Stress Transfer between FRP Reinforcement and Concrete

by

Jianru Yu

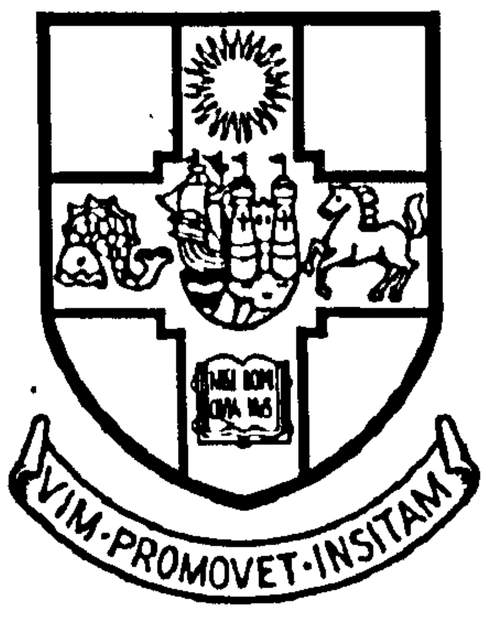

A dissertation submitted to the University of Bristol in accordance with the requirements of the degree of Doctor of Philosophy in the Faculty of Engineering, Department of Civil Engineering

July 2007

To my parents
Xianghe and Jumei

Abstract

This thesis investigates gaps in the current understanding of some key aspects of Fibre Reinforced Polymer (FRP) strengthened reinforced concrete (RC) members. There are four important issues have been investigated. Firstly, a novel pullout test was developed to investigate the stress transfer mechanics and failure modes of near surface mounted (NSM) FRP strengthened RC blocks at a fundamental level. Secondly, the finite element analysis (FEA) was used to gain a detailed understanding of stress distribution both along the bond line and through the thickness of the adhesive layer for the RC members strengthened either by NSM or externally bonded plate (EBP) FRP technique. Thirdly, through both experimental and FEA methods, the brittle separation failure modes not only at the ends but also in midspan zones of FRP strengthened RC beams was fatherly studied. Finally, structural behaviour of an adhesively bonded composite bridge structure (being composed of a glass FRP deck and concrete beam adhesively bonded to each other) and the influence of initial cracks in the RC beam were investigated preliminarily.

To investigate the above issues, a combination of laboratory experiments and numerical analyses was used. In the lab experiments, RC specimens with NSM FRP were fabricated with various strengthening ratios and tested to failure. Each specimen consisted of one middle block (somewhat representative of the midspan region near flexural cracks in real FRP-enhanced RC beams) and two side blocks (somewhat representing the FRP curtailment zones in FRP enhanced RC beams). Each specimen was subjected to axial load and the length of the middle block varied between specimens. From the tests, two brittle separation modes were observed: The fractural separation took place either in the concrete layer horizontally due to cracks propagating along the side blocks or at the adhesive-rod interface. The experimental data show that the ultimate load increased with the length of middle block but was hardly influenced by the amount of strengthening Carbon Fibre Reinforced Polymer (CFRP) rods. Beam theory was used to investigate the structural mechanics associated with the horizontal cracks on the middle block. The calculated results are consistent with experimental observation, which gives fundamental insight into the problem.

Then FE analyses were used to verify the experimental results. In modelling the adhesive layer, the 2D 4-noded quadrilateral plane stress element shows better performance than the 4-noded line interface element. By using a few layers of quadrilateral elements across the thickness of adhesive, the variations of adhesive through-thickness stress are clearly demonstrated, especially at certain critical positions, such as the ends of the adhesive layer or the bond near concrete beam cracks, which are the zones of connection stress concentration.

Based on the validity of the FEA programme, parametric FE analyses were done to investigate how the structural responses of the strengthened blocks to the load are influenced by the variation of material properties. It is found that the model stiffness increased with the increment of concrete strength and Young's modulus of FRP, especially at the post-cracking stage and before steel yielding. Inside the concrete block, both the steel and FRP strains decrease with the increment of the concrete strength because concrete with higher tensile strength can carry a larger share of the tensile load so that reinforcing bars could take smaller loads. The variation of adhesive material properties may only affect the distribution of adhesive shear stress rather than load-displacement plots or steel/CFRP strain distributions. Generally, their influences on adhesive shear stress distributions increased with the load and higher shear stress values are found in the models with higher adhesive Young's modulus E_a, tensile strength f_{ta}, and ratio of ultimate strain to crack strain $\varepsilon_u / \varepsilon_{cr}$. It is concluded that FE analyses with suitable elements are good for further investigation.

Acknowledgments

I would like to express my gratitude to my supervisor Dr. Wendel Sebastian, for his invaluable advice and guidance throughout the course of this research. He provided strong references to secure the scholarships for my PhD study, and then provided further funding for the extensive lab work and for the training course in the use of DIANA which formed the core of my analytical work. Dr Sebastian has further provided an unfailing source of encouragement and leadership that has been essential to completion of the study. I am also grateful to Professor David Blockley, to Professor Colin Taylor, to the late Dr. Bill Smith and to Dr. Wendy Daniell for their help and kindness towards me during my study. In addition, I would like to thank the Overseas Research Students Award Scheme (ORSAS) and the University of Bristol for granting me a scholarship.

My thanks are due to all those at the structures lab who spent their time and effort providing a wealth of information, advice and necessary guidance during the project. Special thanks go to Mr Peter Whereat, Mr Dave Hooper, Mr Mark Fitzgerald and Mr Ian Milnes for their help in fabrication and testing of the large-scale concrete specimens. I would also like to offer my sincere thanks to the computer technicians Messrs Duncan Clay and Chris Hawkins, for their help to set up the computer and address problems as they arose. I gratefully acknowledge the help from the DIANA training course in Wilde FEA Limited, in particular from Dr Andrew Mar and Dr. Justin Morris.

I am grateful for help rendered during the experimental work by my colleagues Chao Zhang and Giorgi Gegeshidze. Further gratitude is due to my colleagues and friends for their friendship and encouragement through my time at Bristol in particular: Dr. Dongkeun Kim, Dr. Wijiaya Salim, Dr. Shivendren Anandakrishnan, Dr. Matthew Dietz, Dr, Luiza Dihoru, Riccardo Sabatino, Dr. Xiaoxia Ni, Dr. Junhui Li, Yanli Tan, and Jie Gu.

Finally, I will always have special gratitude and love to my parents and my bother for their moral support and tolerance.

Declaration

The accompanying dissertation is submitted for the Degree of Doctor of Philosophy in the Faculty of Engineering at the University of Bristol. The work was carried out in the Department of Civil Engineering, University of Bristol, under the supervision of Dr. W. M. Sebastian.

I declare that the work in this dissertation was carried out in accordance with the Regulations of the University of Bristol. The work is original, except where indicated by special reference in the text, and no part of the dissertation has been submitted for any other degree. Any views expressed in the dissertation are those of the author.

The dissertation has not been presented to any other University for examination either in the United Kingdom or overseas.

Jianru Yu

Signed: Date: July 2007

Table of Contents

List of Tables

List of Figures

Notation

A_f	Cross sectional area of the bottom flange of the GFRP deck
D	Diameter of a single circular bar
E_a	Young's modulus of adhesive
E_c	Young's modulus of concrete
E_f	Young's modulus of NSM strengthening rod
E_p	Young's modulus of strengthening plate
E_s	Young's modulus of steel
F_{Gu}	Upper section force of GFRP deck
F_{Gl}	Lower section force of GFRP deck
F_{ad}	Force of adhesive layer
F_c	Tensile force of concrete on the side of block
F_{cc}	Compressive force of concrete beam
F_{ct}	Tensile force of concrete beam
F_p	Loading force
F_{su}	Upper section force of steel reinforcement
F_{sl}	Lower section force of steel reinforcement
G_a	Shear modulus of adhesive
G_f	Fracture energy
I_y	Initial moment
I_{yi}	Initial moment of component
M	Moment of cantilever
P	Loading force
R_f	FRP rod radius
S_y	static moment
S_{yi}	static moment of component

V	Shear force
b	Cross-sectional width of the adhesive layer
dx	Distance between the two locations along the rod
e	Eccentricity of CFRP force from root of covercrete cantilever
f_{ta}	Tensile strength of adhesive
f_{tc}	Tensile strength of concrete
f_{cc}	Copressive strength of concrete
h	Estimated numerical crack bandwidth
k_h	Stiffness of the horizontal spring elements
k_v	Stiffness of the vertical spring elements
l	Length of a single GFRP beam
n	The times of stiffness of vertical spring elements to the bottom flanges
$s(x)$	Slip along x axis
t_a	Thickness of adhesive layer
t_p	Thickness of plate (assumed constant, as is commonly the case)
w	Width of GFRP deck
x	Coordinate along the bond length
Δx	Distance between the two locations along the plate
$\Delta\varepsilon$	Difference in mid-plane axial strain of the plate between the two locations
ε	Axial strain of the bar
ε_1	Strain at position 1
ε_2	Strain at position 2
ε_{cr}	Crack strain of concrete
ε_f	Axial strain of CFRP rod
ε_u	Ultimate tensile strain of concrete
$\varepsilon(x)$	Strain along x axis

τ	Shear stress
τ_{avg}	Average shear bond stress between the two locations
$\tau(x)$	Shear stress along x axis
ν_a	Possion's ratio of adhesive
ν_c	Possion's ratio of concrete
ν_f	Possion's ratio of FRP
ν_s	Possion's ratio of steel

Abbrevation

AC	Adhesive-concrete
CFRP	Carbon fibre reinforced polymer
EBP	External bonded plate
EBR	External bonded reinforcing
ERSG	Electrical Resistance Strain Gauge
GFRP	Glass fibre reinforced polymer
FCB	Flexural cracked beam
FE	Finite element
FEA	Finite element analysis
FEM	Finite element model
FRP	Fibre reinforced polymer
ICB	Inclined cracked beam
IEM	Interface Element Model
NSM	Near surface mounted
PA	Plate-adhesive
PEM	Plane stress Element Model
RC	Reinforced concrete

Chapter 1

Introduction

1.1 Scope of thesis

This thesis is concerned with the structural action up to failure of reinforced concrete (RC) members strengthened with fibre reinforced polymer (FRP) either as externally bonded reinforcing (EBR) strips or as near surface mounted (NSM) bars.

The use of FRPs for strengthening existing civil engineering structures has been recognized as a promising technique with many potential advantages including low weight, easy installation, high durability and tensile strength, large deformation capacity, electromagnetic permeability and practically unlimited availability in FRP sizes, geometries and dimensions (Barros & Fortes (2005)). The types of FRPs available for strengthening are carbon, glass and aramid in the shapes of plates, sheets, rods and strips. Their basic applications to existing RC structures can be grouped into axial, shear and flexural strengthening. Two most commonly used FRP strengthening methods, which either use EBR strips or NSM bars, form the focus of this thesis.

Figure 1-1 shows one application of the FRP NSM technique to a floor slab at the Naval Station San Diego. The importance of NSM strengthening has been recognized

in civil engineering in recent years, but published research in the literature on its mechanical behaviours and failure modes is limited. For example, a survey of the literature reveals that the potential exists for modification of the fundamental rod embedded in concrete block (pullout) test needed to gain a better understanding of bond performance at both the end and midspan zones of NSM strengthened members.

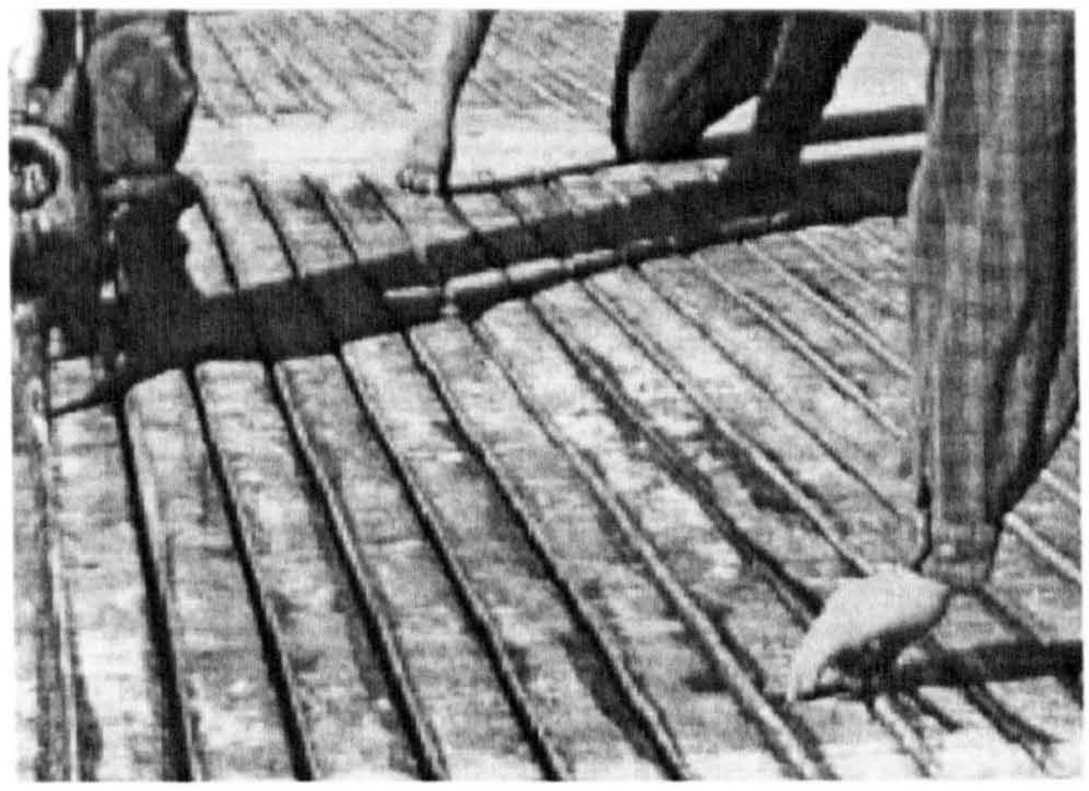

Figure 1-1 CFRP NSM strengthening for Pier 12 at the Naval Station San Diego (USA) (Warren (1998))

Another focus of this thesis refers to the application of bonded plates to the tension faces of structural members (Figure 1-2). For externally strengthened RC structures, there is a critical failure mode called brittle separation failure, which is very rarely found in conventional RC structures. This brittle separation failure is characterized by fracture of the FRP-concrete connection and consequent separation of the FRP plates from the bonded concrete member. Although the brittle separation failure modes of FRP plated members have been commonly reported and investigated in previous research programmes, there is still an urgent need for gaining a detailed understanding of the mechanics of some less studied but critical failure modes such as the midspan debonding mode. Furthermore, virtually no work has been done to date to establish the influence of initial imperfections such as flexural and inclined cracks of concrete beams on these brittle failure modes. The complex stress states which develop within

the plate-to-beam connection of such cracked beams can be described in theoretical analysis only with great effort, but can be studied with ease and care by reliable finite element (FE) analyses. However, the choice of a suitable element to model the behaviour of the connections is crucially important to the success of FE analyses. This is an area of research which needs focussed attention.

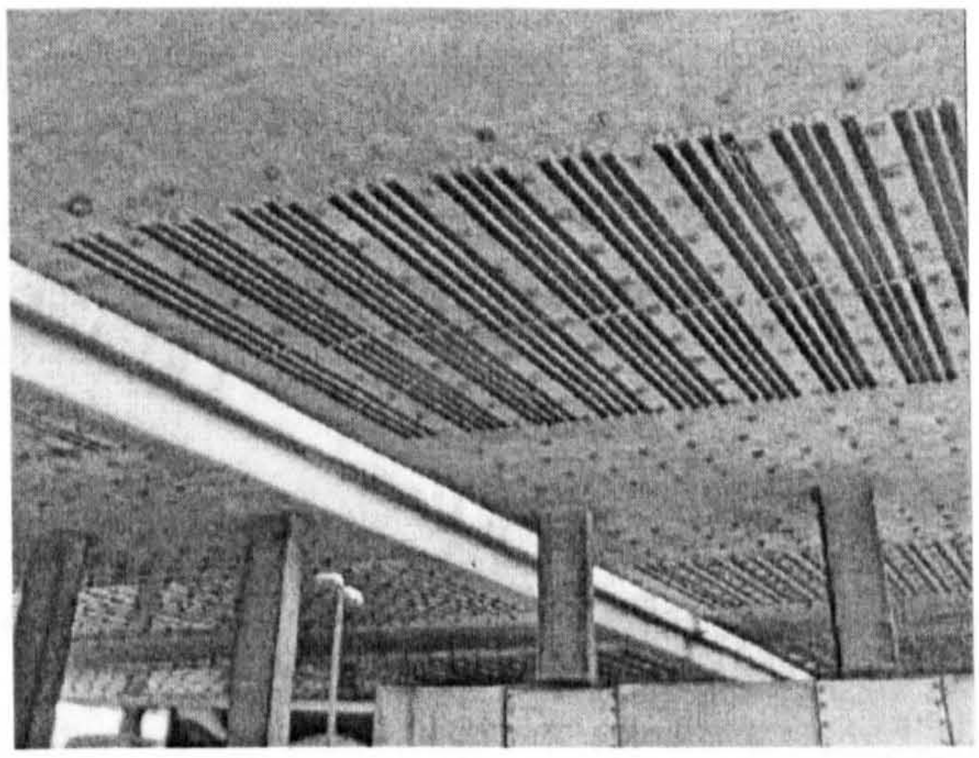

Figure 1-2 CFRP plate bonding of M60 Barnes Bridges at Cheadel in Greater Manchester (Keble et al (2001))

Consistent with these gaps in the existing knowledge, in this thesis, the stress transfer between FRP and concrete both in FRP NSM and plated strengthened members, which directly reflects the mechanical behaviours of structures and finally induces the bond failures, is to be studied carefully.

In the remainder of this chapter, the background to the current study is introduced, then a brief explanation of the issues on stress transfer of FRP strengthened structures is presented, after which the objectives of this PhD thesis are described. Finally, the structure of the thesis is outlined.

1.2 Background

In recent years, there has been a globally increasing number of RC structures which urgently require remedial action for a variety of reasons including: structural deterioration due to internal reinforcement corrosion or freeze-thaw action, increments of load beyond those for which the structures were originally designed, errors at the time of construction due to faulty workmanship or design, or changes of use. Accidental damage due to vehicle impact, fire and earthquakes also generate requirements for enhancement of existing RC structures. In those cases, the structures are no longer considered satisfactory in terms of load carrying capacity for these reasons and/or the changes in the loading specifications of design codes. In order to keep buildings operational, such structures must be upgraded or rebuilt so that they could meet the same requirements demanded of structures built today and in the future.

The choice between upgrading and rebuilding is based on factors specific to each individual case, but certain issues are considered in every case. These are the periods of time during which the structure will be out of service or providing a reduced service, relative costs of upgrading and rebuilding in terms of labour, materials and plant and disruption of other facilities. It is becoming both environmentally and economically preferable to upgrade structures rather than rebuild them, particularly if rapid, effective and simple strengthening methods are available. Therefore, the urgent need to upgrade under-reinforced structures places considerable importance on strengthening techniques.

Externally bonded steel plates were originally employed in the strengthening of RC structures. However, disadvantages in the use of steel materials include transporting,

handling and installing heavy plates, corrosion of steel, limited delivery lengths, difficulty of forming joints, the need for massive and expensive falsework to hold plates in position during adhesive cure and the need to prepare the steel surface for bonding, which is labour intensive and time consuming. The use of polymer composite materials overcomes these problems and provides equally satisfactory solutions. FRP materials possess the qualities of high strength-to-weight ratio and corrosion resistance, resulting in low maintenance costs. FRP materials have mechanical and physical properties superior to those of steel, particularly with respect to tensile and fatigue strengths and these qualities are observed under a wide range of temperatures.

The prime fibres used as reinforcement are glass, carbon and aramid (Rostasy et al. (1992)). The main disadvantages in using these materials are high material cost and possible brittle failure modes due to no yield behaviour. Carbon fibre reinforced polymer (CFRP) materials are much more expensive than mild steel but material cost usually constitutes approximately 20% of the total cost of a strengthening project (Meier & Kaiser (1991)), the remaining 80% being labour costs. The easy handling of FRP plates reduces labour costs considerably. The problem of having to join limited lengths of steel plate is overcome by the fact that FRP plates may be delivered to site in rolls of 300 m or more (Meier (1994)).

1.3 Stress transfer on FRP strengthened RC structures

With the wide applications of the FRP strengthening technique, it is very important to develop a comprehensive understanding of the structural response to loads and corresponding failure modes of such applications so that reliable guidance could be given on the design and practical implementation of FRP strengthening schemes.

Although many investigations have been done to make contributions, there is still a considerable scope to make more effort to enhance such guidance.

Among the strengthening techniques based on FRP composites, the use of NSM FRP is emerging as a promising technology for increasing the strength and durability of deficient concrete, masonry and timber members. The literature currently available on this technique is relatively limited. Beside field applications and experimental field projects, laboratory projects on NSM FRP for structural strengthening of concrete members have been carried out as discussed in Chapter 2.

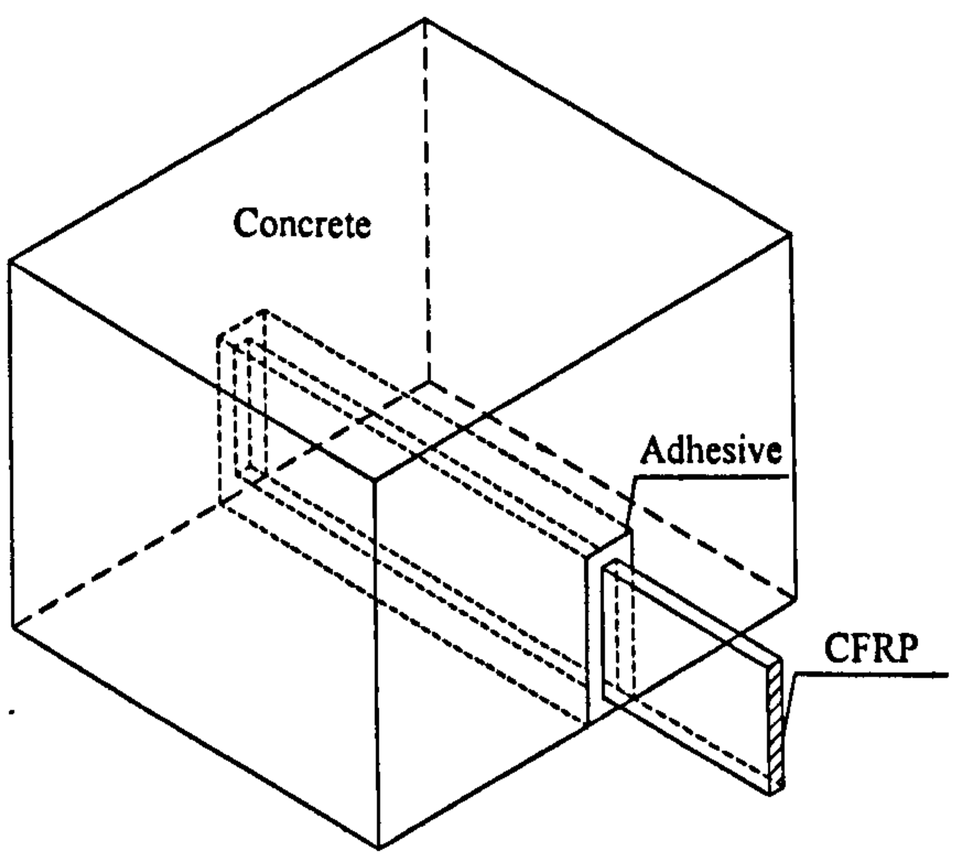

Figure 1-3 NSM technique

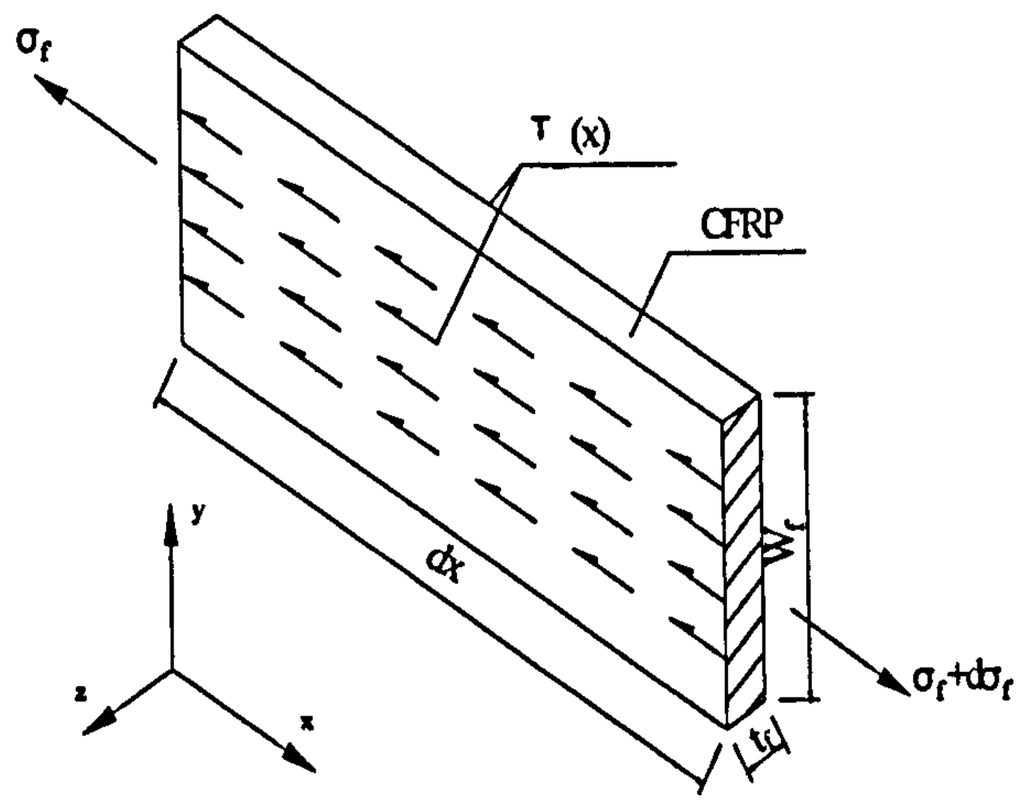

Figure 1-4 Equilibrium of the CFRP

In order for this technique to perform effectively, bond between the NSM reinforcement and surrounding material is a critical issue (Figure 1-3 to Figure 1-5). The aim of this PhD study is to investigate the mechanics of bond between NSM FRP bars and concrete, and to analyse the influence of a few critical parameters on the bond performance and failure modes. Building on previous investigations, an enhanced specimen has been designed in this PhD study in order to obtain a test procedure that is capable of illustrating the bond performance not only in bond curtailments zones but also in the mid-span zones of the beam as well as near the

critical zones such as cracks. Among the investigated variables are FRP reinforcement ratio (area of FRP rods divided by concrete section area), bonded length and groove size. Results of the project are presented and discussed and compared with results from FEA.

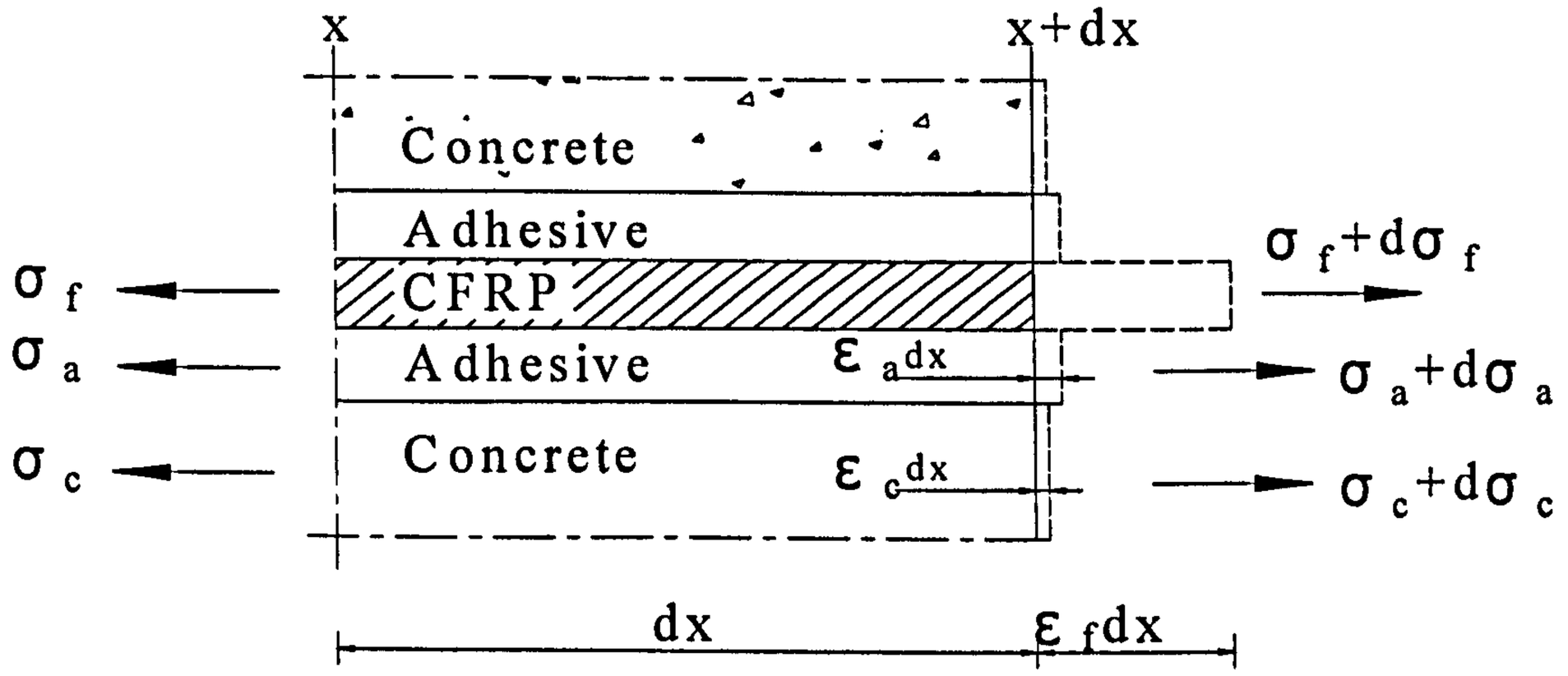

Figure 1-5 Strain of the individual materials of the bond region (bottom view)

Composite plate bonding is now recognized as an appropriate strengthening method. In particular, beam strengthening using bonded composite plates has been studied widely in recent years. According to previous research programmes, brittle separation failure, which results in complete loss of connection between the FRP plate and concrete, is very common in FRP plated concrete members, and can give dramatic reduction in load-carrying capacity.

Figure 1-6 shows an exploded view of the three-layer plate-adhesive-concrete connection with these bond stresses clearly identified. High bond stresses eventually trigger failure of one of these layers. When this occurs, the plate-to-beam connection is lost and the plate separates from the beam. Of the materials in the three connecting layers, the covercrete (concrete layer forming cover to the reinforcement) usually possesses the lowest strength, so debonding commonly occurs through delamination

of the covercrete layer. Concrete is a brittle material, so any mode of debonding can propagate rapidly, with little advance warning.

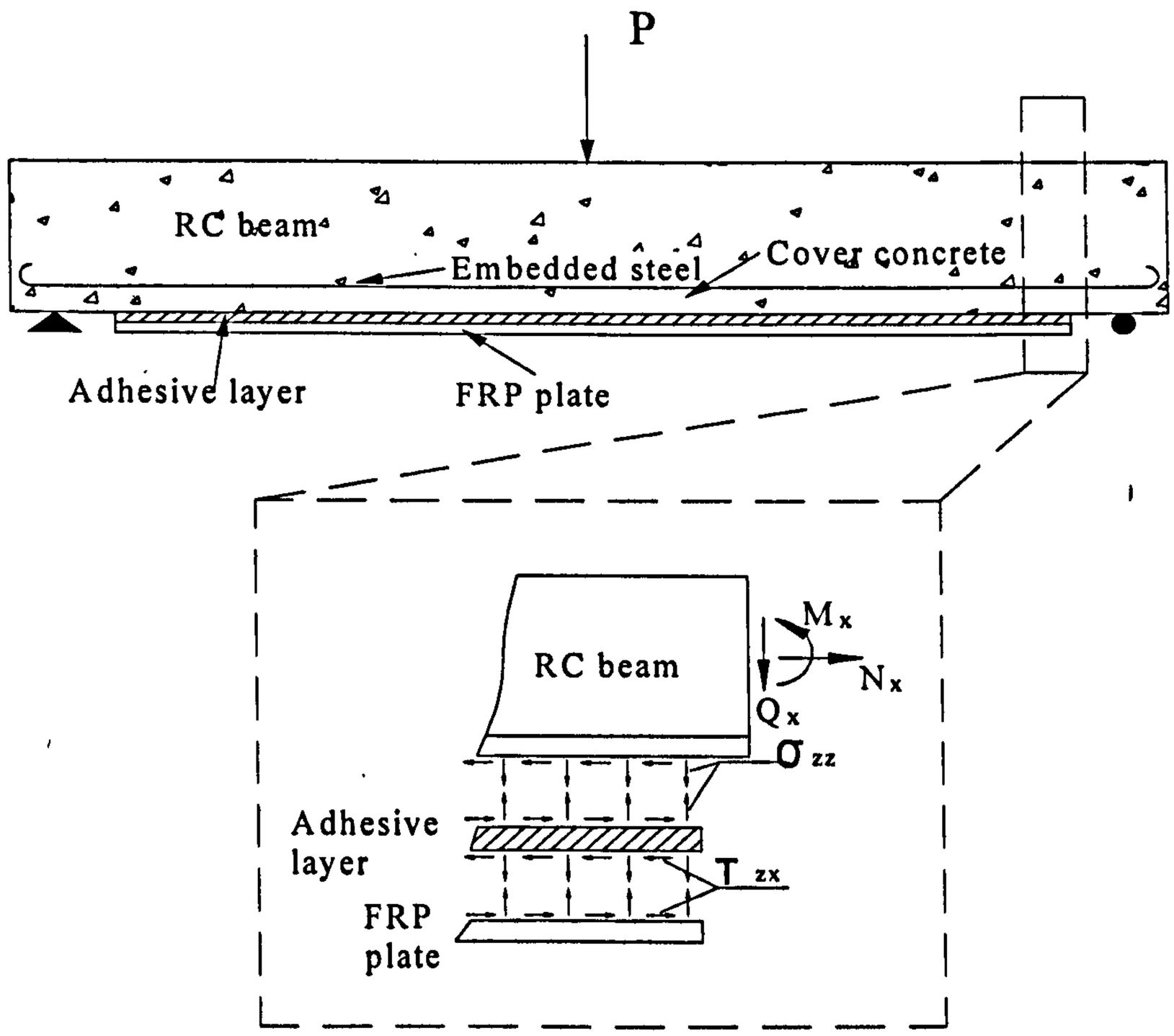

Figure 1-6 Plate bonding technique

Most research effort to date on brittle failure modes of FRP plated beams has focused almost singularly on the End Peel Mode, which initiates at the ends of the plates and progresses inwards along the beam. However, other brittle failure modes (e.g. the midspan debond mode) have been observed recently and are regarded as critical. Therefore, there is an urgent need for research into these topics. This PhD thesis reports the results of one such research programme.

FRP composite bridge decks are a relatively new application of FRPs. The main differences between it and conventional FRP applications include: a) the FRP decks are primarily in compression while the FPR plate or bars are normally in tension; b) FRP decks are individual units which are bonded to each other which may cause

uneven stress transfer while plates are more likely to have continuous stress transfer. In this thesis, a composite bridge specimen comprising a triangular profile GFRP deck adhesively bonded to a RC main beam underneath is presented and its structural response to loading is investigated. This study will give a fundamental insight into the stress transfer at the adhesive bond line between GFRP deck and RC concrete.

Little literature has focussed on the likely influence of initial cracks on the failure behaviour of plated concrete members. An understanding of the influence of such cracks is of interest and has been investigated in this study.

1.4 Aims of the research

The overall aim of this research is to gain a better understanding of stress transfer behaviour between FRP and concrete and the resulting failure modes in the FRP strengthened RC members.

The fundamental research topics under investigation in this thesis are:

- Developing a pullout test to investigate the stress transfer between FRP bars and anchoring material at a fundamental level, which reflects conditions not only in end zones but also mid-span zones of NSM FRP strengthened RC beams.
- Establishing the validity of FEA models by choosing suitable elements to simulate the adhesive bond.
- Developing a comprehensive understanding of the mechanics of the stress distribution both along the bond line and through the thickness of the adhesive layer.
- Gaining an enhanced understanding of the mechanics of the brittle separation failure modes, especially for the mid-span debonding mode that was less investigated in previous studies.

- Investigating the effects of initial flexural and shear cracks on the structural responses of FRP strengthened RC members.

1.5 Layout of the thesis

This thesis is constructed in 7 chapters including the present introductory chapter. The contents of the remaining chapters are given below.

Chapter 2 reviews research work to date on experimental studies and FE analyses of FRP strengthened concrete members. In particular, two commonly used strengthening methods, namely the near surface mounted (NSM) and externally bonded reinforcing (EBR) techniques, as identified in the previous studies, are described and discussed. Most significantly, the lack of research into bond behaviour and failure modes associated with the NSM technique and the lack of understanding of the critical midspan debonding failure mode for FRP plated members are highlighted. Then, the need for a reliable finite element analysis to study the topics mentioned above in detail, is emphasized.

Chapter 3 presents the verification study of the FEA package used in the present PhD study. The elements and associated material models used in the study are described. Three examples are presented of strengthened RC members and associated FE meshes. Then the FEA results are compared with experimental and theoretical data previously published. A suitable choice of elements is discussed for studying both thru-thickness and axial variations of adhesive bond stress.

Chapter 4 is devoted to experimental work performed in this PhD study on a specialised pullout test developed for the NSM technique. The design of the experiments, fabrication of the specimens, and instrumentation, are described. In

particular, the modified set-up of the NSM strengthened block to investigate both midspan debonding and end peel is highlighted. Important observations and data from the tests are presented and discussed in terms of their significance in acquiring an understanding of the midspan debonding mechanics of NSM strengthened RC members.

Chapter 5 focuses on FEA verification of the obtained experimental data, to try and give further physical insight into the mechanics of bond behaviour associated with failure modes of the NSM strengthening technique. Parametric analyses by the FE method to investigate the influences of various material properties on structural responses of the NSM FRP strengthened specimens are also highlighted in this chapter.

Chapter 6 describes further FEA work on FRP strengthened members. In particular, the FEA method is used to predict complex stress transfer mechanics in a composite bridge specimen composed of a top Glass FRP deck and a bottom RC beam, both with and without initial cracks. The stress transfer mechanics and failure modes in FRP plated beams with initial flexural or shear cracks are also analysed and presented by the FEA method, which cannot be caught and easily expressed in current available algebraic research. The localised effects of cracks on the structural behaviours are also investigated.

Chapter 7 summarises the work done and the main results from this research programme. Conclusions are drawn and suggestions for continuation of the work are presented.

Chapter 2

Literature review

2.1 Introduction

This chapter reviews both experimental and finite element (FE) research to date into reinforced concrete (RC) structures externally strengthened by fibre reinforced polymers (FRPs). In the following section, a brief overview is given of the status quo on research into the applications of FRPs for strengthening of existing structures. Studies on various strengthening types and adhesive bond techniques are summarised. In particular, previous research on the near surface mounted (NSM) technique, externally bonded reinforcing (EBR) method and FRP composite bridge decks are reviewed in detail. The discussion focuses on both the experimental and FEA research into stress transfer between FRP and concrete. Finally, conclusions are drawn from the discussions of this chapter.

The review aims to demonstrate that although much of the research to date has focussed on the general failure behaviour of FRP-bonded RC members and on the stress transfer between FRP and concrete, there are still some very important outstanding issues specific to the adhesive stress distribution and mechanics of the

brittle separation failure modes on which significant further light must be shed. In particular, this chapter highlights the important need for further work in the following areas:

- Development of a pull-out test to investigate the stress transfer on FRP bar to anchoring material at a fundamental level, which reflects conditions **both** in midspan zones and end zones of NSM FRP strengthened RC beams.
- Establishing the best choice of elements to simulate the adhesive connection.
- Development of an enhanced understanding of the mechanics of stress distribution both along the bond line and through the thickness of the adhesive layer.
- Gaining an enhanced understanding of the mechanics of the brittle separation failure modes, especially for the mid-span debonding mode which was less investigated.
- Achieving a fundamental understanding of structural behaviour of FRP composite bridge system in which FRPs are under compression rather than tension compared to those in conventional FRP strengthened structures.

2.2 Application of FRPs in Structural Engineering

2.2.1 Advantages and general application of FRP

A fibre-reinforced polymer is a composite material comprising a polymer matrix reinforced with fibres. The fibres are usually glass, carbon, or aramid, while the polymer is usually an epoxy, vinylester or polyester thermosetting plastic. FRPs are commonly used in the aerospace, automotive, marine, and construction industries.

Some of the favourable characteristics of FRP materials are high stiffness and a high strength to self weight ratio, excellent fatigue and corrosion resistance, reduced installation time and maintenance costs, as well as superior resistance to environmental degradation compared to traditional building materials.

The superior characteristics of FRP make it attractive for use in new construction or retrofit of existing ones. Among the more common uses of FRPs on existing RC structures are their applications to flexural and shear strengthening of RC beams in bridges and buildings. For flexural strengthening (Figure 2-1), previous research reported narrower and more evenly distributed flexural cracks, higher member stiffness and significantly improved load capacity. For example, in experiments conducted within Meier's research group (Meier & Kaiser (1991), Meier (1992), Meier et al (1992)) in Switzerland, 2 m span RC beams bonded with 0.3 mm thick FRP plates exhibited 100% increase in ultimate capacity and 50% reduction of deflection, both over the un-strengthened RC member.

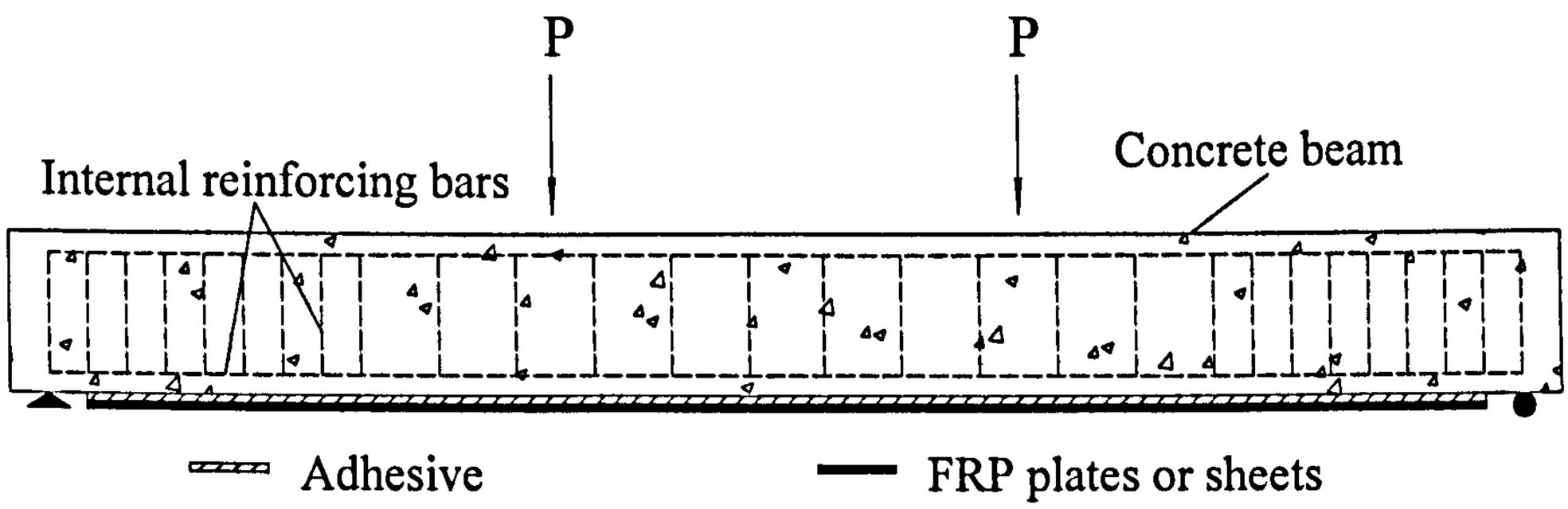

Figure 2-1 FRP flexural reinforcement of beams

As can be seen in Figure 2-2, shear strengthening of beams can be achieved by bonding FRP fabric around the sections of the concrete members with various arrangements of FRP fabric including diagonal fabric (Salles Neto et al (2001)), vertical fabric continuous along the entire length of the beam (Grace et al (1999) and Oehlers (2001)), or vertical fabric laid in strips intermittently along the member (Mukhopadhyaya et al (1998), Triantafillou (1998), and Tann et al (2001)). Furthermore, the axial strengthening of beams in the critical compression concrete zone can be achieved by confinement within fabric, or by bonding FRP plate and / or fabric to the maximum moment region.

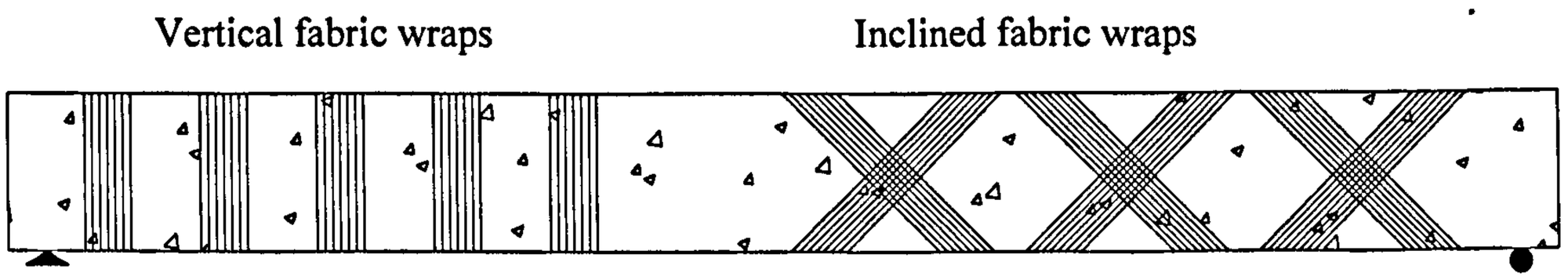

Figure 2-2 FRP shear reinforcement of beams

Other main applications of FRPs on existing RC structures include the strengthening of columns and slabs. A popular strengthening technique for concrete columns is wrapping a few layers of FRP fabric around the column. In that case, the tendency of the concrete column to expand radially under axial compression is resisted by the FRP fabric. The column flexural capacity is also enhanced in this way. Several bridge columns have been strengthened with CFRP fabric in Japan and the USA to improve seismic resistance, while in the UK RC columns in several car parks have been strengthened with FRP materials (The Concrete Society Report TR55 (2000)).

For slabs, flexural strengthening is applicable with FRPs. Besides, it has been suggested that shear strengthening of slabs may be possible via vertical through steel or FRP rods anchored at the top and base of the member (Buyukozturk et al (1999)).

Research into the structural uses of FRPs confirms that the materials also can be successfully employed in new-build applications, including dual role in both permanent formwork and external permanent reinforcement in concrete structures (Canning et al (1999)), the use of FRP rods as embedded reinforcement in RC structures (Cosenza et al (1997) and Grace et al (1998)), the use of FRP tendons for prestressing purposes in both pre-tensioned (Lees & Burgoyne (1999)) and post-tensioned (Meier (2000) and Choi et al (2001)) concrete structures, and the use of concrete-filled FRP tubes or shells as composite columns (Saafi et al (1999)). In addition, Sebastian (1996) has investigated the use of a Glass Reinforced Plastic (GRP)

enclosure as a load-bearing component within the Composite Space Truss Bridge (CSTB) form.

2.2.2 Near surface mounted (NSM) technique

2.2.2.1 Description

In recent years, among the strengthening techniques based on FRP composites, the use of NSM FRP bars is emerging as a promising technology for increasing flexural and shear strength of deficient concrete, masonry and timber members.

The term 'near' is used to distinguish this technique of structural strengthening from that using externally bonded FRP composites. The NSM strengthening technique is based on the use of FRP bars as shear or flexural reinforcement. Embedment is achieved by cutting a groove into the surface of the member to be strengthened along the desired direction and to the desired depth and width. The groove is filled halfway with epoxy or cementitious paste. Then the FRP bars of circular, square or rectangular cross sections are placed in the groove and lightly pressed, forcing the paste to flow around the bar and fill completely the space between the bar and the sides of the groove. The groove is then filled with more paste and the surface is levelled.

The NSM FRP reinforcement may be round, square, rectangular or oval bars, as well as strips (Figure 2-3 and Figure 2-4). For brevity, the term "bars" is used herein as a generic term encompassing all cross section shapes, while the term "strips" is reserved for thin narrow strips. Different cross section shapes have different advantages, and offer different choices for practical applications. For example, square bars maximize the bar sectional area for a given size of square groove while round bars are more readily available and can be more easily anchored in pre-stressing operations. Narrow

strips maximize the surface area-to-sectional area ratio for a given volume and thus minimize the risk of debonding, but require a thicker cover for a given cross-sectional area.

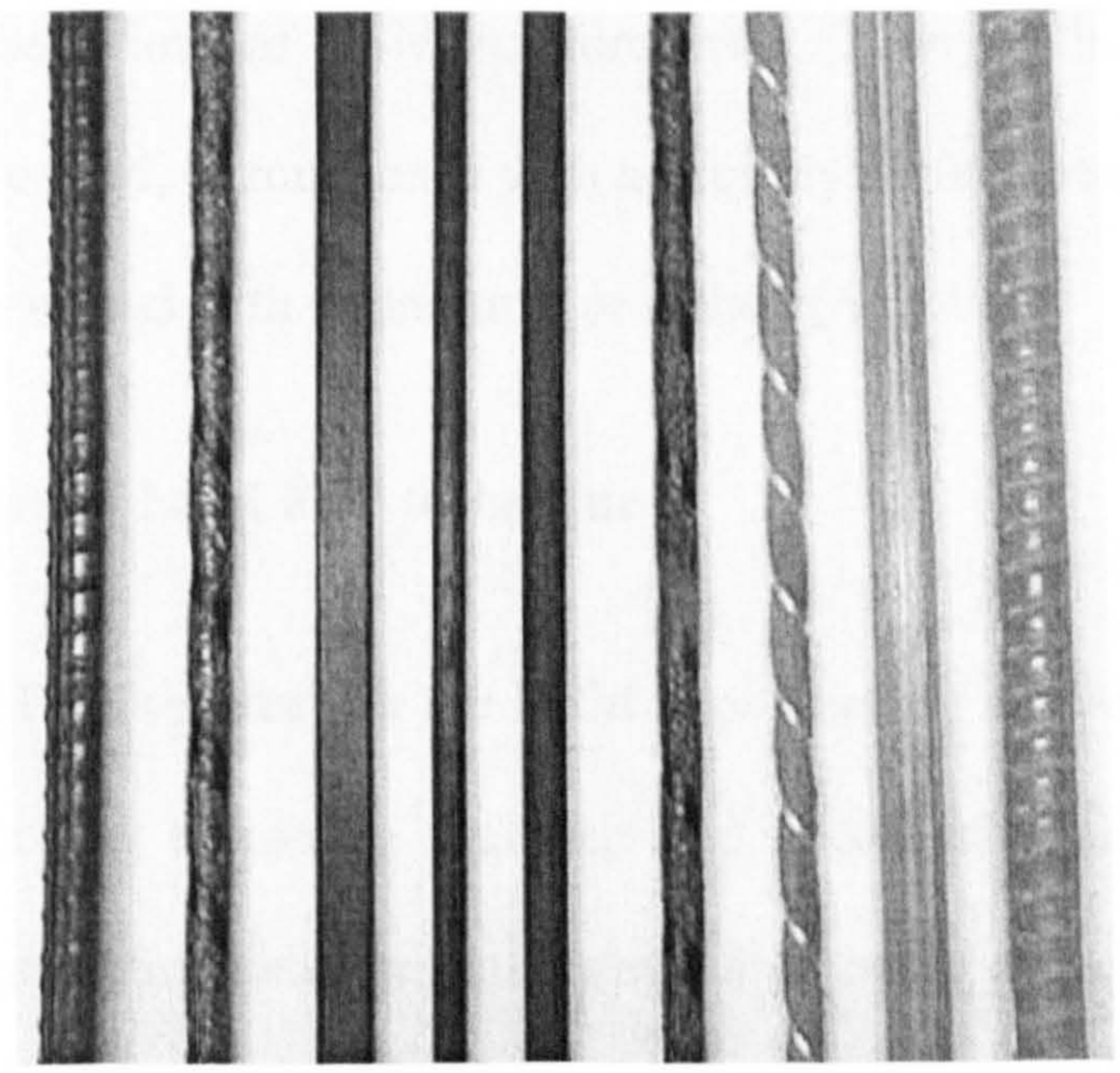

Figure 2-3 Types of FRP bars for NSM applications (De Lorenzis & Teng (2007)).

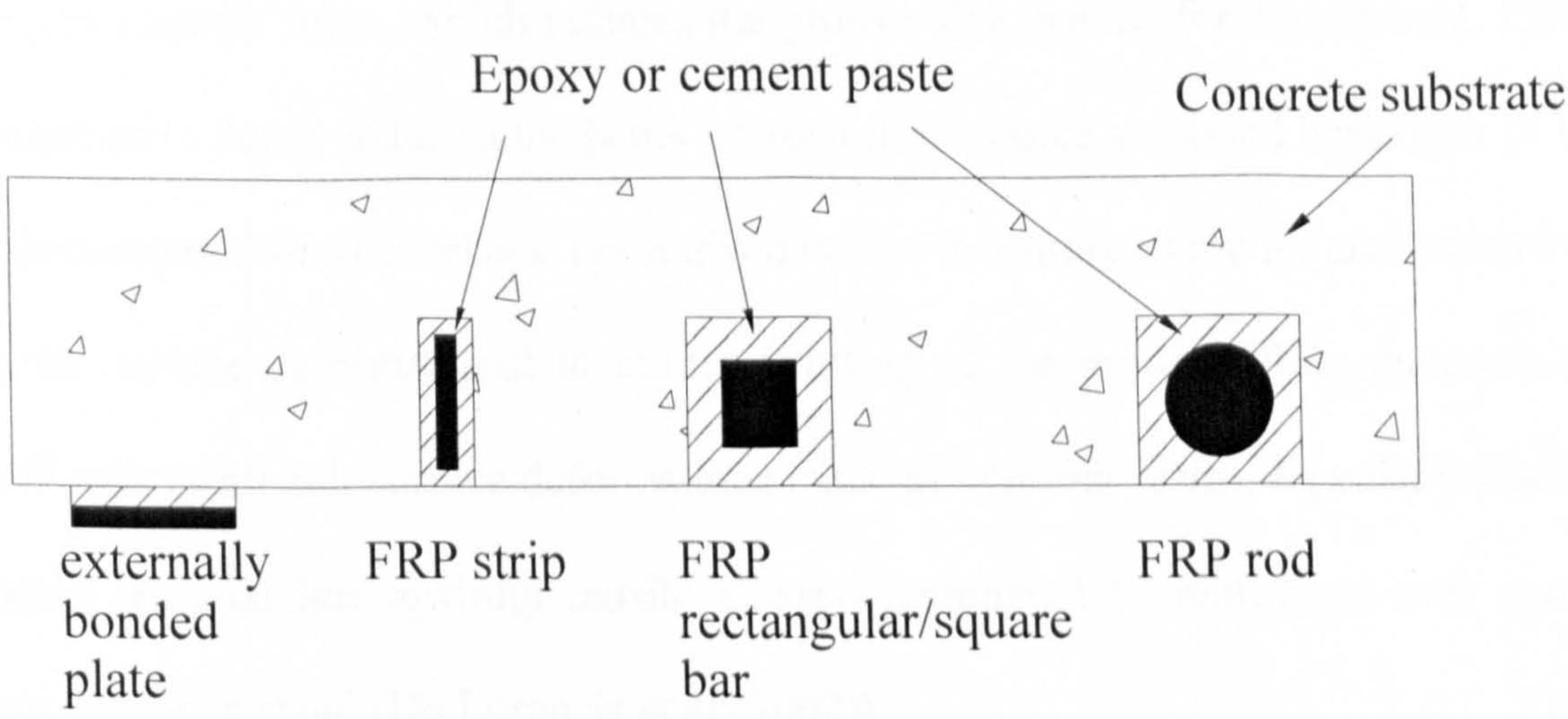

Figure 2-4 Cross section comparing different NSM systems with externally bonded plate

El-Hacha & Rizkalla (2004) has compared equivalent amounts of NSM reinforcement provided as round bars or strips. As expected, strips performed better and failed by tensile rupture rather than debonding like the round bars, due to the higher local bond strength and larger lateral surface to cross-sectional area ratio of NSM strips. In practical applications, the choice depends strongly on the constraints of a specific

situation, such as the depth of the cover, and the availability and cost of a particular type of FRP bar.

FRP bars are also manufactured with a variety of surface textures, which strongly affect their bond behaviour as NSM reinforcement. Their surface can be smooth, sand-blasted, sand-coated, or roughened with a peel-ply surface treatment. Round bars can also be spirally wound with a fiber tow, or ribbed (ACI 440).

2.2.2.2 Advantages of NSM FRP technique

The advantages of FRP vs. steel for the NSM strengthening application are primarily the better resistance to corrosion, the ease and speed of application due to the lightweight properties, and the optimization of the grooving process. Due to the high tensile strength of the FRP, rods with smaller diameters can be used for a given required tensile force, which reduces the groove size needed for embedment. Further reduction in depth is due to the better corrosion resistance and bond behaviour of FRP rods compared to steel rebars. For a given cover, it is more likely for steel rebar (with stiffer surface deformations) to induce splitting of the groove-filling materials than FRP rods (with soft surface deformations made of polymer resin), especially when the filling material has medium tensile strength compared to reinforced rods and the groove size is small (De Lorenzis et al (2002)).

In certain cases, the NSM strengthening technique can be more convenient than using externally bonded reinforcing (EBR) methods due to better reinforcement anchoring systems and resistance to external corrosion as well as the minimal surface preparation work and installation time necessary (Nanni et al. (1999)).

Firstly, for the EBR technique, the research carried out up to now has revealed that this technique cannot mobilize the full tensile strength of the FRP materials, due to their premature debonding (Spadea et al (1998)). To improve the efficiency of the EBR technique, some anchorage systems have been proposed (Khalifa et al (1999)). NSM strengthening technique makes it possible to anchor the FRP reinforcing rods/strips into RC members so that reliable anchorage could be achieved.

Another advantage of NSM embedment is that it significantly reduces the probability of harm resulting from fire, acts of vandalism, mechanical damage, and aging effects. While in the EBR technique, the reinforcing performance of these composites can be negatively affected and decreases significantly when submitted to high and low temperatures (Tommaso et al (2001)).

In particular, the NSM technique becomes attractive for strengthening in the negative moment regions of slabs and decks, where external reinforcement would be subjected to mechanical and environmental damage and would require protective cover which could interfere with the presence of floor finishes.

Furthermore, NSM technique requires minimal surface preparation work (other than grooving) and implies minimal installation time compared to the externally bonded technique. The use of customized grooving tools can allow technicians to cut the appropriate grooves in one pass, whereas the choice of high viscosity epoxies as groove-filling material allows for ease of gunning the material into the grooves.

2.2.2.3 Previous applications of NSM FRP technique

Although the use of FRP rods for this application is very recent, NSM steel bars have been used in Europe for strengthening of RC structures since the early 1950's. The

earliest reference that could be found in the literature dates back to 1949 (Asplund (1949)), an RC bridge in Sweden which experienced excessive settlement during construction, so that the moment capacity needed to be increased. This was accomplished by grooving the surface, filling the grooves with cement mortar and embedding steel rebars in them.

Gentile and Rizkalla (1999) conducted a comprehensive experimental program to investigate the feasibility of using NSM GFRP bars for flexural strengthening of timber bridge stringers. Based on test results, the Tourond Creek bridge constructed 39 years ago in Manitoba, Canada, was strengthened using GFRP bars. The bars were inserted longitudinally into specially constructed grooves in the stringers and adhered to the wood beams with an epoxy resin. Using this technology, the bridge is capable now of carrying the current design loads for less than 15% of the cost estimated to replace the bridge.

Figure 2-5 shows a few applications of NSM technique on deficient structures. Hogue et al. (1999) carried out a strengthening project to upgrade the structural floor of Myriad Convention Centre (Oklahoma City, USA) in 1997-1998. A combination of externally bonded steel plates, CFRP sheets and NSM CFRP rods was adopted. NSM rods were used for shear strengthening in this case. Figure 2-5(a) shows that vertical grooves were saw-cut along the side surfaces of the joist and the CFRP rods were inserted.

Figure 2-5(b) shows that Pier 12 at the Naval Station San Diego (USA) was strengthened in November 1998 (Warren (1998)). NSM CFRP rods were placed in sequence into the epoxy-filled slots to increase the capacity of the deck slab in the

negative moment regions. Strain gauges were attached to the CFRP rods in order to monitor the performance of the strengthening system, which proved to be satisfactory.

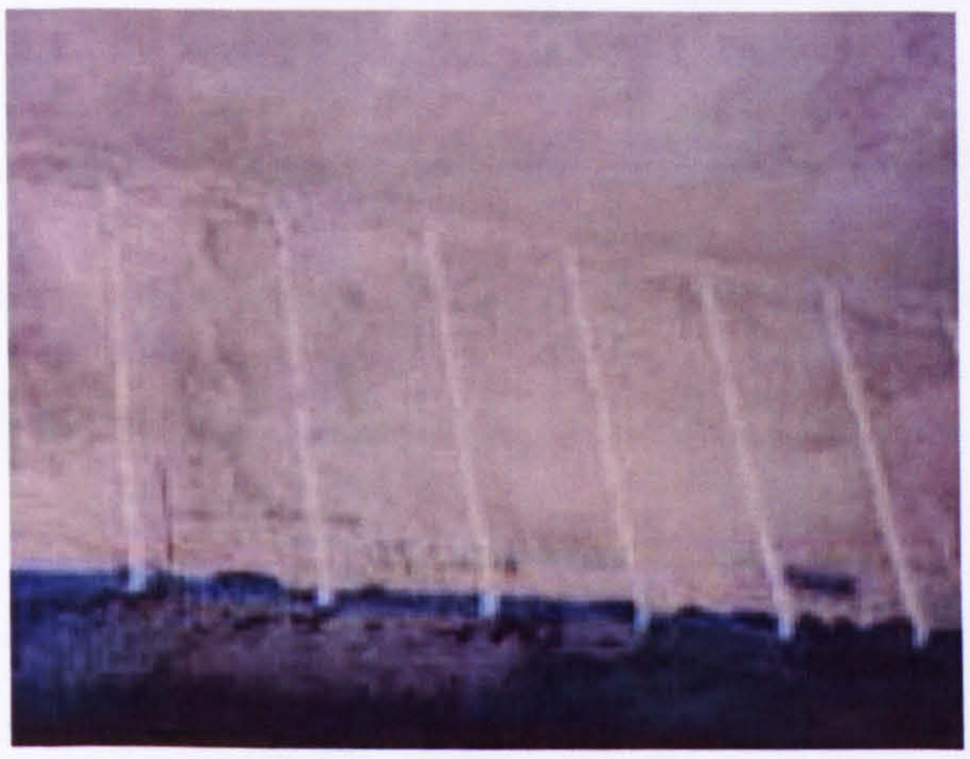

(a) Upgrading floor of Myriad Convention Centre (Hogue et al. (1999))

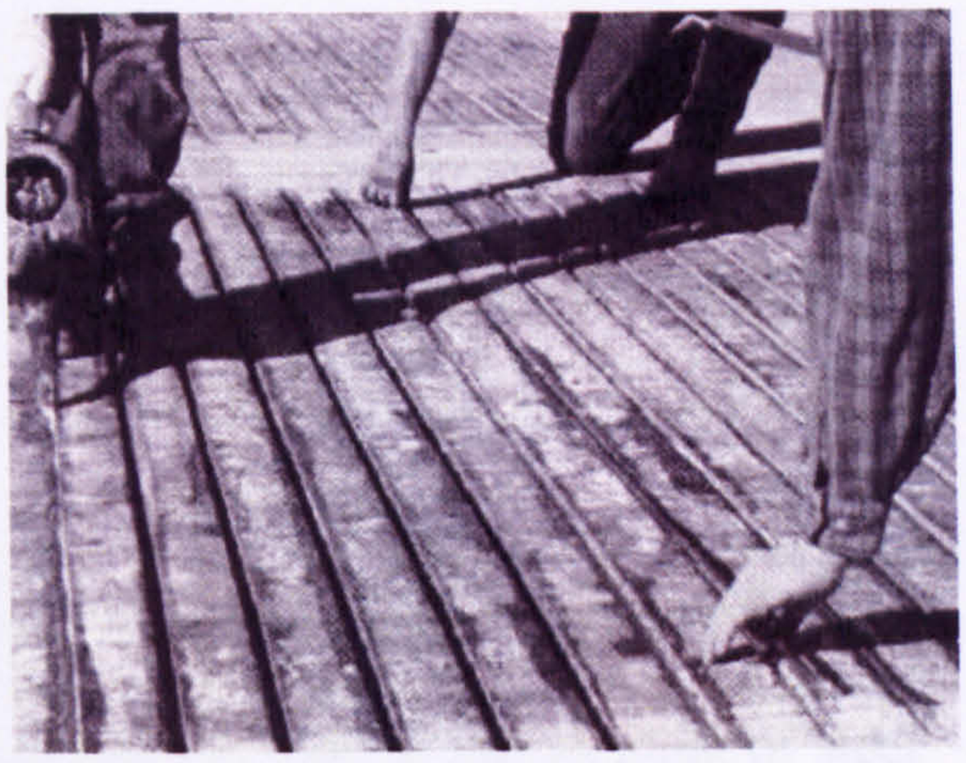

(b) Strengthening Pier 12 at the Naval Station San Diego (Warren (1998))

(c) Strengthened Bridge in service (Alkhrdaji et al. (1999))

(d) Strengthening and load testing program at Malcolm Bliss Hospital (Tumaialan et al. (1999))

Figure 2-5 Examples of previous applications of NSM FRP Rods

Alkhrdaji et al. (1999) strengthened Bridge J-857 (Phelps County, USA) in service in August 1998. One of the three solid RC decks was strengthened by embedding NSM FRP rods in grooves cut onto the soffit of the bridge deck parallel to its longitudinal

axis. Two columns were also strengthened with NSM CFRP rods to increase their flexural capacity Figure 2-5(c). The rods were mounted on two opposite faces of the columns and anchored into footings.

A strengthening and load testing program at Malcolm Bliss Hospital in St. Louis, USA was conducted by Tumaialan et al. (1999). Figure 2-5 (d) shows the installation of NSM FRP rods on a masonry wall.

All existing test results of strengthened beams, slabs, and columns indicate that the NSM reinforcement improved the ultimate load and the load at the yielding of steel reinforcement, as well as the post-cracking stiffness.

2.2.3 FRP composite bridge decks

Maintenance of transportation infrastructure, especially bridges, is a growing concern worldwide. Bridge decks are subjected to severe environmental conditions and heavy traffic loads. Finding innovative, cost-effective solutions for the repair and replacement of concrete and steel in bridges is a necessity. A FRP deck weighs approximately 80% less than a concrete deck. Reducing the dead load will increase the allowable live load capacity of the bridge without significant repair to the existing superstructure, thus lengthening its service life. Hence, lightweight and durable FRPs can be an excellent candidate for replacing concrete decks. Actually, the use of FRP composite bridge decks has gained momentum in the past few years with the successful installation of several composite bridges around the world.

Composite bridge decks are typically made of glass fibre and a polyester resin or vinyl ester resin matrix. Most bridges constructed to date use deck elements from pultruded (The term is a portmanteau word: "pull" + "extruded") structural shapes

(henceforth called "profile") that are glued together. Basic profile cross sections are including hexagonal plus half-depth trapezoidal sections (Keller (2001)), triangular single or dual cell sections (Brown & Zureick (2001), Crocker et al. (2002), Luke et al. (2002)), box sections (Hayes et al. (2000)) and trapezoidal dual-cell sections (Cassity et al. (2002)).

Each of these deck systems is factory assembled into deck panels that are sized appropriately for shipping to the work sites. The panels are then erected and bonded together at the site using high performance adhesives, mechanical connections, or both. For example, Figure 2-6 shows a trapezoidal dual-cell profile being formed through a pultrusion process. Fibre reinforcements are wetted with the resin and pulled through heated metal dies which binds and cures the composite into a precise cross-section. The profiles are assembled by bonding with a structural polyurethane adhesive. The deck shows a strongly orthotropic load-carrying behaviour due to the different fibre architectures and the different structural behaviours in longitudinal and transverse directions. However, it is found that there is little published data for the bolt connected composite deck up to date. Therefore, the adhesively bonded composite deck will be the focus of this thesis and FE analyses are done and compared to experimental data.

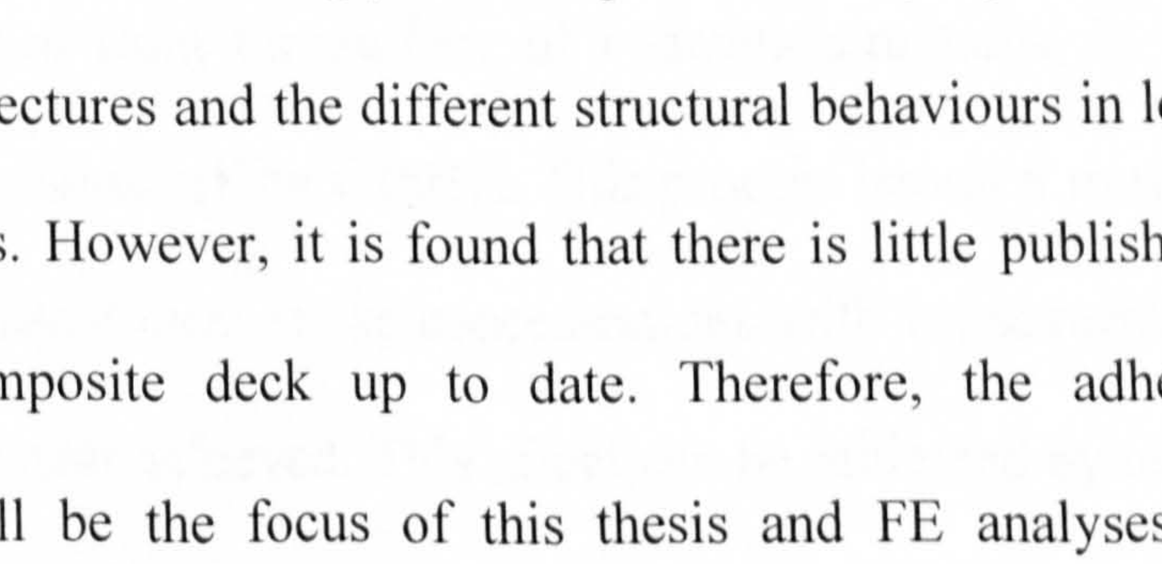

Figure 2-6 Schematic of the pultruded GFRP bridge deck

2.2.4 Adhesive bond technique

With regard to the connections, adhesively bonded connections are used more and more due to their favourable behaviour with respect to anisotropic composite fibre materials (Keller & Gurtler (2003)). Compared to bolted connections, adhesive connections allow for a much smoother and uniform load transfer and offer better durability because the adherends are not subjected to additional drilling operations that cut and expose the fibres to environmental impact. The advantages of adhesively bonded joints also include less stress concentrations, superior fatigue resistance, high strength-weight ratio, low fabrication cost, improved visual appearance, excellent electrical and thermal insulation properties, corrosion prevention, etc. (Pandey (1998)).

Structural adhesives are generally thermosets such as epoxy, acrylic, polyurethane and phenolic adhesives. A minor degree of grit-blasting is necessary to remove laitance and general impurities from the surface of concrete structures, in preparation for bonding of the FRP fabrics (Kim (2003)). This process leaves a roughened concrete surface which can cause local stress concentrations with consequential reduction in the level of enhancement achieved. This effect can be mitigated by using epoxy resin to fill and smooth out the asperities generated by the grit-blasting.

Pandey (1999) concluded that there are mainly three types of failure modes in the bonded joints: (1) cohesive failure within the adhesive; (2) adhesive failure which occurs at the interfaces of the adhesive and adherends; and (3) failure of adherends which also includes delamination in the composite adherends. Other possible failure modes are cyclic debonding in which progressive separation of adherends occurs due to the failure of the adhesive under cyclic loading. An accurate analysis of adhesively

bonded joints is needed in order to determine stress distribution for predicting strength and failure.

2.3 Structural behaviour of FRP-strengthened concrete members

2.3.1 Introduction

The growing number of applications of adhesively bonded FRP-strengthened concrete members requires improved testing methods to evaluate the behaviour of the bonded joints. Destructive tests are performed to evaluate the mechanical performance of adhesive bonded joints. A great variety of test geometries and specimens are used to obtain adhesive properties and strength of adhesive joints. The measured parameters are the load and strain needed to create failure.

The remainder of this section reviews the research work to date in the field, and in so doing draws attention to the important outstanding areas which require further focused research.

2.3.2 Study of RC elements strengthened with NSM FRP

Besides field applications and experimental field projects, laboratory projects on NSM FRP rods for structural strengthening of concrete members have been carried out in recent years. De Lorenzis & Nanni (2001[1], 2001[2], 2002) and De Lorenzis et al (2002) have comprehensively analysed the bond performance of NSM FRP rods. Other researchers have proposed similar strengthening techniques but, instead of rods, have used laminate strips of CFRP (Blaschko & Zilch (1999), Ferreira (2000)).

2.3.2.1 Bond test and discussion of failure modes

Bond is of primary importance, since it enables the stress transfer between the concrete and the FRP reinforcement to develop composite action. The bond behaviour influences the ultimate capacity of the reinforced element as well as serviceability aspects such as crack width and crack spacing. Among the many different types of bond tests to investigate the stress transfer from the concrete to the FRP bars and the effective bond length reported in the literature, the most common are the direct pullout test (Figure 2-7) and the beam pull-out test (Figure 2-8).

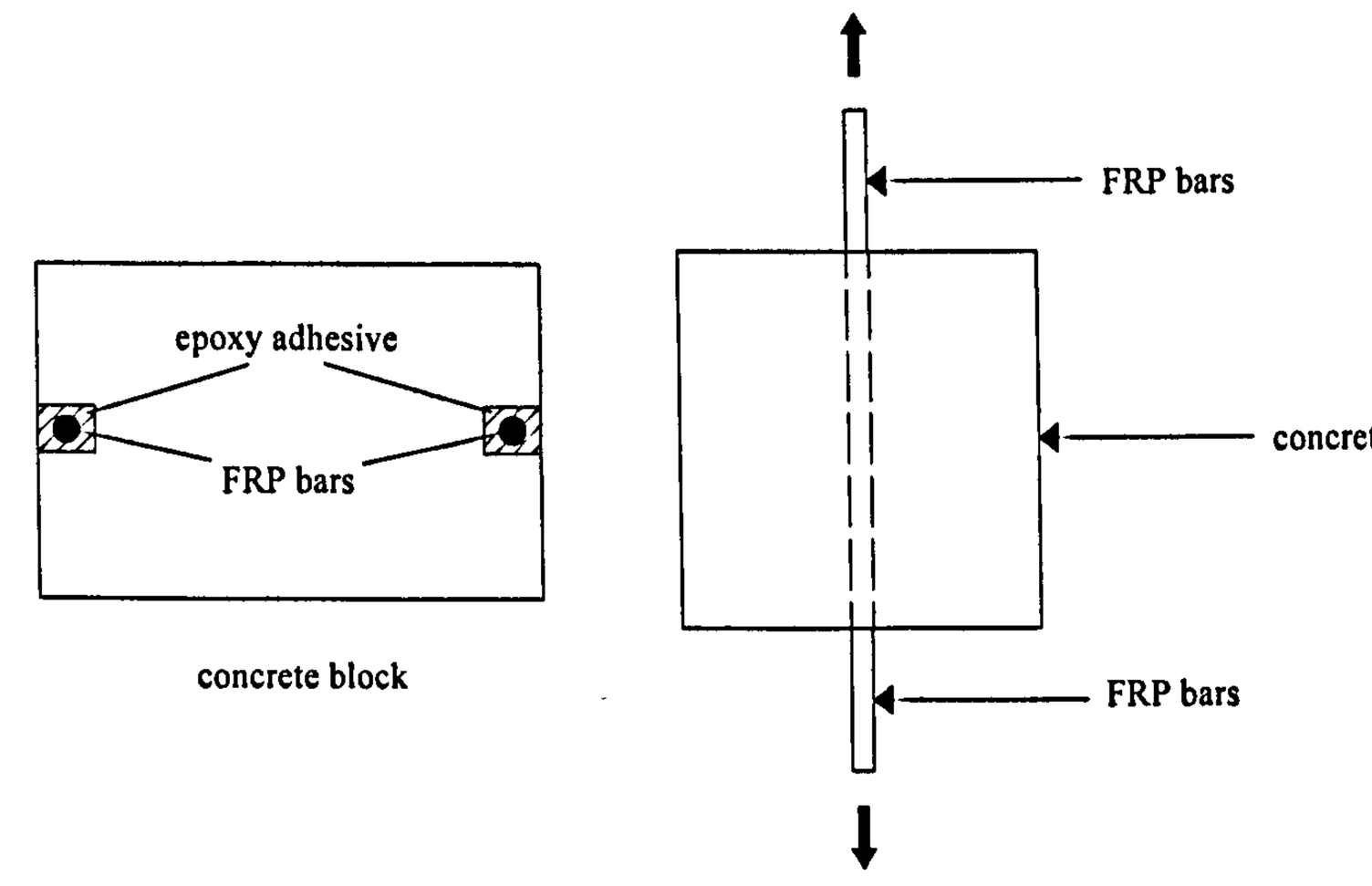

(a) Cross section (b) Loading set up

Figure 2-7 Direct pull-out bond test specimen

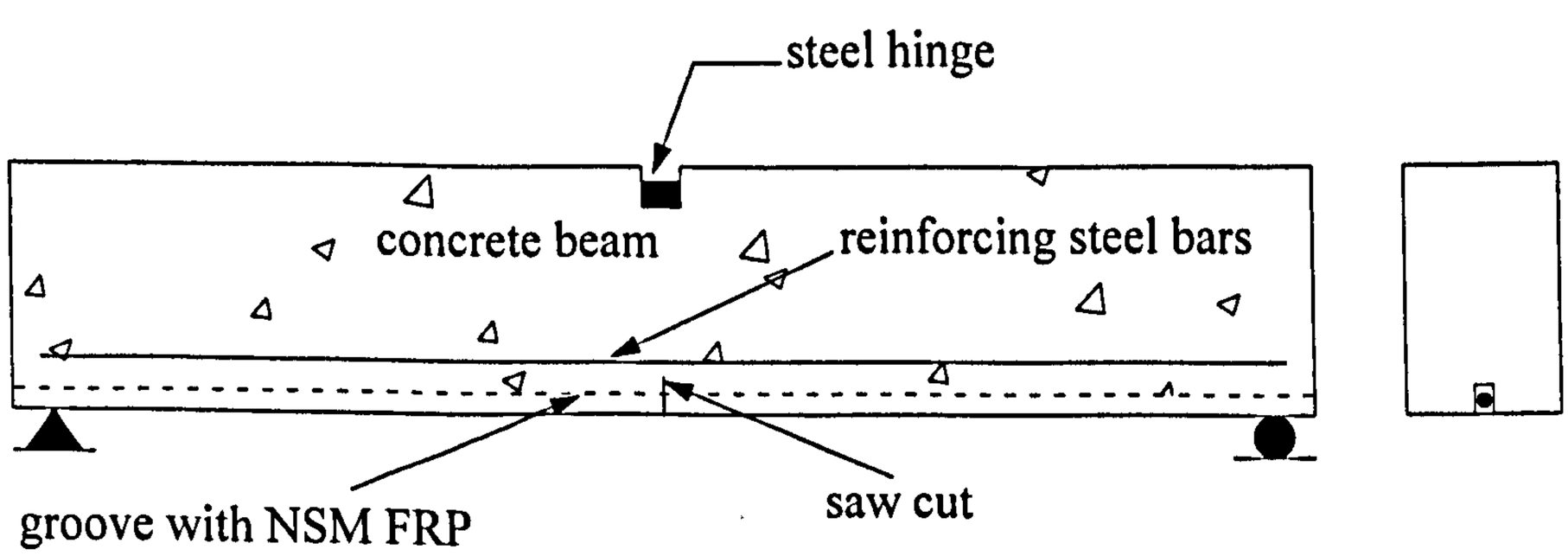

Figure 2-8 Beam pull-out bond test specimen

For the direct pull out test, the specimen usually consisted of a concrete block with epoxy-filled grooves cut on two opposite faces and the CFRP rods or strips inserted into the grooves. Then the load was applied to the NSM bars while a steel frame restrained the concrete block. For the beam pullout test, each beam had a steel hinge at the top and a saw cut at the bottom, both located at midspan. The purpose of the hinge and saw cut was to control the distribution of the internal forces. During loading, the saw cut caused a crack to develop at the centre of the beam and extend up to the hinge. Therefore, the compressive force in the beam at midspan was located at the centre of the hinge and the internal moment arm was known and constant for any given load level above the cracking load. This allowed an accurate computation of the tensile stress in the rod. Only one side of the beam was the test region, with the FRP rod having a limited bonded length and being unbonded in the remaining part. The rod was fully bonded on the other side of the beam, so that bond failure would occur in the test region.

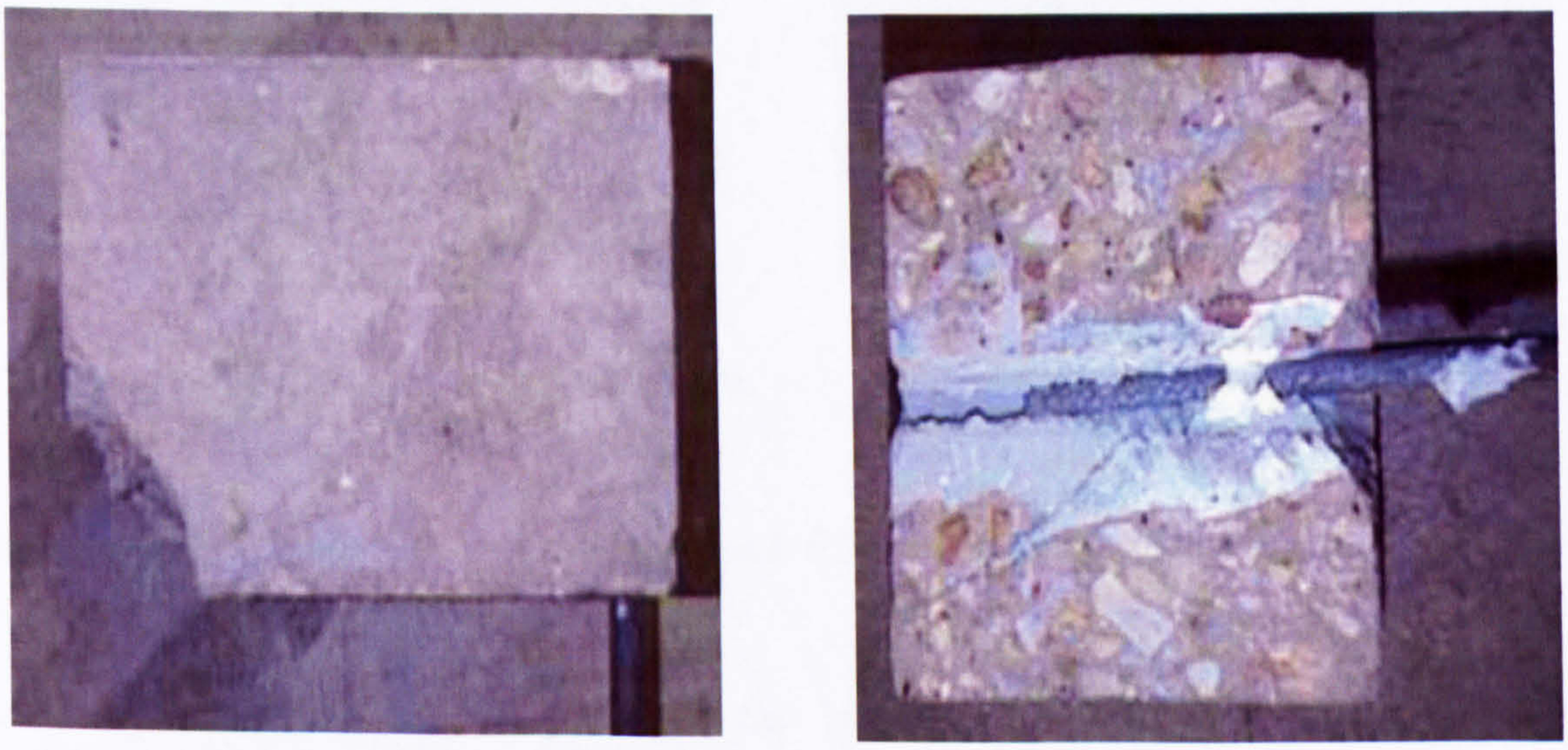

(a) Failure in concrete (b) Failure in bar-epoxy interface

Figure 2-9 NSM failure modes reported by Yan et al. (1999)

Based on the results from bond tests, Yan et al. (1999) reported that two different failure modes were found in the tests: the specimens with the two shorter bonded

lengths failed by rupture of the concrete at the edge of the block (Figure 2-9 (a)) and those with the longest bonded length failed as pull out at the rod–epoxy interface (Figure 2-9 (b)). The former failure mode may be due to the closeness of the bonded length to the edge of the concrete block so that the concrete edge failed in shear before proper bond failure occurred.

Another series of bond tests was performed by Warren (2000). Half of the specimens were tested at room temperature while the other half at 60 °C. It was found that the room temperature specimens failed by splitting and shearing of the concrete while the elevated temperature ones failed at the epoxy-concrete interface.

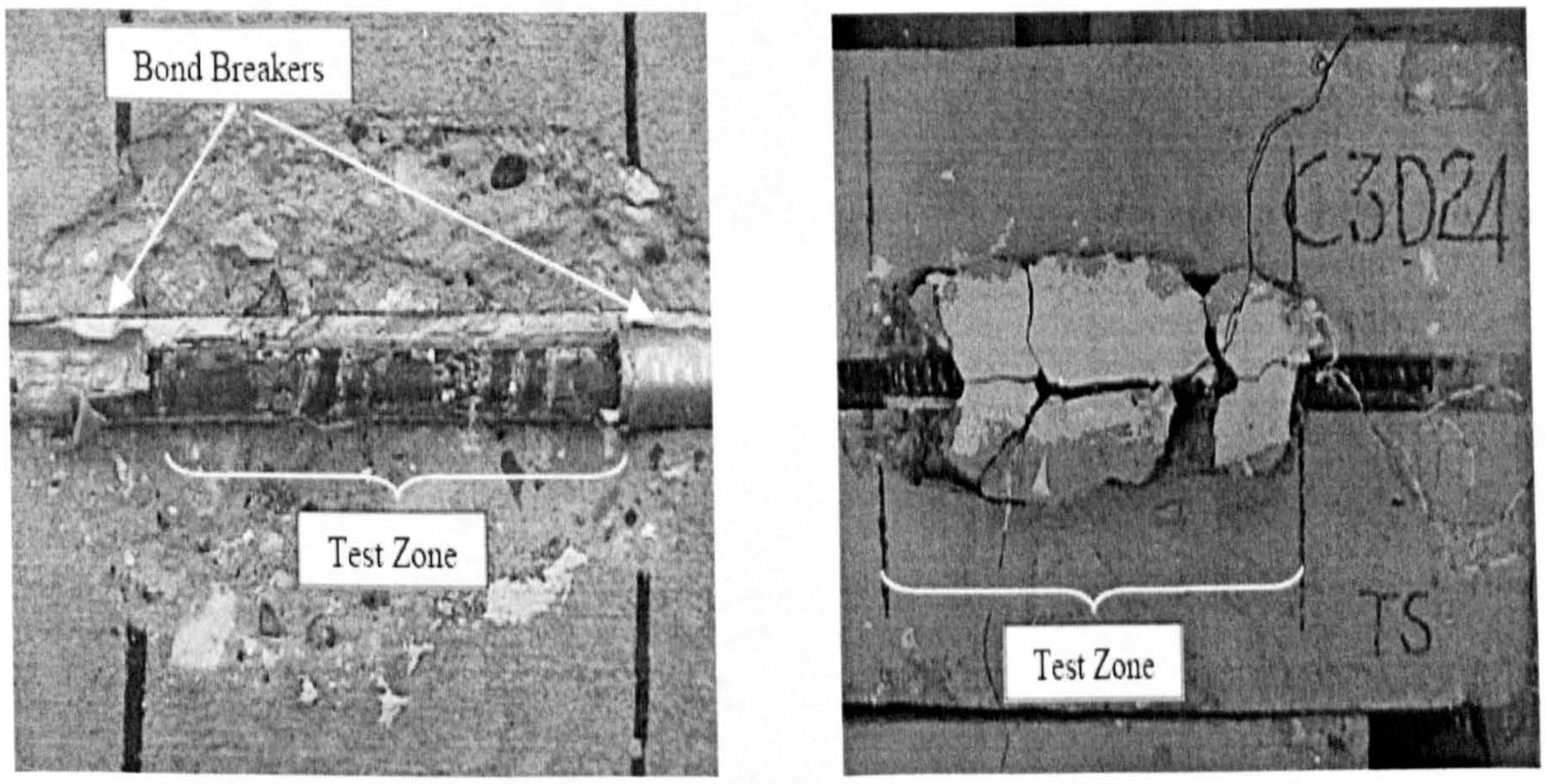

(a) Failure by splitting of epoxy adhesive (b) Failure by concrete cracking

Figure 2-10 NSM failure modes reported by De Lorenzis and Nanni (20012)

De Lorenzis & Nanni (2001[2]) carried out beam pull-out tests on five specimens strengthened by CFRP deformed rods. Two bond failure modes were observed: splitting of the epoxy cover Figure 2-10 (a) and cracking of the concrete surrounding the groove Figure 2-10 (b), depending on the groove size. As the groove size increases, the thickness of the epoxy cover increases, so offering a higher resistance to

splitting. The ultimate load increases correspondingly, and failure may eventually shift from the epoxy to the surrounding concrete. The average bond strength results were approximately constant with the bonded length, indicating an even distribution of bond stresses at failure.

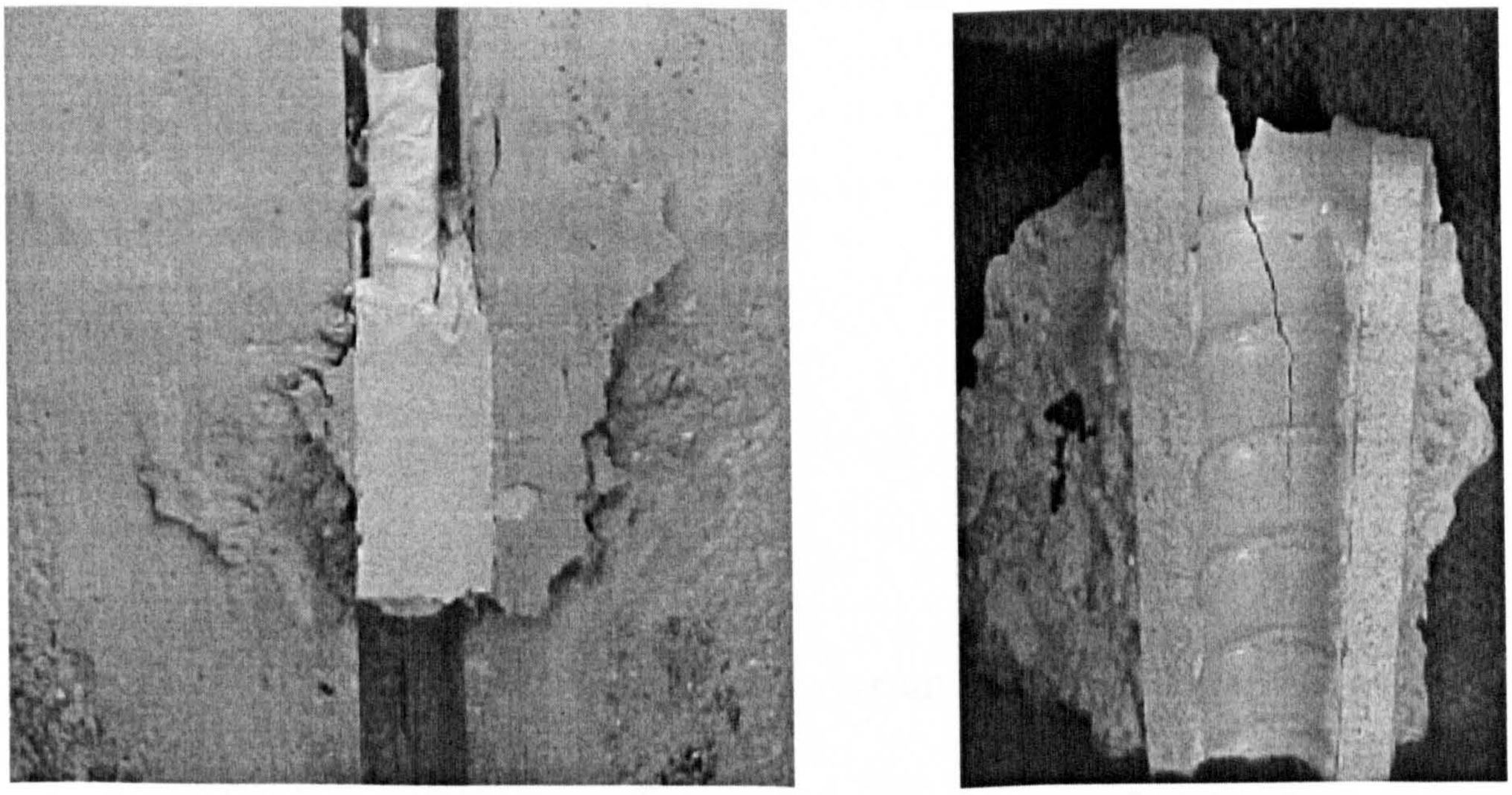

(a) Concrete cracking

(b) Longitudinal splitting crack

(c) Failure at the epoxy-concrete interface

(d) Splitting of the cement mortar

Figure 2-11 NSM failure modes reported by De Lorenzis et al (2002)

A modified pull-out test was developed by De Lorenzis & Nanni (2002) on NSM CFRP and GFRP ribbed and sandblasted rods, with varying bond length and groove size. In total a series of tests on 36 specimens were performed. The encountered failure modes shown in Figure 2-11 were: splitting of the epoxy, accompanied or not by cracking of the concrete surrounding the groove, for ribbed rods, and pull-out at the rod–epoxy interface for sandblasted rods.

2.3.2.2 Flexural strengthening for RC beams

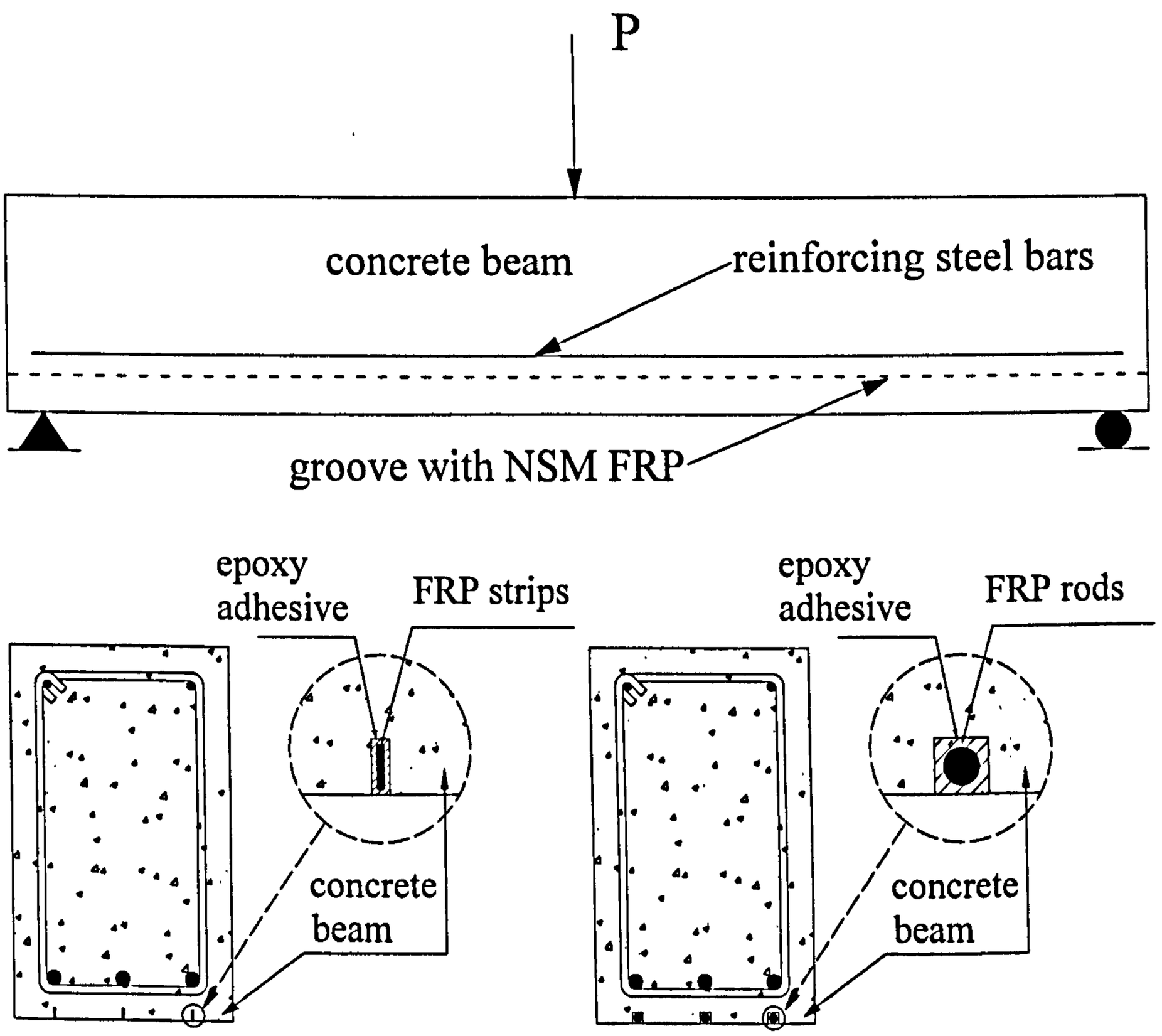

Figure 2-12 Diagram of NSM FRP technique

The benefits in terms of load-carrying capacity and ductility showed that this technique is promising for strengthening concrete elements failing in bending. Some existing studies were conducted on simply supported RC beams flexurally reinforced

with NSM bars (Figure 2-12). Based on the available experimental evidence, the possible failure modes include: concrete cover separation, bar-epoxy interfacial debonding, epoxy-concrete interfacial debonding and other secondary debonding failure mechanisms (De Lorenzis & Teng (2007)). Note that the debonding failures observed in the flexural tests differ greatly from those found in the bond tests, due to the presence of flexural and shear cracks altering the bond stress distribution, the curvature of the beam, and the dowel forces generated by the opening up of the bond cracks, phenomena which are all absent in a bond test specimen.

De Lorenzis et al (2000[3]) reported bar–epoxy interfacial debonding that involves interfacial debonding between a bar and the epoxy for sand-blasted round bars. It was found that the epoxy cover in the beam was intersected by flexural cracks which facilitated the initiation of longitudinal splitting cracks and hence accelerated interfacial debonding (Figure 2-13 (a)).

Hassan and Rizkalla (2003 & 2004) conducted flexural tests on RC beams with NSM CFRP round ribbed bars and strips of varying embedment length. Failure of beams with NSM round ribbed bars occurred by splitting of the concrete cover followed by the complete debonding of the bars in all cases. These authors concluded that the tensile rupture of this type of bar is unlikely to occur, regardless of the embedment length, that the maximum usable strain of these bars should be limited to 0.7 - 0.8%, and that the anchorage length should not be shorter than 800 mm. In the case of beams with NSM strips, rupture of the strips occurred when the embedment length was larger than 850 mm. They also reported the cohesive shear failure in the concrete at the epoxy-concrete interface starting from the cut-off section as shown in Figure 2-13 (b).

(a) Bar-epoxy interface debonding

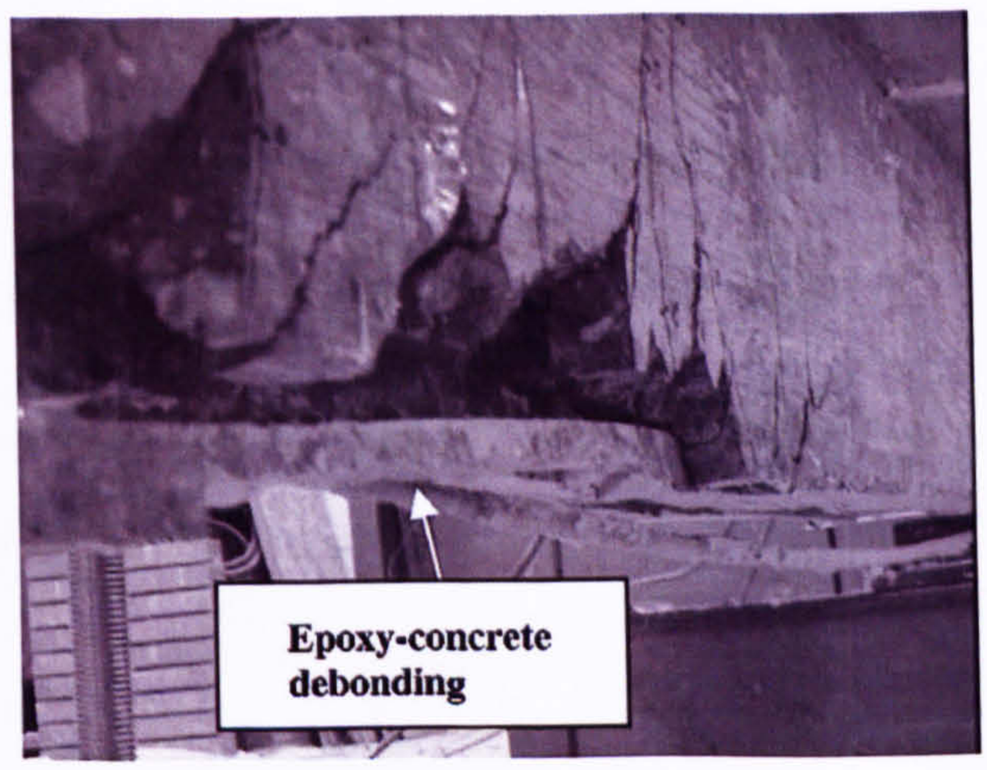

(b) Epoxy-concrete debonding

(c) Separation mode I of concrete cover

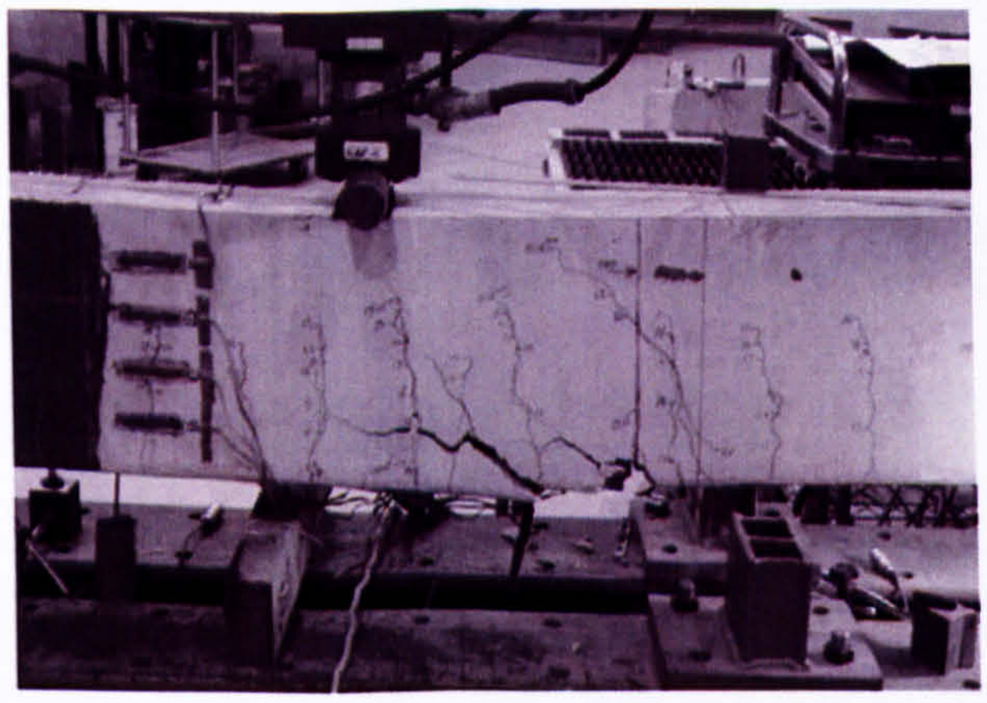

(d) Separation mode II of concrete cover

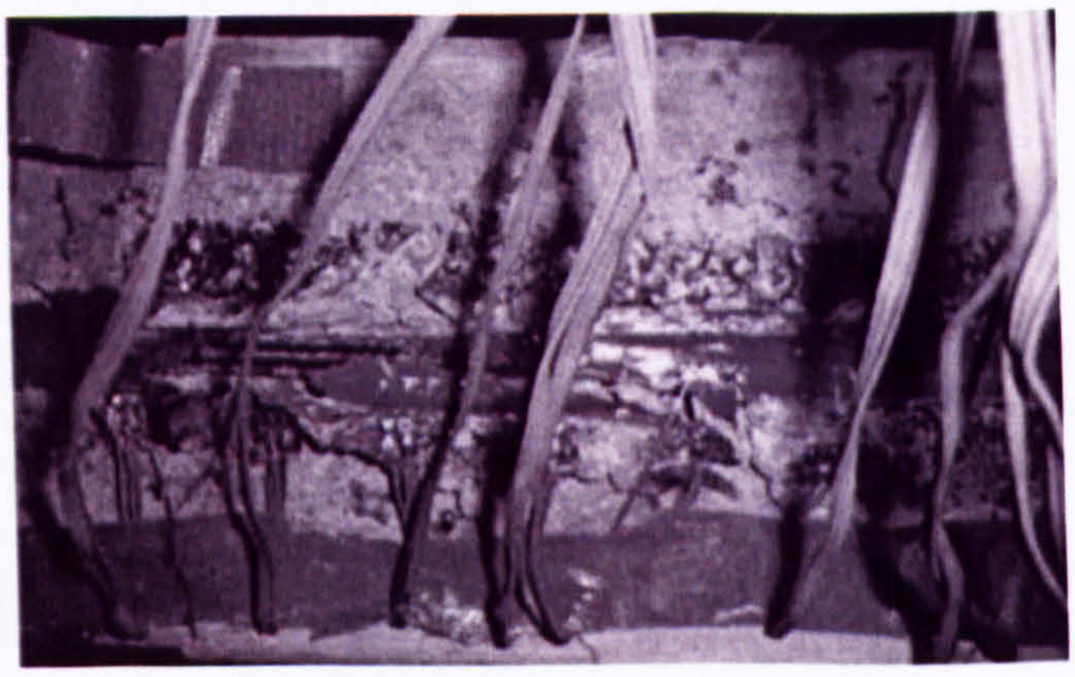

(e) Splitting of the epoxy cover

Figure 2-13 Debonding failure modes on flexurally strengthened beams

Barros and Fortes (2005) applied the NSM technique on beams failing in bending by testing four series of beams under four-point loading. Taking the results obtained it was observed that this strengthening technique provided significant increase of the load corresponding to the deflection of the serviceability limit state, concrete cracking and the yielding of conventional reinforcement, the service load of the strengthened

beams, and the maximum load of the reference beams respectively. The maximum strains in the CFRP laminates ranged from 62% to 91% of its ultimate strain, indicating that this strengthening technique can mobilize stress levels in the CFRP reinforcing elements close to the tensile strength of this composite material. Figure 2-13 (c) shows the failure mode of beam, which was characterized by the detachment of a layer of concrete at bottom of the beam.

Teng et al. (2006) conducted flexural tests on RC beams with NSM strips of varying embedment length. As the embedment length increased, the failure mode changed from concrete cover separation starting from the cut-off section (Figure 2-13 (d)), to concrete crushing followed by secondary cover separation close to the maximum moment region. In the beams with the two longest embedment lengths, secondary debonding mechanisms were also observed (Figure 2-13 (e)).

2.3.2.3 Shear strengthening for RC beams

The use of NSM FRP reinforcement is also effective in enhancing the shear capacity of RC beams. In the studies for this purpose, the bars are embedded in grooves cut on the sides of the member at a desired angle to the beam axis.

De Lorenzis & Nanni (2001[1]) carried out shear-strengthening tests on eight large size T-beams by puting CFRP ribbed round bars in epoxy-filled grooves. The test variables included bar spacing, inclination angle and anchorage of the bars in the flange. An increase in shear capacity as high as 106% was achieved.

Two different failure modes were identified in the tests, namely the debonding of the FRP bars by splitting of the epoxy cover and cracking of the surrounding concrete, associated with the diagonal tension failure of concrete (Figure 2-14 (a)), and

separation of the concrete cover of the steel longitudinal reinforcement (Figure 2-14 (b)). The authors suggested that debonding of the FRP bars is the most important failure mode and could be prevented by providing better anchorage of the NSM bars crossing the critical shear crack, by either anchoring the bars in the beam flange or the use of inclined (e.g. 45 degree) bars at a sufficiently close spacing to achieve a longer total bond length. The second mode, however, may be attributed to the fact that no or very limited steel stirrups were present in these beams, and is unlikely in beams with a significant number of steel stirrups.

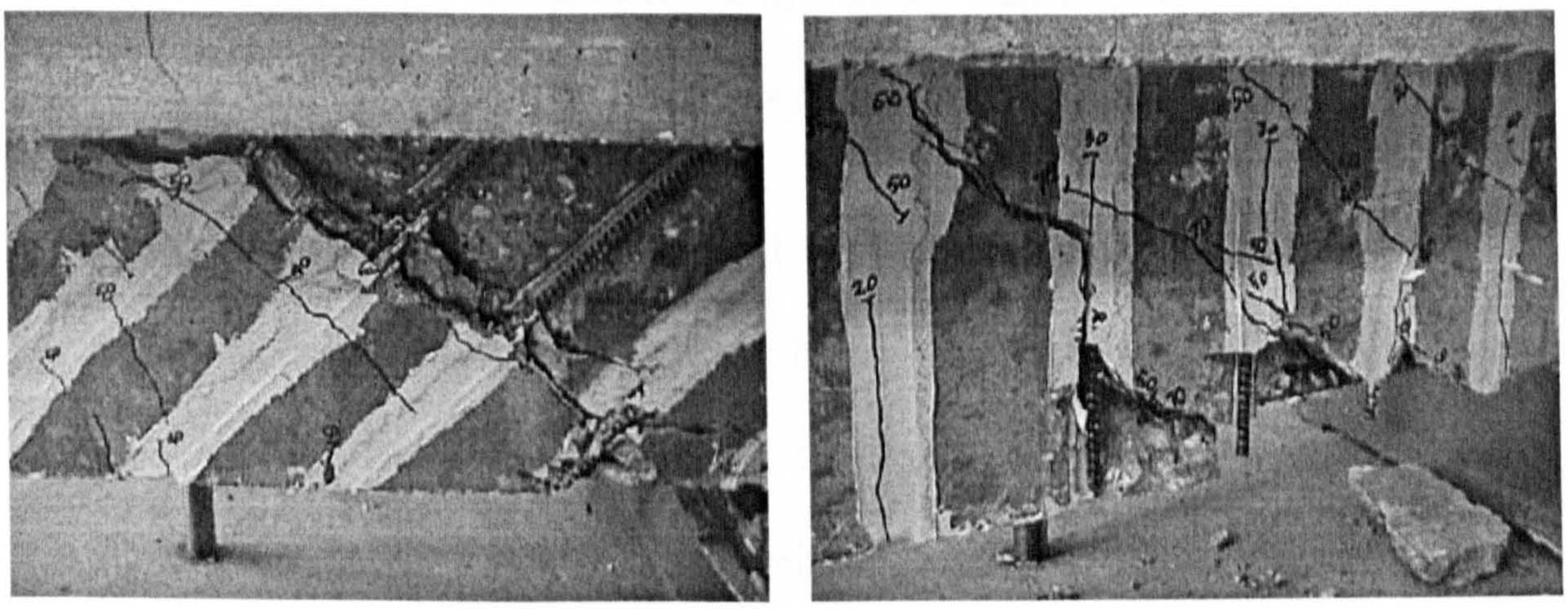

(a) Splitting of epoxy cover (b) Local separation of concrete cover

Figure 2-14 Debonding failure modes on shear strengthened beams

Barros & Dias (2003) tested beams of different sizes strengthened by NSM CFRP, conventional stirrups and CFRP sheets respectively. The reported results showed that the first one is the most effective not only on the load bearing capacity but also on the ductility of strengthened beam. Although failure modes were not described, based on the reported load-deflection curves, at least some of the beams are believed to have failed in bending.

Nanni et al (2004) applied CFRP rectangular bars installed as NSM reinforcement for shear strengthening in conjunction with an externally bonded pre-cured CFRP laminate to increase the flexural capacity of a prestressed concrete bridge girder. The

specimen, which was removed from an overloaded bridge in Kansas was strengthened and tested in the laboratory. Test results showed that the proposed NSM reinforcement technique represents an effective solution to increase shear capacity.

2.3.2.4 Other research on NSM strengthening applications

Nordin & & Täljsten (2006) conducted a pilot study on concrete beams strengthened with prestressed NSM CFRP strips. Test results showed a substantial increase in cracking and failure loads for the strengthened specimens. Prestressing the strips did not influence the mode of failure. Compared to unstrengthened specimens, the prestressed beams had considerably smaller deflections at failure.

Prota et al. (2004) proposed the combined use of FRP laminates and NSM bars for upgrading RC beam-column connections. NSM bars were installed on the column prior to wrapping and anchored through the beam. Such installation enabled the transition of the failure mode from the column to the shear failure of the joint. In further specimens, additional strengthening was provided to the joint to suppress joint shear failure by placing the FRP reinforcement either along the beam axis or along the column axis. With this strengthening scheme, failure shifted to the column-joint interface at the termination of the FRP laminate. The upgrading of the joint zone increased its deformability and hence provided a significant contribution to the ductility of the system. This topic deserves further investigation as similar advantages may be realised by suitable combinations of the two techniques in solving other strengthening problems.

2.3.2.5 Theoretical analysis of bond stress-slip relationship

Based on the average bond stress–slip curves of the specimens with the shortest bonded length, De Lorenzis et al (2002) approximated and modelled analytically the local bond–slip relationships in the two cases of specimens failed by splitting and at the epoxy–concrete interface. This allowed computation of some quantities of interest from a design standpoint, such as the bond failure load as a function of the bonded length, the load at onset of free-end slip corresponding to the ascending portion of the bond–slip curve, and the corresponding minimum bonded length. A design approach based on the limit state philosophy was proposed to compute the anchorage length of NSM bars, and a design example was carried out.

Hassan & Rizkalla (2002) proposed a general methodology to evaluate the development length of NSM FRP bars of different configurations and types of fibers. The influence of the groove dimensions, groove spacing, and the limited adhesive cover was investigated. The authors concluded that the tensile stresses both at the concrete-adhesive interface and the FRP-adhesive interface are highly dependent on the groove dimensions and controls the failure mode of NSM FRP bars. Design charts were provided to establish code specifications for the use of NSM FRP reinforcement.

Hassan & Rizkalla (2003) proposed a closed-form analytical solution to predict the interfacial shear stresses. The model was validated by comparing the predicted values with test results as well as nonlinear FE modelling. A quantitative criterion governing the debonding failure of NSM CFRP strips was established. The influence of various parameters including internal steel reinforcement ratio, concrete compressive strength, and groove width was discussed.

By using the results of an experimental program with pullout-bending tests, Cruz & Barros (2004) developed a numerical strategy to obtain an analytical bond-slip relationship. This relationship was converted into a bond-slip constitutive law for a line interface finite element, used to simulate the concrete-CFRP bond behaviour. The numerical model developed predicted all the significant aspects registered experimentally, and can be used to assess relevant information in the design of concrete structures strengthened by the NSM technique.

2.3.2.6 Further research needed

From a comprehensive literature review, it was found that there is still limited understanding of the mechanics of debonding in beams strengthened with NSM systems. In spite of all these experimental investigations on the NSM FRP strengthened concrete members, few tests have been done to fully characterize the stress transfer conditions between FRP and anchoring material, especially in midspan zones rather than end zones. Besides, descriptions of failure modes in the existing literature are often not sufficiently detailed to understand the progression of the failure process. The interactions between the different failure modes described above are still unclear and deserve further investigation.

For this reason, one of the main focuses of the work reported in this thesis is *an in-depth experimental investigation and finite element analysis of stress transfer between NSM FRP bars and anchoring material in a novel pullout specimen which somewhat represents conditions both in mid-span zones and end zones as well as relative failure modes*. Given the variability of material properties and groove geometry, it also requires that *the influence of the most critical parameters on the bond performance* to be investigated and therefore a comprehensive parametric FE analysis is conducted

along with experimental tests. These issues are in particular represented in detail in Chapter 4 and Chapter 5.

2.3.3 Investigation of FRP plated RC elements

2.3.3.1 Debonding mechanisms of FRP plated RC elements

Previous research shows that the external FRP plate bonding for enhancement of RC structures is one of the most popular FRP strengthening methods and has attracted much research attention. Experiments have been carried out using several setups, including single shear tests (Chajes et al. (1996), Bizindavyi & Neale (1999), Täljsten (1997)), double shear tests (Swamy et al. (1986), Brosens & Van Gemert (1997), Hiroyuki & Wu (1997), Neubauer & Rostãsy (1997)), and modified beam tests (Van Gemert (1980), Ziraba et al. (1995)).

It is concluded that RC members enhanced via FRP plate mostly fail in the following three ways: flexure failure by FRP rupture or concrete crushing, shear failure, and failure by brittle fracture of the plate-to-concrete connection and consequent separation of the plate from the original concrete member (Kim (2003)). Among them, the brittle separation failure is one of the most common and critical (Bonacci & Maalej (2001)). In particular, such failure was found to be very undesirable, since it not only can occur at a load much lower than that which induces conventional flexural failure by concrete crushing but also can precipitate large and sudden reductions in load capacity. Also, once separation occurs, the un-plated member can be left exposed to loads far greater than that for which it was originally designed, with potentially catastrophic consequences.

It is therefore important to understand the mechanism of brittle separation failure. To that end, much experimental and analytical research effort has been invested in this subject and it is found that more than one debond mode exists. The remainder of this section reviews the work to date in the field and describes the physics of two of these debond modes. In so doing, attention is drawn to the important outstanding areas which require further focussed research.

2.3.3.2 Discussion of various brittle separation failure modes

Probably the most extensively researched and commonly reported brittle separation failure mode is End-peel, so-named because it initiates at the ends of the plates and propagates inwards along the beam by peeling of the plates, as shown in Figure 2-15 (a). This occurs by horizontal fracture of the cover concrete, usually at the level of the embedded steel reinforcement or near the adhesive-concrete interface.

End-peel failure has been reported by a number of researchers including Täljsten (1994), Brosens & Van Gemert (1997), Buyukozturk & Hearing (1998), Ahmed & Van Gemert (1999), Hassanen & Raoof (2001), and Nguyen et al (2001). The previous work shows that the bond stresses which trigger such failure develop at locations of rapid change of section of the plated beam, i.e., the abrupt transition from the un-plated section A to the plated section B in Figure 2-15 (a). Roberts & Haji-Kazemi (1989) analytically demonstrated that such section change causes high shear and normal bond stresses to develop and to be transmitted through the plate-to-concrete connection over a short distance from plate curtailment.

The research into End-peel has identified some parameters which strongly influence this failure mode, including the strength of the plate-to-concrete connection, the offset

of section change from the near support, the width-to-thickness ratio of the plate, the shear span-to-beam depth ratio, and the stiffness of the connecting adhesive layer.

Recently, another important failure mode, termed midspan debond, was found in the midspan region of the beam, initiating at the toes of flexural cracks and propagating out to the ends of the plates. As shown in Figure 2-15 (b), the delaminated concrete, adhesive, and plate remain an integral part of the original beam. During the initiation phase, inclined cracks form in the covercrete.

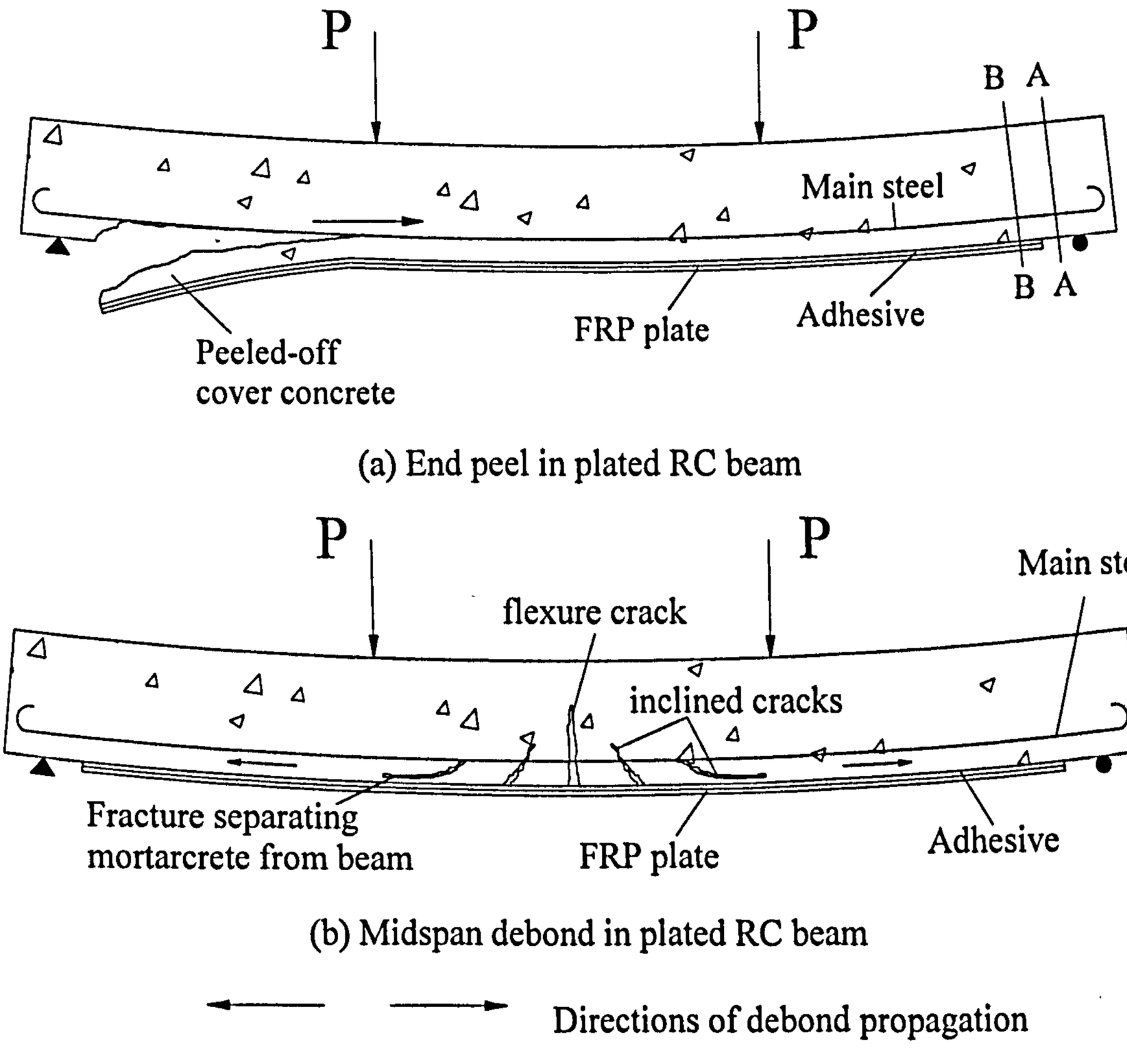

(a) End peel in plated RC beam

(b) Midspan debond in plated RC beam

Figure 2-15 Diagrams of major failure modes (Sebastian (2001))

Arduini & Nanni (1997) reported this failure mode starting at flexural cracks in the maximum moment region and propagating out towards the ends of the plates. Out of

16 reinforced concrete beams bonded with CFRP plates, 6 were reported to have failed in this manner.

Meier & Kaiser (1991), Meier (1992) and Meier et al (1992, 1993) also reported a brittle separation mode which initiated from one of the shear cracks well away from the end of the plate in FRP-plated concrete beams. As shown in Figure 2-16, this failure mode occurs because the opening of the shear crack induces dowel action in the FRP plate across the toe of the crack, thereby inducing high vertical tensile stresses and consequent horizontal fracture of the concrete-to-adhesive connection on one side of the crack. Note also from Figure 2-16 the potential for horizontal splitting of the cover concrete at the level of the embedded steel rebar, owing to a similar dowel effect in that rebar. Quantril et al (1996), Kishi et al (2001), Rahimi & Hutchinson (2001), and Fanning & Kelly (2001) have reported this type of separation failure.

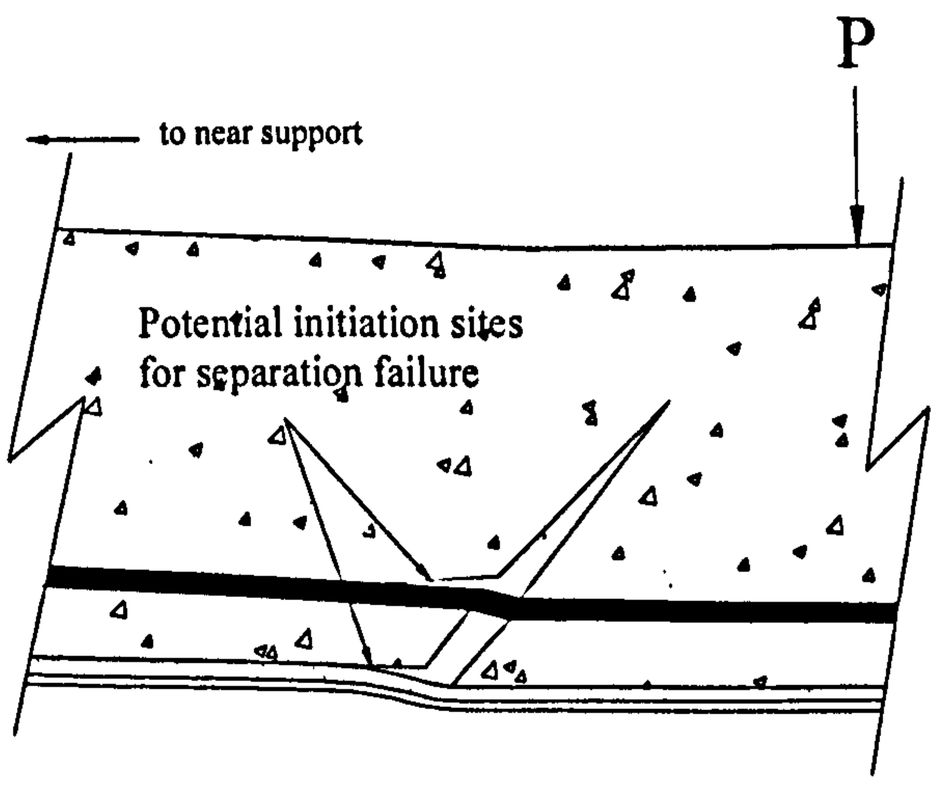

Figure 2-16 Shear-crack separation mode

Swamy & Mukhopadhyaya (1999) reported that the integrity of the bond between the CFRP plate and the concrete is particularly sensitive to cracks in the shear span, which could cause vertical and/or horizontal displacement of the bonded elements at

the toes of the cracks. Garden (1997) suggested that this mode of separation failure is likely to occur when the shear span-to-depth ratio of the plated beams is high.

2.3.3.3 Stress transfer and anchorage length

Brittle separation failure of adhesive bonding is triggered mainly by high shear bond stresses transmitted through the adhesive and adjacent cover concrete layers. Experimental determination of the magnitudes of the critical shear stresses is thus a crucial starting point for gaining a proper understanding of structural failure modes. To that end, many analyses have been done on the FRP-plated beam specimens loaded to failure, focusing on the shear strengths of the plate-to-concrete connection (usually that of the cover concrete).

Specifically, the average shear bond stress between two longitudinally adjacent locations of a plated member cannot be measured directly, but is instead inferred from axial strain readings at those locations. Due to the difficulties of putting strain gauges along the bonded surfaces of strengthening plates, these strains have been achieved mostly from strain gauges attached to the surfaces of the bonded plates. The expression used to work backwards from the test strain gauge data to the average shear bond stress between the two locations τ_{avg} is as follows:

$$\tau_{avg} = t_p E_p \frac{\Delta\varepsilon}{\Delta x} \qquad \text{(Equation 2-1)}$$

Where: t_p is thickness of plate (assumed constant, as is commonly the case); E_p is Young's modulus of strengthening plate; $\Delta\varepsilon$ is the difference in mid-plane axial strain of the plate between the two locations; and Δx is the distance between the two locations along the plate.

It is noted that the strains used must be those at the mid-plane of the plate. Because the FRP plates used are very thin, it is usually assumed that the strains measured from the exposed surfaces of the plates are virtually equal to those at the mid-planes of the plates.

Most of the reported strengths lie in the range from 1 to 5 N/mm^2, which is reasonable. For example, Sharif et al (1994) stated that the maximum sustainable interface shear stress was from 3 to 4 N/mm^2. However, higher stresses were found in other researches up to be 15 N/mm^2 (Bizindavyi & Neale (1999), Quantril et al (1996)).

The possible reasons for the wide range of concrete material strengths reported could be the well-known statistical variation in properties of concrete and the local bending of the plate in the vicinity of the shear crack. In the latter case, the strain at the mid-thickness of the plate can be very different in magnitude from that at the outer surface of the plate, even for thin plates. Kim (2003) took a new measuring method to reduce this error by attaching the strain gauges to both the bonded and exposed surfaces of the plates, and by using the linear through-thickness strain assumption to deduce the mid-plane strains.

Kim (2003) also mentioned the existence of very low values of connection shear strength. The reason may be the presence of imperfections such as bubbles in the connecting adhesive layer. If the experimental instrumentation layout used to deduce the shear strength does not coincide with the locations of the imperfections, then the stress concentrating effects of the imperfections will not show up in the test data, and so lower shear strengths than those which actually existed at separation failure will have been measured.

The tension in the plate is transferred to the concrete mainly via shear stresses in the adhesive over a short length nearest to the applied load. Experiments show that at any one time, only part of the bond is effective (Täljsten (1997)). As cracking in the concrete propagates, bond resistance is gradually lost in the zone near the load, but in the mean time it is activated further away from the load. Therefore, a key issue in the design of effective externally bonded plates is the anchorage strength and substantial research has been carried out on this issue.

Shear anchorage strength models have been advanced in the last few years. They may be classified into three categories: a) empirical models based directly on the regression of test data (Hiroyuki & Wu (1997)); b) fracture mechanics models (Neubauer & Rostasy (1997)), and c) design proposals that generally make use of some simple assumptions (Khalifa et al. (1998), Chen & Teng (2001)).

It was found that the anchorage strength cannot always increase with an increase in the bond length, and the ultimate tensile strength of a plate may never be reached, however long the bond length is. This phenomenon leads to the important concept of effective bond length, beyond which any increase in the bond length cannot increase the anchorage strength, as confirmed by many experimental studies (Chajes et al. (1996), Täljsten (1997)) and fracture mechanics analyses (Yuan et al. (2001)). However, a longer bond length may improve the ductility of the failure process.

In spite of this large volume of research, there are still several crucial aspects of brittle separation failure which require elucidation. By building on that of these previous researchers, the work reported in the present thesis seeks to quantify the influence of stress transfer between bond of concrete and strengthening plates on the brittle failure modes by presenting both experimental data and finite element analyses results.

2.3.4 Investigation of FRP composite bridge decks

FRP composite bridge decks are relatively new application of FRPs. The main differences between it and conventional FRP application are including: a) the FRP decks are in compression at bending zone while the FPR plate or bars are in tension mostly; b) FRP profile decks normally have joints section which may cause uneven stress transfer while plates have continuous uniform shape.

Currently there are no proven analysis procedures or design standards available for its construction. Thus, FRP deck behaviour under live loads and long-term durability are not well understood by civil engineers. An as-installed field evaluation through load testing and further analytical investigations is considered essential to ensure the safe and cost-effective use of FRP decks (Kumar et al. (2004)).

Alampalli et al. (2002) presented the design, fabrication, and installation procedures, and proof testing of FRP composite bridge deck panels for a short span bridge. Bakht et al. (2000) presented the design procedures of FRP structures in the Canadian Bridge Design Code Provisions for fibre-reinforced structures. Burgueno et al. (2001) studied the behavior of FRP composite bridge superstructure conducting experimental and analytical studies. Dutta et al. (2003) performed fatigue tests on FRP deck panels and studied their behavior under extreme weather conditions. Harik et al. (1999) determined the factor of safety against failure of hybrid FRP/concrete composite bridge deck panels based on experimental studies. Hayes et al. (2000) and Kumar et al. (2004) developed and studied FRP composite bridge decks by assembling the pultruded components. Static and fatigue tests were conducted on models of hybrid FRP/concrete composite bridge structures (Kitane et al. (2004)) and on models of composite bridge decks (Youn & Chang (1998).

However, in the field of adhesive connections of pultruded profiles, still very little research has been done up to present. In this thesis, a composite bridge specimen comprising a triangular profile GFRP deck on the top adhesively bonded to a RC beam on the bottom is presented and its structural response to loading is discussed. This study will give a fundamental insight into the stress transfer at the adhesive bond line between GFRP deck and RC concrete.

2.4 FE study on stress transfer between FRP and concrete

2.4.1 Introduction

Alongside laboratory testing, mathematical modelling of FRP strengthened concrete structures is important in order to help elucidate the fundamental structural mechanics of the connections in such structures under loads. Consistent with that objective, comprehensive symbolic models have in the past been developed for predicting stress distributions in the connecting adhesive layer. However, the complications of structural analysis involved in the adhesive bonding of the structural system include behaviour near discrete cracks, effect of steel yield, effect of progressive loss of bond with load increase, through-thickness interfacial stress distribution, and interfacial nonlinear bond-slip behaviour. It is difficult to obtain a classical analytical solution for the joint, which can take into account all the above complexities. Hence, it becomes necessary to employ numerical techniques like the FEA method.

The FEA method is usually used to model and evaluate the experimental work. To make a correct analysis it is important to take into account the following: adhesive nonlinear mechanical properties, the occurrence of high stress gradients in certain regions of the joint, the effects of adherent stiffness. Here, the relevant literatures pertaining to the study have been reviewed. It is found that both linear and nonlinear

FE analyses have been carried out on different types of adhesive joints, and stresses and strains of joints components have been evaluated.

2.4.2 Choices of elements and corresponding material properties for adhesive

The adhesive bond layer between concrete and strengthening materials (either EBR strips or NSM bars) is usually epoxy resin, which is thin compared with the thickness of the adherends. To simulate its special mechanical properties, it is essential to choose proper elements. According to the review on available literature, it is found that generally there are four types of structural elements in use, namely 2D/3D interface elements, 2D quadrilateral plane elements, and 3D brick elements. Material properties were defined respectively corresponding to the different element configurations.

The idea of using the interface elements for modelling the bond between concrete and strengthening materials has been transferred from its earlier applications in the simulation of the concrete-reinforcement bond in RC members. Ziraba et al. (1995) chose a six-node steel-glue-concrete interface element to model the epoxy adhesive between RC beams and steel plates. A three-point Gaussian integration rule was used for the element that can pick up not only the normal and shear stress concentrations at the plate curtailment, but is also capable of separation if the peak normal and shear stresses are exceeded. The shear modulus of the interface has been determined from the line relating the average shear stress to slip relationship in experiments. In the modelling of bond between NSM CFRP laminate strips and concrete, Cruz & Barros (2004) implemented a line interface element in the FEMIX computer code. A bond stress-slip relationship was obtained through experimental pullout-bending tests. Then the tangential component of the constitutive law of a line interface element was

defined to simulate the concrete-CFRP bond behavior. To estimate crack spacing and tension stiffening effects in RC members with externally bonded FRP sheets, Sato & Vecchio (2003) used a four-noded joint element to model the bond between concrete and the FRP. The bond characteristic is modelled according to a concept of average bond, i.e. bilinear simplification from bond tests.

In many 2D analyses, several layers of quadrilateral plane elements were also utilized to model the adhesive bond line. The fine mesh across the adhesive thickness makes it possible to investigate the stress gradient in this direction. Either the plane stress or plane strain elements could be found in most commercial FEA packages such as ANSYS, ABAQUS and LUSAS. The elements could be elastic or even have plasticity, creep, swelling, stress stiffening, large deflection, and large strain capabilities. The summary of parametric studies on adhesive joints are given in Table 2-1 to Table 2-4.

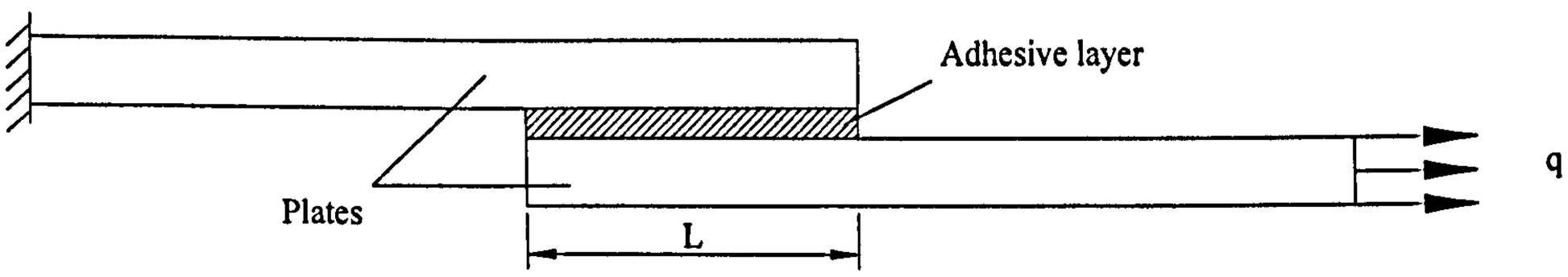

Researcher	Element type for adhesive layer	Parameters
Crocombe (1995)	3 layers of 4-node quadrilateral plain strain element (ANSYS)	
Pandey (1999)	2 layers of 8-node quadrilateral plane strain element	Lap length (L) Adhesive thickness (d) Adhesive tapering
Li (1999)	Various layers of 4-node quadrilateral plain strain element (ANSYS)	Layers of elements across adhesive Adhesive thickness (d) Adhesive elastic modulus (E)

Table 2-1 Single lap joint

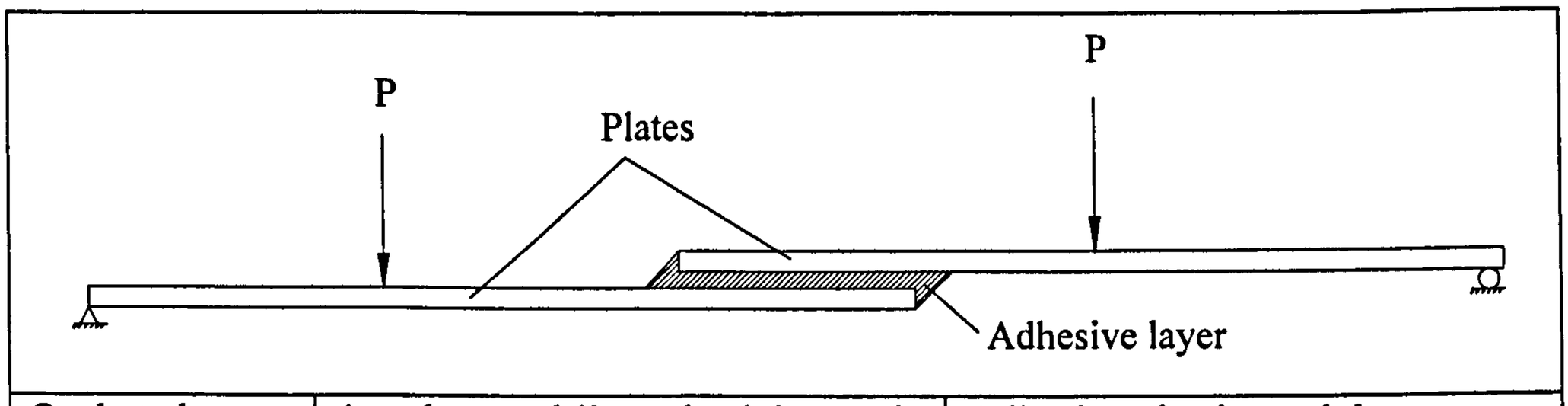		
Ozel et al (2003)	4-node quadrilateral plain strain element (ANSYS)	Adhesive elastic modulus Plate thickness

Table 2-2 Lap joint under four point load

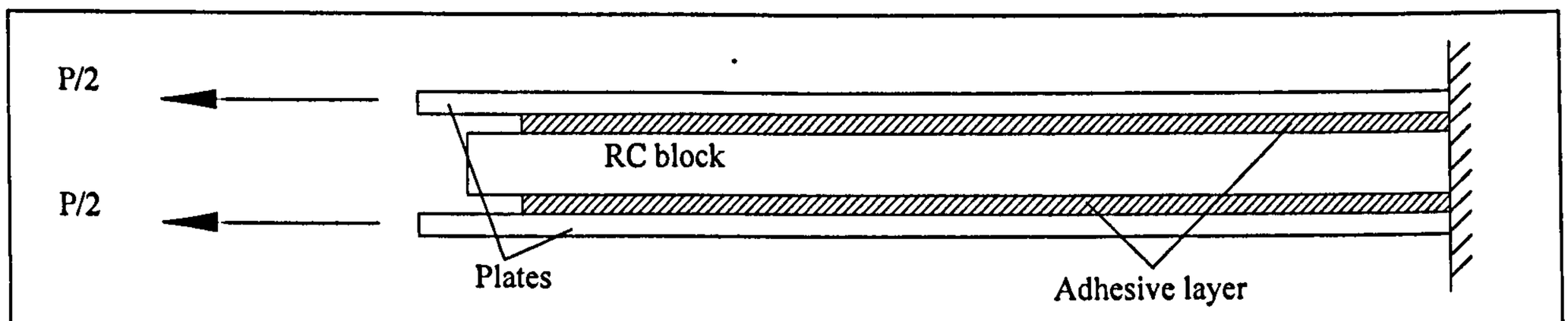		
Barnes et al (2001)	4-node quadrilateral plane stress element (ABAQUS)	Plate thickness Adhesive thickness

Table 2-3 plate bonded RC block

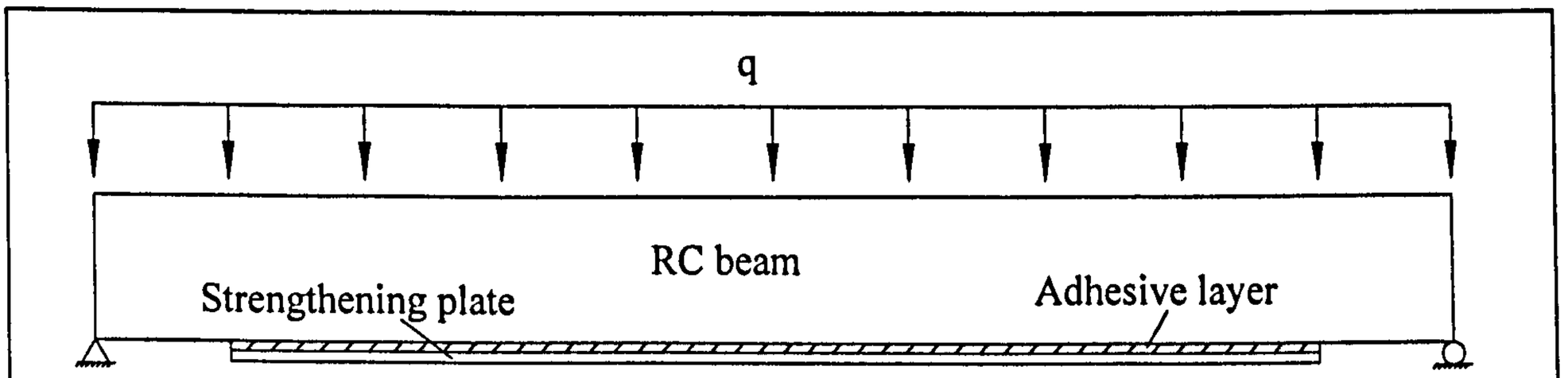		
Teng (2002)	4-node quadrilateral plane stress element (LUSAS)	Adhesive thickness Adhesive elastic modulus Plate thickness Plate elastic modulus

Table 2-4 Simply supported beam

In a few 3D FE analyses, special elements were used to model the adhesive layers. Mahfuz et al. (1998) developed a model idealizing the composite as a regular rectangular array of fibres in $0^{o}/90^{o}$ orientations embedded in the matrix, in which 3D contact elements were introduced between the fibre and the matrix to simulate the interface conditions between the two phases. Slippage between 0^{o} and 90^{o} layers is also considered by introducing another set of contact elements at the layer separation planes. Pandey et al. (1999) presented 3D viscoplastic analysis of adhesively bonded

single lap joint considering material and geometric nonlinearity. The adherends and adhesive layers are modelled using 20-noded solid elements. The constitutive relations for the adhesive is developed using a pressure dependent (modified) von Mises yield function and Ramberg-Osgood idealization for the experimental stress-strain curve.

In the following chapter, verification studies are done by utilising various finite elements, including 2D/3D interface element, 2D plane element and 3D brick element, to investigate their general potential to model the epoxy resin adhesive layer between concrete and FRP. The advantages and disadvantages are discussed. It appears that the 2D quadrilateral plane stress element and 3D brick element show better performance in modelling the adhesive layer rather than 2D/3D interface element because the effects of adhesive through-thickness stress variation can be clearly demonstrated by using a few layers of plane stress or brick elements across the thickness of the adhesive. But the interface element is more suitable for modelling the surface between two materials rather than one certain material such as adhesive, while the surface preferably has no thickness or has much smaller thickness than the surrounding materials.

2.4.3 Analysis of adhesive stress distribution and parametric study

Understanding of stress mechanics in both the adhesive layer and the adherends is essential for the prediction of adhesively bonded joints strength. Although such problem is 3D in nature, it is mentioned by Pandey et al. (1999) and Adams & Peppiatt (1973) that the major stress distributions are not significantly influenced by the transverse stress caused by the effects of Poisson's ratio. Therefore, to reduce the computational efforts, many researches have pursued 2D FE analyses of bonded lap

joints or connections in bending beams.

Crocombe (1995) analyzed FE models for a lap joint by putting three layers of plane strain quadratic elements across the adhesive layer. The resulting peel and shear stress distribution is essentially uniform along the entire overlap length, peaking slightly before dipping at the overlap ends. The stress distributions along the centre of the adhesive layer are compared with a closed form analysis. The correlation between the two shear stress distributions is excellent while that between the peel stresses is reasonable. Given the refinement of the finite element mesh, it is more likely that assumptions made in developing the closed form model (i.e. neglecting adherend shearing and adhesive longitudinal stresses and assuming a constant adhesive stress across the adhesive thickness) are the cause of the mismatch that occurs between the stress distributions.

In practice, joints are made of non-identical components with various thickness, materials, etc, which may play an important role in the distribution and concentration of stresses, as well as the failure mode predictions. It is therefore necessary to achieve a basic understanding of the influences of some important parameters such as lap length, adhesive thickness, adherends tapering, adhesive tapering and relative stiffness of adherends. The summary of parametric studies can be seen in Table 2-1.

In nonlinear FE analysis of adhesively bonded lap joints, Pandey et al (1999) illustrated that an increase in the lap length reduces the maximum peel and shear stress and joint flexibility increases with an increase in the adhesive thickness. It is also observed by Li et al (1999) that the peak shear and peel stress increase with the bond thickness and adhesive elastic modulus. Two interface conditions, namely, infinitely strong and weakly bonded, are considered to establish FE study of the bond

of laminated composites under tensile loading by Mahfuz et al (1998). The strong interface has been observed to agree well with the experimental data.

A study of the adhesive bond stress transfer was undertaken by Barnes et al (2001) in specimens comprising a concrete block with steel plates bonded to two opposite faces using a two part structural epoxy adhesive. He claimed that the shear stress in a steel-to-concrete adhesive joint is distributed exponentially, peaking at the loaded end of the specimen. For the specimen configurations used, the strain was distributed over a 130mm anchorage length. The further parametric study varied the plate thickness and adhesive thickness and it is concluded that the increment of either plate or adhesive thickness led to a general reduction in peak stress levels and an increase in total bond capacity.

Teng et al (2002) investigated interfacial stresses in plate bonded RC beams. The FE results show that stresses vary strongly across the adhesive layer. In particular, near the end of the plate, the interfacial normal stress is tensile along the adhesive-concrete (AC) interface but compressive along the plate-adhesive (PA) interface, offering a plausible explanation for the fact that PA interfacial failure in tests has rarely been if at all reported. A comprehensive parametric study is then presented and the results show the conclusion as following: reducing the thickness of the adhesive layer leads to an increase in both the normal stress and the shear stress; as the elastic modulus of the adhesive is increased, the interfacial normal and shear stresses also increase; an increase in the plate thickness leads to increased interfacial stresses; an increase in the elastic modulus of the plate leads to an increase in the interfacial stresses.

Ozel et al (2003) developed FE analysis of adhesive joints in four-point bending load. Two adhesive, one stiff and one flexible, and hard steel as adherend with four

different thicknesses, were analyzed. It was shown that while the stiff adhesive gave stronger joint strength when using thick adherends, the opposite was the case for the flexible adhesive when using thin adherends.

Computational models for reinforced concrete beams strengthened by epoxy bonded steel plates of various thicknesses were presented by Ziraba et al (1995). It is illustrated that as the plate thickness is increased, depth of flexural cracks in concrete is reduced but with accompanying increase in zone of cracking along length of beam.

It can be seen from the above literature review, most FE analyses have been focused on the 2D modelling of members strengthened by externally bonded plates. As discussed earlier in this chapter, the NSM strengthening technique is also important and needs further investigation. Therefore, one essential emphasis of this PhD study is to investigate the mechanics of stress transfer in NSM strengthened members.

2.4.4 Strengthening of cracked structures (influence of initial imperfections)

In practice, there are imperfections in the FRP-to-concrete connection caused by workmanship errors during implementation of the FRP strengthening scheme, shrinkage of the adhesive and so on. Under load, high bond stress concentrations can arise near the edges of the imperfections, which can potentially lead to reduced separation failure loads. In spite of this, an extensive search of the literature revealed no documented work on the likely influence of bond imperfections on the failure behaviour of plated concrete members. Part of the reason for this may well be that the high levels of quality control employed in fabricating lab specimens result in negligible bond imperfections in those specimens. Even so, there must be some variability in the levels of quality control adopted in different labs worldwide, and so

it may be that significant imperfections have arisen in many lab specimens which have been reported on in the literature.

Clearly, an understanding of the effect of the imperfections is crucial for achieving appropriate levels of quality control on the plate bonding process to be developed. Besides, it will also enable safe, informed, economic decisions to be made in practice on the effects of such imperfections. In particular, a brittle separation failure mode, due to elasto-plastic activity at the inner ends of the shear spans, could well be critical in the presence of defects, and so an understanding of the influence of defects in this region was of interest in this study. *Therefore, another major emphasis of this PhD study was to investigate the influence of bond imperfections on separation failure behaviour of FRP-plated concrete members.* These investigations are reported in Chapter 6.

2.5 Conclusions

From the discussions of this chapter, the following points have emerged:

- Brittle fracture of the connection is common in the failure of FRP strengthened concrete members. By far most of the research to date has focussed almost exclusively on identifying the detailed mechanics of *end-peel* separation failure, with other equally critical modes receiving relatively little attention. ***As a result, much work remains to be done to properly understand the mechanisms of these other modes. In this thesis, use of a novel pullout test to understand both the mid-span debonding and end-peel failure modes is presented.***
- Understanding of **stress distributions** in the adhesive layer as well as the adherends is essential for the prediction of joint strength. By using multi-layer plane or brick elements across the adhesive layer, it is found that the peel and shear stress vary

strongly with the stresses along the adhesive-concrete interface being very different from those along the plate-adhesive interface, which gives insight to the failure behaviour of the strengthened concrete specimens. ***Much of the work has been done on the FRP plated concrete beam, while the stress transfer along the bonding line of near-surface mounted concrete members and FRP decks which remain less investigated.***

- Various finite elements, including 2D/3D interface element, 2D plane element and 3D brick element, have been investigated for their general potential to model the epoxy resin adhesive layer between concrete and FRP. The advantages and disadvantages are discussed. It appears that ***the 2D quadrilateral plane stress element and 3D brick element show better performance in modelling the adhesive layer rather than 2D/3D interface element because the effects of adhesive through-thickness stress variation can be clearly demonstrated by using a few layers of plane stress or brick elements across the thickness of the adhesive.***
- Imperfections can arise in the adhesive connection layer and concrete members for a variety of reasons. ***Therefore, an experimental program and FEA of beams with initial imperfections, such as adhesive debonding and concrete cracks to address this issue is therefore timely.***

These outstanding issues have guided the approach adopted in the present PhD study. In the following chapter, a detailed study is presented to verify the FEA package used in this thesis. This study establishes the relative levels of reliability of different elements for modelling the structural action of the adhesive layer. Chapter 4 describes the experimental work conducted within this study to properly understand the mechanics of stress transfer between NSM FRP bars and concrete. The present experiments look at both end-peel and mid-span debonding failure mechanism while

most of the previous lap shear tests investigate end-peel debonding only. The specific designs of specimens for such modelling and relevant experimental results are also addressed in detail. FE analysis for the test samples is then presented in chapter 5, in which the FEA technique discussed in chapter 3 is used. In chapter 6, the FEA technique was further employed to reveal the stress transfer mechanism of adhesive bonding layer in the beams with initiated flexural/shear cracks and the beams under temperature loads. Finally, Chapter 7 summarises the main findings of this thesis and puts forward suggestions for extension of this work.

Chapter 3

Details and verification of finite element analyses

3.1 Introduction

The finite element (FE) analysis method is a powerful tool for simulating the behaviour of RC structures. As discussed in Chapter 2, many linear and nonlinear FE analyses have been carried out on the study of adhesive joints' stress transfer in RC structures strengthened with steel or FRP materials. However, previous work has been directed largely at structures reinforced by externally bonded reinforcing (EBR) plates, with much less research on strengthening by *near surface mounted* (NSM) bars. Therefore it is essential to study the interfacial stress transfer behaviour between FRP and anchoring materials in NSM strengthened members. In addition, for the members strengthened via either the NSM or EBR approach, on important topics such as the *mid-span brittle separation* failure mode of strengthened RC structures and *through-thickness variations* of stress in the adhesive near discrete cracks in zones of significant flexure and shear, further deeper research is required. In the present study, these topics are explored in detail via the FEA commercial package, DIANA, in Chapters 5 and 6.

The level of success achieved in predicting mechanical characteristics of strengthened RC structures through FEA can be very dependent on the adoption of suitable models to account for bond stress concentrations and distributions along the adhesive layer. By employing suitable elements and material properties, along with appropriate fine meshes at critical zones, the FE approach may well find a reliable application for assessing structural action. It is thus important to establish the relative levels of reliability of different elements for modelling the structural action of the adhesive connections.

To that end, this chapter presents the FE modelling techniques used in the present PhD study and it presents a verification study of the FE analysis. In the following sections, the elements and associated material properties are described. In particular, the interface elements, the plane stress elements, and the brick elements which are alternately used to model the adhesive layers are described. The geometries and FE meshes of strengthened RC members used to illustrate these ideas are presented. Then the FEA results are compared with experimental and theoretical data previously published. Finally, conclusions are drawn.

3.2 Finite element modelling

3.2.1 Choice of elements

As discussed in Chapter 2, the action of plated RC beams and lap joints under load is largely 2D. Therefore, 2D FE models of these members have been constructed and analysed in this thesis. The concrete member and attached plate are each simulated, in their vertical planes, by the four-noded quadrilateral iso-parametric plane stress element Q8MEM (Figure 3-1 Element Library, DIANA 8.1). The basic variables of Q8MEM are the translations of the nodes in two directions.

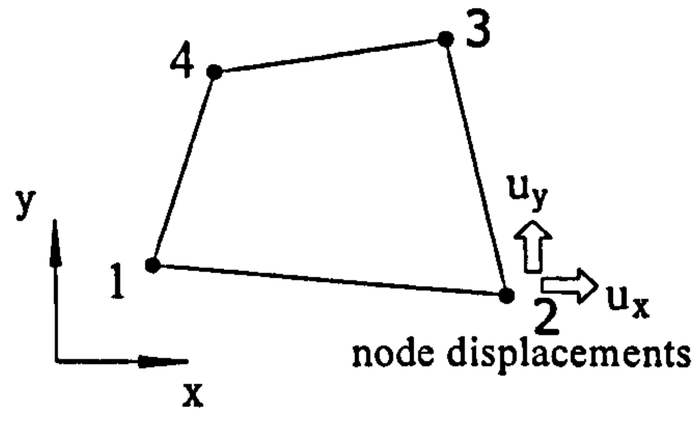

Figure 3-1 Q8MEM element

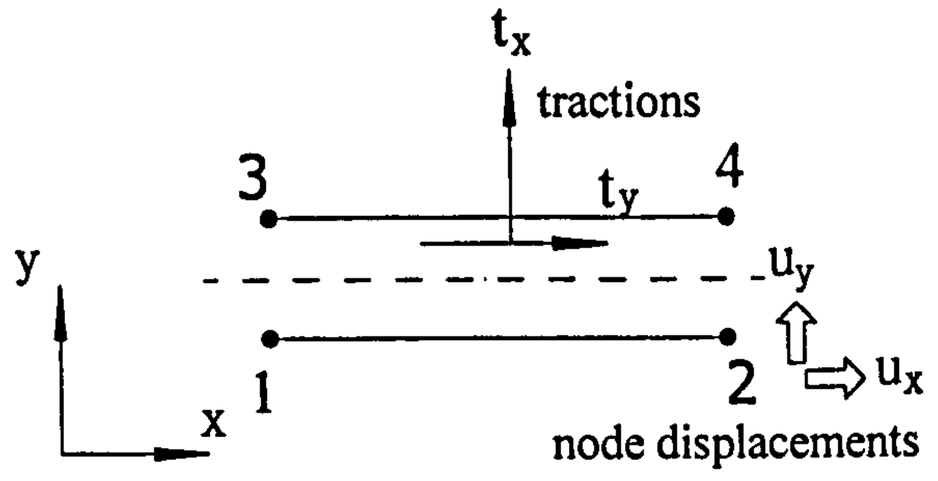

Figure 3-2 L8IF element

For the adhesive layer, two types of elements have alternatively been used in the present study. One of the choices is the L8IF element which is an interface element between two lines in a 2D configuration (Figure 3-2). This interface element incorporates a relation between the normal and shear tractions and the corresponding relative displacements across the interface. In the FE model, the nodes of the L8IF element were connected to those of adjacent concrete and steel rectangular Q8MEM elements as illustrated in Figure 3-3.

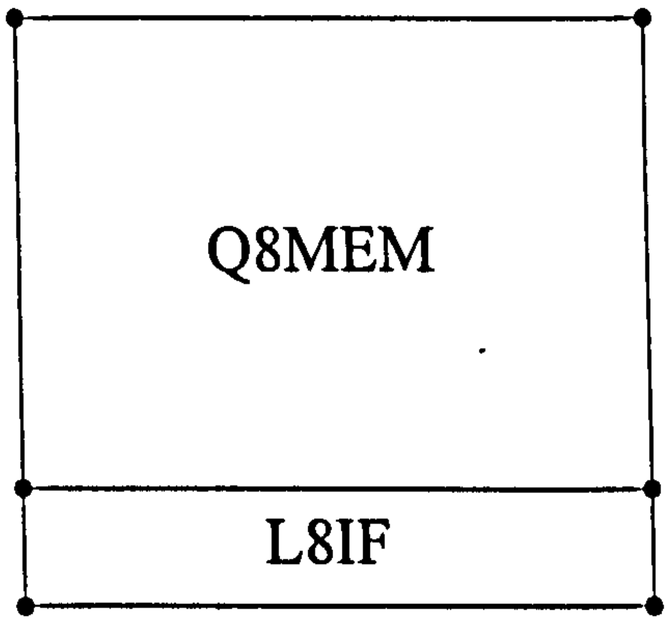

Figure 3-3 Connection between L8IF and Q8MEM elements

The second choice is using the same Q8MEM element as for concrete and plate members. In this case, by employing a few layers of plane stress elements through the thickness of the adhesive, it is possible to demonstrate through-thickness adhesive normal and shear stress variations, especially at certain critical positions, such as the

ends of the adhesive layer or the bond near cracks in the concrete beam, which are the zones of connection stress concentration.

In other cases, such as for RC members strengthened with NSM FRP bars, 3D actions within the adhesive connection constitute an important facet of load response. For example, cross sectional shrinkage of the bars due to lateral Poisson's ratio effect from longitudinal tensile stress can cause cracks in the adhesive and concrete around bars. Therefore, it is necessary to employ 3D modelling for these members. In the 3D modelling, the concrete prism, FRP bars and epoxy adhesive were modelled by the eight-noded brick element HX24L (Figure 3-4) or six-noded brick element TP18L (Figure 3-5). The basic variables in the nodes of solid elements are the translations of the nodes in three directions. Using multi-layer brick elements instead of interface elements for the adhesive layer can capture the through-thickness stress variation.

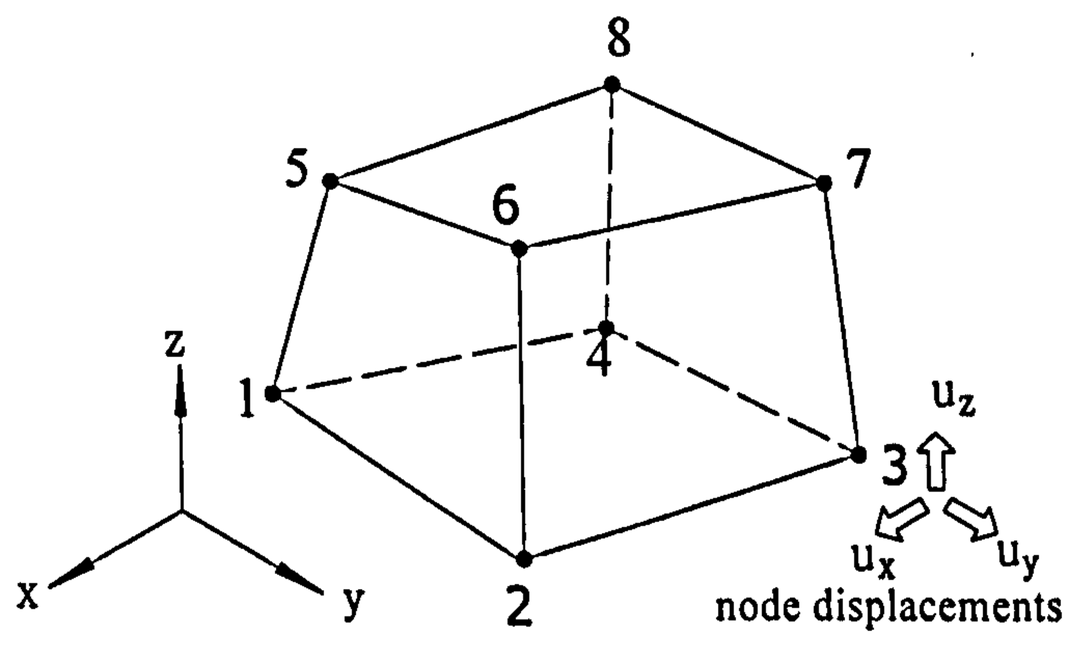

Figure 3-4 HX24L brick element

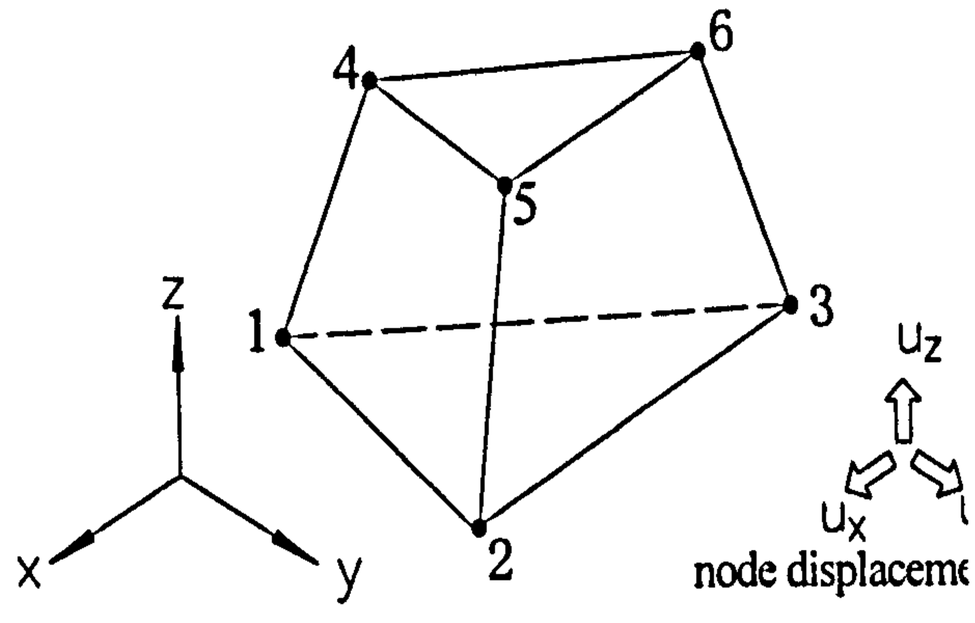

Figure 3-5 TP18L brick element

3.2.2 Material properties

3.2.2.1 Steel and FRP

For the reinforcing steel bars and bonded steel plates, a linear elastic-plastic model as used both in tension and compression, with the Von Mises yield criterion. The uni-axial stress-strain relationship is shown in Figure 3-6.

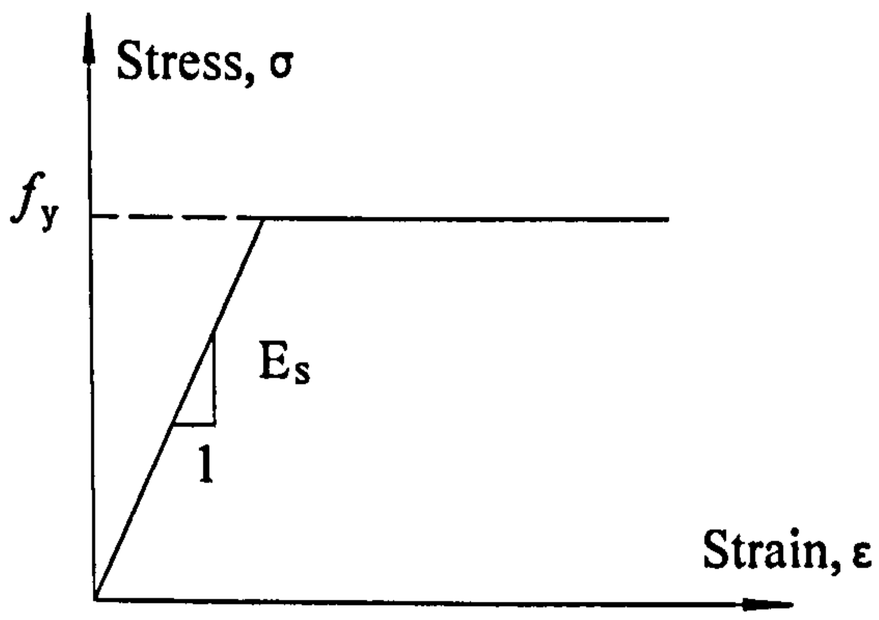

Figure 3-6 Elastic-perfectly plastic model for steel

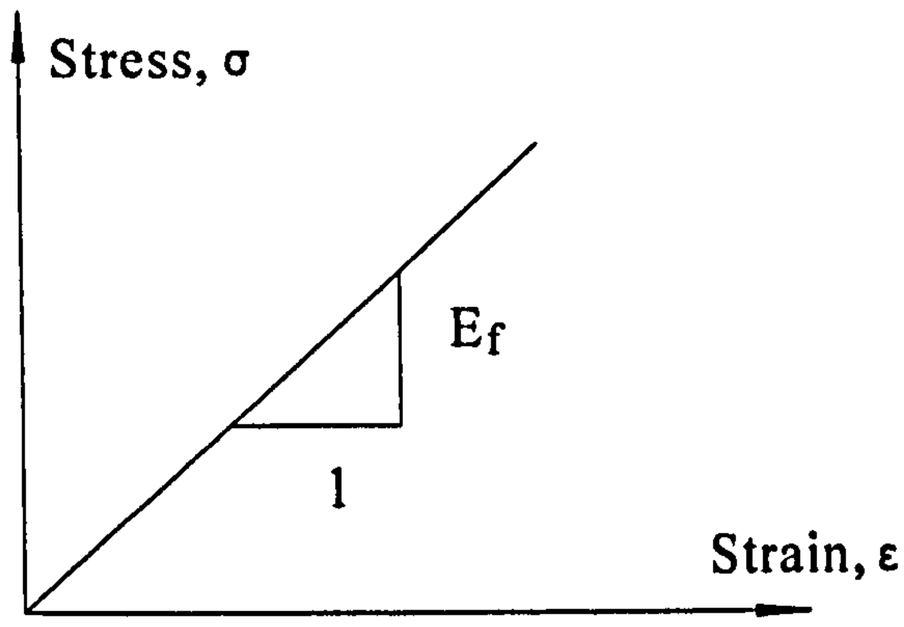

Figure 3-7 Elastic model for FRP

FRP plates or bars generally behave in a linear elastic fashion until rupture. In practice, FRPs are mainly used to carry the tensile stress along their longitudinal direction in the strengthened beam. Hence linear elastic behaviour was assumed for the FRP, as shown in Figure 3-7.

3.2.2.2 Concrete

To model the nonlinear behaviour of concrete structures, DIANA offers a broad range of constitutive behaviours for quasi-brittle materials. In the present study, smeared cracking first proposed by Litton (1974) is applied to the modelling of concrete. Cracking is specified as a combination of tension cut-off, tension stiffening and shear

retention. Actual values are presented along with other relevant details for the examples used to verify the program.

The tension-stiffening curve in Figure 3-8 is based on fracture energy by the definition of the crack bandwidth of the element, for which DIANA assumes a value related to the area or the volume of the element. This method is useful for reducing mesh dependency problems (Bazant (1983)).

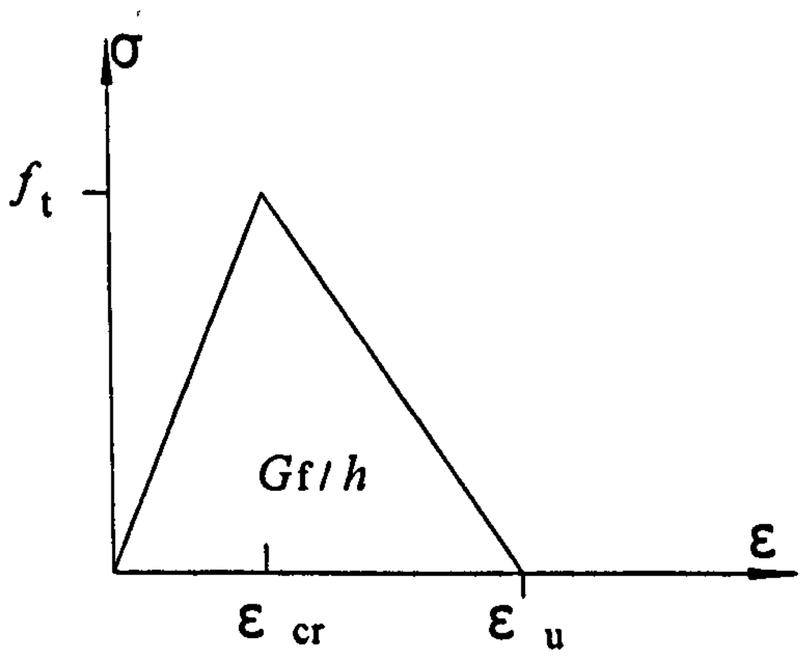

Figure 3-8 Linear tension stiffening in smeared cracking

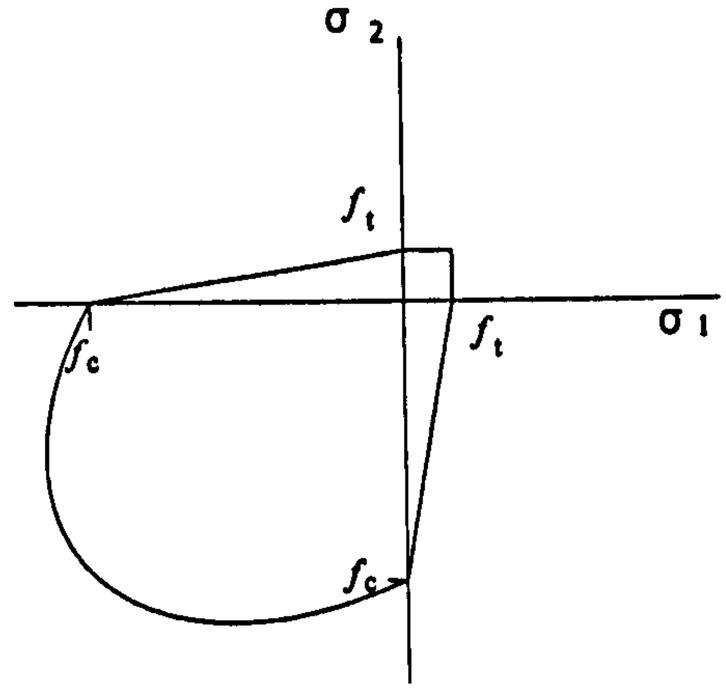

Figure 3-9 Combination of linear tension cut-off in and compressive plasticity model in 2D principal stress space

The following equation is normally taken to calculate the ultimate concrete strain ε_u:

$$\varepsilon_u = 2G_f / f_{tc}h \qquad \text{(Equation 3-1)}$$

where f_{tc} is the tensile strength of concrete. However, the fracture energy G_f and the estimated numerical crack bandwidth h are difficult to be measured and sometimes are not available from test data. Therefore, the ultimate strain ε_u is taken as 5 to 10 times of the crack strain ε_{cr} which has been defined as:

$$\varepsilon_{cr} = f_{tc} / E_c \qquad \text{(Equation 3-2)}$$

The combination of tensile and compression stresses can be modelled with a multi-surface plasticity approach, available for biaxial stress states, as shown in Figure 3-9. However, in analyses where tension and compression arise simultaneously in one particular stress point, these models may lead to numerical oscillation, especially in plane stress situations. In addition, a pure "compression" failure of concrete is unlikely. In a compression test, the specimen is subjected to a uniaxial compressive load, with tensile strains induced by Poisson's effect occuring perpendicular to the load. Because concrete is relatively weak in tension, these actually cause cracking and the eventual failure (Mindess & Young (1981), Shah et al. (1995)). Therefore, in this study, the crushing capability is turned off and cracking of the concrete controls the failure of the finite element models.

3.2.2.3 Adhesive layer and interfacial model

As stated before, there are two types of elements, namely the plane stress element Q8MEM and the interface element L8IF, available in DIANA for 2D analysis of the adhesive layer.

For the model in which the adhesive layer is represented via plane stress element, the smeared cracking model (similar to that used for concrete) is applied. For the other 2D model, the line interface elements are used for the relationship between debonding and slipping behaviour (displacement in shear direction and normal directions). In order to calibrate the FE model with the experimental results, the initial shear and normal stiffnesses of the interface elements varied between 100 and 300 N/mm^2. The chosen shear stiffness value was assumed and kept constant throughout the linear and the nonlinear analyses. The normal stiffness is represented based on the linear

elasticity and linear tension softening (Figure 3-10). The value for the maximum bond stress was accepted as 5 N/mm^2 in the linear zone.

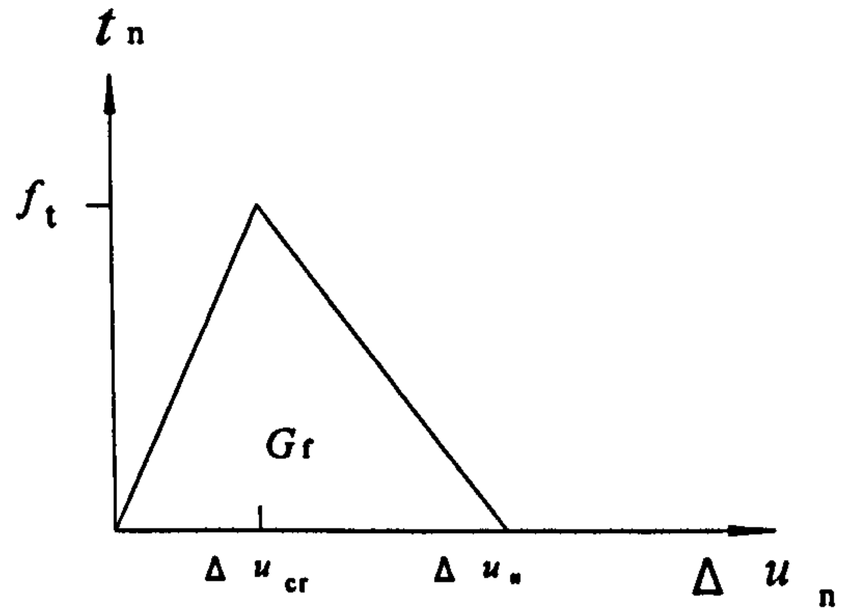

Figure 3-10 Linear tension stiffening for 2D interface element

3.2.3 Convergence techniques and mesh configuration

Energy convergence criteria are used in all of the verification studies. Also, the arc length method was combined with the constant stiffness method as this was found to give the most stability to the computation.

To accurately simulate the complicated fracture behaviour involving concrete cracking and interfacial debonding, a proper mesh needs to be used. Too coarse a mesh may lead to inaccurate results, while too fine a mesh may require more computation time. In order to achieve a comprehensive understanding of adhesive behaviour, finer meshes are used through the thickness of the adhesive layers, near the ends of the adhesive layers and near cracks in the concrete member. To minimize problems with ill conditioning, gradation of meshes was employed near discontinuities, with a fine mesh immediately adjacent to the discontinuities and gradually increasing mesh size as distance from the discontinuity increases.

3.3 Verification study

Four numerical experiments were conducted with the FEA package DIANA to establish the validity and degree of accuracy of the analytical models used in this study. The examples include a 2D model of a plated RC beam, a 2D model of a FRP-concrete lap shear test, a 2D model of a FRP composite bridge deck and a 3D model of a concrete block with a NSM FRP bar. To that end, in what follows, the FE results are compared with published experimental data and also with theoretical data published by other researchers. Unless stated otherwise, the term predicted is used to describe results obtained from the present FE study, while the term measured is used to describe the data obtained from the actual laboratory experiments conducted.

3.3.1 Steel plate bond to concrete beam (Roberts & Haji-Kazemi (1989))

3.3.1.1 Geometry and loading

A simply supported concrete beam was reinforced with externally bonded steel plate and was analysed under UDL first by Roberts & Haji-Kazemi (1989), then by Teng et al. (2002) and Shen et al. (2001). The geometric and material properties are shown in Figure 3-11.

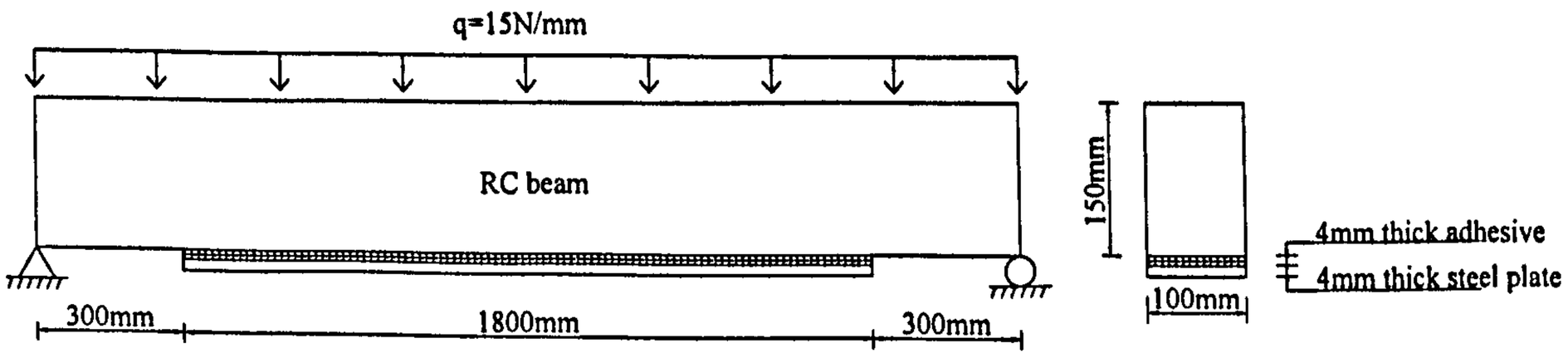

Figure 3-11 The RC beam with externally bonded steel plate under UDL

For the FE model of the beam, interface element L8IF and plane stress element Q8MEM were alternatively used to model the adhesive layer. The corresponding results are referred to as the Interface Element Model (IEM) and Plane stress Element Model (PEM) results respectively. The number of elements used across the adhesive layer for both element types was, respectively, 1, 4 and 16. In the horizontal direction, a graded mesh was used with the fine mesh near the plate end. Figure 3-12 shows the FE model with the finest mesh.

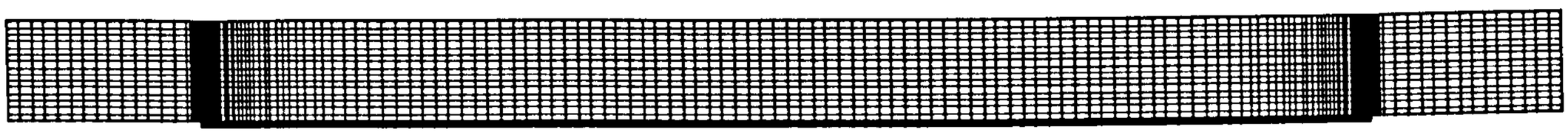

Figure 3-12 Finite element model of steel plate bonded concrete beam

The material properties are summarised as follow:

Concrete beam: $E_c = 20$ kN/mm^2, $\nu_c = 0.2$

Steel plate: $E_s = 200$ kN/mm^2, $\nu_s = 0.3$

Adhesive: $E_a = 2$ kN/mm^2, $\nu_a = 0.25$

3.3.1.2 Non-uniform Through-thickness Effects in Adhesive layer

The approximate analytical solution by Roberts & Haji-Kazemi (1989) assumes a uniform through-thickness stress distribution for both the normal and shear stresses in the adhesive layer, and so leads to monotonically increasing interfacial shear stresses from the mid-span of the beam towards the plate end, with a maximum value at the plate end. However, the normal and shear stresses do vary across the thickness of the

adhesive layer, especially near the ends of the plate. Such variations cannot be captured by the approximate analytical solution.

For example, the normal stress near the plate end is tensile at the adhesive-concrete (AC) interface but compressive at the plate-adhesive (PA) interface, which gives a plausible explanation for the fact that most interfacial failures in tests reported lay on the AC interface rather than the PA interface (Jones et al. (1988), Roberts & Haji-Kazemi (1989), Oehlers & Moran (1990), Ross et al. (1999)). The shear stress in the adhesive layer also varies significantly, particularly near the two interfaces. At the mid-thickness of the adhesive layer, the shear stress tends to zero at the plate end as expected. The divergent stresses may be due to the stress singularity on the two interfacial surfaces at plate ends. By using the finest mesh, such effect is limited to tiny zones near the singularity points. Therefore, the results from the finest mesh model are believed to be the most accurate obtained from such model.

The FE results are then compared with Shen et al's (2001) high-order analytical solution assuming linearly varying interfacial stresses through the thickness of the adhesive layer in Figure 3-13. In this thesis, tension is positive and compression is negative for the normal stresses. The FE predictions are seen to agree well with the comprehensive analytical predictions in general, with some differences occurring within the vicinity of the plate end.

For the normal stresses, the FE model gives very good agreement with Shen et al's (2001) analytical solution on AC interface. The two peak values are slightly different, with the FE model value being higher. Shen et al's (2001) solution predicts that the normal stress on PA interface is smaller than that on AC interface and stays tensile (positive). The FE model also predicts the divergence between AC and PA interface

but shows that the normal stress on PA interface is compressive (negative) as stated before. For the interfacial shear stresses, those predicted by Shen's solution are almost identical for the PA interface and the AC interface. They increase towards the plate end but then reduce rapidly to zero at the plate end, complying with the stress-free boundary condition. The FE model predicts the exact same tendency for shear stress on PA interface and middle-adhesive (MA) section, except there is divergence on AC interface due to singularity effect there.

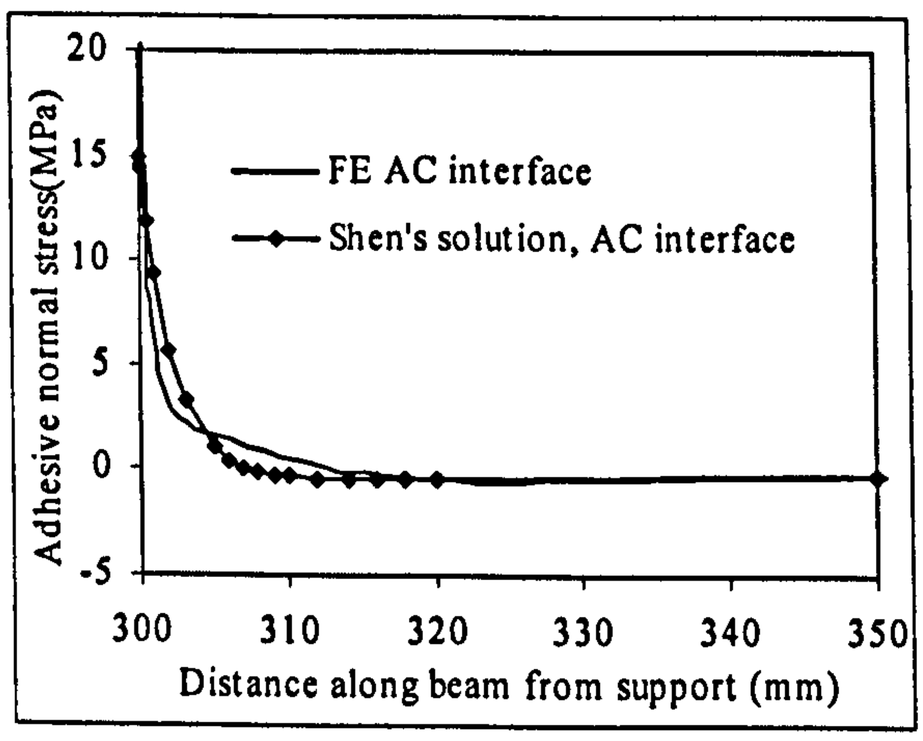

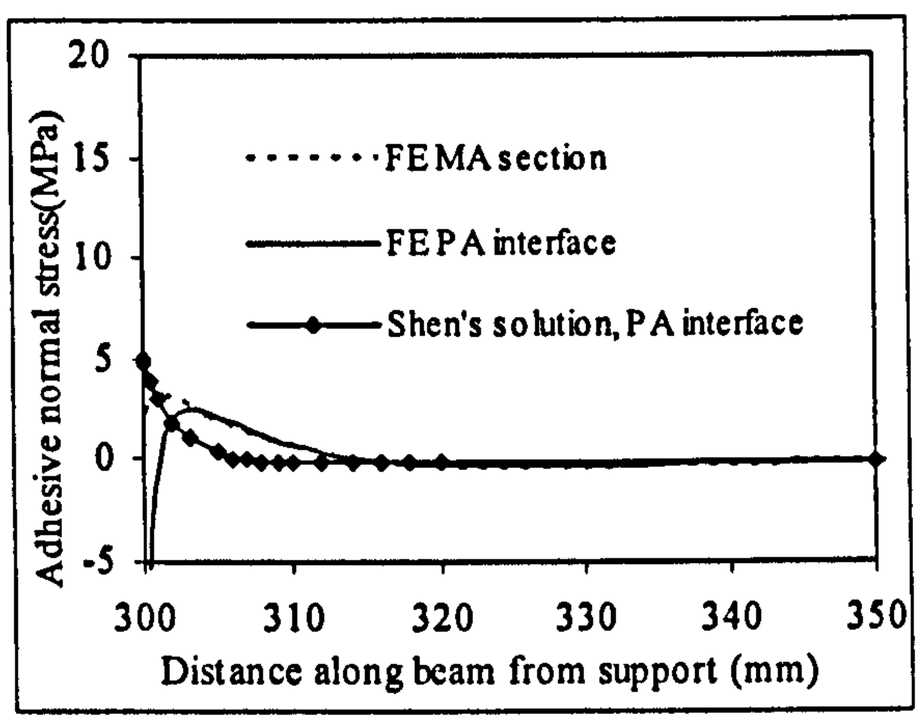

(a) Adhesive normal stress distribution

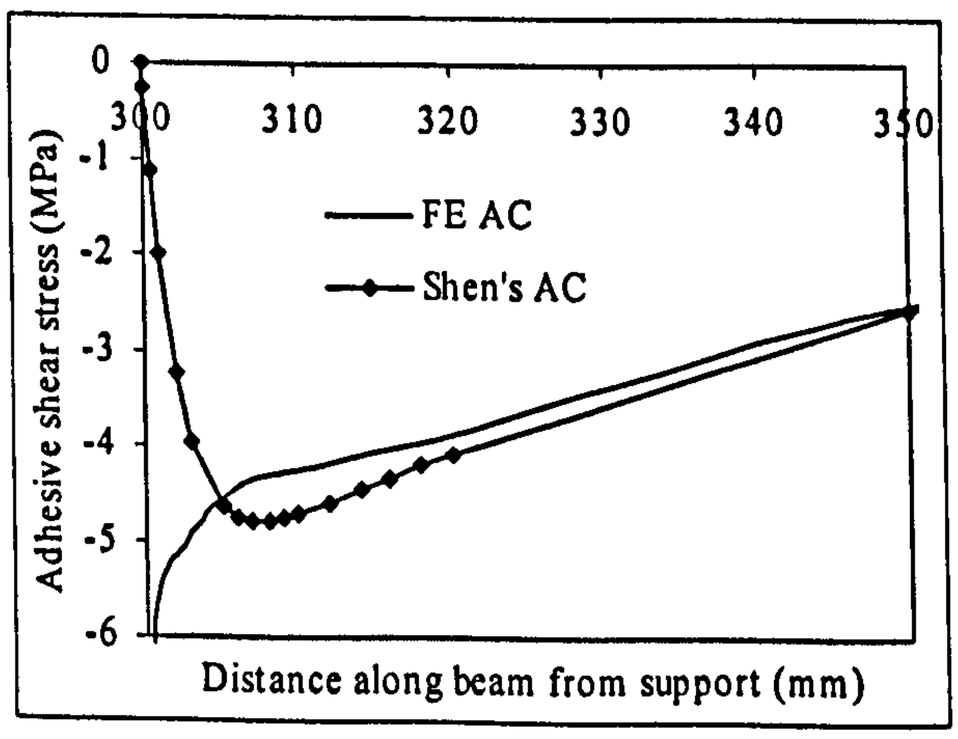

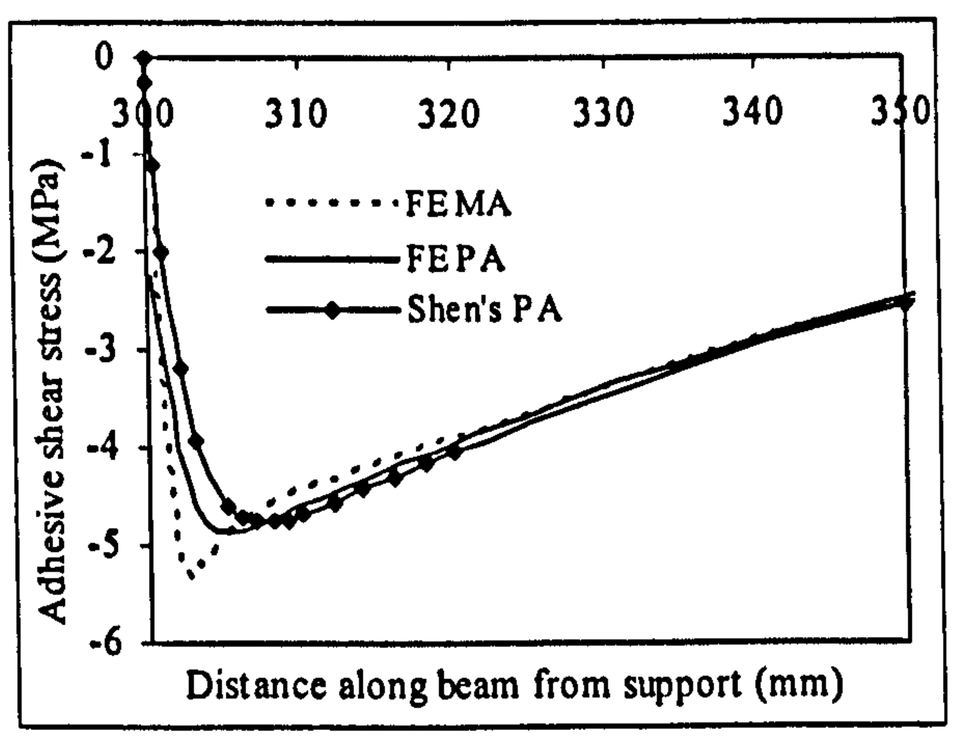

(b) Adhesive shear stress distribution

Figure 3-13 Adhesive stress comparison between FE model and Shen's solution

The reasonably close agreements between the FE results and the analytical results prove the validity and reliability of the FE model used in the present study. It is then

possible to use this FE technique to predict the important structural behaviour in the critical zones not only near plate ends but also near cracks in the cracked beam. Based on the prototype of this beam, two types of cracked beams, namely flexure-cracked beam and shear-cracked beam, are presumed and modelled via the FEA package later on in this thesis. The flexure-cracked beam is modelled by putting three vertical cracks at the mid-span area while the shear-cracked beam is modelled by putting an inclined crack near plate end. Mechanical behaviour of these beams are analysed and predicted in detail in Chapter 6.

3.3.1.3 Convergence investigation

More than one layer of elements has been used across the thickness of adhesive, to reveal the variation of adhesive stresses at different thickness positions. In this section, the reliability and convergence of multi-layer Interface Element Models (IEMs) and Plane stress Element Models (PEMs) are investigated.

For the IEMs, the FE results show that both the normal and shear stresses of the adhesive in each layer are exactly the same in value with other layers, which is not in line with the results of more reliable analytical treatments of the problem. As a result, it is not possible to investigate the adhesive stress variations at different thickness positions by using multi-layer IEMs.

Moreover, as shown in Figure 3-14, the IEMs with different numbers of elements through-thickness adhesive layers give very different results from each other for both the adhesive normal and shear stress. It indicates that results from IEMs may not converge so that they are not stable and reliable. The reason for such divergence may be due to the interface element's basic property that represents the relation between the traction and the nodal relative displacement. Due to such property, interface

element is suitable for modelling the surface between two materials rather than one certain material, while the surface preferably has no thickness or has much smaller thickness than surrounding materials. However, in this case, the adhesive layer is 4mm and as thick as the bonded plate. Therefore, it is better to model the adhesive layer as one certain body with volume and material property rather than the surface between concrete beam and steel plate.

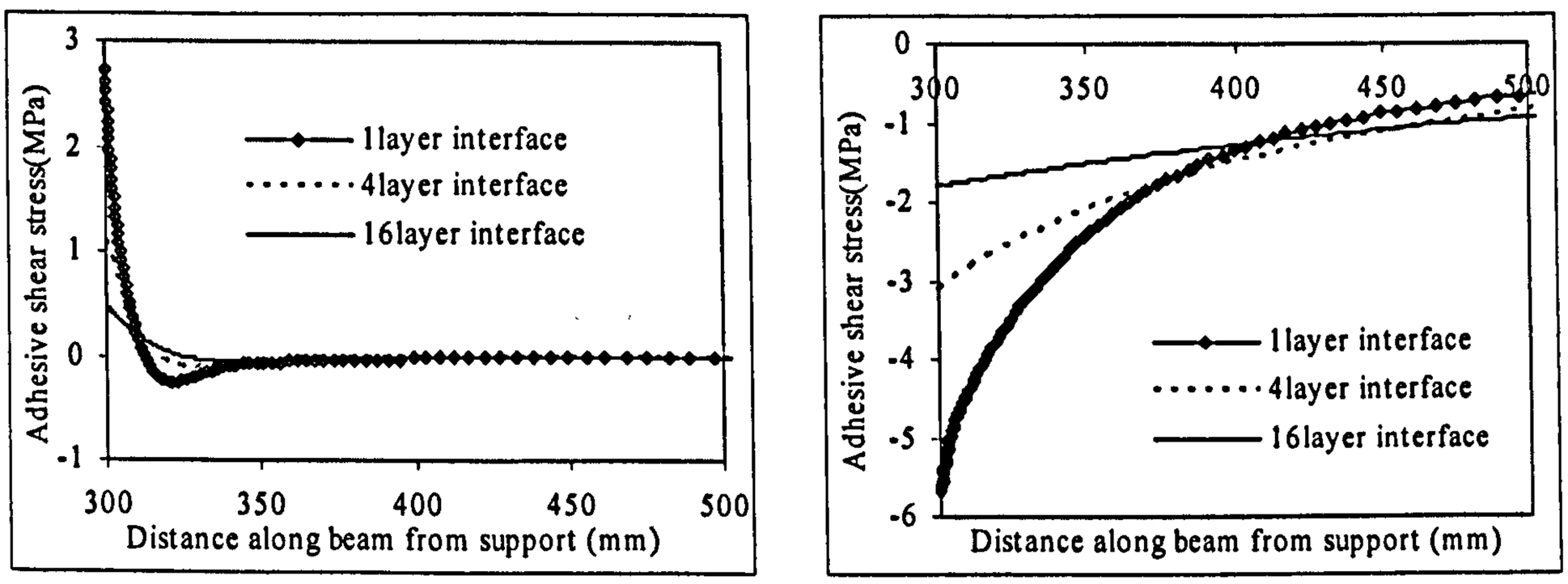

(a) Normal stress distribution (b) Shear stress distribution

Figure 3-14 Detailed adhesive shear stress distribution near plate end for IEMs

The multi-layer PEMs were also analysed and the average values of results are compared in Figure 3-15. Both the normal and shear stress distributions from these three models show good agreement with each other along the plate length, which indicates the convergence among PEMs. At the ends of the adhesive along the beam length, which are the critical zones of connection stress concentration, the multi-layer PEMs work better than the mono-layer PEM. The analysis from the multi-layer PEMs show the right tendency that the shear stress turns down towards zero near plate curtailment, which closely satisfies the stress-free boundary condition at the ends of the adhesive layer.

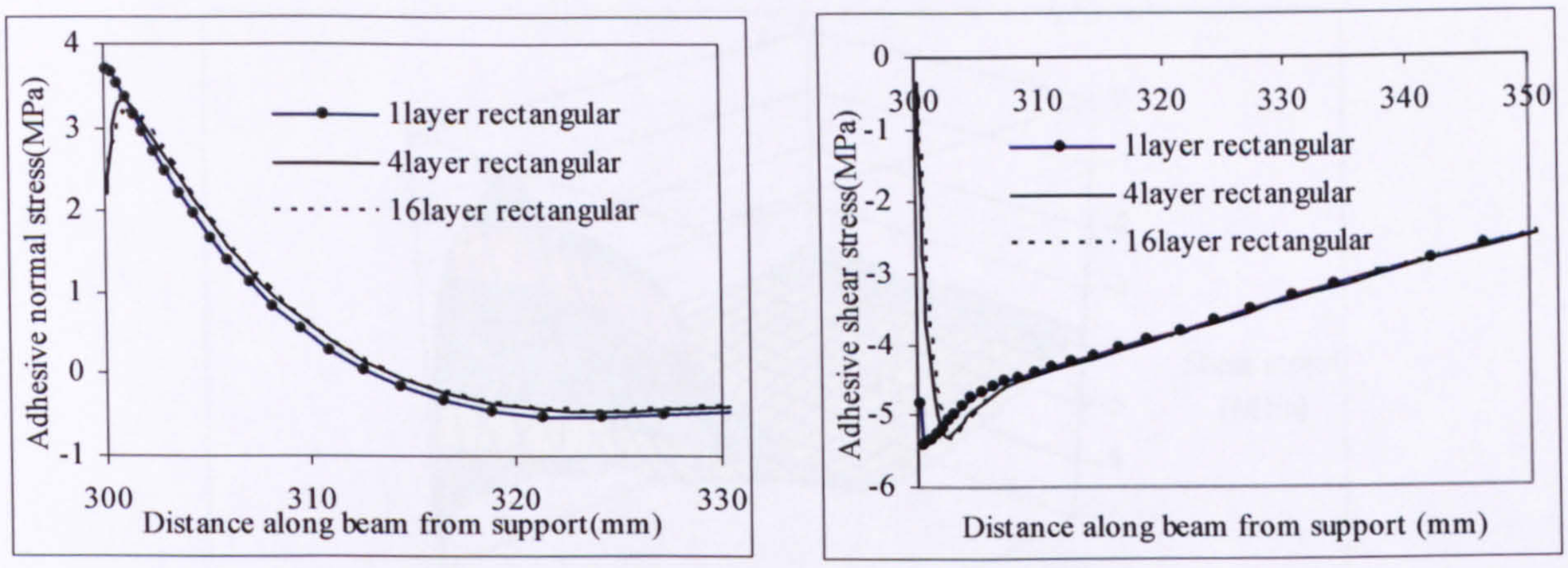

(a) Normal stress distribution (b) Shear stress distribution

Figure 3-15 Adhesive stress distribution near plate end for PEMs

In the present study, important information on interfacial behaviour of adhesive can be obtained by examining the results based on the PEM with finest mesh. Figure 3-16 demonstrated in 3D the complex variations of both normal and shear stresses across the adhesive layer thickness in the vicinity of the plate end respectively. It can be seen that both the normal and shear stresses vary strongly across the thickness of the adhesive layer in the vicinity of the plate end but are uniform at a small distance from the plate end.

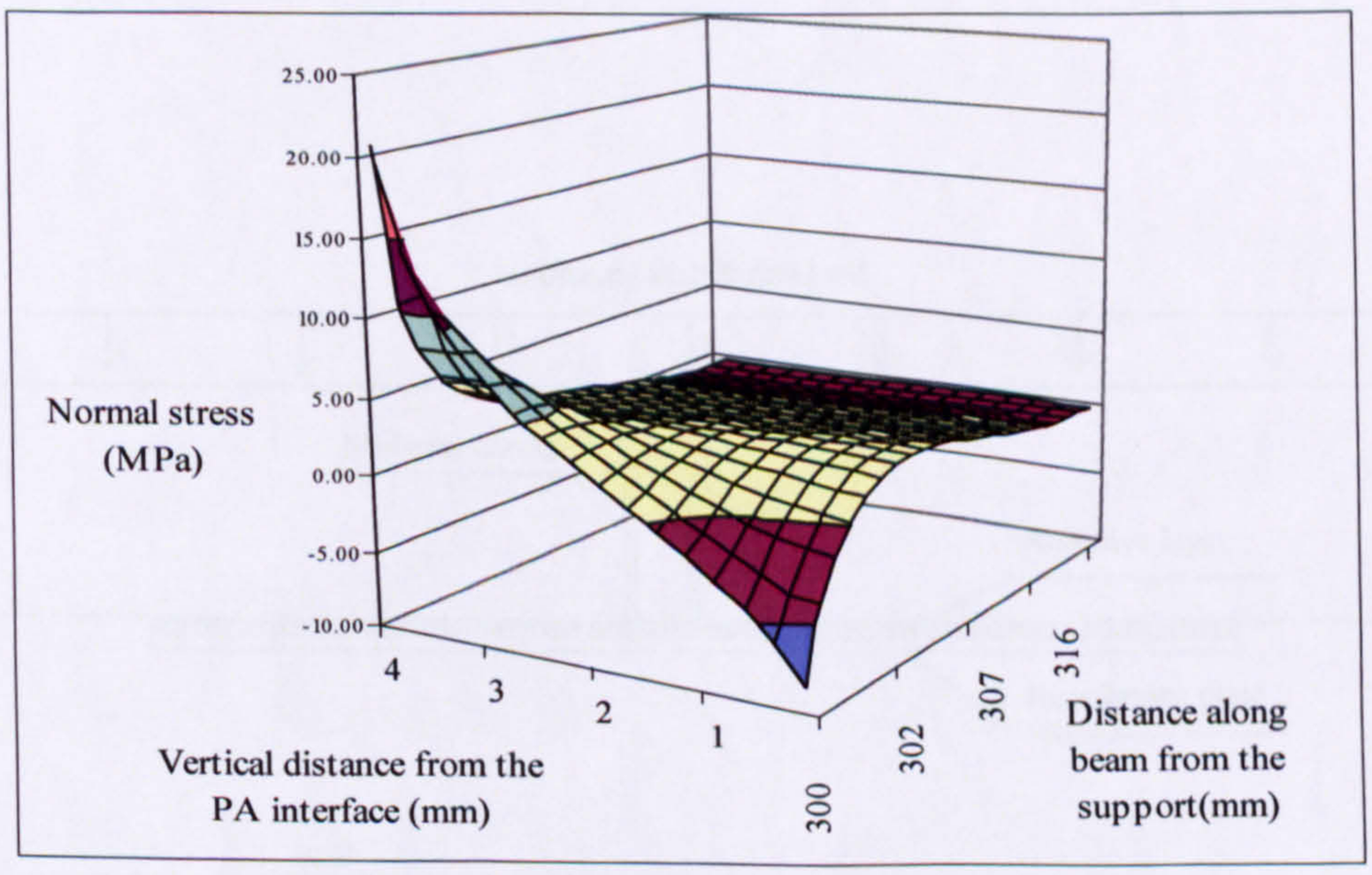

(a) Normal stress

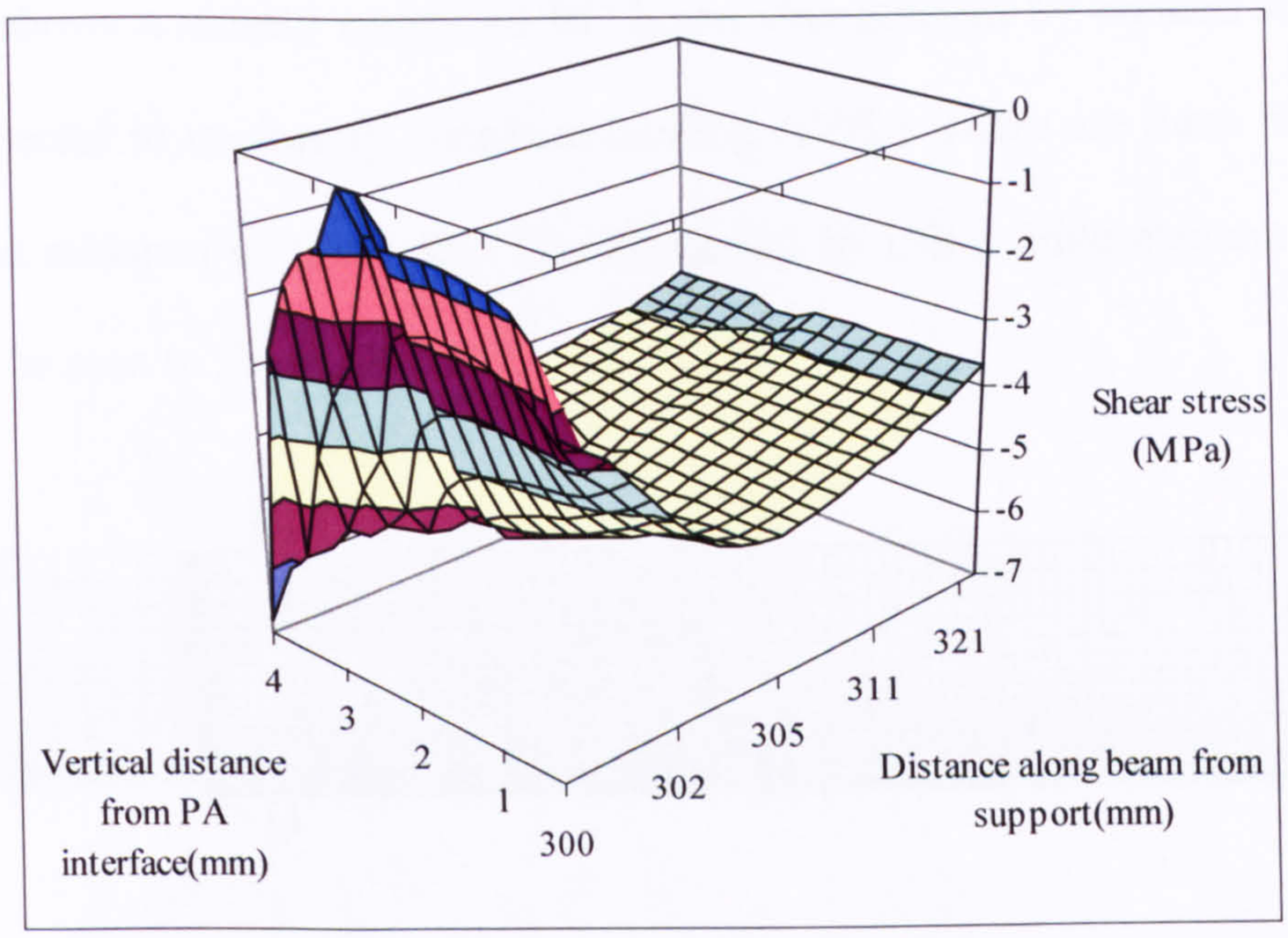

(b) Shear stress

Figure 3-16 3D views of stress distributions in the adhesive layer

3.3.1.4 Equilibrium check

In the present study, the element aspect ratio is as high as 16 in some areas. It was therefore considered essential to perform equilibrium and other checks on the FE output to establish whether these high aspect ratios had an adverse effect on the results.

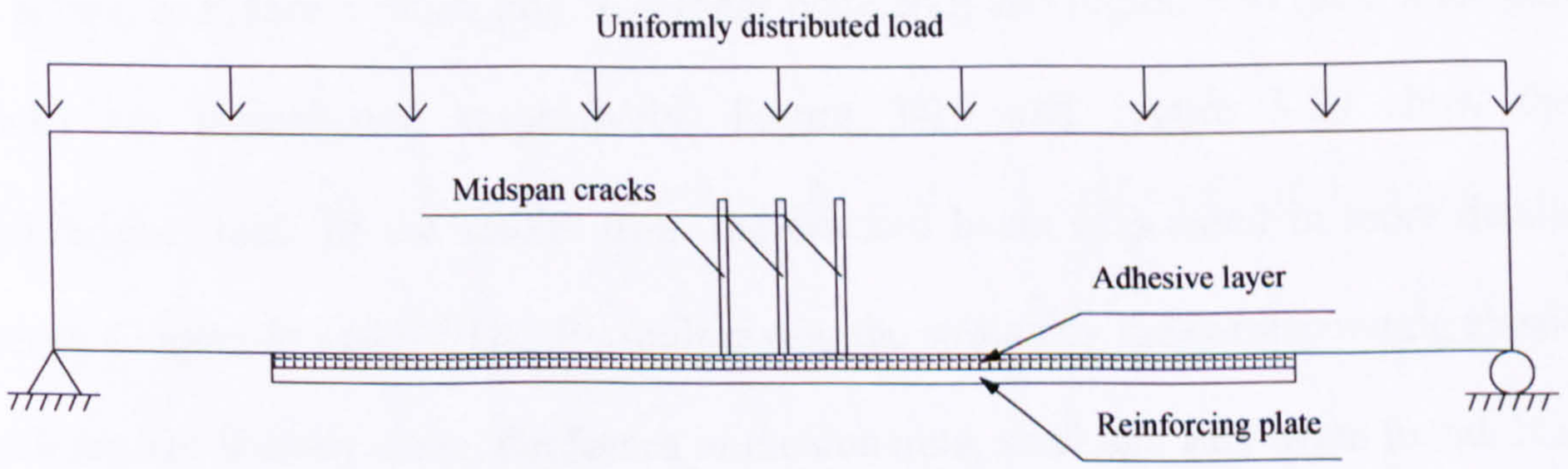

Figure 3-17 Cracked concrete beam strengthened by bonded plate under UDL

Figure 3-17 shows a simply supported RC beam strengthened by bonded steel plate and was subjected to uniformly distribute loading (UDL). There are three pre-cracks located in the midspan of the beam. The FE model by using finite element package DIANA can be seen in Figure 3-18.

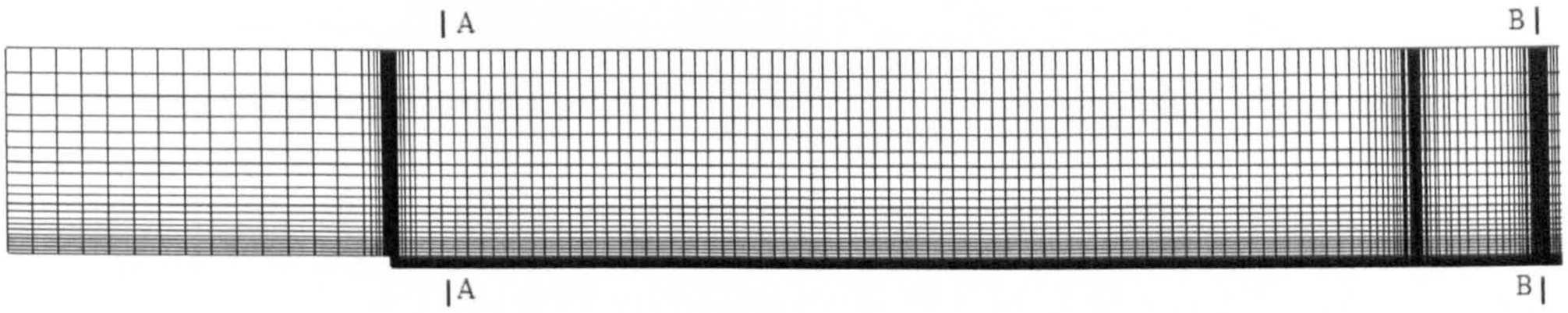

(a) Overall view

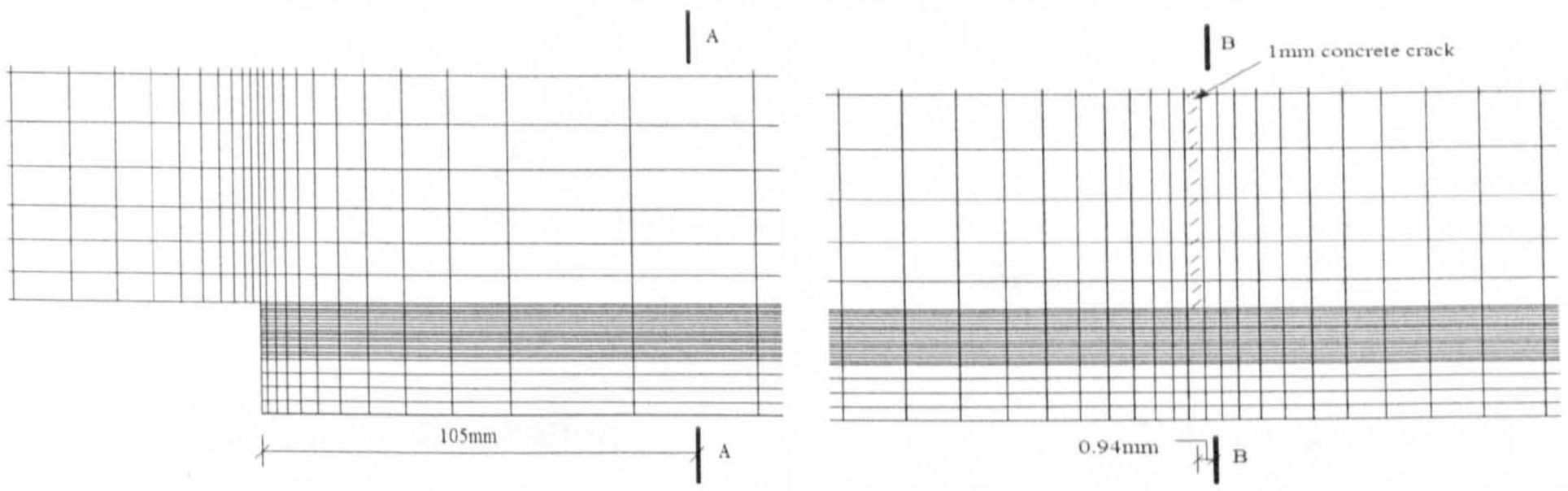

(b) Detailed elevation near end of plate and near the mid-span concrete crack

Figure 3-18 FE mesh of concrete beam

As shown in Figure 3-18, region A-A (near plate end) and region B-B (near mid-span crack) are investigated respectively. Figure 3-19 and Figure 3-20 show the equilibrium check of the results from the cracked beam (discussed in more details later in Chapter 6) under UDL. By multiplying the strains by the corresponding elastic modulus and then by areas, the forces in the concrete, steel and FRP were found. It is seen that longitudinal force equilibrium is very nearly satisfied by the results.

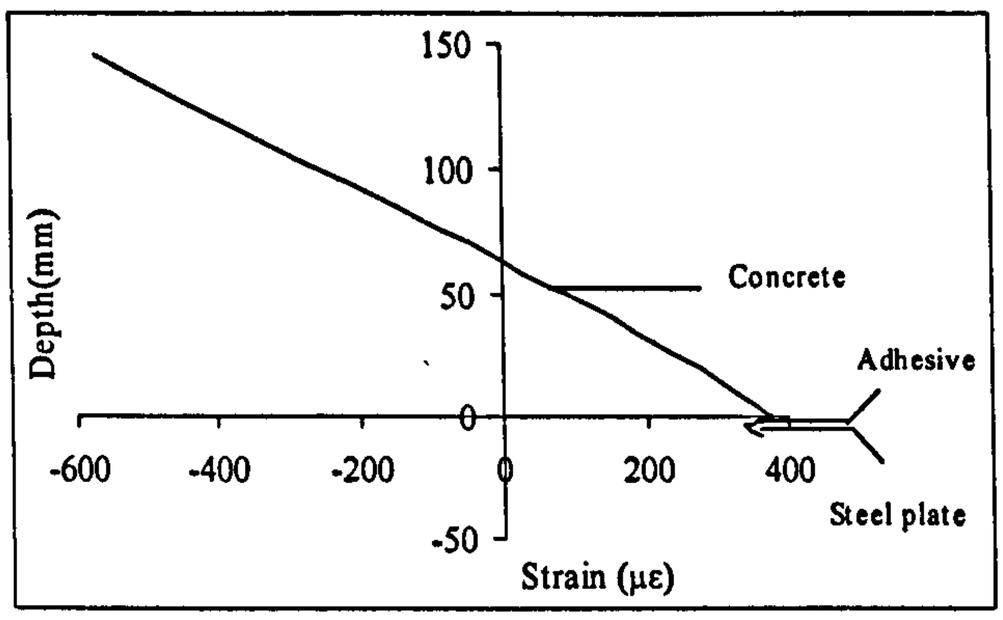

(a) Strains distribution

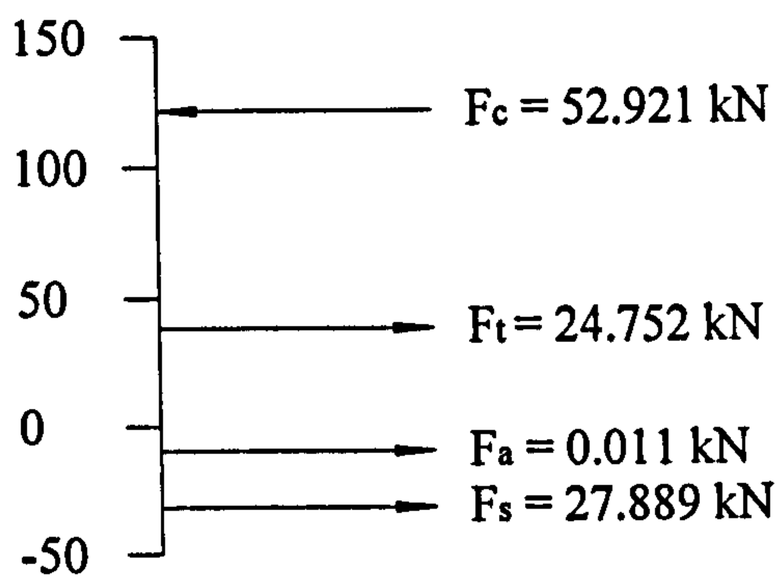

(b) Force diagram

Figure 3-19 Equilibrium check for Elements near plate end (region A-A)

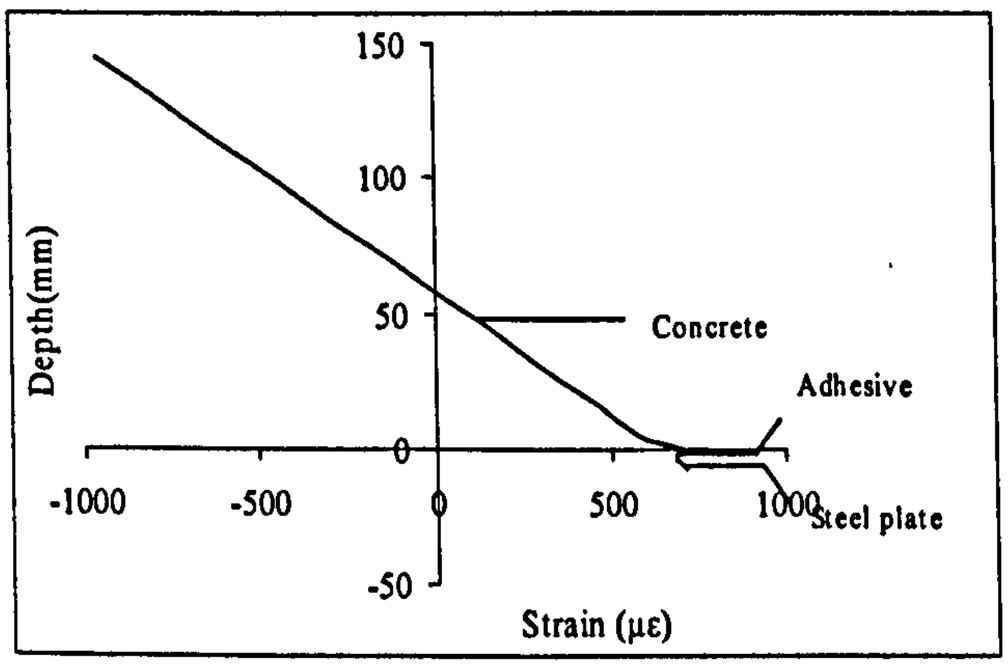

(a) Strains distribution

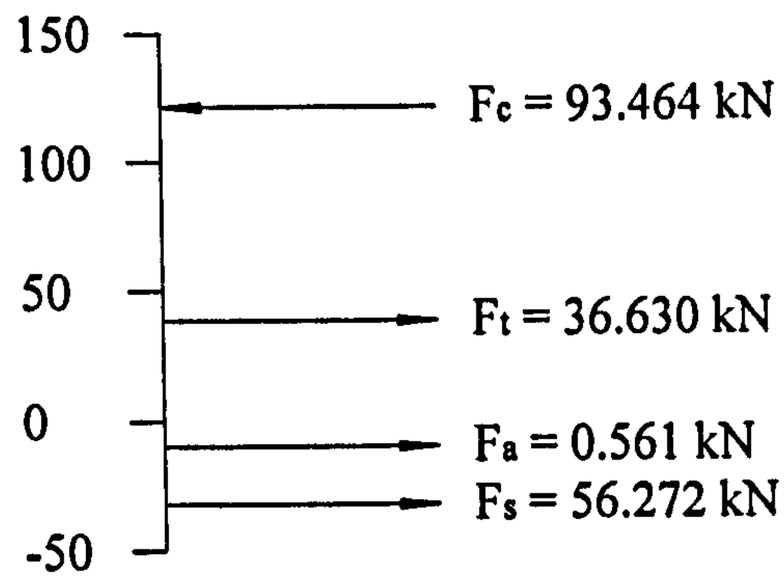

(b) Force diagram

Figure 3-20 Equilibrium check for Elements close crack (region B-B)

Further calculations give the section moment based on the stresses, which is compared in Table 3-1 with the moment required for equilibrium. Again very good agreements are obtained, indicating the reliability of the results from equilibrium perceptive.

Table 3-1 Equilibrium check for EBR plate strengthened RC beam

	M_c (kNm)	M_{FE} (kNm)	Error (%)
Near plate end	6.04	6.64	9.07
Near crack	10.76	10.80	0.35

3.3.2 Single lap joint (Täljsten (1997))

Täljsten tested a series of concrete prisms bonded with steel plates. The specimen S200 40A, of anchor length 200mm and width 40mm, was modelled and analyzed in the present paper (Figure 3-21).

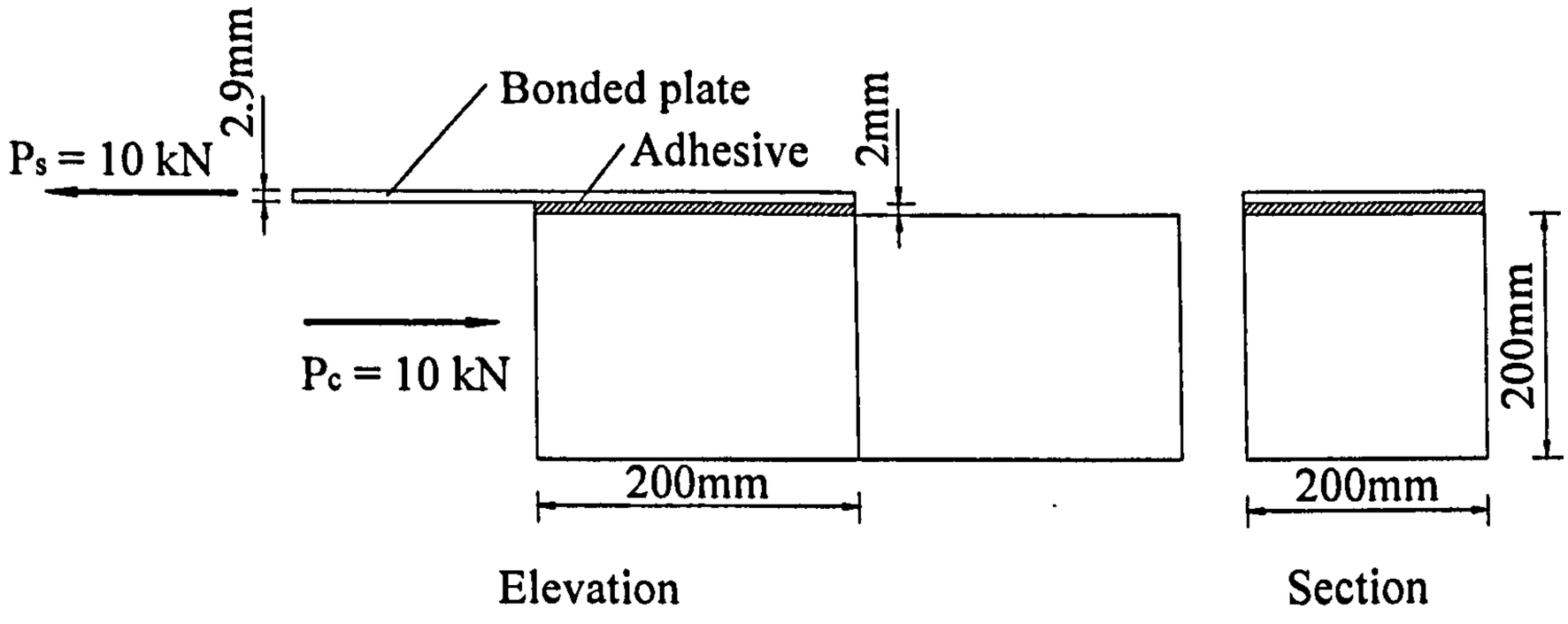

Figure 3-21 Concrete prism bonded to steel plate

The specimen was loaded to failure in the actual test. In the FE analysis, however, only one load step, which was 10 kN, was applied to the model. Material properties were applied to the FE model in line with the experiment data.

Concrete prism: $E_c = 35$ kN/mm^2, $f_{cc} = 39$ N/mm^2, $f_{tc} = 3.5$ N/mm^2;

Steel plates: $E_s = 205$ kN/mm^2, $f_{ys} = 340$ N/mm^2

Adhesive: $E_a = 6.7$ kN/mm^2, $f_a = 24$ N/mm^2

FE model of the specimen is shown in Figure 3-22. The concrete prism and the steel plate are modelled by the plane stress element Q8MEM while the adhesive layers are modelled by 1, 4 and 16 layers of Q8MEM and interface element L8IF respectively.

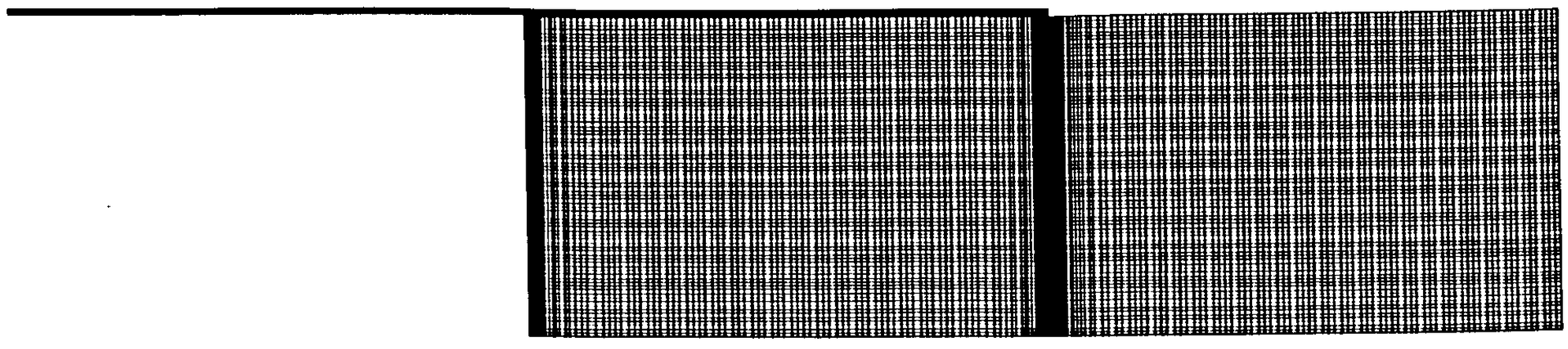

Figure 3-22 Finite element model of concrete prism

The comparisons among FE results, experimental and theoretical data for steel plate strain, adhesive shear and normal stress are shown in Figure 3-23 to Figure 3-25.

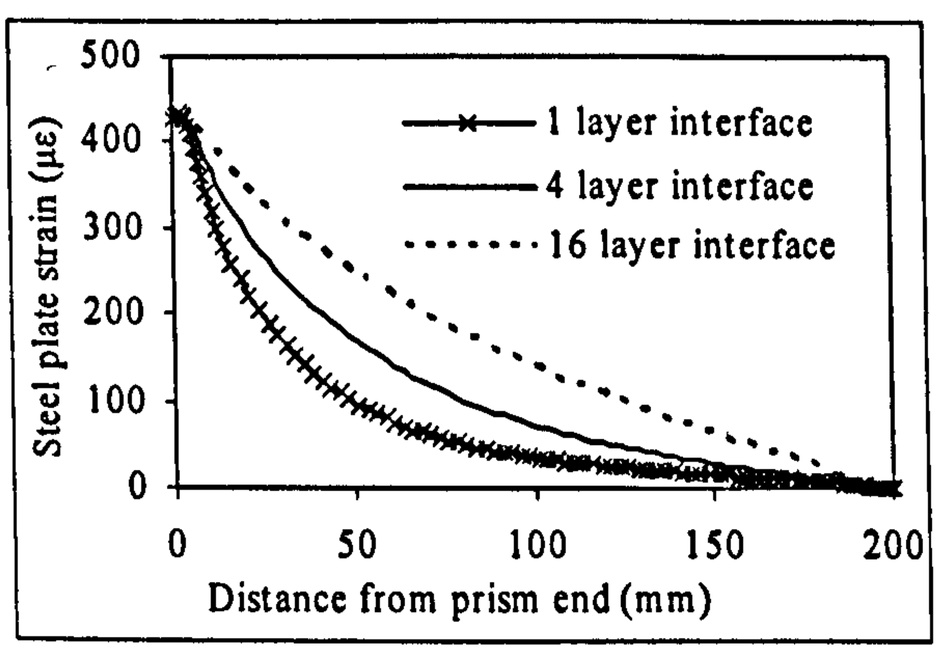

(a) Interface element models

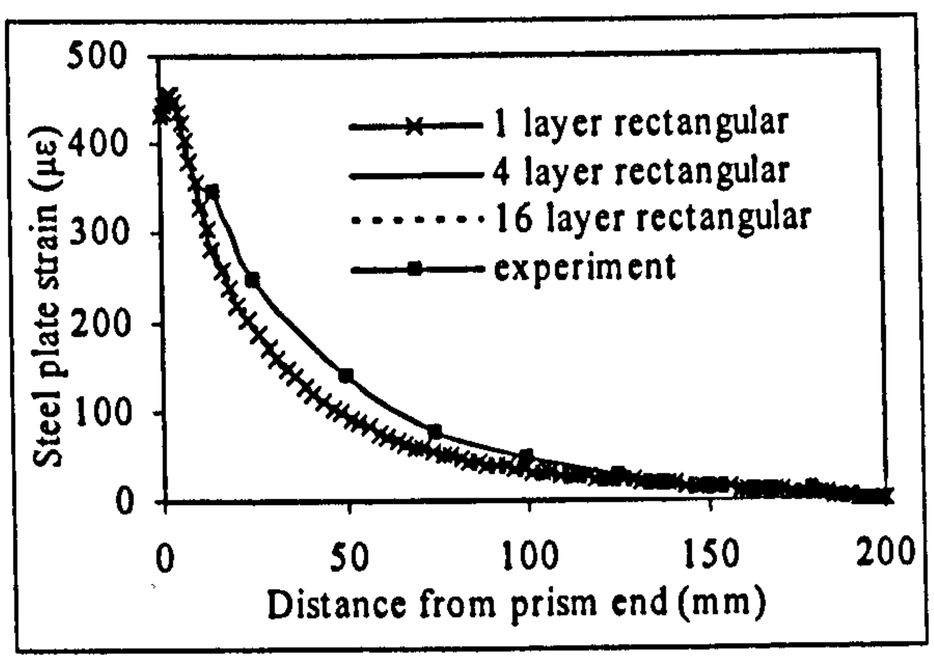

(b) Plane stress element models

Figure 3-23 Steel plate strain distribution

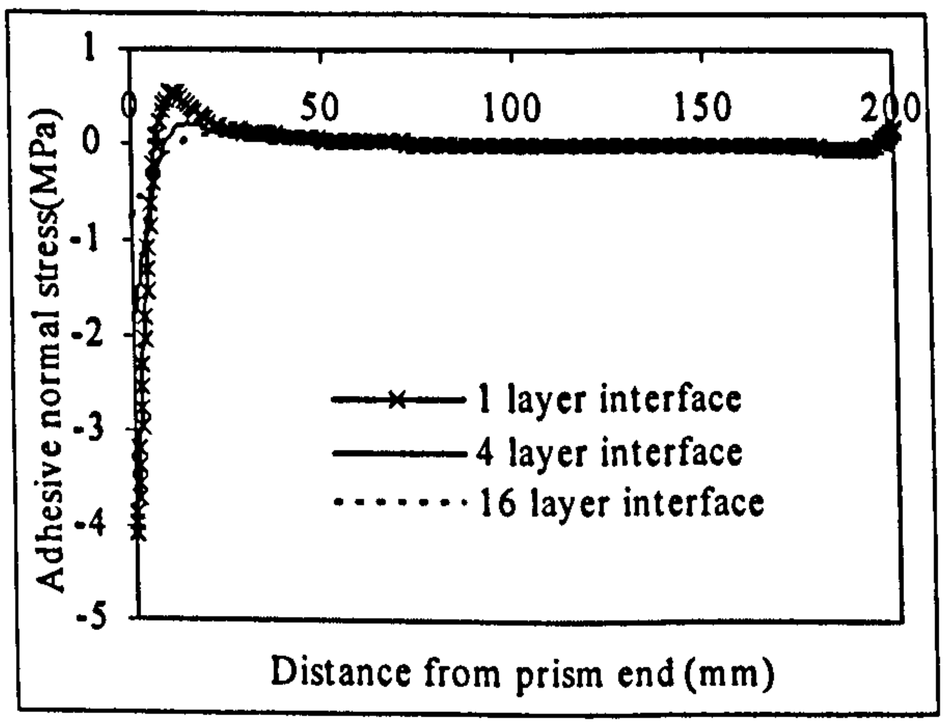

(a) Interface element models

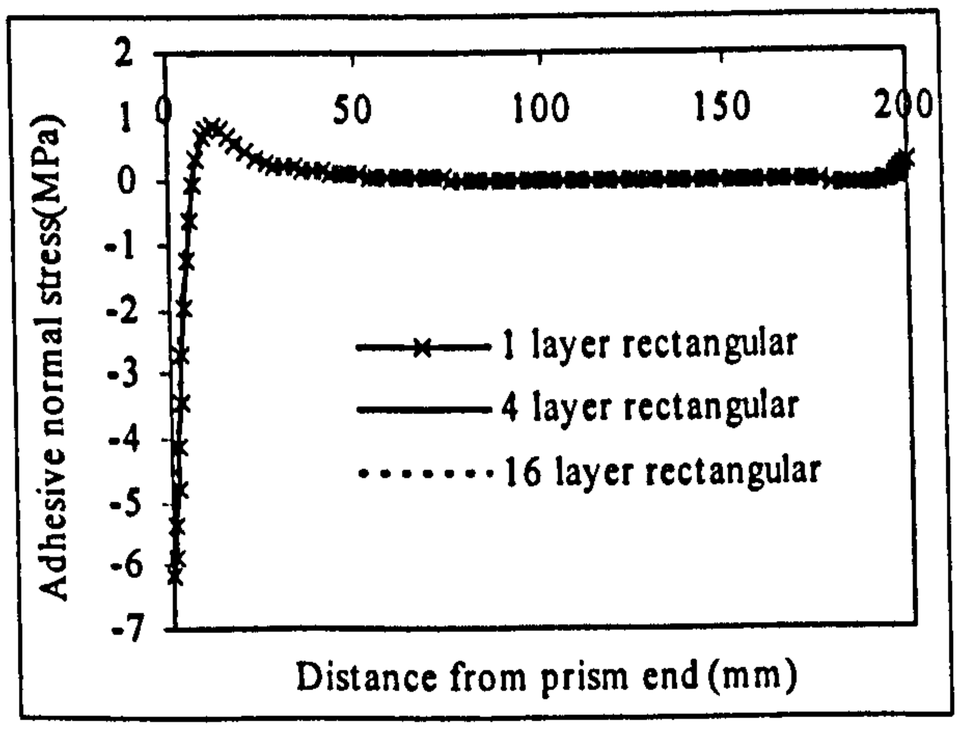

(b) Plane stress element models

Figure 3-24 Adhesive normal stress distribution

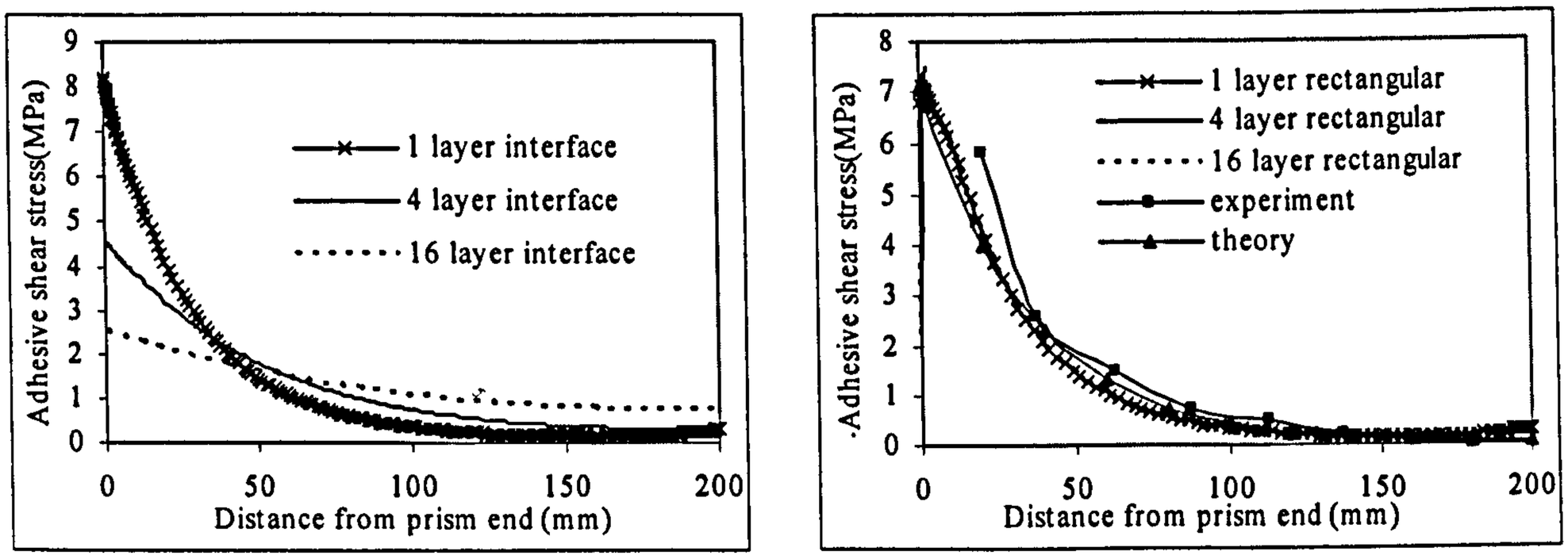

(a) Interface element models (b) Plane stress element models

Figure 3-25 Adhesive shear stress distribution

Similar trends are observed in the previous analysis for the plate bonded RC beam: the adhesive stresses in each layer of the multi-layer IEMs are exactly the same in value with those in other layers, which makes it impossible to investigate the through-thickness stress variations. In addition, as shown in Figure 3-23 to Figure 3-25 (a), the result of using different numbers of interface element layers through the thickness of the adhesive was significantly divergent in the output figures, which once again demonstrate that the results from the interface element models have not converged and so are not reliable.

On the contrary, as shown in Figure 3-23 to Figure 3-25 (b), average results from 1, 4 and 16 layer PEMs agree very well with each other and also agree reasonably with the test data, with the only small differences emerging mainly in a zone very near to the plate end. By comparing with the experimental data, we can see that both the interfacial shear stress and steel plate strain from the experimental data are consistently higher than the FE results and theoretical solutions.

As seen from Figure 3-25 (b), the peak interfacial shear stress of both the 1-layer PEM and theoretical analysis are at the end of the plate, violating the free surface

condition of zero shear stress. To the contrary, the peak shear stress from 4-layer and 16-layer PEM occurs at approximately 0.5 mm from the plate end and tends to go back to zero at the plate end, which agrees with the free surface condition of zero shear stress.

3.3.3 Composite bridge specimen

3.3.3.1 Geometry and FEA mesh

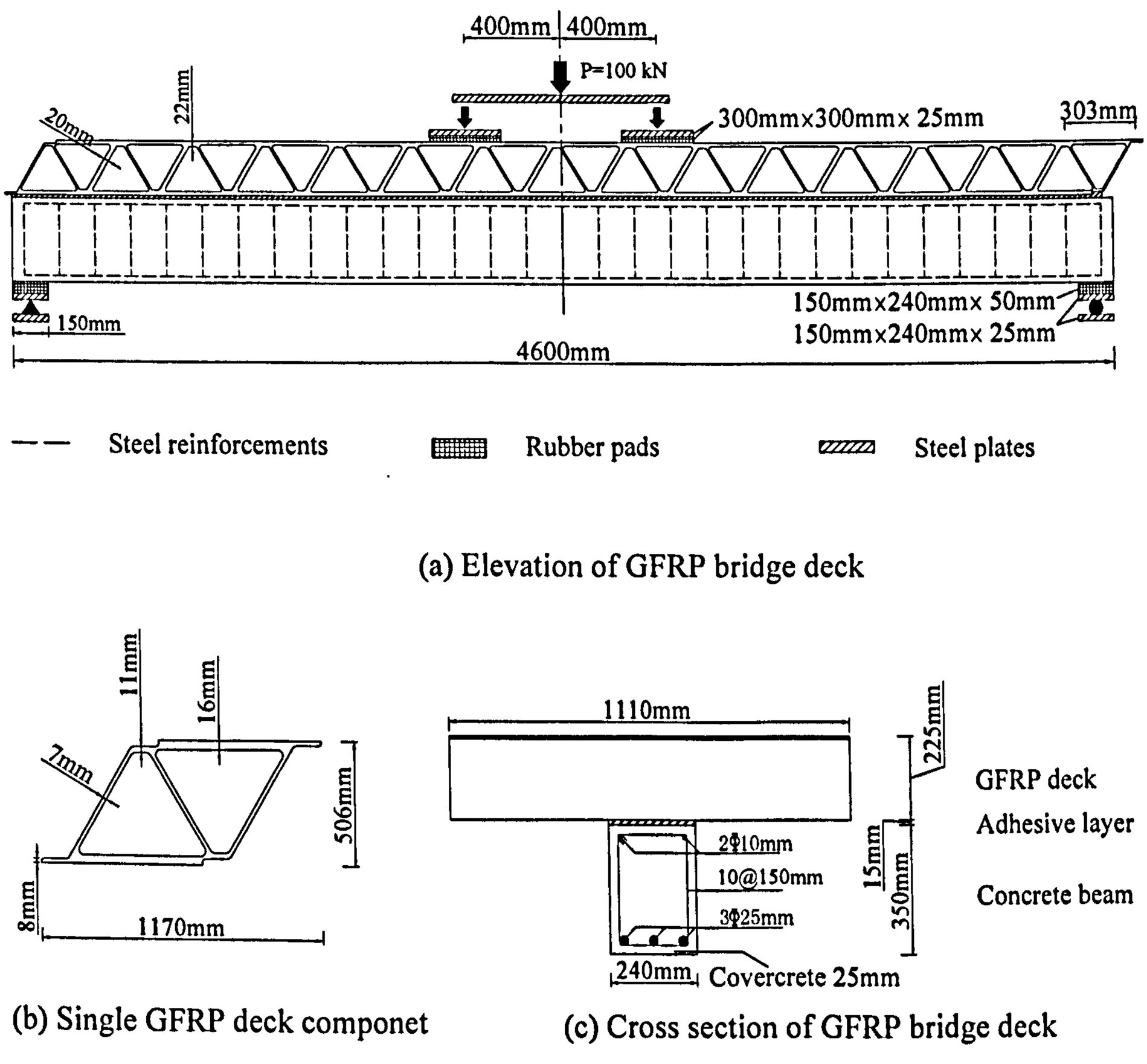

Figure 3-26 shows the geometry of the composite bridge specimen comprising triangulated GFRP deck adhesively connected to a RC beam. The whole was subjected to four-point loading. The material properties input to the FE models are also given below.

Concrete beam: E_c = 35 kN/mm^2, ν_c = 0.2, f_{cc} = 50 N/mm^2, f_{tc} = 3.5 N/mm^2;

Adhesive: E_a = 2 kN/mm^2, ν_c = 0.3, f_{ca} = 100 N/mm^2, f_{ta} = 4 N/mm^2

GFRP: E_f = 18 kN/mm^2, ν_f = 0.4

Steel plates: E_s = 205 kN/mm^2, ν_s = 0.3, f_{ys} = 500 N/mm^2

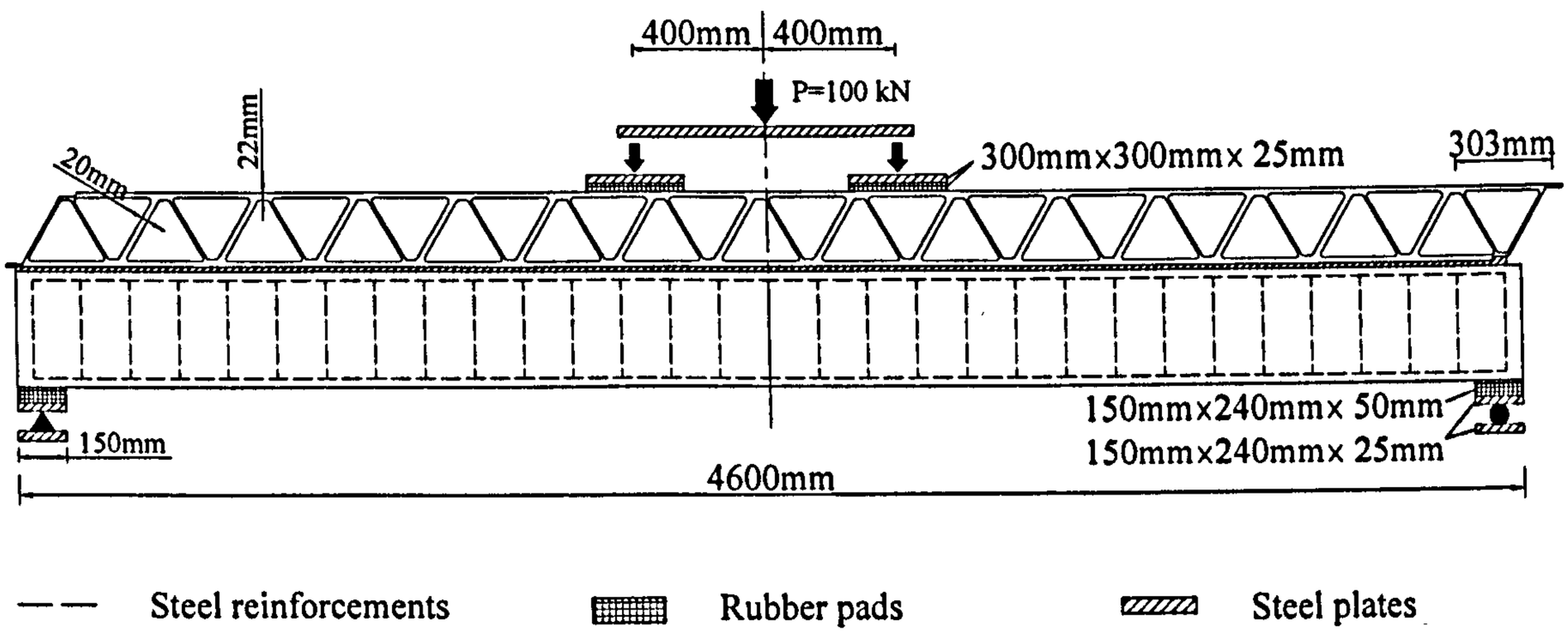

(a) Elevation of GFRP bridge deck

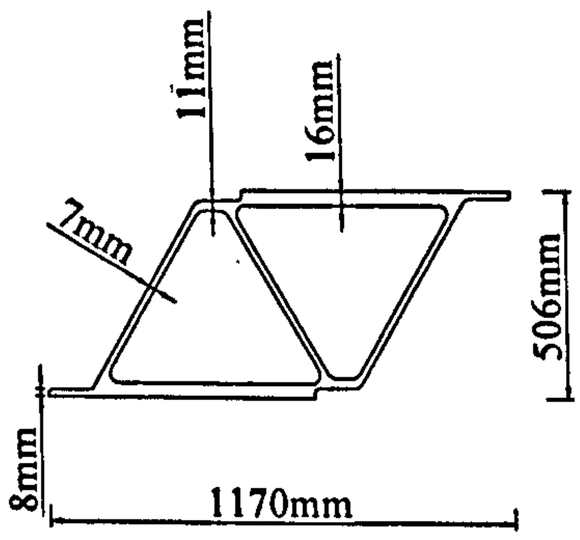

(b) Single GFRP deck componet

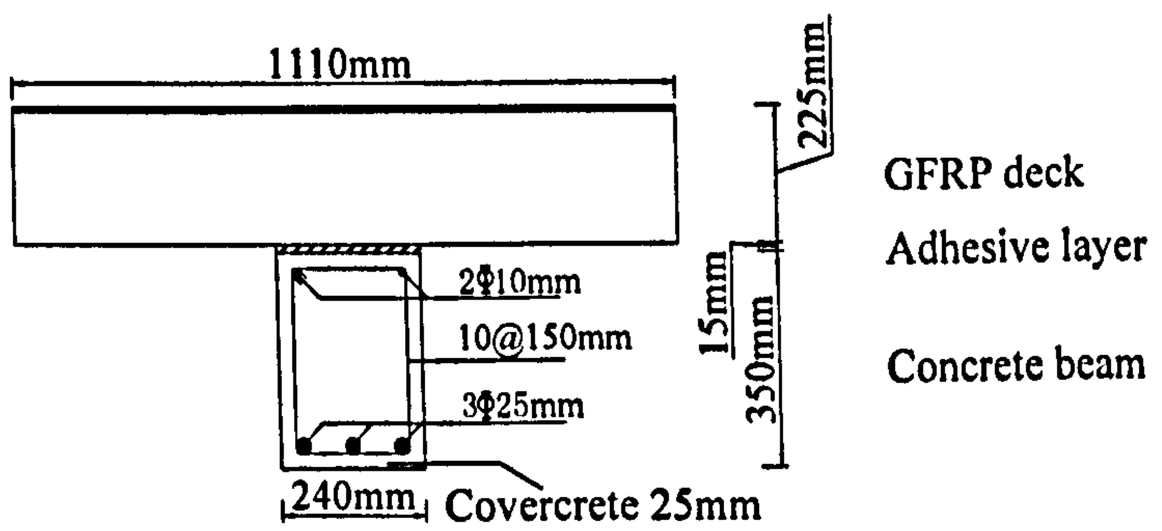

(c) Cross section of GFRP bridge deck

Figure 3-26 Geometry of the composite bridge specimen

The 2D FE mesh of the composite bridge specimen is shown in Figure 3-27. The four-noded plane stress element Q8MEM was used for modelling RC beam and adhesive layer, while the three-noded plane stress element T6MEM was used for modelling the

GFRP deck and the two-noded truss element L2TRU was used for the reinforcing steel bars.

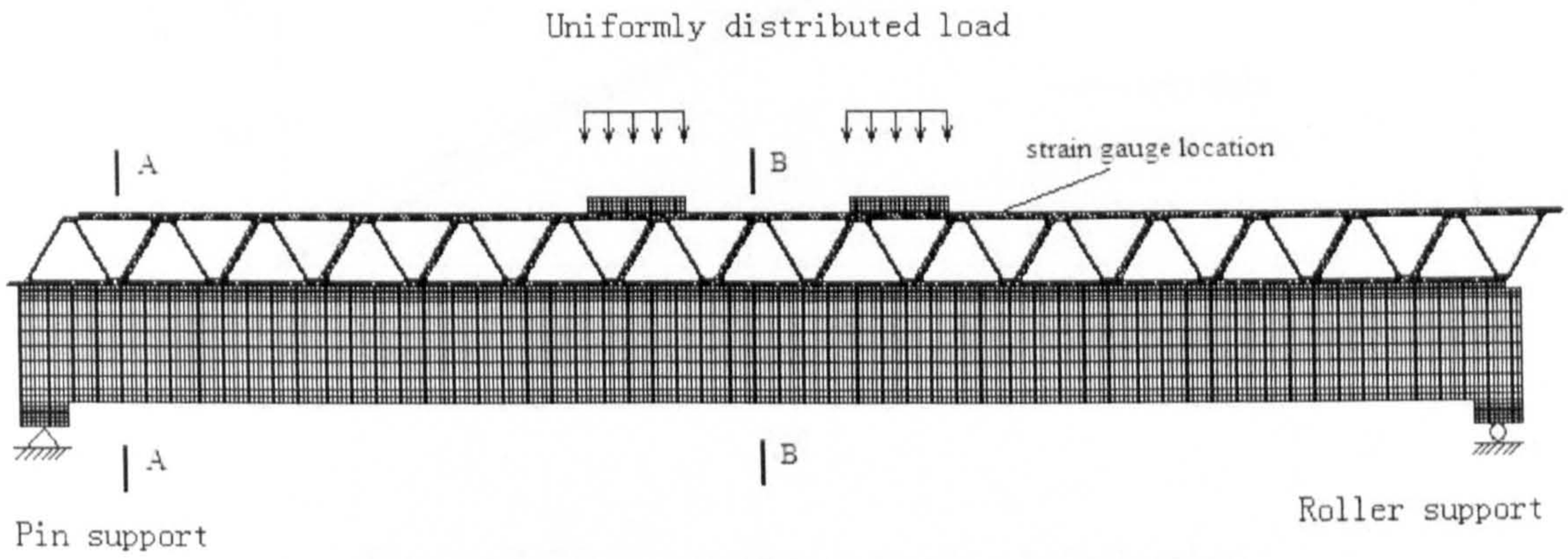

Figure 3-27 2D fine mesh model of the composite bridge specimen

3.3.3.2 Comparison with test data

Figure 3-28 to Figure 3-30 show the comparison plots between FEA results and test data for load vs. deflection and steel/GFRP strain for the load up to P = 200 kN, respectively. The plots show that the deflection and strain behaviours were nearly linear elastic throughout the test.

In Figure 3-28, the deflections are measured at the bottom of RC beam mid-span. The results were highly encouraging as the FEA prediction agrees very well with the test data. Both data found quite small deflection (up to 7.5 mm) at this loading stage.

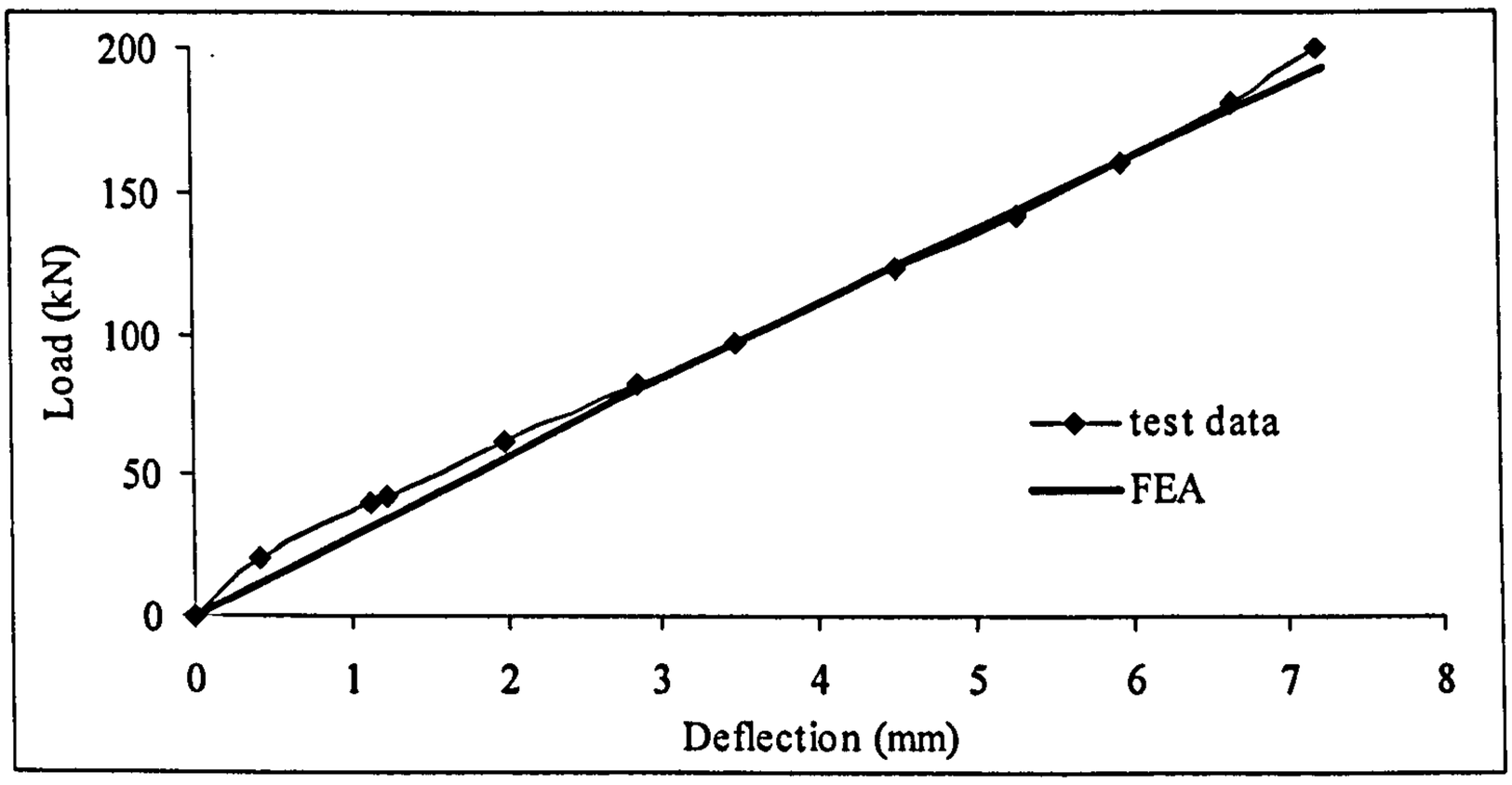

Figure 3-28 Comparison for load-deflection

The steel strain was measured at the midspan of one of the bottom reinforcing steel bars inside the RC beam. Again, very good comparison was found between FEA results and test data (Figure 3-29). It can be seen that the bottom steel strains keep in tension during the loading and the steels have not yielded at this stage.

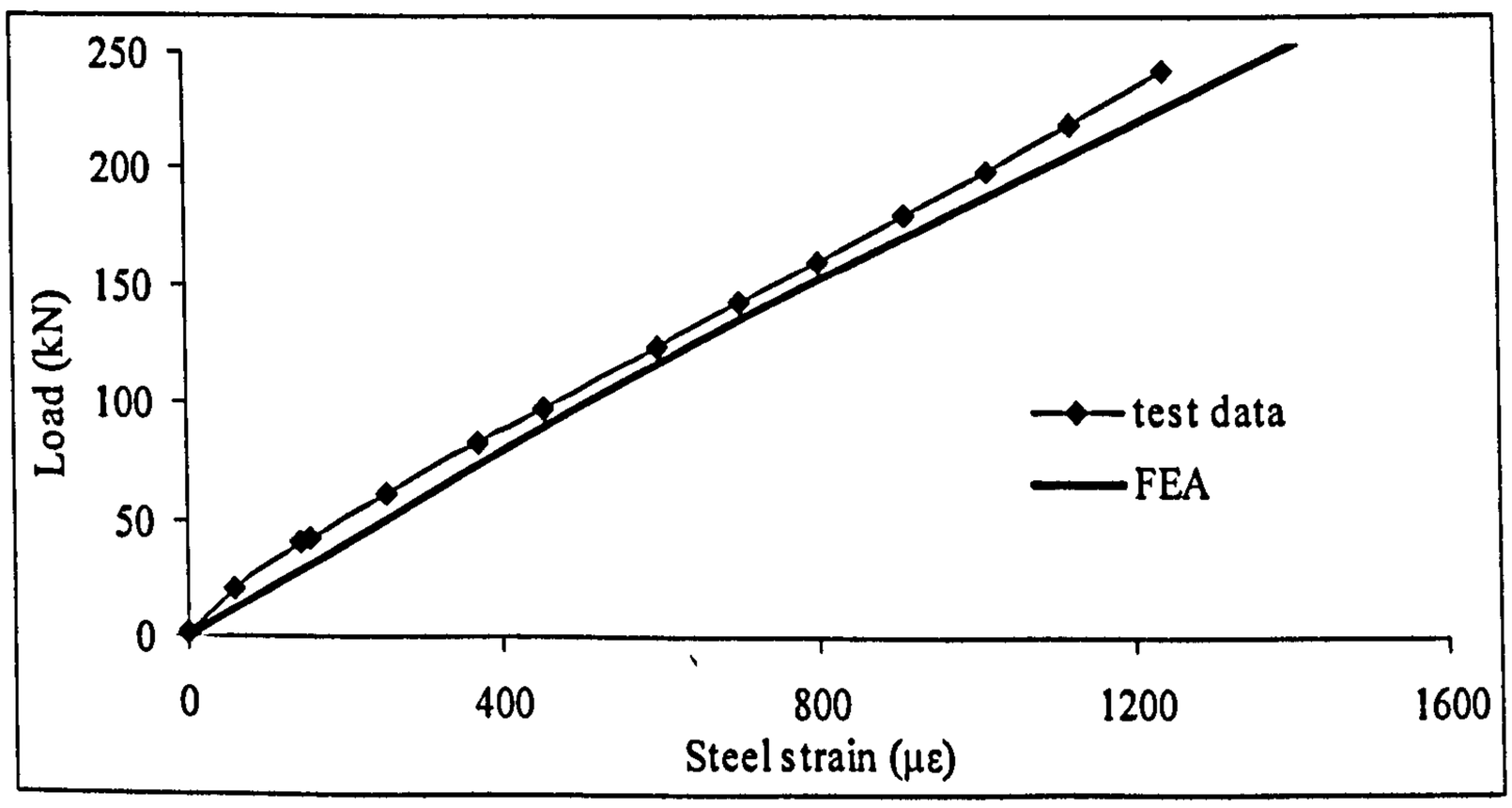

Figure 3-29 Comparison for load-steel strain

The GFRP strain shown in Figure 3-30 was measured on the top of one of the single GFRP deck near midspan (see exact location in Figure 3-27). The GFRP deck is in

compression at this zone. It can be seen that the comparison is relatively good except that the FE analysis predicting slightly higher strains under the same loading.

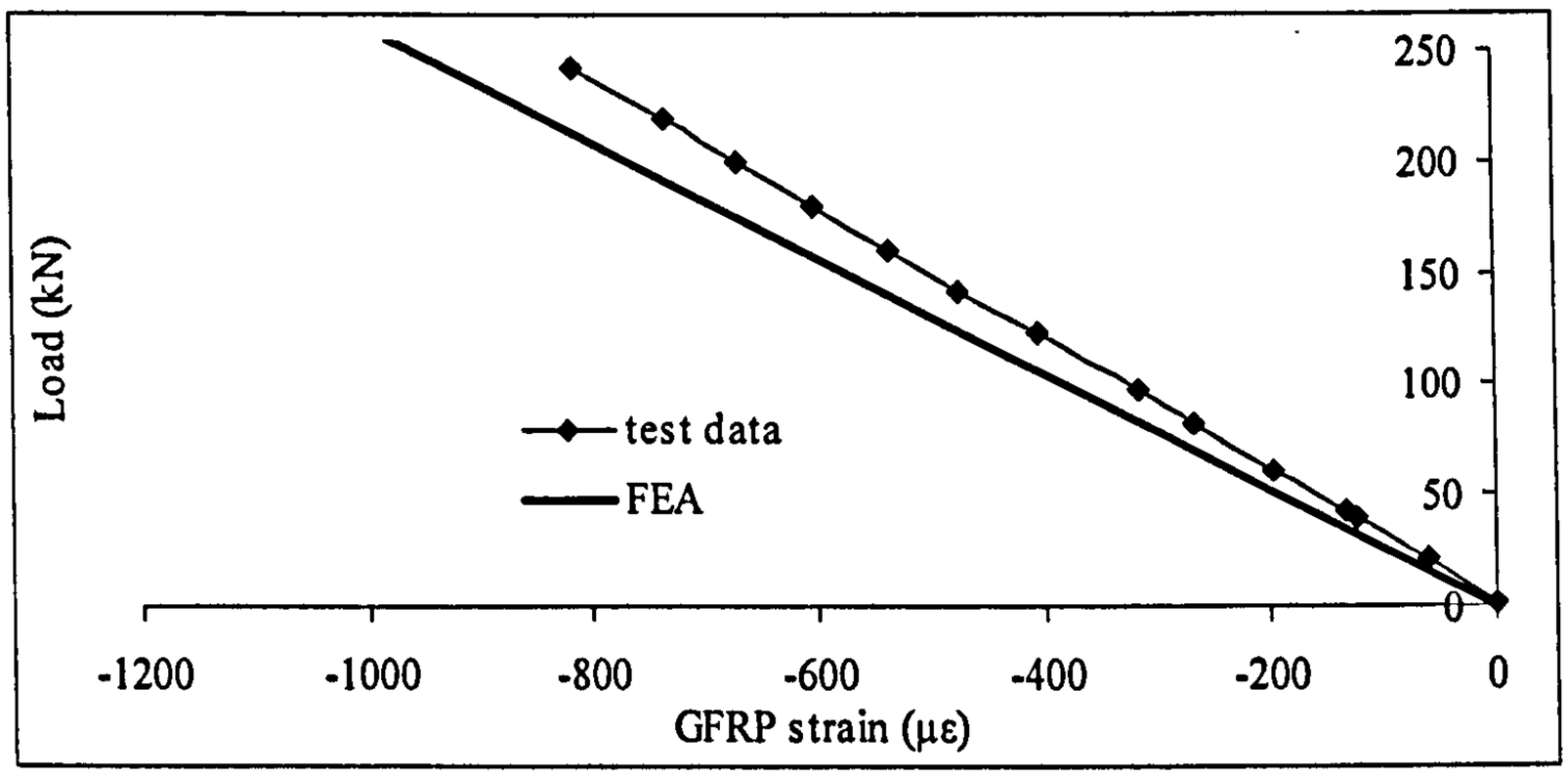

Figure 3-30 Comparison for load-GFRP strain

3.3.3.3 Equilibrium check

Equilibrium checks on the FE output are presented in this section to establish the level of reliability of the FE output. As can be seen in Figure 3-27, section A-A near the pin support and section B-B near midspan were chosen to perform this check. Figure 3-31 shows the enlarged mesh near those sections.

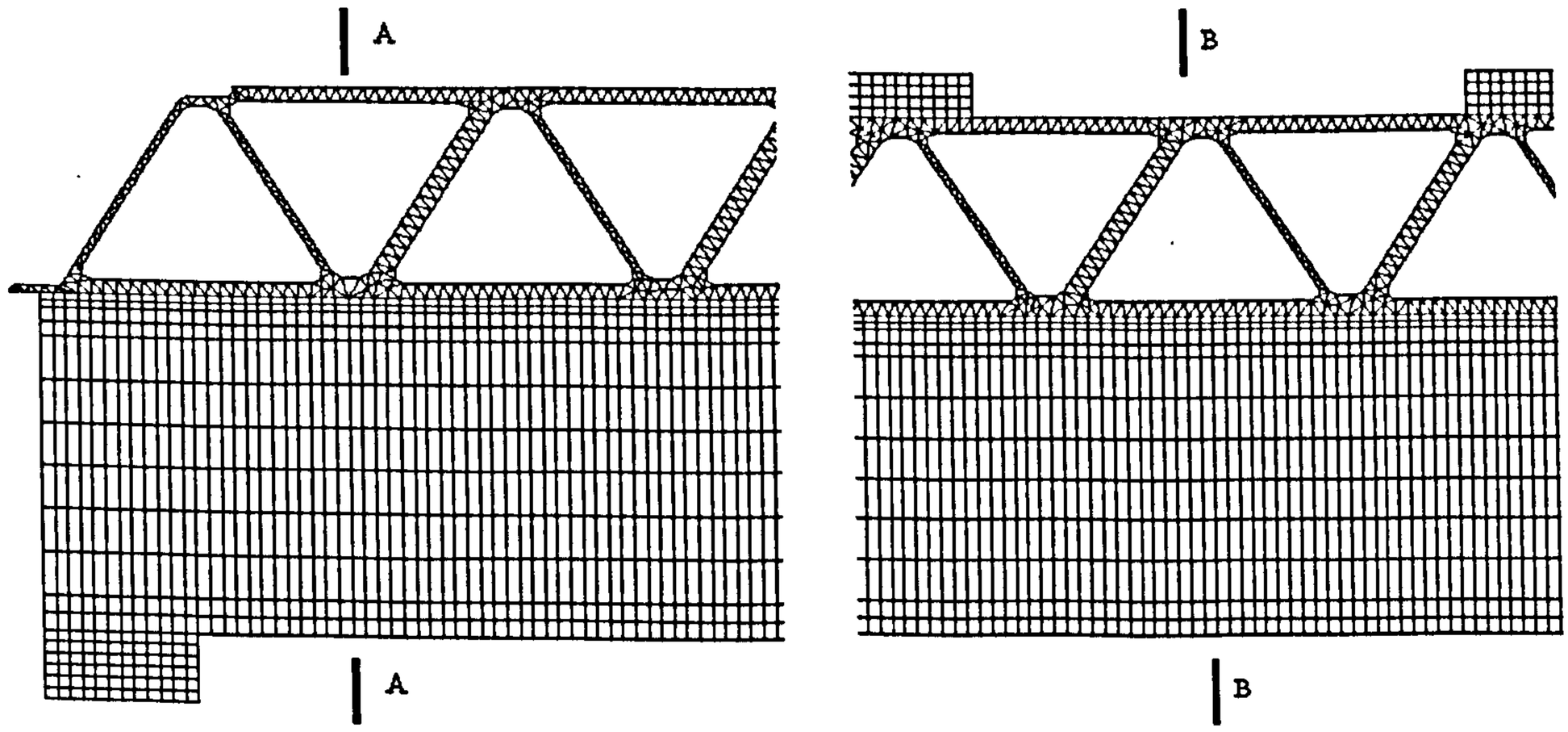

(a) Section A-A near support

(b) Section B-B near midspan

Figure 3-31 Enlarged mesh of the specimen parts near support and midspan

The strain distributions of the concrete, steel bars and GFRP along the cut sections are shown in Figure 3-32 (a) and Figure 3-33 (a). By multiplying the strains by the corresponding elastic moduli and then by areas, the forces in the concrete, steel bars and GFRP decks were found. It can be seen from Figure 3-32 (b) and Figure 3-33 (b) that the sum of the longitudinal forces is found to be small enough to satisfy the equilibrium. Further calculations give the section moment based on the stresses and relative distance from the base of the beam. The results are compared in Table 3-2. with the moment required for equilibrium. Again very good agreements are obtained, indicating the reliability of the results from the equilibrium perspective.

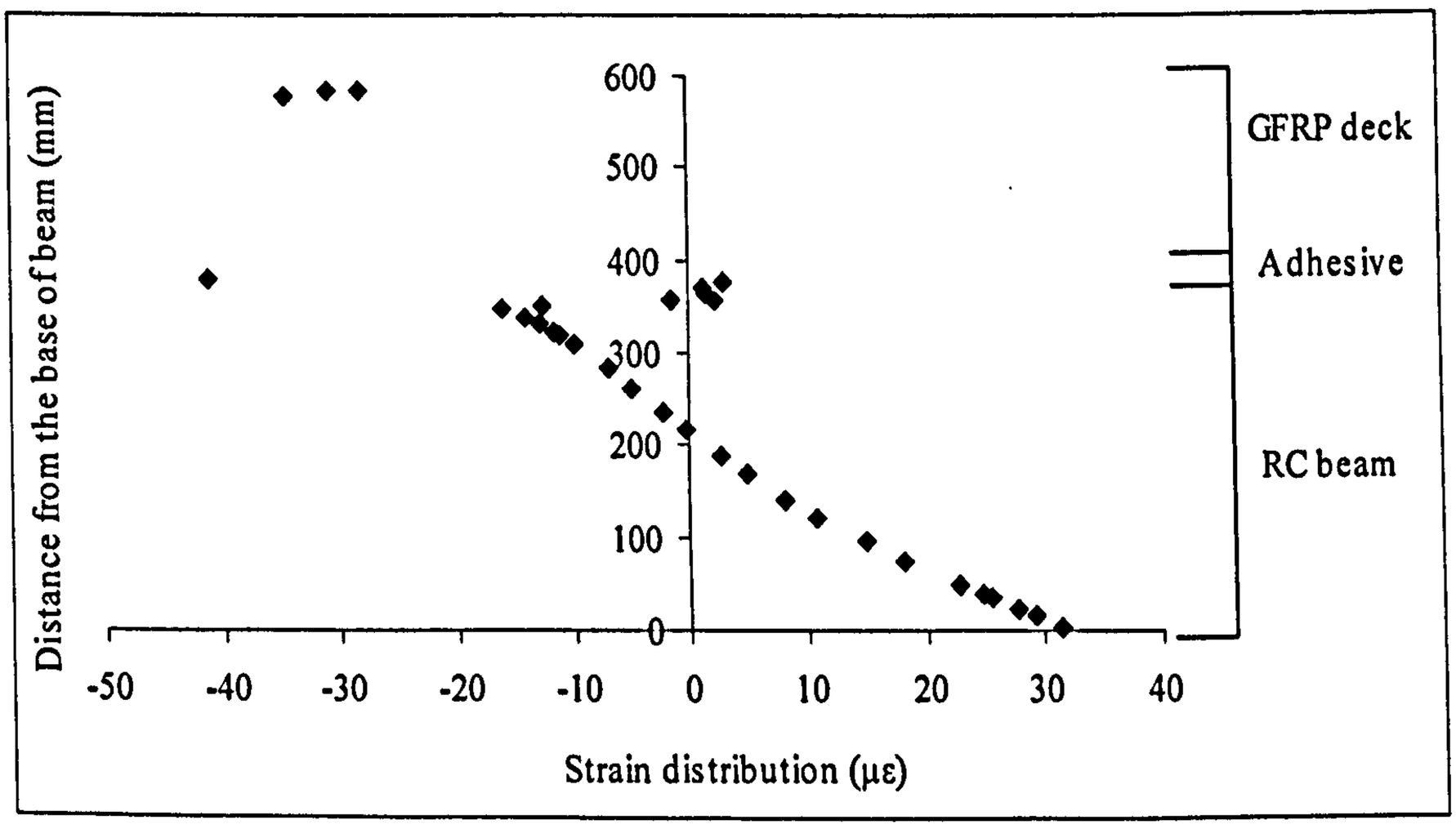

(a) Strain distribution along cutting section

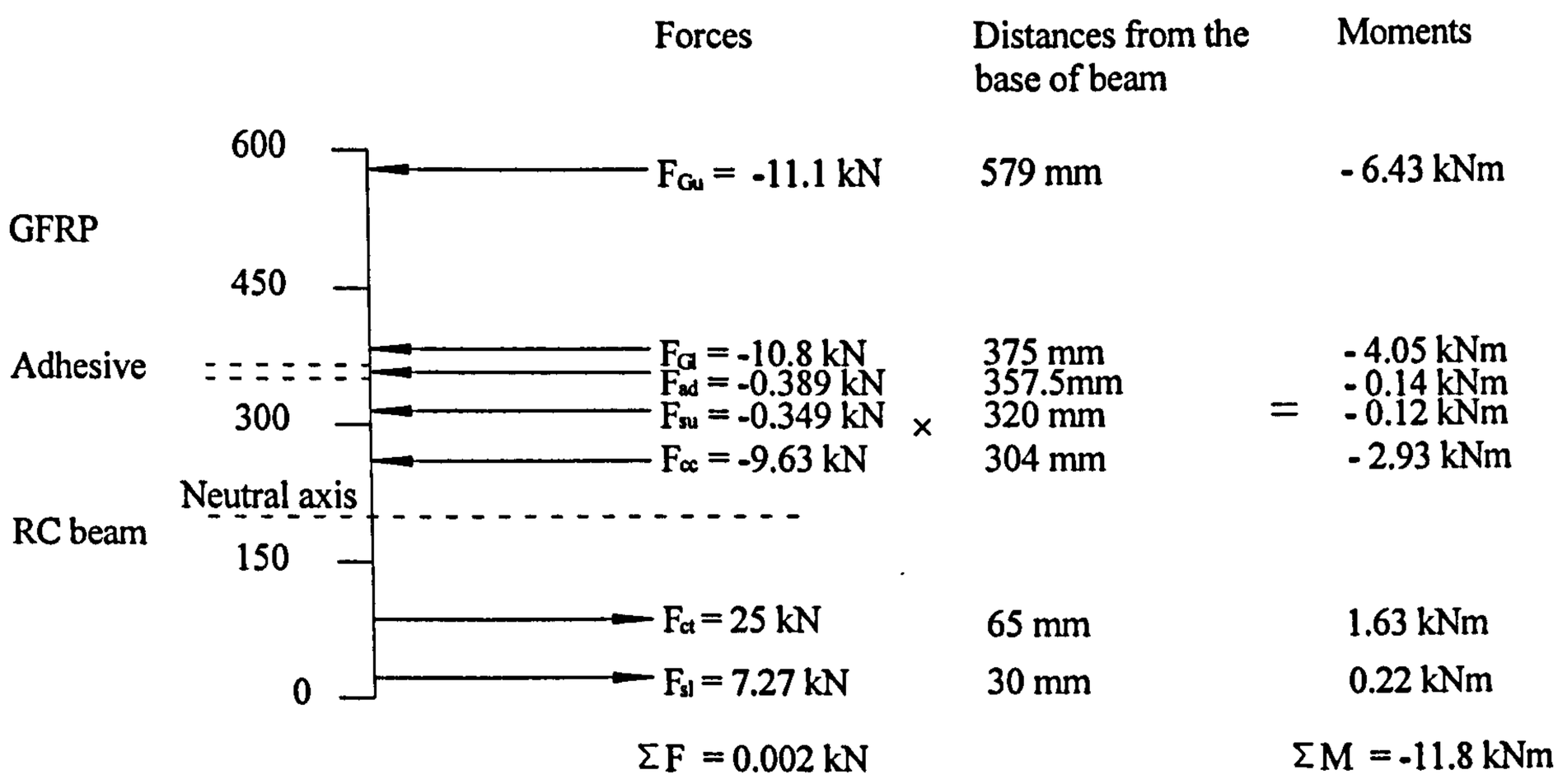

(b) Force and moment checks

Figure 3-32 Equilibrium check for elements near support (section A-A)

Where F_{Gu} is upper section force of GFRP deck; F_{Gl} is lower section force of GFRP deck; F_{ad} is force of adhesive layer; F_{cc} is compressive force of concrete beam; F_{ct} is tensile force of concrete beam; F_{su} is upper section force of steel reinforcement; F_{sl} is lower section force of steel reinforcement.

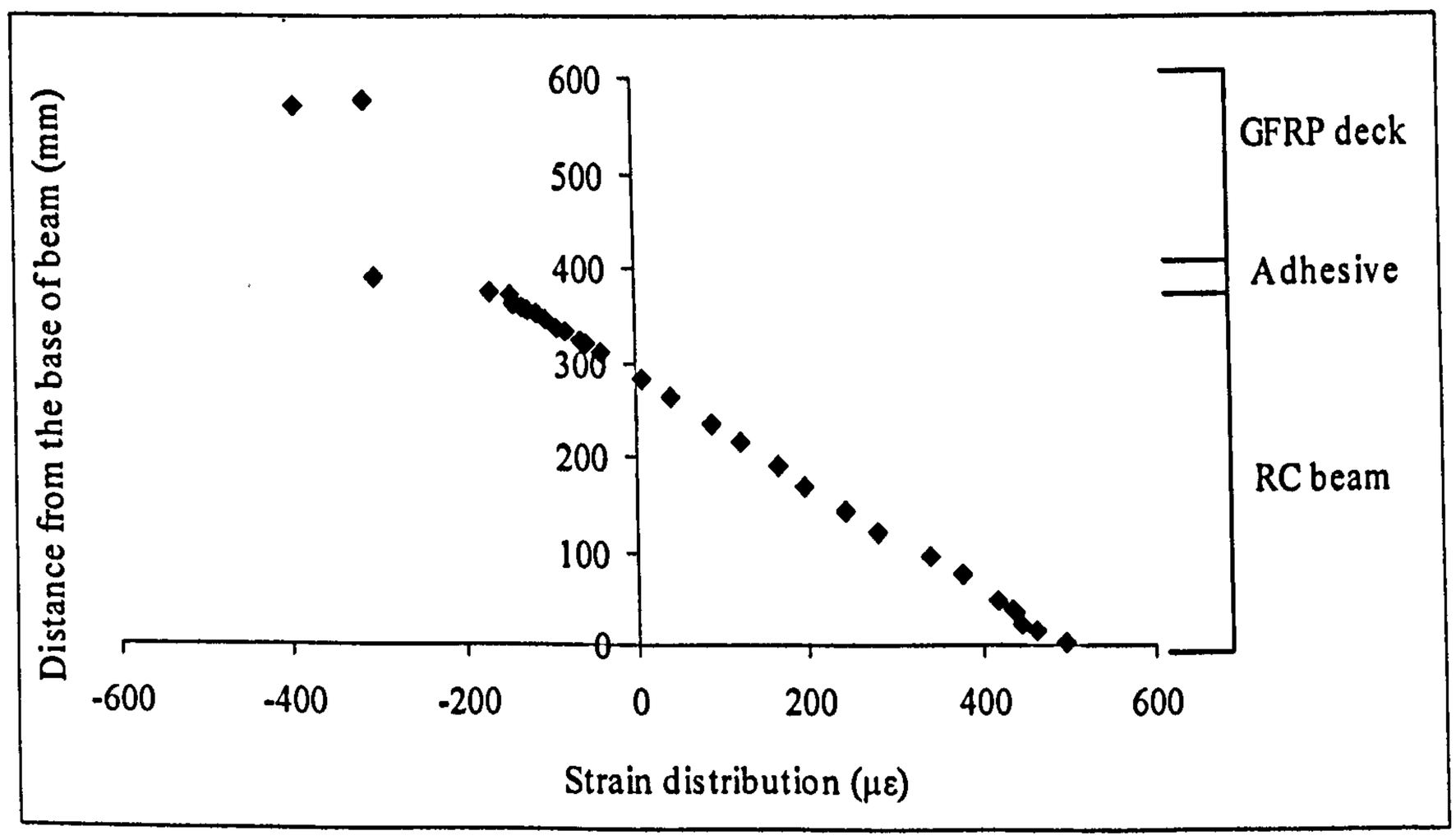

(a) Strain distribution along cutting section

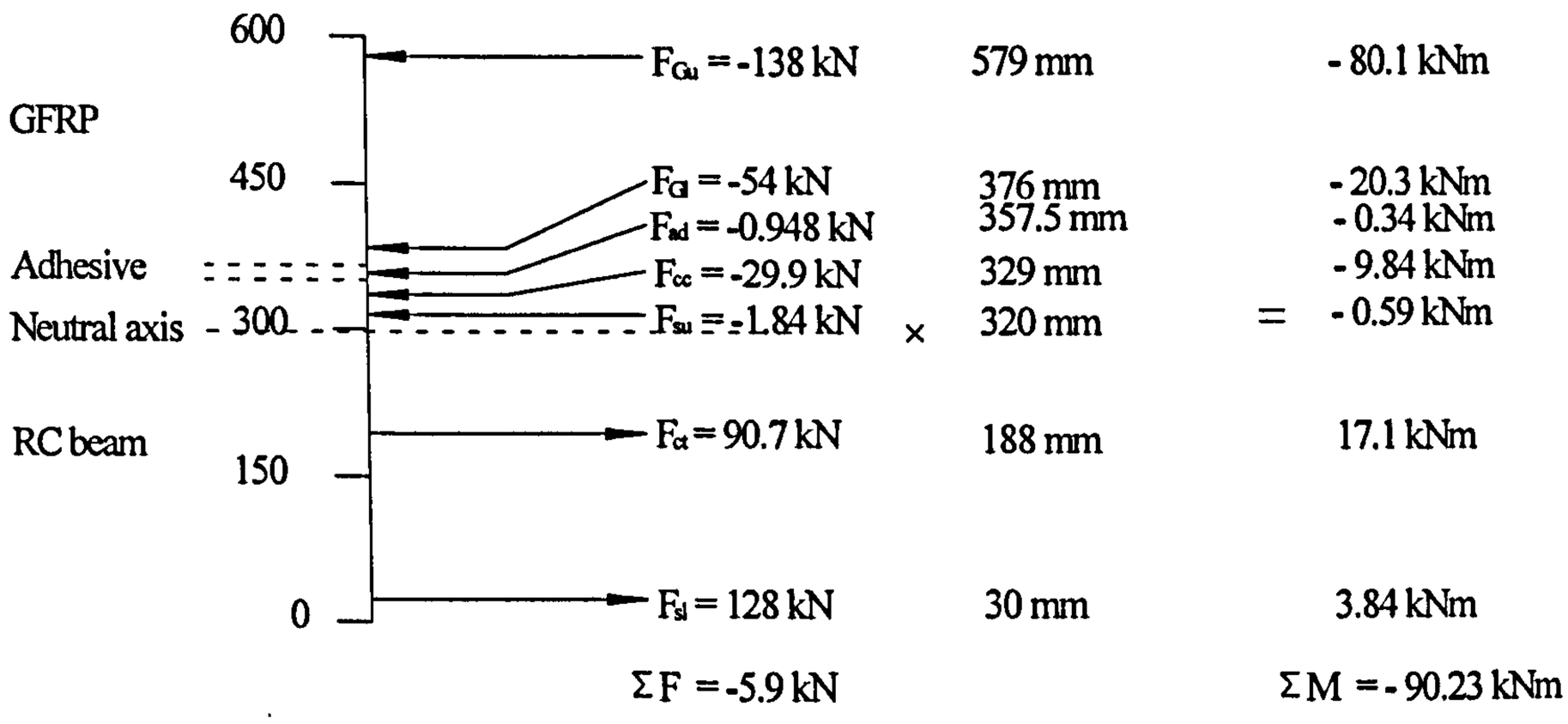

(b) Force and moment checks

Figure 3-33 Equilibrium check for elements near midspan (section B-B)

Table 3-2 Equilibrium check for the composite bridge deck

	M_c (kNm)	M_{FE} (kNm)	Error (%)
Near support	11.3	11.8	4.72
Near midspan	91.25	90.23	1.12

3.3.4 NSM FRP strengthened concrete block (Teng et al. (2006))

A series of bond tests were carried out by Teng et al. (2006). The bond specimen details are shown in Figure 3-34. In the tests the bond length was varied from 30 to 250 mm. Then the specimen with longest bond length being 250 mm was chosen in this FE analysis.

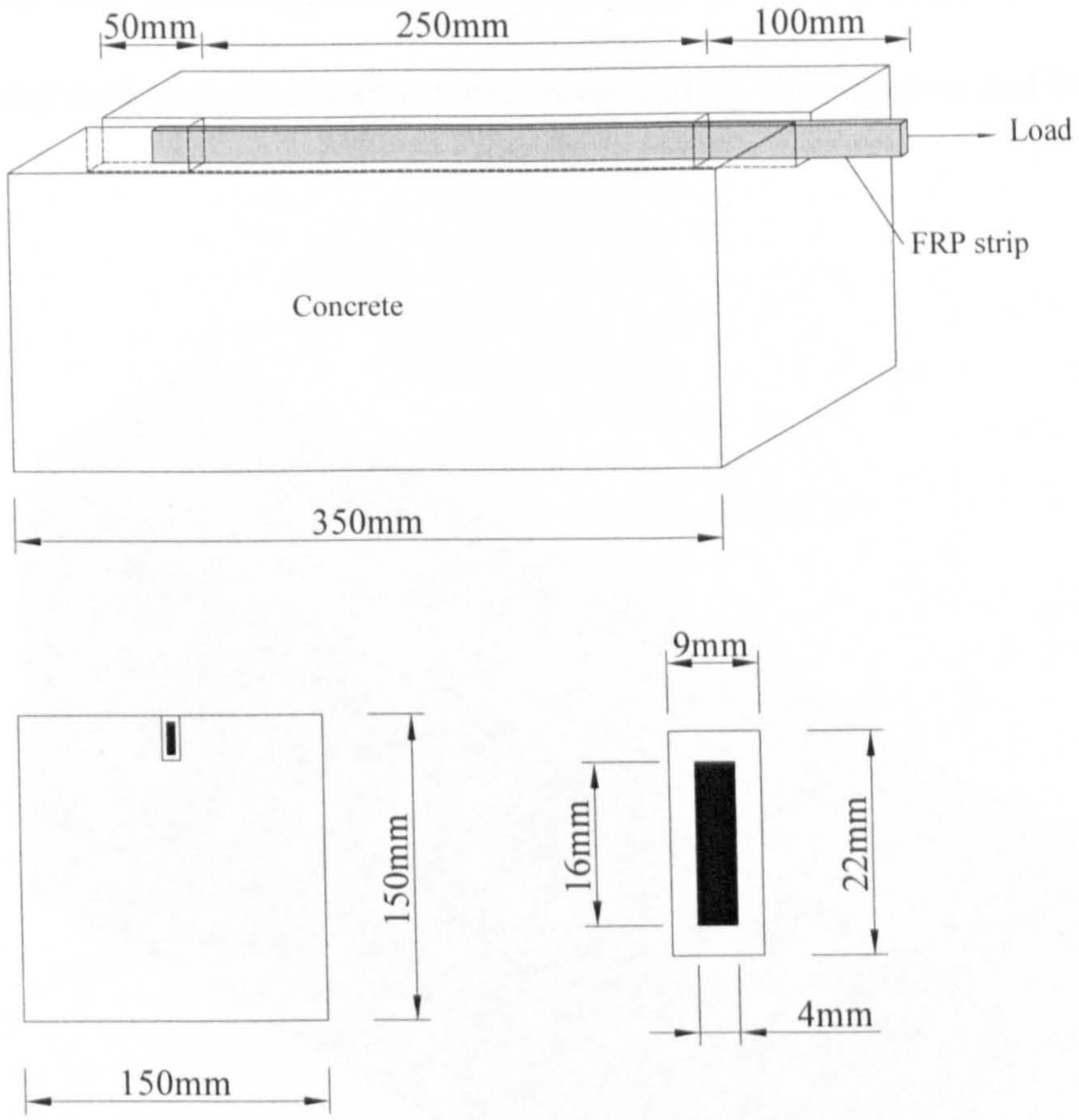

Figure 3-34 Schematic of bond test specimens

The material properties of specimen are from experimental data and are given below:

Concrete: $E_c = 30$ kN/mm^2, $\nu_c = 0.2$, $f_{cc} = 29$ N/mm^2, $f_{tc} = 2.5$ N/mm^2;

Adhesive: $E_a = 2.63$ kN/mm^2, $\nu_c = 0.3$, $f_{ca} = 100$ N/mm^2, $f_{ta} = 42.6$ N/mm^2

CFRP: $E_f = 151$ kN/mm^2, $\nu_f = 0.4$

As mentioned earlier on, 3D actions within the adhesive connection in NSM FRP strengthened RC members constitute an important facet of load response. The cross sectional shrinkage of the bars due to lateral Poisson's ratio effect from longitudinal tensile stress can cause cracks in the adhesive and concrete around bars. Therefore, 3D modelling was employed for this NSM specimen (Figure 3-35). Due to the

symmetry, only half of the specimen was modelled in the FE analyses. The concrete block, FRP strip and epoxy adhesive were modelled by the eight-noded brick element HX24L.

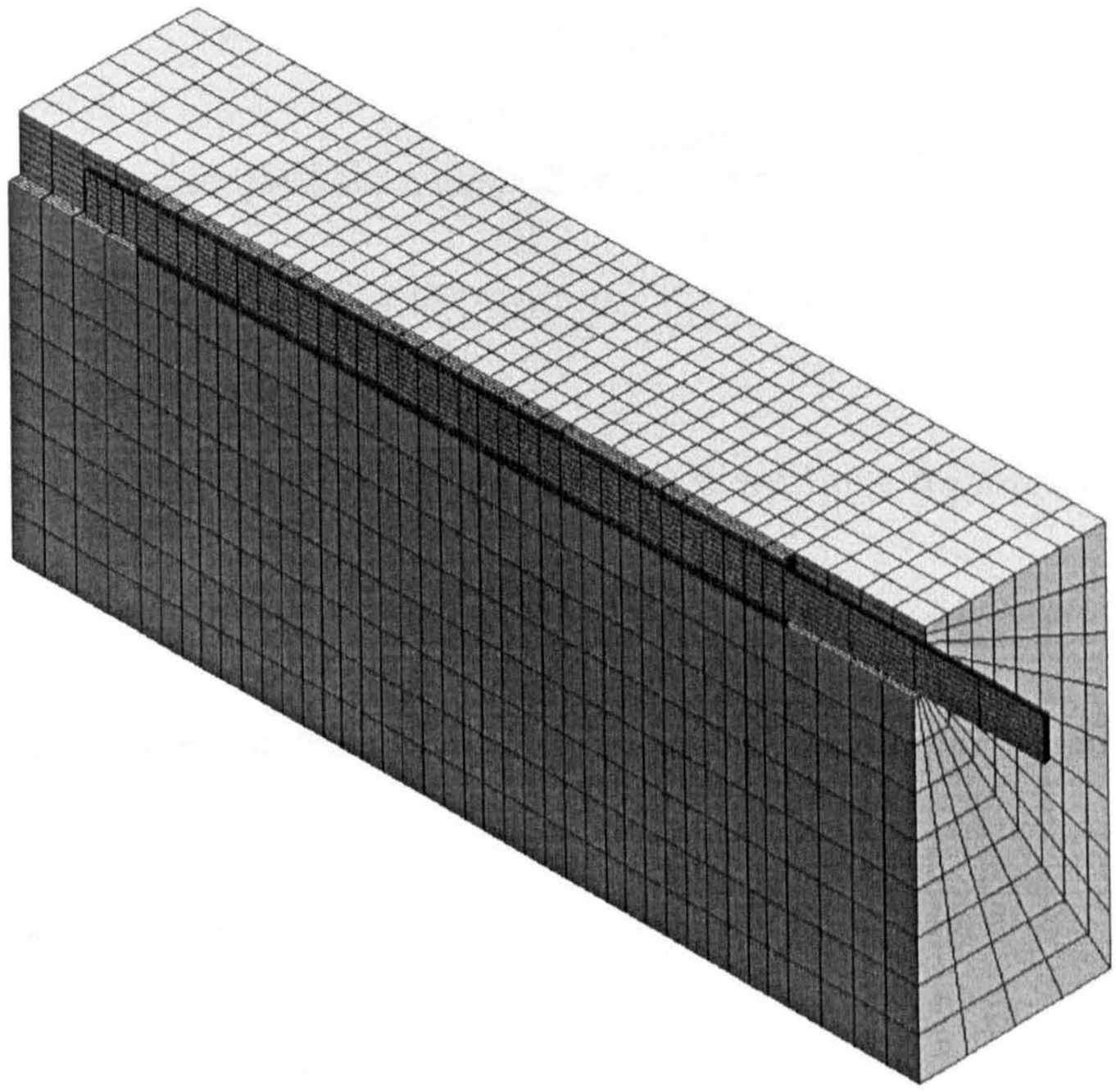

Figure 3-35 3D Finite element model of bond test specimens

Figure 3-36 shows the comparison plots between FEA results and test data corresponding to three load stages for CFRP strain distributions along the adhesive bonded line. It can be seen that the correlation between the two curves is very good for the lower load before P = 32 kN. However, for the higher load P = 51.2 kN, there are certain differences between the FEA results and test data.

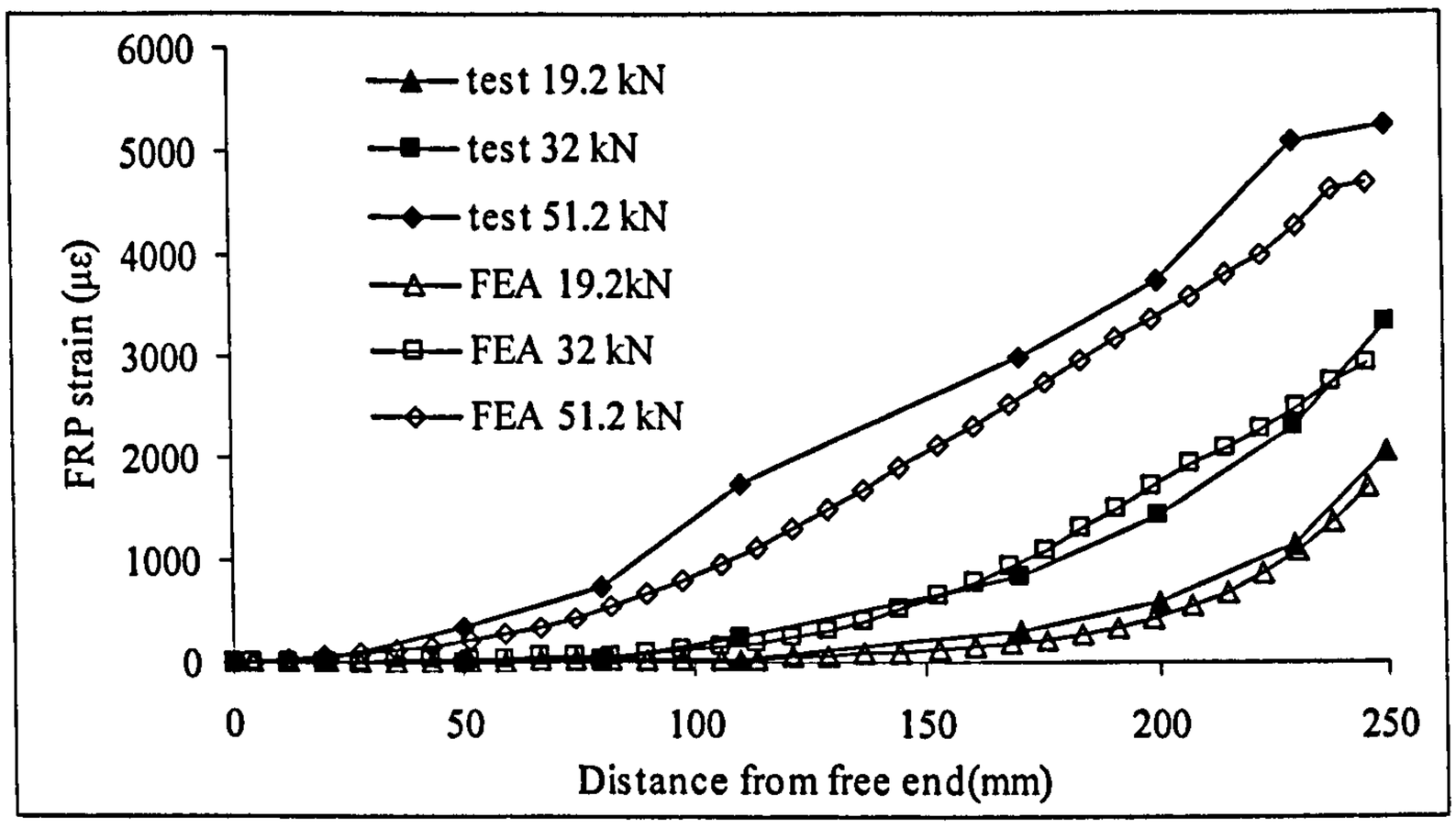

Figure 3-36 Comparisons between FEA results and test data for FRP strain distributions

Similar trends were found for adhesive shear stress distributions in Figure 3-37.

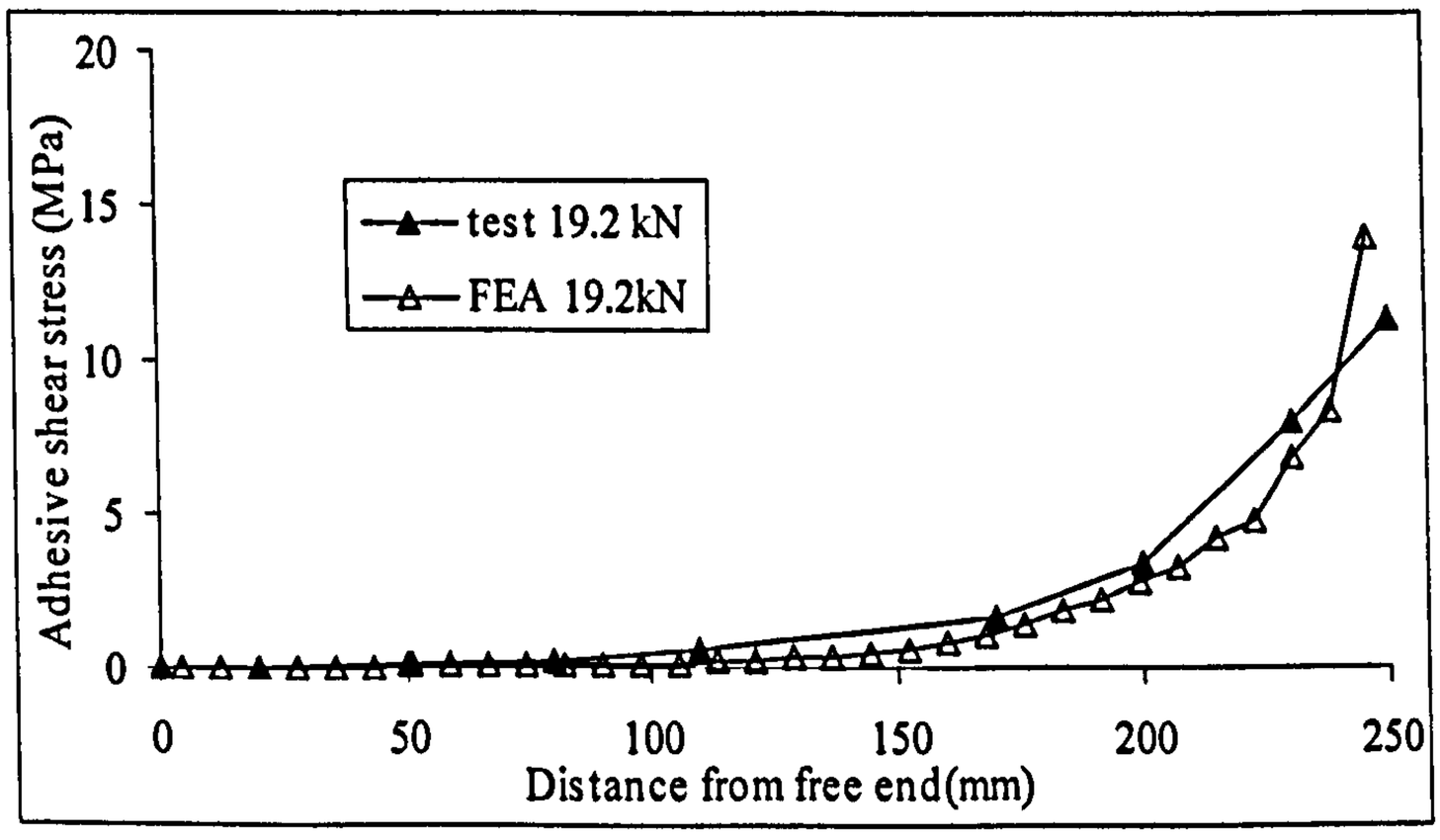

(a) P = 19.2 kN

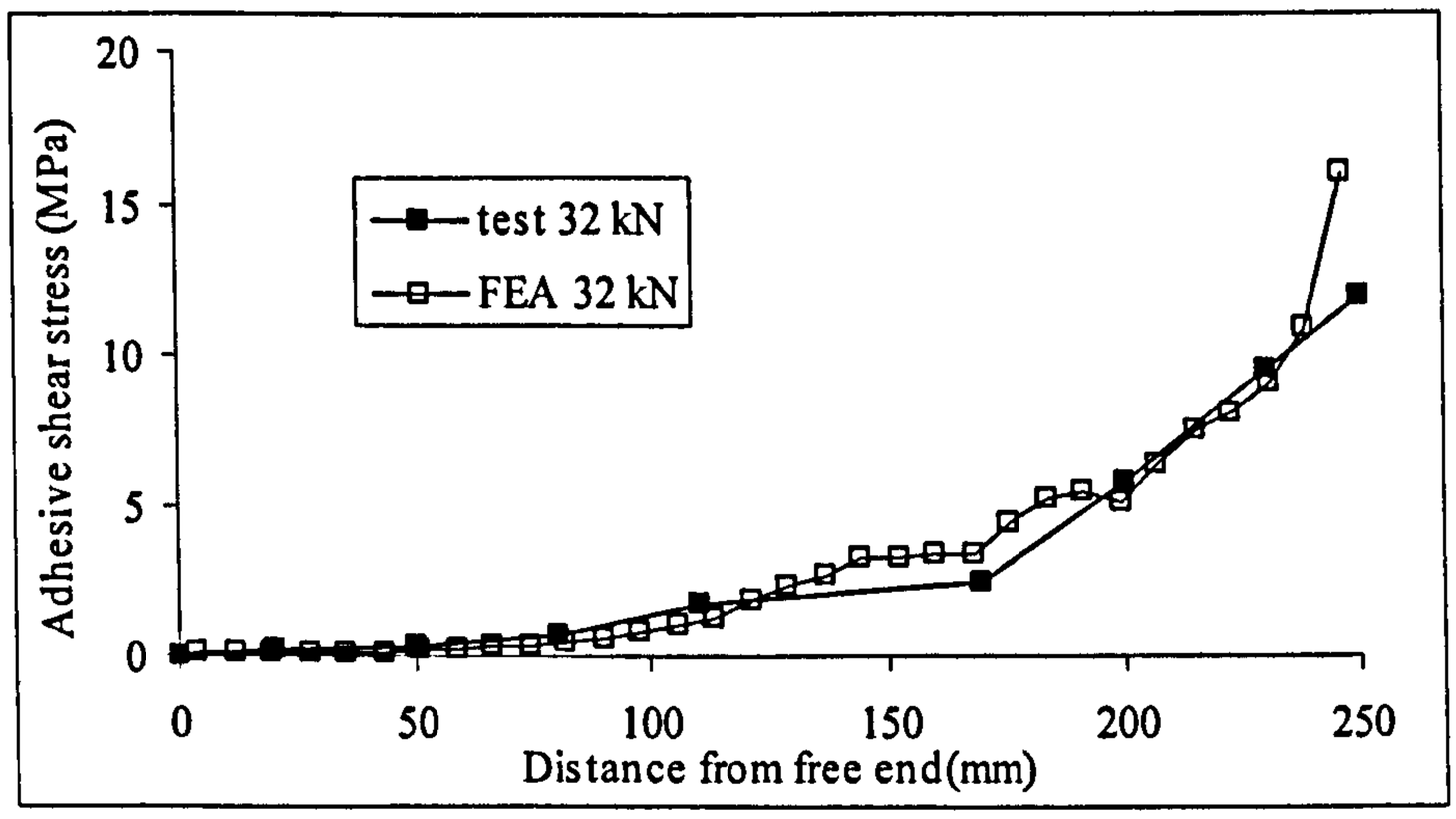

(b) P = 32 kN

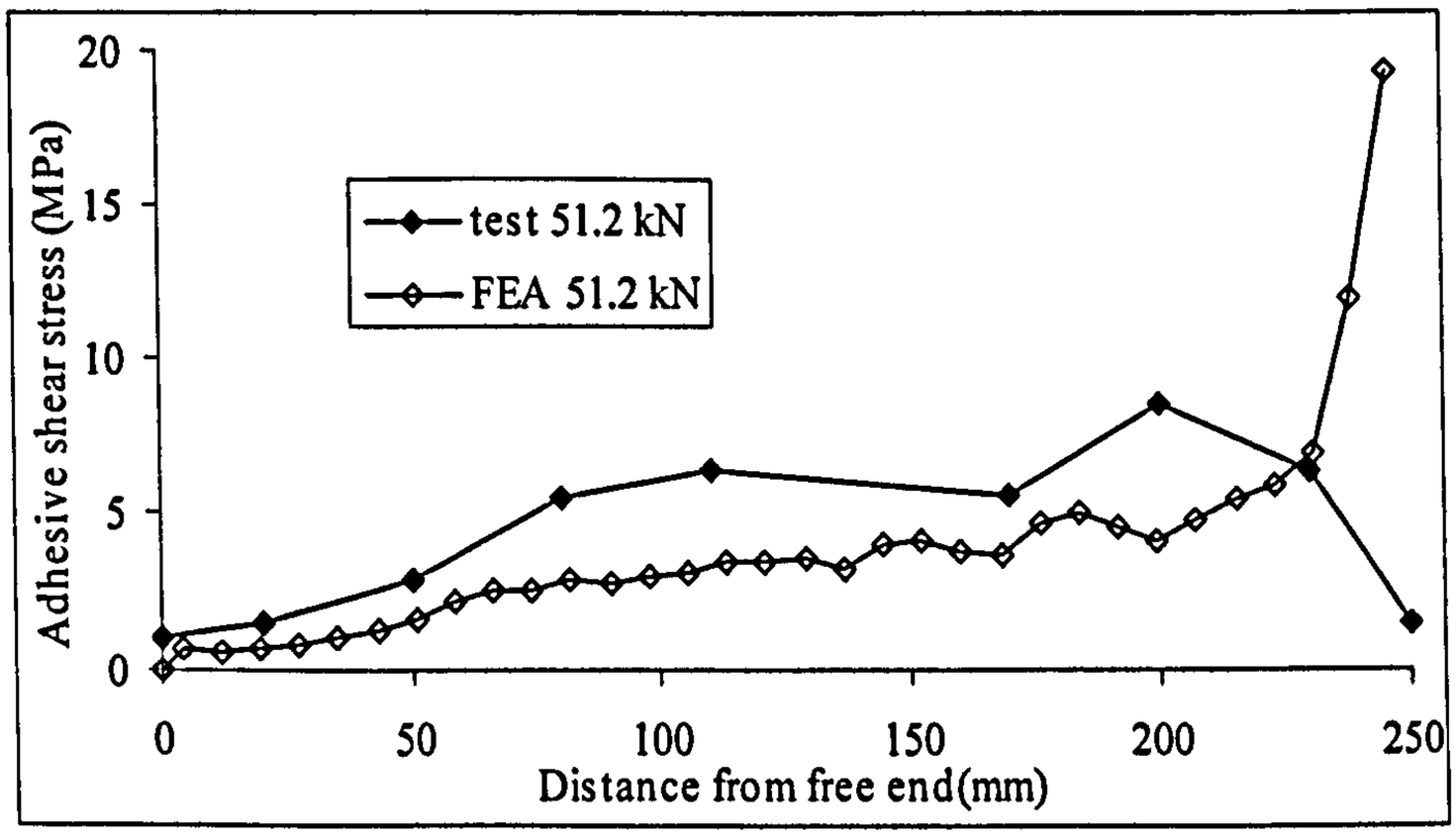

(c) P = 51.2 kN

Figure 3-37 Comparisons between FEA results and test data for adhesive shear stress distributions

Although certain differences exist between FEA results and test data, the comparisons are reasonably satisfying. Therefore, the 3D modelling technique was used for simulating the structural responses of NSM specimens tested in this PhD study and the comparisons were presented in Chapter 5.

3.4 Conclusions

The advanced FEA package DIANA presented here provides robust predictions of the stress transfer behaviour between steel/FRP and concrete in the composite structures. Strains of FRP plates and steel bars, bond stress slip and slip distributions are reliably determined.

In 2D FE modelling, it appears that the four-noded quadrilateral plane stress element shows better performance in modelling the adhesive layer rather than the four-noded interface element. By using a few layers of plane stress elements across the thickness of adhesive, the effects of adhesive through-thickness stress variation can be clearly demonstrated, especially at certain critical positions, such as the ends of adhesive layer or the bond near concrete beam cracks, which are the zones of connection stress concentration. On the other side, the interface element is more suitable for modelling the surface between two materials rather than one certain material such as adhesive, while the surface preferably has no thickness or has much smaller thickness than surrounding materials. Although these results are presented for elastic response, the ideas also apply probably in magnified form after any material nonlinearity (e.g. steel yield or concrete in high compression) occurs.

In the 3D model, the eight-noded brick element HX24L is employed to model the adhesive layer, the concrete block and the FRP bars. Reasonable agreement was found between the FEA results and the test data so that this modelling technique could be further used in other analyses.

However, it is inappropriate to assume the rigid connection of nodes between strengthening rods and adhesive elements in certain cases if there is significant slip between them. In this case, an interface element could be introduced between

adhesive layer and FRP rod to describe a relation between the tractions and the relative displacements across the interface. The extension study about FEA program's capabilities to deal with this issue is then discussed later in Chapter 6.

Chapter 4

Novel pullout tests with NSM CFRP rods

4.1 Introduction

The use of near surface mounted (NSM) Fibre Reinforced Polymer (FRP) rods is a promising technology for increasing the strength of deficient concrete members. As discussed in Chapter 2, although externally strengthened RC beams have been researched extensively, there are still a few important areas to be investigated with regards to NSM strengthening of structures. This relates to investigation of bond-stresses between FRP and concrete up to failure.

Hence, there is scope for fundamental work in these areas. To that end, a carefully designed experimental programme was developed in this PhD study, to give insight into characteristics of stress transfer between NSM FRP rods and concrete in both the mid-span and end zones of beams. As can be seen in Figure 4-1, the specimen comprised a middle RC block joined to 2 side RC blocks via steel and FRP reinforcements continuous across the 3 blocks. The specimen is loaded axially. Use of instrumentation in the specimen permits estimation of local bond stress distributions within the middle block (which gives insight into bond behaviour in the

midspan zone of a real FRP-strengthened RC beam) and the end blocks (giving insight into bond behaviour in end anchorage zones of FRP-strengthened RC beams).

The influence of various geometry parameters such as length of middle block, the amount of strengthening CFRP rods and the width of near surface grooves on the bonding performance of blocks under certain loads were investigated by comparing and analysing the experimental data.

A preliminary study of the mechanics of the splitting cracks was then done to give rise to NSM FRP-to-concrete bond failure.

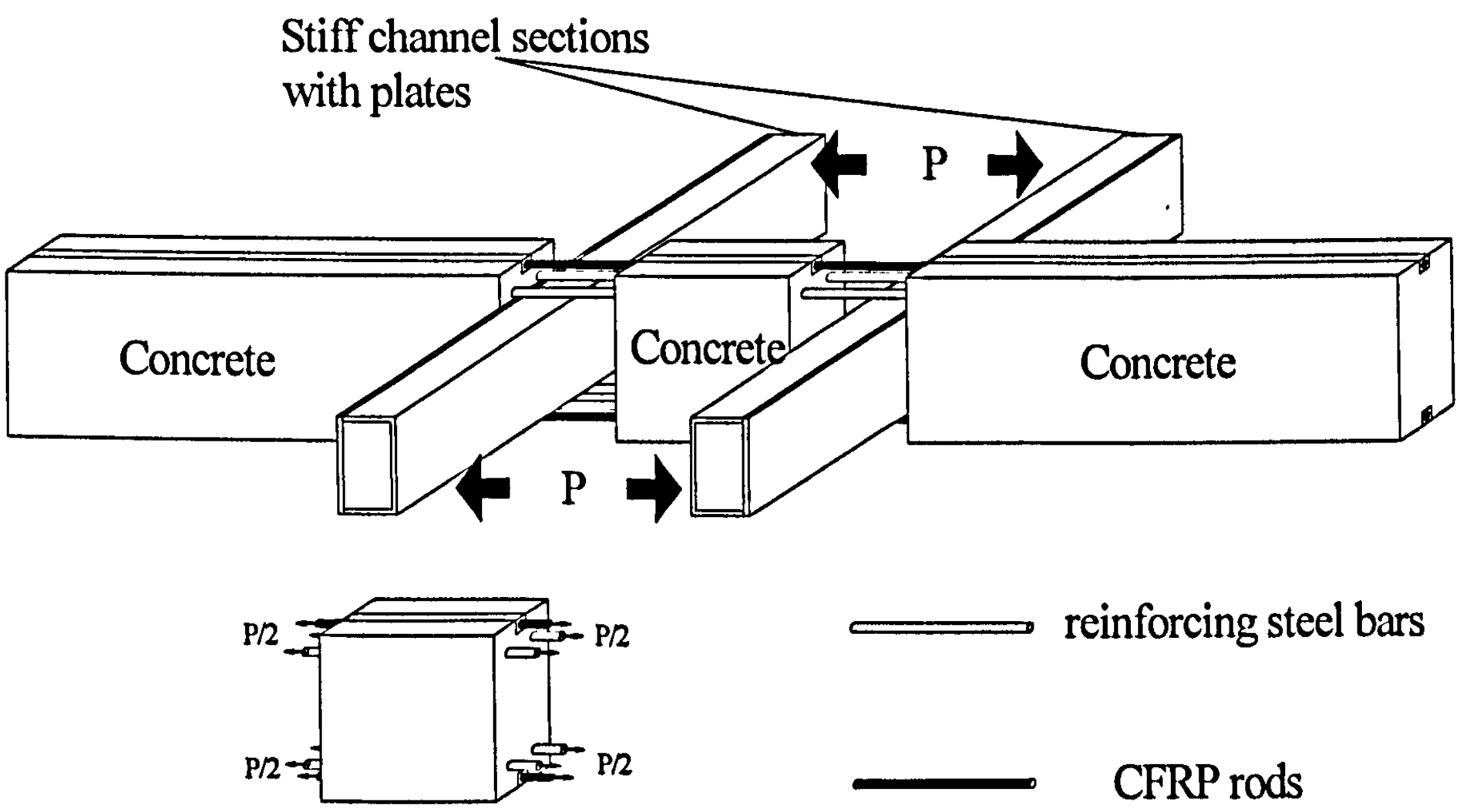

Figure 4-1 Loading configuration of specimen

In what follows, the details of the NSM CFRP strengthened specimens are presented, the recorded visual observations and measured data from the tests to failure of these specimens are discussed, and the inferences drawn from these test results on the nature of the important structural actions are put forward.

4.2 Description of experimental study

4.2.1 Details of strengthened RC blocks

Four CFRP NSM pullout specimens to the general details of Figure 4-1 were fabricated and tested to failure. Each specimen consisted of three concrete blocks reinforced with ribbed steel bars inside and CFRP rods near surface mounted (NSM) on two opposite faces.

The cross section details are given in Figure 4-2. Stirrups were used in the side blocks at intervals of 300 mm to represent the beam ends near supports. The middle block was used to represent the midspan of beam with little shear force. Therefore, no stirrup was used for middle block.

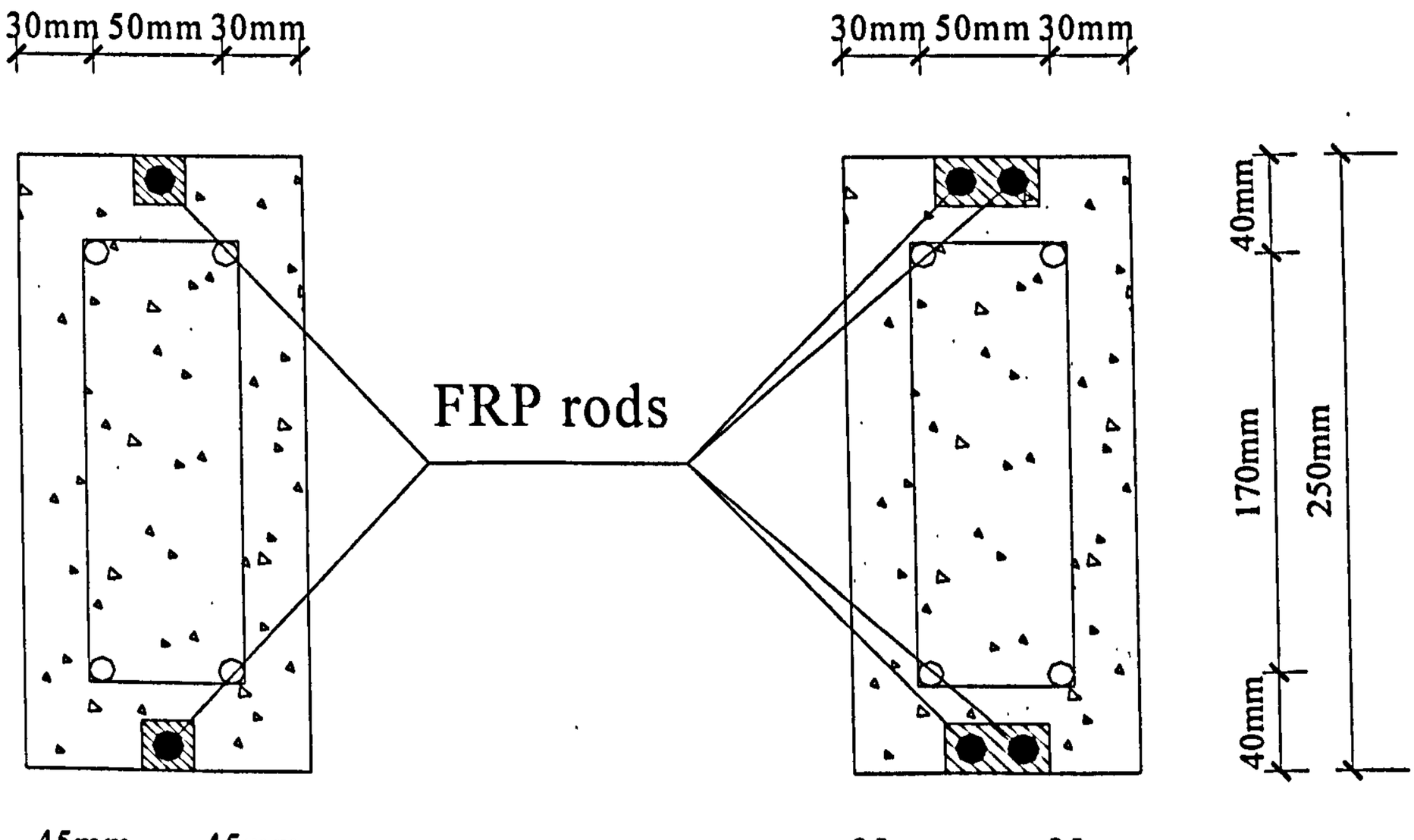

(a) B1 and B3 (b) B2 and B4

Figure 4-2 Cross section dimensions of specimens

Dimension parameters of specimens are given in Figure 4-3. As can be seen, the primary test variables were the length of the middle block and the amounts of CFRP rods bonded onto the blocks. The four specimens are henceforth termed B1 to B4.

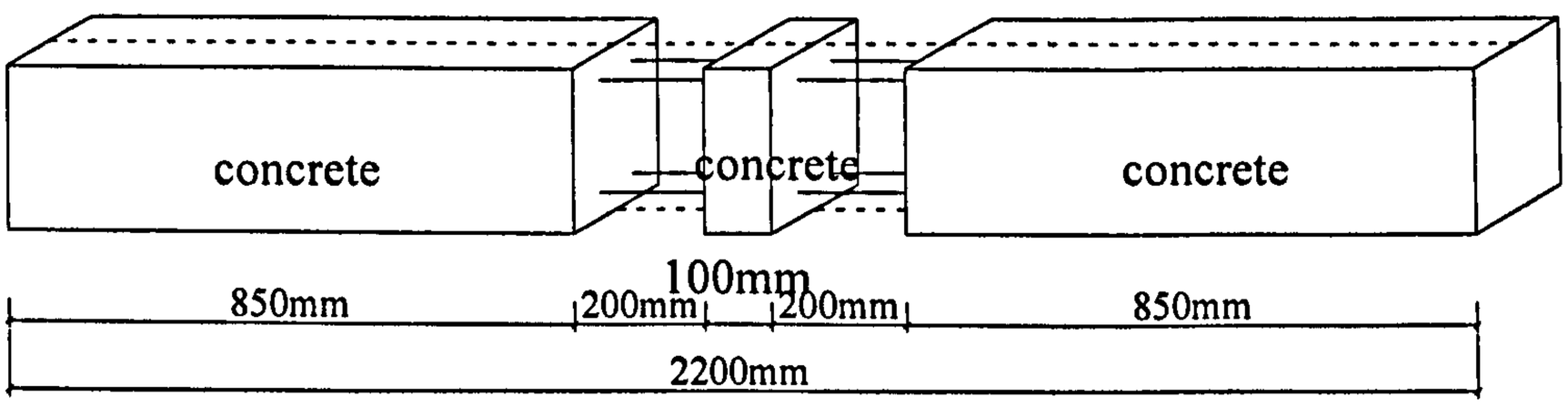

(a) B1 (short middle block+1 rod each side)

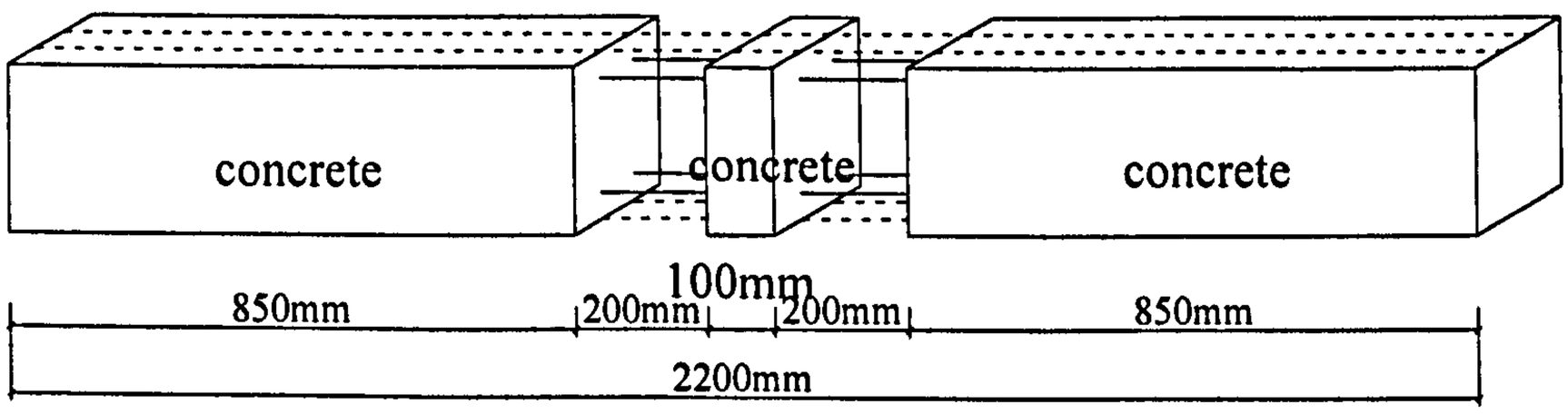

(b) B2 (short middle block+2 rods each side)

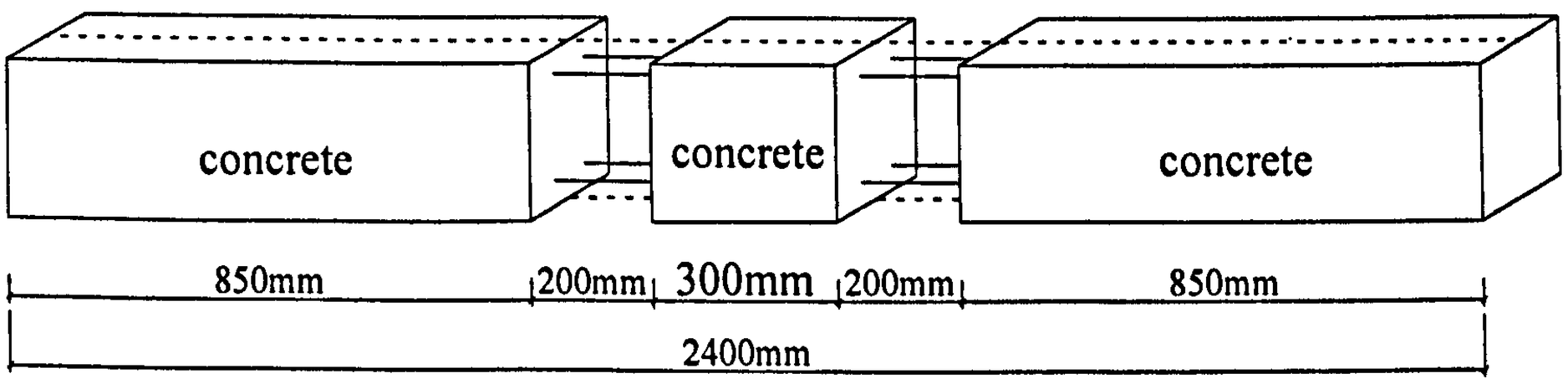

(c) B3 (long middle block+1 rod each side)

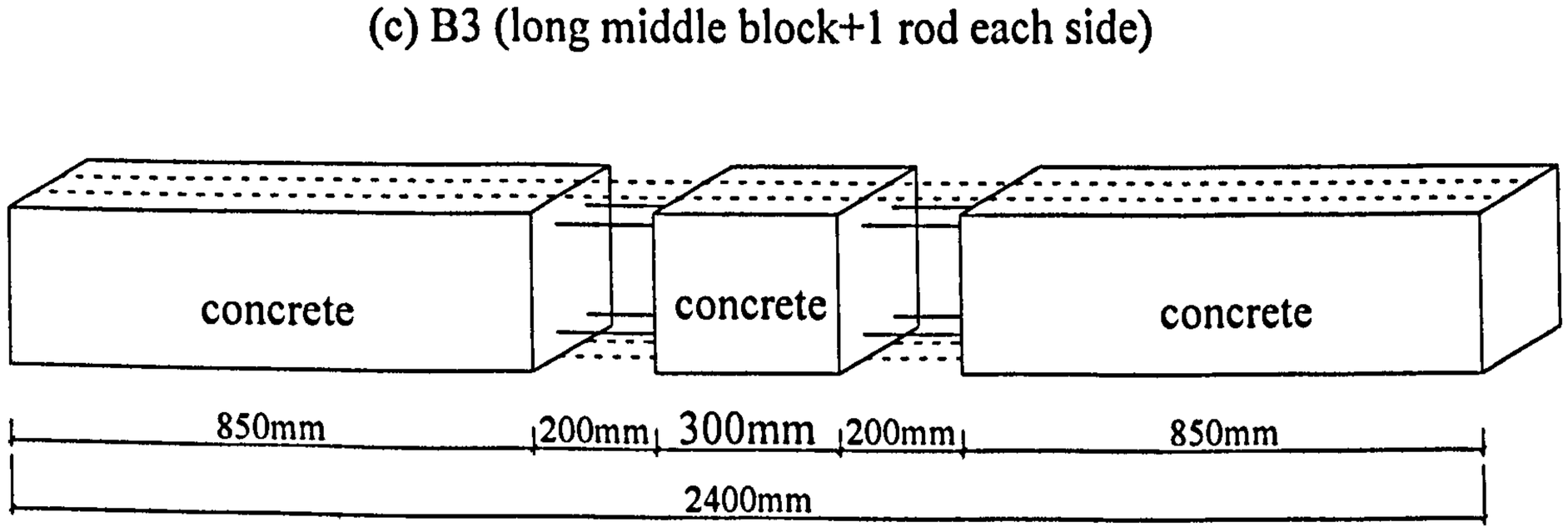

(d) B4 (long middle block+2 rods each side)

Figure 4-3 Dimension parameters of specimens

Table 4-1 shows the geometry details for all the four specimens.

Table 4-1 Geometry details of four specimens

Specimen	Length of middle block (mm)	Number of CFRP rods on each side	Width of near surface groove (mm)
B1	100	1	20
B2	100	2	40
B3	300	1	20
B4	300	2	40

4.2.2 Material properties

4.2.2.1 Concrete

The covercrete strength is a major parameter influencing the onset of brittle separation failure of FRP-plated concrete members. However, the present investigation is focused on the effects of other parameters on the behaviour of FRP-strengthened concrete members. Therefore, all the concrete specimens were carefully cast to minimise any variation in concrete quality. The influence of variability in concrete strength can be considered in future work. Indeed, the concrete blocks were all cast from one batch of ready-mixed concrete. The target concrete strength was 40 N/mm^2. The freshly cast specimens were covered with polythene for at least 28 days, to permit proper curing of the concrete.

4.2.2.2 CFRP rods

The CFRP rods, supplied by Degussa Ltd., were tested in this experimental programme. These CFRP rods are 12mm diameter and all contained unidirectional carbon fibres, with a minimum fibre content of 68% by volume.

The Young's modulus was obtained from tensile tests performed on 200mm long coupons in an extensometer (Figure 4-4 (a)). Strain gauges were attached at mid-length of each coupon, to measure the elongation of the coupon without having to allow for local effects and slip between the jaws of the testing machine and the ends of the coupon. Two strain gauges were attached diametrically opposite each other for each coupon (Figure 4-4 (b)) to account for any bending effect.

Failure of the FRP strengthened specimens occurred by bond failure at the adhesive - FRP interface and by splitting of the cover concrete, not by rupture of the FRP rods. For this reason, the CFRP coupons were tested to sufficiently high strains to permit quantification of Young's modulus of the material, but were not tested to failure. The measured average Young's modulus of CFRP rods is 140 kN/mm^2.

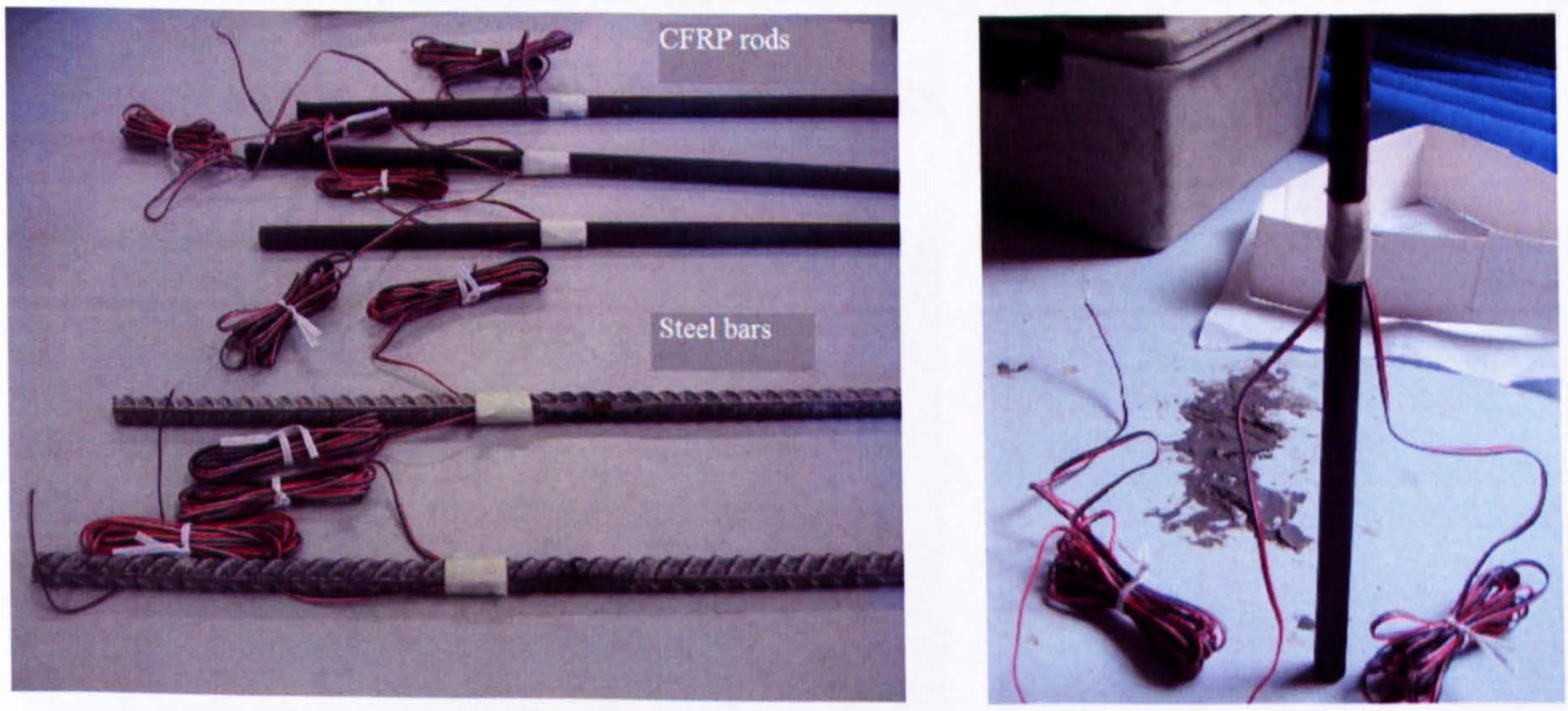

(a) Steel and CFRP rods coupons

(b) Two strain gauges for each rod

Figure 4-4 Tensile test coupons

4.2.2.3 Rebar

High tensile deformed steel reinforcing bars of diameter 12mm were used in all concrete blocks, while 8 mm round steel bar was used for the stirrups. Sample steel

rebar coupons of 200 mm length were tested, as shown in Figure 4-4 (a). The average Young's modulus of steel bars was then found as 185 kN/mm^2.

4.2.2.4 Epoxy adhesive

Epoxy resin is widely used as the bond product for several materials in construction such as concrete, masonry units, wood, glass and metals. A high strength non-flow epoxy bedding and repair mortar with a Trademark of FEBSET NF, supplied by Degussa construction chemicals (UK), was used to bond the prefabricated CFRP rods to the concrete, into the grooves.

The adhesive is a two-part, fast curing material, consisting of a white resin and a black hardener component provided in 3 kg units. In preparing the adhesive, these two parts are mixed until a uniform grey colour is achieved (Figure 4-5). It cures to give high mechanical properties typical to epoxy compounds.

(a) Two-part adhesive (b) Mixture in the bucket

Figure 4-5 Components of FEBSET NF adhesive

According to the manufacturer's product information, the adhesive is resistant to oils, greases, petroleum, salts, many acids and alkalis and most commonly-met corrosive

media. It does not shrink on curing, and is designed to be used when cured from 5°C to 60°C. Its impact resistance and mechanical strength are significantly greater than that of concrete. The typical applications of these adhesives include grouting anchor bars into drilled holes, and bonding of steel or FRP plates to concrete or steel members. According to the supplier, the epoxy adhesive has the properties indicated in Table 4-2.

Table 4-2 Technical data and typical properties of FEBSET NF adhesive

Composition	Two-component epoxy based mortar
Colour	Pale grey
Specific gravity	1.80@ 20℃
Compressive strength	50N/mm^2@ 7 days
Tensile strength	6.5N/mm^2@ 7 days
Flexural strength	50N/mm^2@ 7 days
Full cure 25	3 to 5 days
Pot life	1 hour @ 25℃
	30 mins @ 40℃
Cure rates	5 hours @ 25℃
	2 hours @ 40℃
Full cure	5 days @ 25℃
	3 days @ 40℃

(Degussa product information (2004))

4.2.3 NSM bonding procedure

Each specimen was strengthened using CFRP rods inserted into grooves cut on the two opposite sides of the block. These two sides are supposed to be the top and bottom sides of the beam.

Embedment of the rods was achieved by grooving the surface of the member to be strengthened along the desired direction and to the desired depth and width. The groove was filled halfway with epoxy. The FRP rod was then placed in the groove and lightly pressed, so forcing the epoxy to flow around the bar and fill completely the space between the bar and the sides of the groove. The groove was then filled with more adhesive and the surface is levelled. Installation procedures of the CFRP rods are illustrated in Figure 4-6.

Figure 4-7 shows the diagrams of the four specimens before and after strengthening. Two of the four blocks were strengthened by bonding one CFRP rod on each side, the others by two rods on each side.

(a) The cut groove

(b) Half fill the groove with epoxy

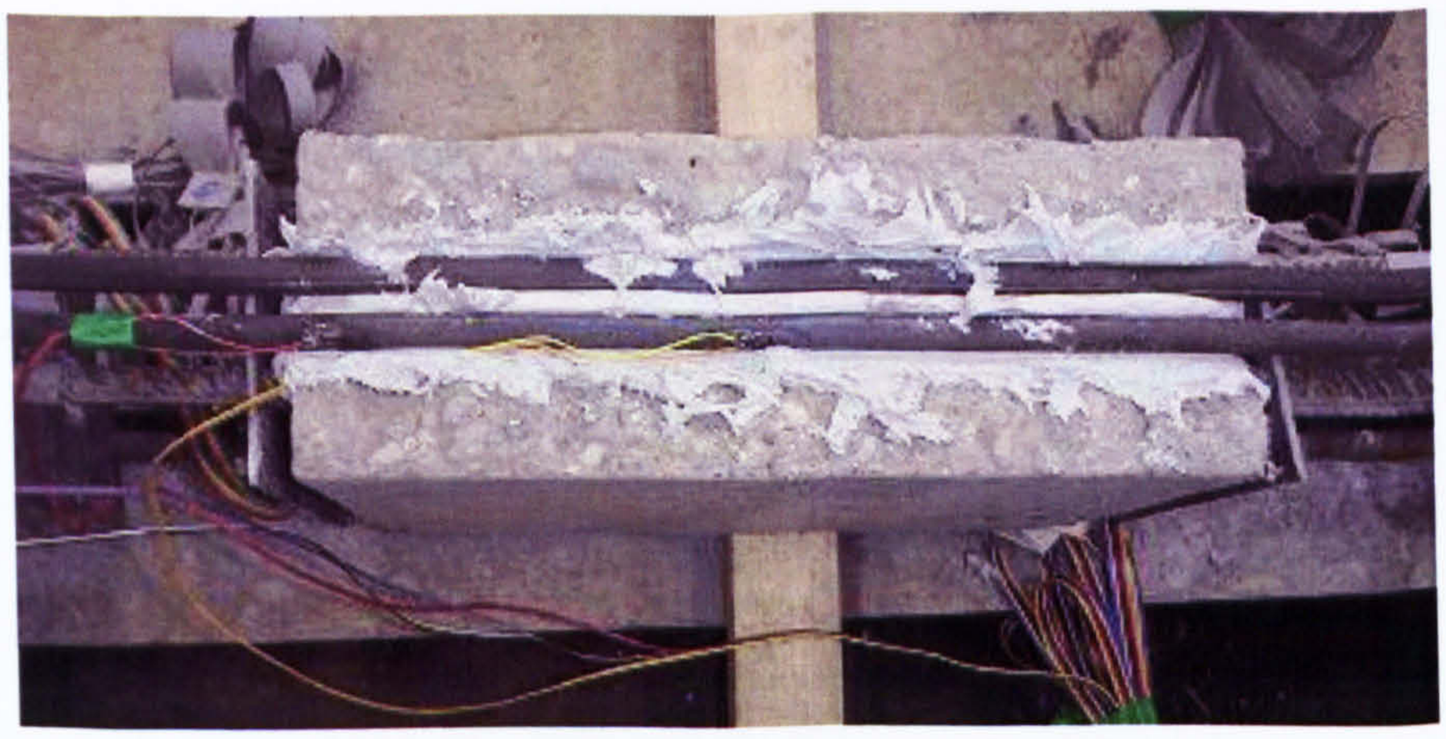

(c) Press the CFRP rods into the groove

(d) Pour the remaining epoxy

(e) The levelled surface

Figure 4-6 Strengthening procedure for specimens

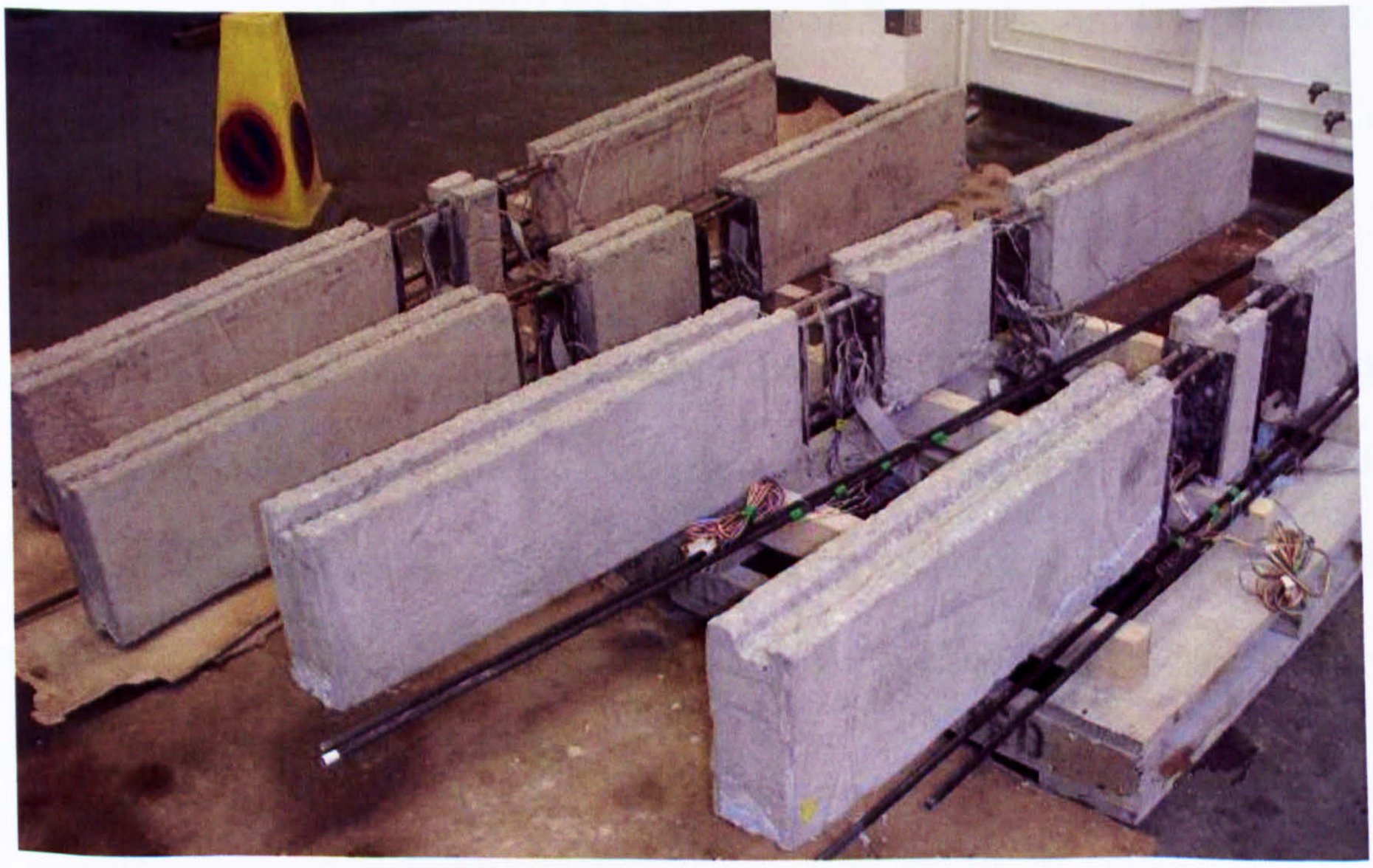

(a) Specimens before bonding CFRP rods

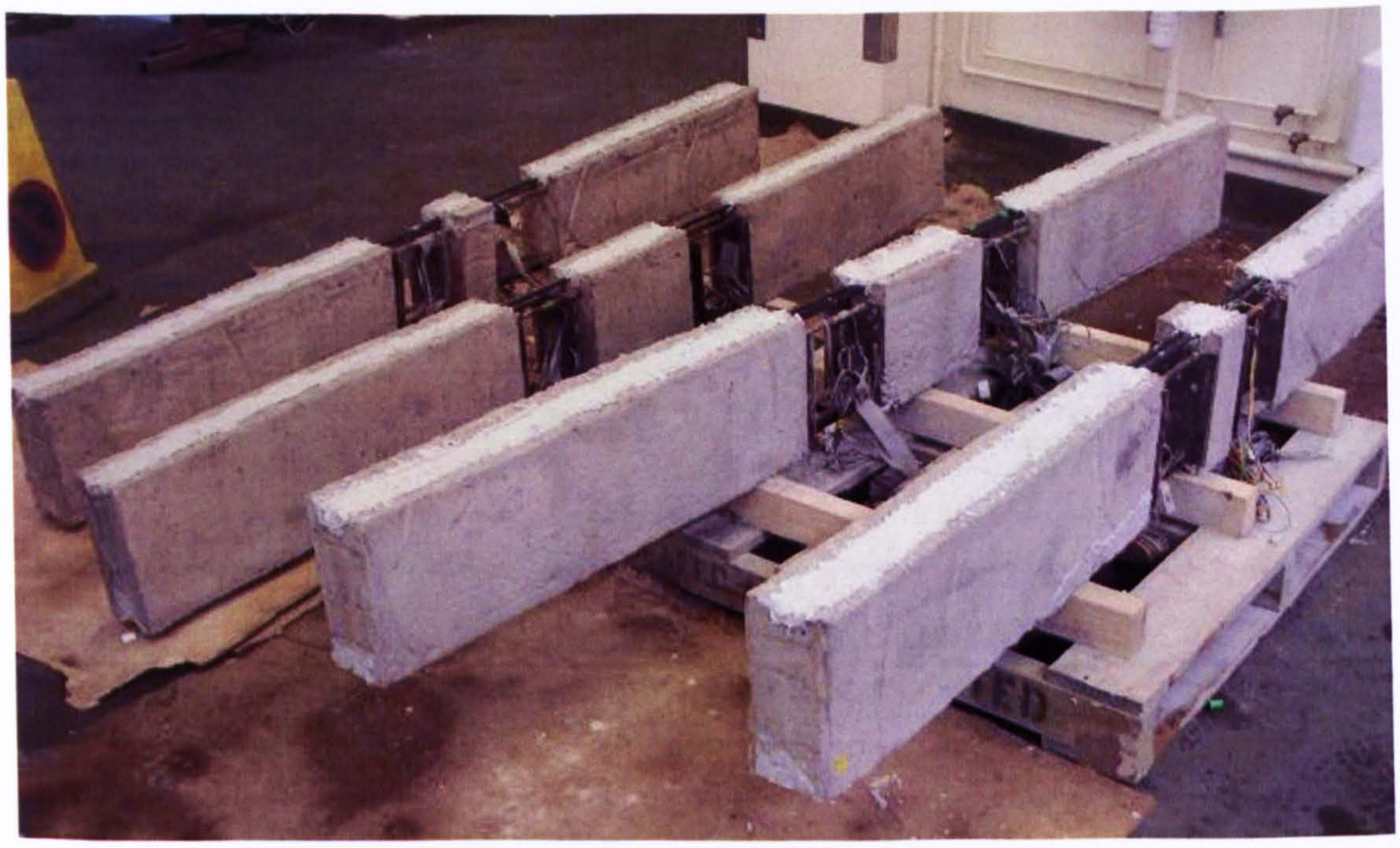

(b) Specimens after bonding CFRP rods

Figure 4-7 Specimens before and after CFRP rod strengthening

4.2.4 Test apparatus and instrumentation

Various layouts of Electrical Resistance Strain Gauges (ERSGs) of 2 mm gauge length were applied to the different specimens, as shown in Figure 4-8. High gauge densities were employed near the middle parts of the specimens. The gauges and accompanying leads on the bonded surfaces of the rods were attached before bonding the rods to the blocks.

One strain gauge was installed on each exposed surface of steel bar near the mid span position to measure the strain in the steel reinforcement. Gauges were also attached to the embedded surfaces of the steel reinforcing bars before casting the concrete blocks, particularly near the middle of block, to quantify the steel strain developed inside the concrete block.

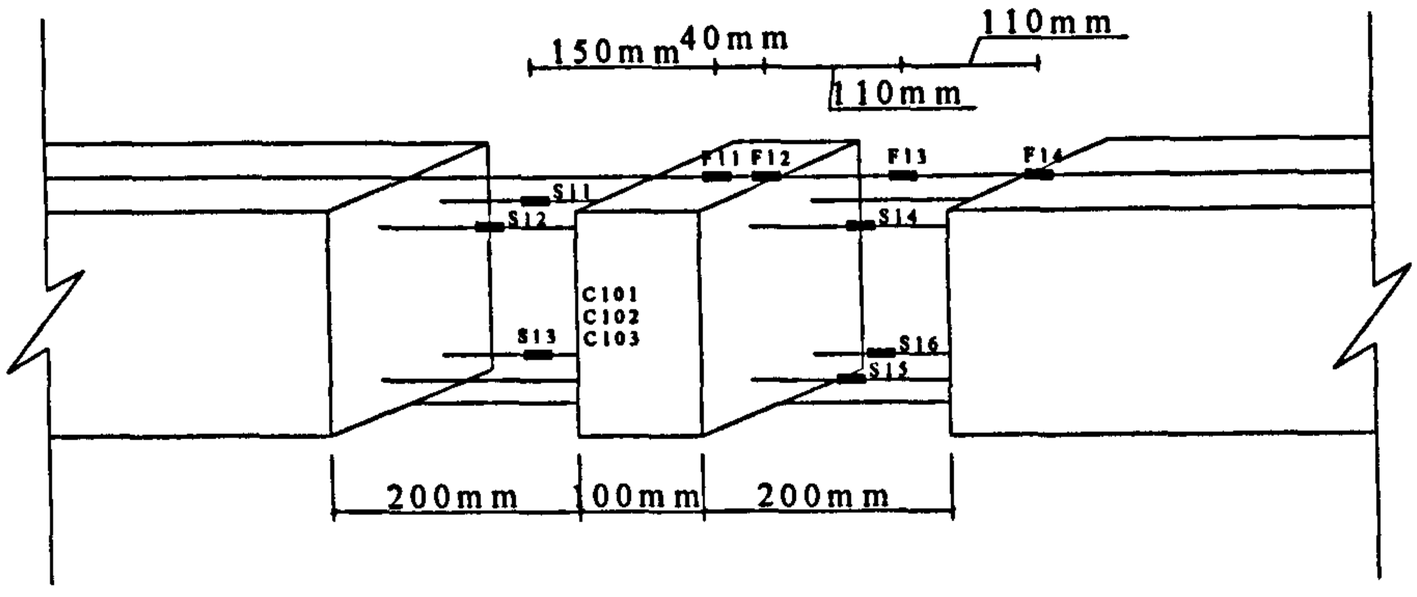

(a) B1

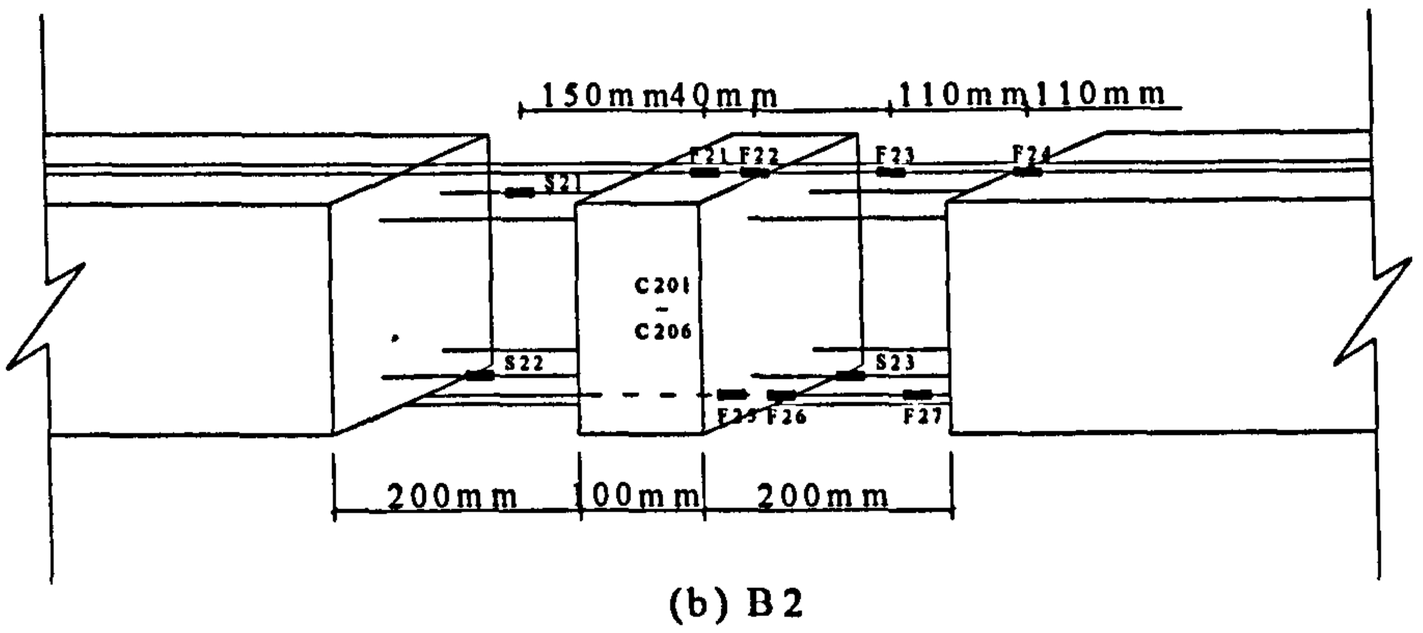

(b) B2

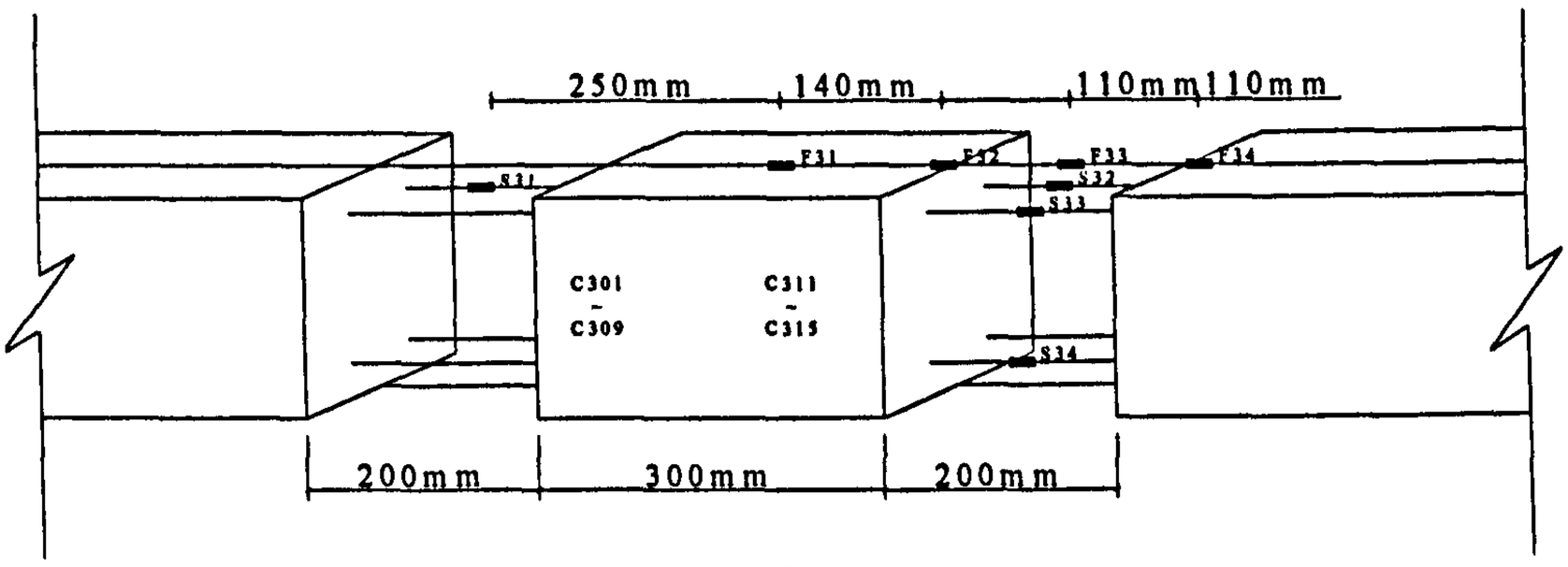

(c) B3

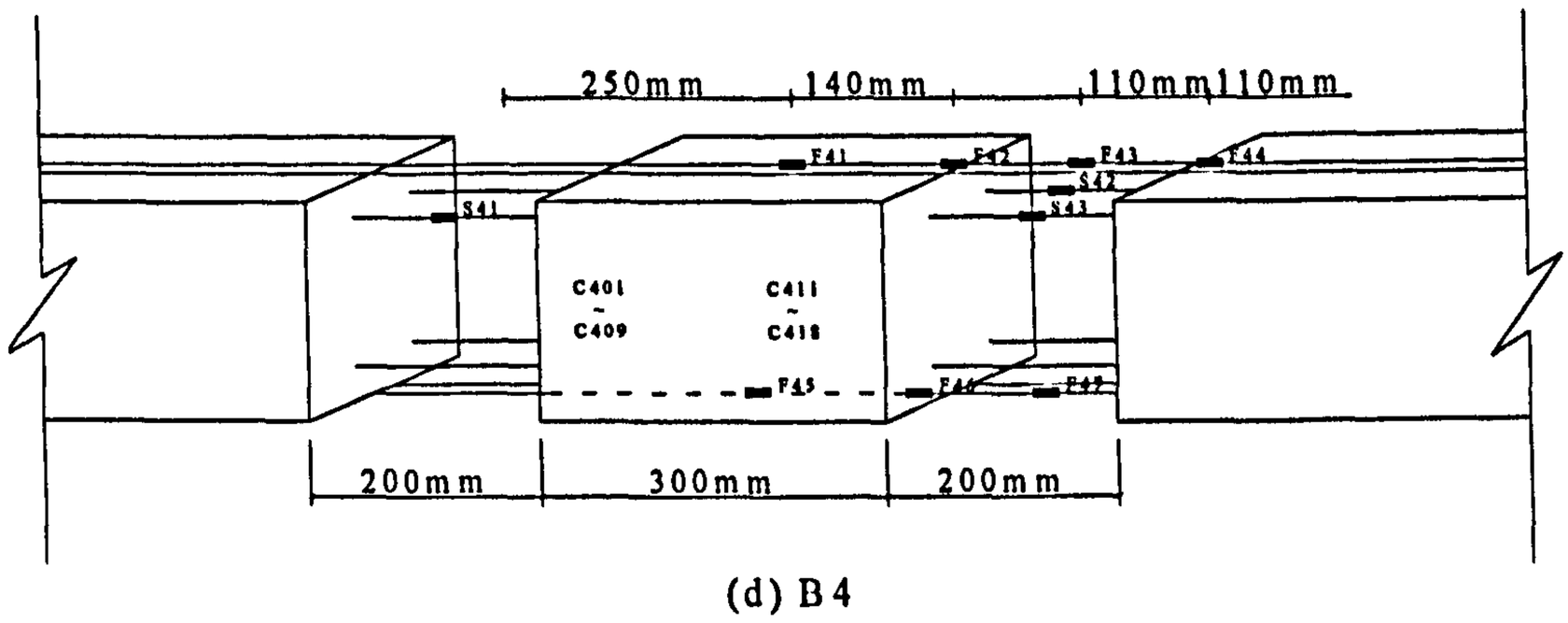

(d) B4

Figure 4-8 Strain gauges location

Strain gauges were attached longitudinally to the surfaces of the CFRP rods at close spacing along the middle of each block. In some cases, strain gauges were attached to

one of the rods in the specimen; while in other cases, strain gauges were attached to two of the rods. In the latter cases, such arrangements could be used to check the symmetry and avoid errors caused by eccentricity effects during pure tensile testing.

On the diagrams, F_{ij}, S_{ij} and C_{ij} refer to gauges on the FRP bars, and on the exposed and embedded steel surfaces respectively, where i means the numbering of specimen and j means the numbering of strain gauge in each specimen.

Throughout testing, development of crack patterns and the progression of any form of failure (brittle separation or otherwise), were monitored using a camera.

4.2.5 Test set up and procedure

All specimens were tested under pure axial loading up to failure. As shown in Figure 4-1, the hydraulic jack was originally designed to be put between two side blocks in order to push them away, which consequently enforce the middle block under tensile force. However, the spaces between the two side blocks (especially for the smaller specimen B1 and B2) are found to be too small to fit in the jack. Therefore, an end positioned hand-operated hydraulic jack was used in a self-reacting steel frame system as shown in Figure 4-9.

When the jack pushed the end steel channel section, the load was transferred via two steel rods into the middle steel channel section, which consequently pushed the side RC block away. The other side RC block was fixed with another end welded steel box section via two steel rods. Such set up enables the middle RC block under axial tensile force. The tension in the specimen was then counterweighted by compression in the I-section steel beam frame. The buckling of I-section steel beams due to compression was checked and no bracing member was found needed between two steel beams.

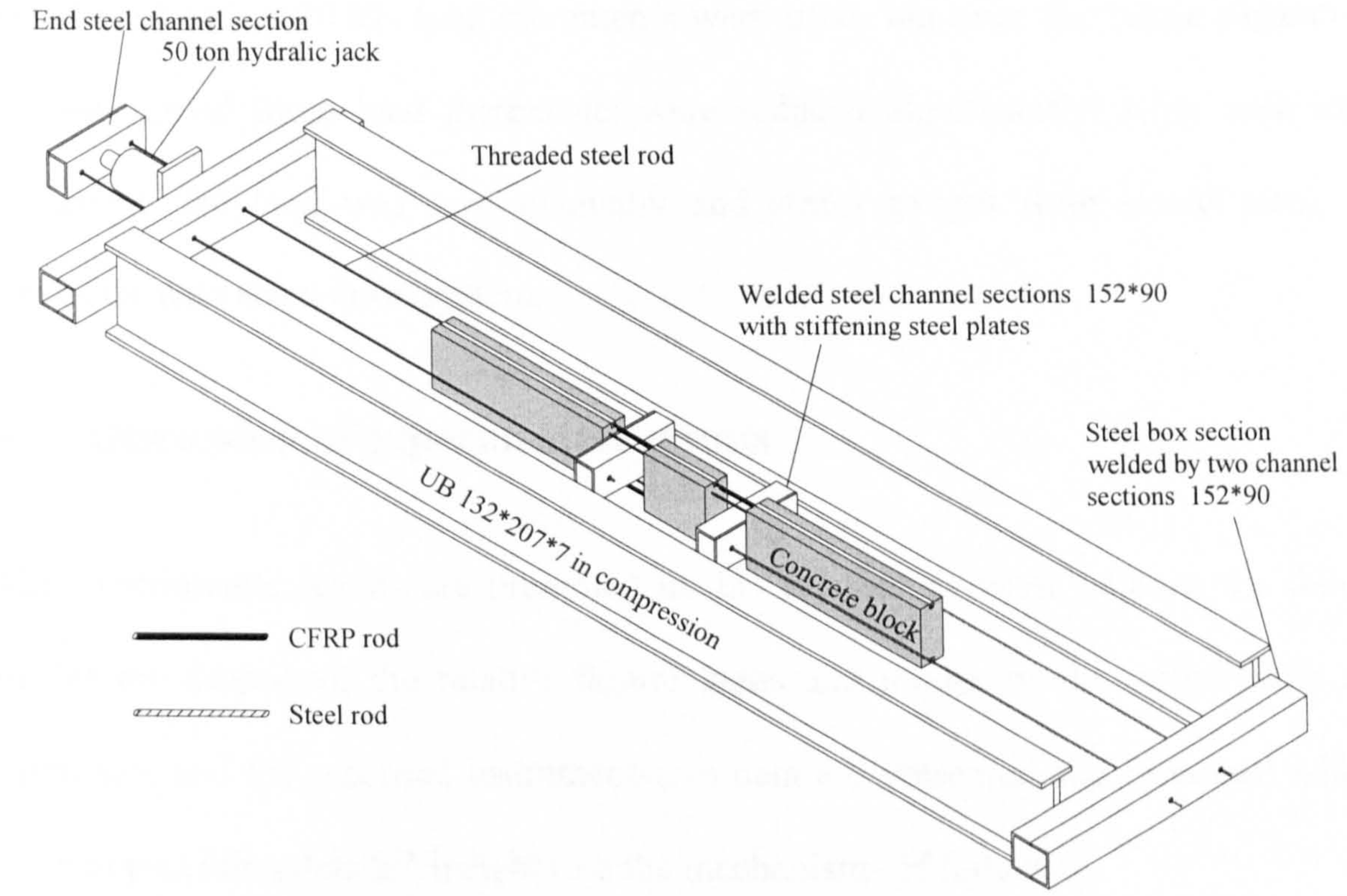

(a) Isometric view

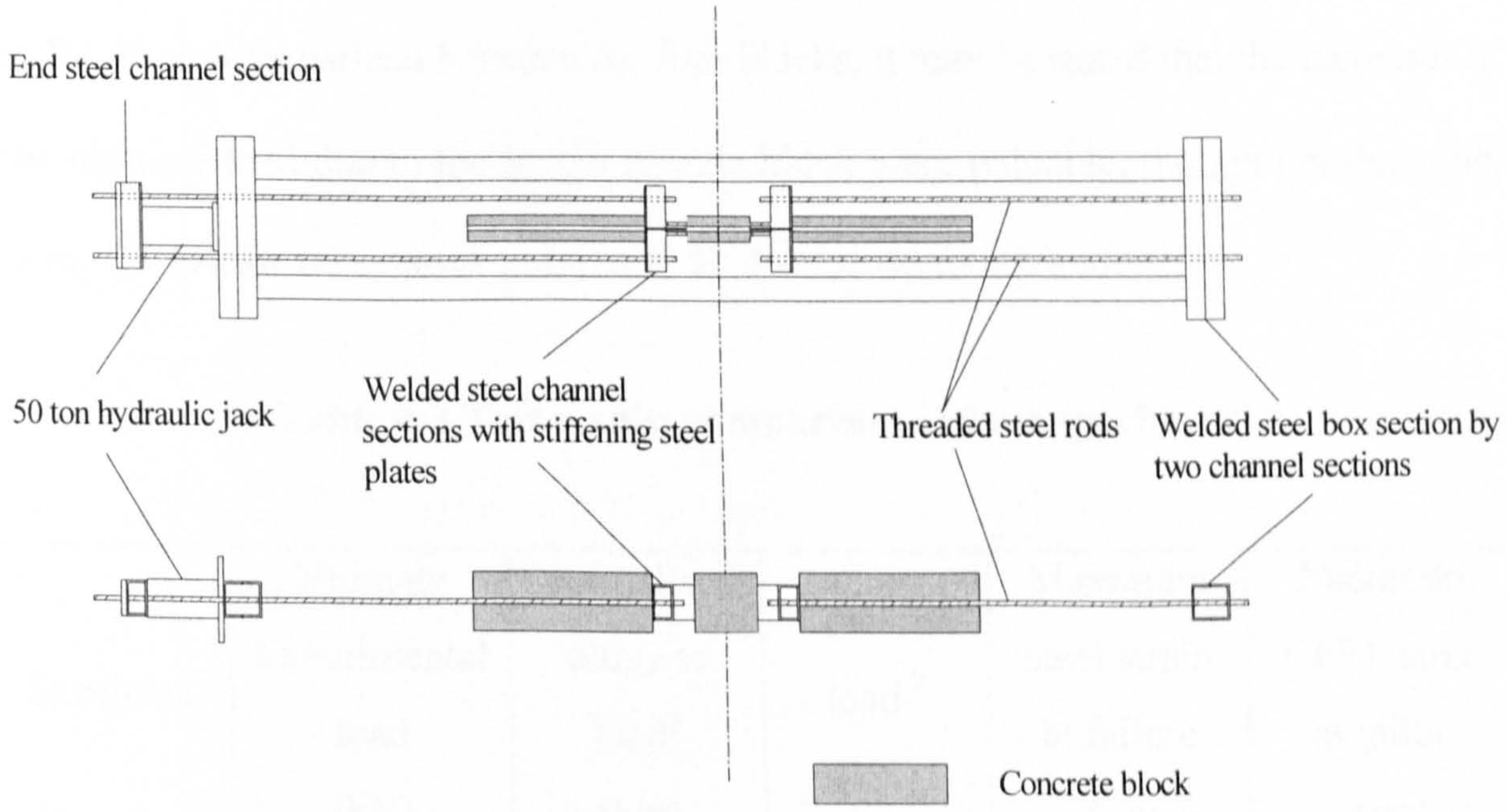

(b) Plan and elevation views

Figure 4-9 Specimen set up

Initially 10 kN or 20 kN load increments were used, but once the brittle separation process started these load increments were reduced significantly. After each load increment, the load was read manually and strain gauges were stored using an electronic data acquisition system.

4.3 Discussion of experimental results

The experimental results are presented in this section. In what follows, the failure modes are described, the relative failure loads and modes of the tested beam are discussed, and the recorded instrumentation data are presented and discussed with a view to providing detailed insight into the mechanisms of failure.

4.3.1 Failure loads and failure modes

Table 4-3 shows the experimental failure loads and maximum strains of specimens B1 to B4. From comparison between the four blocks, it may be stated that the increases of the ultimate load due to the longer middle block were palpable, though not dramatic, being 24.5% for B3 relative to B1, and 31.7% for B4 relative to B2.

Table 4-3 Test results comparison of four specimens

Specimen	Ultimate Experimental load (kN)	Normalised ultimate load[1] (kN)	Cracking load [2] (kN)	Maximum steel strain at failure (με)	Maximum CFRP strain at failure (με)
B1	289.8	1.0	118.2	2806	N/A
B2	294.0	1.014	127.4	3235	2689
B3	360.7	1.245	108.2	2877	3442
B4	385.6	1.331	135.7	2742	2369

[1] Normalized with respect to failure load of control specimen B1

[2] Cracks initiated on either side concrete block and propagated outwards

However, with the same length of middle block (300 mm), when the amount of strengthening CFRP rods doubled from 2 to 4 rods, the ultimate load of B4 increased slightly 9% more than B3. Also, B1 and B2 failed at very similar loads in spite of doubling the strengthening CFRP rod on both sides.

Figure 4-10 shows the crack developments in B2 and B4. As can be seen, the first visible cracks initiated near the loading areas on the side blocks and then propagated horizontally outwards. According to Table 4-3, the first crack load is not very variable between the specimens.

The initial crack patterns in middle blocks, either horizontal or vertical, are shown in Figure 4-11. In B1 and B2, deep horizontal cracks suddenly occurred on both sides of short middle blocks in the loading stage near failure (around P = 270 kN, see Figure 4-11 (a) and (b)) while there are no such original horizontal crack found in B3 and B4 before specimens failure. Basically, such horizontal cracks occurred when the normal stress on the fracture plane exceed the concrete tensile strength. A detailed study was then carried out in 4.3.3 and a cantilever beam theory was used to calculate these normal stresses to give insight into the crack mechanism.

On the other hand, one vertical crack was observed in the centre of each middle block at the early load stage (around P = 155 kN, see Figure 4-11 (c) and (d)) in both B3 and B4 rather than in B1 and B2 which have shorter middle blocks. This could explain that the minimum crack spacing under pure tensile force is bigger than the size of shorter middle block (100 mm).

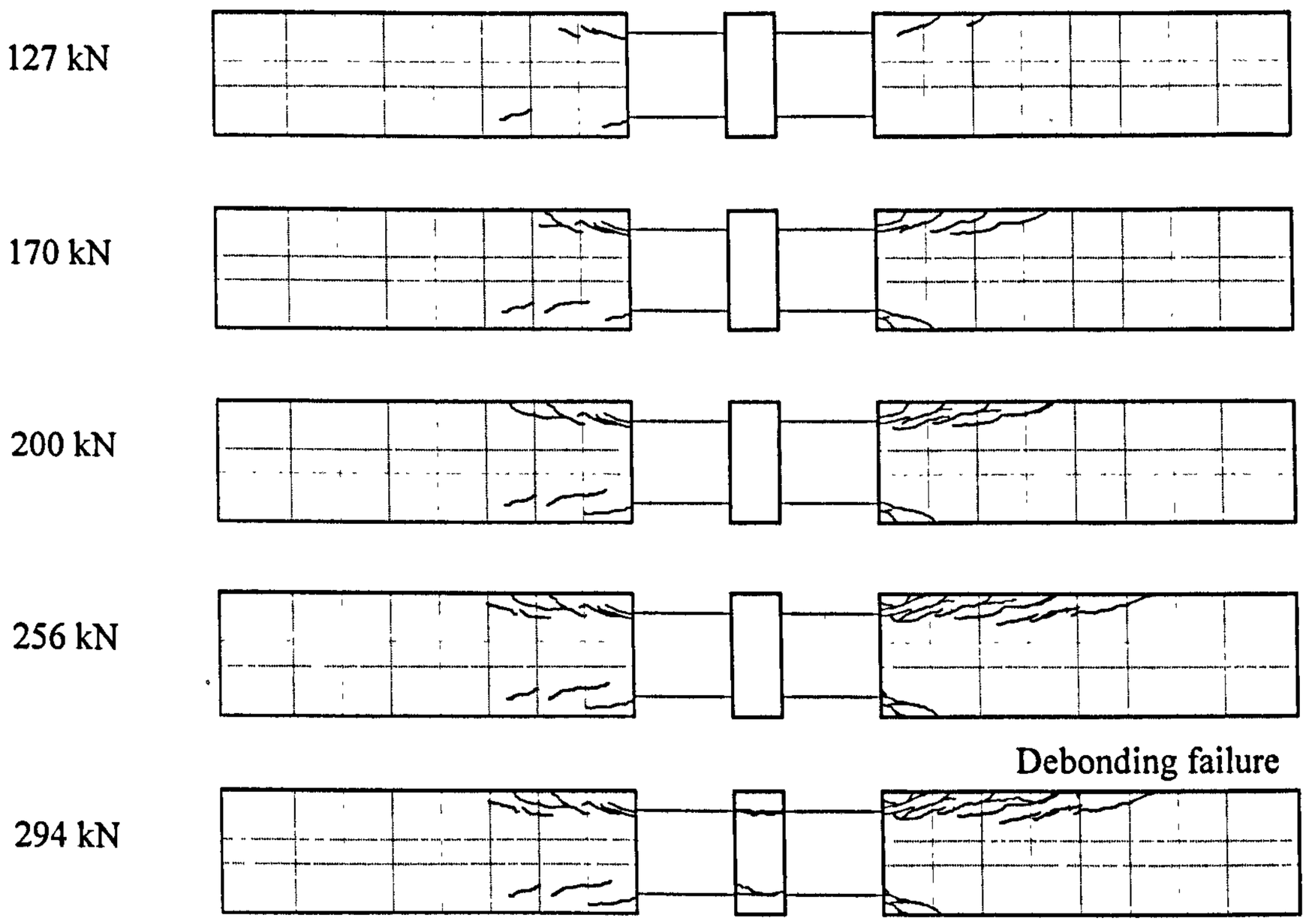

(a) B2

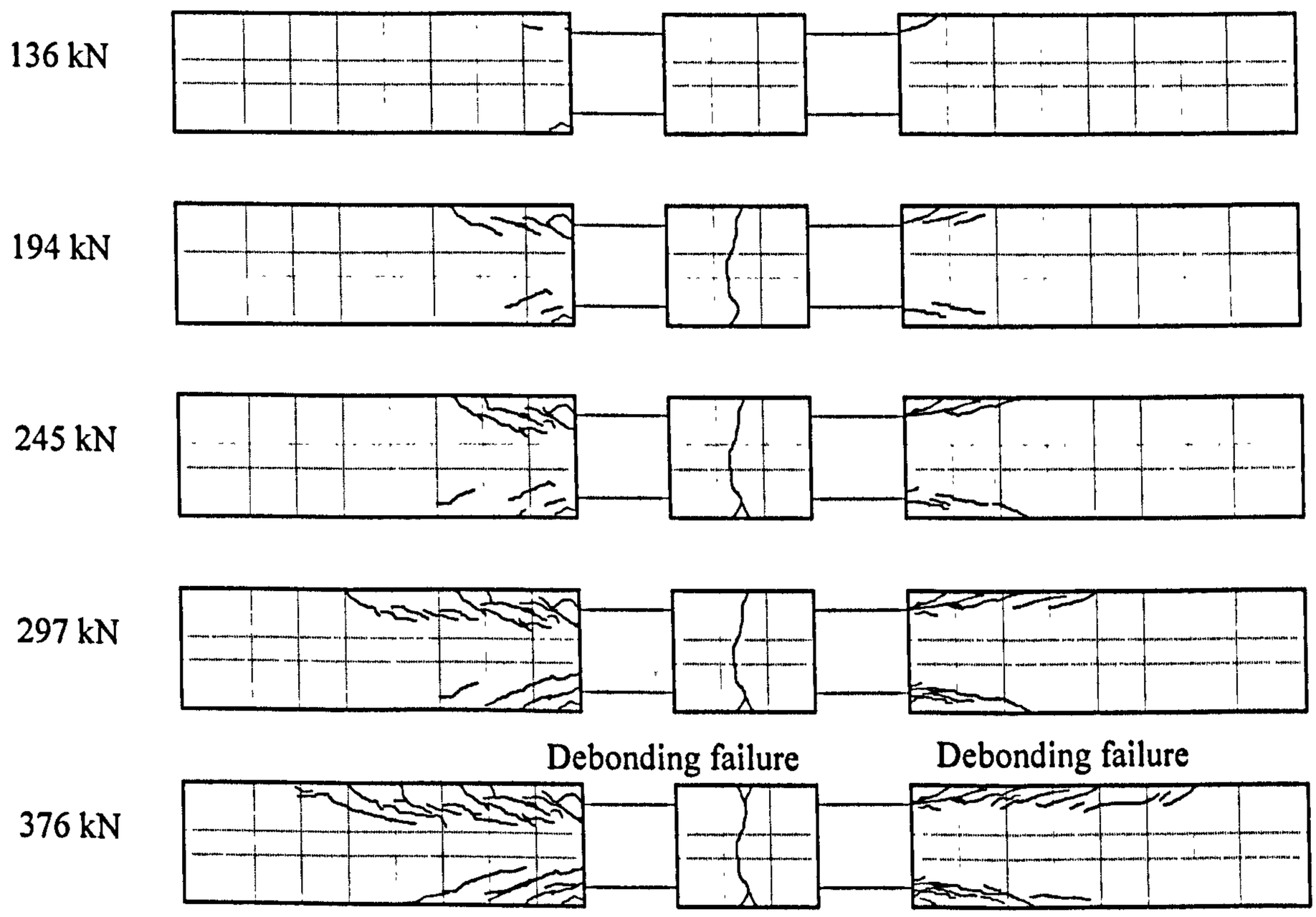

(b) B4

Figure 4-10 Elevation views of crack developments in the specimens B2 and B4

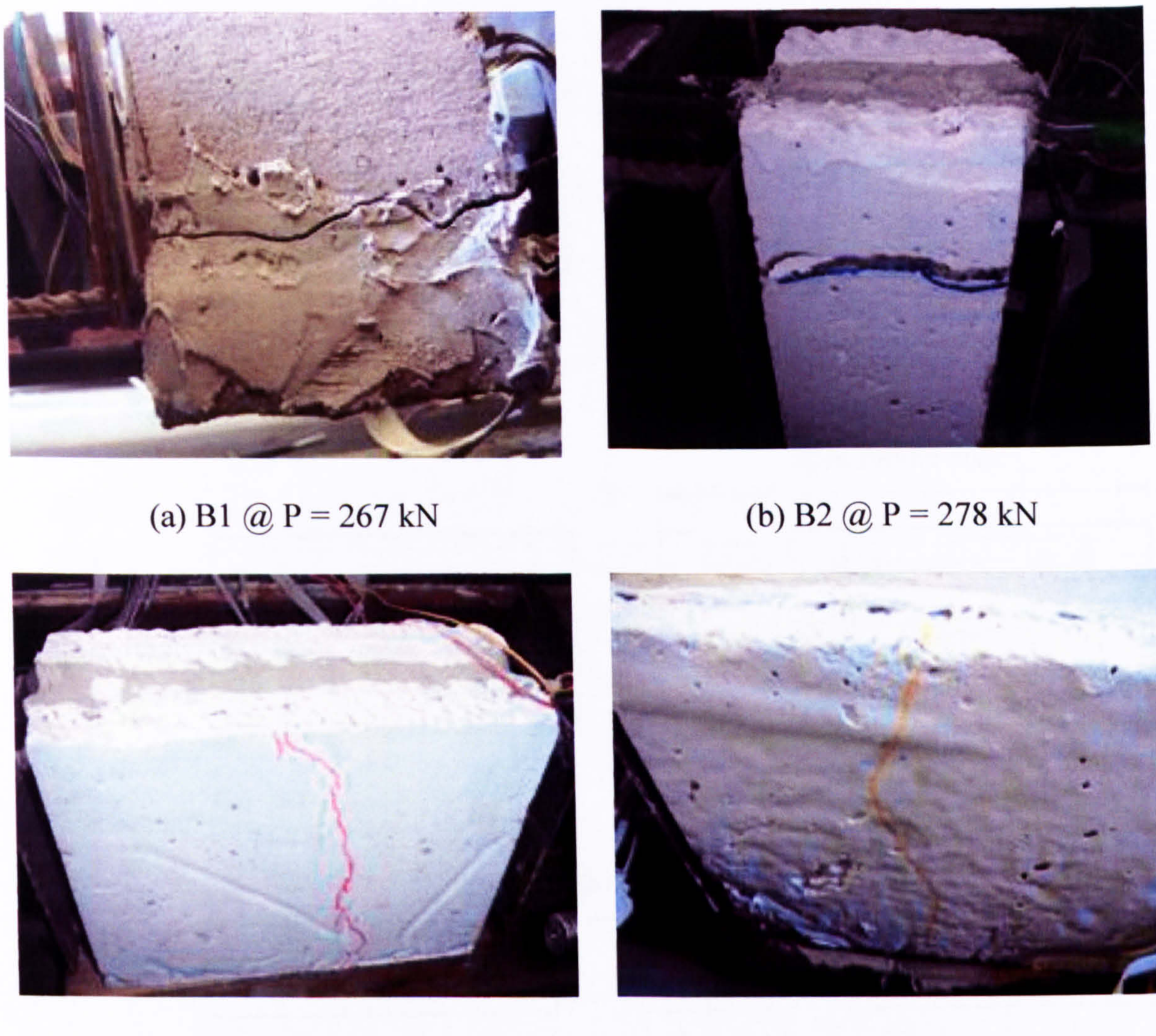

(a) B1 @ P = 267 kN

(b) B2 @ P = 278 kN

(c) B3@ P = 160 kN

(d) B4 @ P = 152 kN

Figure 4-11 Initial cracks in the middle blocks

The crack patterns of specimens B1 to B4 before final separation failure are shown in Figure 4-12. Extensive cracks formed horizontally on the side blocks as the applied load increased beyond the points that just caused yield of the embedded steel. Cracks propagated and covered most of the length of the side blocks just before the final brittle separation failure. However, fewer cracks were observed in B1 and B2 compared to B3 and B4 before failure. This may indicate that specimens with shorter middle block are more brittle than those with longer middle block so that they fail under the smaller loads without showing too much ductility.

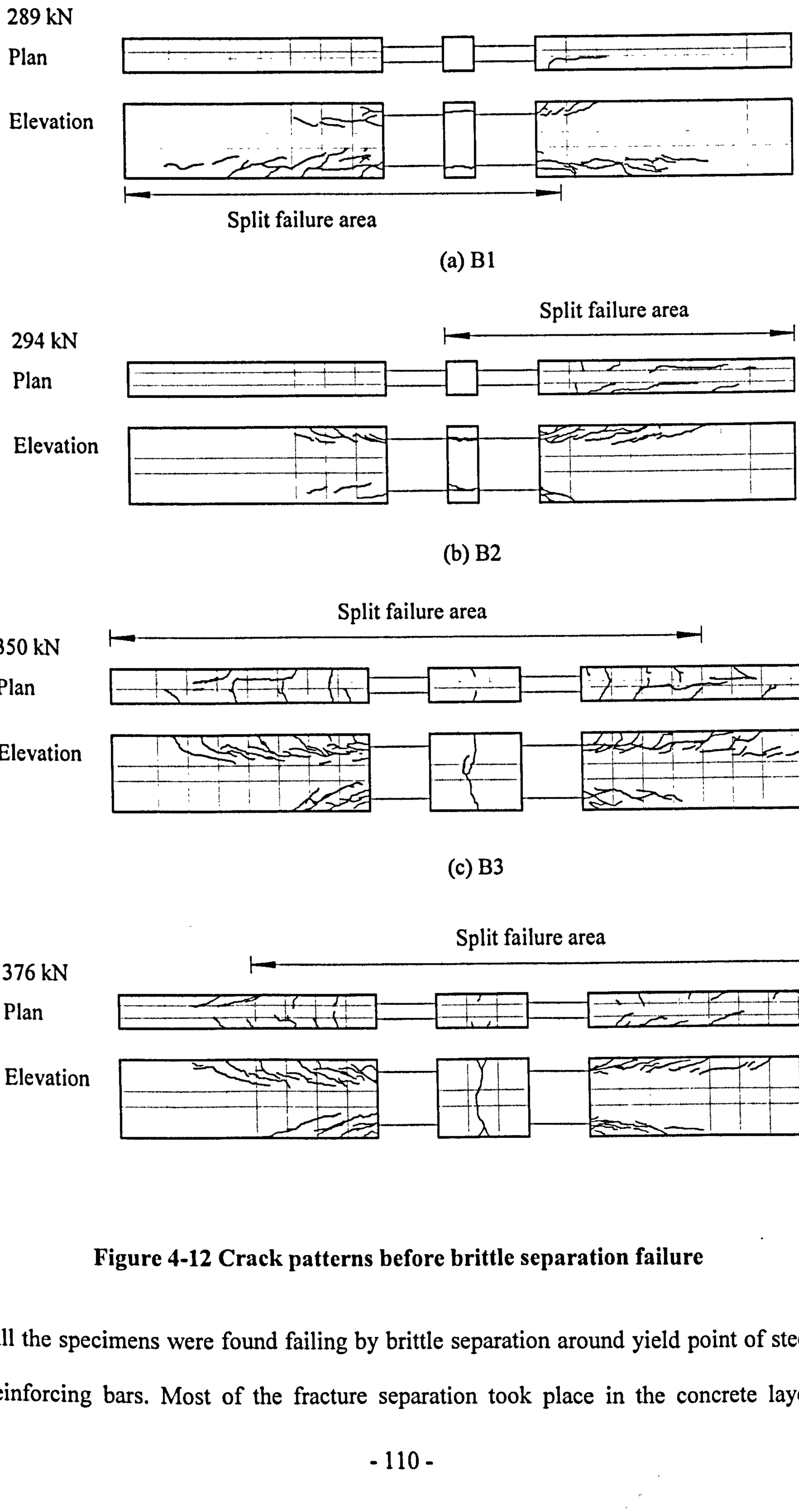

Figure 4-12 Crack patterns before brittle separation failure

All the specimens were found failing by brittle separation around yield point of steel reinforcing bars. Most of the fracture separation took place in the concrete layer

horizontally (Figure 4-13) initiated by the shear cracks near the inner end of the side blocks and propagated towards the outer ends of the side blocks. In certain cases, the brittle separation also occurred at the adhesive-FRP interface (Figure 4-14). Basically, the fracture separation lengths in B1 and B2 are shorter than those in B3 and B4, which again, may be caused by brittle behaviour of the formers. Figure 4-15 and Figure 4-16 show B2 and B4 after brittle separation failure. In both cases, note the large chunks of cover concrete that have been ripped off.

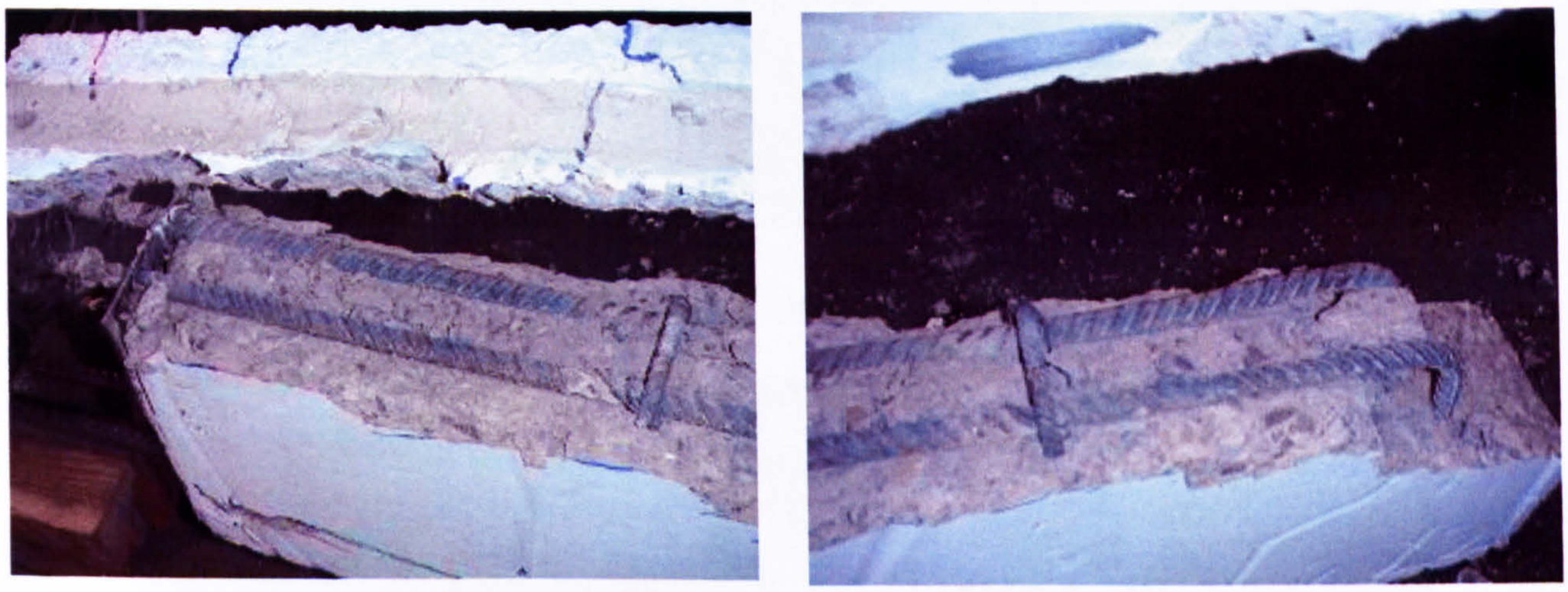

(a) Separation in the cover concrete 1 (b) Separation in the cover concrete 2

Figure 4-13 Separation in the cover concrete

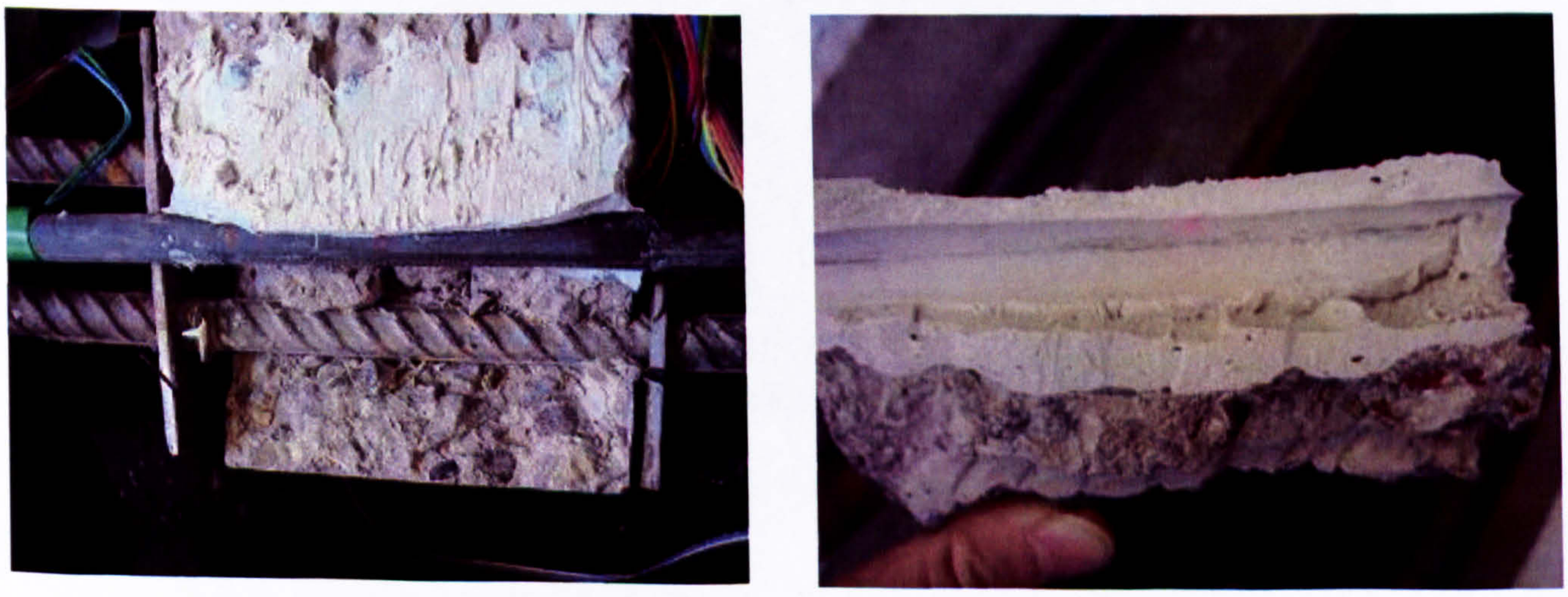

(a) Separation between concrete and adhesive (b) Block of concrete after fracture

Figure 4-14 Separation between concrete and adhesive

(a) B2 (entire specimen)

(b) B2 (fracture of end concrete block)

Figure 4-15 Fracture failure mode of B2

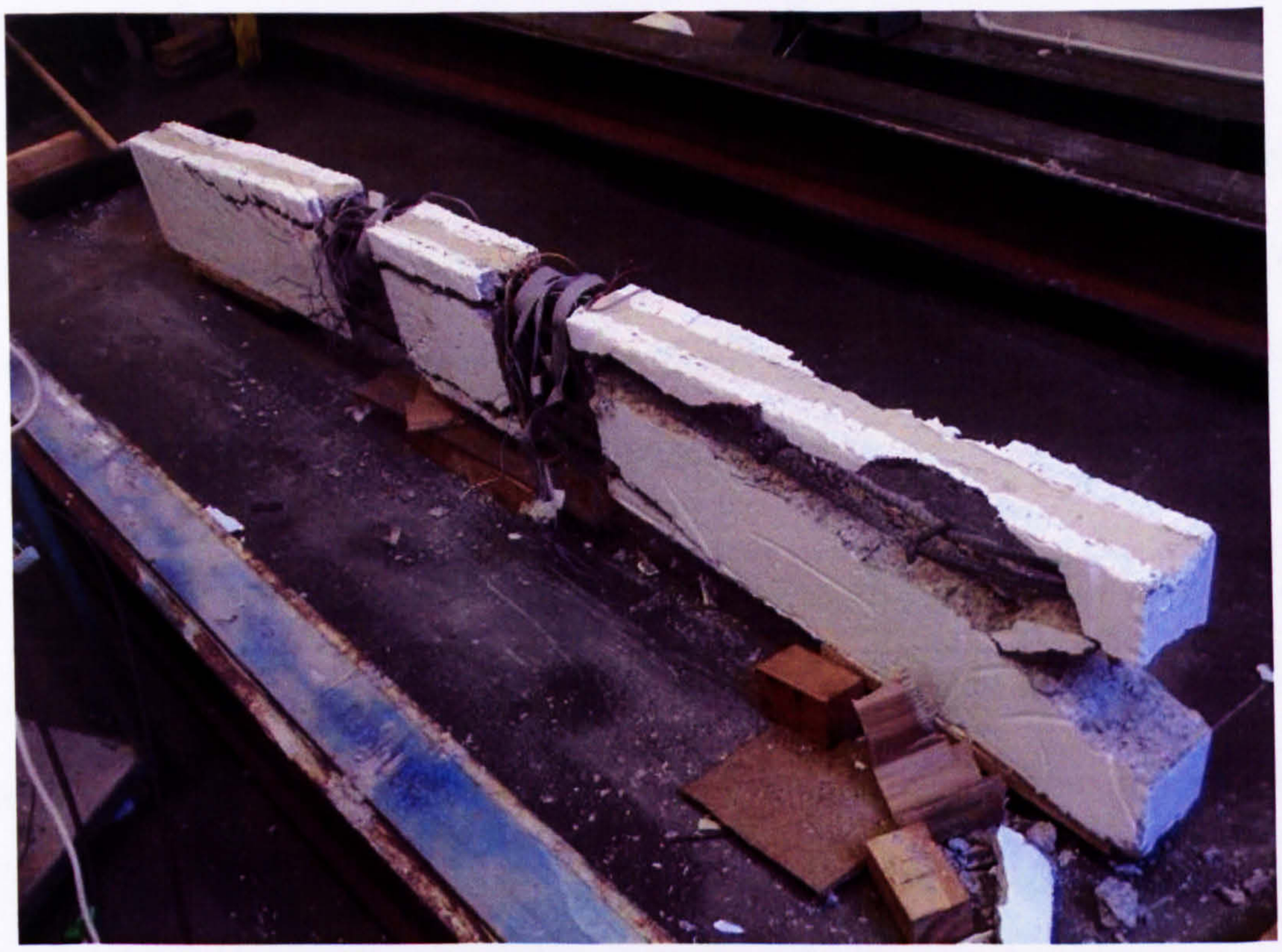

(a) B4 (entire specimen)

(b) B4 (fracture of end concrete block)

Figure 4-16 Fracture failure mode of B4

4.3.2 Equilibrium check on results

The shear bond stresses within the CFRP-to-concrete connection which trigger separation failure are deduced from the strains measured on the CFRP rods. It was therefore essential to perform a preliminary check on the strengthened specimens to verify that these recorded strains satisfied equilibrium.

Figure 4-17 shows the strain and stress (force) distribution for both the steel bars and CFRP rods at the exposed region between middle block and side block. Ideally, both steel reinforcing bars and CFRP rods were stretched simultaneously, with the same strain throughout the loading period. In Figure 4-17 (c), stresses of steel bars are bigger than CFRP rods due to the higher Young's modulus of steel. However, after steel yield, CFRP rods continued to carry the tensile load until specimens failed (see Figure 4-17 (d)).

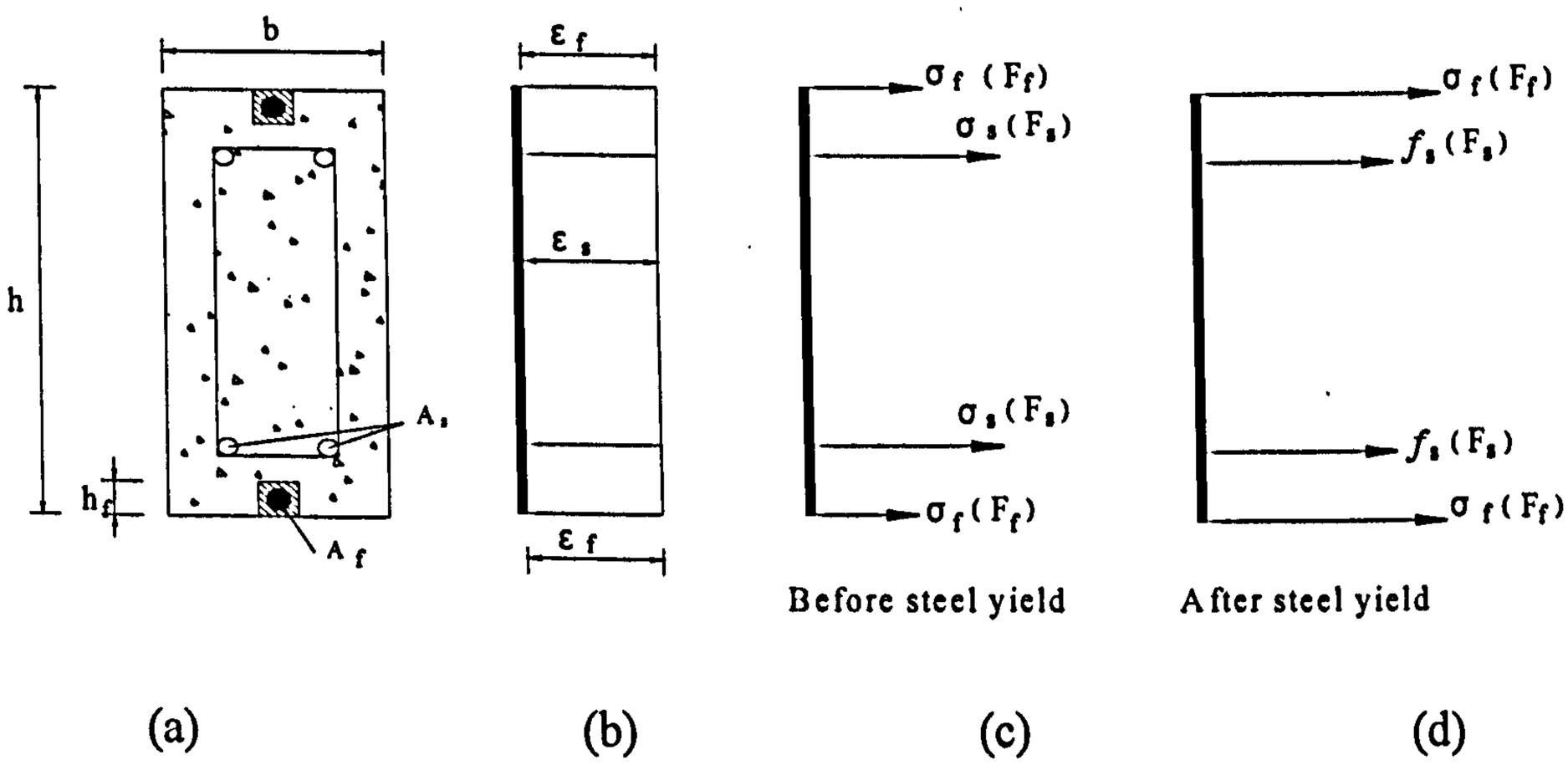

Figure 4-17 Internal strain and stress distribution of cross section under tension

The tensile forces in the steel and CFRP were found based on the measured strains. The sum of these forces is compared with the corresponding load applied. Good

agreement is obtained, indicating the reliability of the results. Table 4-4 shows the equilibrium check for sections of beam B2, B3 and B4 at the ultimate stage.

Table 4-4 Equilibrium check for beam section

Specimen	Experimental load P_e (kN)	Average steel strain (με)	Average CFRP strain (με)	Calculated load P_c (kN)	Disparity (%)
B2	294.0	2171	2112	315.3	7.25
B3	349.0	2621.7	3282.5	323.2	7.39
B4	375.6	2481.3	2420.6	360.8	3.95

4.3.3 Verification of normal stress on the fracture surface in middle blocks

As discussed earlier, the middle blocks of specimens with different length cracked in different modes. In the shorter middle block (B1 and B2), deep horizontal cracks suddenly occurred on the both sides of short middle blocks at the load around 270 kN. However, the longer middle block (B3 and B4), one vertical crack rather than horizontal one was observed in the centre of each middle block at the load around 155 kN. To understand the mechanics of these various failure modes, calculations were performed for the normal stress on the fracture surface.

The deep horizontal crack across the middle block for B2 is shown in Figure 4-18 (a). To work out the normal stress on the fracture plane, half of the top fracture part just above the reinforcing steel bars (shaded area in Figure 4-18 (b)) was taken out to be investigated. The simplified model of this part is shown in Figure 4-19. There is in fact a deep cantilever beam actually exists so that a simple beam theory is now used. It can be seen that eccentricity of FRP rod force F_p action on covercrete cantilever caused normal stresses at root of cantilever and eventually could cause fracture when

the normal stresses exceed concrete tensile strength. The limitation of this modelling approach does exist but still gives fundamental insight into the problem.

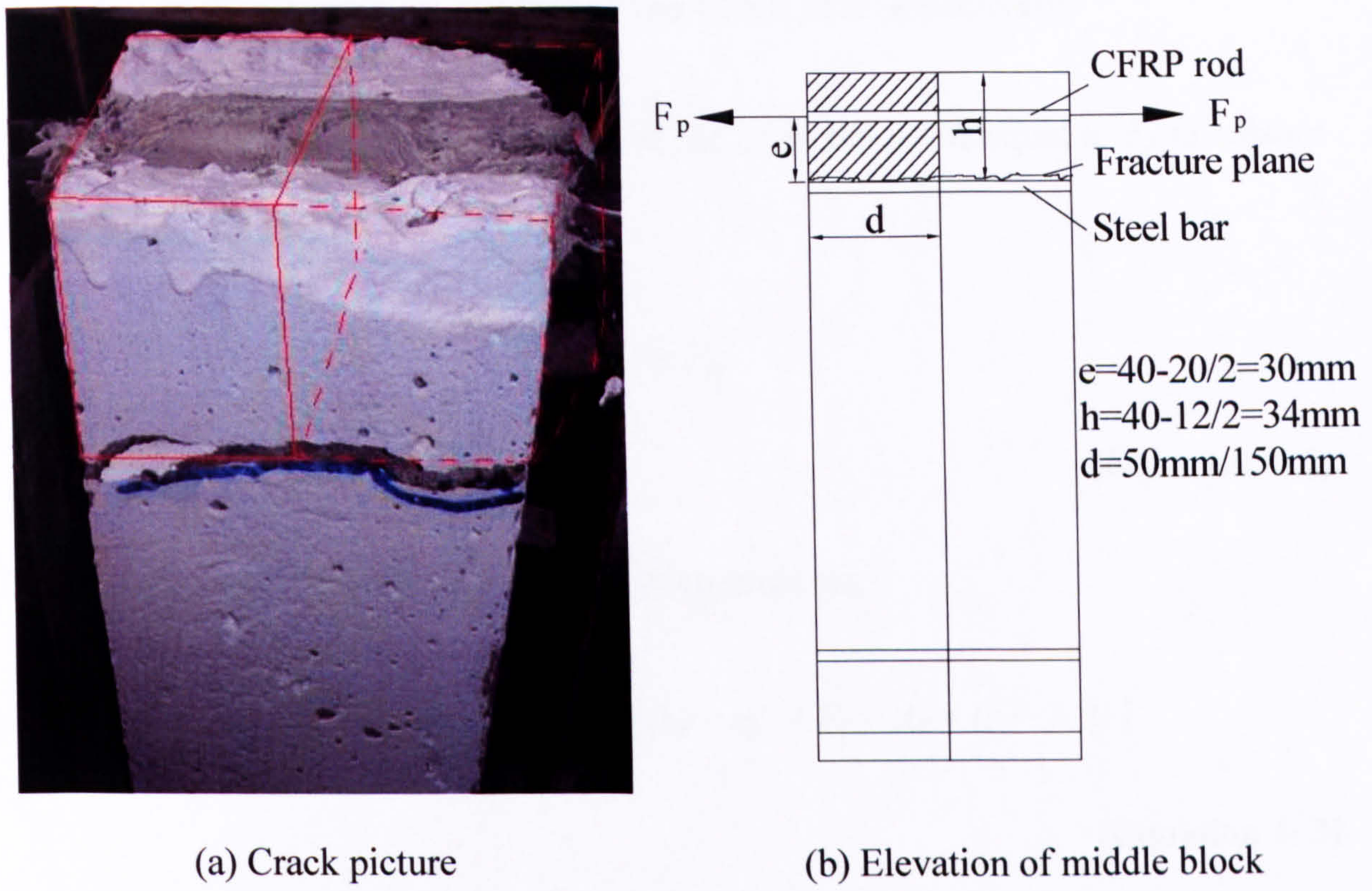

(a) Crack picture (b) Elevation of middle block

Figure 4-18 Crack patterns in middle block of B2

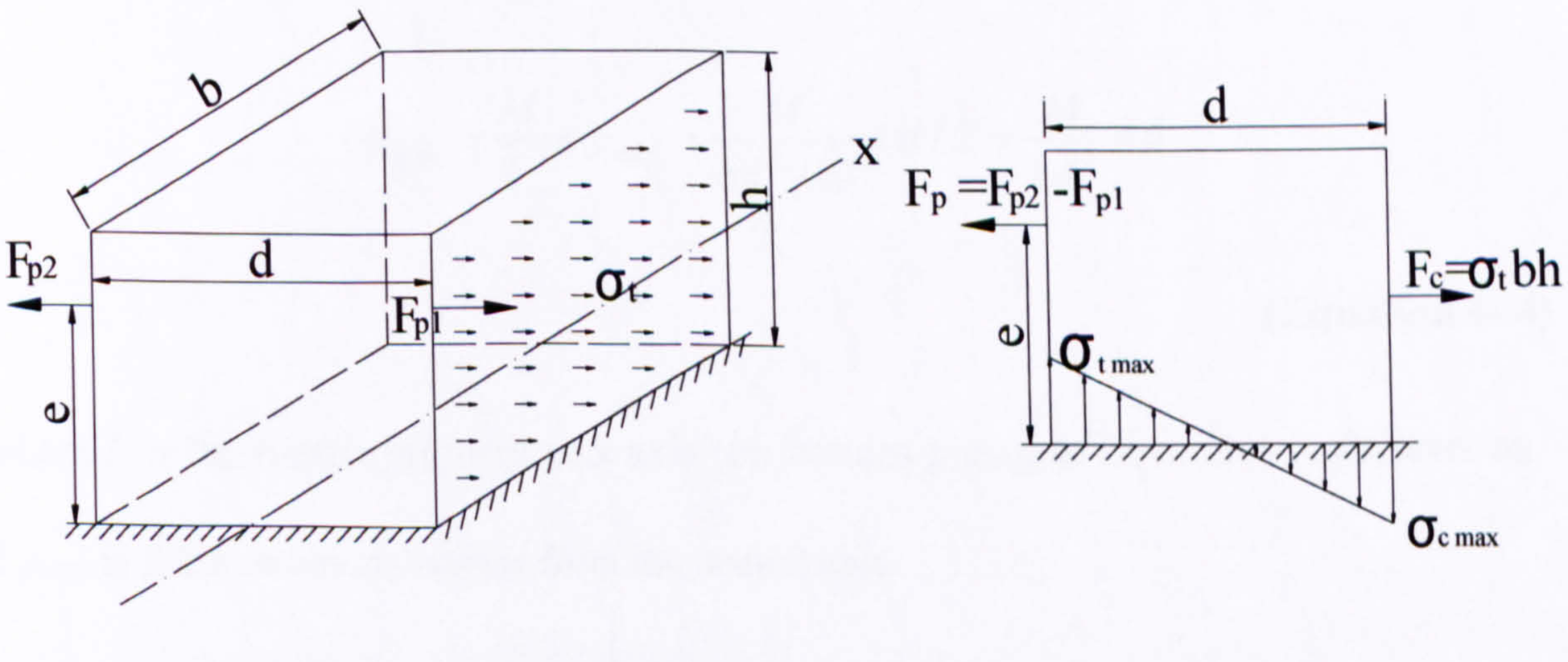

(a) 3D view of shaded area (b) Elevation diagram

Figure 4-19 Diagram of crack part

The force F_p can be calculated from the difference of CFRP rods strains between the gauges at the mid-block ε_1 and near the edge of middle block ε_2:

$$F_p = \Delta\varepsilon \times E_f \times A_f = (\varepsilon_2 - \varepsilon_1) \times E_f \times A_f$$

(Equation 4- 1)

where E_f and A_f are modulus and area of the CFRP rods respectively.

The tensile force of concrete on the side of block F_c should be equal to F_p to balance the horizontal forces:

$$F_c = F_p$$

(Equation 4- 2)

Then the moment of cantilever M can be interpreted as:

$$M = | F_p \times e - F_c \times h/2 | = | (\varepsilon_2 - \varepsilon_1) \times E_f \times A_f \times (e - h/2) |$$

(Equation 4- 3)

where e is eccentricity of CFRP force from root of covercrete cantilever.

Then the normal stress σ_{max} on the fracture plane is:

$$\sigma_{max} = \frac{M}{I_x} \times y_{max} = \frac{M}{bd^3/12} \times d/2 = \frac{M}{bd^2} \times 6$$

(Equation 4- 4)

where I_x is the inertia moment in x axis (on bottom plane) of covercrete cantilever an d y_{max} is the maximum distance from the neutral axis.

The results are presented in Table 4-5 and Table 4-6 for B2 and B4 respectively. As can be seen, for B2, the calculated maximum normal stress went up with the increasing of the load and reach as high as up to 6.94 N/mm^2, which are higher than the tensile strength of the concrete and therefore caused the horizontal crack. As for

B4, the normal stress was up to 0.45 N/mm^2, which is much lower than the tensile strength of the concrete. In this case, a horizontal crack in the middle block was not the originally observed mode of failure in the test.

Table 4-5 Calculation of normal stress on the fracture plane for B2

Load (kN)	F_p (N)	M (Nm)	Normal stress σ (N/mm^2)
77	10610	137.9	3.01
127	15783	205.2	4.48
171	19734	256.6	5.60
212	22518	292.7	6.39
278	24455	317.9	6.94
294	22451	291.9	6.37

Table 4-6 Calculation of normal stress on the fracture plane for B4

Load (kN)	F_p (N)	M (Nm)	Normal stress σ (N/mm^2)
69	7035	91.5	0.22
194	12870	167.3	0.41
246	13095	170.2	0.41
337	14265	185.5	0.45
376	13590	176.7	0.43

4.3.4 Axial strain and shear bond stress profiles along specimens

The free body diagram for an infinitesimal length of rod is given in Figure 4-20.

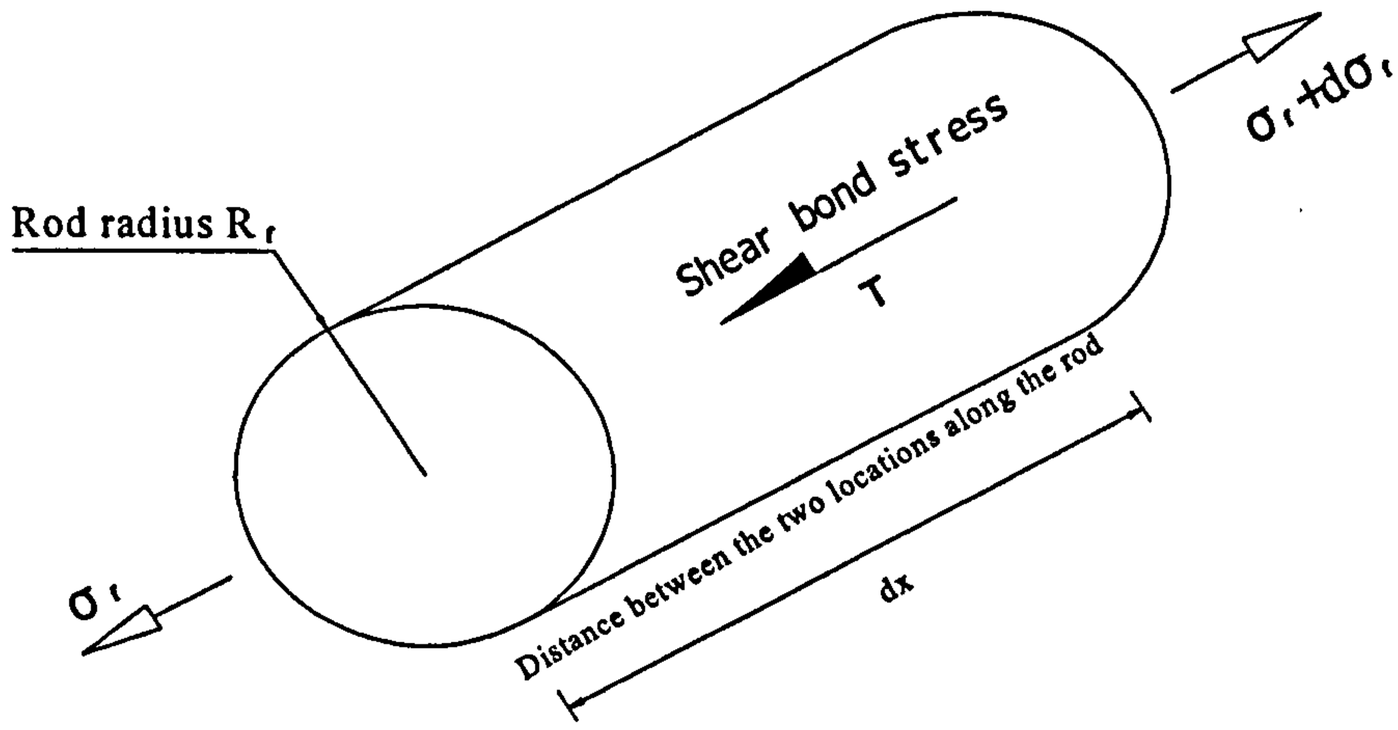

σ_f = Axial stress in the rod

$d\sigma_f$ = Difference of rod axial stress between the two locations

Figure 4-20 Free body diagram for infinitesimal length of rod

The axial equilibrium equations emerging from Figure 4-20, along with the linear material constitutive expression for the FRP, produces the following relationship:

$$\sigma_f \pi R_f^2 + 2\tau\pi R_f dx = (\sigma_f + d\sigma_f)\pi R_f^2$$

$$2\tau dx = R_f d\sigma_f$$

$$\tau = \frac{R_f}{2}\frac{d\varepsilon_f E_f}{dx}$$

$$\tau = \frac{R_f E_f}{2}\frac{d\varepsilon_f}{dx}$$

(Equation 4- 5)

Where E_f is Young's modulus of CFRP and ε_f is axial strain of CFRP rod.

It is noted that, in the derivation of (Equation 4- 5), the axial force must be based on the *average* axial strain of rod at that section. Under ideal pure tensile forces, it may be argued that the average strain is, to a very good approximation, equal to the strains on the surface of the rod.

It is recognised that, in practice, gauges on the bonded surface of the CFRP rod and the accompanying leads through the adhesive will have the negative effect of introducing imperfections in the rod-to-concrete bond. Therefore, the number of bonded surface gauges used in practice should be a compromise between the need to determine representative values of the shear bond stress, whilst simultaneously not unduly weakening the bond.

It should be appreciated that no matter how gauges are closely spaced, the finite spacing of the gauges renders the bond stresses based on these gauge readings *average*, rather than point, bond stresses. Using the strains recorded from the strain gauges installed on the CFRP rods, the average CFRP-concrete bond stresses developed along the CFRP rods can be evaluated in Figure 4-21.

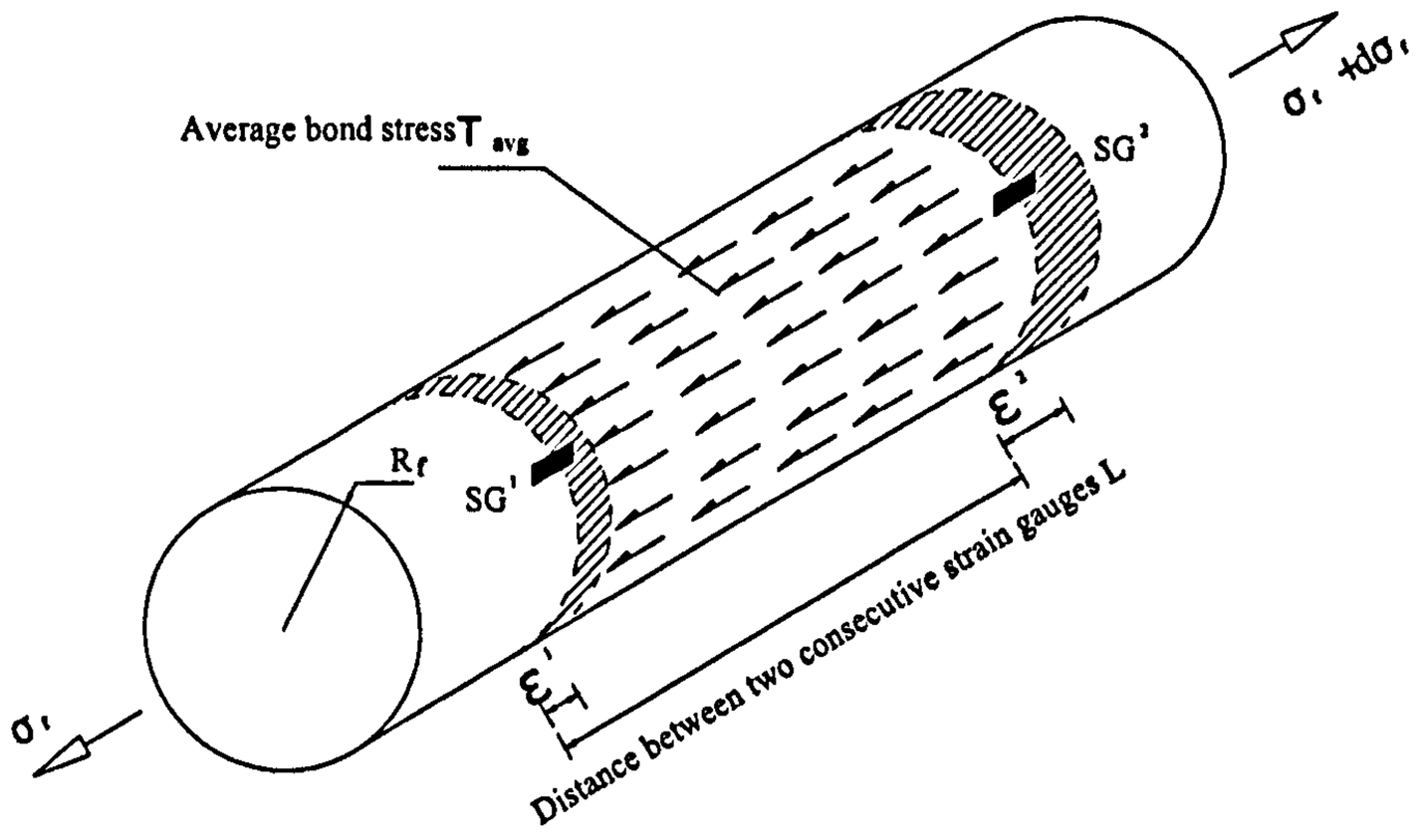

Figure 4-21 Average bond stress τ_{avg} in-between two consecutive strain gauges installed to the CFRP rod.

Therefore, the average bond stress τ_{avg} on the CFRP rods, in-between the strain gauges positions (SG^1 and SG^2), was determined according to the following equations:

$$\tau_{avg} = \frac{R_f E_f (\varepsilon_2 - \varepsilon_1)}{2L}$$

(Equation 4- 6)

where $\Delta\varepsilon$ is the difference in mid-plane axial strain of the plate between the two locations (ε_1 - ε_2). In this treatment, it is assumed an average bond stress in-between the two strain gauges.

Figure 4-22 to Figure 4-24 show, for different load levels, the axial strain profiles in the CFRP rod and the average shear stress profiles of specimens B2 to B4.

For B2 and B4, strain gauges were respectively bonded to the two CFRP rods inserted into the opposite faces of the concrete block. Then the average reading of two strain gauges on the positions with same distance from mid-span was taken to represent the strain distributions. However, strain gauge F44 did not work well so that there are only three strain values for each load step for B4.

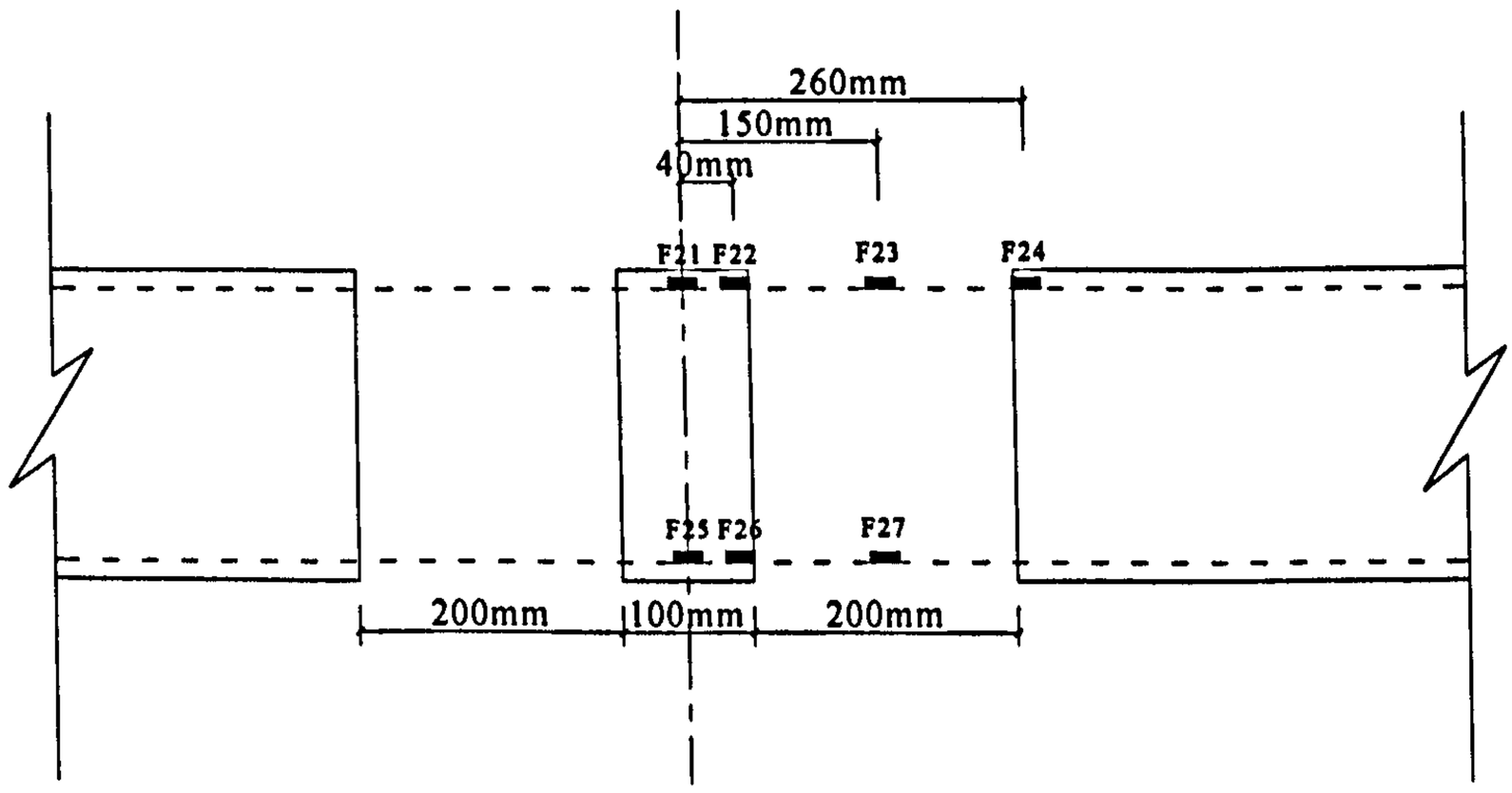

(a) B2 strain gauge location on CFRP rods

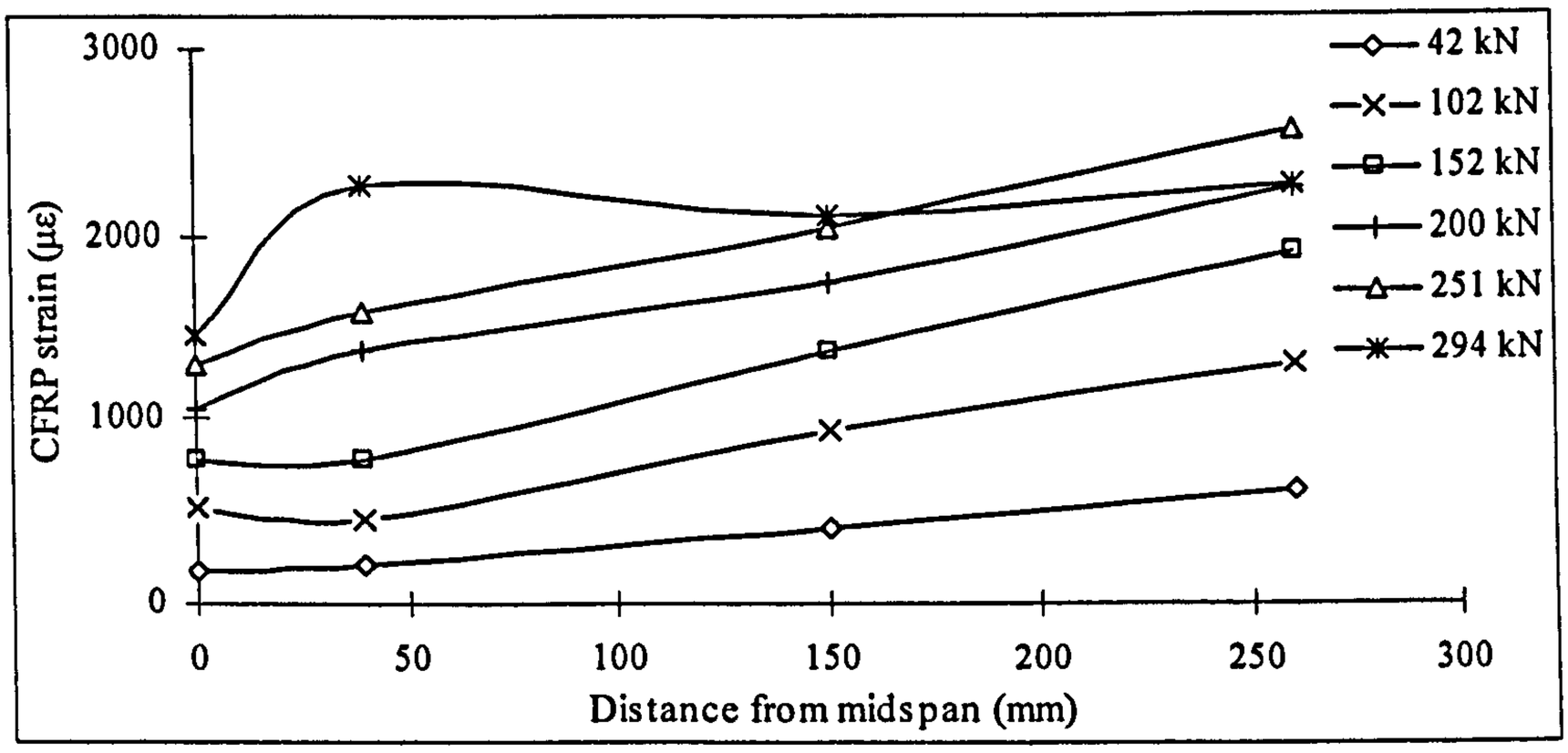

(b) B2 CFRP strain distribution

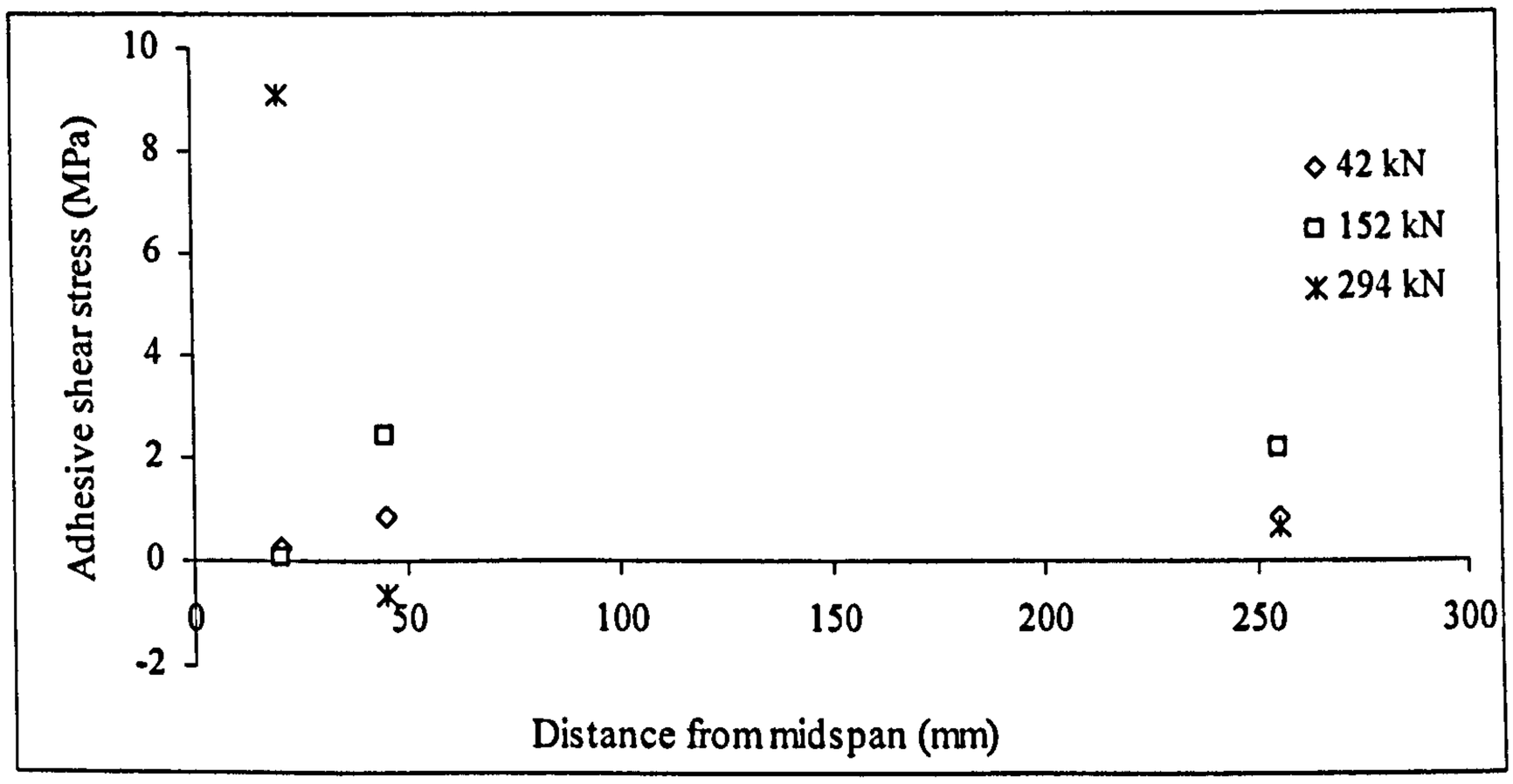

(c) B2 adhesive shear stress distribution

Figure 4-22 CFRP axial strain and adhesive shear stress distributions for B2

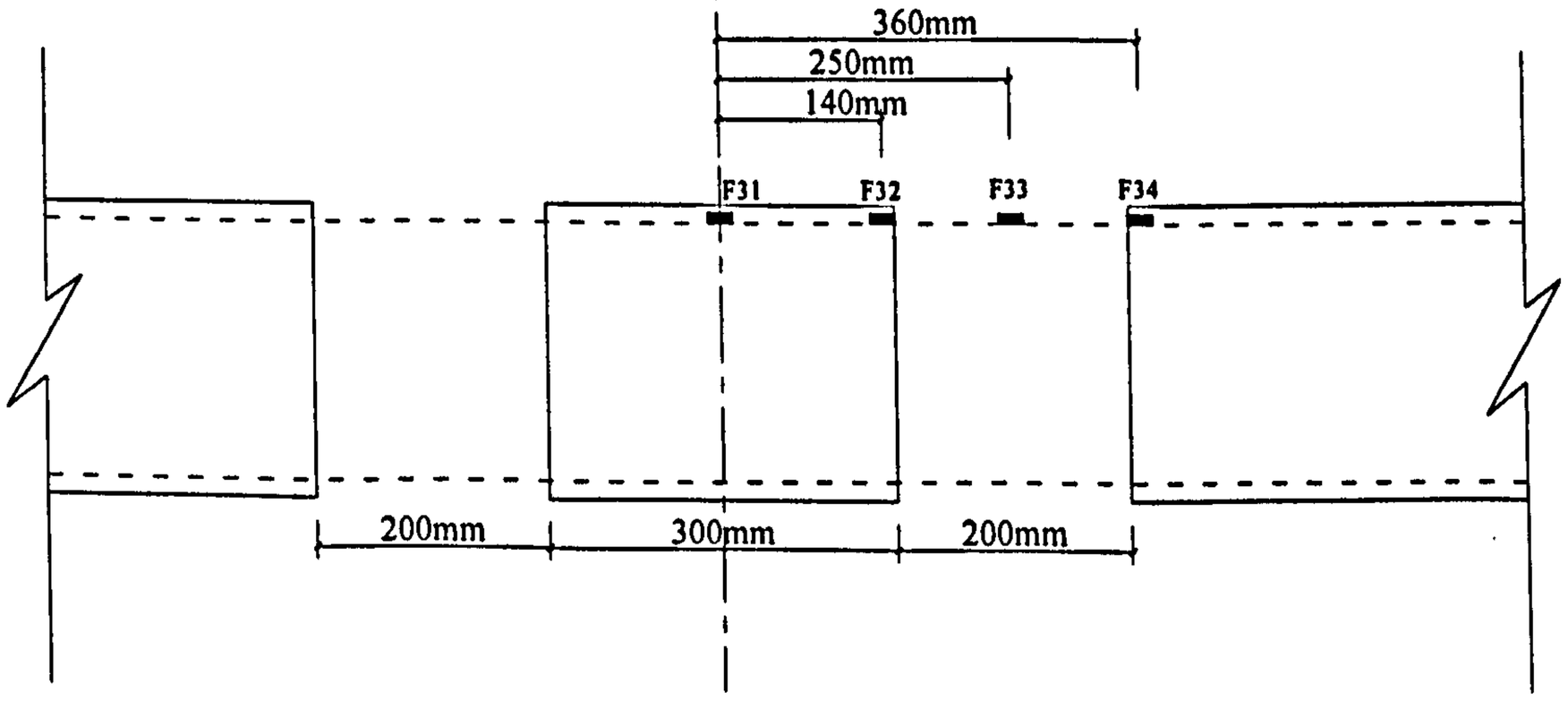

(a) B3 strain gauge location on CFRP rods

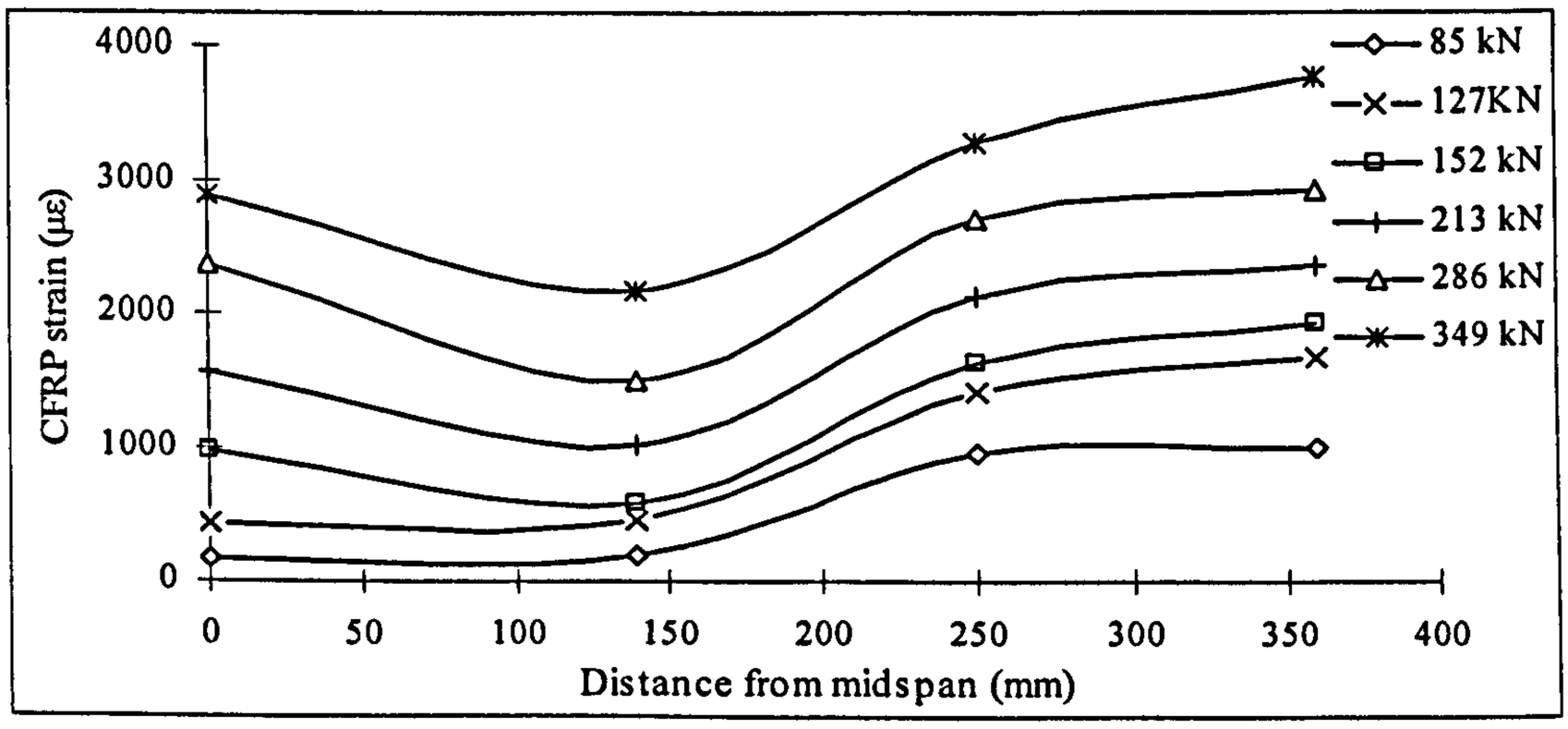

(b) B3 CFRP strain distribution

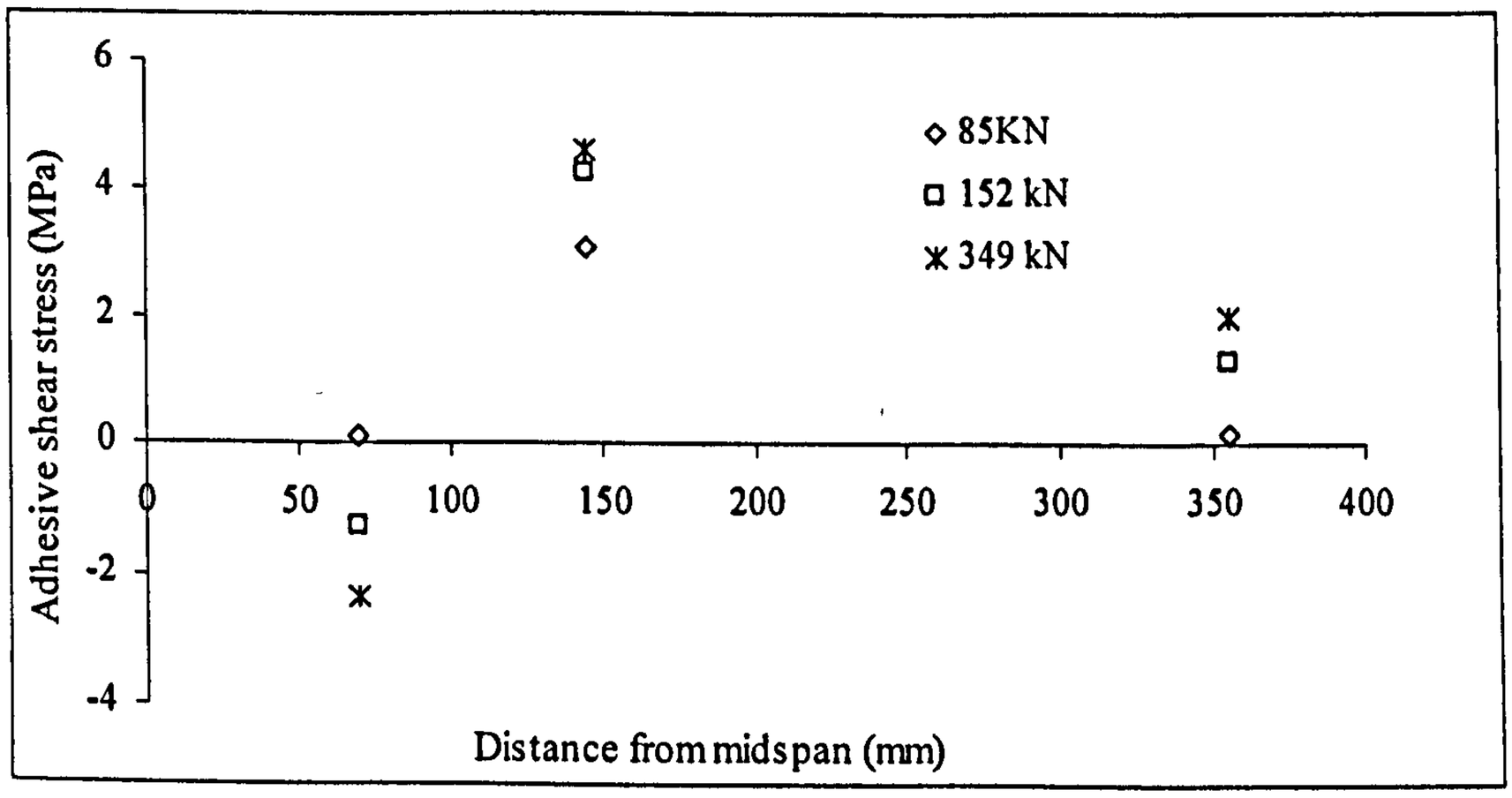

(c) B3 adhesive shear stress distribution

Figure 4-23 CFRP axial strain and adhesive shear stress profile for B3

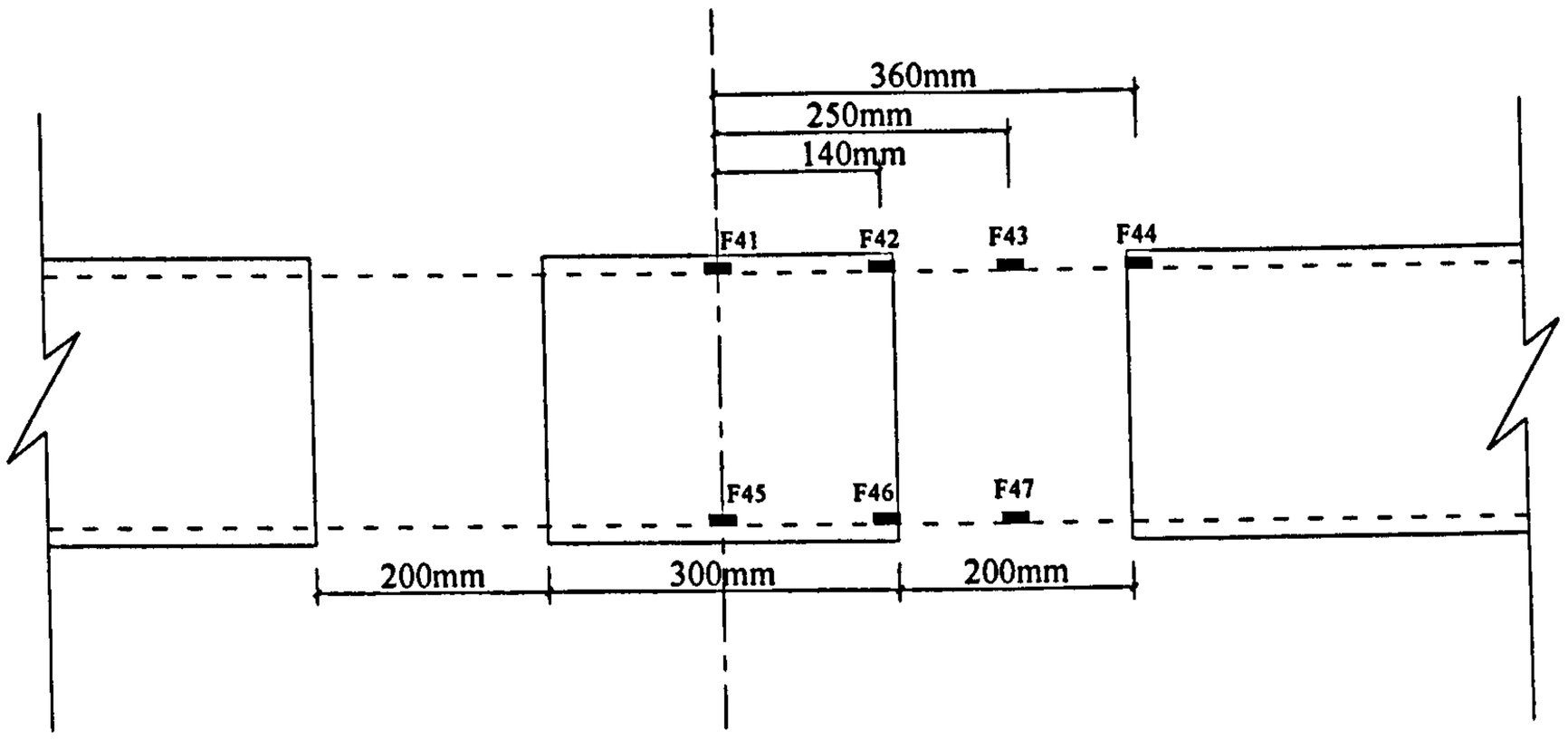

(a) B4 strain gauges location on CFRP rods

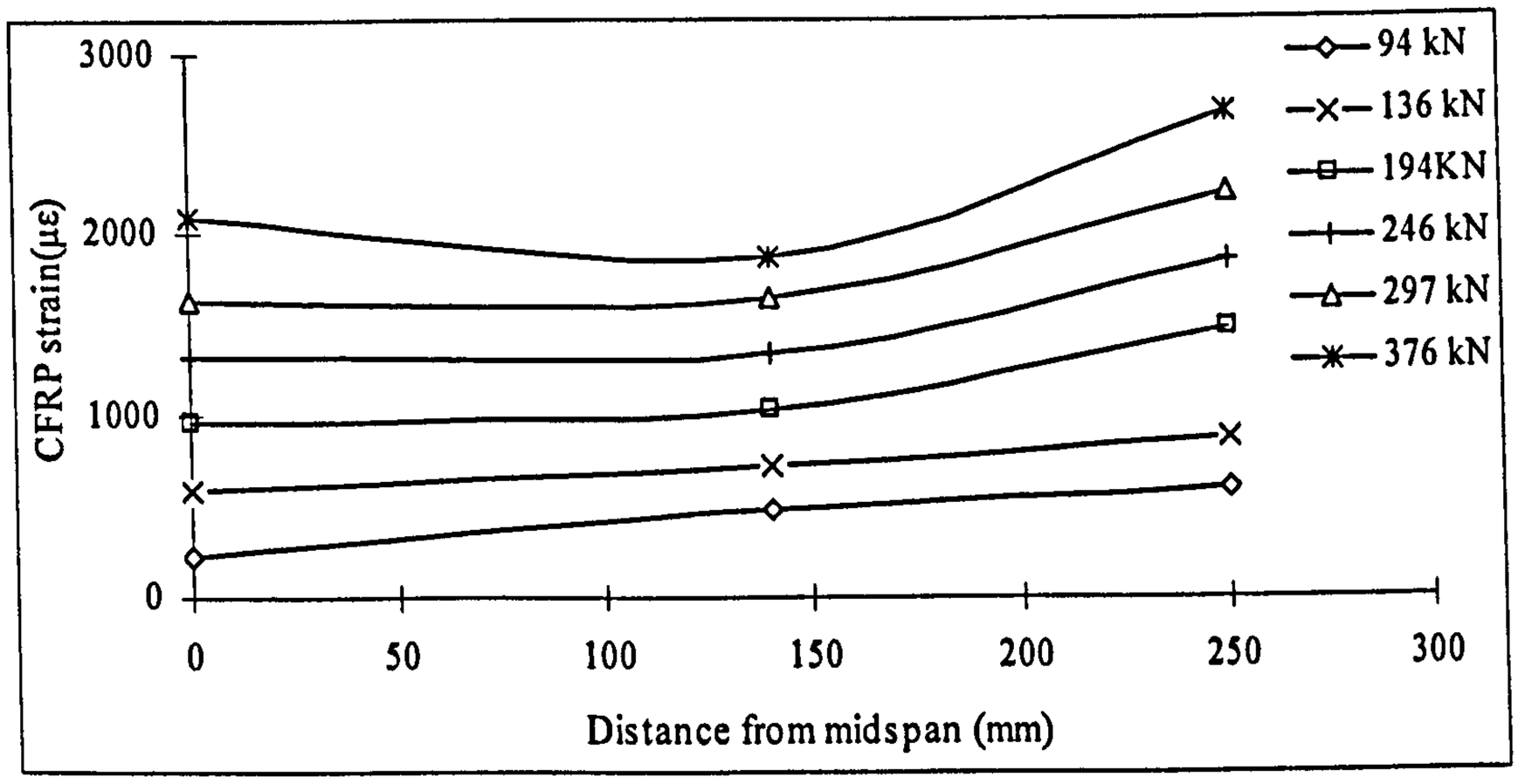

(b) B4 CFRP strain distribution

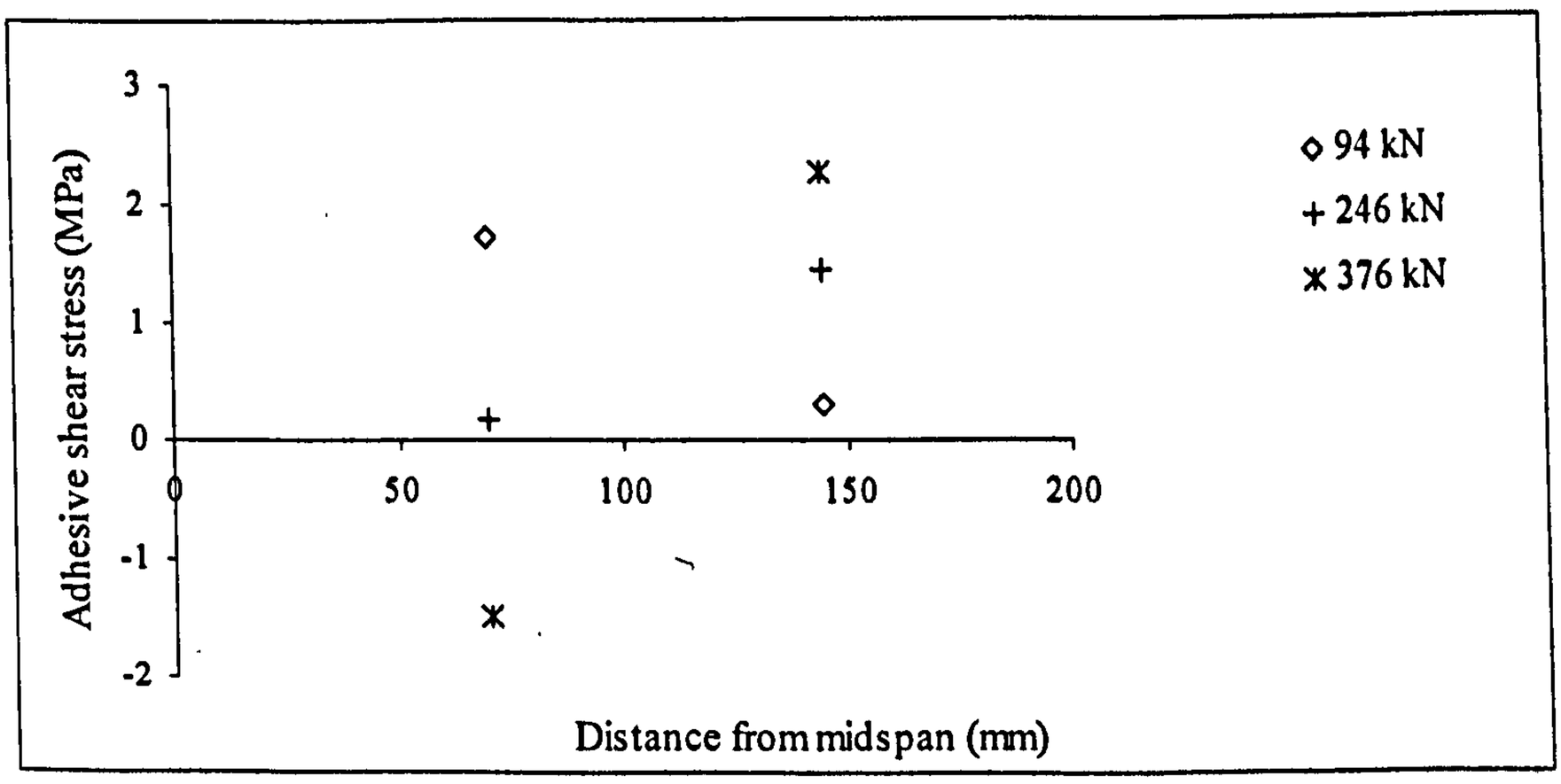

(c) B4 adhesive shear stress distribution

Figure 4-24 CFRP axial strain and adhesive shear stress profile for B4

From Figure 4-22, it can be seen that the CFRP strains for B2 generally increased with the distance from mid-block. However, just before specimen failure at P = 294 kN, the strain inside middle block with 10 mm distance from the edge suddenly went up while the strain inside side block dropped. It could be possibly explained by the massive cracks occurred in the concrete block at this load stage which induced the eccentric loading of specimen and subsequently caused the local bending of the CFRP rods. The sudden change also cause unrealistically high deducted shear stress (around 9 N/mm^2) while other shear stresses reasonably varied between 0 to 4 N/mm^2.

It can be seen from Figure 4-23 that the CFRP strains for B3 increased with the distance from mid-block before P = 127 kN. However, after first vertical crack at mid-block, higher CFRP strains are found at mid-block than those at the position near block edge. The shear stresses varied from 0 to 4.5 N/mm^2 which are relatively reasonable. Similar trends are found in Figure 4-24 for B4 and it tell from the figure that the first vertical crack load at mid-block for B4 is around P = 136 kN.

4.3.5 Load-strain profiles

Figure 4-25 shows the comparisons of load-CFRP strain plots among B2 to B4 for various locations. From Figure 4-25 (a), it can be seen that at the mid-block position, the load-strain plot for B2 keep linear up to failure, which is according with the observation that there is no vertical crack found in concrete at this area. For B3 and B4, the plots are similar and keep linear until the vertical cracks were observed in the middle concrete block at the mid-block area. After concrete crack, B3 has higher strains than B4 at the same load since there are double amount of the CFRP rods in B4 to undertake the loads.

Figure 4-25 (b) indicate the load-strain plots for strain gauges putting on the CFRP rods inside middle concrete block with 10 mm distance from the edge. The gradient for each specimen is close with each other. The reversing strain in B2 at around P = 210 kN is possibly due to the occurrence of a deep horizontal crack in the middle concrete block.

By comparing the plots in Figure 4-25 (c), we can see that both B2 (the specimen with shorter middle block) and B3 (the specimen with double amount of strengthening CFRP rods) have higher strains than B4 at the same load. From Figure 4-25 (d), the strain in B2 reverses due to the horizontal cracks in the side blocks.

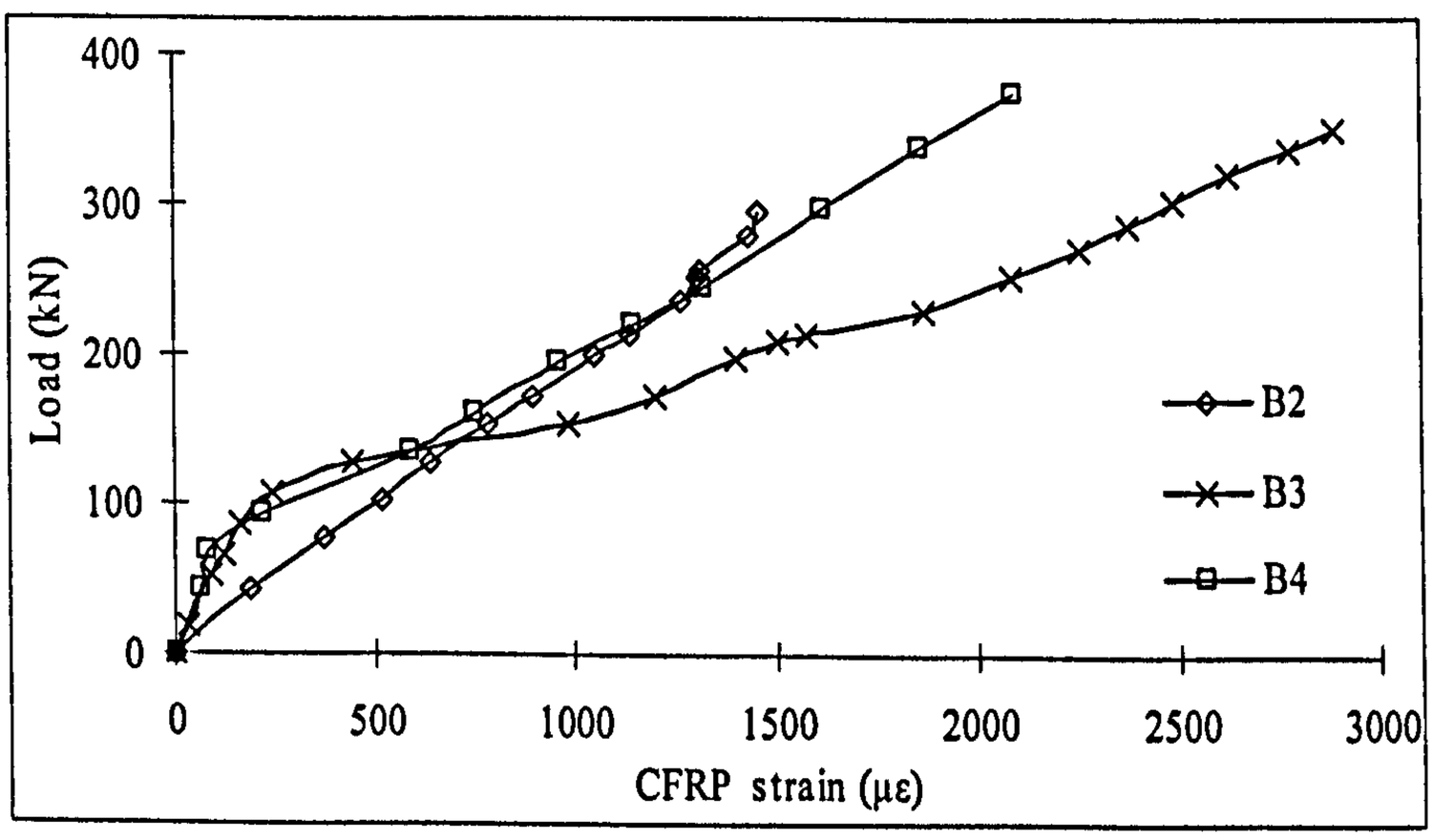

(a) s= 0mm

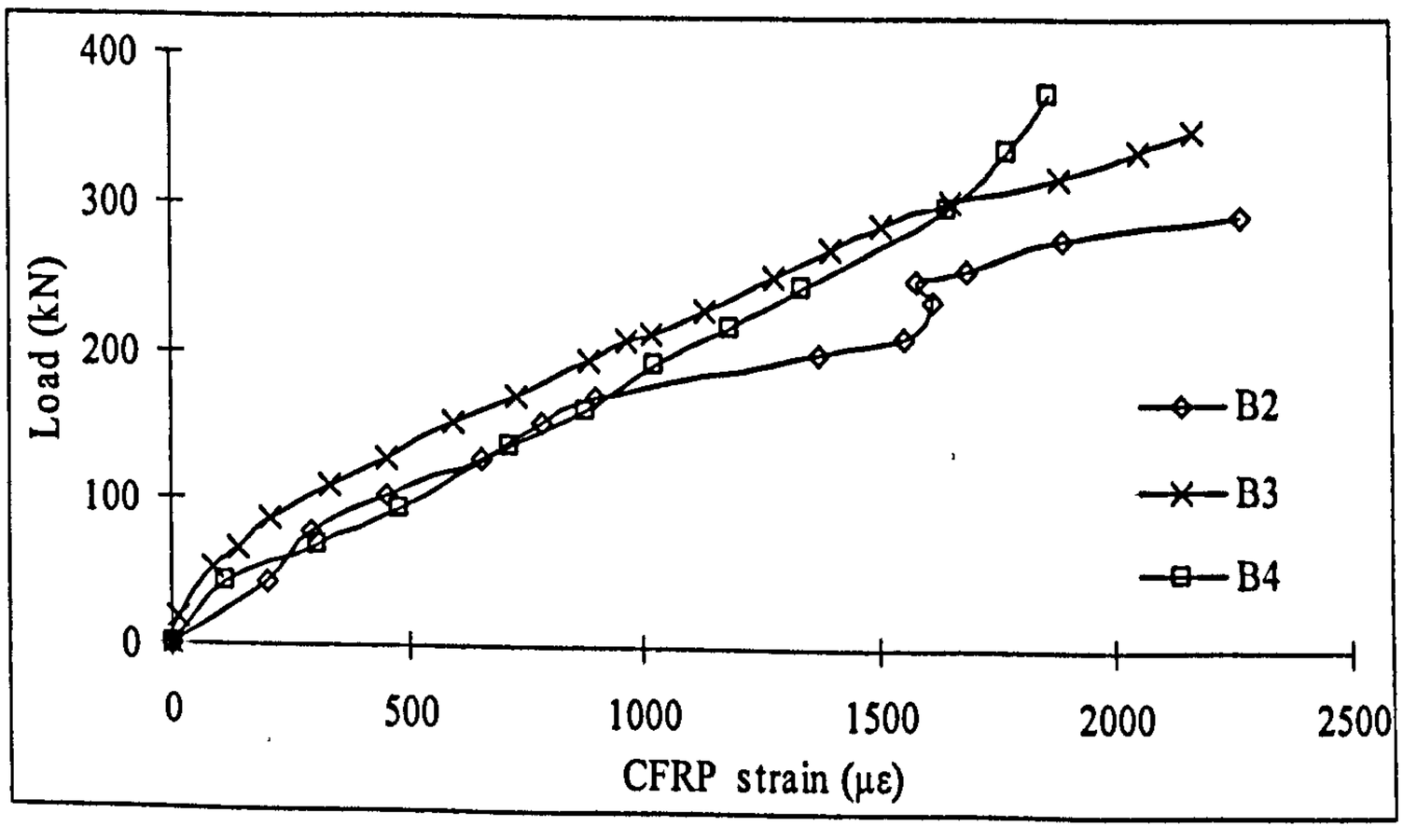

(b) s= 140 mm (s= 40mm for B2)

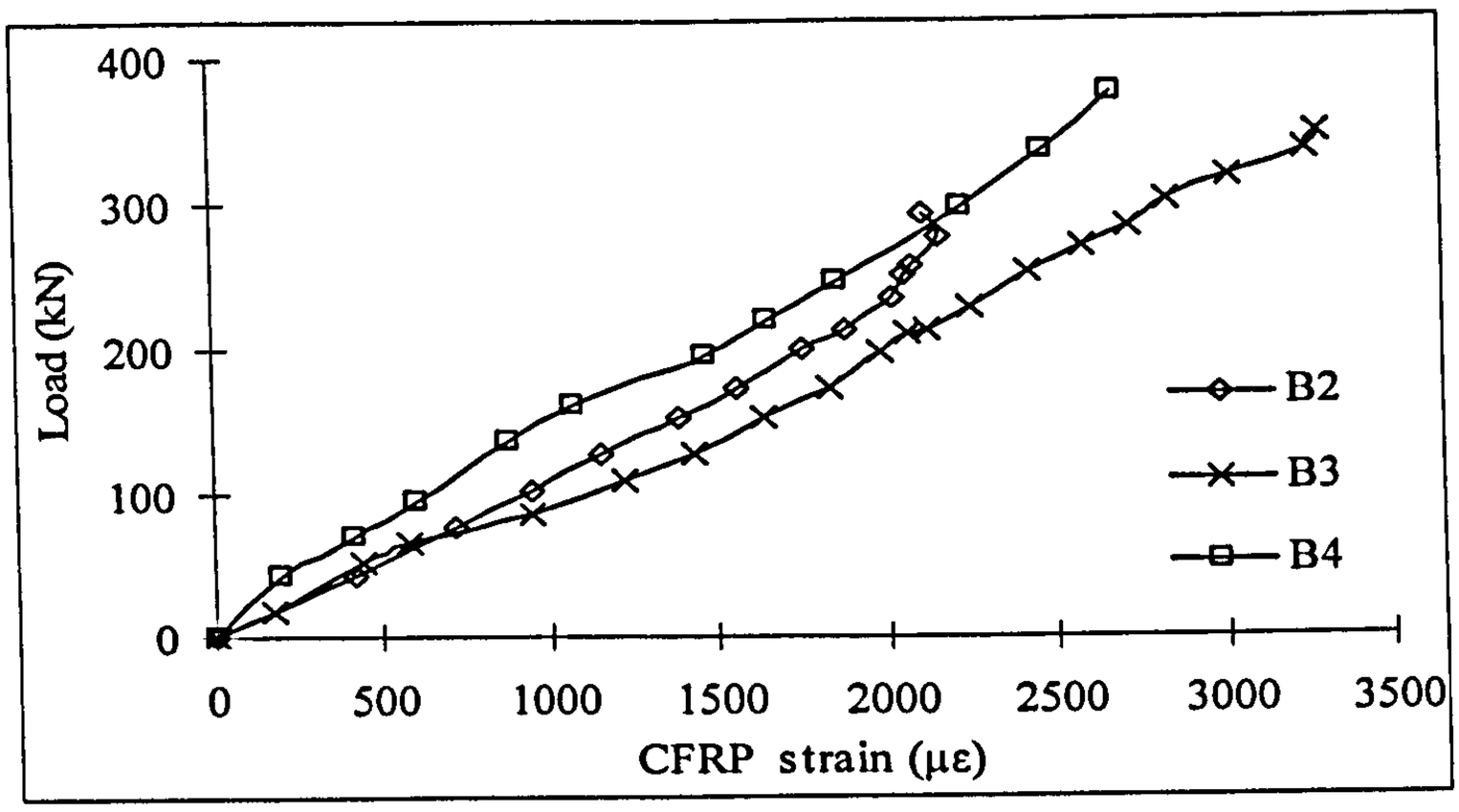

(c) s= 250 mm (s= 150mm for B2)

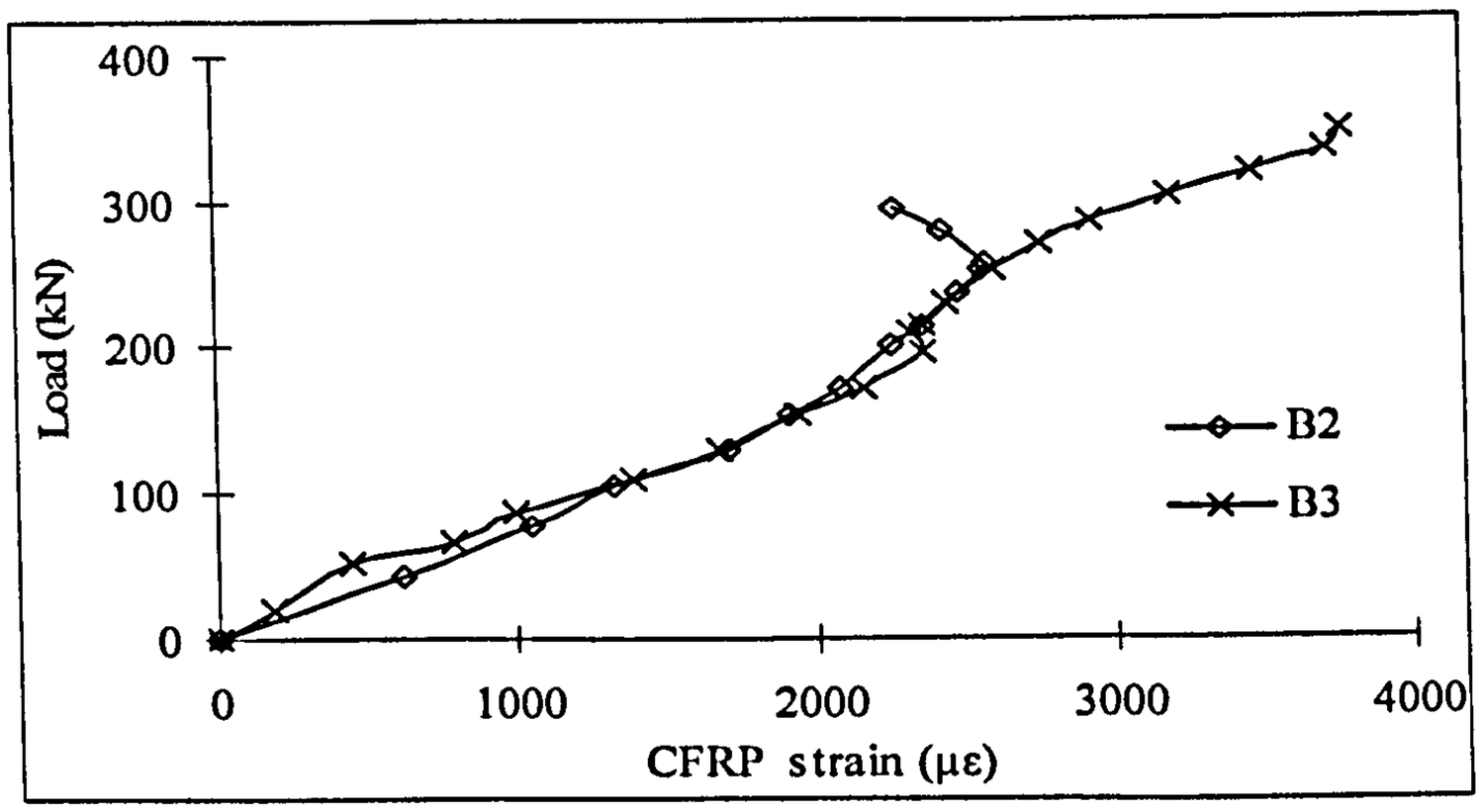

(d) s= 360 mm (s= 260mm for B2)

Figure 4-25 Load – CFRP strain profile for B2 to B4

Figure 4-26 shows the load–steel strain profile for specimen B1 to B4. As shown in Figure 4-8, one strain gauge was put on each exposed steel rod and the locations of the strain gauges have the same distance to mid-block for each specimen. The average steel strain was then taken to represent the typical steel strain for each specimen. According to Figure 4-26, the curves are almost linear until failure and there is no obvious yield stage for the steel in this area.

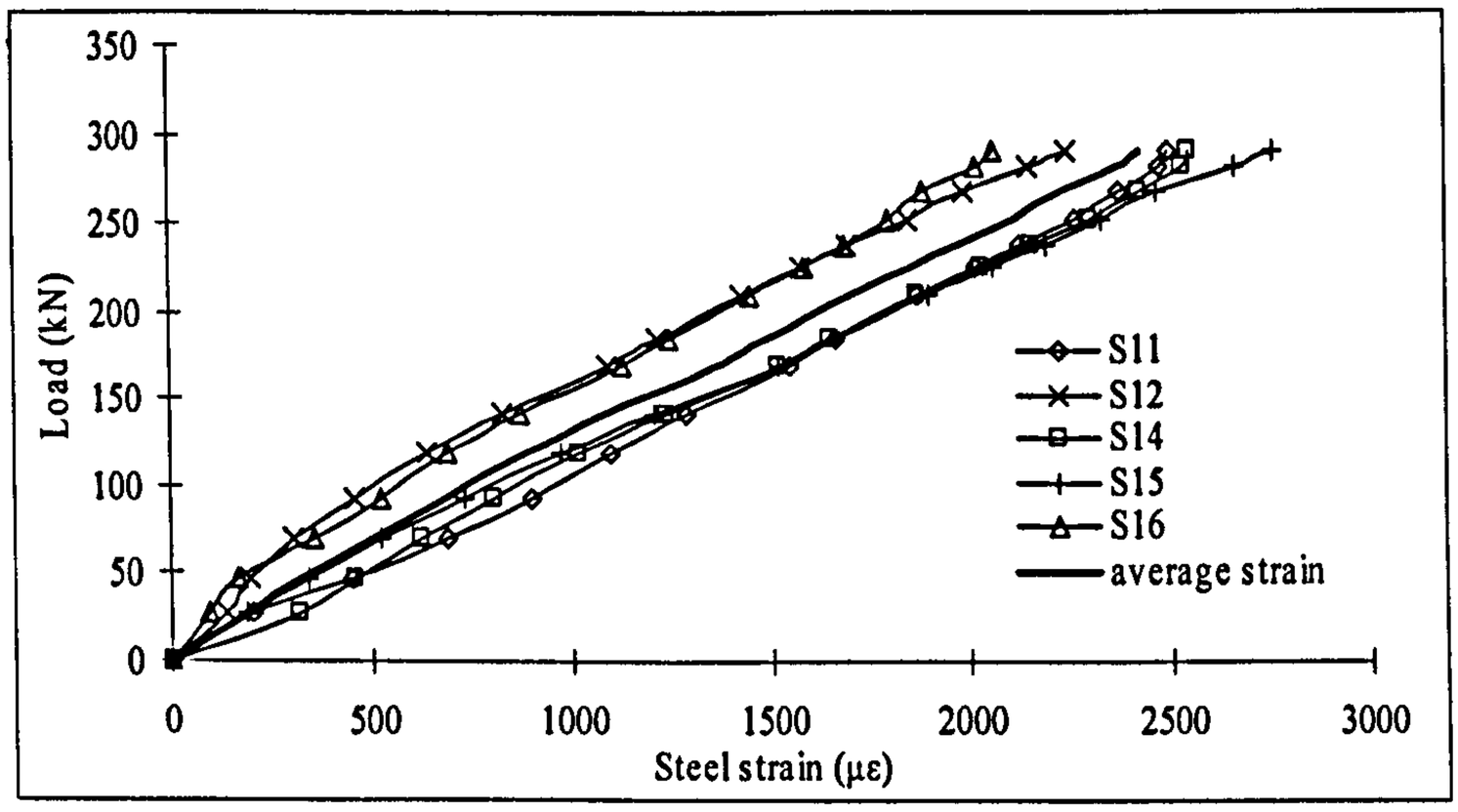
Load (kN)
350
300
250
200
150
100
50
0
0
500
1000
1500
2000
2500
3000
Steel strain (με)
S11
S12
S14
S15
S16
average strain

(a) B1

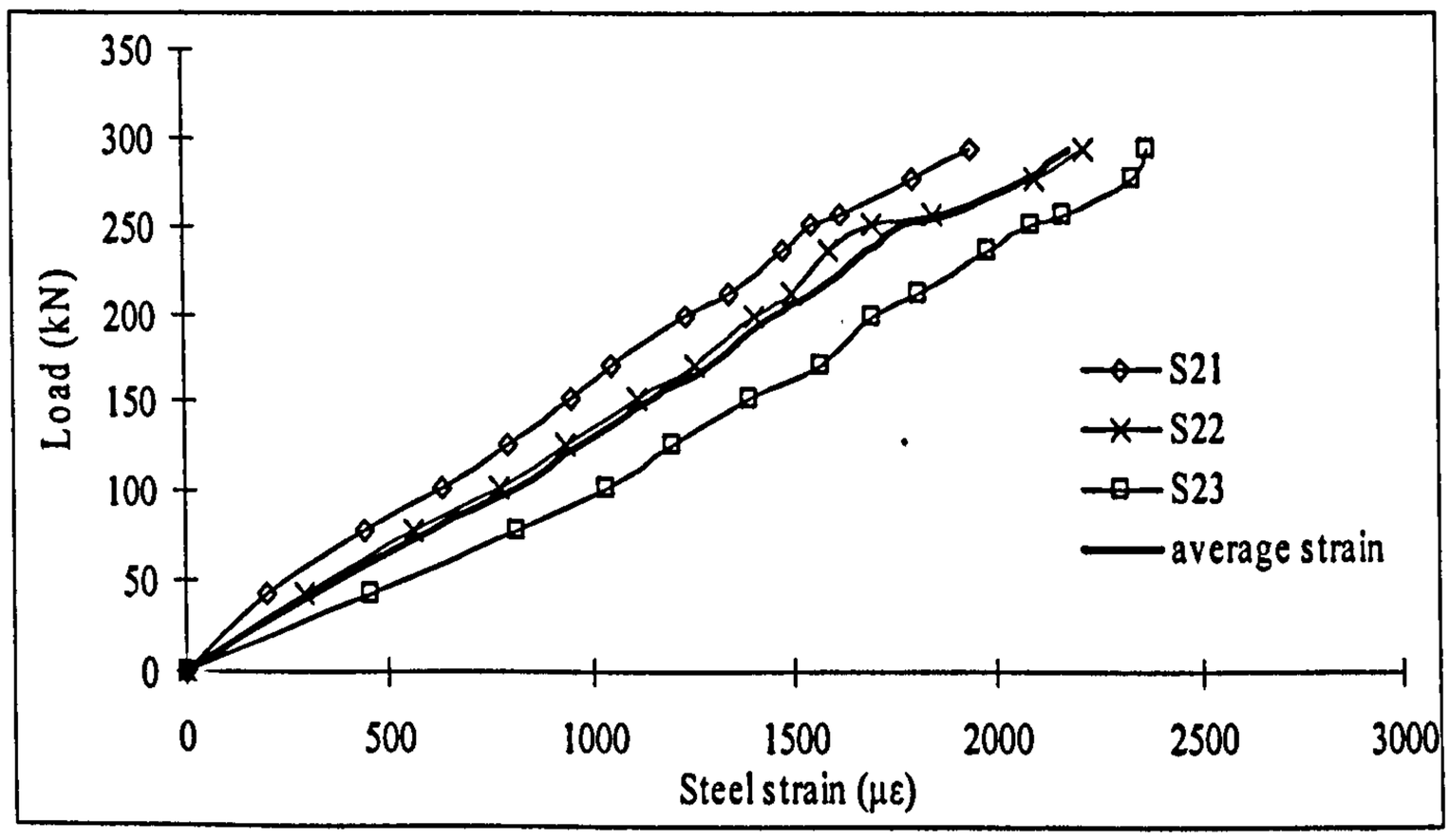
Load (kN)
350
300
250
200
150
100
50
0
0
500
1000
1500
2000
2500
3000
Steel strain (με)
S21
S22
S23
average strain

(b) B2

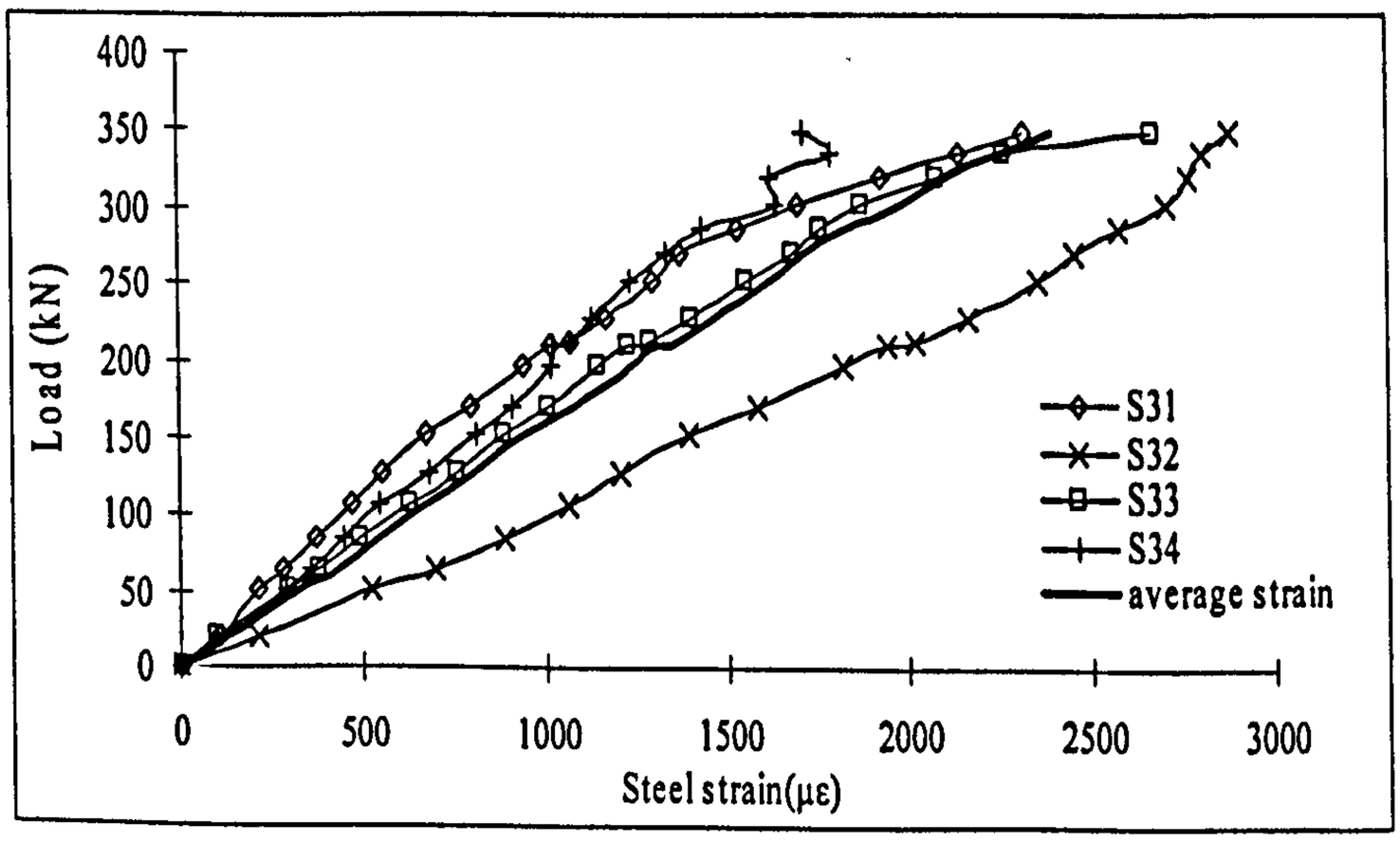
Load (kN)
400
350
300
250
200
150
100
50
0
0
500
1000
1500
2000
2500
3000
Steel strain(με)
S31
S32
S33
S34
average strain

(c) B3

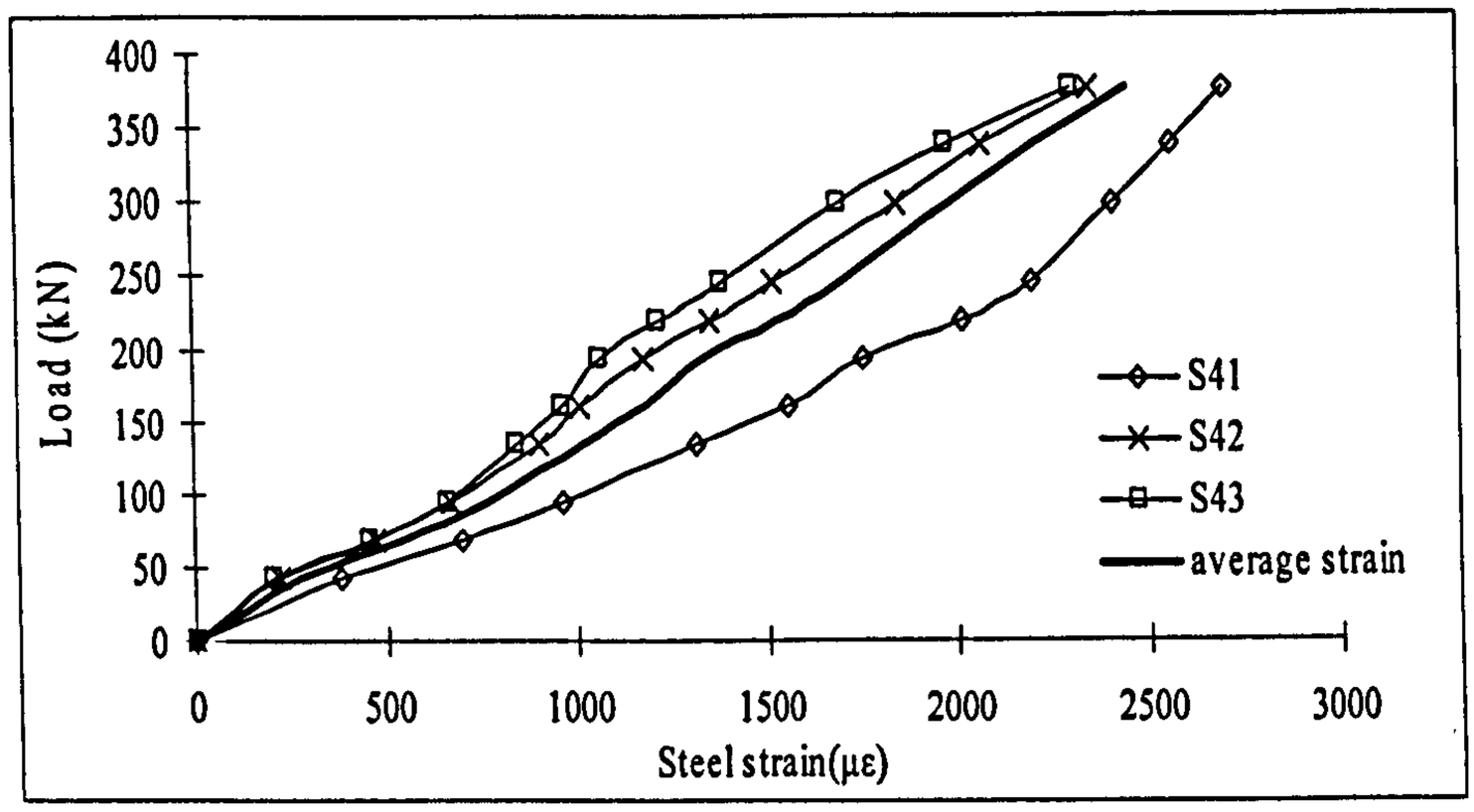

(d) B4

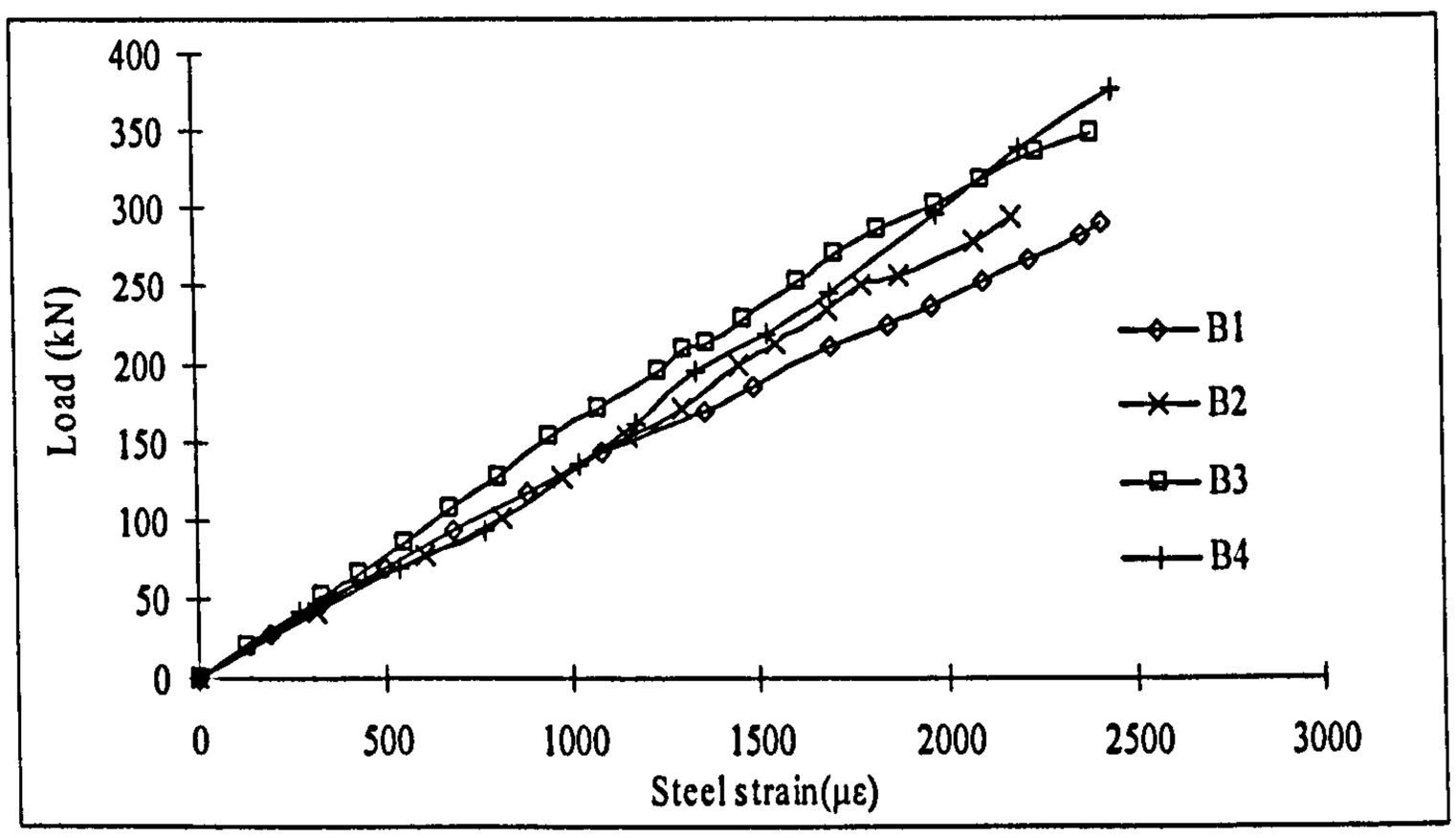

(e) Average strain of B1 to B4

Figure 4-26 Load – external steel strain profile for B1 to B4

A few strain gauges were closely attached to the steel bars inside the middle block. However, these gauges produced erratic readings. The load-internal steel strain curves are given in Figure 4-27. It can be seen that not only tensile strains but also high compressive strains are found for the steel bars embedded inside the concrete block. The reason for these erratic load-strain curves could possibly due to the internal cracking of the middle concrete block because these strain gauges behaviours are strongly influenced by the surrounded concrete.

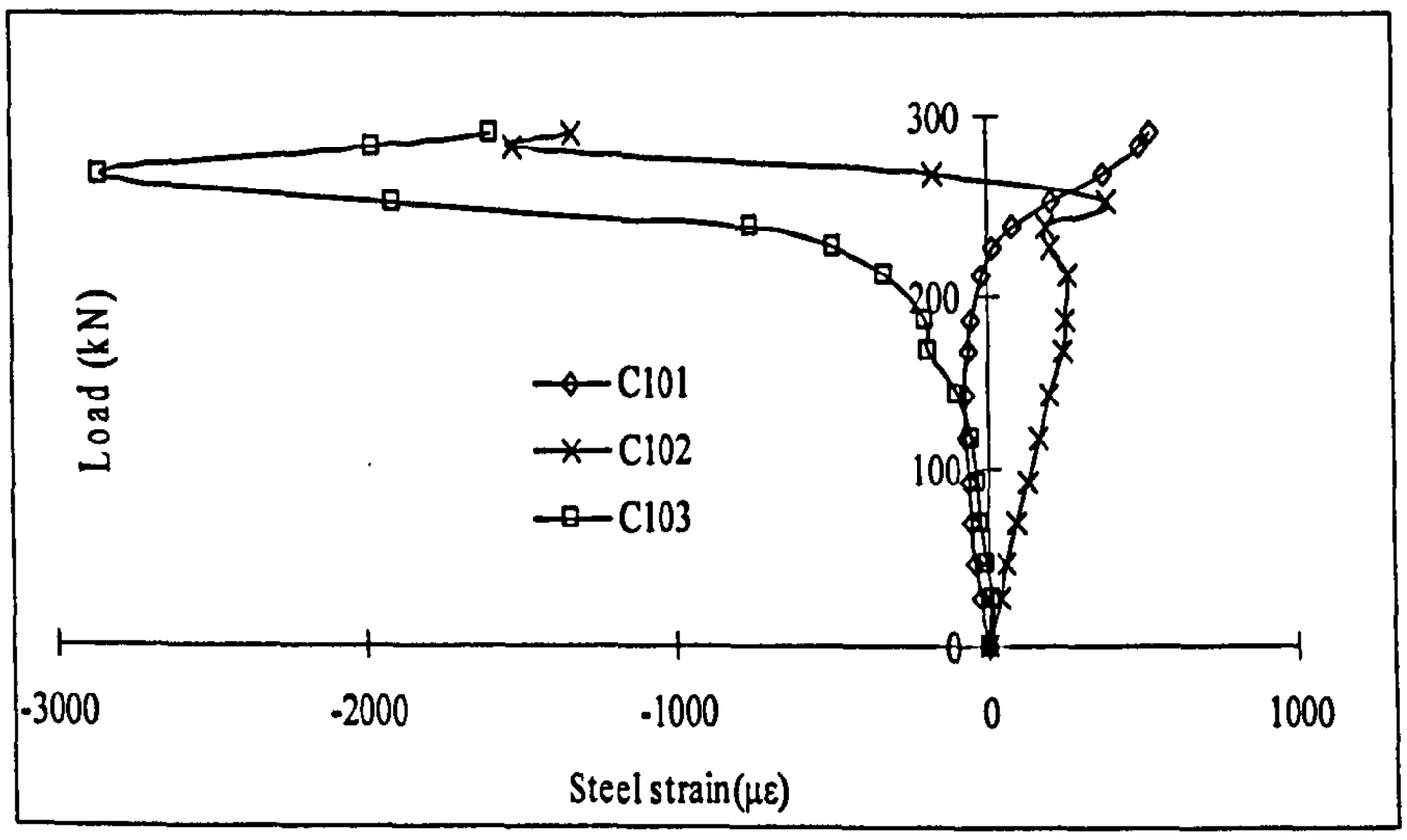
Load (kN)
300
200
100
0
C101
C102
C103
-3000
-2000
-1000
0
1000
Steel strain(με)

(a) B1

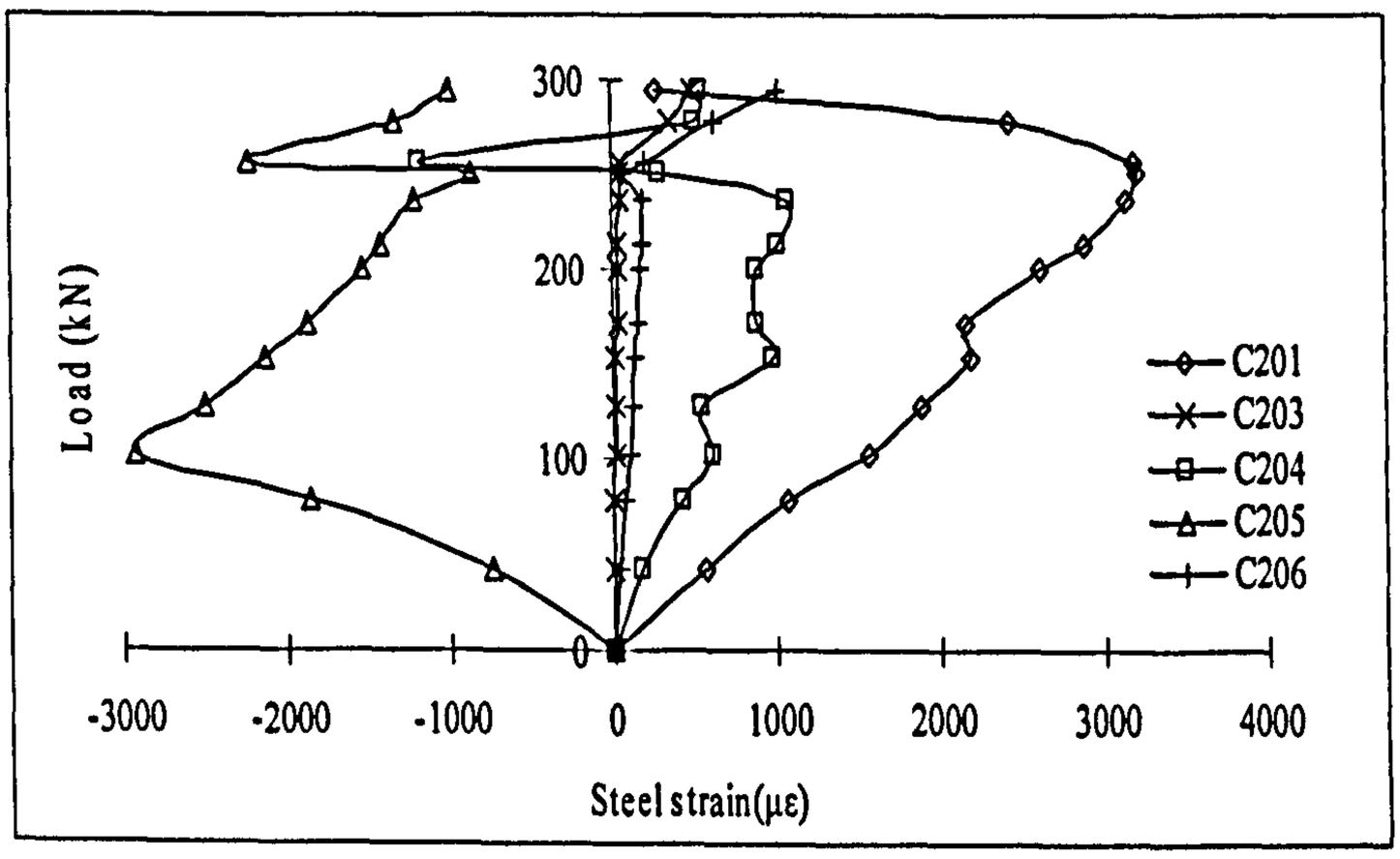
Load (kN)
300
200
100
0
C201
C203
C204
C205
C206
-3000
-2000
-1000
0
1000
2000
3000
4000
Steel strain(με)

(b) B2

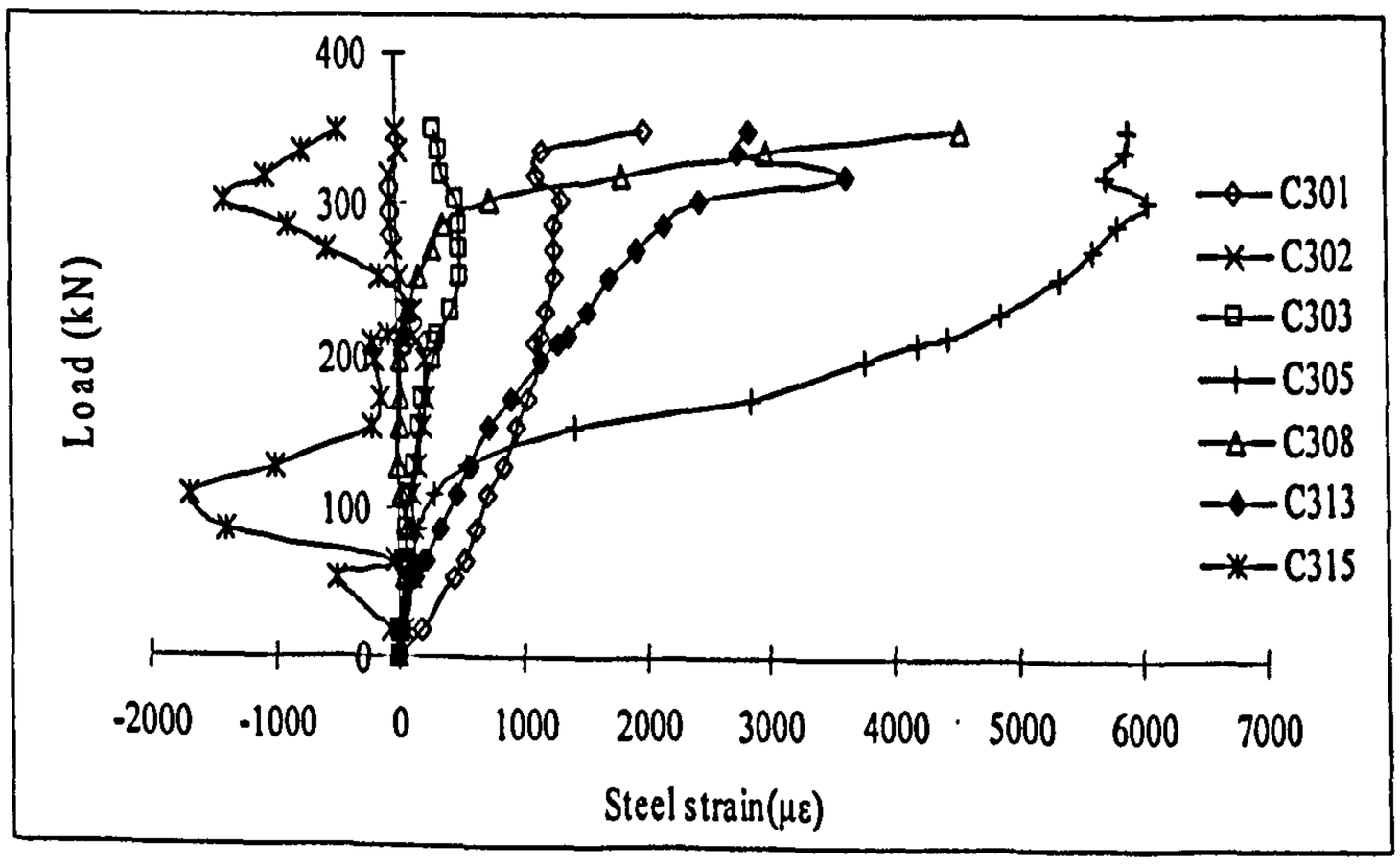
Load (kN)
400
300
200
100
0
C301
C302
C303
C305
C308
C313
C315
-2000
-1000
0
1000
2000
3000
4000
5000
6000
7000
Steel strain(με)

(c) B3

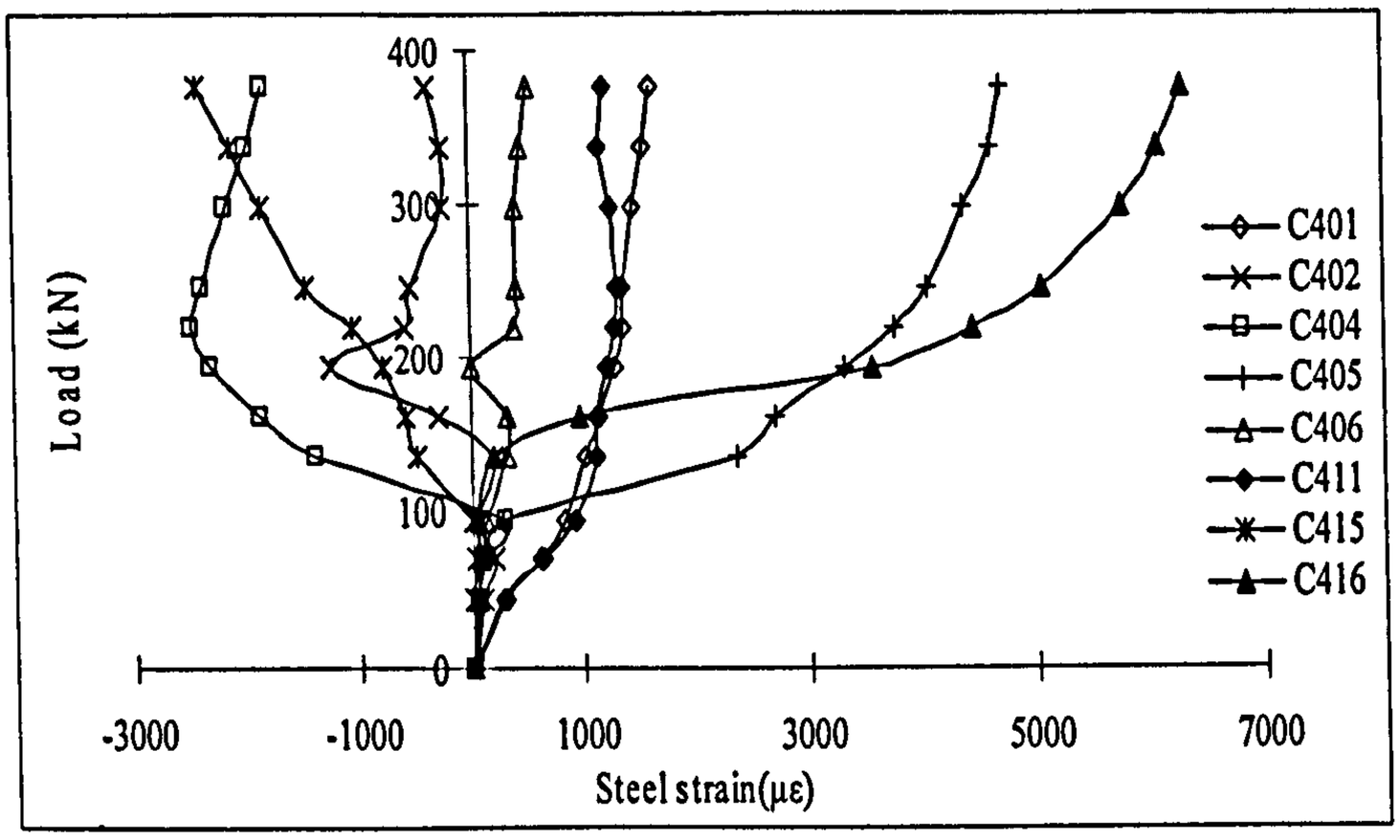

(d) B4

Figure 4-27 Load – internal steel strain profile for beam B1 to B4

4.4 Conclusions

Four NSM CFRP strengthened RC blocks have been fabricated and tested to failure. The parameters varied between the specimens include the length of middle block, the amount of reinforcing CFRP rods, and the near surface groove size. Commercial materials were used in all tests, to increase the realism of the lab simulations. All blocks failed by sudden brittle separation failure.

From the physical observations made and data collected during these experiments, the following general points may be made:

- When the length of middle blocks increased from 100mm to 300mm, the ultimate load of B3 is 24.5% higher than that of B1 while the load of B4 is 31.7% higher than that of B2.
- The ultimate failure loads were not influenced by the amount of strengthening CFRP. With the same length of middle block, the ultimate load of B4 increased slightly 9%

more than B3 when the CFRP rods doubled from 2 to 4 rods. Both B1 and B2 failed at very similar loads in spite of doubling the strengthening CFRP rod on both sides.

- Specimens were observed to fail in two brittle separation modes. The fractural separation took place either in the concrete layer horizontally due to shear cracks propagated along the side blocks or at the adhesive-rods interface.
- Being consistent to the failure modes, the cracks typically occurred either through a 30mm thick concrete layer adjacent to the reinforcing steel rod or on the bond line between the adhesive and CFRP rods. Fewer cracks were observed in B1 and B2 compared to B3 and B4 before failure, indicating that specimens with shorter middle block are more brittle than those with longer middle block so that they fail under the smaller loads without showing too much ductility.
- Beam theory was used to investigate the mechanism of horizontal cracks on the middle block. The calculated results of normal stress on the fracture plane are consistent with experimental observation, which gives fundamental insight into the reasons of various crack modes. The calculated maximum normal stress for B2 went up with the increasing of the load and reached as high as up to 10.25 N/mm^2 at the load P = 278 kN, which are higher than the tensile strength of the concrete and caused the horizontal crack at the middle block. However, throughout the loading period, the normal stress of B4 stayed up to 1.12 N/mm^2, which is much lower than the tensile strength of the concrete. Therefore, no horizontal crack was observed in the test.
- According to the experimental data, the CFRP strains for B2 (specimen with shorter middle block) generally increased with the distance from mid-block. However, the CFRP strains for B3 and B4 (specimens with longer middle blocks) increased with the distance from mid-block before vertical crack at mid-block. After then, higher CFRP strains are found at mid-block than those at the position near block edge. The shear stresses varied from 0 to 4.5 N/mm^2 which are relatively reasonably.

- With the same length of middle block, the specimen with double the amount of strengthening CFRP rods (B4) generally has smaller CFRP and steel strains under the same tensile load comparing to B3, especially after concrete block crack. The reversing strain in B2 at around P = 210 kN is possibly due to the occurrence of a deep horizontal crack in the middle concrete block.

The experimental analysis discussed in this chapter gives insight into the stress transfer characteristics between strengthening CFRP and concrete both near the mid-span and end zones. The next chapter is going to describe finite element analysis verified by the test data recorded in this chapter, along with a comprehensive investigation into the influence of more parameters on specimen failure behaviour.

Chapter 5

Finite element analyses of experimental specimens

5.1 Introduction

Chapter 4 presented a series of experiments conducted on RC specimens retrofitted with CFRP rods by the NSM technique to investigate the strengthening performance, failure modes, bond mechanisms and effects of some important design parameters such as length of middle block and the amount of strengthening CFRP rods. In what follows, these blocks are analysed using commercial FEA program DIANA. The distributions of both the reinforcing steel bar strains and CFRP rod strains along with the adhesive stresses for the four blocks are illustrated and compared to the experimental data. The FE analyses are also used to identify load-displacement curves which were not investigated in the lab tests. Subsequently, further parameters regarding the geometry and material properties of the specimens were chosen and their effects on structural behaviour are analysed and presented.

5.2 Finite element analyses of the specimens

5.2.1 Specimen configuration and FEA modelling

Geometry details of the specimens and test procedures are discussed in detail in Chapter 4. The test set-up is schematically represented in Figure 5-1. The specimen is composed of three parts: two side blocks, where the CFRP rod is inserted into the concrete along the anchorage length of 850 mm; and the middle block, where the CFRP rod is bonded to concrete over a length varying from 100 mm to 300 mm. To focus the investigation on the middle block, the side blocks are not considered in the following simulations.

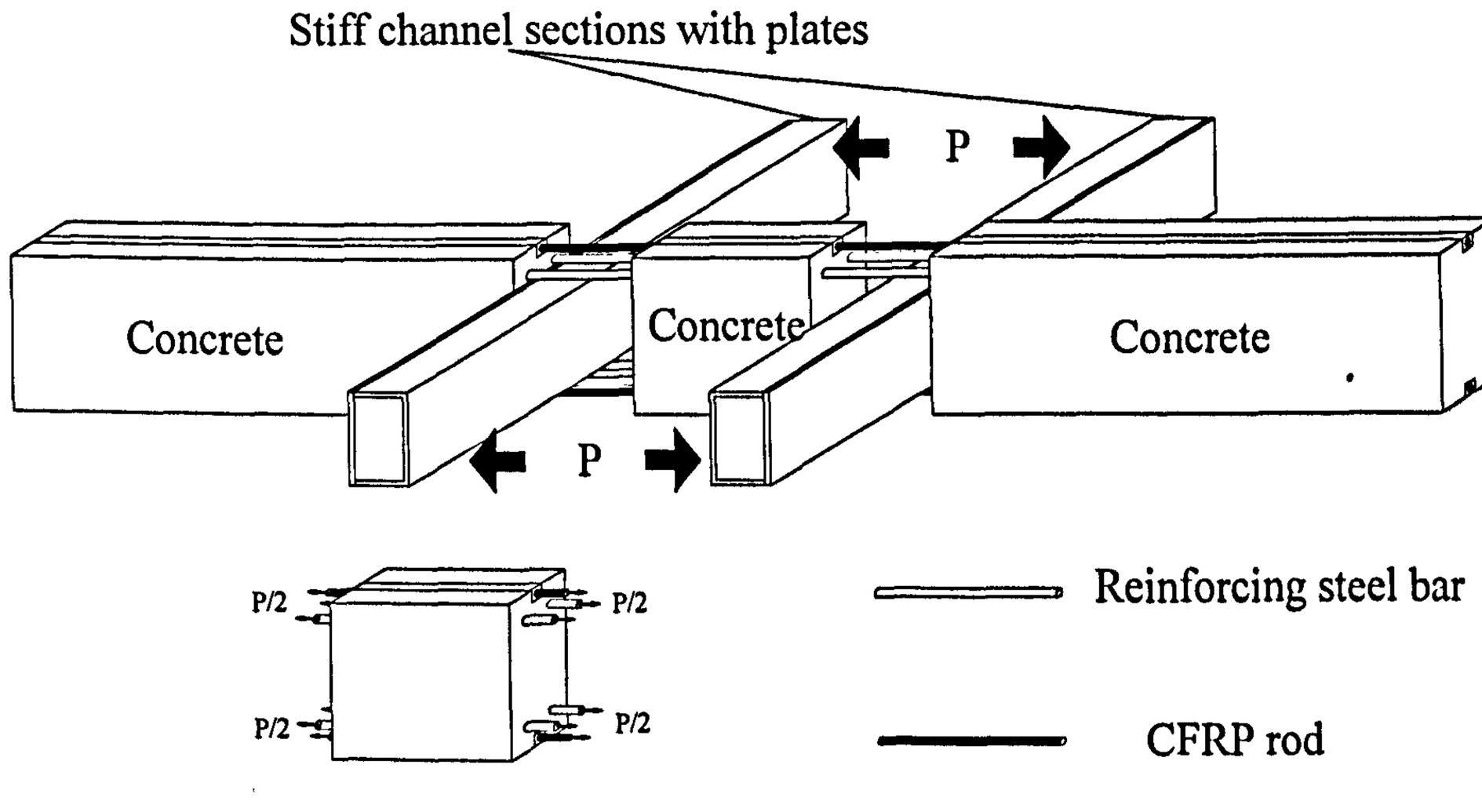

Figure 5-1 Loading and set up of test specimen

In this Chapter, 3D models were employed for simulating the CFRP NSM strengthened specimens. Taking advantage of symmetry of the models to achieve the balance between the speed of analysis and the accuracy of results, only one eighth of the original middle block was analysed with appropriate boundary conditions and the applied load in the FE program. The eight-noded brick element HX24L is used for the

modelling of concrete beam, reinforcing steel bars and adhesive layer while the six-noded brick element TP18L is used for CFRP rods due to their round shape. The FEM meshes can be seen in Figure 5-2.

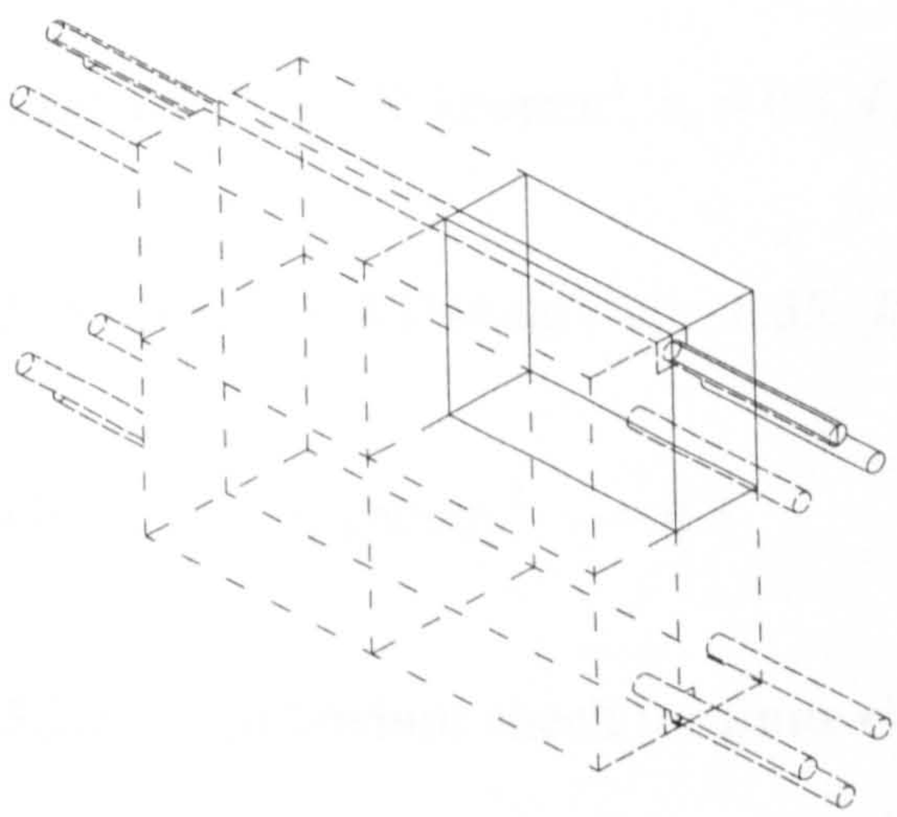

(a) Geometry for B1 or B3

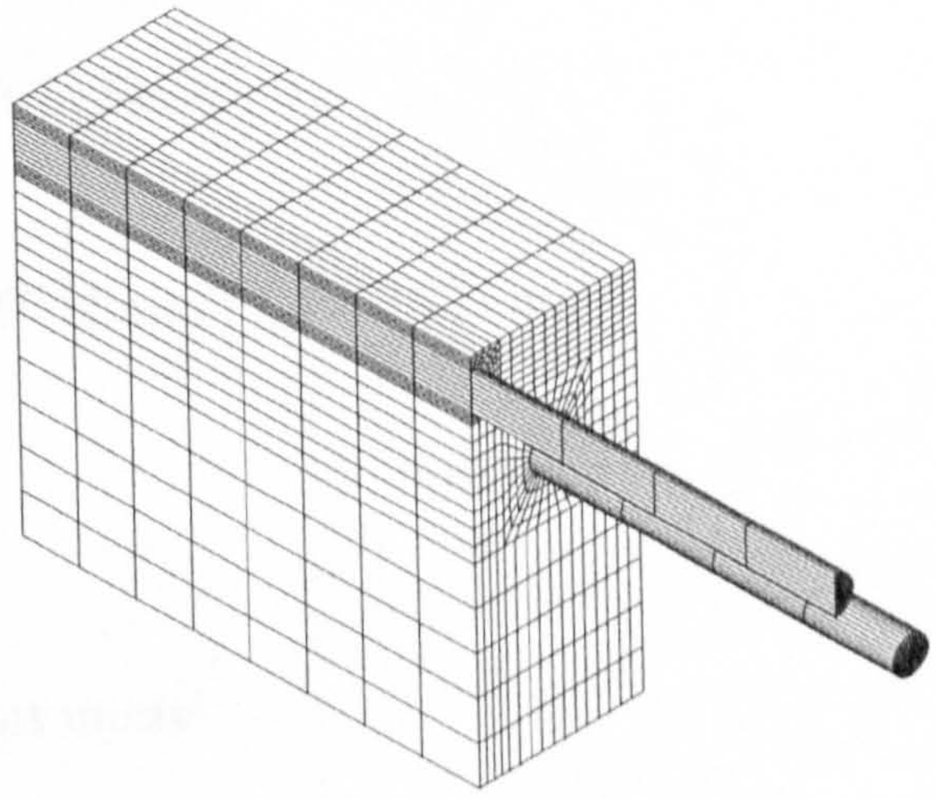

(b) Mesh for B1 or B3

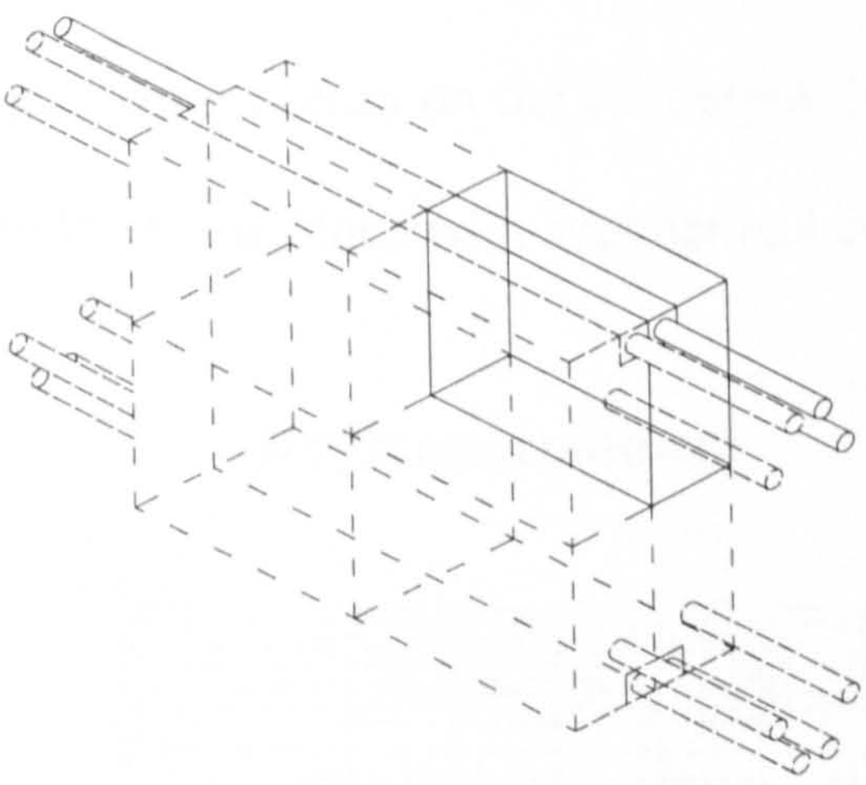

(c) Geometry for B2 or B4

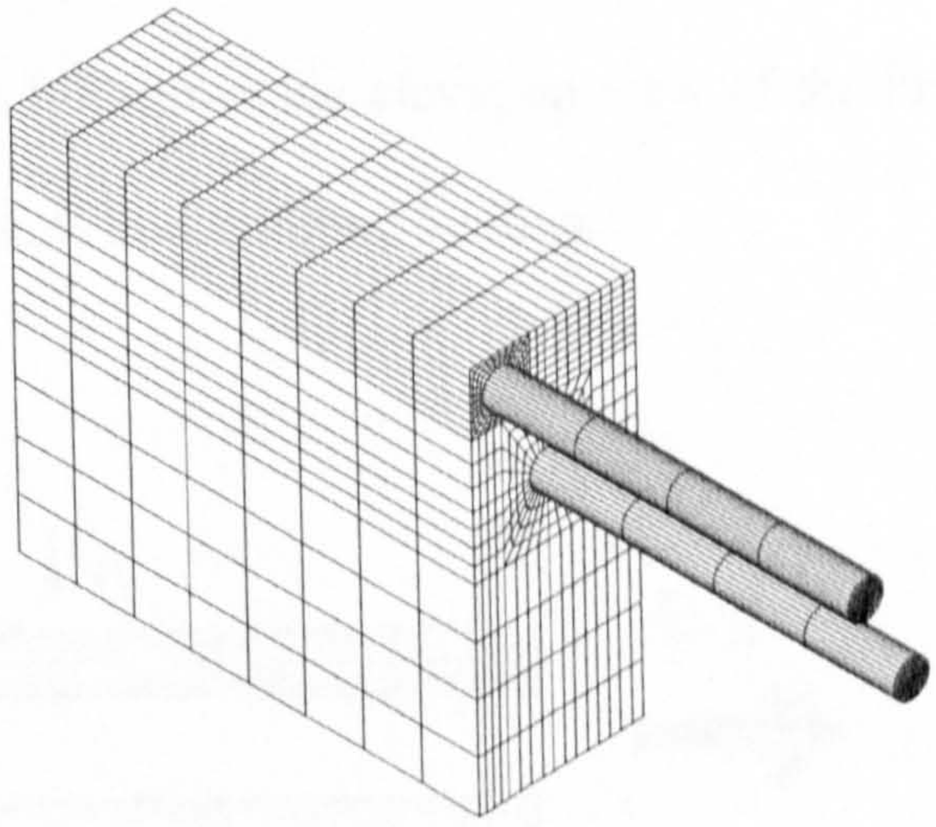

(d) Mesh for B2 or B4

Figure 5-2 Geometry and mesh of the middle block for B1 to B4

The material properties input to the FE models are based on the data from lab tests described in Chapter 4. Please refer to Chapter 3 (3.2.2 Material properties) for the corresponding modelling technique. Because Young's modulus of concrete is not available from the lab test, the value is assumed to be 28 kN/mm^2 according to the compressive strength as 40 N/mm^2. Both the steel bar and CFRP rod samples were

not tested to yield in the lab. In this case, the yield strength of steel bar is assumed to be 500 N/mm^2. The summary of material properties is given below:

Concrete block: E_c = 28 kN/mm^2, ν_c = 0.2, f_{cc} = 40 N/mm^2, f_{tc} = 3 N/mm^2

Steel rod: E_s = 200 kN/mm^2, ν_s = 0.3, f_{ys} = 500 N/mm^2

Adhesive: E_a = 8 kN/mm^2, ν_a = 0.35, f_{ca} = 50 N/mm^2, f_{ta} = 6.5 N/mm^2

FRP: E_f = 150 kN/mm^2, ν_f = 0.3

5.2.2 Equilibrium check for finite element model

To make sure the FEA results are reliable, it was considered essential to perform equilibrium checks on the FE output. Figure 5-3 shows the elevation view of the FE model for the block with symmetrical constraints and assigned loading.

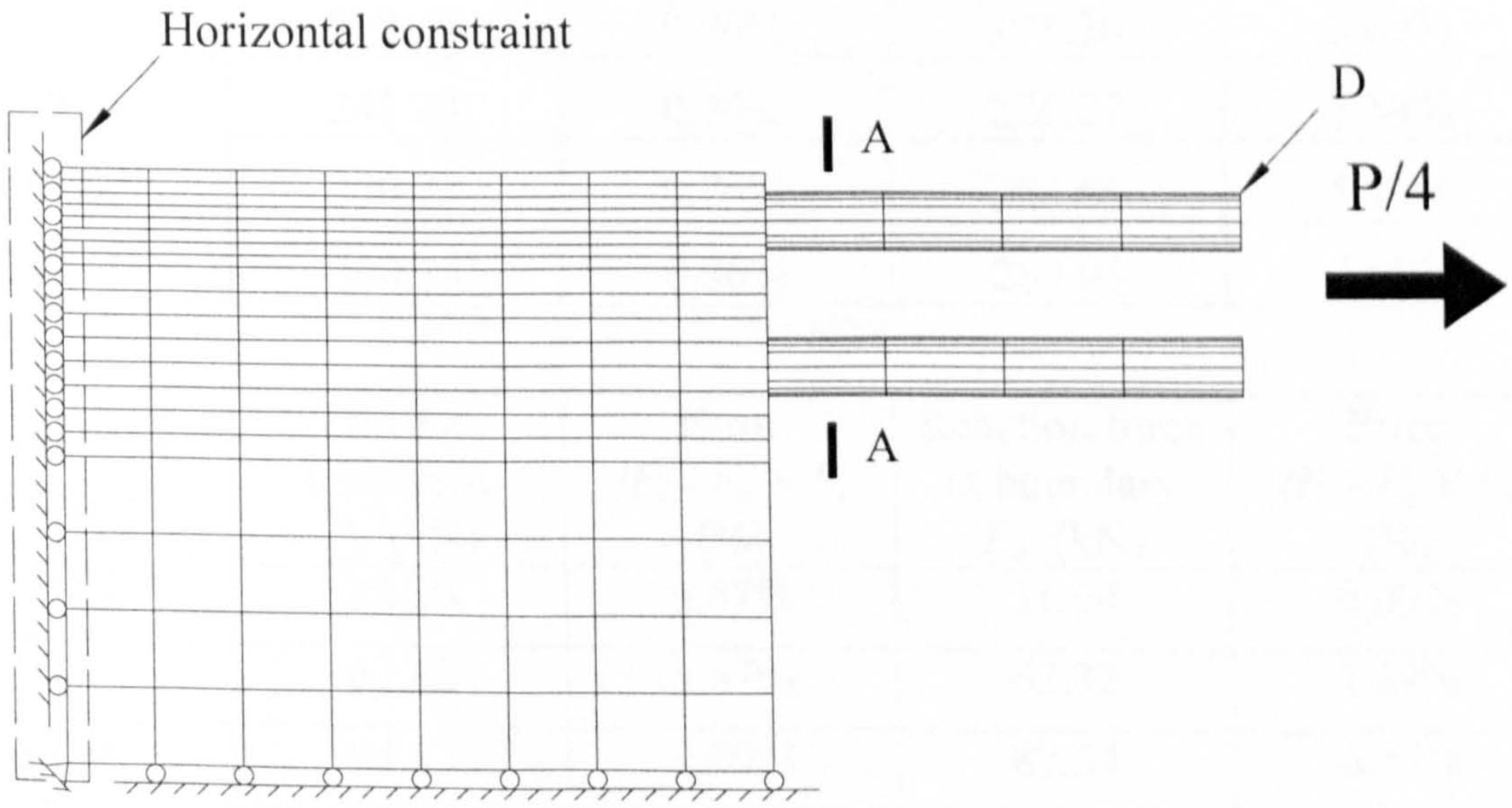

Figure 5-3 Elevation view of FE mesh

Section A-A was chosen to be investigated because there is no concrete stress to be taken into account in that area. As described before, the blocks were under pure

tensile load. By multiplying the steel and CFRP strains by the corresponding elastic moduli and then by areas, the forces in the steel and FRP rods were found. The sums of the tensile forces are then compared with the initial loading. Table 5-1 shows the calculations and comparisons for each model at every load step. It can be seen that the tensile force equilibrium is very nearly satisfied by the results.

Table 5-1 Equilibrium check for Elements at region A-A

(a) B1

Initial load F_i (kN)	Force at section A F_a (kN)	Error $(F_i - F_a)/ F_i$ (%)	Reaction force at boundary F_b (kN)	Error $(F_i - F_b)/ F_i$ (%)
32.70	32.85	0.46%	32.70	0.00%
64.27	64.64	0.57%	62.28	3.10%
93.60	94.20	0.64%	89.69	4.18%
122.65	123.56	0.74%	116.80	4.77%
152.65	153.85	0.78%	140.75	7.80%
180.42	181.54	0.62%	172.24	4.54%
210.26	212.29	0.96%	198.30	5.69%
239.54	241.23	0.70%	226.27	5.54%
268.62	270.73	0.79%	254.69	5.19%
297.67	300.23	0.86%	283.08	4.90%

(b) B2

Initial load F_i (kN)	Force at section A F_a (kN)	Error $(F_i - F_a)/ F_i$ (%)	Reaction force at boundary F_b (kN)	Error $(F_i - F_b)/ F_i$ (%)
31.94	32.20	0.67%	31.94	0.00%
63.20	63.62	0.67%	62.32	1.39%
93.38	94.12	0.79%	87.54	6.25%
121.71	122.69	0.81%	116.13	4.59%
151.24	152.92	1.11%	140.49	7.10%
179.93	181.59	0.92%	166.78	7.31%
208.40	210.39	0.95%	195.39	6.24%
236.83	238.43	0.67%	224.28	5.30%
265.36	267.86	0.94%	252.88	4.70%

293.90	296.66	0.94%	281.07	4.37%

(c) B3

Initial load F_i (kN)	Force at section A F_a (kN)	Error $(F_i - F_a)/ F_i$ (%)	Reaction force at boundary F_b (kN)	Error $(F_i - F_b)/ F_i$ (%)
50.24	50.29	0.09%	50.25	0.00%
94.10	94.20	0.11%	93.08	1.07%
128.91	128.92	0.01%	125.44	2.69%
160.71	160.40	-0.19%	146.53	8.82%
188.42	188.28	-0.07%	163.70	13.12%
218.74	219.25	0.24%	191.22	12.58%
256.02	256.42	0.15%	224.64	12.26%
290.85	291.71	0.30%	260.17	10.55%
325.06	325.78	0.22%	296.23	8.87%
358.78	359.85	0.30%	332.46	7.34%

(d) B4

Initial load F_i (kN)	Force at section A F_a (kN)	Error $(F_i - F_a)/ F_i$ (%)	Reaction force at boundary F_b (kN)	Error $(F_i - F_b)/ F_i$ (%)
51.81	51.92	0.21%	51.75	0.11%
97.25	97.28	0.04%	96.19	1.09%
134.01	133.87	-0.11%	131.45	1.91%
168.01	167.62	-0.23%	153.69	8.52%
197.59	197.23	-0.18%	170.66	13.63%
231.62	231.55	-0.03%	196.62	15.11%
265.92	265.87	-0.02%	238.51	10.31%
303.60	304.26	0.22%	274.01	9.75%
339.41	339.44	0.01%	311.17	8.32%
374.83	375.25	0.11%	348.46	7.04%

5.3 Comparisons with experimental results

5.3.1 Tensile strain in steel reinforcement

For the specimens B1 to B4, axial strains of steel reinforcement from the FE models. are presented and analyzed in Figure 5-4 and Figure 5-5.

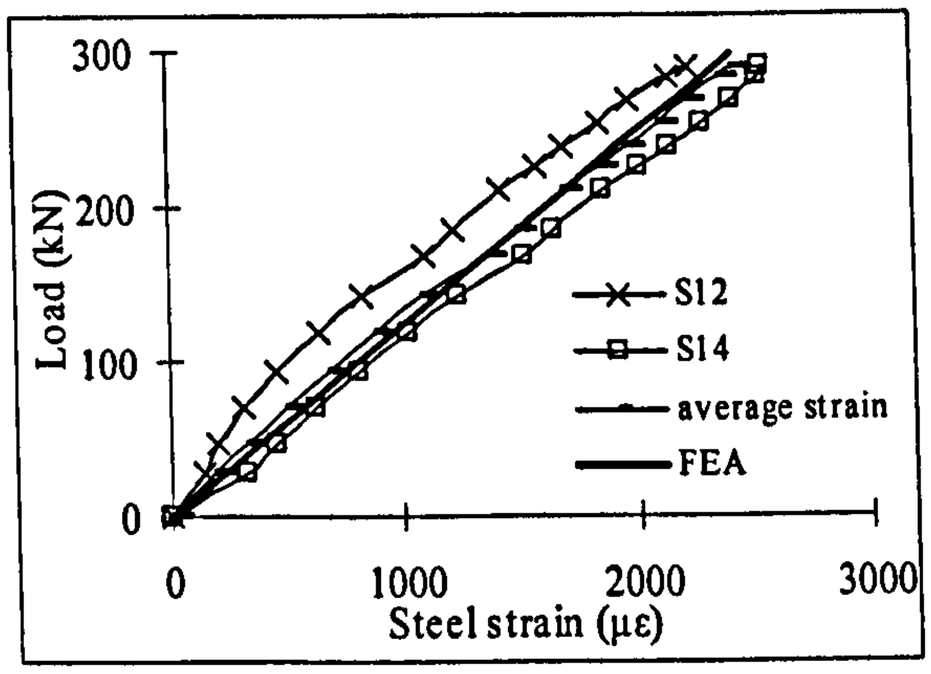

(a) B1

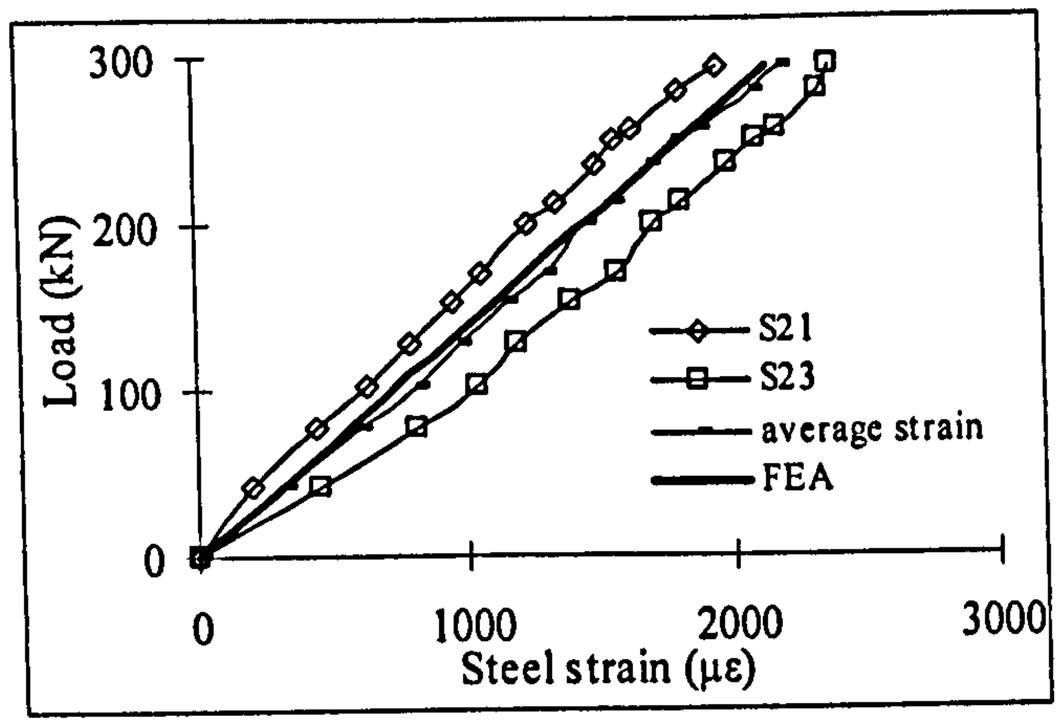

(b) B2

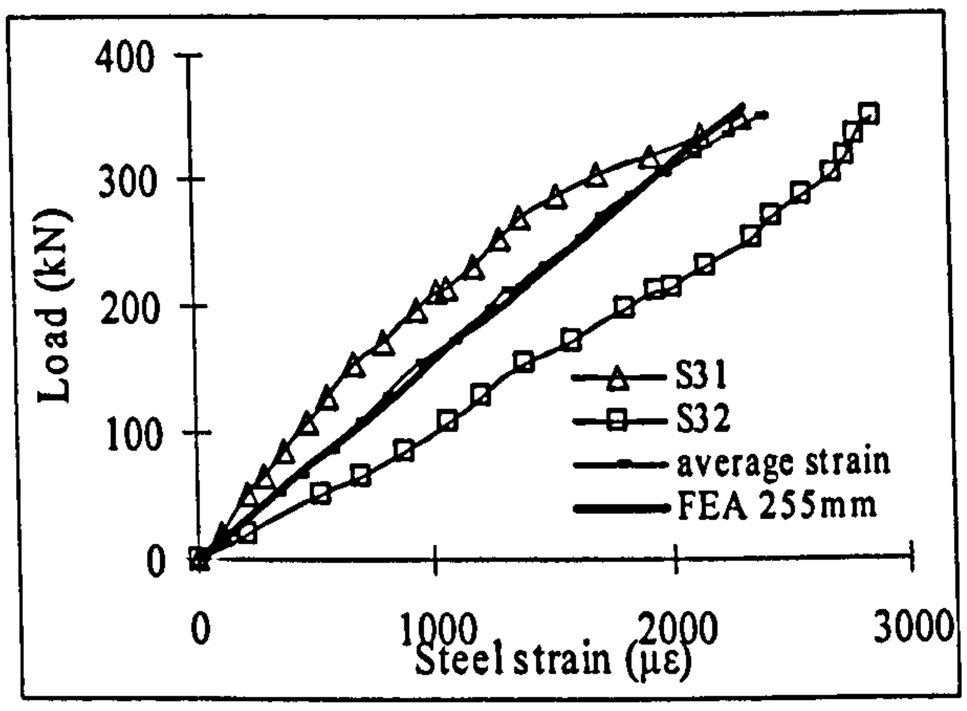

(c) B3

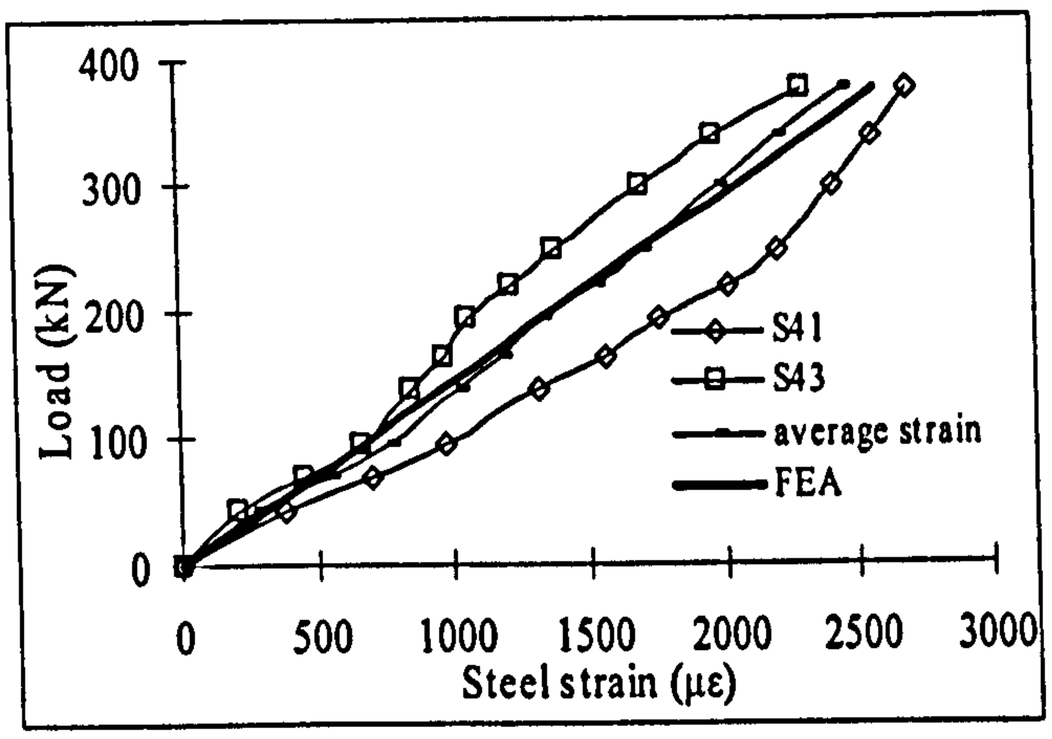

(d) B4

Figure 5-4 Comparisons between test data and FEA results of load- Steel strain for B1 to B4

The experimental data of steel strain were collected from the strain gauges on the middle area of the exposed steel rods. As can be seen Figure 4-7, the strain gauges are symmetrically located and have the same distance to the mid-block. As discussed earlier on Chapter 4, for each specimen, average values were taken from these readings to represent the typical strain at this location. In the FE analysis, one eighth of the specimen was modelled due to symmetry of the specimens, which means that only one steel rod was modelled and one strain reading could be taken from the corresponding location. In this case, the maximum, minimum and average strain gauge readings from test data are taken for each specimen and compared to the FEA results. Comparisons of the load-steel tensile strain plots between the FEA results and

the experimental data are then shown in Figure 5-4. Good agreements were found between the average value and the FE results.

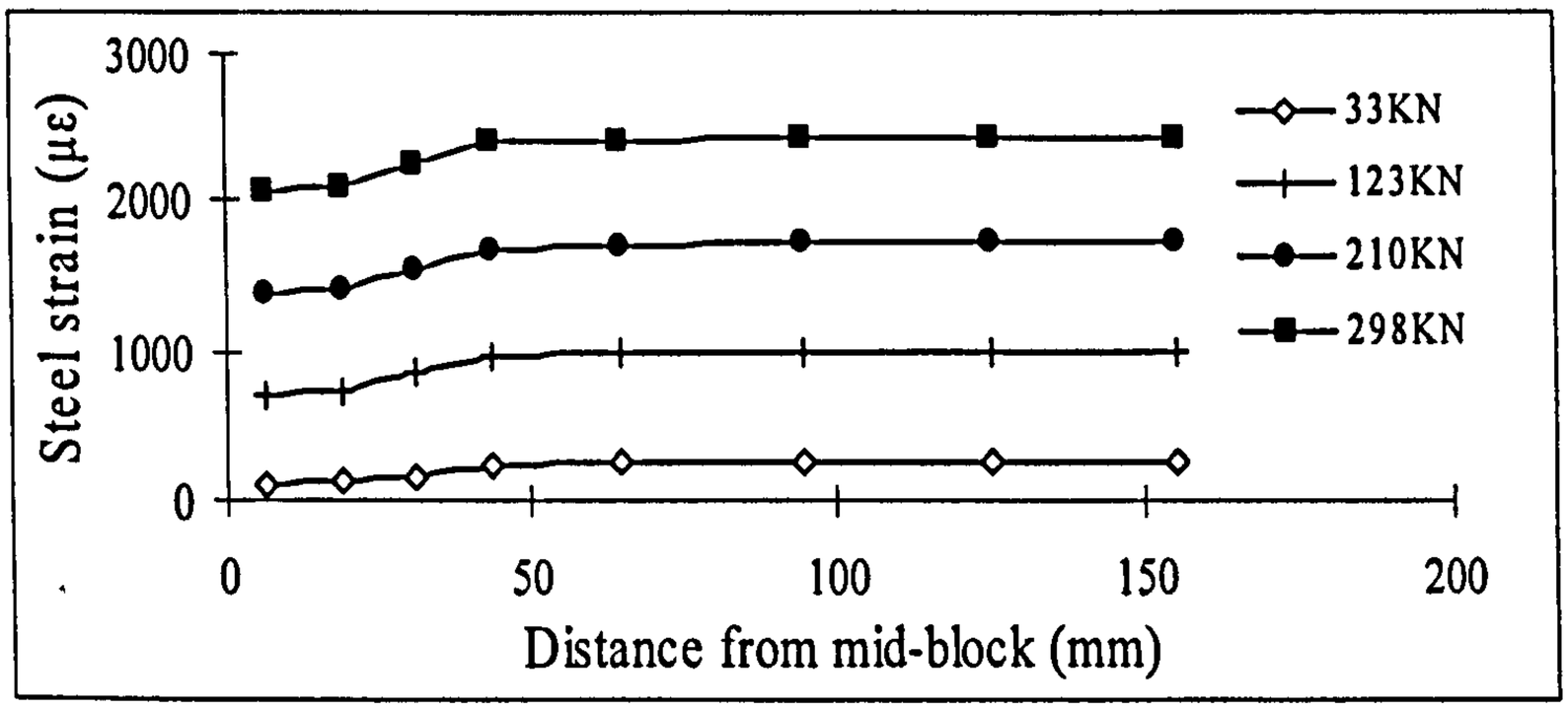

(a) B1 steel strain distribution

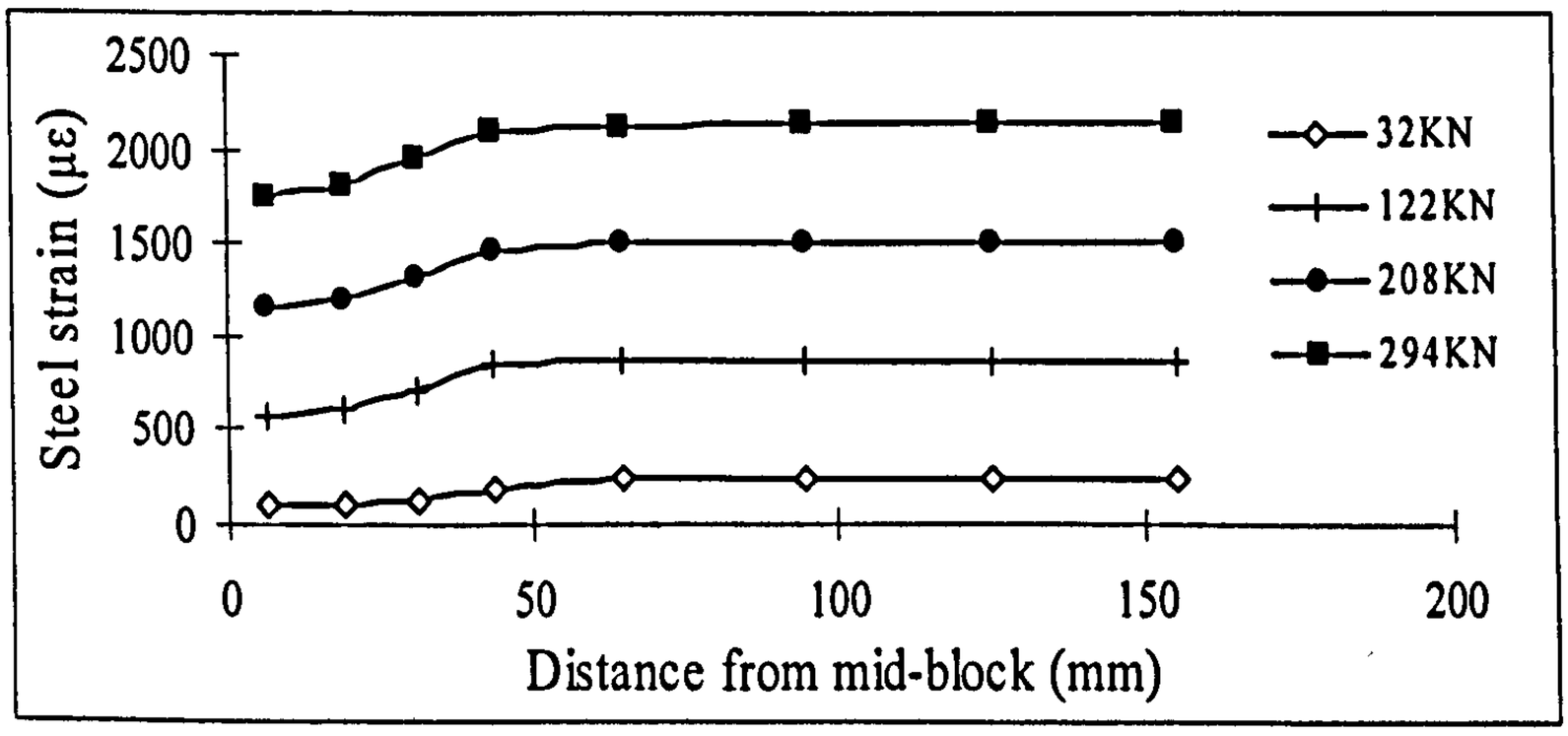

(b) B2 steel strain distribution

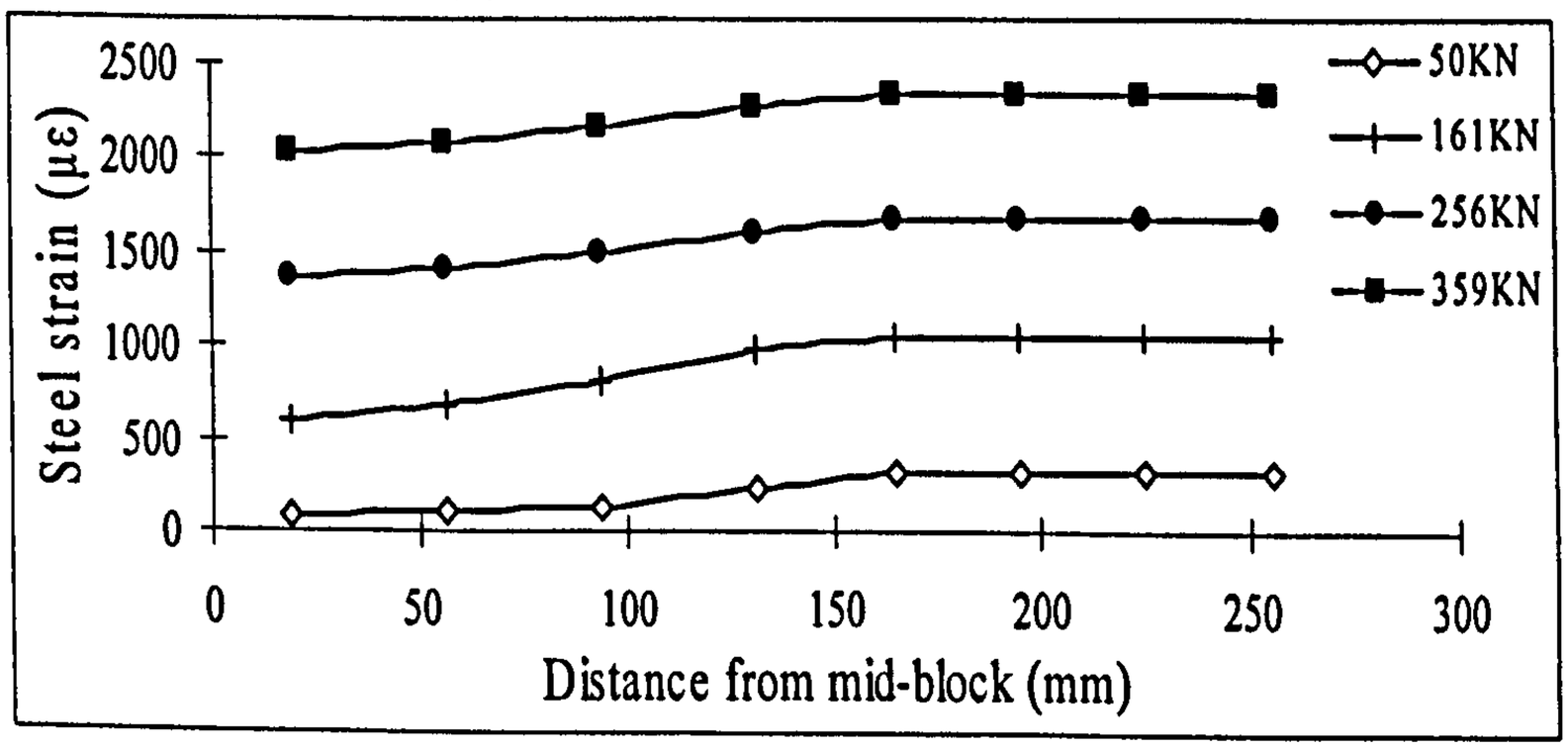

(c) B3 steel strain distribution

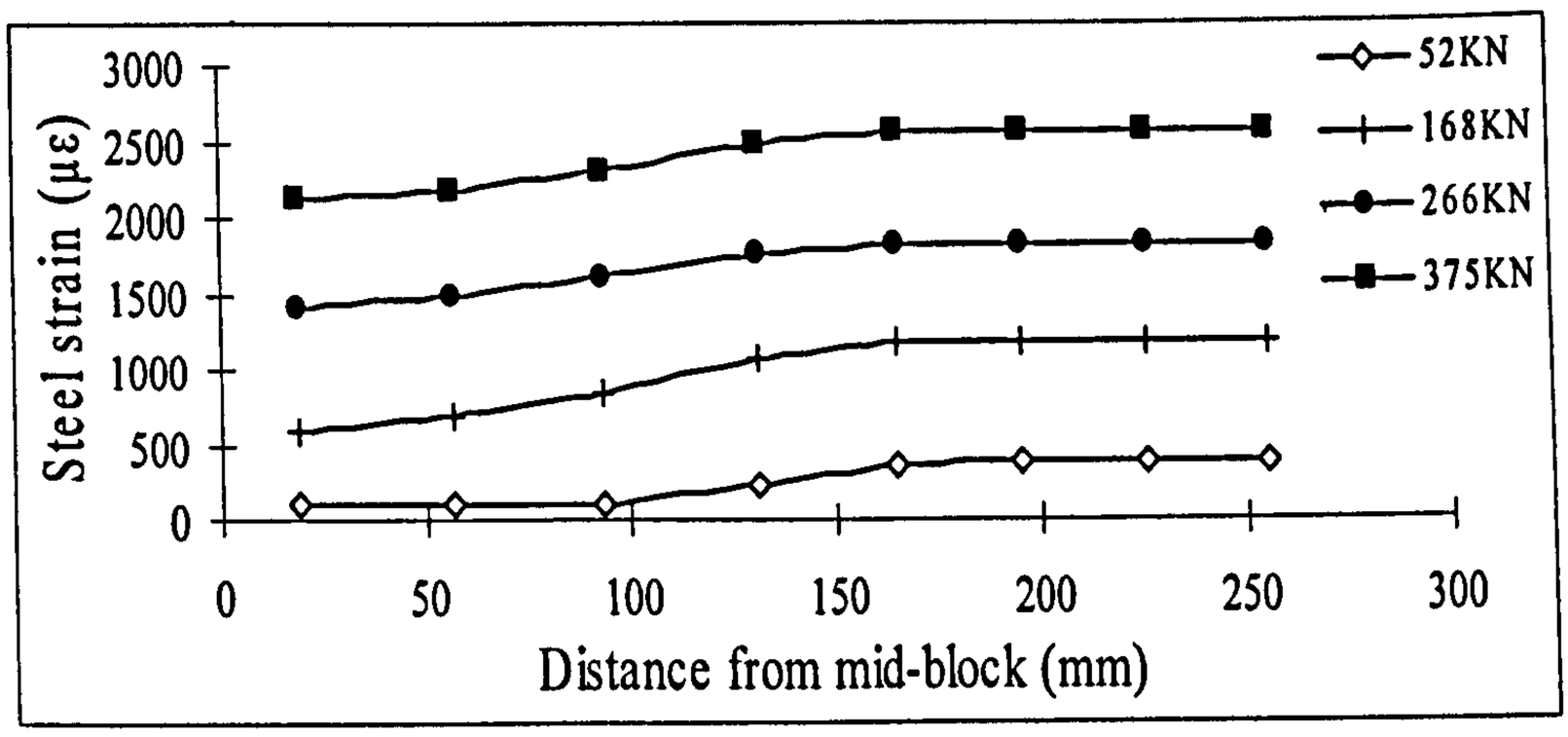

(d) B4 steel strain distribution

Figure 5-5 FEA results of Steel strain distributions for B1 to B4

Figure 5-5 shows the steel strain distributions along the bar from FEA results. Clearly, the strain increased with the distance away from the middle of the block and then kept constant in the exposed area of CFRP rods. The smaller strain was found inside the block than the exposed area, which may be due to the fact that part of the tensile force in the former area is partly taken by the concrete.

5.3.2 Tensile strain in CFRP rods

The experimental data of FRP strain were collected on the CFRP rods in a short distance from the mid-block. The locations of the strain gauges are shown in Figure 4-22 to Figure 4-24 in Chapter 4. The FE results were then taken at the corresponding locations.

The comparison between test data and FEA results of CFRP strain distribution for B2 to B4 at certain load stages are then shown in Figure 5-6. There is no comparison for B1 because the CFRP strains from test data of for this specimen are absent. In general, the strain distributions of both the test data and the FE models have similar trends. Very good correlation was found at the lower load stages. But at the higher load stages, the FEA results show certain level of difference from the test results. The

adhesive shear stress from FEA results are also compared with the shear stress deducted from measured CFRP strains from test data. However, the comparisons are not very good.

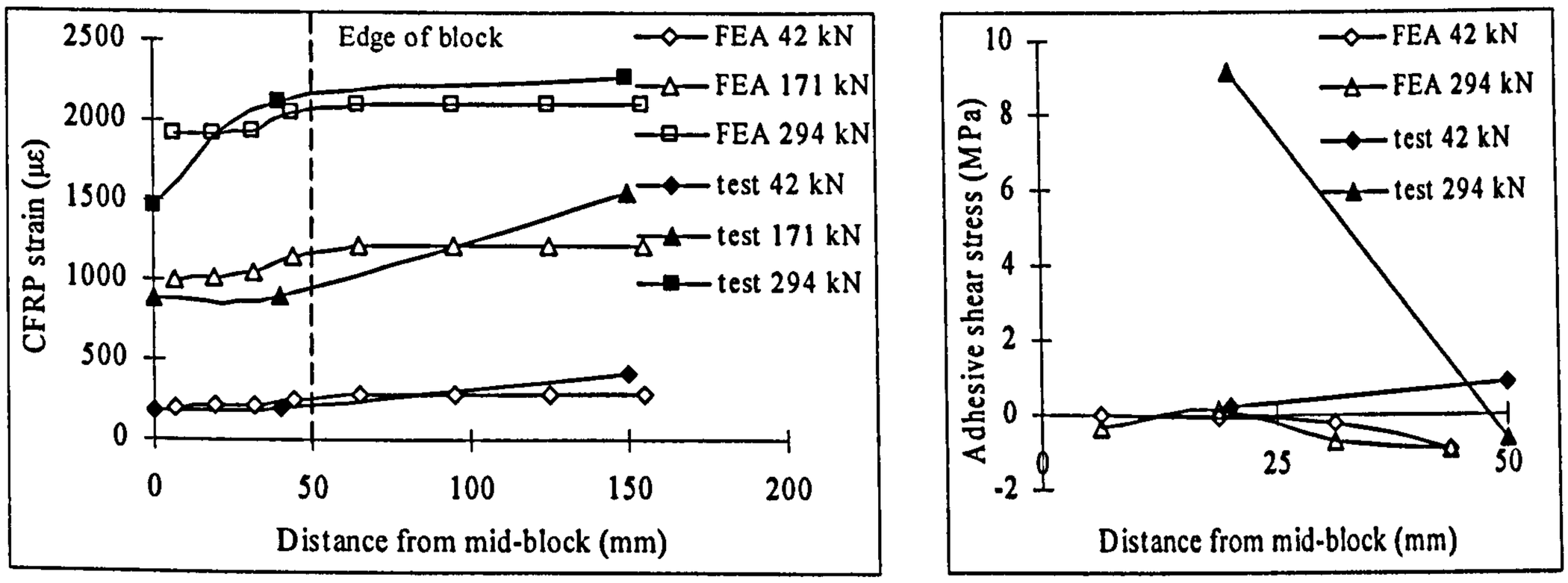

(a) Distributions of CFRP strains and adhesive shear stresses for B2

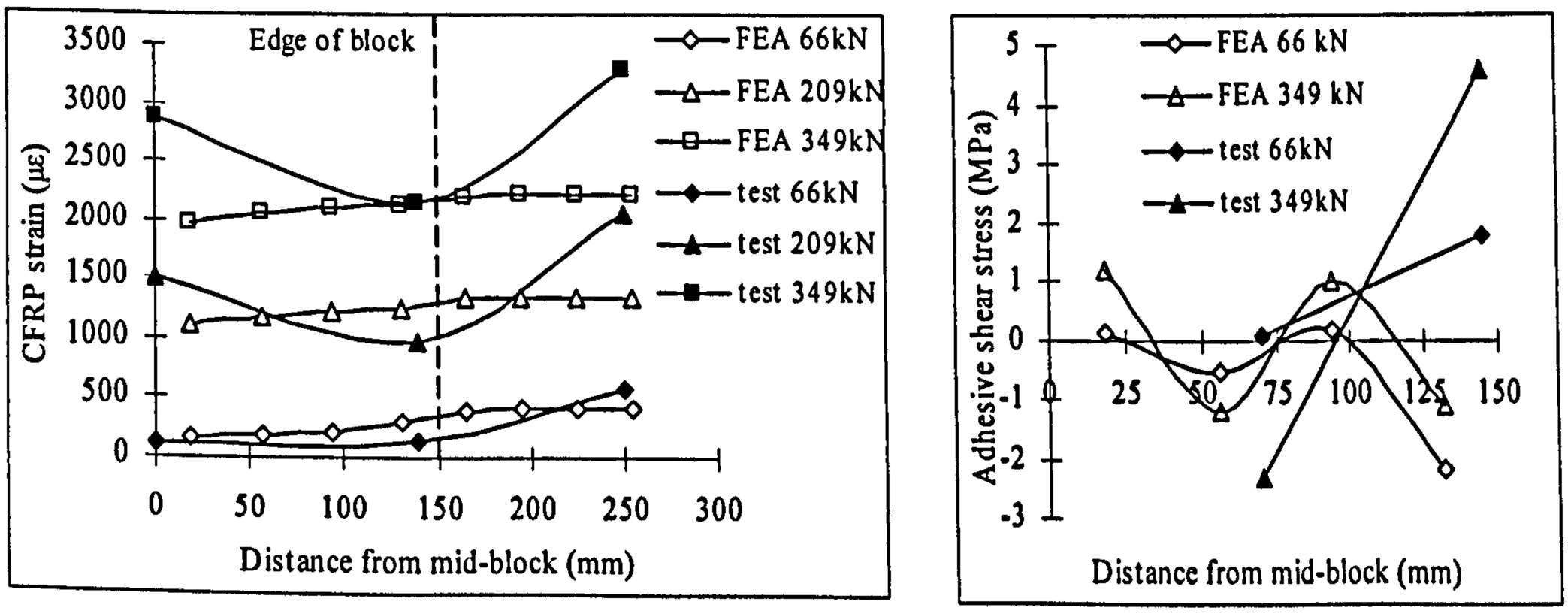

(b) Distributions of CFRP strains and adhesive shear stresses for B3

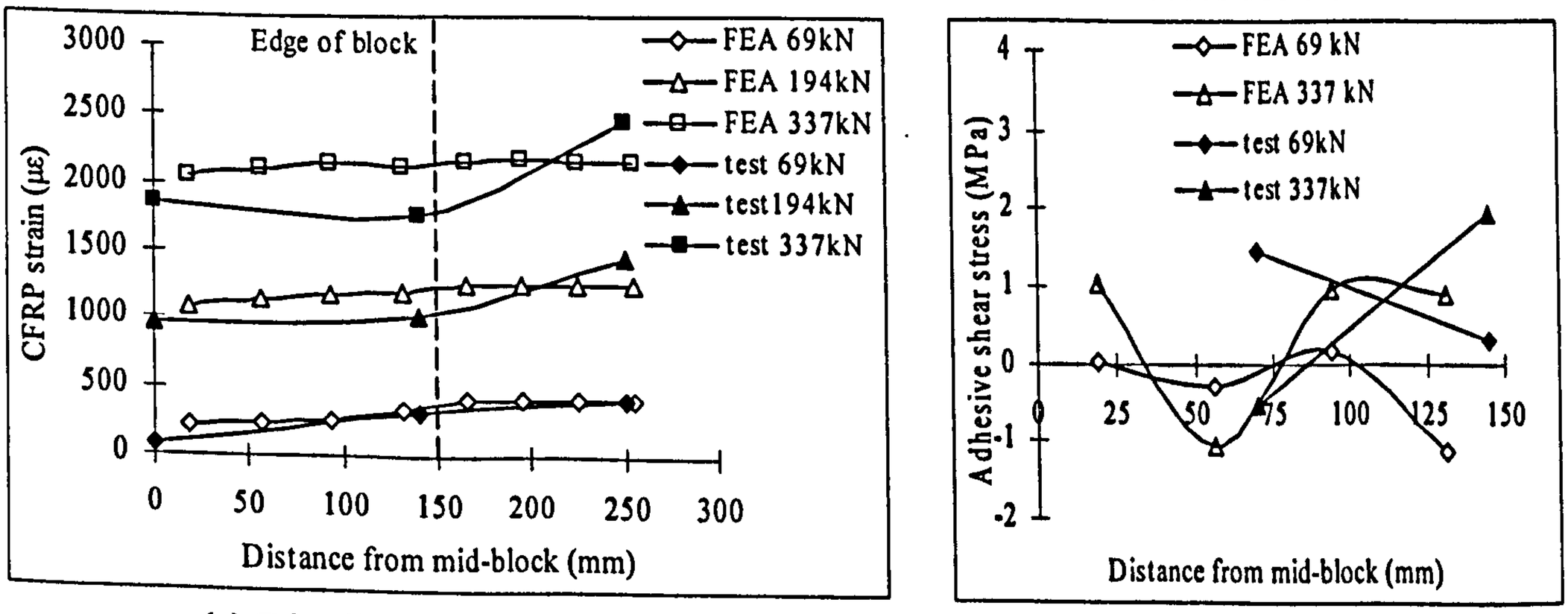

(c) Distributions of CFRP strains and adhesive shear stresses for B4

Figure 5-6 Comparisons between test data and FEA results of CFRP strain distribution for B2 to B4

The inconsistency between the FEA results and test data is possibly due to a few reasons.

The first reason is the local bending of CFRP rods where the strain gauges are located. It cannot be guaranteed that the specimen set-up in the lab are under a perfectly axial loading scheme. In this case, the local bending may exist on the CFRP rods, which could cause high tensile strain. Basically, it can be seen that for the FEA results, the CFRP tensile strains increase with the distance from the mid-block to the edge of the block due to the tensile force inside of block is partly taken by concrete. On the exposed area, the CFRP strains remain nearly constant. However, as seen from the test data in Figure 5-6 (b) and (c), the CFRP strains on the exposed area for B3 and B4 are up to 1000 micro strains higher than those near the edge of the block. This may plausibly be explained by the existence of local bending near the mid-block because if there is no local bending exists on the exposed CFRP rods in the lab test, the strains on the exposed area should keep constant as FEA results.

To moderately lower the effect of local bending, strain gauges can be put on the two CFRP rods on the opposite sides of the middle concrete block and taking the average reading of the corresponding strain gauges, which has been done for B2 and B4. As can be seen in Figure 5-6, B2 and B4 show better agreements between FEA results and test data than B3 does. In addition, the effect of local bending could also be eliminated by putting two strain gauges on the opposite sides of the same section on the CFRP rods and then taking the average reading of both values. To avoid damaging the bonding between FRP rod and surrounding adhesive, such arrangement of strain gauges should be used with care. It could be considered in future investigations.

Another possible reason is the local effects caused by the major cracks which took place close to the strain gauge locations in the experiment, while the smeared cracking approach is used in the FE analyses.

For B2, the local bending of CFRP rods in test could also be caused by the deep ***horizontal*** cracks on the middle block. As seen from Figure 5-6 (a), at load P = 294 kN, the CFRP strain at midspan is 600 micro strain smaller than that near the block edge which resulted much higher shear stress than the FEA results.

However, for B3 and B4, the ***vertical*** cracks of surrounding adhesive and concrete in close proximity to the strain gauges at mid-block can cause the inconsistent distribution of CFRP strains. The mechanism of crack influence is illustrated below.

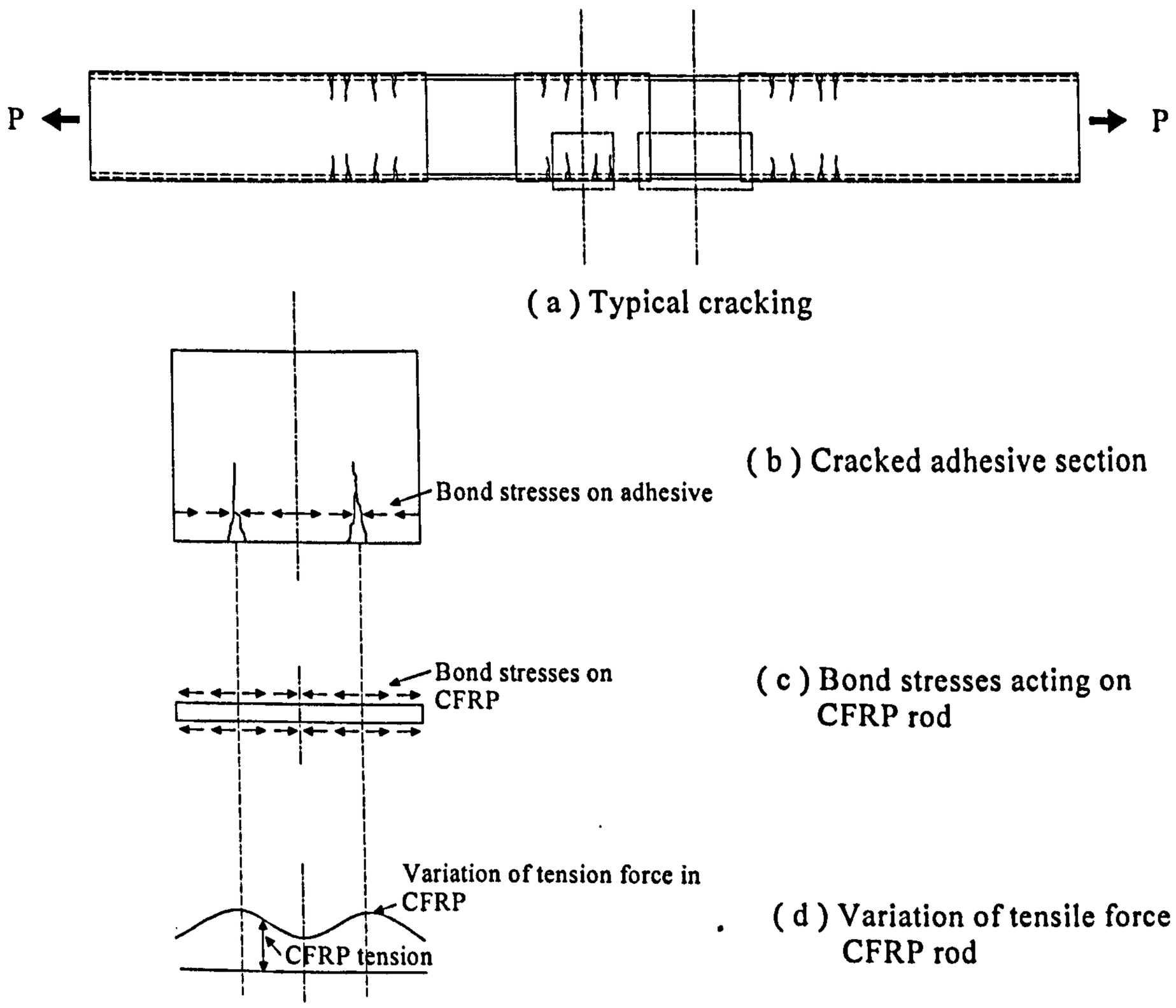

Figure 5-7 Variation of tensile force in CFRP rods near surrounding adhesive

In the experimental specimen at a sufficiently high load, the adhesive and concrete may fail to resist tensile stresses only where the cracks are located as shown in Figure 5-7 (a) and (b). Between the cracks, the adhesive and concrete resist moderate amounts of tension introduced by bond stresses acting along the interface in the direction show in Figure 5-7 (c), which reduce the tensile forces in the CFRP rods, as illustrated by Figure 5-7 (d).

(a) Typical smeared cracking

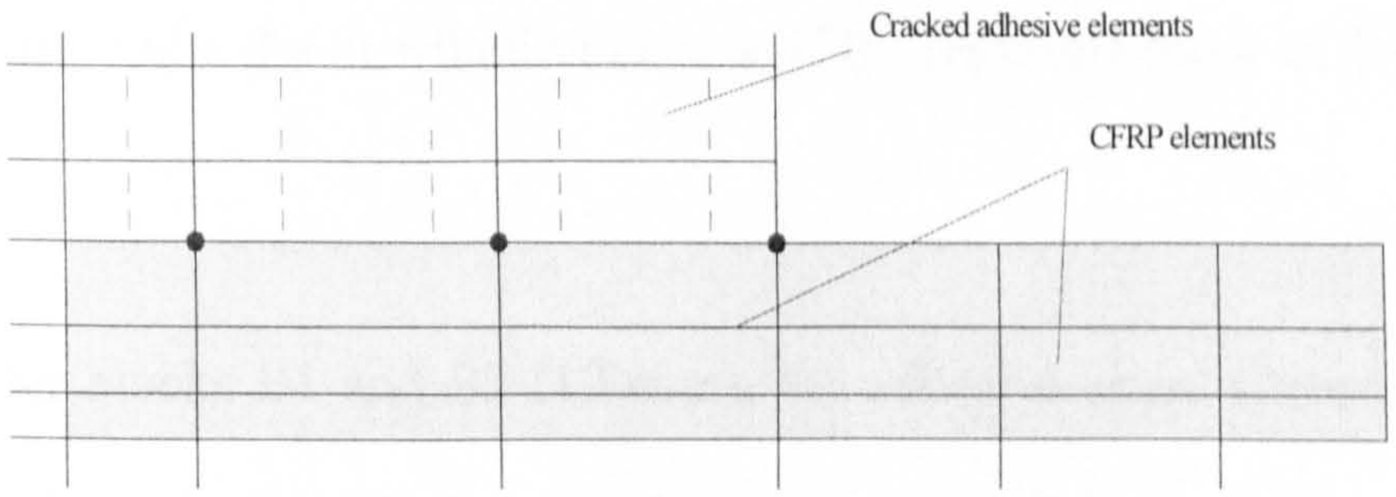

(b) Cracked adhesive and CFRP rod element

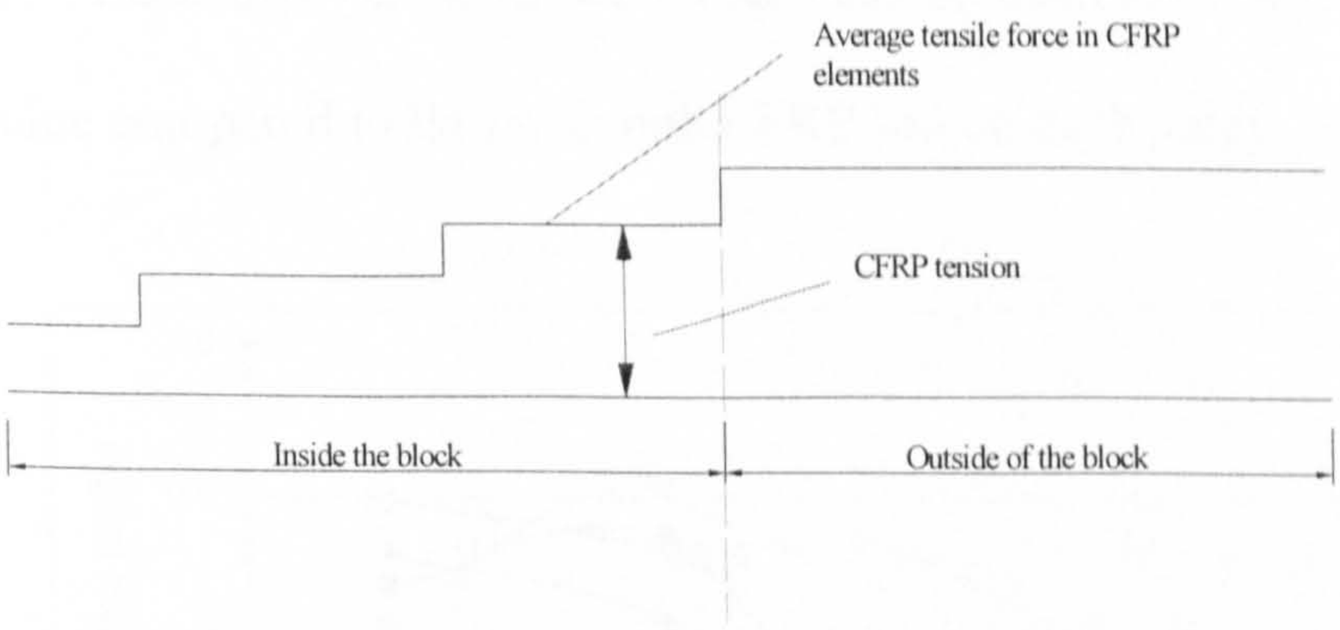

(c) Profile of tensile force in CFRP element

Figure 5-8 Development of tensile force in the CFRP for finite element models

Figure 5-8 then shows the development of the tensile force in the CFRP rods for the FE models. In the smeared cracking approach, the smeared cracks spread over the region where the principal tensile stresses in the adhesive elements exceed the

ultimate tensile strength rather than having discrete cracks, as shown in Figure 5-8 (a) and (b). Therefore, the tension in the CFRP elements for the FE model does not vary as in the actual block specimen but remains constant across each element (Figure 5-8 (c)). For this reason, CFRP strains of the FEA results could be different from those of lab test.

5.3.3 Adhesive shear stress distribution

Distributions of adhesive shear stresses along CFRP rods are presented in Figure 5-9. Generally, the models with same length of middle block have the similar trend of stress distribution, e.g. the distribution curves of B1 resemble those of B2 (Figure 5-9 (a) and (b)), while the distribution curves of B3 resemble those of B4 (Figure 5-9 (c) and (d).

For shorter blocks B1 and B2 (100mm), the adhesive shear stresses of both models fluctuate along the bond line and peak near the end of block, ranging from 2.0 N/mm^2 to 4.0 N/mm^2. Basically, B2 (with two CFRP rods on each side) shows nearly half of the stress value compared to B1 (with one CFRP rod on each side).

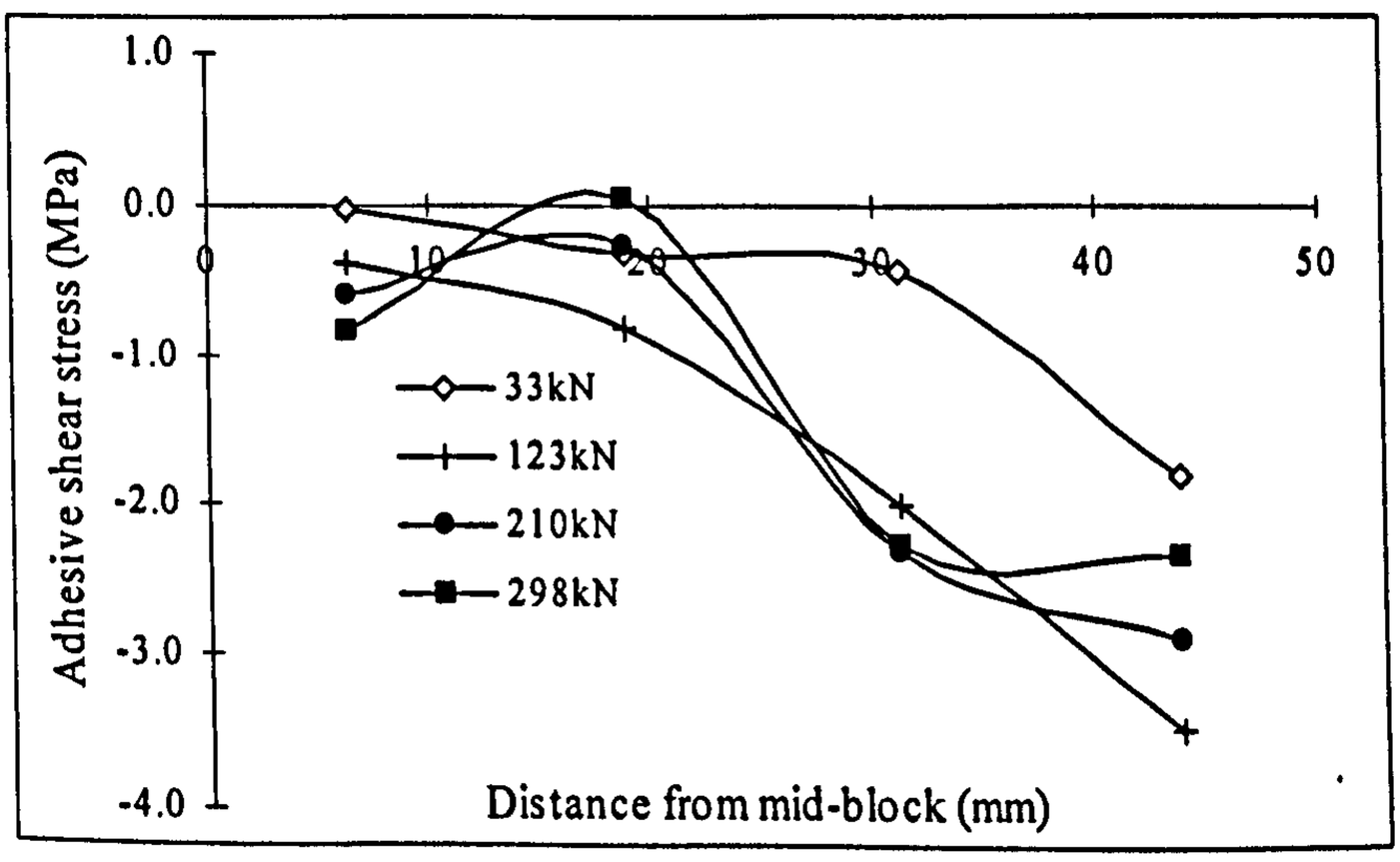

(a) B1 adhesive shear stress distribution

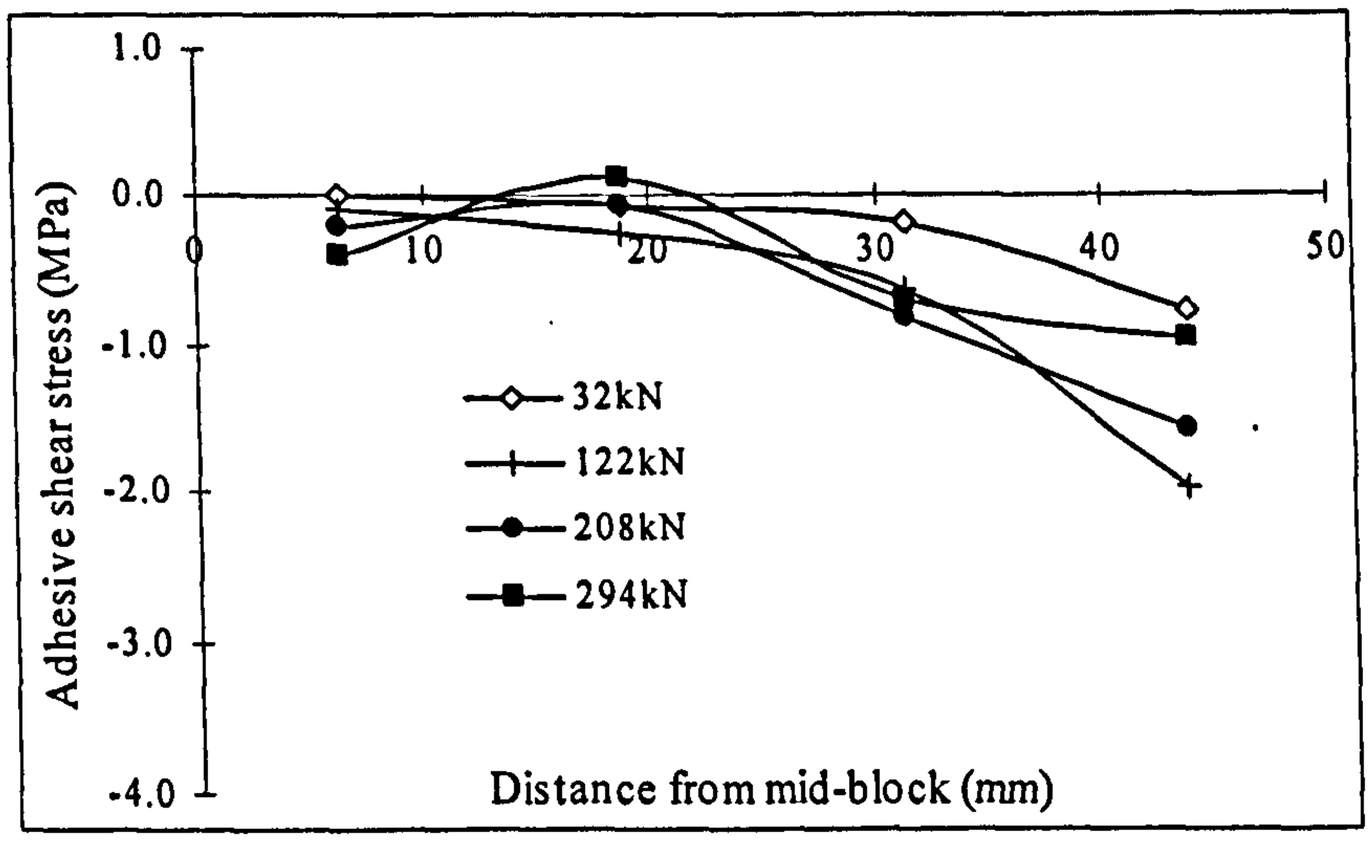

(b) B2 adhesive shear stress distribution

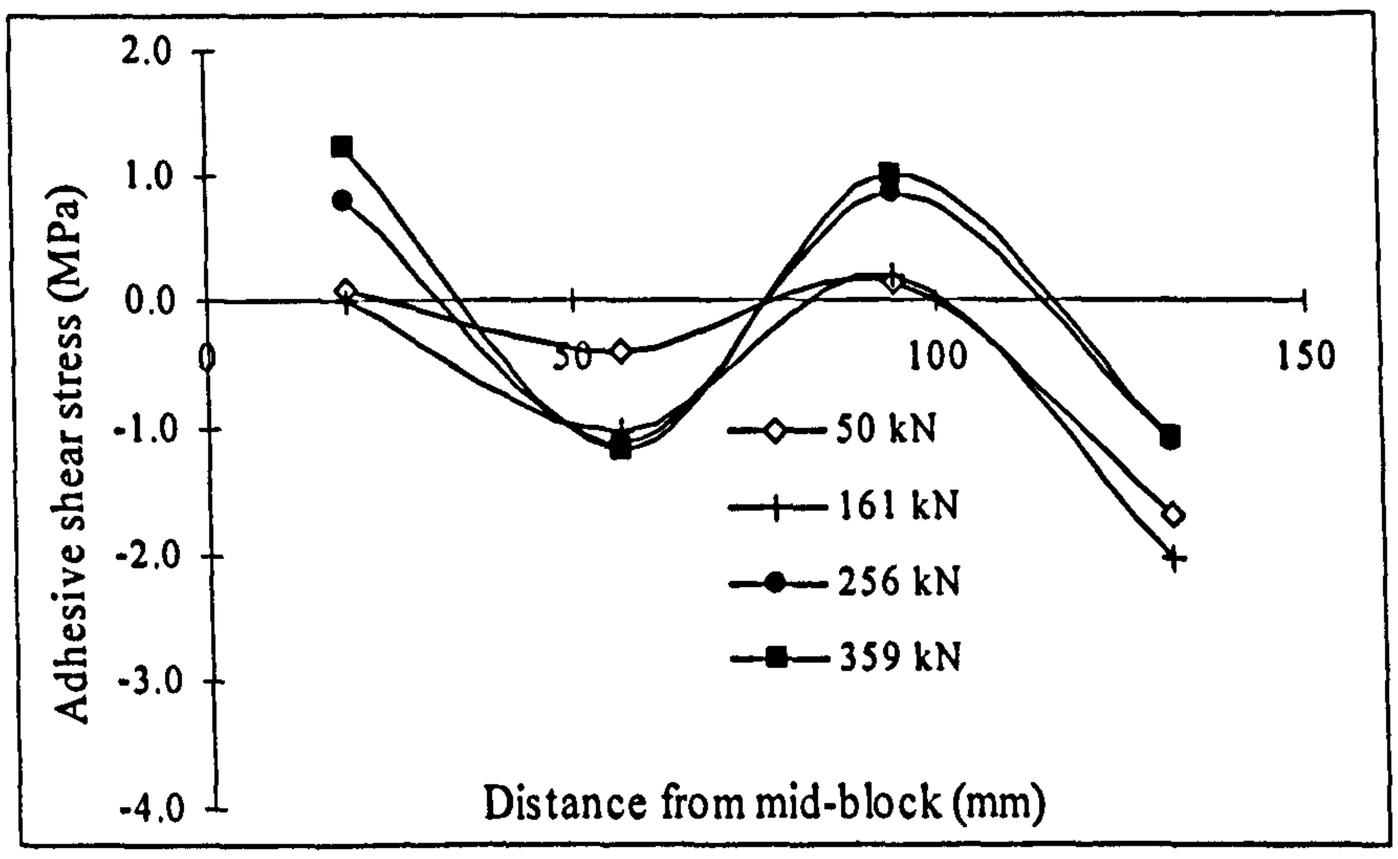

(c) B3 adhesive shear stress distribution

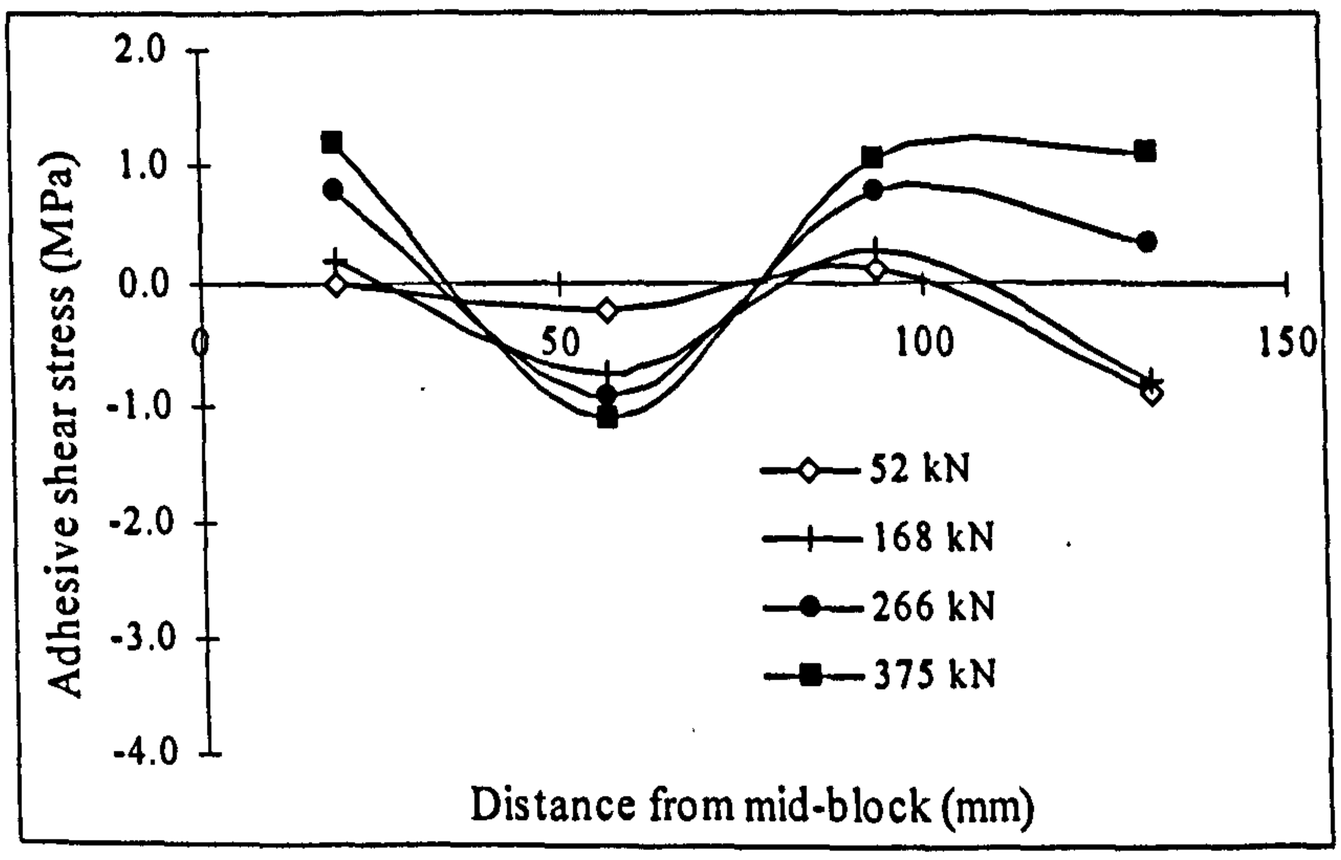

(d) B4 adhesive shear stress distribution

Figure 5-9 FEA results of adhesive shear stress distribution for B1 to B4

Peak shear stress values are also found near the end of the block for the longer blocks B3 and B4 (300 mm). The maximum value ranges from 2.0 N/mm^2 (B4) to 4.0

N/mm^2 (B3). In addition, higher shear stresses near the mid-block were found in B3 and B4 than B1 and B2.

It is stated earlier in Chapter 3 that the shear stress could vary across the thickness of adhesive layer. The similar variations were also found in these FE analyses.

Basically, four layers of brick elements are put through the thickness of each adhesive layer with the distances to the FRP rods are 0.5, 1.5, 2.5 and 3.5 mm respectively. The variations of the adhesive shear stress distribution for B4 are shown in Figure 5-10. As can be seen from Figure 5-10 (a), at lower load stage P = 52 kN, the adhesive shear stresses went up to 1.0 N/mm^2 and there are a little bit variations found between different layers. When the load went up, much bigger different is found between adhesive layers in load stage P = 168 kN. The stress variations along the bond line decreased with the increment of layer's distance to the CFRP rods. When the load went further and specimen is near failure, at P = 375 kN, the variations between layers are even bigger and the shear stress peak at 1.5 N/mm^2.

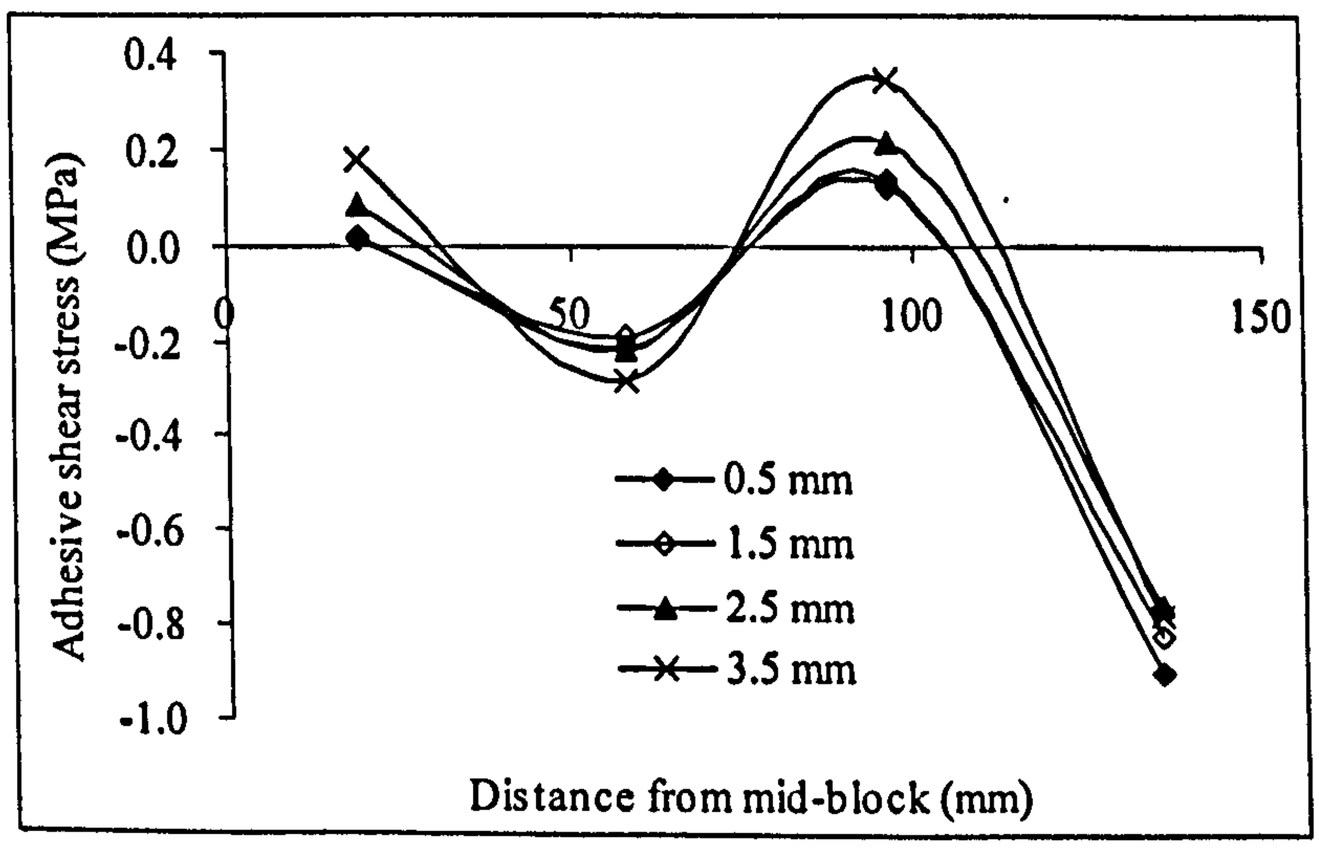

(a) P = 52 kN

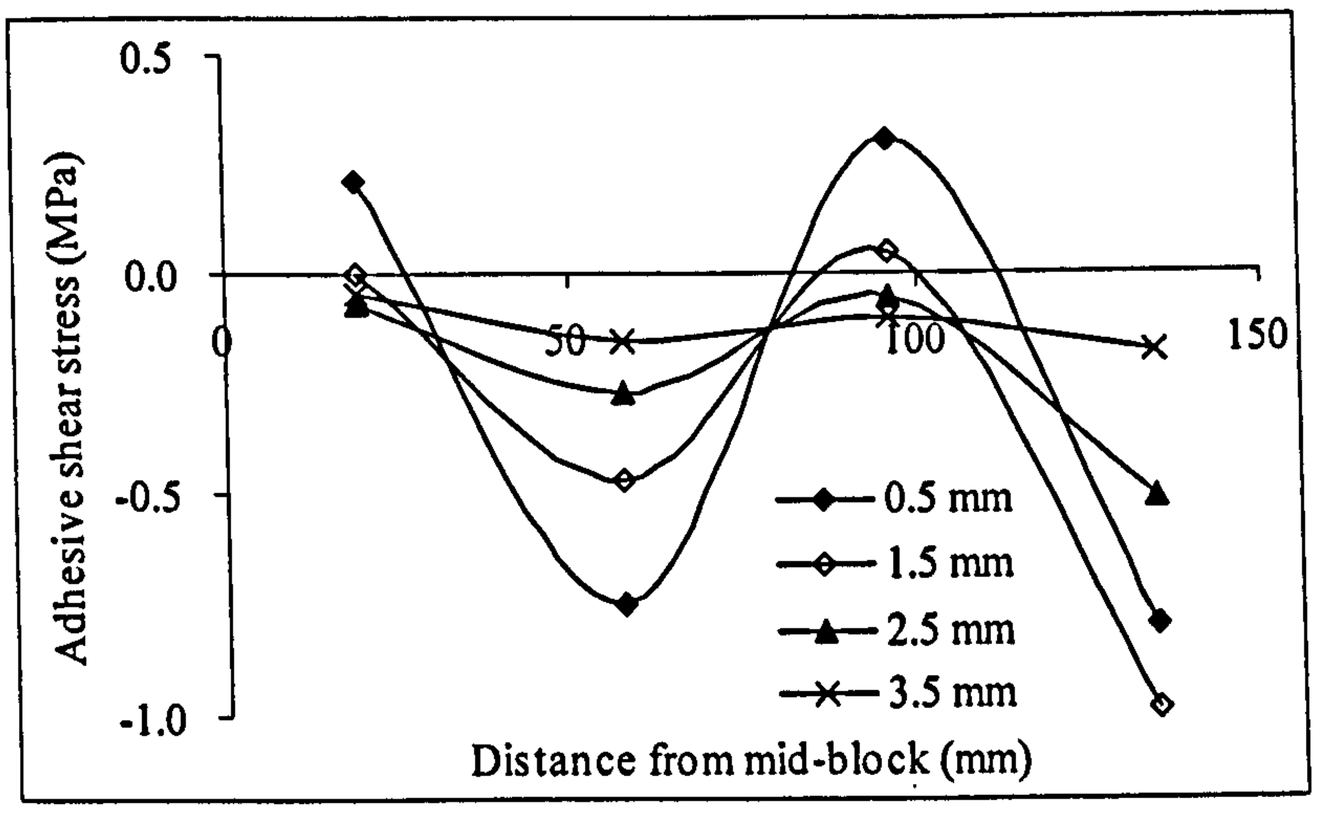

(b) P = 168 kN

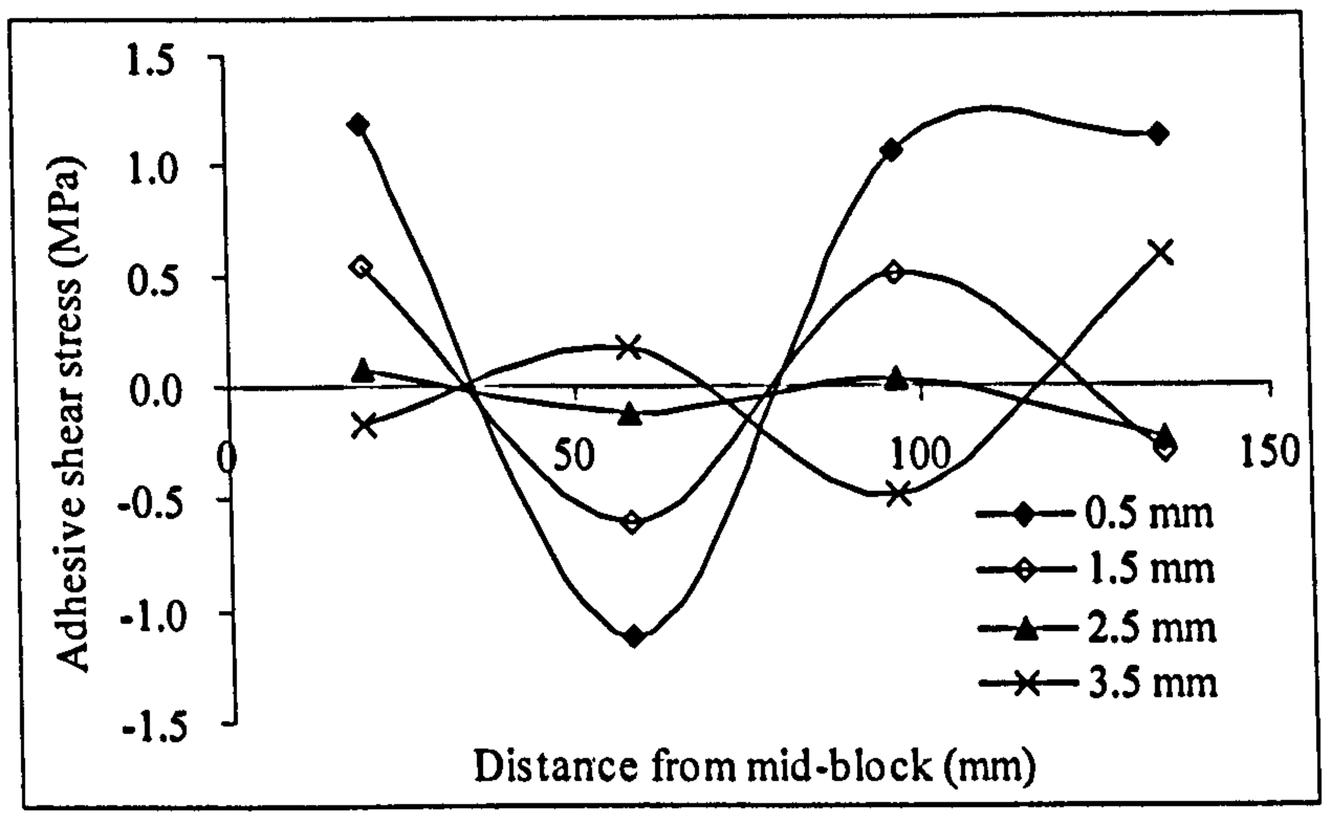

(c) P = 375 kN

Figure 5-10 Variations of adhesive shear stress distributions through thickness for model B4

5.3.4 Load-displacement plots

Due to the shortage of equipment, the displacements of specimen were not recorded in the lab test. For the FE analyses, the horizontal displacements are measured at the point D in Figure 5-3, where is the centre between the middle block and the side block for each specimen. Figure 5-11 shows load-displacement plots from the FE analyses for all four specimens, with the displacements shown on the horizontal axis and the loads shown on the vertical axis. The stiffness of the structure can be illustrated by the

gradient of the load-displacement curves. The bigger gradient reflects the larger stiffness of the specimen.

By comparing the load-carrying capacities of the models, the blocks with longer middle block generally have higher load carrying capacities than those with the shorter middle blocks. The figure also shows that the stiffness of each blocks is approximately the same as other's in the linear range. After first cracking at around P = 50 kN, the stiffness of the models with shorter middle block are approximately 20% higher than those with longer middle blocks. Both the shorter specimens kept nearly linear afterwards until failure at around P = 280 kN.

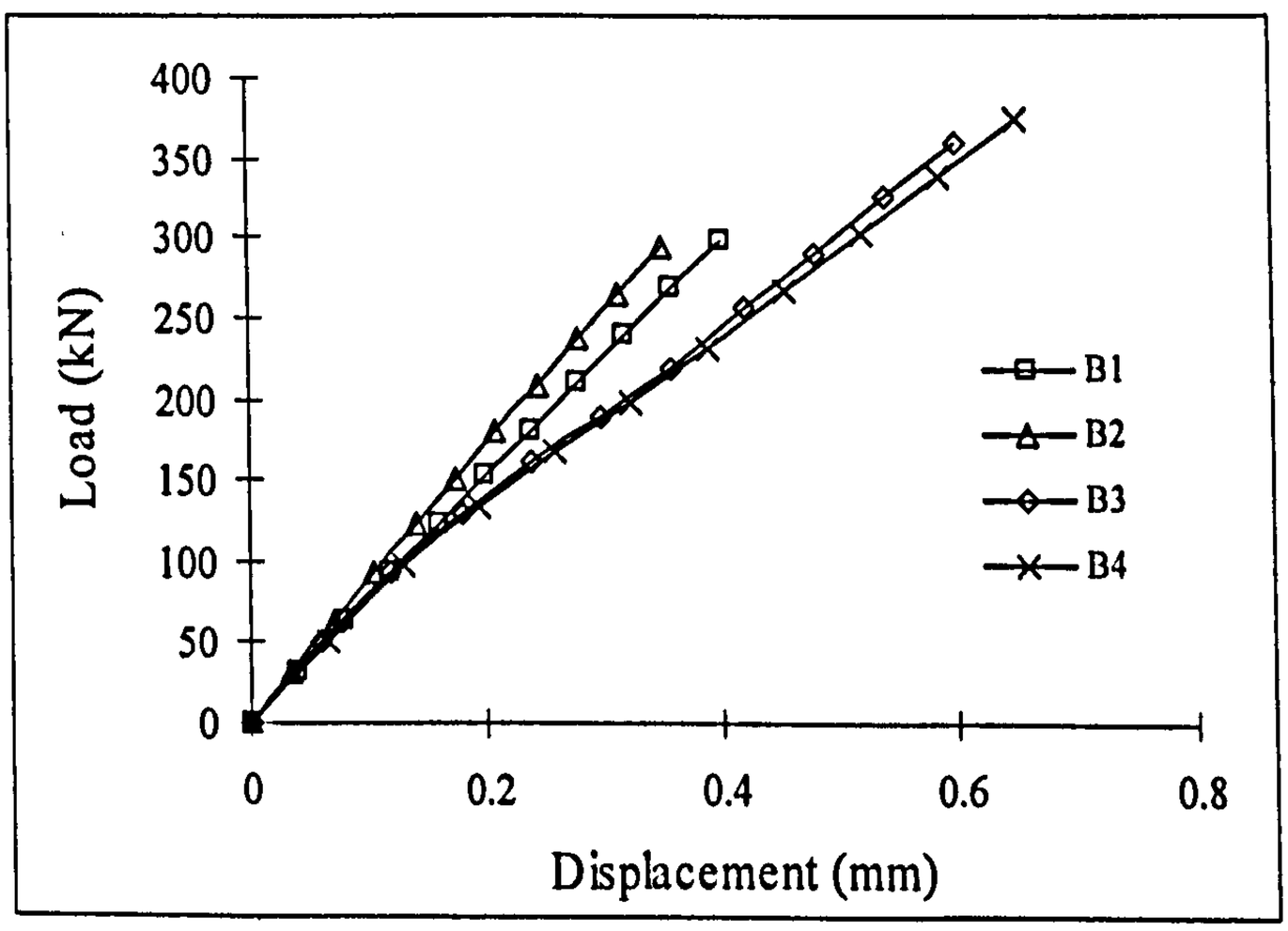

Figure 5-11 Load-displacement curves for B1 to B4

However, there are several factors that may cause the higher stiffness in the finite element models. Micro cracks produced by drying shrinkage and handling are present in the concrete to some degree. These would reduce the stiffness of the actual blocks, while the finite element models do not include micro cracks. Perfect bond between the concrete and reinforcing element is assumed in the FE analyses, but the assumption would not be true for the actual blocks. As slip between two materials occurs, the

bond is reduced. Thus, the overall stiffness of the actual specimens could be lower than what the FE models predict, due to factors that are not incorporated into the models.

5.4 Parametric analysis

In practice, there are materials of various properties available to construct and strengthen the structures. How do these material properties affect the performance and failure behaviour of the strengthened structure? A clear explanation of these influencing factors is essential to an effective application of NSM FRP technique in practice.

In the present study, the original FE model of NSM FRP rods strengthened blocks discussed earlier on this chapter was used to investigate the effect of relevant parameters on the structural performance and failure behaviours of the blocks.

The parameters are including concrete tensile strength f_{tc}, NSM rod Young's modulus E_f, adhesive Young's modulus E_a, tensile strength f_{ta} and the ratio of ultimate strain to crack strain $\varepsilon_u / \varepsilon_{cr}$, as shown in Table 5-2.

Table 5-2 Material properties for the Finite Element Analysis

Materials	Concrete	Adhesive	Steel	CFRP
Young's modulus (kN/mm2)	28	***2-20***	200	***15-150***
Poisson's ratio	0.2	0.35	0.3	0.3
Yield strength (N/mm2)	--	--	500	--
Compressive strength (N/mm2)	40	50	--	--
Tensile strength (N/mm2)	***3-6***	***4-16***	--	--
$\varepsilon_u / \varepsilon_{cr}$	5	***2-10***	--	--

According to the values identified by test data and the FEA results presented earlier in this chapter, the values such as f_{tc} = 3 N/mm^2, E_f = 150 kN/mm^2, E_a = 8 kN/mm^2, f_{ta} = 8 N/mm^2 and $\varepsilon_u / \varepsilon_{cr}$ = 5 were chosen as reference values for the material properties of strengthened structures. As shown in Table 5-2, the concrete tensile strength f_{tc} was varied from 3 to 6 N/mm^2 to simulate the concrete of different grade. The strengthening rod tensile strength E_f was varied from 15 to 150 kN/mm^2 to simulate the NSM rods with different moduli, such as glass FRP, carbon FRP and steel rods. The adhesive material properties E_a, t_a and $\varepsilon_u / \varepsilon_{cr}$ were varied from 2 to 20 kN/mm^2, 4 to 16 N/mm^2 and 2 to 5 respectively to simulate different types of adhesive.

Table 5-3 Main parameters investigated in FE analyses

<table>
<tr><th rowspan="2">Name of models</th><th rowspan="2">Material parameters</th><th rowspan="2">Concrete tensile strength f_{tc} (N/mm^2)</th><th rowspan="2">FRP Young's modulus E_f (kN/mm^2)</th><th colspan="3">Adhesive mechanical parameters</th></tr>
<tr><th>Young's modulus E_a (kN/mm^2)</th><th>Tensile strength f_{ta} (N/mm^2)</th><th>$\frac{\varepsilon_u}{\varepsilon_{cr}}$</th></tr>
<tr><td>CT3</td><td rowspan="2">f_{tc}</td><td>3</td><td rowspan="2">150</td><td rowspan="5">8</td><td rowspan="10">8</td><td rowspan="10">5</td></tr>
<tr><td>CT6</td><td>6</td></tr>
<tr><td>FE4</td><td rowspan="2">E_f</td><td rowspan="11">3</td><td>15</td></tr>
<tr><td>FE5</td><td>150</td></tr>
<tr><td>AE2</td><td rowspan="4">E_a</td><td rowspan="11">150</td><td>2</td></tr>
<tr><td>AE8</td><td>8</td></tr>
<tr><td>AE20</td><td>20</td></tr>
<tr><td>AT4</td><td rowspan="4">f_{ta}</td><td rowspan="5">8</td><td>4</td></tr>
<tr><td>AT8</td><td>8</td></tr>
<tr><td>AT16</td><td>16</td></tr>
<tr><td>AS2</td><td rowspan="3">$\frac{\varepsilon_u}{\varepsilon_{cr}}$</td><td rowspan="3">8</td><td>2</td></tr>
<tr><td>AS5</td><td>5</td></tr>
<tr><td>AS10</td><td>10</td></tr>
</table>

As shown in Table 5-3, the models are named according to the varying material parameters. Firstly, CT3 means model with weaker concrete tensile strength f_{tc} = 3 N/mm^2 while CT6 means model with stronger f_{tc} = 6 N/mm^2. Secondly, FE4 means model with lower strengthening rod's Young's modulus E_f = 1.5×10^4 N/mm2, while FE5 means model with higher E_f = 1.5×10^5 N/mm^2. Thirdly, AE2 means model with lower adhesive Young's modulus as E_a = 2 kN/mm^2; AE8 means model with moderate E_a = 8 kN/mm^2. while AE20 means model with higher E_a = 20 kN/mm^2. Fourthly, AT4 means model with weaker adhesive tensile strength f_{ta} = 4 N/mm^2, AT8 means model with moderate f_{ta} = 8 N/mm^2 while AT16 means model with stronger f_{ta} = 16 N/mm^2. Finally, AS4 means model with smaller ratio of ultimate strain to crack strain $\varepsilon_u/\varepsilon_{cr}$ = 2, AS5 means model with moderate $\varepsilon_u/\varepsilon_{cr}$ = 5 while AS10 means model with largest $\varepsilon_u/\varepsilon_{cr}$ = 10.

5.4.1 Effect of concrete tensile strength f_{tc}

Figure 5-12 demonstrates the effect of concrete tensile strength f_{tc} on the load-displacement behaviour of the strengthened blocks.

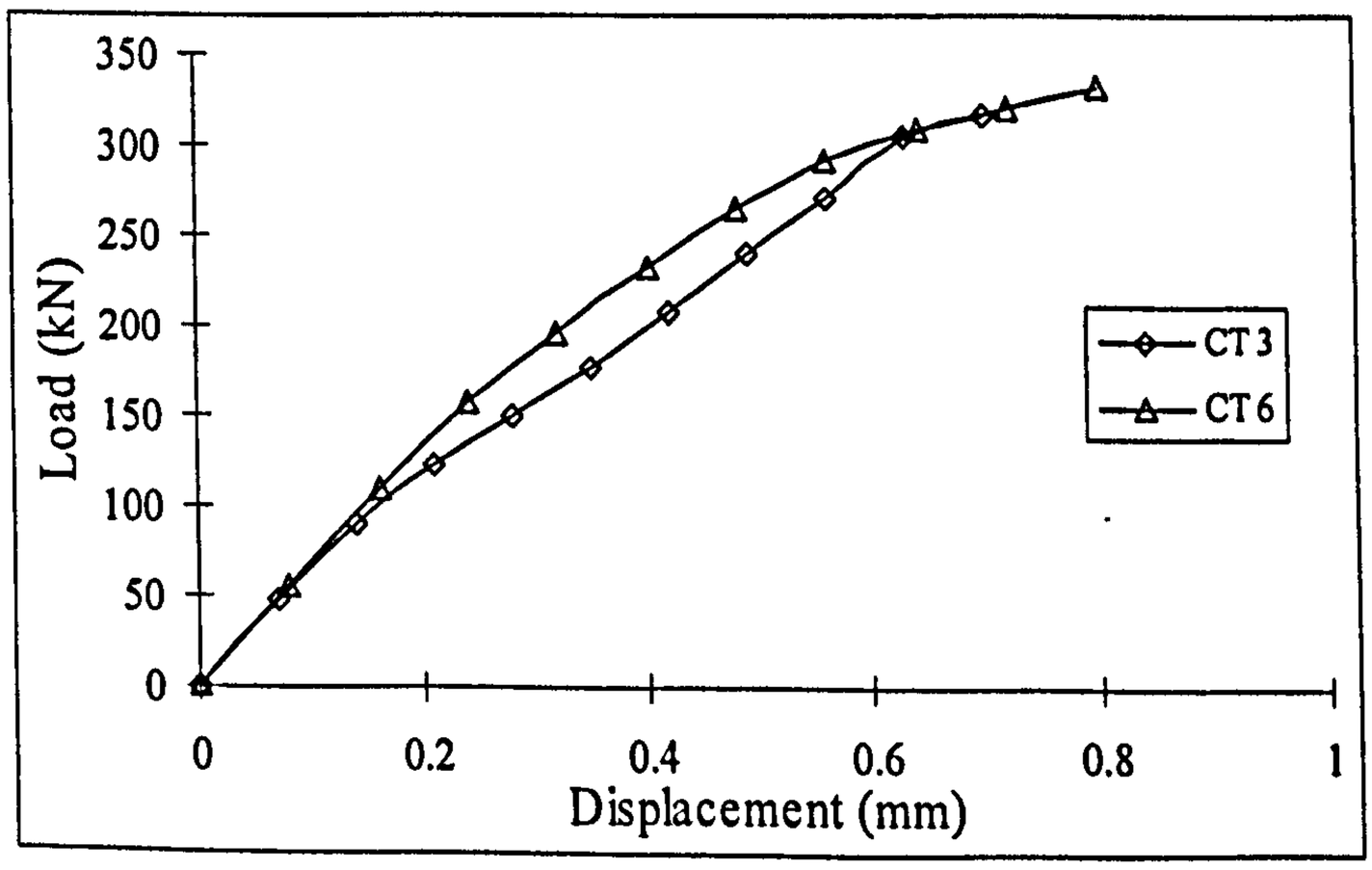

Figure 5-12 Load-displacement curves for various concrete strengths

It can be seen that the stiffness of both blocks are the similar in the linear stage. After concrete cracking, around $P = 70$ kN, the stiffness of the block with weaker concrete tensile strength $f_{tc} = 3$ N/mm^2 (CT3) became 20% smaller than the one with $f_{tc} = 6$ N/mm^2 (CT6). However, both curves joined at $P = 310$ kN after yield of steel bars.

Then the nonlinear behaviours of both models' steel strain corresponding to different loading stages are discussed. As can be seen from Figure 5-13 (a), the steel strains of both models are nearly the same at the position outside of the middle concrete block under the same load. However, there is big difference between the two curves at the position inside of the middle concrete block (Figure 5-13 (b)). Under the same load, the steel strain decreased with the increment of concrete tensile strength under the same load because concrete with higher tensile strength can carry a larger share of the tensile load so that steel rebar could take smaller loads.

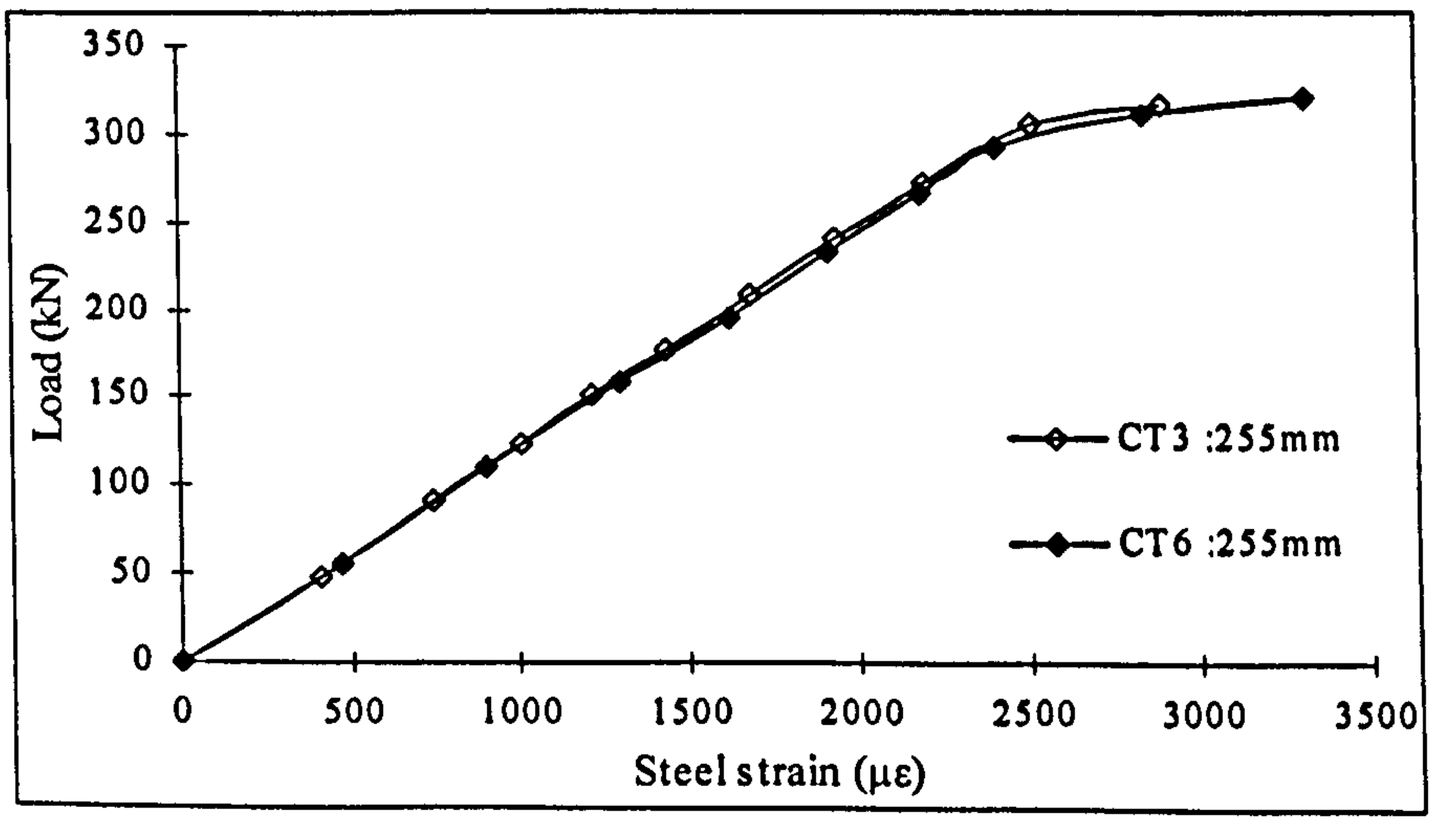

(a) Outside of concrete block near loading end

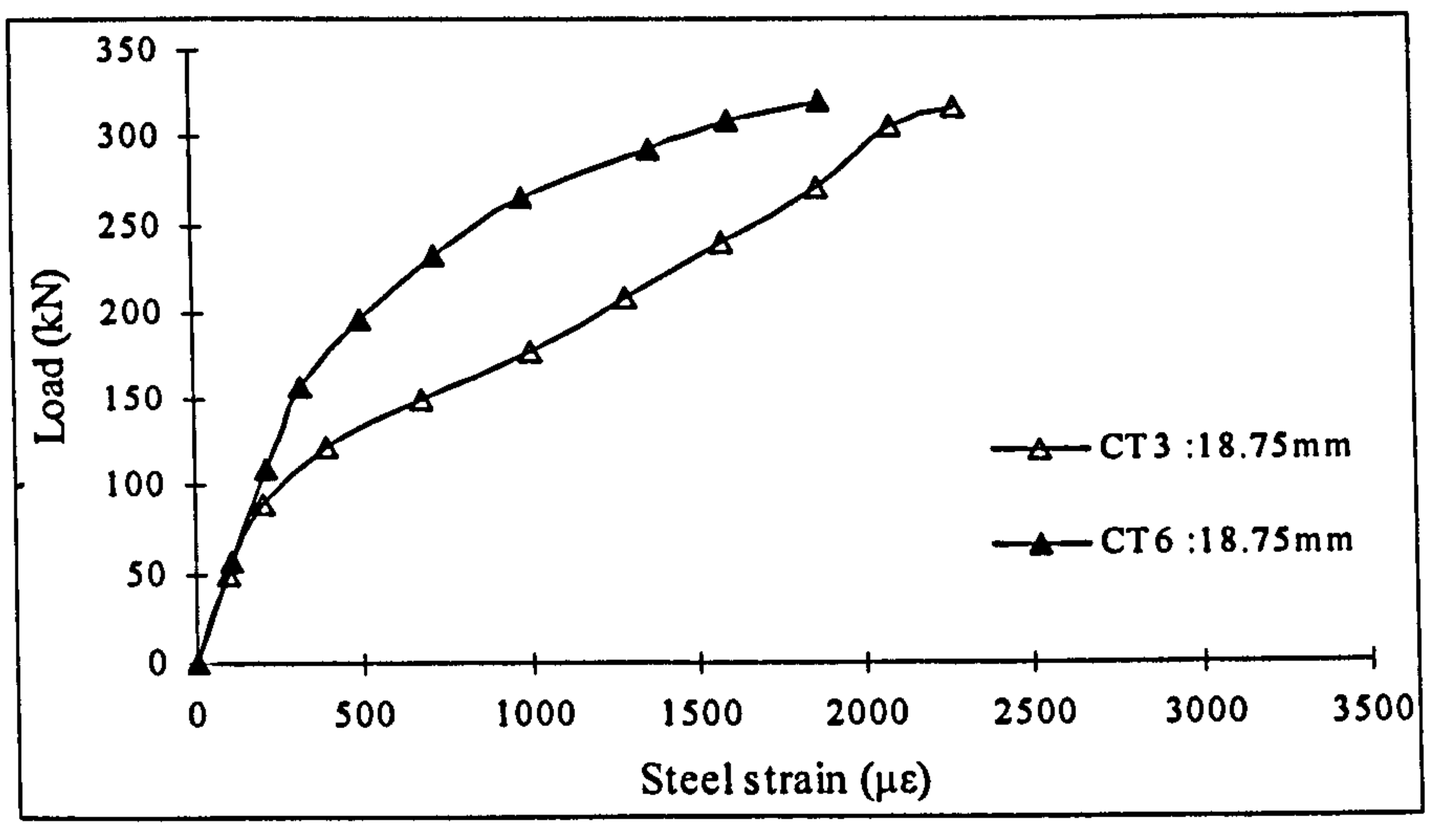

(b) Inside the concrete block near mid-block

Figure 5-13 Load-steel strain curves for various concrete strengths

Figure 5-14 shows the strain distributions of steel rebar for the two models. It can be seen clearly that under the lower load P = 100 kN, when the concrete just began to crack, both curves are relatively close to each other. With the increment of tensile load, the difference between both curves increased. Under the same load, the strains in model CT3 is up to 700 με bigger than the strains in CT6. The similar trends of strain distributions are found for the FRP bars in Figure 5-15 and Figure 5-16.

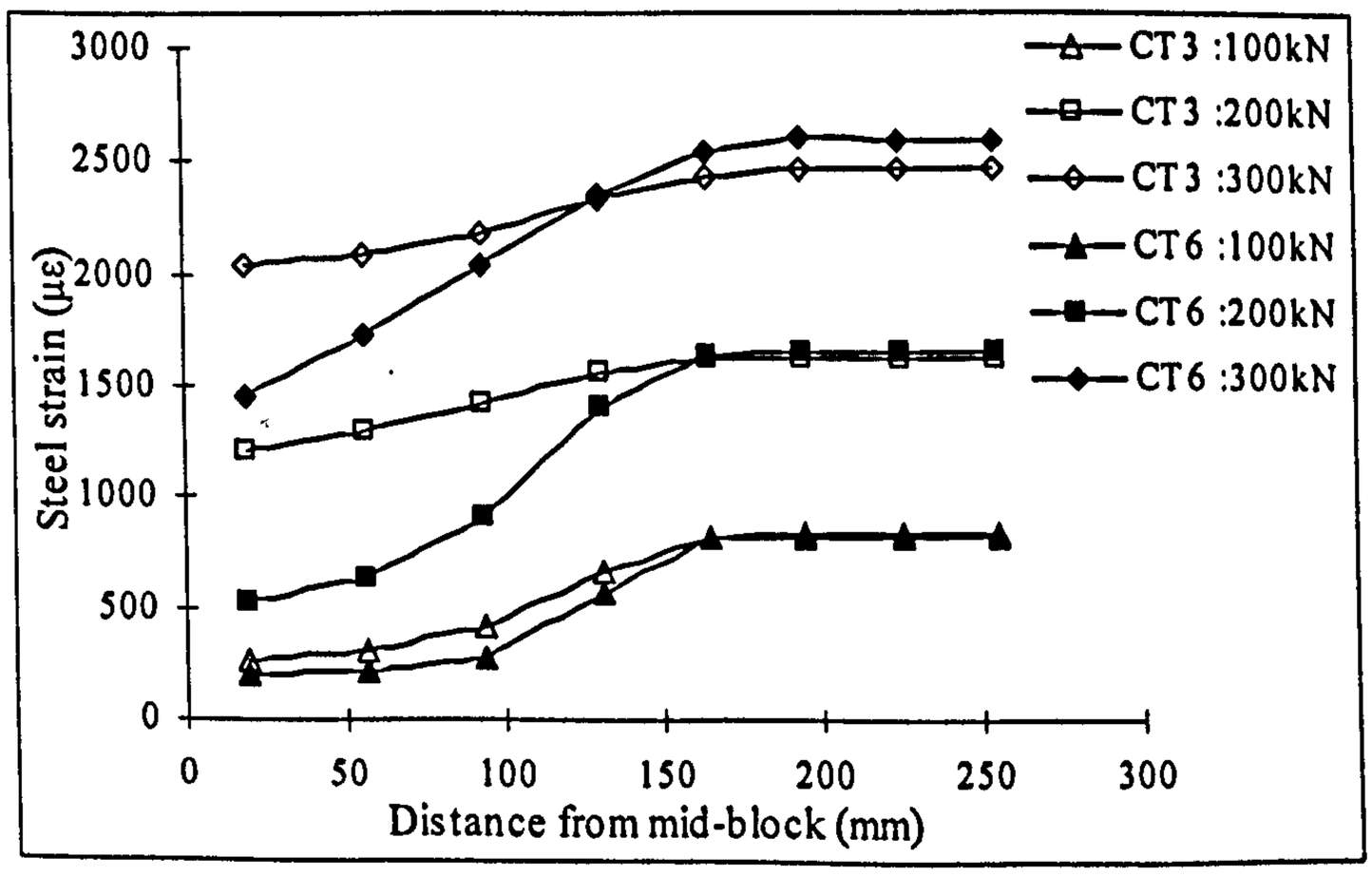

Figure 5-14 Steel strain distributions for various concrete strengths

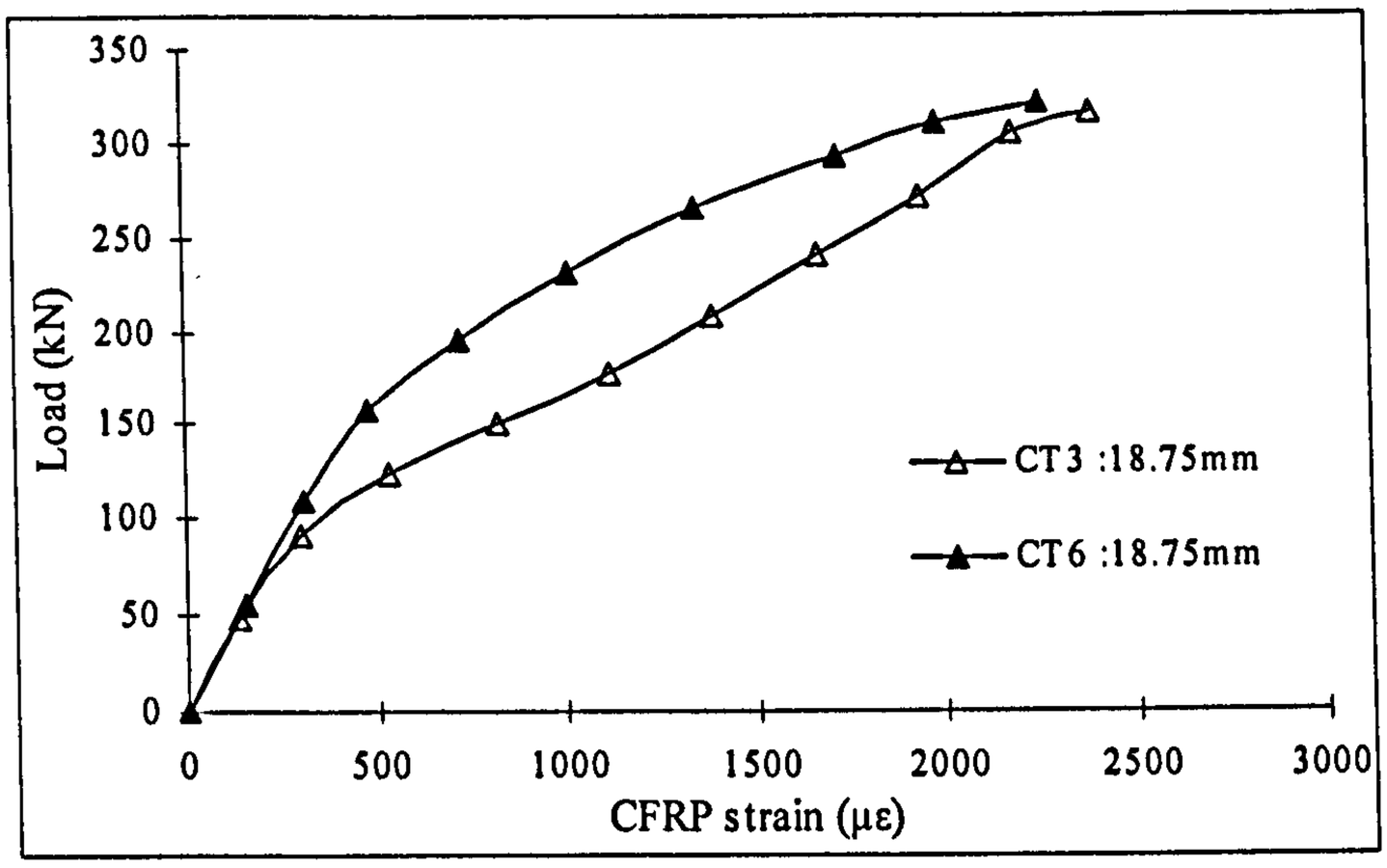

(a) Inside the concrete block near mid-block

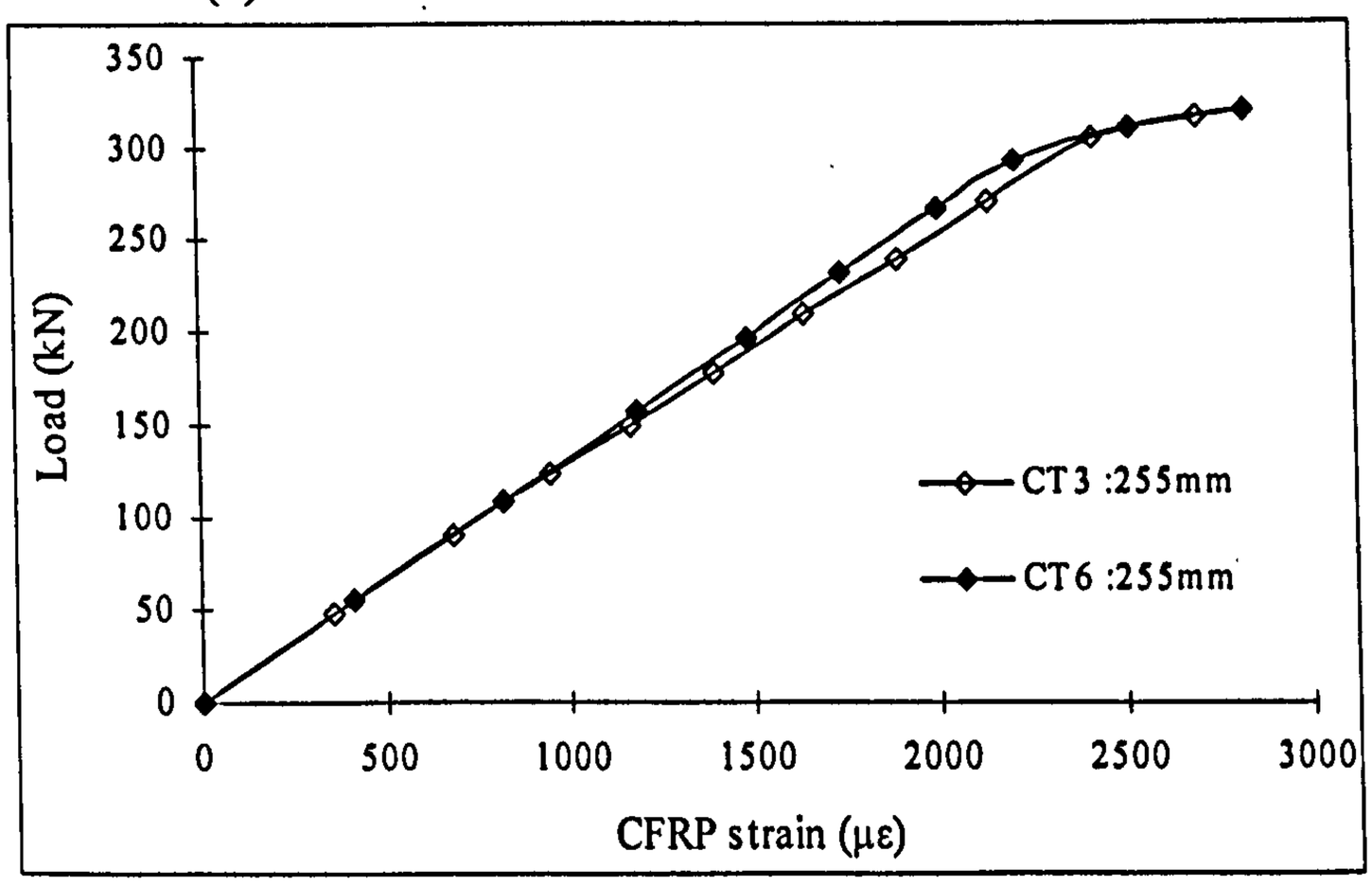

(b) Outside of concrete block near loading end

Figure 5-15 Load-CFRP strain curves for various concrete strengths

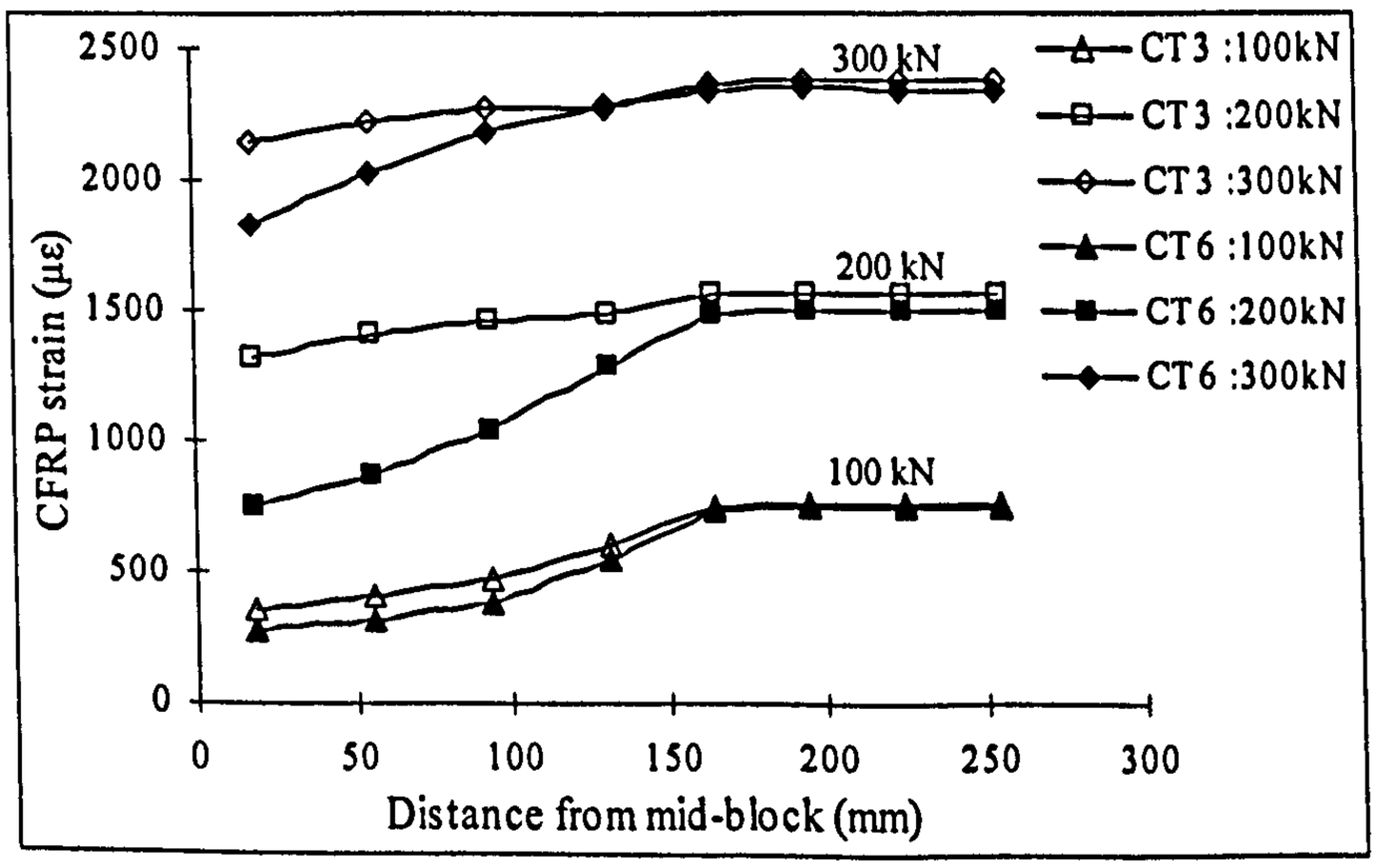

Figure 5-16 FRP strain distributions for various concrete strengths

The adhesive shear stress distributions of both models are shown in Figure 5-17. The curves for two models are very close to each other and fluctuate between -4.2 to 0.3 N/mm^2 under the load P = 100 kN. However, at P = 200 kN when cracks occurred on both concrete and adhesive materials, the adhesive shear stresses in model CT6 became higher than those in model CT3 and the difference between two models range from 1 to 3 N/mm^2. The differences became even bigger under higher load P = 300 kN. The reason for these differences may due to that the stiffer concrete body because more stress transfer between concrete and inserted FRP bars.

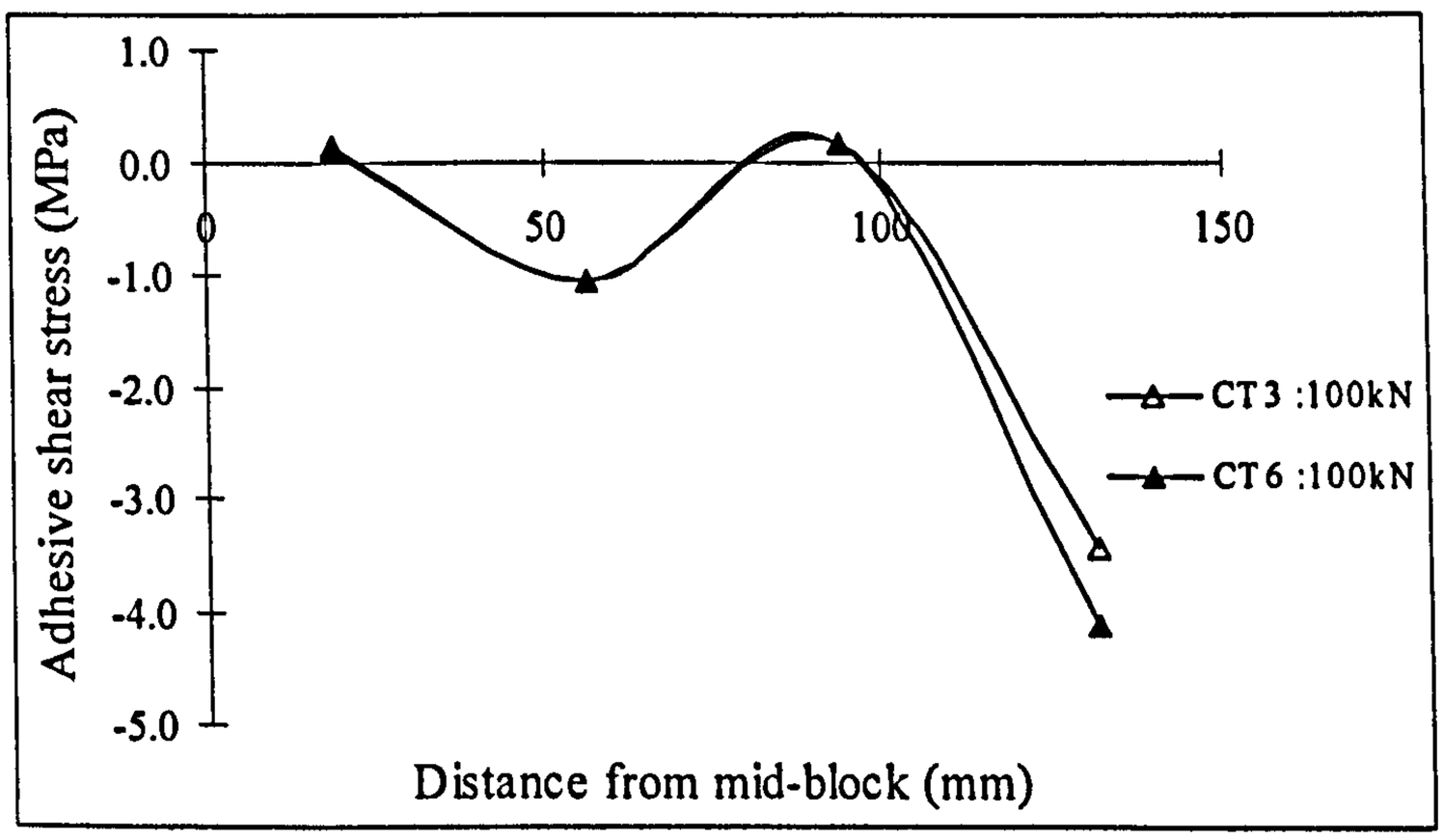

(a) P = 100 kN

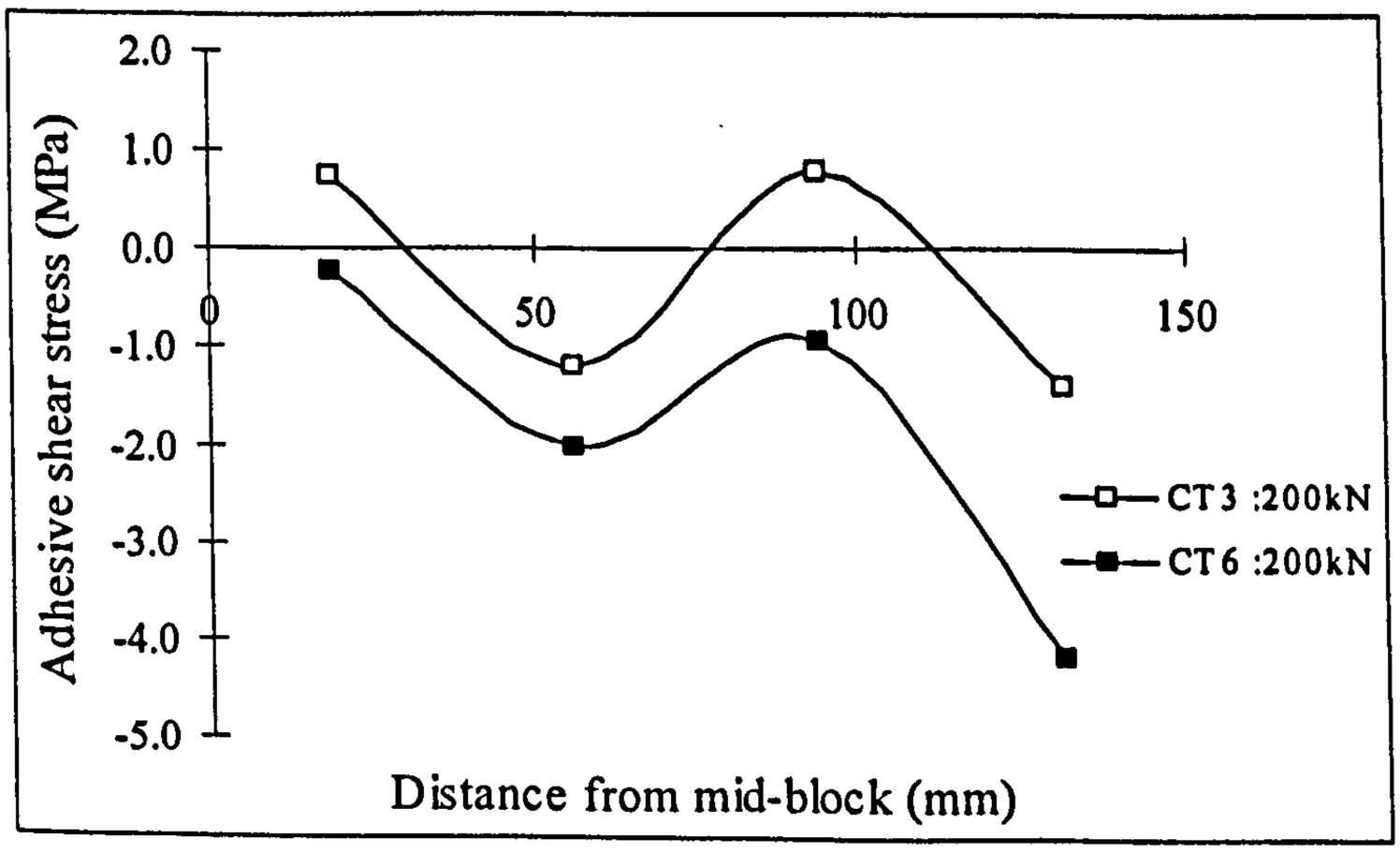

(b) P = 200 kN

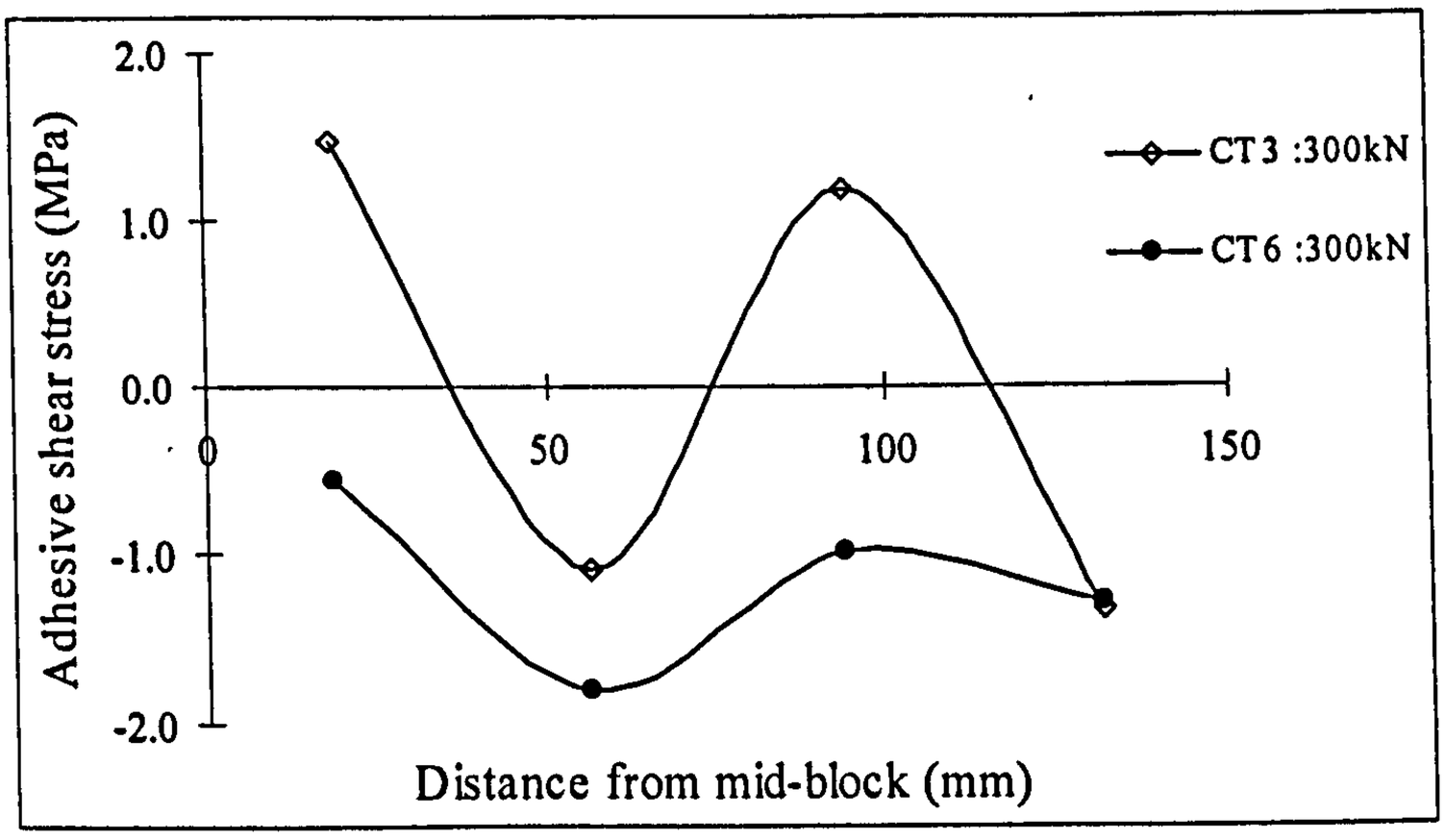

(c) $P = 300$ kN

Figure 5-17 Adhesive shear stress distributions for various concrete strengths

5.4.2 Effect of Young's modulus E_f of strengthening FRP bars

Figure 5-18 demonstrates the effect of Young's modulus of FRP bars (E_f) on the load-displacement behaviour of the NSM strengthened block. It can be seen that the stiffness of block with $E_f = 150$ kN/mm^2 (FE5) keeps constantly bigger than the model with $E_f = 15$ kN/mm^2 (FE4). The model FE5 also reaches ultimate load 70 kN higher than the model FE4 does which due to the strengthening FRP rod with higher Young's modulus can undertake more load.

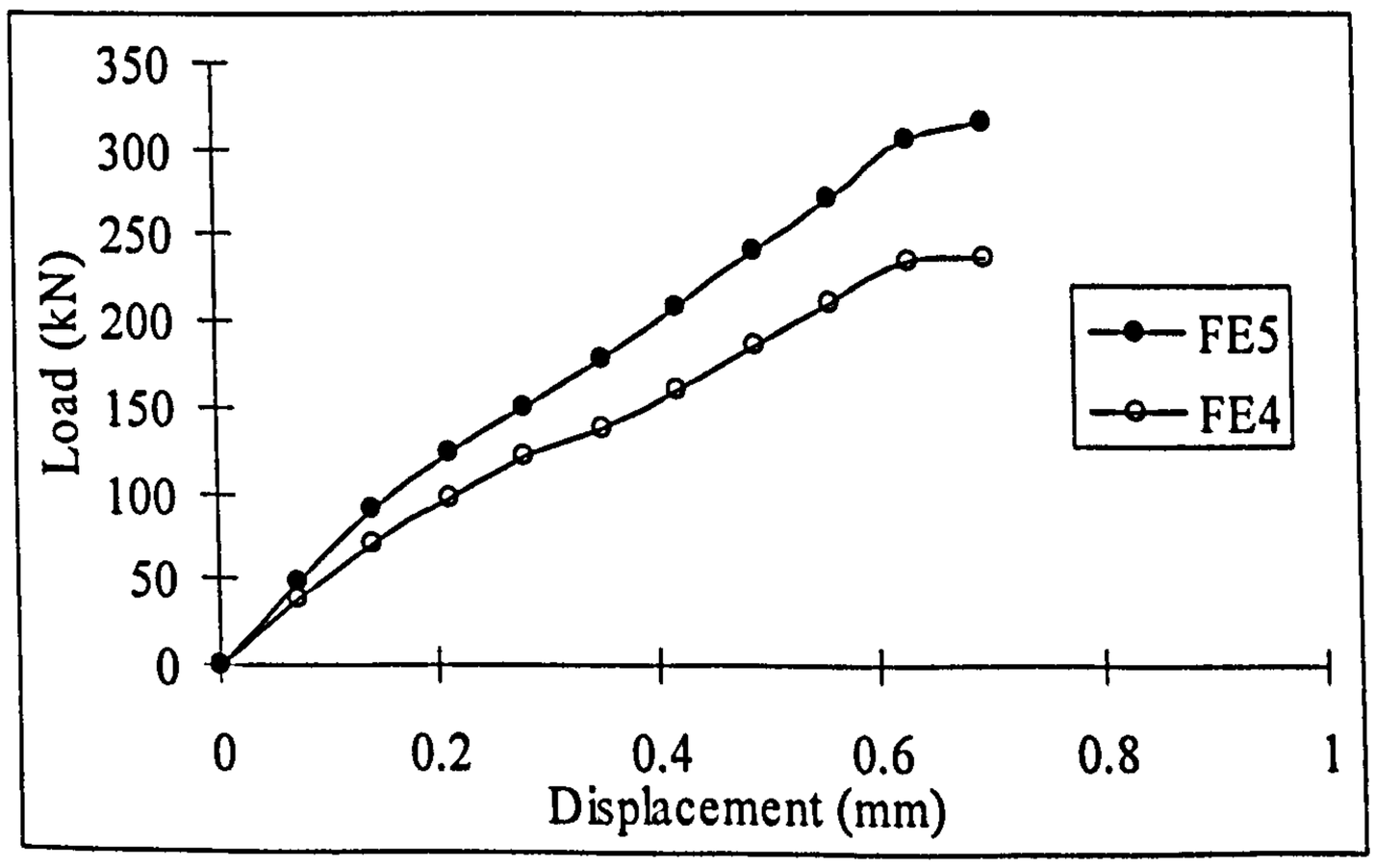

Figure 5-18 Load-displacement curves for various FRP Young's moduli

Figure 5-19 exhibit the nonlinear behaviour of steel strain developments under load for different locations. It can be seen that there is a big difference between the strain curves of the two models. At the position inside of middle concrete block, both the curves remain similar at the linear stage. However, after the cracking of concrete, bigger strain was found in the model FE4 rather than FE5 under the same load (Figure 5-19 (a)). At the position outside of middle concrete block, both the load-strain curve keep linear before material's yielding while the strain under same load increases with the decrement of FRP Young's modulus Figure 5-19 (b)).

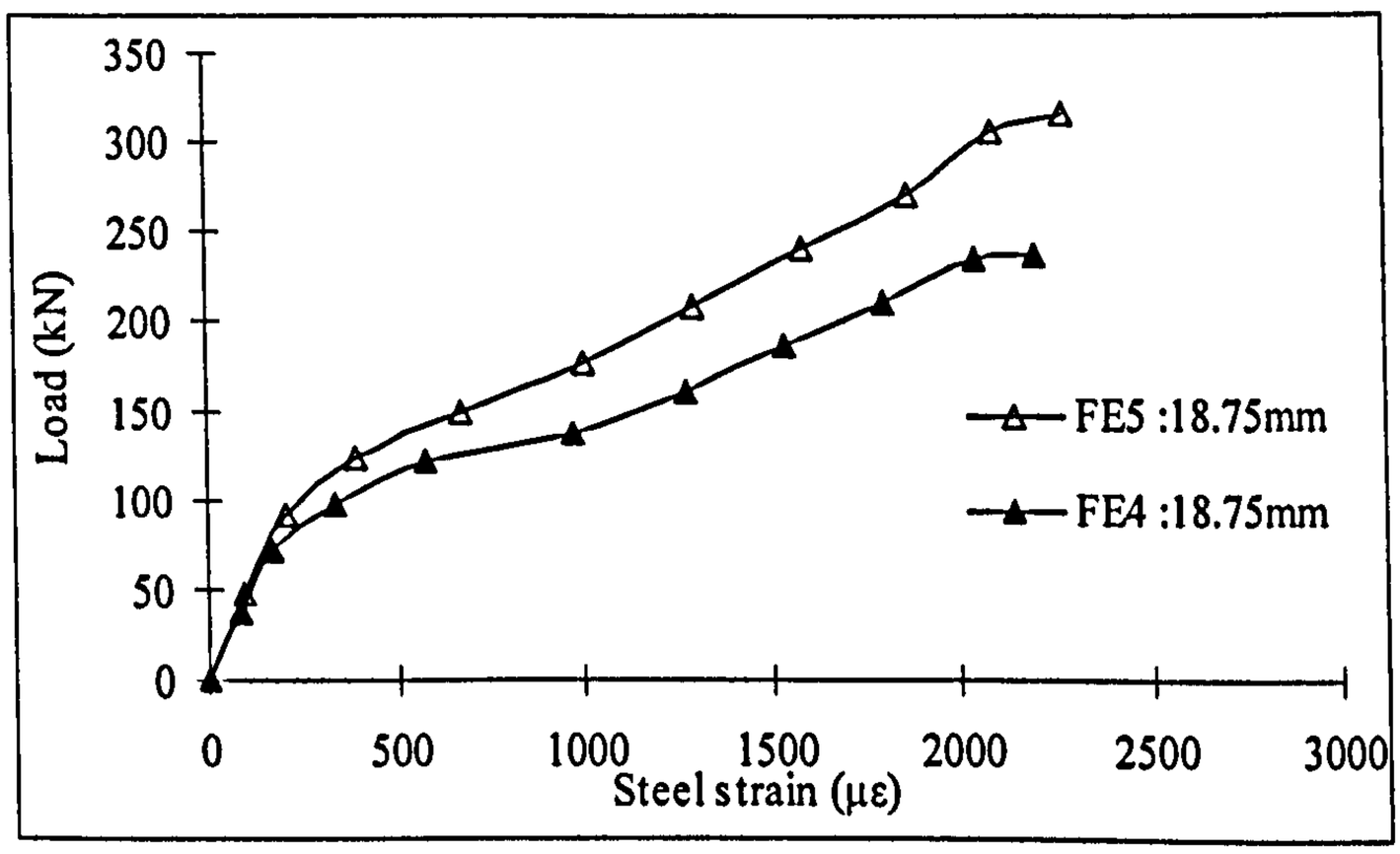

(a) Inside the concrete block near mid-block

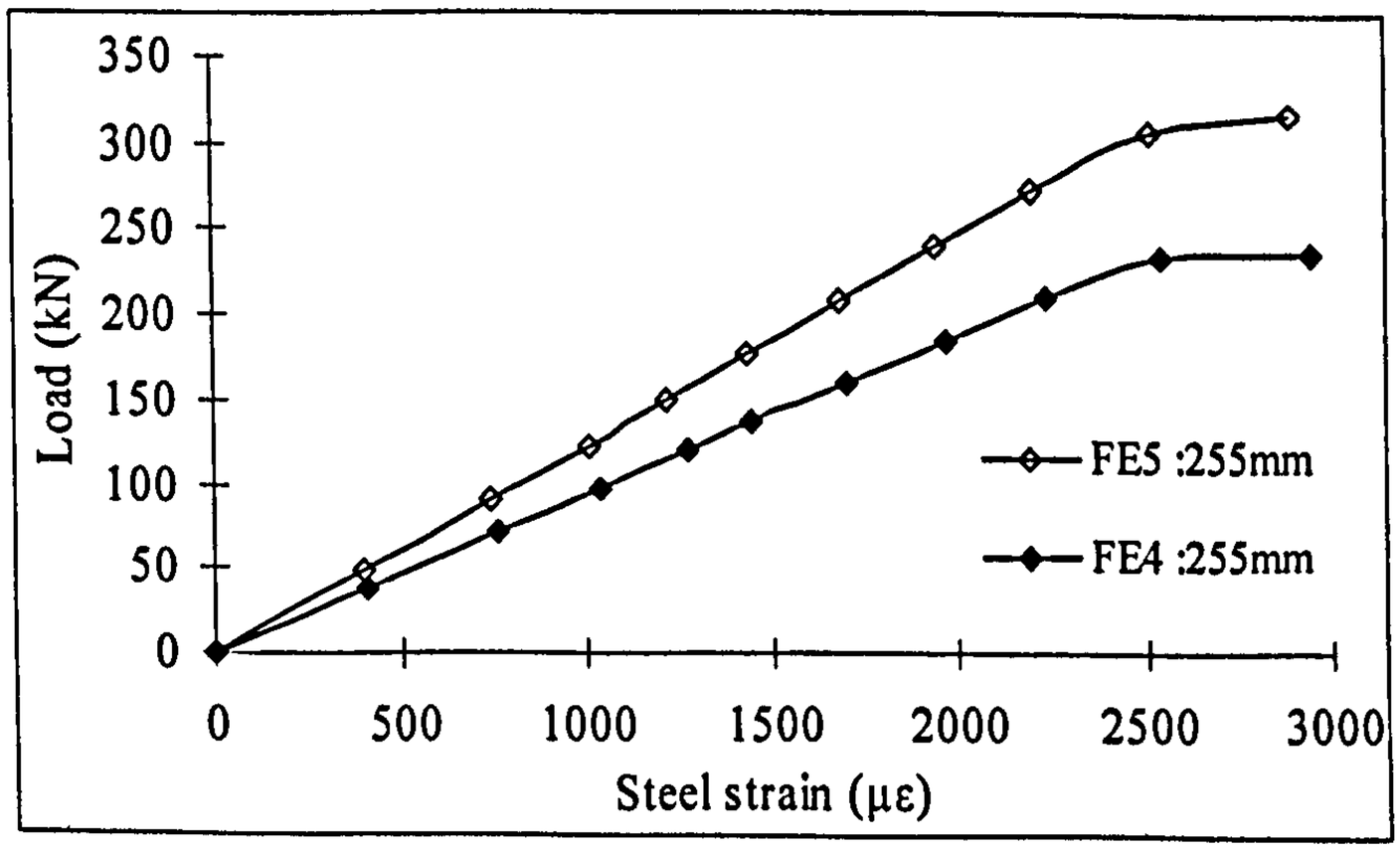

(b) Outside of concrete block near loading end

Figure 5-19 Load-steel strain curves for various FRP Young's moduli

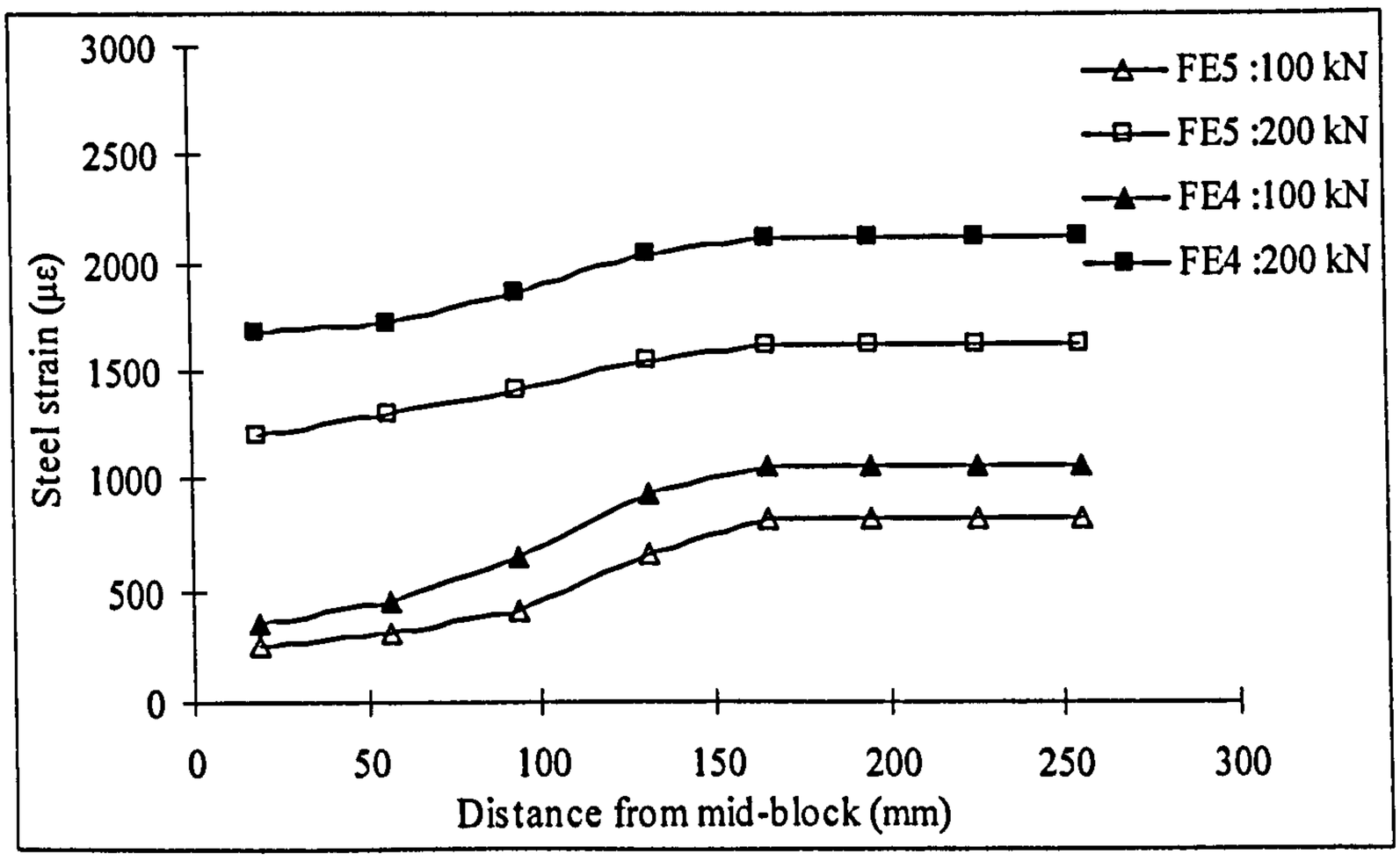

Figure 5-20 Steel strain distributions for various FRP Young's moduli

Figure 5-20 show the steel strain distributions for the two models. It can be seen clearly that both the steel strain distributions have the similar trends but the model with higher FRP Young's modulus (FE5) constantly shows higher strain than the model FE4. The differences are up to 500 με.

Similar trends are found in Figure 5-21 and Figure 5-22 for FRP strains. In particular, the FRP strains in model FE5 increased suddenly up to 1000 με at the position outside of the concrete block due to the loss of concrete constraint.

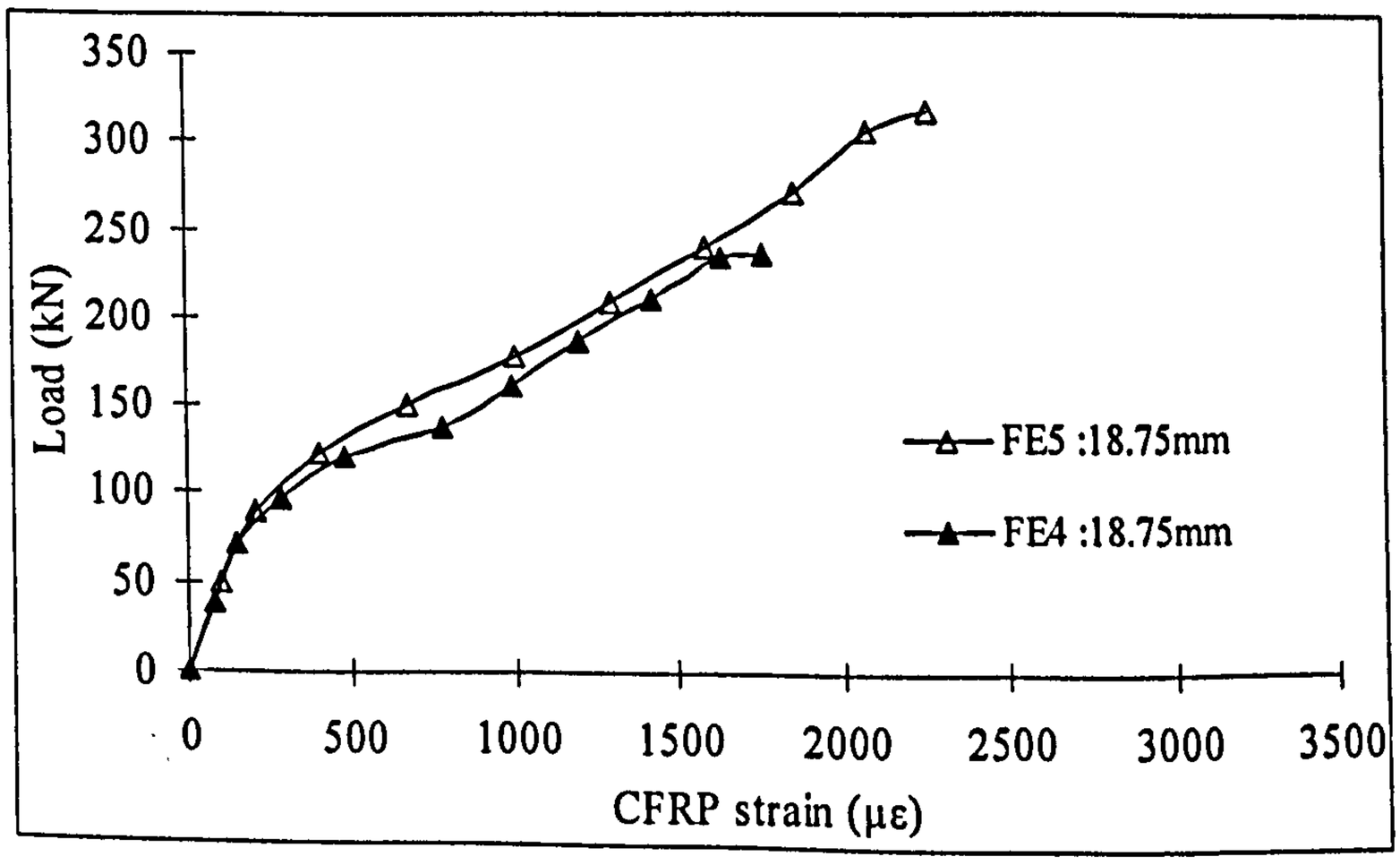

(a) Inside the concrete block near mid-block

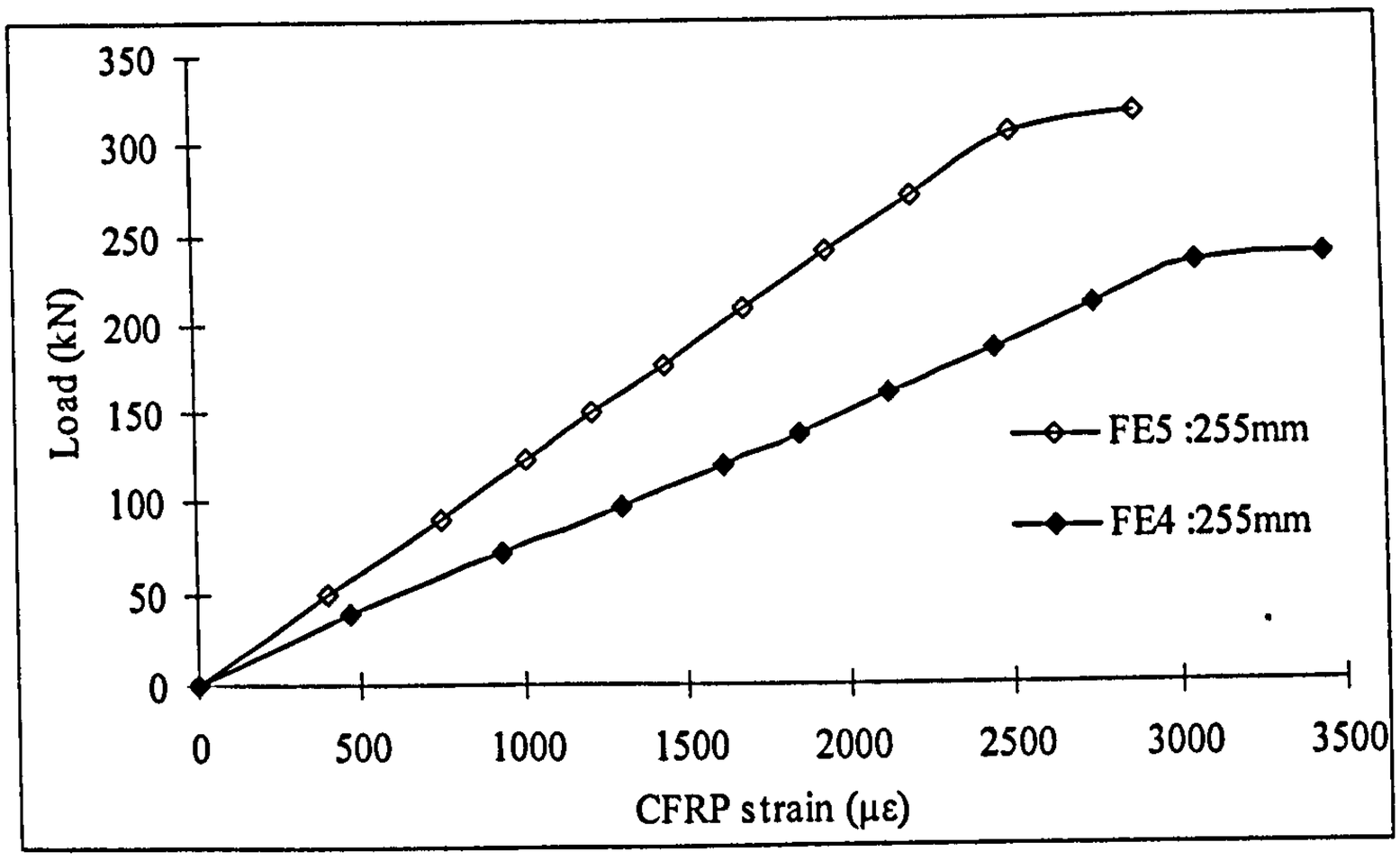

(b) Outside of concrete block near loading end

Figure 5-21 load-FRP strain curves for various FRP Young's moduli

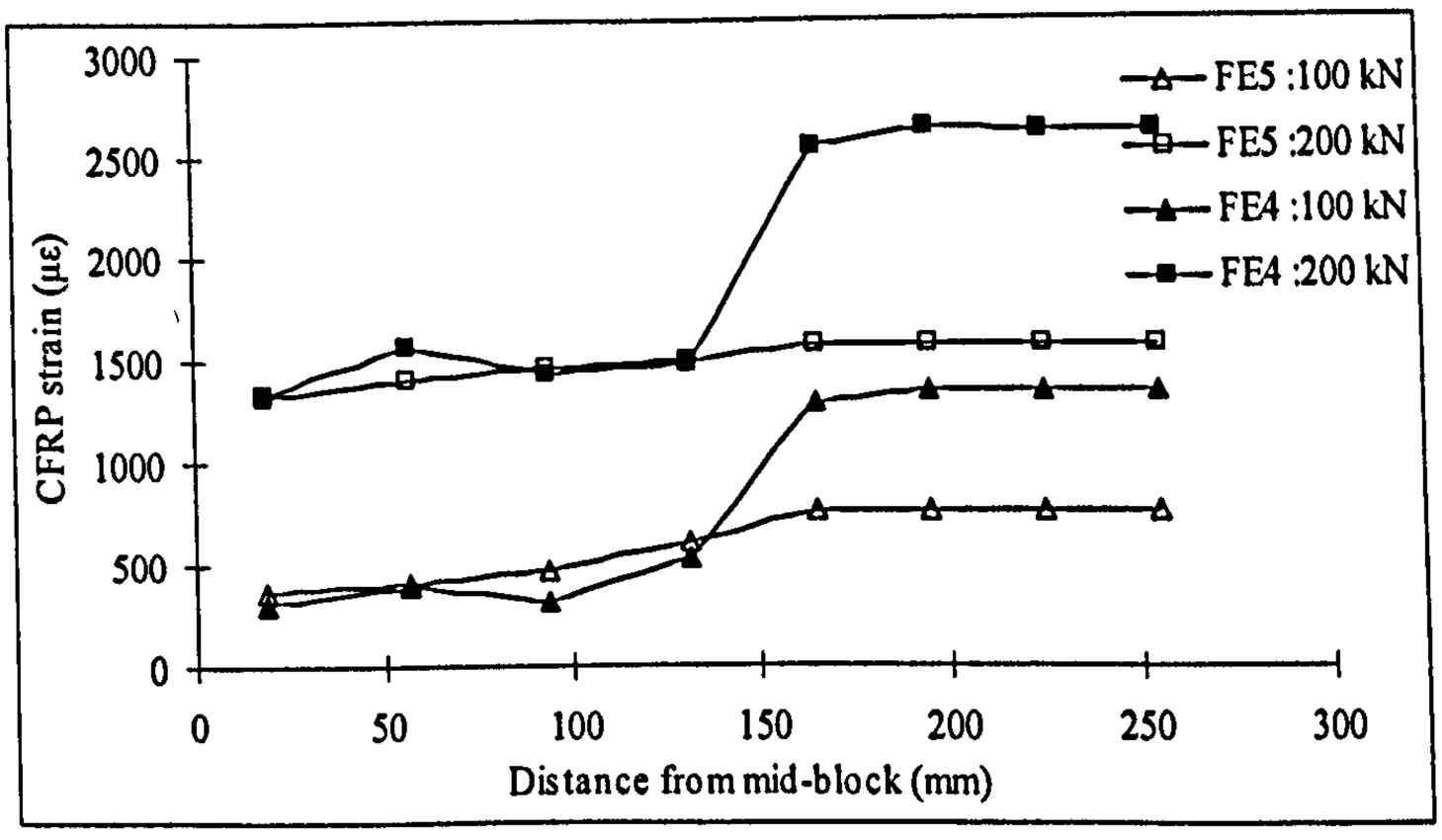

Figure 5-22 FRP strain distributions for various FRP Young's moduli

The adhesive shear stress distributions of both models are shown in Figure 5-23. Both distribution curves are fairly close to each other and fluctuate between -3.5 to 1.5 N/mm^2 under the load P = 100 kN and between -1.5 to 1.5 N/mm^2 under the load P = 200 kN.

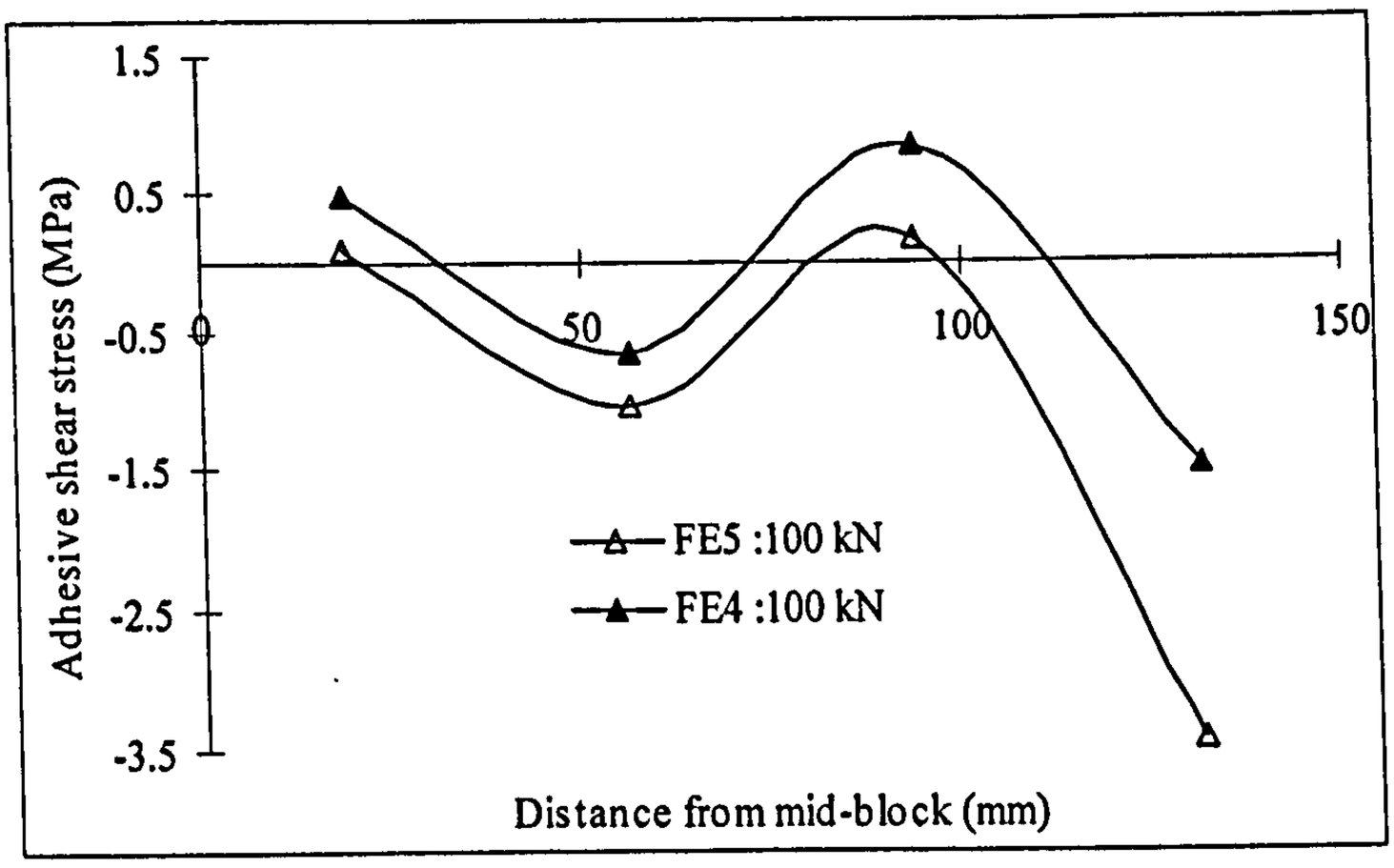

(a) P = 100 kN

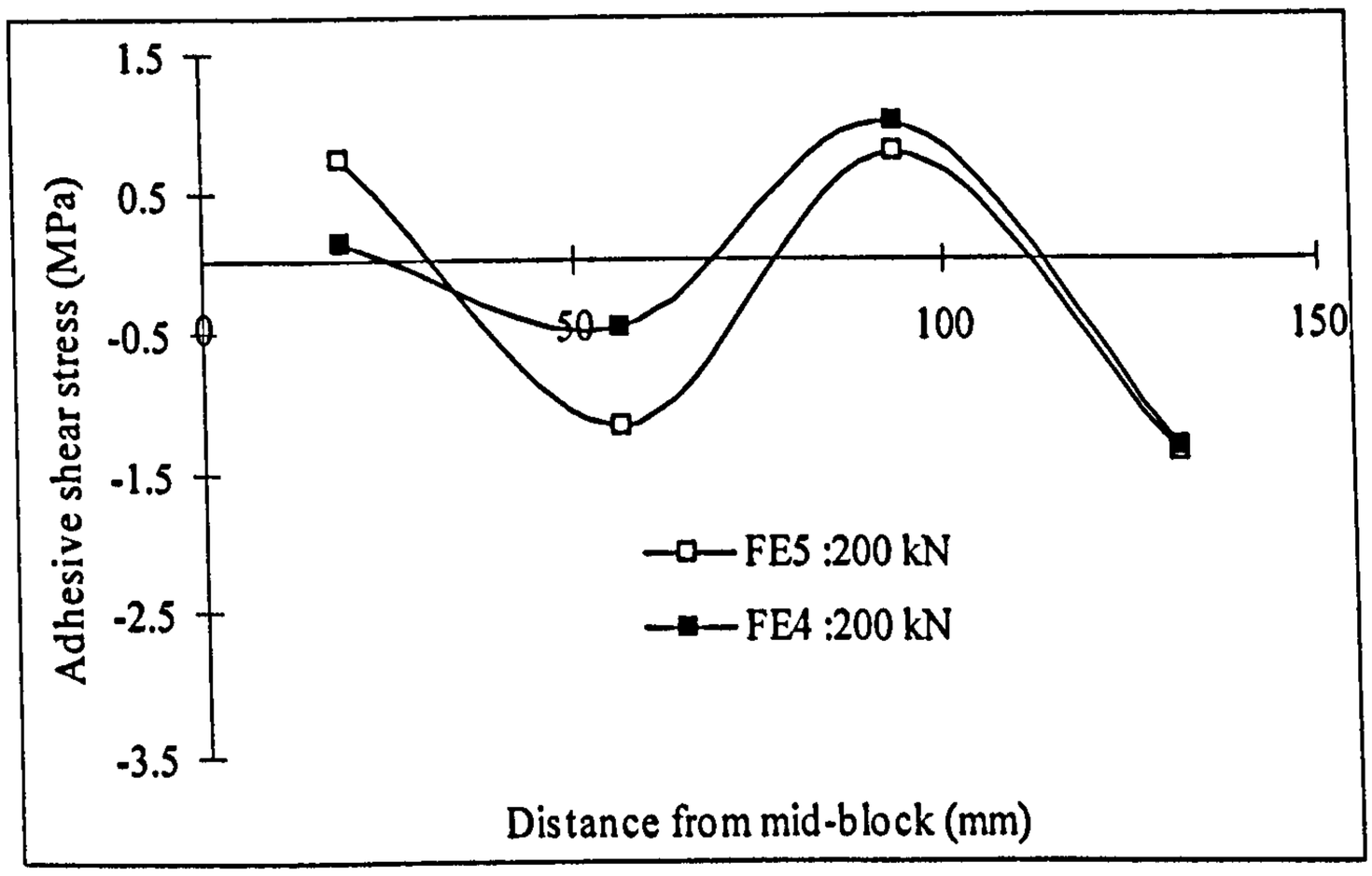

(b) P = 200 kN

Figure 5-23 Adhesive shear stress distributions for various FRP Young's moduli

5.4.3 Effect of adhesive parameters

Three parameters regarding adhesive material properties, adhesive Young' moduli E_a, tensile strength f_{ta} and ratio of ultimate strain to crack strain $\varepsilon_u/\varepsilon_{cr}$, were investigated in the FE Analyses and their influences on the strengthened block models' behaviour were presented.

Figure 5-24 shows the effect of various adhesive Young's moduli E_a on the structural behaviour of the NSM strengthened blocks. It can be seen that the load-displacement

plots stay nearly the same for different models. As for the steel rebar and FRP rod, the strain distributions are almost same except for a few minor differences.

Similarly, the other two adhesive parameters, i.e. f_{ta} and $\varepsilon_u/\varepsilon_{cr}$, have little influence on the load-displacement plots, steel/CFRP strain distributions of different models.

The adhesive shear stress distributions with various adhesive material parameters are shown in Figure 5-25 to Figure 5-27. The curves for different FE models do vary from each other in certain degree but the trends remain similar.

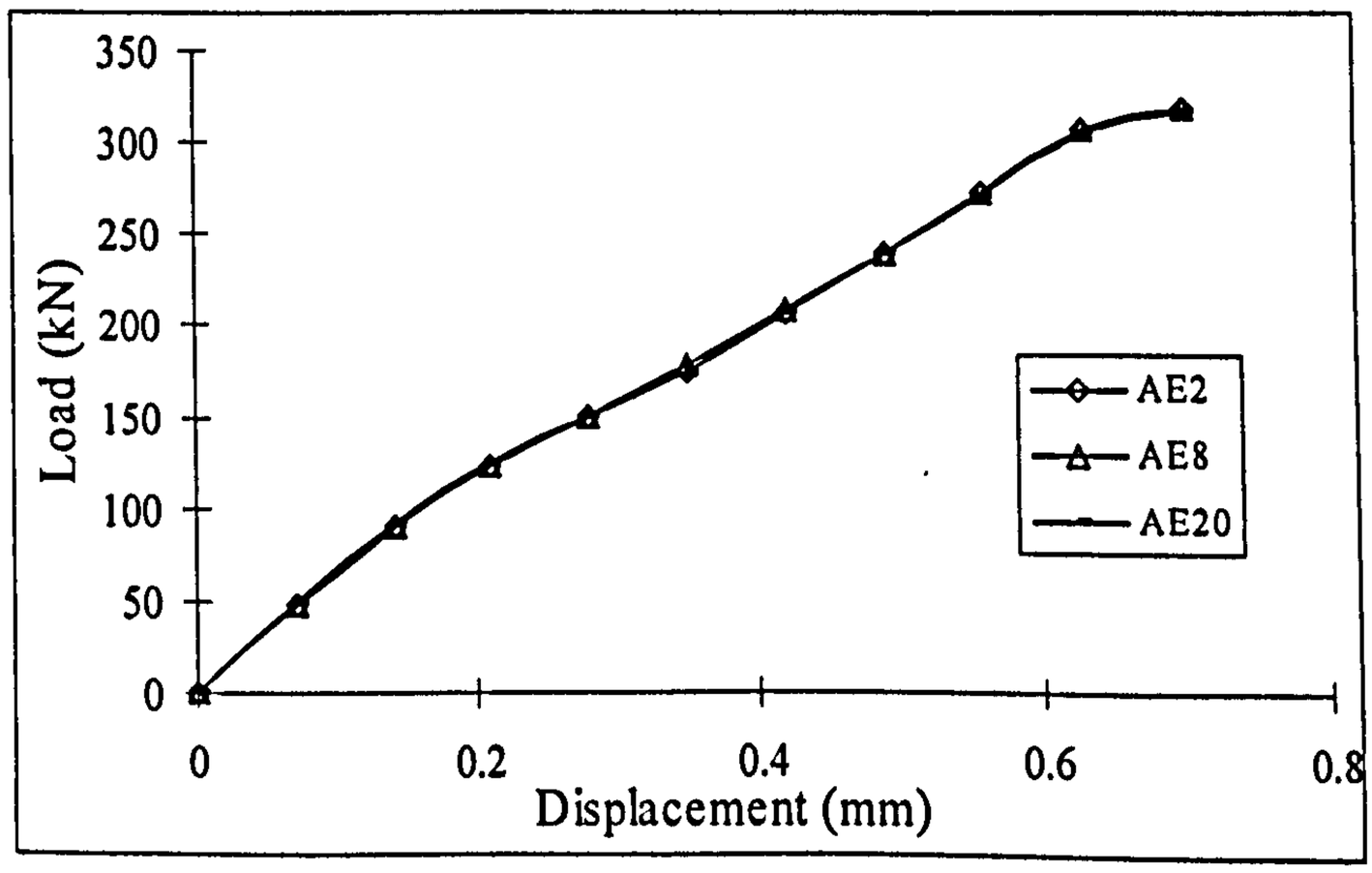

(a) Load-displacement plots

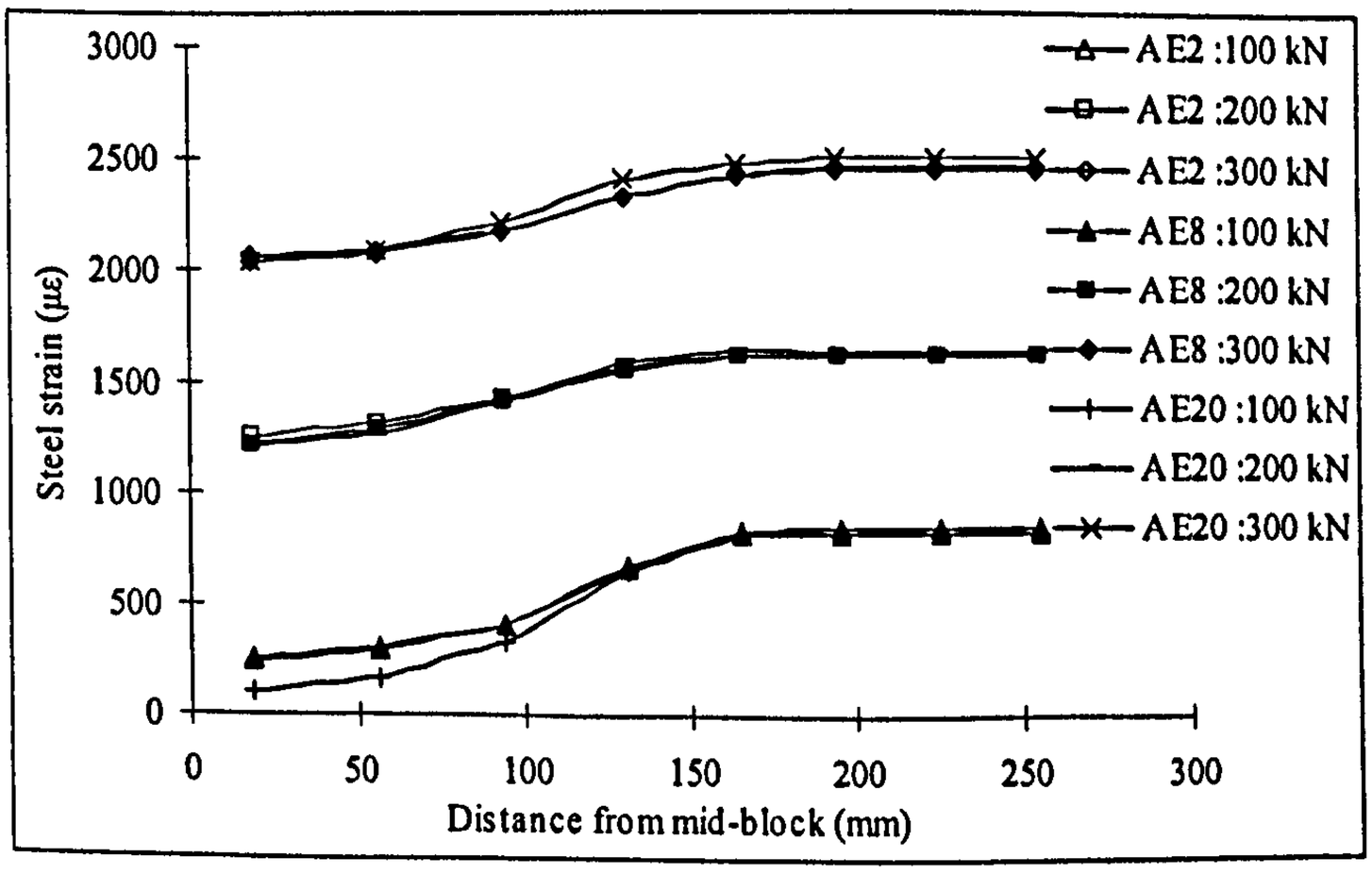

(b) Steel strain distributions

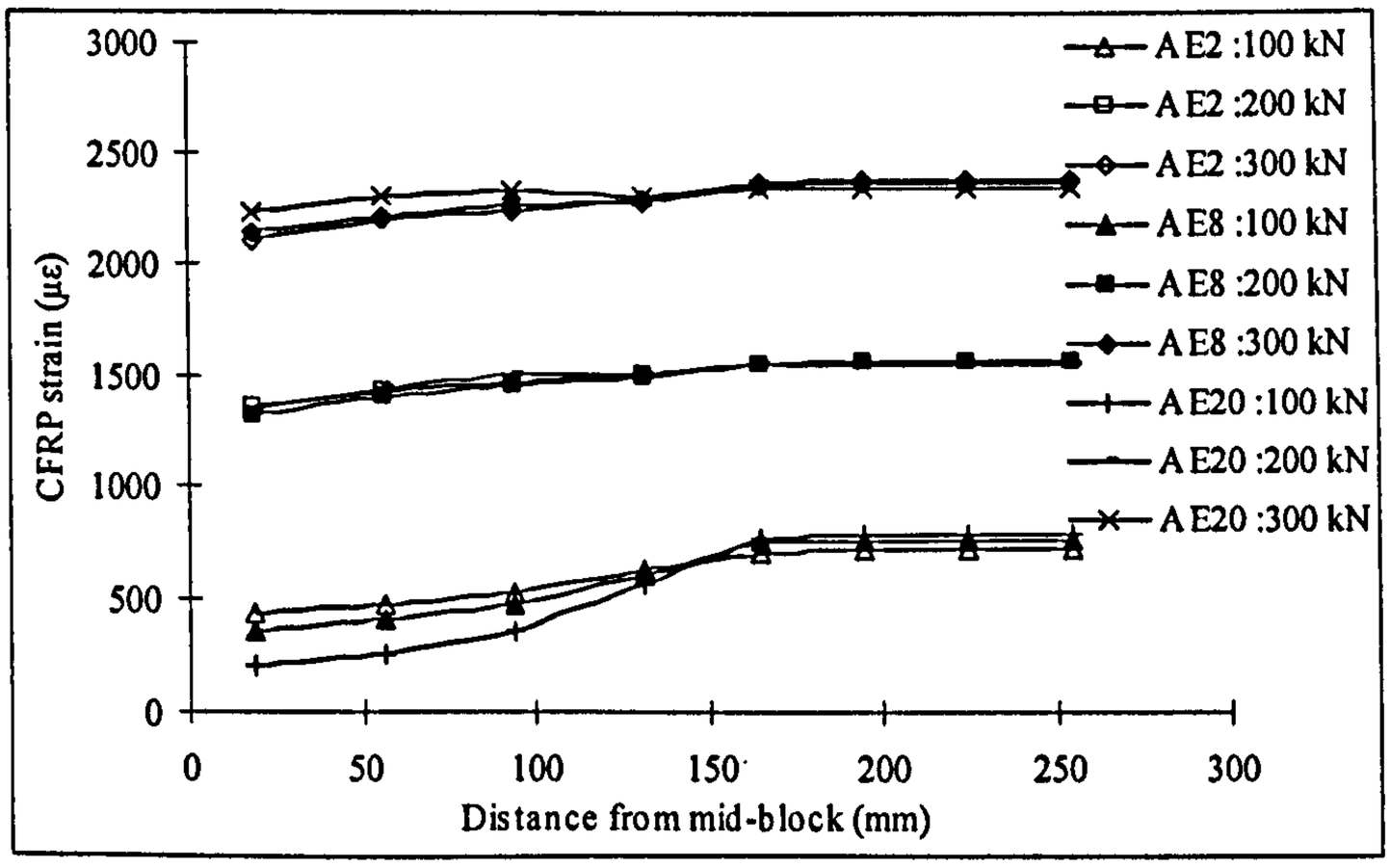

(c) Steel strain distributions

Figure 5-24 Effects of various adhesive Young's moduli on structural responses

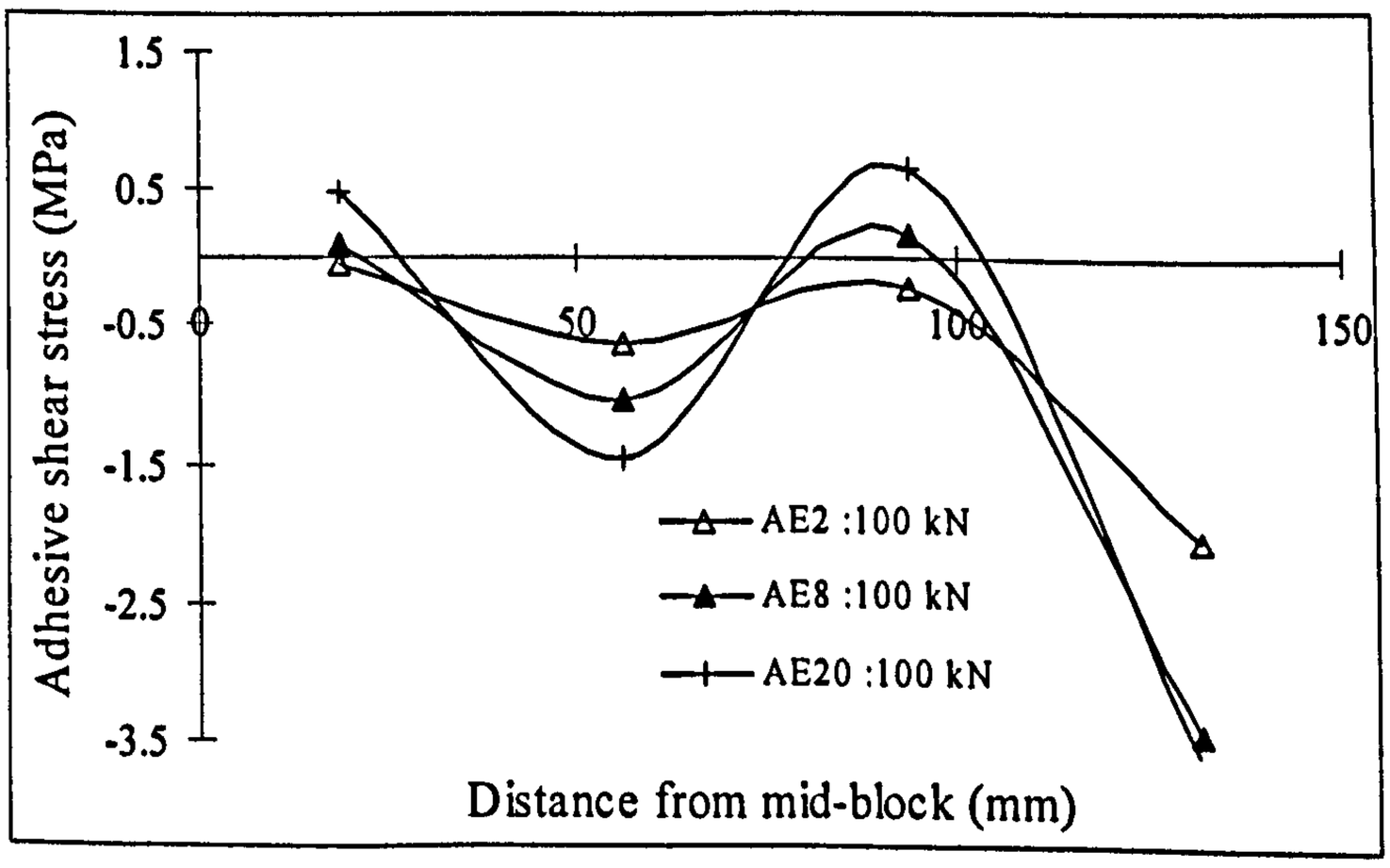

(a) Under load P = 100 kN

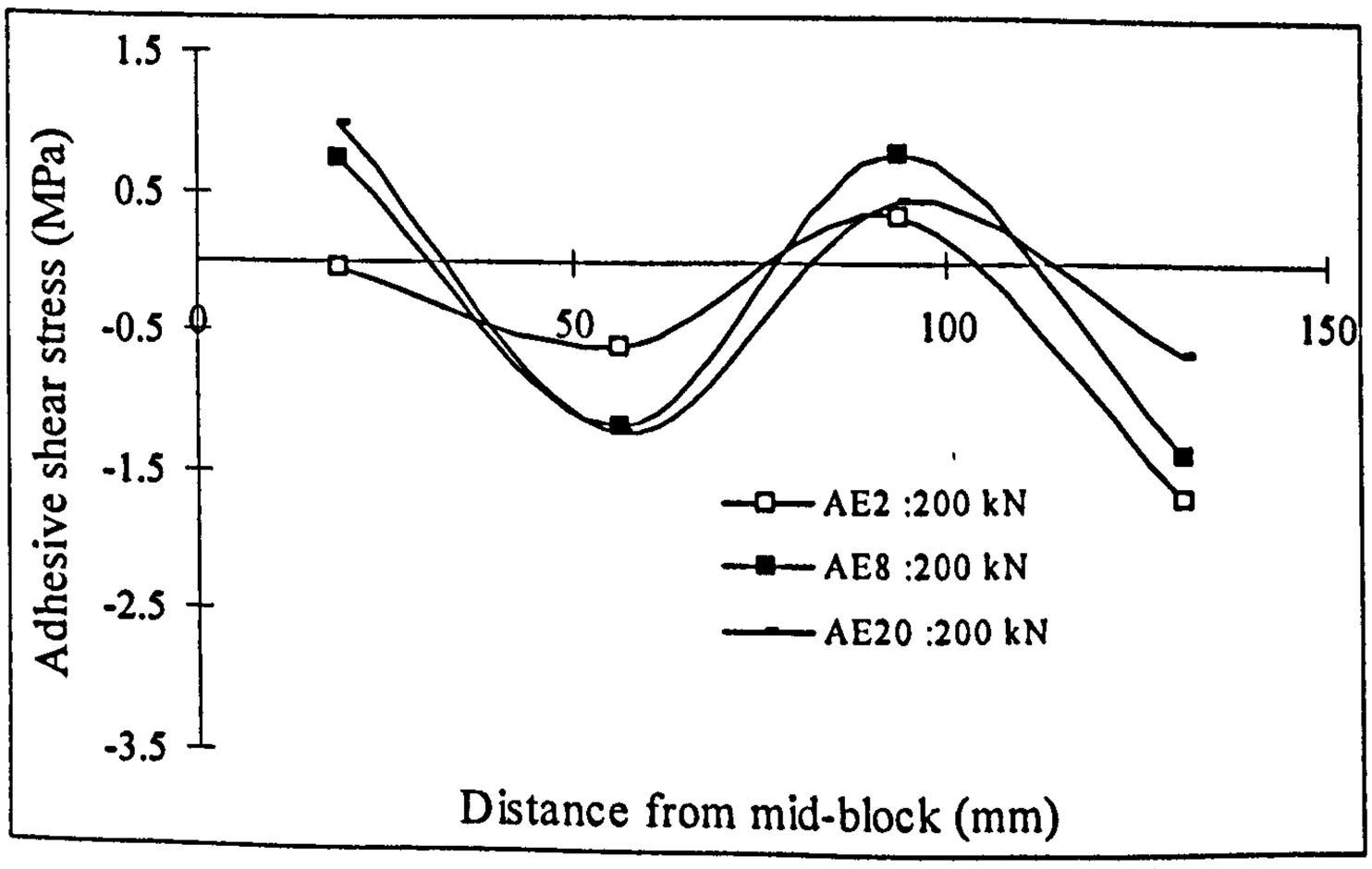

(b) Under load P = 200 kN

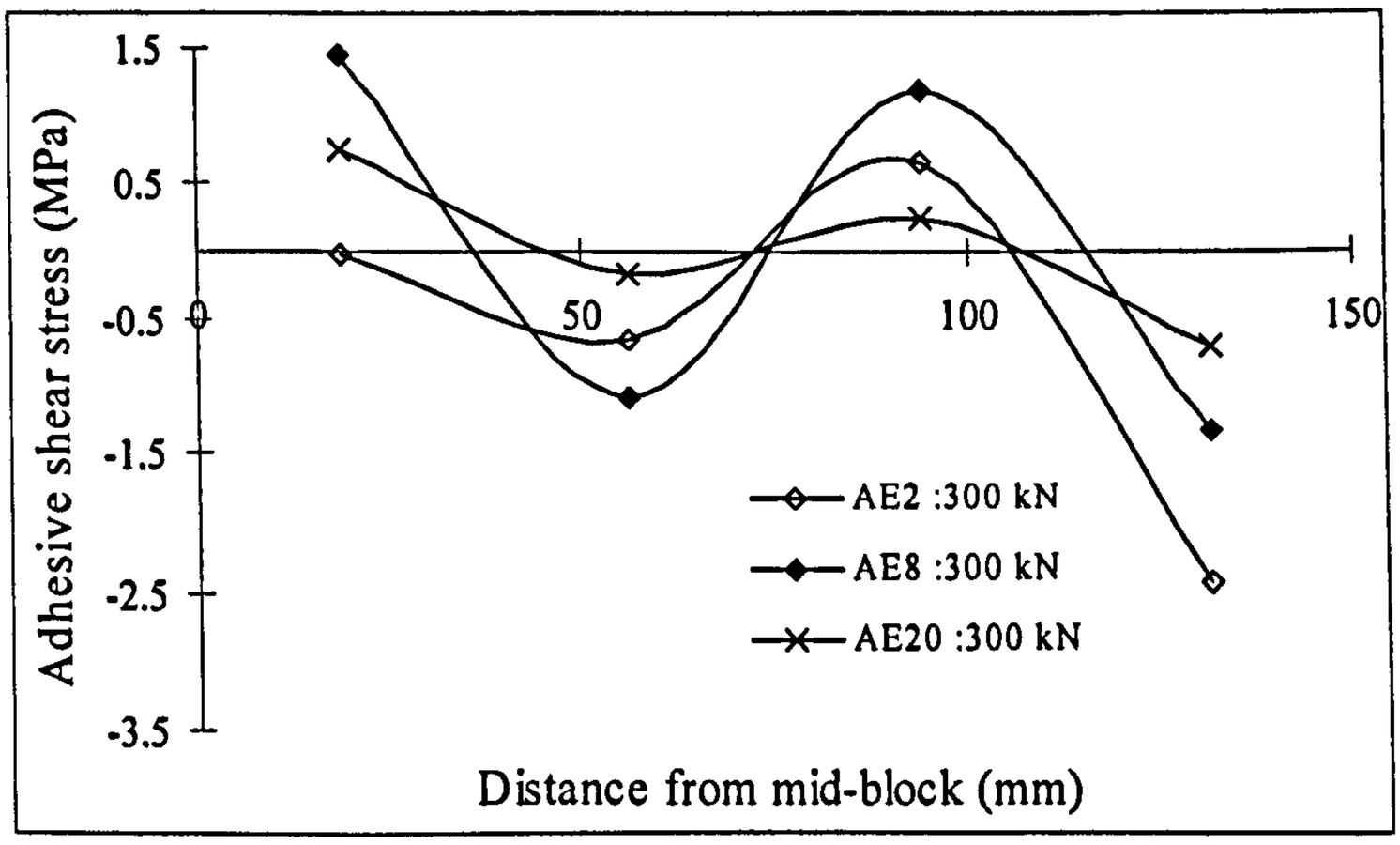

(c) Under load P = 300 kN

Figure 5-25 Adhesive shear stress distributions for various adhesive Young's moduli

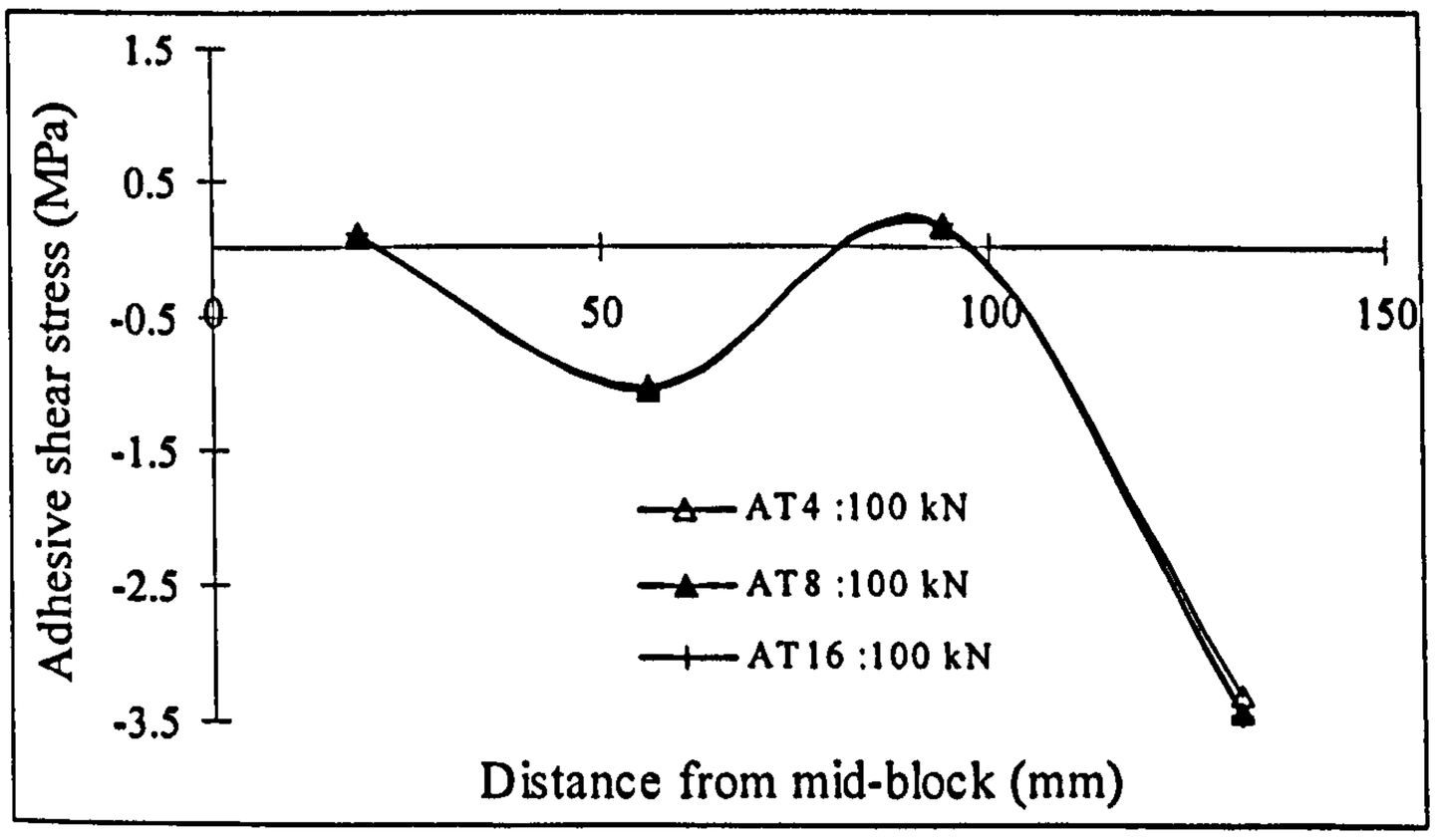

(a) Under load P = 100 kN

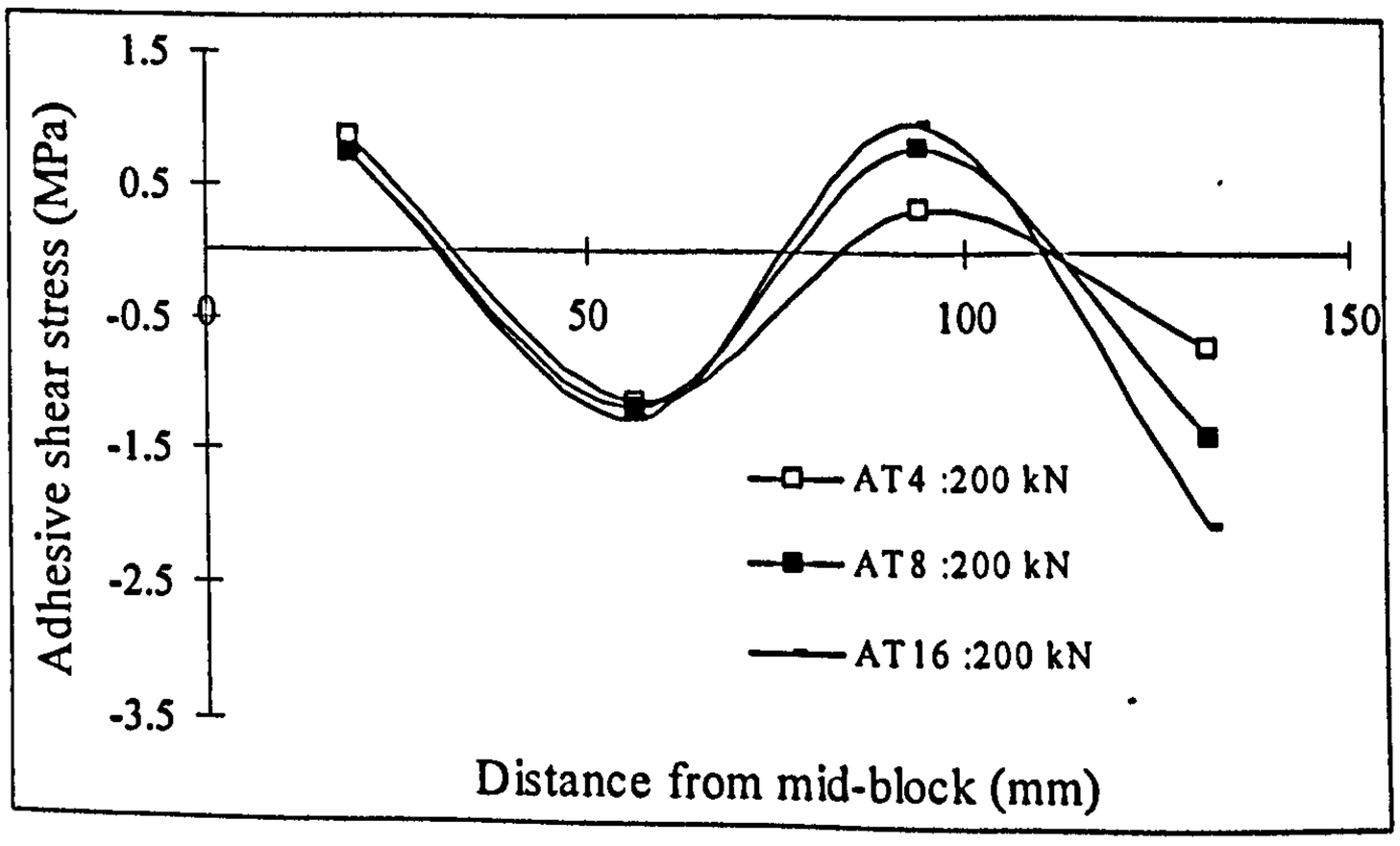

(b) Under load P = 200 kN

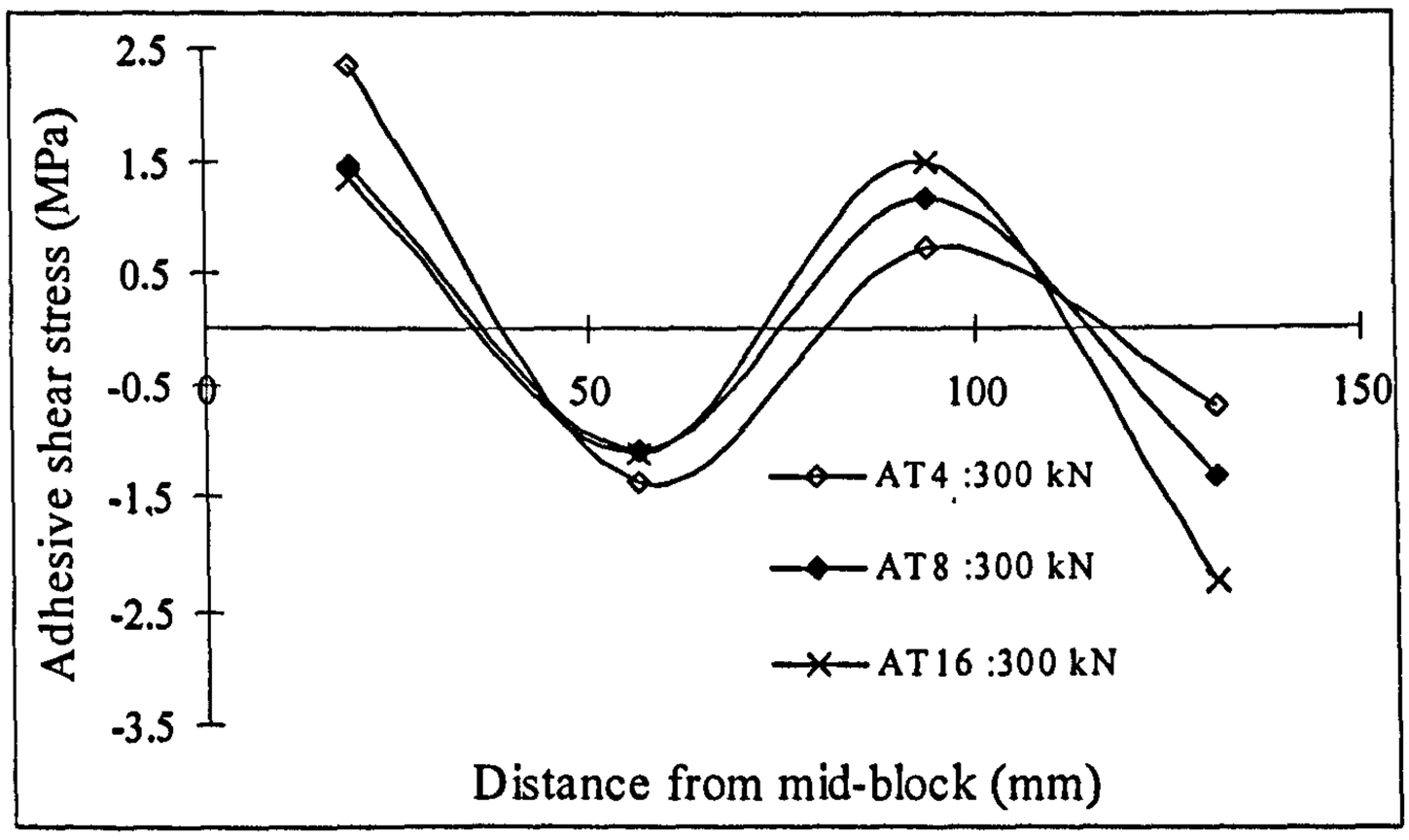

(c) Under load P = 300 kN

Figure 5-26 Adhesive shear stress distributions for various adhesive tensile strength

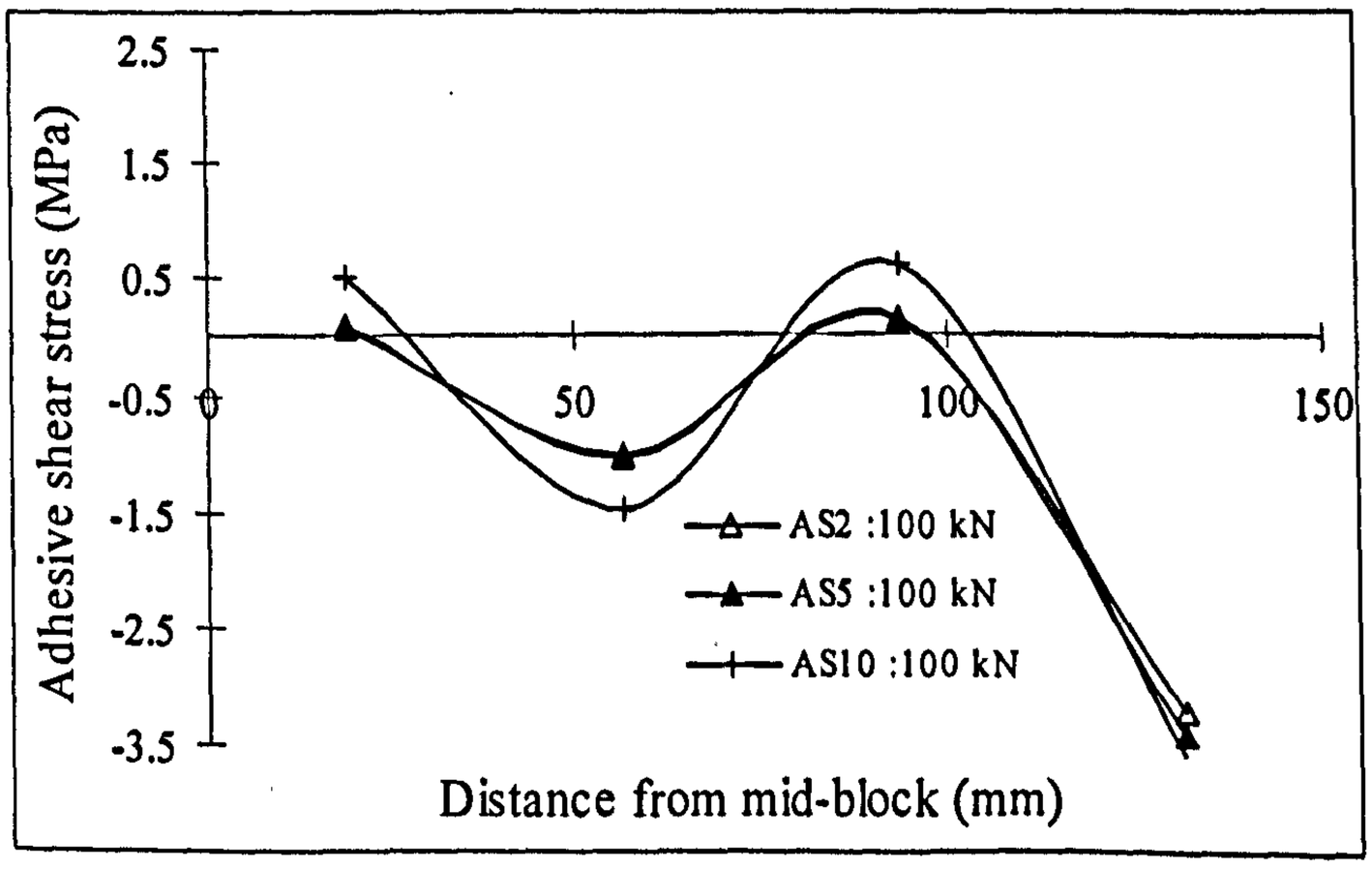

(a) Under load P = 100 kN

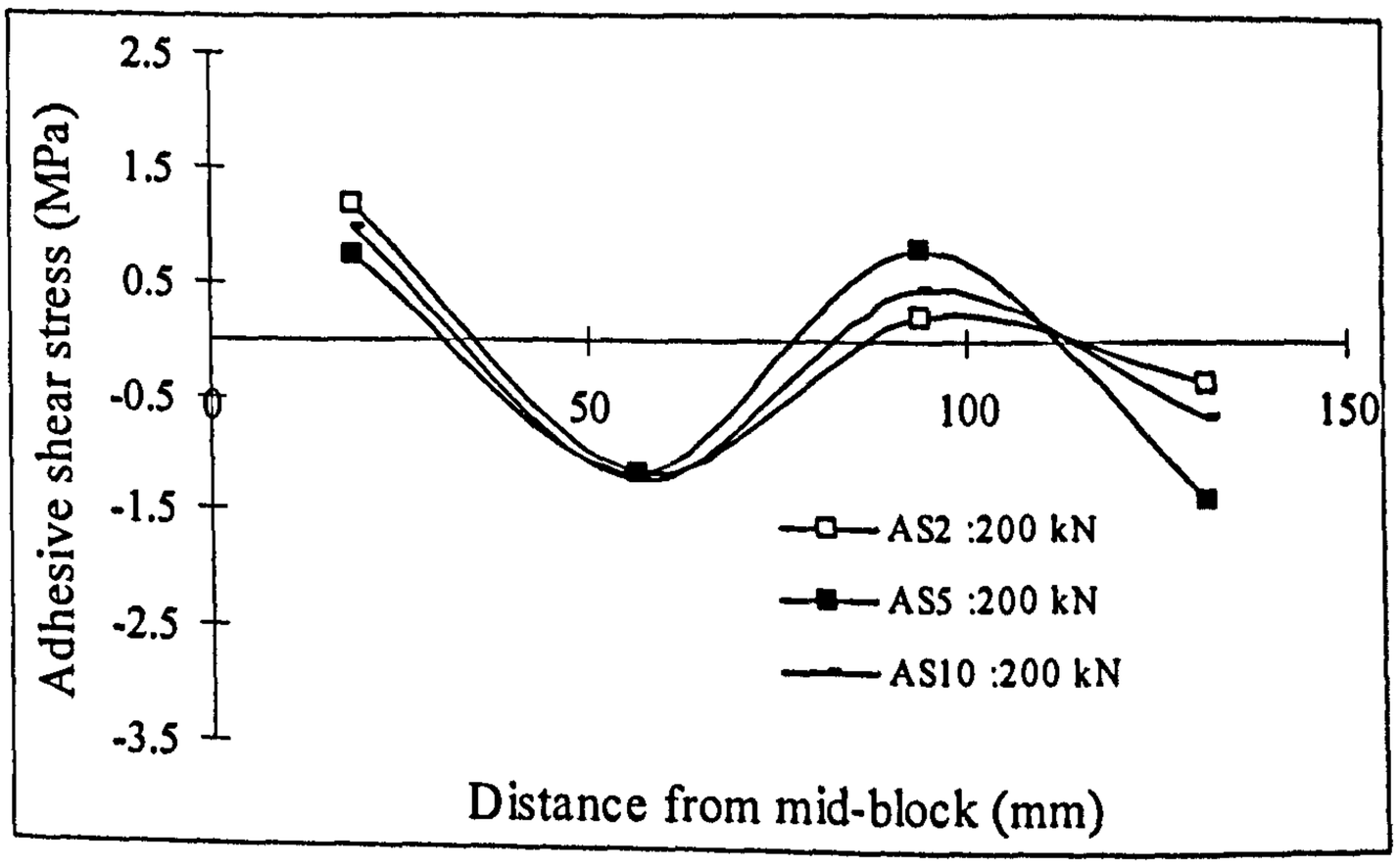

(b) Under load P = 200 kN

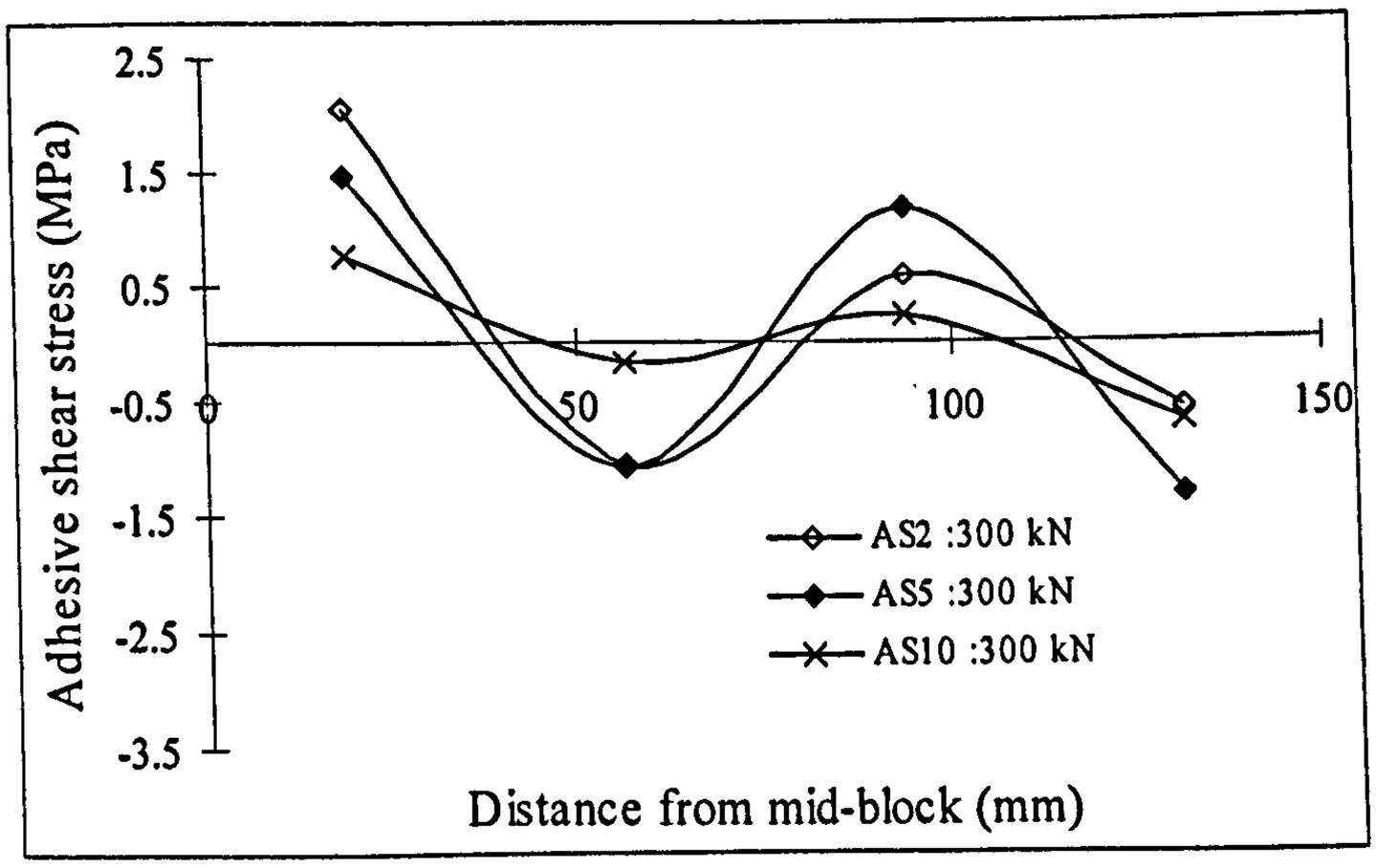

(c) Under load P = 300 kN

Figure 5-27 Adhesive shear stress distributions for various adhesive ratios of ultimate strain to crack strain

Basically, E_a affects the adhesive shear stress distributions most. From Figure 5-25, it can be seen that the value of adhesive stress varied twice or three times while the E_a increased 10 times from 2 kN/mm^2 (AE2) to 20 kN/mm^2 (AE20).

As can be seen from Figure 5-26, the models with various adhesive strength show nearly the same shear stress distribution under the lower load P=100 kN. Then the shear stress of model increased with the increment of adhesive strength as the loading goes up.

The influence from ratio of adhesive ultimate strain to crack strain are shown in Figure 5-27. It can be seen that the distribution curves have the similar trend and fluctuate from –3.5 to 2.5 N/mm^2.

5.5 Conclusions

In this chapter, the NSM strengthened RC blocks discussed in Chapter 4 were analysed in the FEA program DIANA for both verification study and parametric study.

In the first part, the specimens B1 to B4 from lab test were modelled and investigated in FE analysis. Eight-noded brick element HX24L was employed in 3D modelling and the material properties obtained from lab tests were input into the different parts of the FE models separately. The FEA results were presented, including the strains of both reinforcing steel bars and NSM CFRP rods, the adhesive shear stresses, as well as the load-displacement curves for the four specimens. By comparing to the experimental data, it is found that the trends of the FEA results and the test data are similar.

In the second part, FE models are used to characterize the influence of various material parameters on the structural behaviour of the same specimen configuration. These parametric effects are yet unknown or under investigated but very important in the development of an efficient strengthening method with NSM FRP rods. A series of parameters such as concrete tensile strength f_{tc}, NSM rod's Young's modulus E_f and adhesive's tensile strength f_{ta}, Young's modulus E_a and ratio of ultimate strain to crack strain $\varepsilon_u/\varepsilon_{cr}$ are varied to investigate the corresponding effects on the critical strain distributions load-displacement behaviour. The following conclusions can be drawn from the FE analyses and may be used as knowledge for practical design:

- The structural behaviours of the NSM strengthened blocks are influenced by the variation of concrete strength f_{tc}. At the linear stage, before the crack of weaker concrete, both the models behaved similarly. However, at the post-cracking stage and before steel yielding, the model with higher concrete strength (CT6) shows 20% higher stiffness than the model with lower one (CT3). Both the steel and FRP strains outside the middle block keep close to each other. However, inside the concrete block, both the steel and FRP strains decrease with the increment of the concrete strength because concrete with higher tensile strength can carry a larger share of the tensile load so that reinforcing bars could take smaller loads. The influence of concrete

tensile strength on adhesive shear stress distributions between two models increased with load which may due to that the stiffer concrete body cause more stress transfer between concrete and inserted FRP bars.

- The Young's modulus of FRP rod E_f has a significant effect on the structural response of the strengthened blocks. Basically, it is found that the FRP rod with higher Young's modulus can improve more load capacity for the same strengthened specimen. However, despite the ten times of difference of FRP Young's modulus between the two models, the adhesive shear stress distributions of both models are not influenced much and fairly close to each other.
- The variation of adhesive material properties discussed in this thesis hardly affects the ultimate load or strain distributions of reinforcing steel/CFRP rods. For the distribution of adhesive shear stress, the influence dose exist but not significant. For example, the adhesive stress varied twice or three times while E_a increased 10 times from 2 kN/mm^2 (AE2) to 20 kN/mm^2 (AE20). It can be concluded that when choosing the adhesive among the ranges discussed in this thesis, the variation of adhesive material properties dose not matter too much.

Chapter 6

Finite element predictions for FRP-concrete hybrid members

6.1 Introduction

Many finite element analyses (FEA) have been presented in the preceding chapters. Both Chapter 3 and Chapter 5 gave a few verification studies by comparing the FEA results with experimental and theoretical data from the literature and from the lab tests of this PhD study. Furthermore, Chapter 5 presented parametric analyses for the specimen models discussed in Chapter 4.

According to the analytical results discussed earlier on, the reliability and validity of the FEA have been established. The FE technique will now be used in this chapter to set up more models of various structures and to predict their responses to certain loads.

First, the effects of initial cracks on the behaviour of these structures are investigated carefully. In the following sections, FRP plate-strengthened RC beams are analysed with either vertical (flexural) or inclined (shear) cracks under both point loads and uniformly distributed loads (UDL). Then a composite bridge specimen composed of GFRP decking adhesively bonded to a RC beam is modelled and investigated. The

model is also investigated with an initial crack in the concrete underneath one of the loading pads. The FEA results are then presented and interpreted in detail.

The FEA program's capabilities are also extended to deal with the bond-slip behaviour of the interface between steel reinforcement and concrete in 3D FE modelling. A steel-concrete connection is modelled by 8-noded surface interface elements with multi-linear bond slip properties based on experimental data. The FEA results agree reasonably well with the measured and calculated test data.

6.2 Reinforced concrete beam with cracks

6.2.1 RC beam with flexural cracks under UDL

The cracked beams investigated in this prediction study are based on the prototype of the uncracked RC beam discussed in the verification study of Chapter 3. The geometrical dimensions and material properties of the cracked beams are the same as the original un-cracked beam, except that there are either vertical flexural cracks near the midspan (Figure 6-1) or inclined cracks near the ends of the plate (Figure 6-8). Fine meshes are employed in the critical areas such as plate ends and near cracks (Figure 6-2). Specifically, 16 layers of elements are put through the thickness of the adhesive layer. Material properties are appointed to the different parts of the model according to the existing analysis data.

In this section, the flexural cracked beam (FCB) is subjected to 15 N/mm UDL throughout the length of the beam (Figure 6-1). The three flexural cracks near midspan are modelled by 3 columns of 1mm wide plane stress elements (Q8MEM). The mesh is shown in Figure 6-2. The material properties of these elements are chosen to be the same as those of elements in the remainder of the concrete, except

that the tensile strength is set to the very low value of 0.01 N/mm^2, to allow cracks to form easily in these areas.

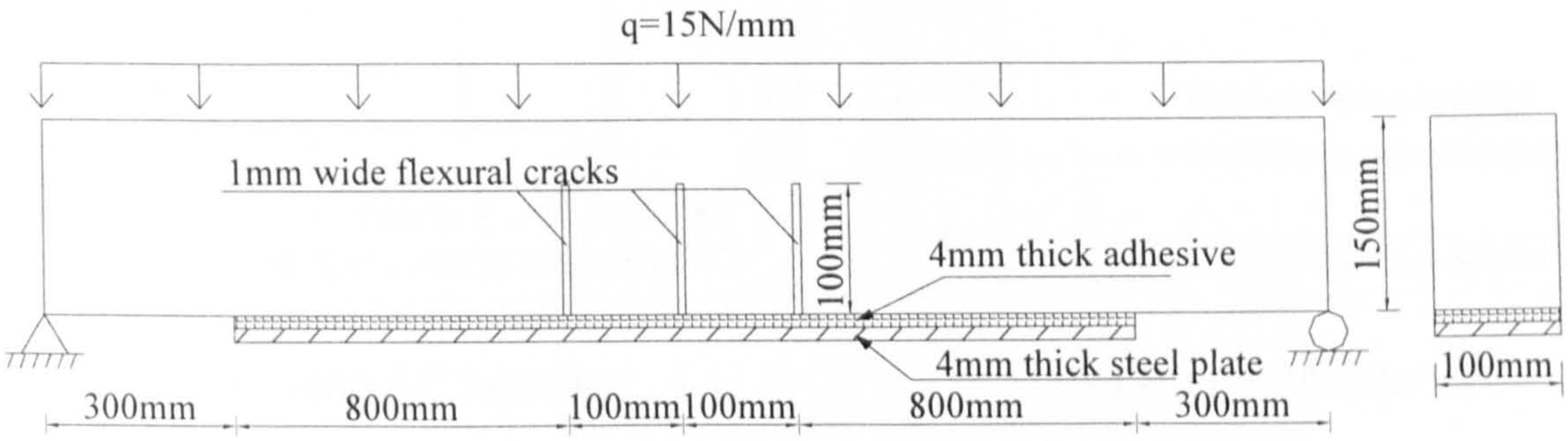

Figure 6-1 Geometry of FCB under UDL

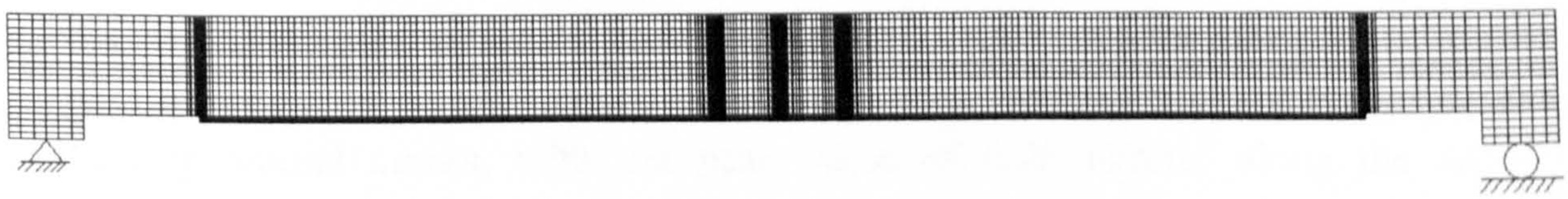

Figure 6-2 Mesh of FCB

It was observed from the FE results that the adhesive interface stress distributions along the beam length in the FCB, including those near the plate ends, are very similar to those in the un-cracked beams. However, the adhesive stresses of the cracked beam in the region around the three flexural cracks differed from that of the un-cracked beam in the same region. In particular, the variation of the stress along the adhesive-concrete (AC) interface is even greater than that along the plate-adhesive (PA) interface, which may be due to the concrete cracking and stress concentration.

As shown in Figure 6-3, the normal stresses of the un-cracked beam in this mid-span area, both along the AC and PA interface, stayed near zero. However, for the cracked beam, the normal stress peaks at 0.14 N/mm^2 along the AC interface and 0.03 N/mm^2 along the PA interface.

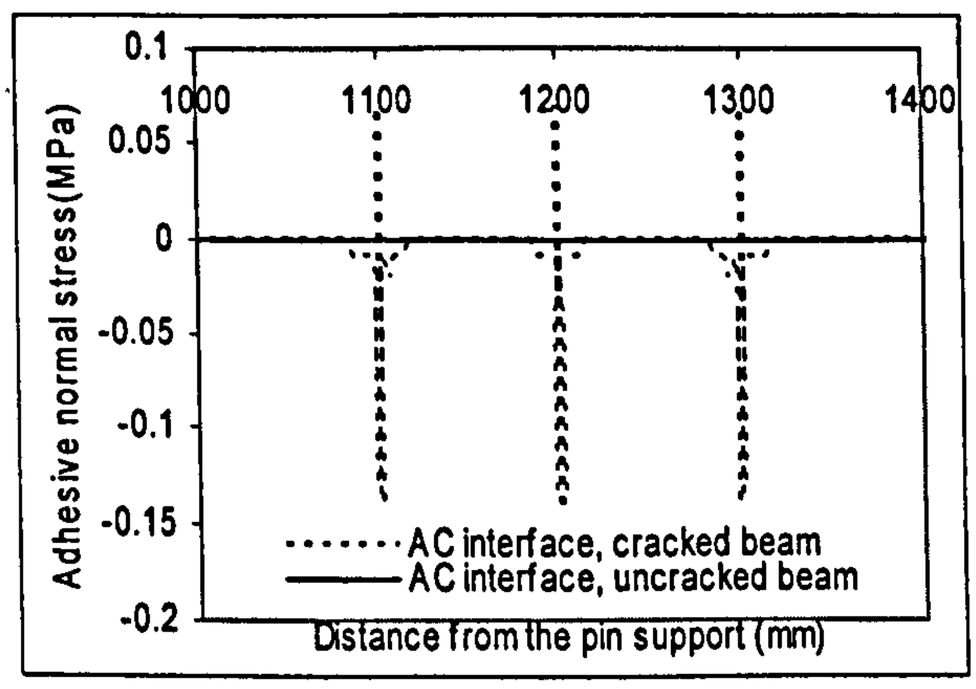

(a) Along AC interface

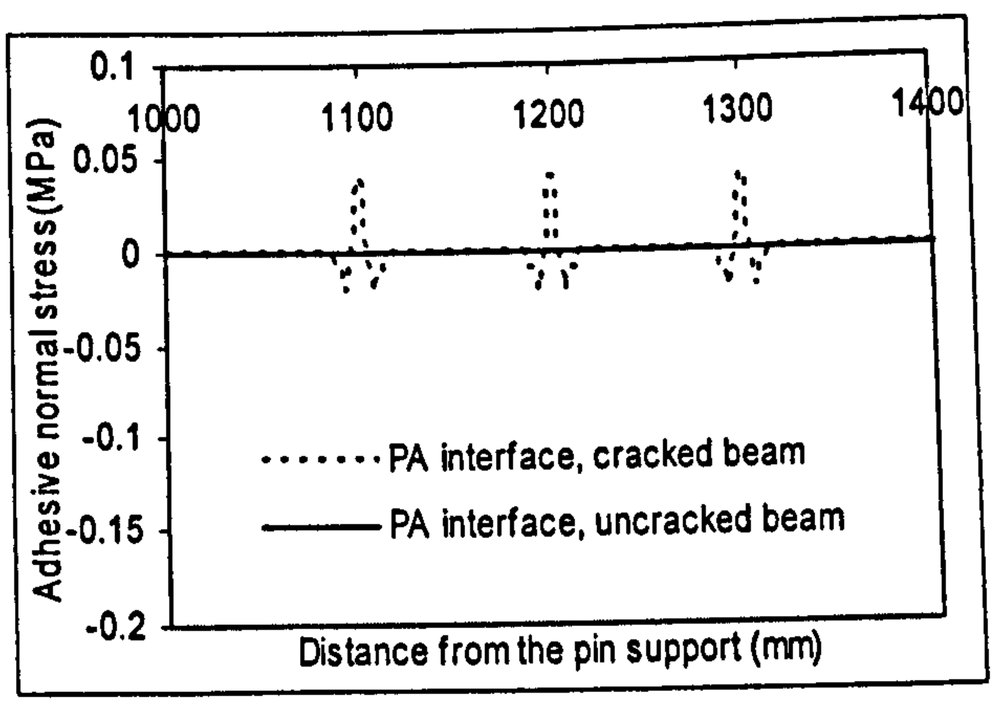

(b) Along PA interface

Figure 6-3 Adhesive normal stress distributions around mid-span cracks in both the cracked beam model and un-cracked beam model under UDL

Similarly, as shown in Figure 6-4, the shear stress of the cracked beam varied significantly around cracks, with the peak value of 0.28 N/mm^2 along the AC interface and 0.04 N/mm^2 along the PA interface respectively, while the shear stress of the un-cracked beam just increases linearly.

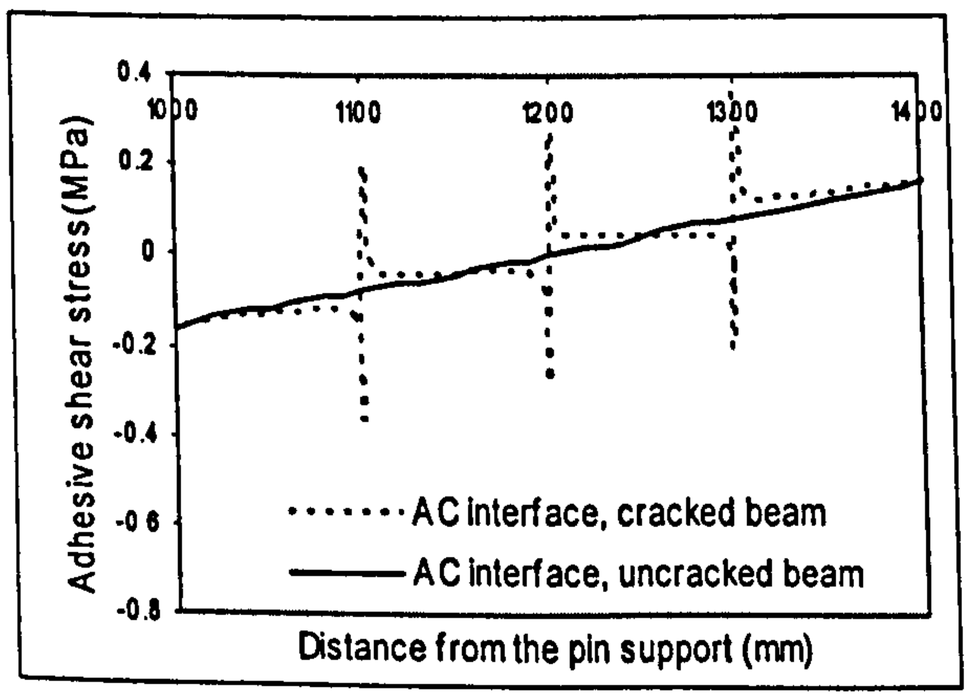

(a) Along AC interface

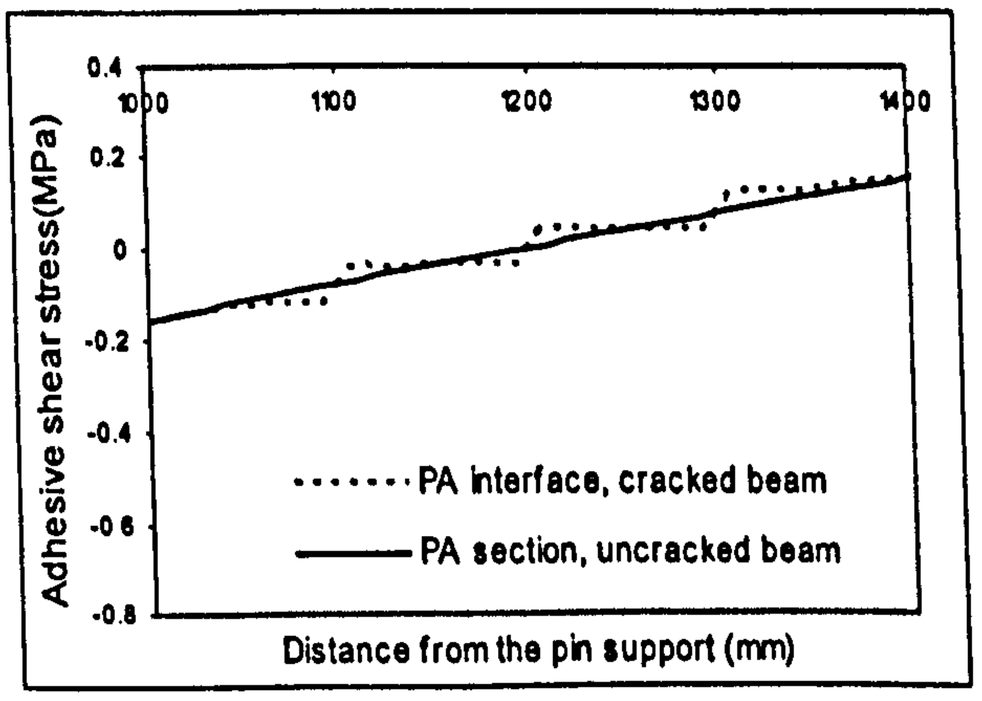

(b) Along PA interface

Figure 6-4 Adhesive shear stress distributions around mid-span cracks in both the cracked beam model and un-cracked beam model under UDL

Of course, with load increasing, these shear and normal peak stresses at the cracks could easily reach levels that induce failure at the adhesive connection.

6.2.2 RC beam with flexural cracks under point load

In this section, the FCB used in the last example is subjected to a point load of 36 kN at midspan instead of the UDL (Figure 6-5). The FE model is the same as the former example (Figure 6-2).

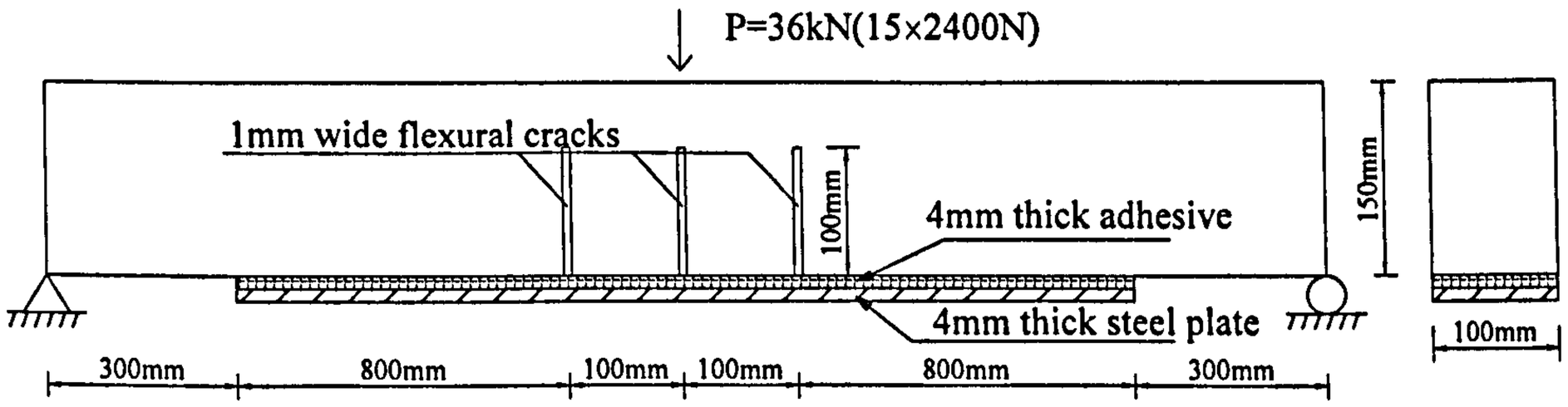

Figure 6-5 Geometry of FCB under point load

Similar to the above analysis, the interface stress distribution of the adhesive layer of the cracked beam under midspan point loading generally agrees with that of the un-cracked beam under the same load, except within the critical zones around the cracks, which can be seen in Figure 6-6 and Figure 6-7.

The cracks clearly introduce local and significant bond stress concentrations at the AC interface. These concentrations do not feed through to the PA interface. It should be noted that such concentration of bond stresses at cracks is pronounced. If loads increase, especially if steel yields, then bond stresses will rise even further.

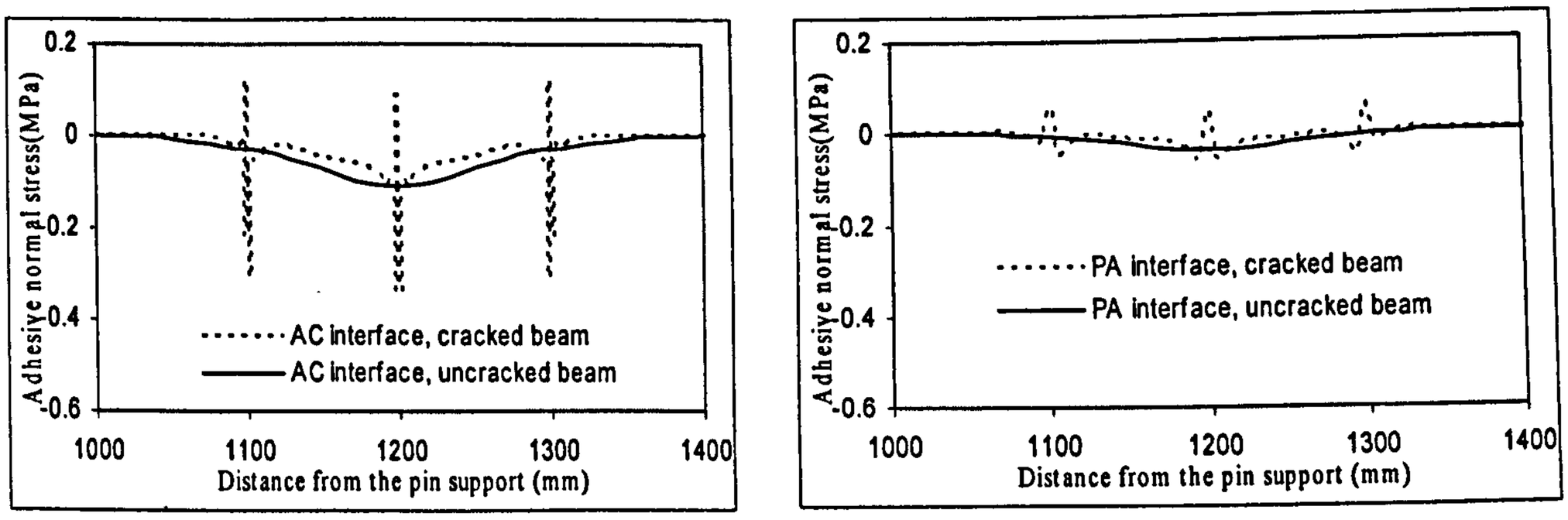

(a) Along AC interface (b) Along PA interface

Figure 6-6 Adhesive normal stress distributions around mid-span cracks in both the cracked beam model and un-cracked beam model under point load

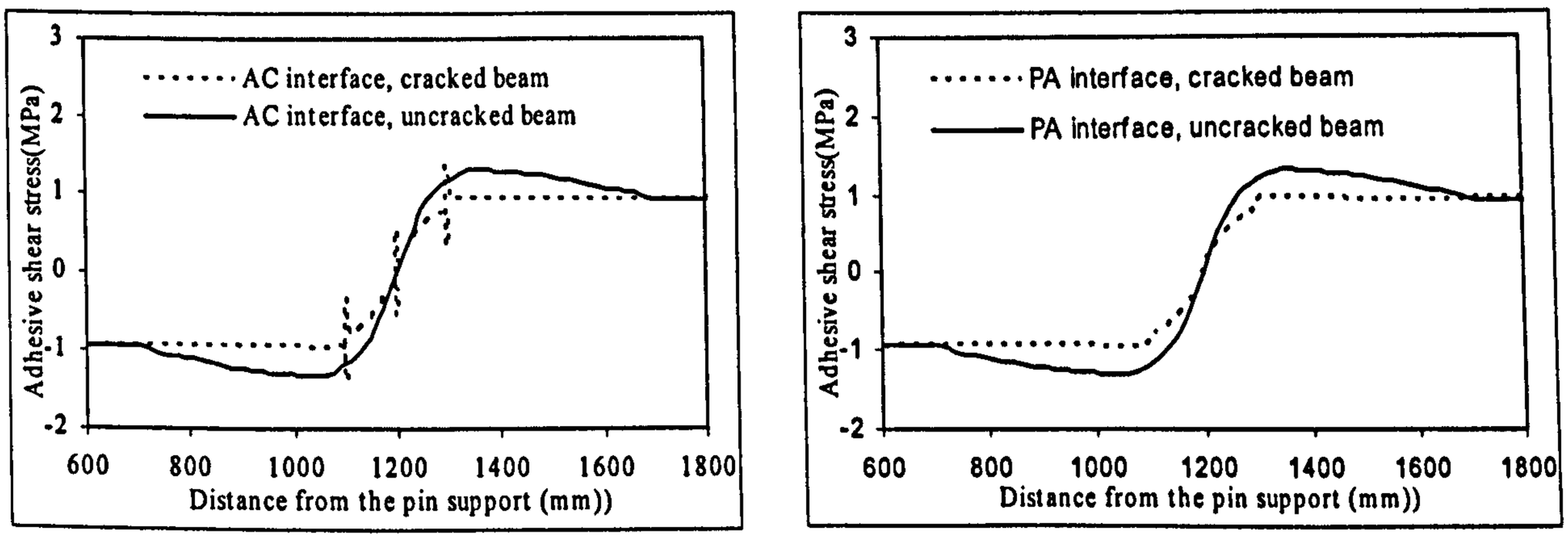

(a) Along AC interface (b) Along PA interface

Figure 6-7 Adhesive shear stress distributions around mid-span cracks in both the cracked beam model and un-cracked beam model under point load

6.2.3 RC beam with inclined cracks under UDL

In practice, FRP plated beams are susceptible to a brittle form of failure named End Peel, in which the plates peel away from the beam starting at the ends of the plate. Therefore, besides the flexural cracks at mid-span of the beam, the inclined cracks at the plate's ends also need investigation. The details of the inclined crack in the beam are shown in Figure 6-8.

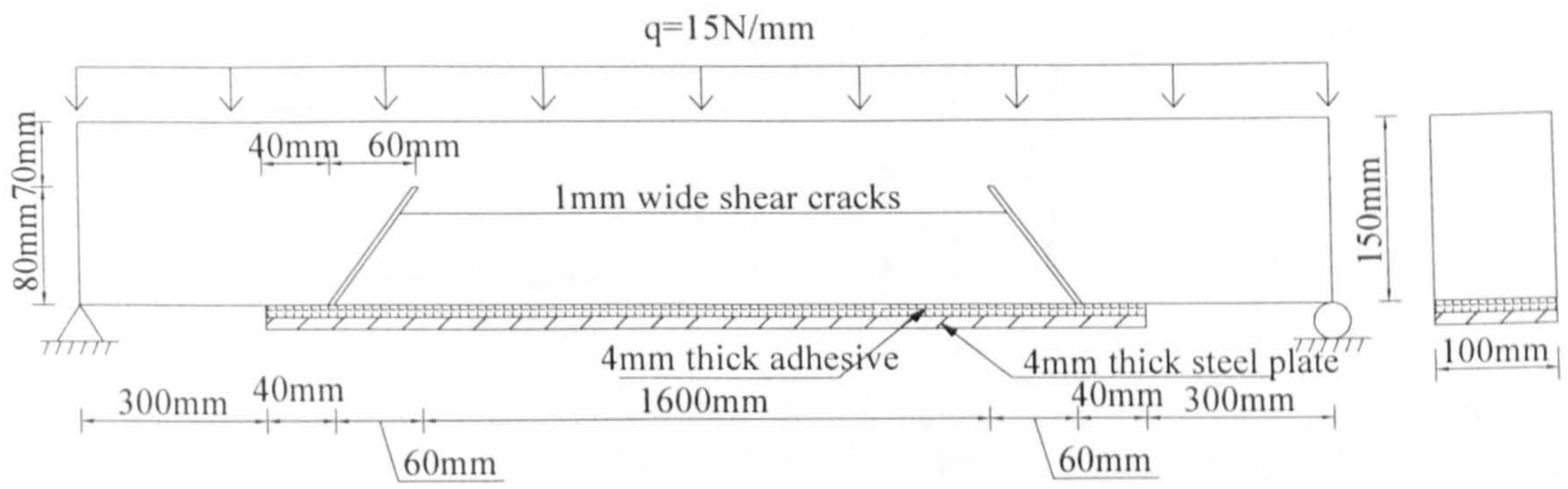

Figure 6-8 Geometry of SCB under UDL

Using symmetry, half of the beam is modelled and analysed as shown in Figure 6-9. Proper constraints are applied on the FE model according to the original supports. The inclined cracks were modelled by the same technique used in the FCB examples.

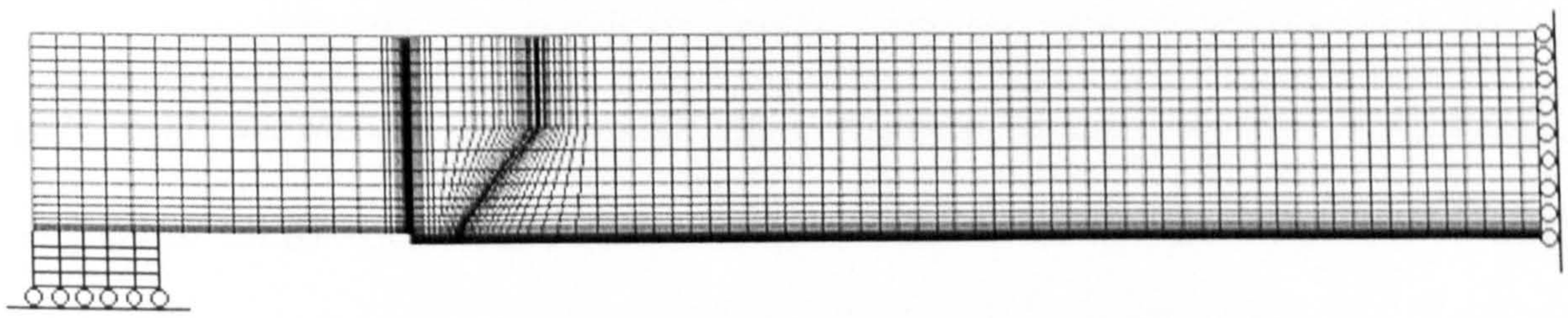

Figure 6-9 Mesh of SCB

The analytical results show that the adhesive stress distributions along beam length both along AC interface and PA interface agree with each other generally except the area around shear cracks. As shown on Figure 6-10, in the area around cracks, both the adhesive shear stress and normal stress around cracks varied dramatically which may be due to nonlinearities caused by concrete cracking and stress concentration.

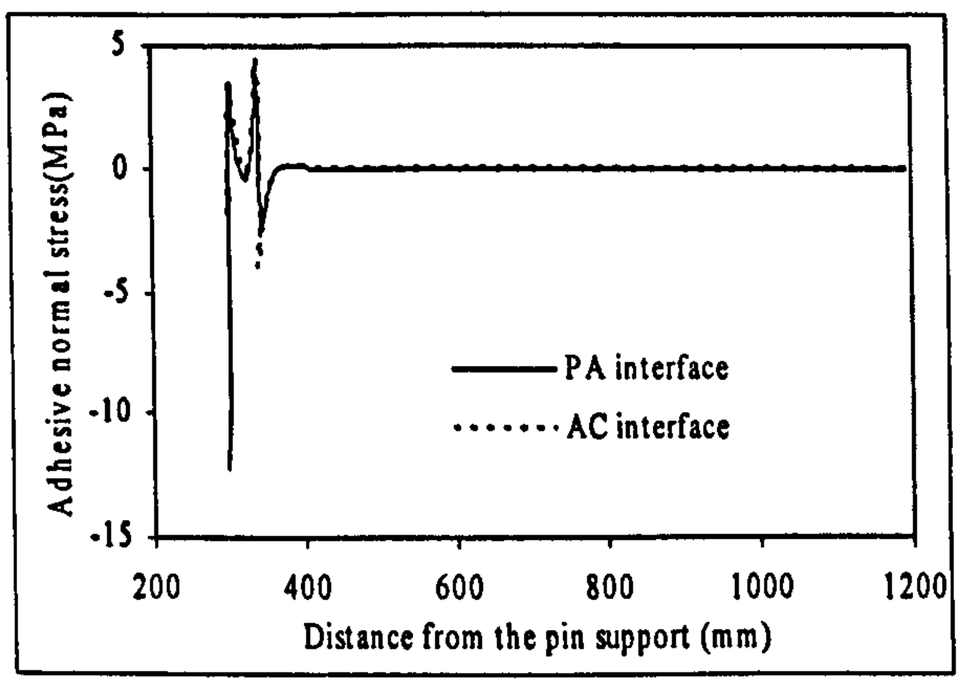

(a) Normal stress distribution

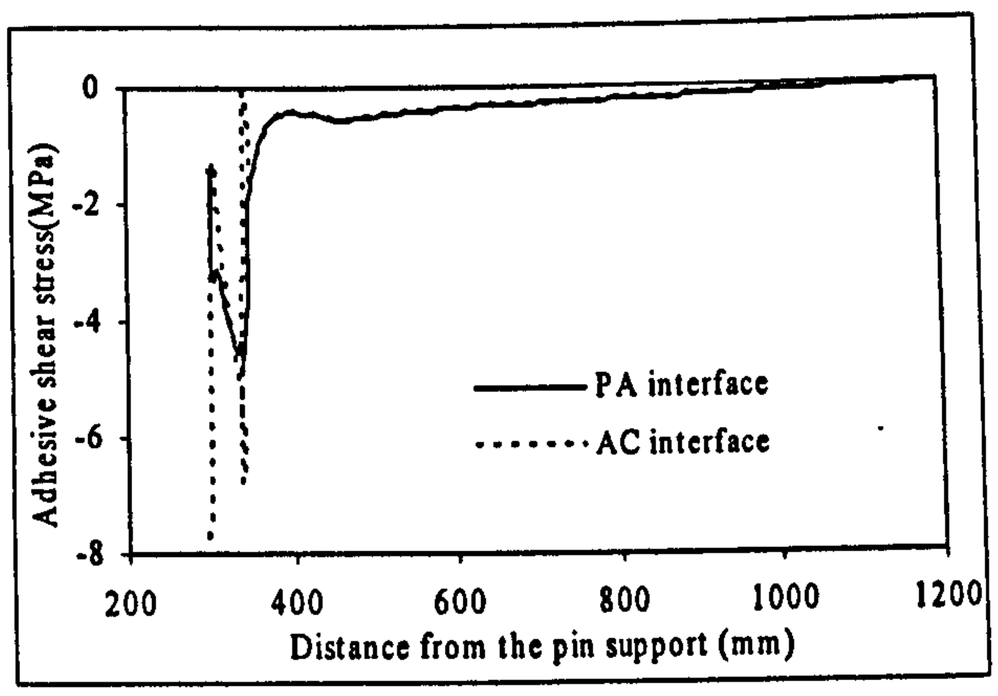

(b) Shear stress distribution

Figure 6-10 Adhesive stress distributions around shear crack around plate end

6.3 Composite bridge specimen

6.3.1 Geometry and material properties

Figure 6-11 shows the geometry of the composite bridge specimen comprising triangulated GFRP deck adhesively connected to a RC beam. The whole was subjected to four-point loading. Some verification studies of this structure have been discussed in Chapter 3. In this section, further investigations are done on the issue of stress transfer between the GFRP deck and the RC beam through the adhesive.

6.3.2 Preliminary modelling of the GFRP deck using beam elements

Before performing the 2D modelling of the bridge specimen using a fine mesh of the plane stress elements, a preliminary FE modelling was done for the top GFRP deck using the two-noded beam element (L6BEN) in a linear analysis. This analysis can help, at the fundamental stage, to gain a preliminary idea as to demonstrate the tension or compression status of each component (top flange, bottom flange and webs) of the GFRP deck as well as to find out the most critical areas with maximum axial force, shear force and bending moment. These results could complement the 2D fine mesh

modelling of the bridge specimen due to the following reasons: (a) the model with plane stress elements does not reveal these results (axial force, shear force and bending moment of each component) directly; (b) use of this information can display the critical area of the specimen and help to set up the model with initial crack discussed in the later sections.

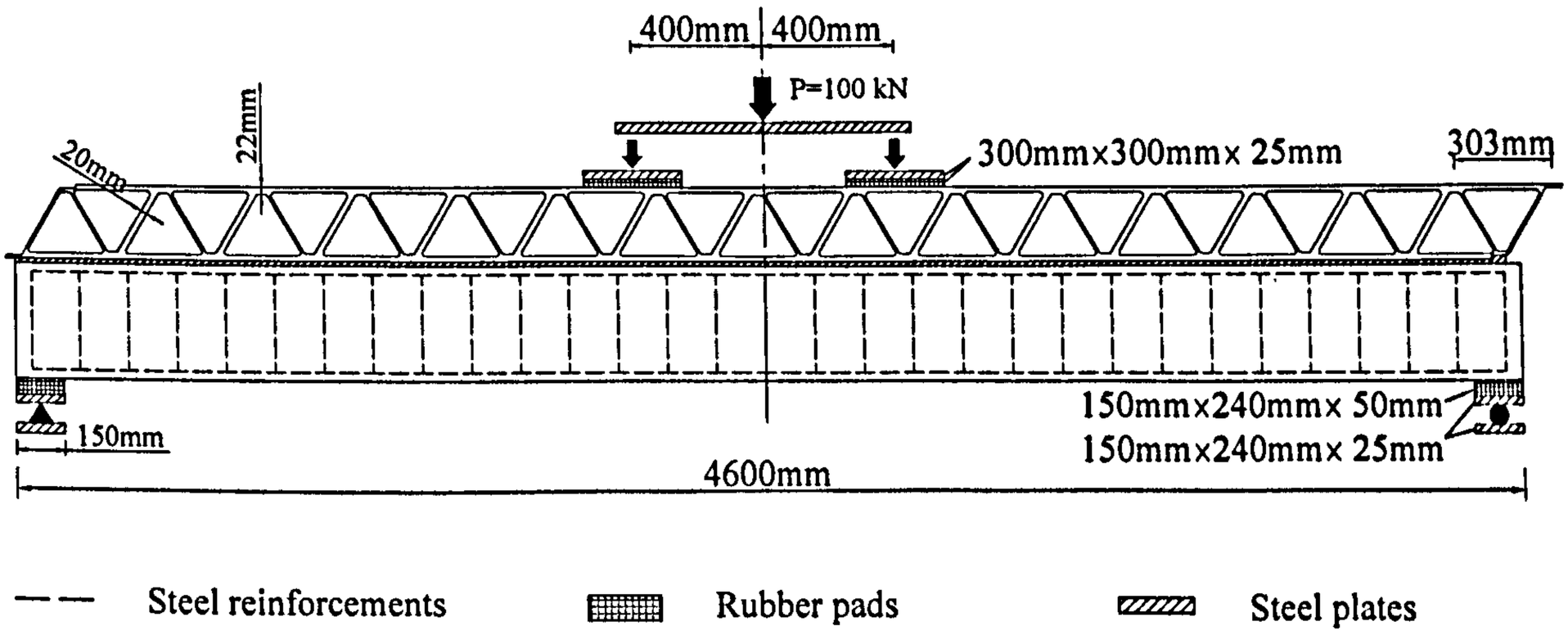

(a) Elevation of GFRP bridge deck

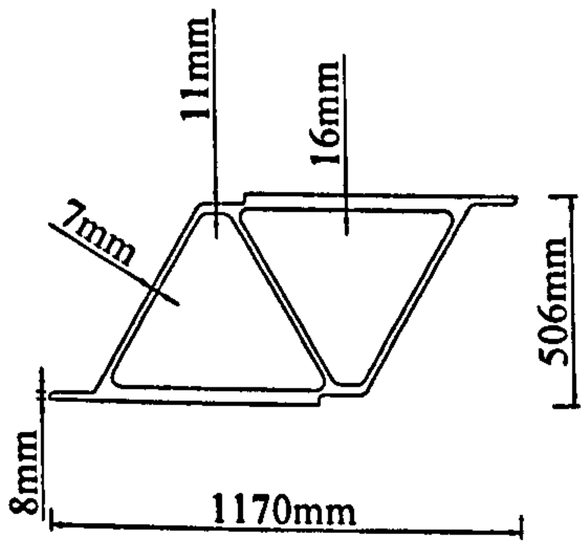

(b) Single GFRP deck componet

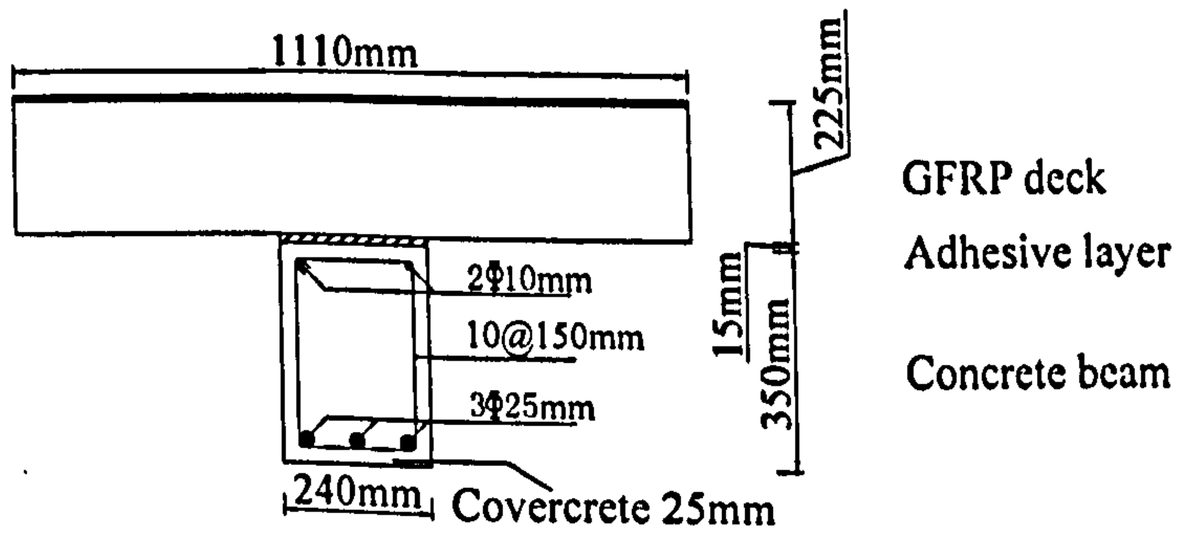

(c) Cross section of GFRP bridge deck

Figure 6-11 Geometry of the composite bridge specimen

As seen from Figure 6-12, the loading on the model was distributed among four nodes equally. As for the boundary condition of GFRP deck, the ends of the GFRP deck were subjected to the pin and roller supports respectively, while the other bottom nodes were connected to both horizontal and vertical 2-noded spring elements SP1TR

with corresponding stiffness to represent the constraint from the adhesive and concrete beam.

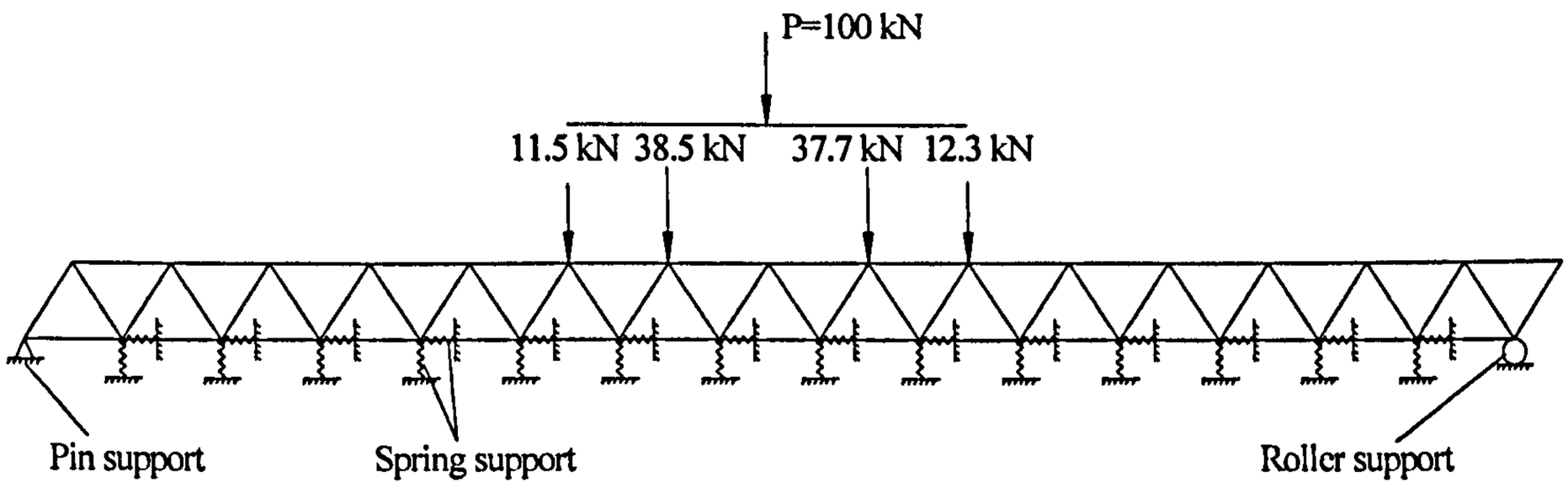

Figure 6-12 Modelling of GFRP deck using two-noded beam element

For the horizontal spring elements, the stiffness k_h could be defined as:

$$k_h = \frac{G_a lw}{t_a} = \frac{E_a}{2(1+\nu_a)} \frac{lw}{t_a} \qquad \text{(Equation 6-1)}$$

Where G_a is the shear modulus of adhesive, l is the length of a single GFRP beam, w is the width of GFRP deck, t_a is the thickness of adhesive layer, E_a is Young's modulus of adhesive and ν_a is Poisson's ratio of adhesive.

For the vertical spring elements, the stiffness k_v could be defined as:

$$k_v = \frac{E_f A_f}{l} \times n \qquad \text{(Equation 6-2)}$$

Where E_f is Young's modulus of GFRP, A_f is the cross sectional area of the bottom flange of the GFRP deck and n is the times of stiffness of vertical spring elements to the bottom flanges. A few parametric analyses were done by choosing the different values for n, e.g. n = 1, 5 and 10. It is found that the variation of n value does not

influence the tension or compression status of each component but slightly changes the value of maximum forces.

Figure 6-13 shows the axial force diagram of the GFRP deck and the locations of maximum values for axial force. The maximum axial forces peaking at around 28.9 kN were found in the thicker webs because members with higher stiffness could attract more loads. In addition, it can be seen that all the thinner webs are under compression. Although the maximum compression forces in the thinner webs are around 10 kN lower than those in the thicker webs, it still can cause buckling due to the lower stiffness.

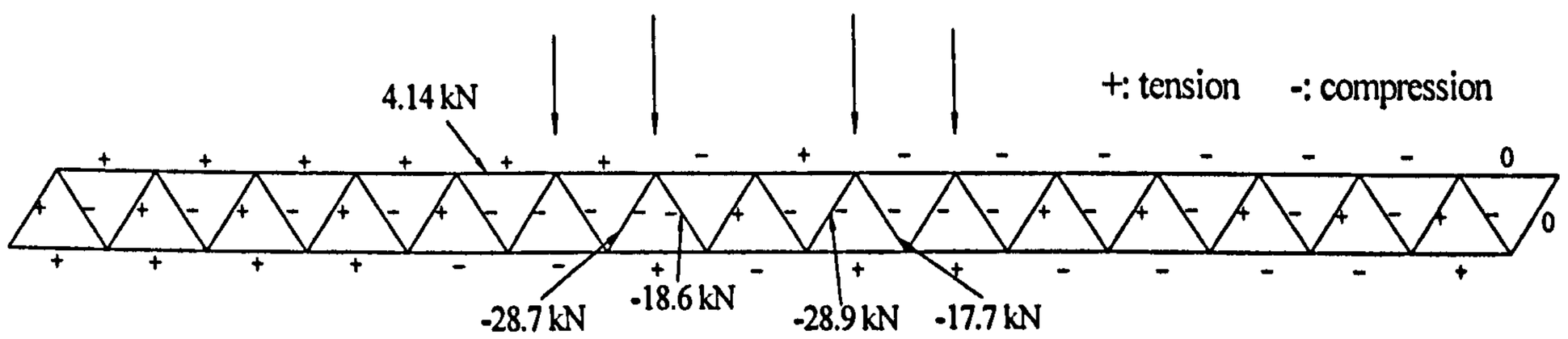

Figure 6-13 Axial force diagram of GFRP deck

High bending moments are found at the joints of webs and flanges near the midspan, which could cause joint failure around that area. The shear forces in the members are relatively small and negligible. The locations of maximum shear force and moment are shown in Figure 6-14 respectively.

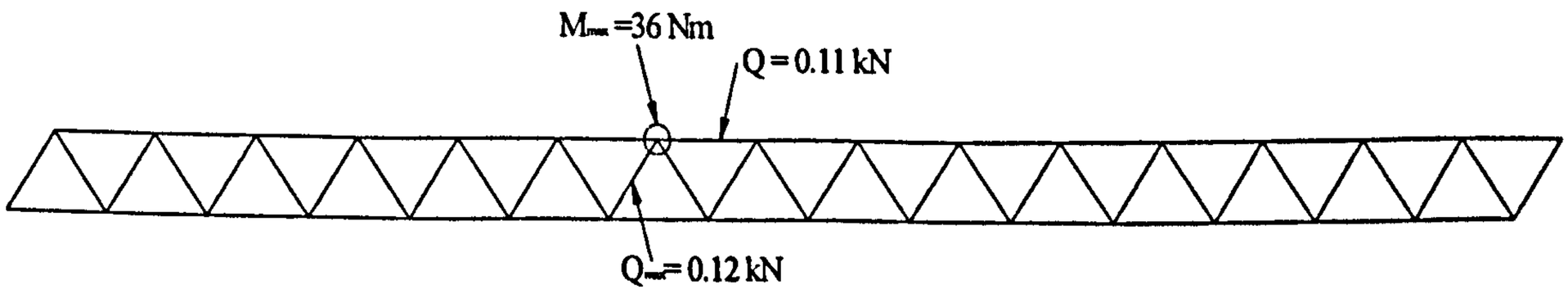

Figure 6-14 Location of maximum shear force and bending moment

Test observations show that failure of the FRP bridge deck-concrete beam specimens occurs by splitting at the joints within the decking itself. The results also show that the bending moments at the joints are indeed significant. Therefore, the use of this preliminary 2D FE analysis was meant to predict local bending / shear effects in the deck - especially near/at the joints -which might have been responsible for the stresses causing this joint splitting failure. In further work, the use of more involved FEanalysis to give detailed stress states at the joints is needed.

6.3.3 2D FEA model of the composite bridge structure

The 2D FE mesh of the composite bridge specimen is shown Figure 6-15. The four-noded plane stress element Q8MEM was used for modelling the RC beam and adhesive layer, while the three-noded plane stress element T6MEM was used for modelling the GFRP deck and the two-noded truss element L2TRU was used for the reinforcing steel bars.

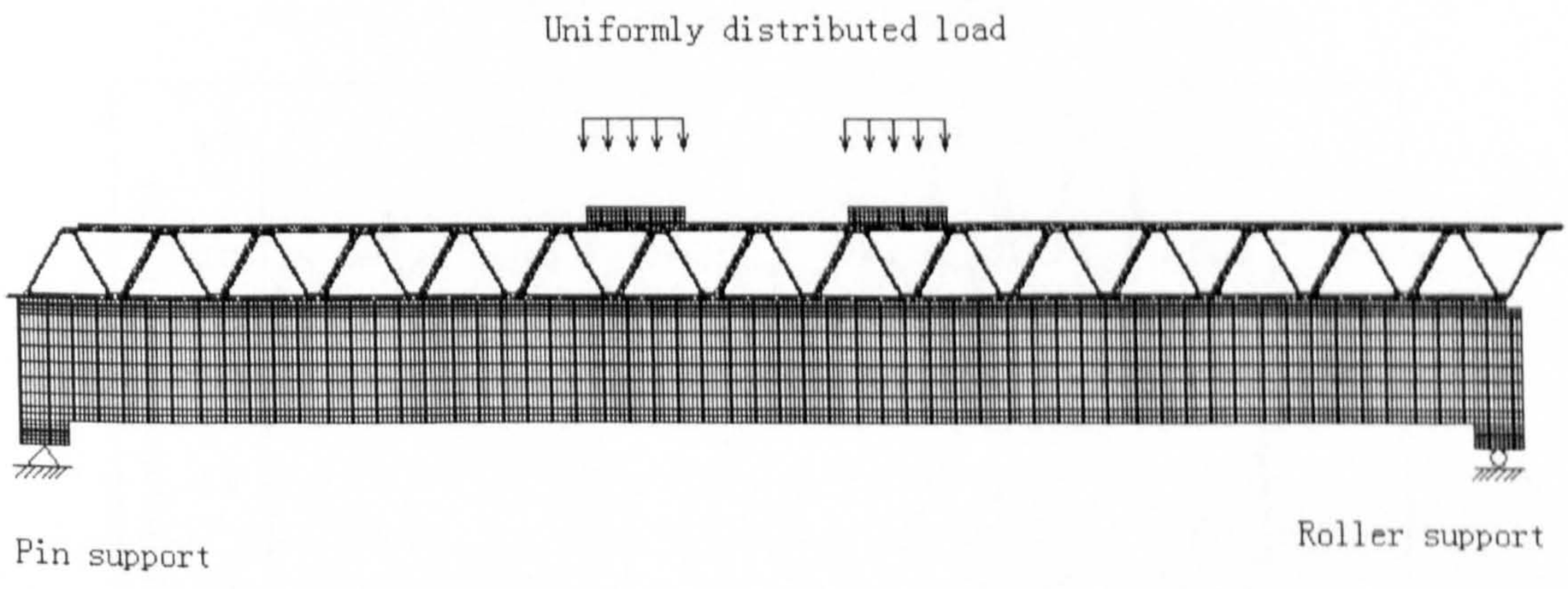

Figure 6-15 2D fine mesh model of the composite bridge specimen

6.3.4 GFRP bridge deck without any initial crack

Figure 6-16 to Figure 6-18 show the results from the FE analysis for the GFRP bridge deck without initial crack under the load P = 100 kN.

The distributions of both shear and normal stresses of the adhesive layer were represented in Figure 6-16. Note the near anti-symmetric nature of the distribution of the shear stress. This is because the shear bond stresses reverse direction across the mid-span in order to achieve zero net horizontal force. The shear stresses peak at 0.8 N/mm^2. The small value at the both ends is expected from the free face boundary condition and complementary shear stress considerations. As for the normal stress, the value oscillated around zero, ranging from -1.5 N/mm^2 to 0.5 N/mm^2.

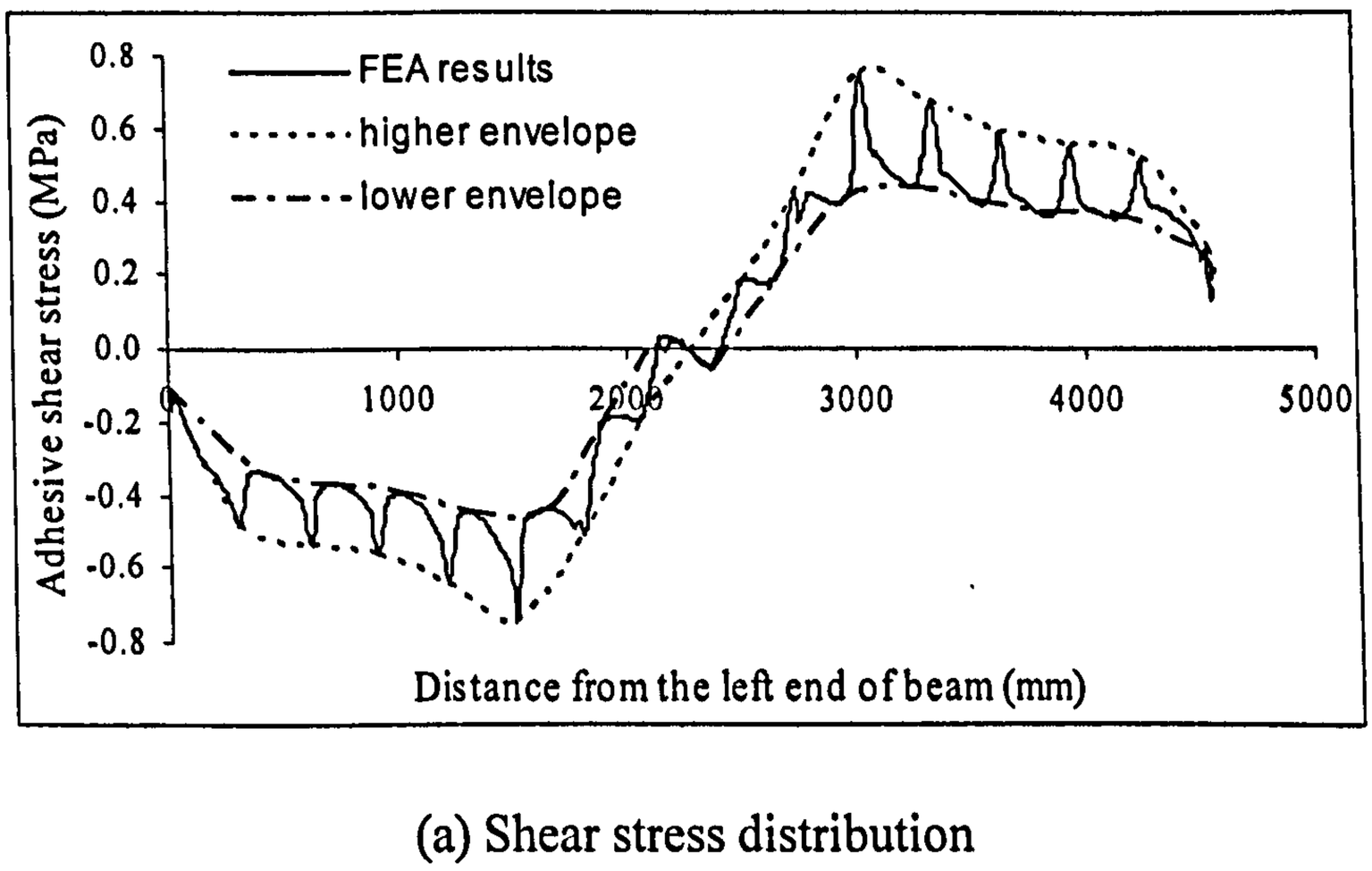

(a) Shear stress distribution

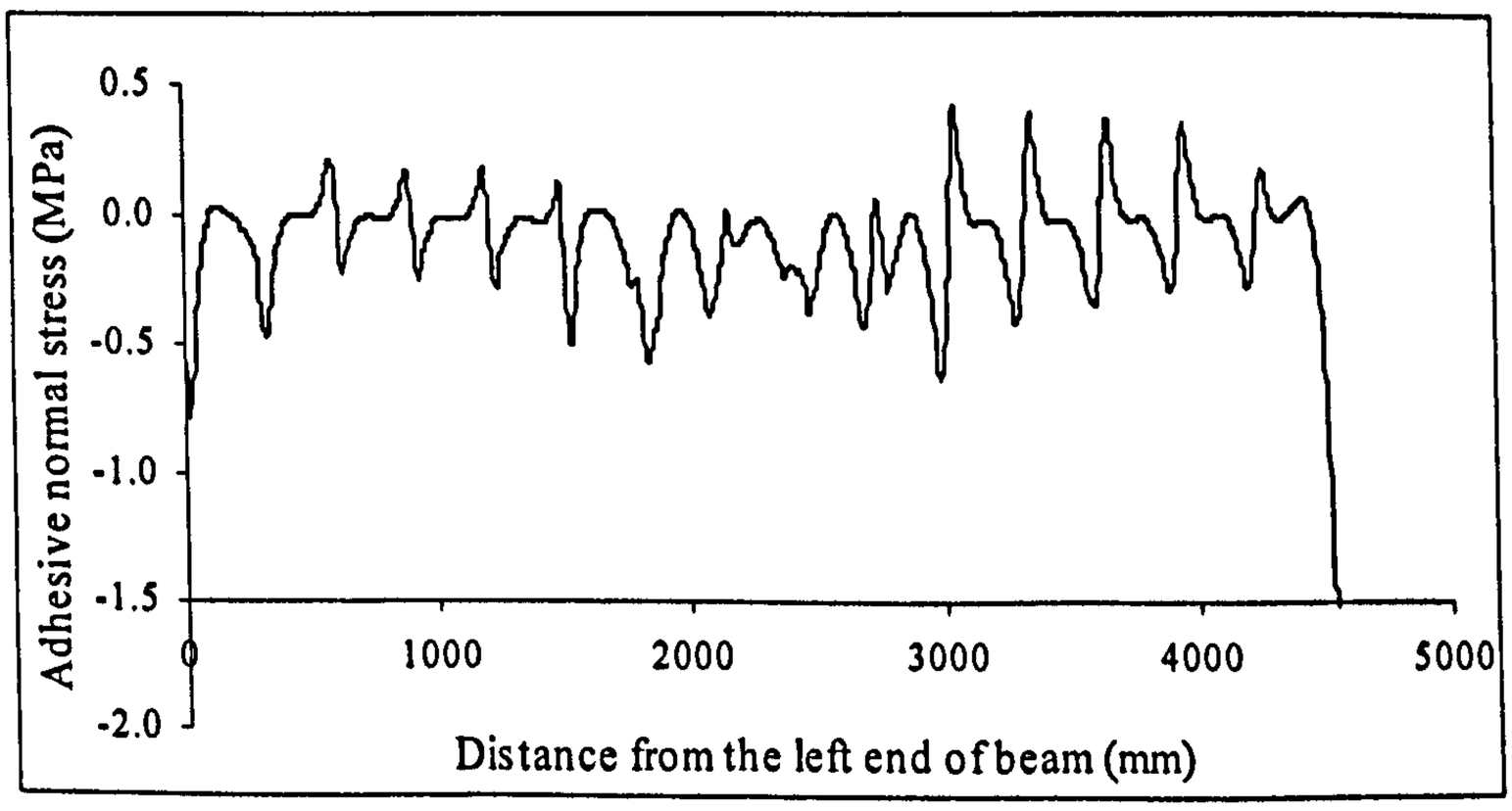

(b) Normal stress distribution (plus tensile, minus compressive)

Figure 6-16 Adhesive shear and normal stress distribution

Note that the distributions are not exactly symmetric because of the asymmetry of the above GFRP deck. The spikes of both shear and normal stresses may stem from the sudden injection of force from the GFRP decks webs. The joints of the GFRP web increase the adhesive layer stresses much more than other areas.

In some cases, people may use equivalent beam models with top & bottom flanges and web to predict the structural behaviours of such composite bridges. For example, Keller et al (2004) brought forward an approximated equation to calculate the shear stress in the adhesive layers:

$$\tau = \frac{VES_y}{EI_y b} \qquad \text{(Equation 6-3)}$$

Where V = shear force, b = cross-sectional width of the adhesive layer, ES_y = corresponding static moment of components, weighted by the Young's modulus, and EI_y = bending stiffness of components. The following two can be calculated by using equations below:

$$EI_y = \Sigma [\, E_i \times (I_{yi} + A_{si} \times z_{si}^2] \qquad \text{(Equation 6-4)}$$

$$ES_y = \Sigma [\, E_i \times A_{si} \times z_{si}] \qquad \text{(Equation 6-5)}$$

For simplification, both values for EI_y and ES_y are assumed to be constant along the longitudinal length of bridge deck in this model, Therefore, this model would not allow for spikes and normally end up as smooth lines somewhere between two envelope lines in Figure 6-16 (a). Because the spikes are significant in magnitude and could cause brittle fracture of structures, this modelling method may not be a safe approach to design connections.

For the cover concrete of the beam attached with the adhesive layer, the distributions of horizontal and vertical stresses are shown in Figure 6-17. The distribution of horizontal stress follows the shape of the global moment diagram. The maximum stress is near midspan and in compression with the value of around 4 N/mm^2. As for the vertical stress, the distribution is similar to the one of adhesive normal stress and the spikes could be found under the joints of the GFRP web.

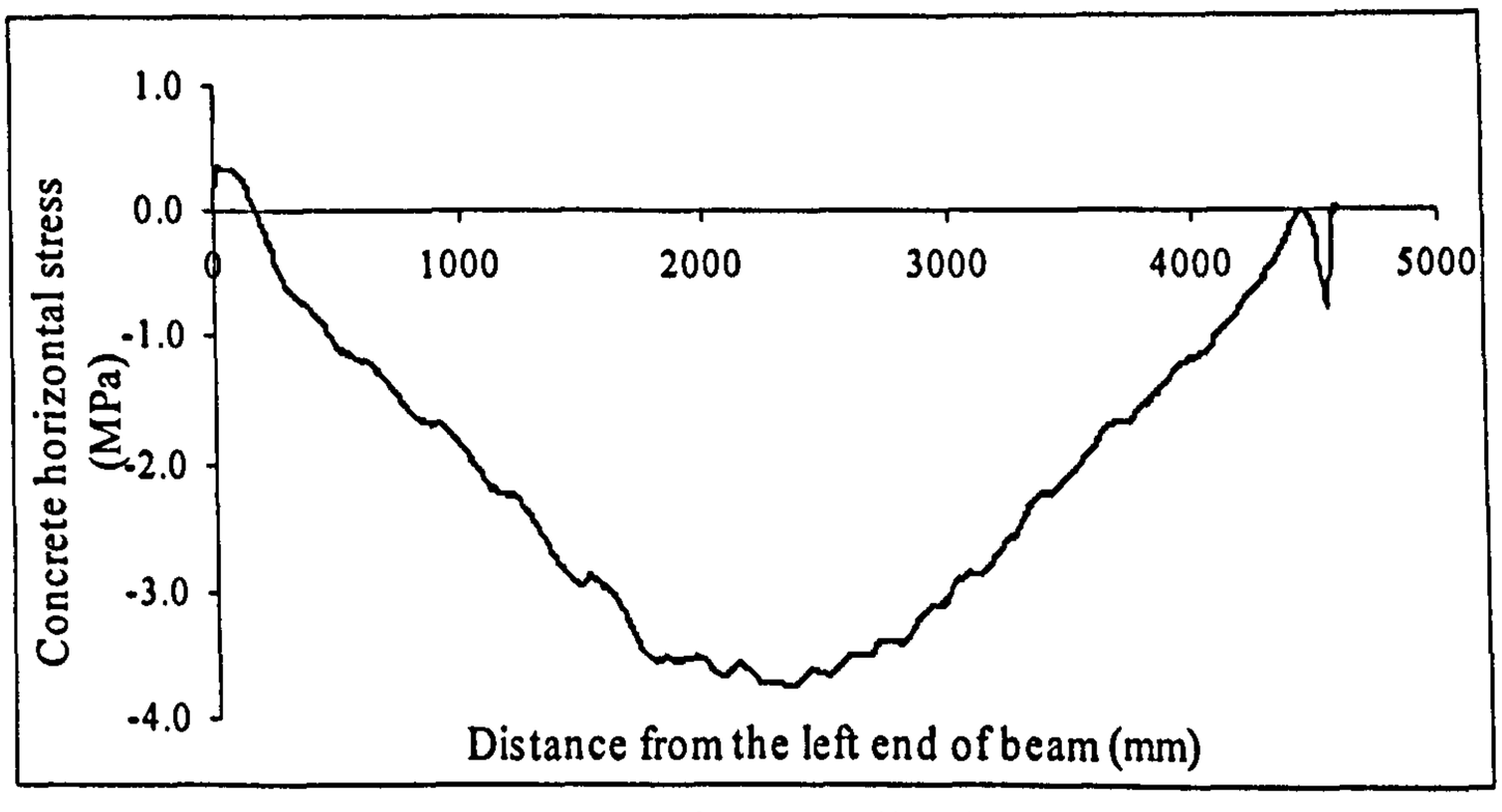

(a) Horizontal stress distribution

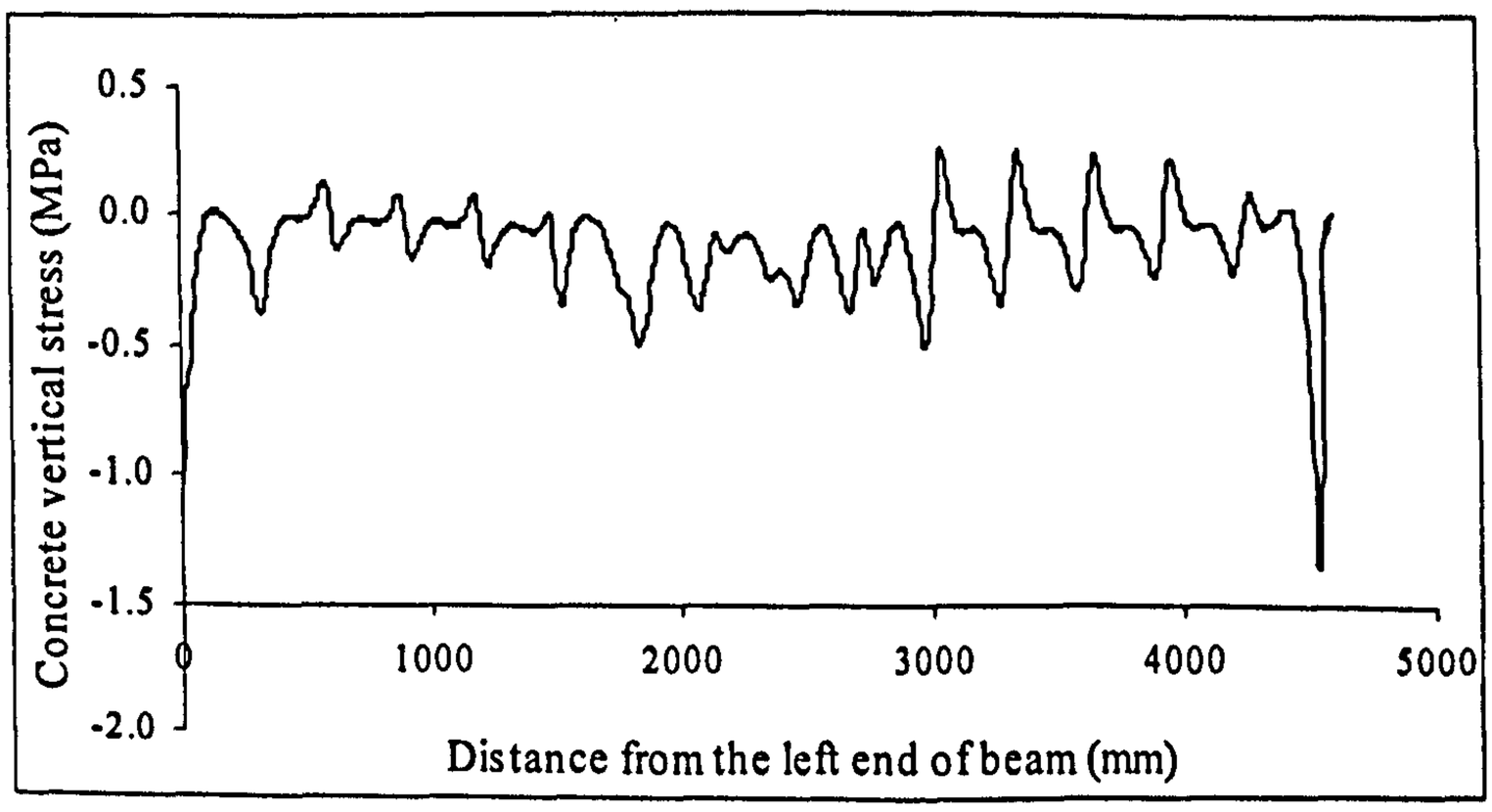

(b) Vertical stress distribution

Figure 6-17 cover concrete horizontal and vertical stress distribution

The distributions of axial stress for reinforcing steel bars both on the top and bottom are also shown in Figure 6-18. It can be seen that the axial stress of the top steel is

mostly in compression up to 13 N/mm^2, which means the neutral axis of the composite cross section composed of GFRP deck and RC beam is still below the top steel. The axial stress of bottom steel is in tension and increase rapidly within middle zone, where the bending moment is the highest and many smeared cracks were found in that area.

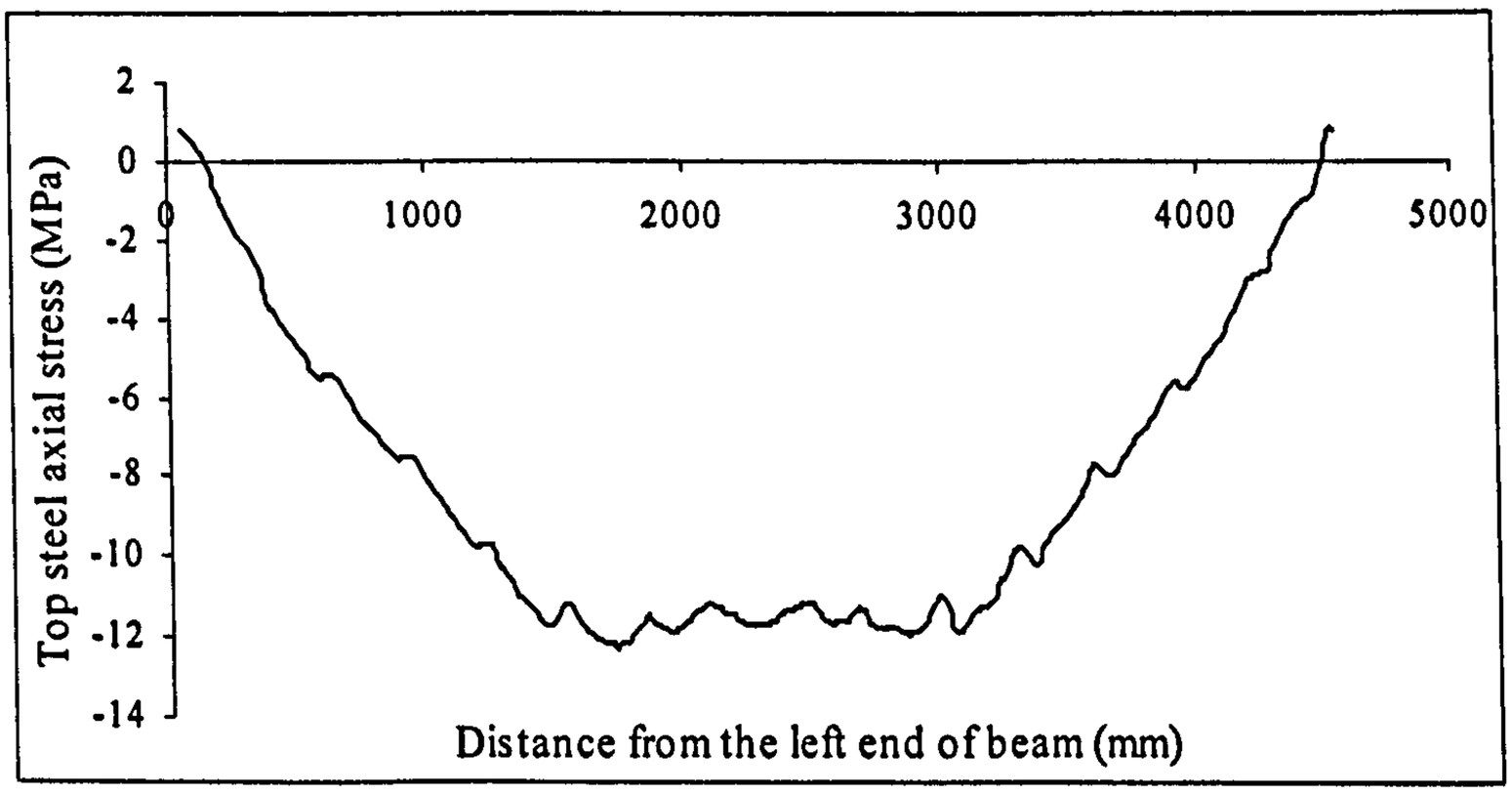

(a) Axial stress distribution for top steel reinforcing bar

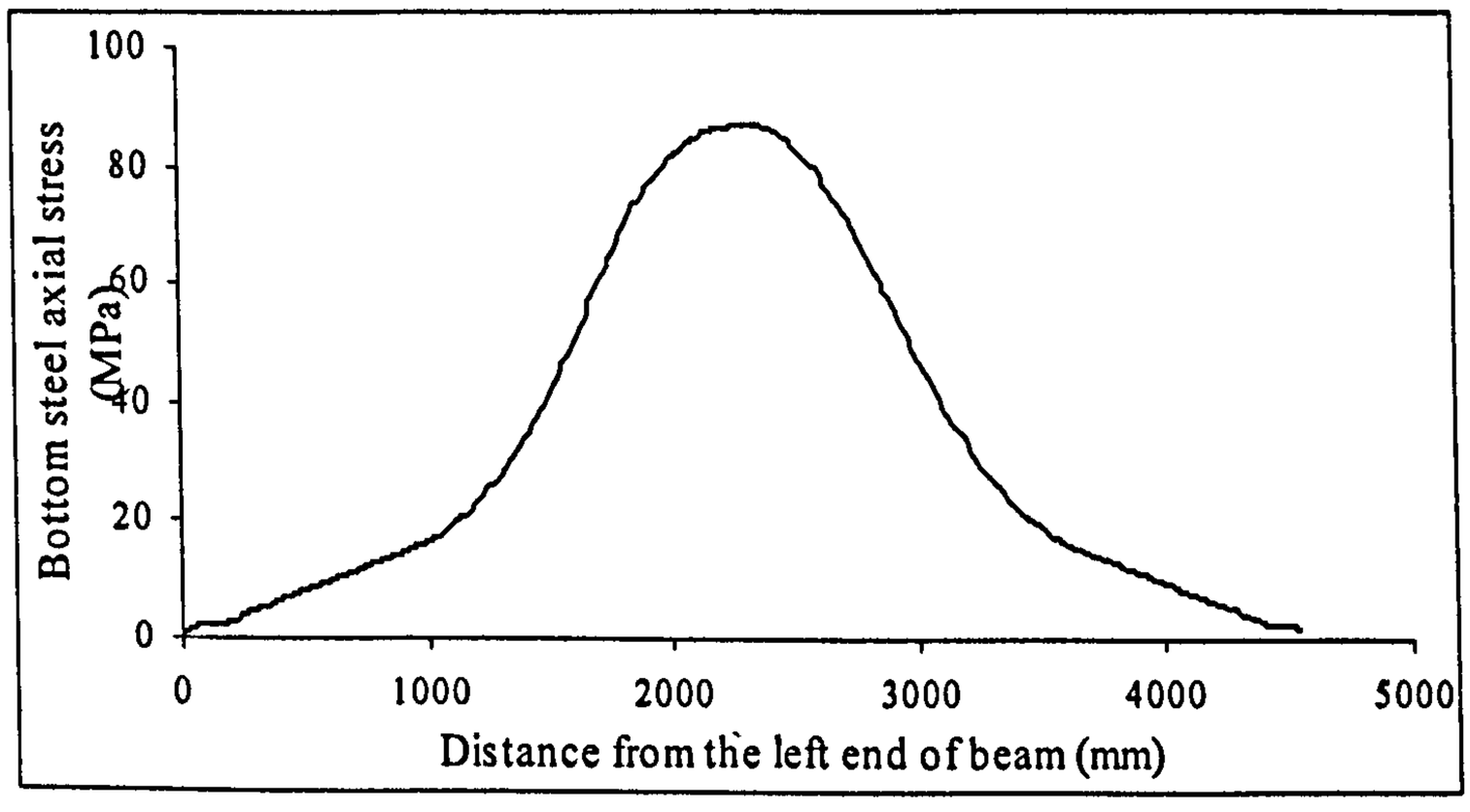

(b) Axial stress distribution for bottom steel reinforcing bar

Figure 6-18 top and bottom steel reinforcement axial stress distribution

6.3.5 GFRP bridge deck with initial crack in RC beam

Vertical cracks can be found near the highest tension area of the RC beam. To investigate the effect of initial crack on the behaviour of the composite bridge, one 1 mm crack was modelled in the concrete beam underneath the loading pad with the bottom steel reinforcing bar going through without breaking (Figure 6-19). The concrete elements inside the crack area were taken off from the analysed model to model the void crack.

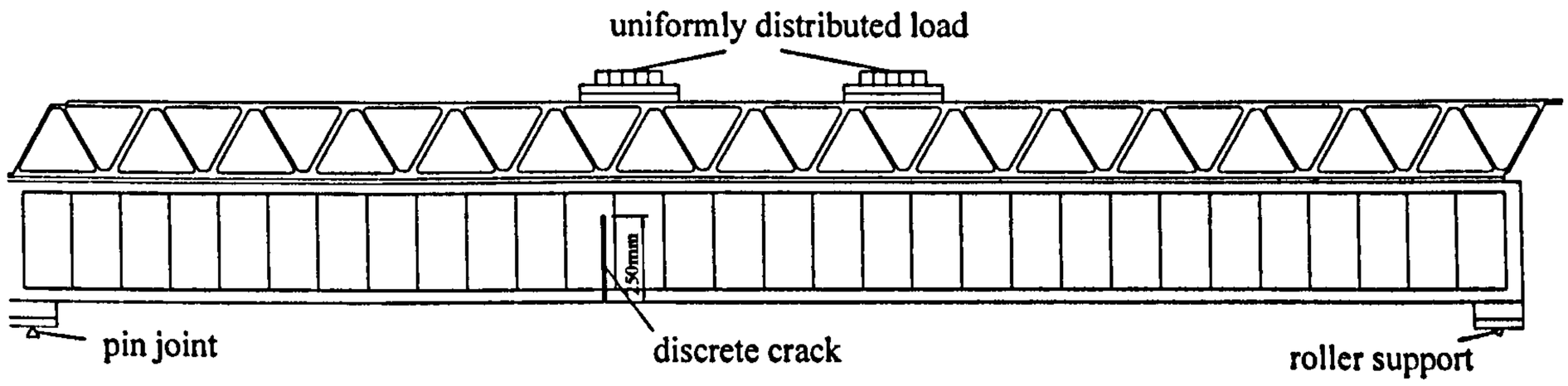

Figure 6-19 2D model of GFRP Bridge deck with initial discrete crack

Figure 6-20 to Figure 6-22 show the results from the FE analysis for the GFRP bridge deck with the initial crack under the load P = 100 kN.

It can be seen from Figure 6-20 that the adhesive stress distributions along the beam length are very similar to those in the model without initial cracks, except that the stress concentrations are found near the crack area. The adhesive shear stress above the crack location almost doubled the value, going up from around 0.45 N/mm^2 to 0.85 N/mm^2. Then the adhesive normal stress above the crack location varied from zero to around 0.5 N/mm^2, indicating the initial crack put a great influence on the stress distribution at this area.

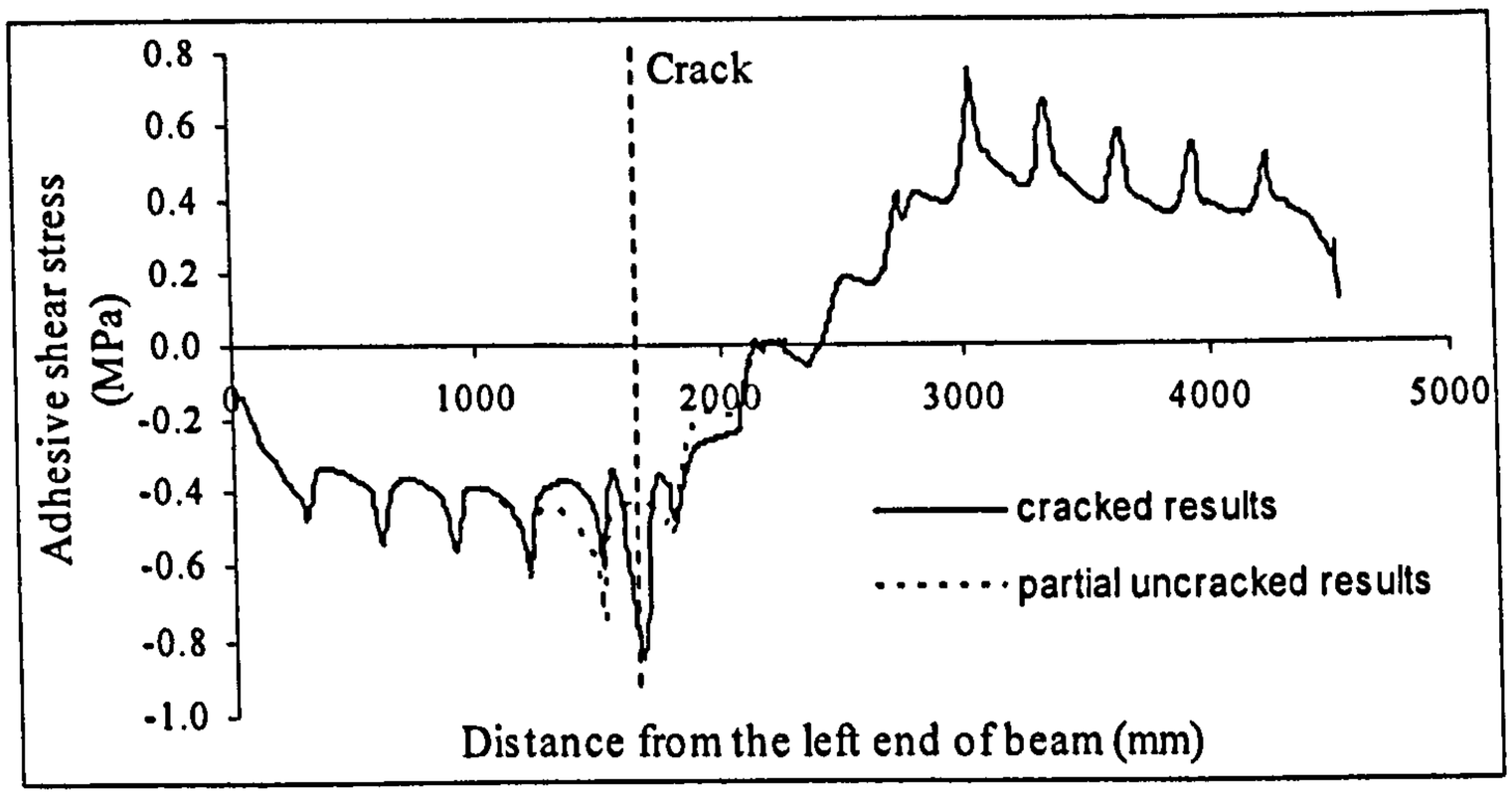

(a) Shear stress distribution

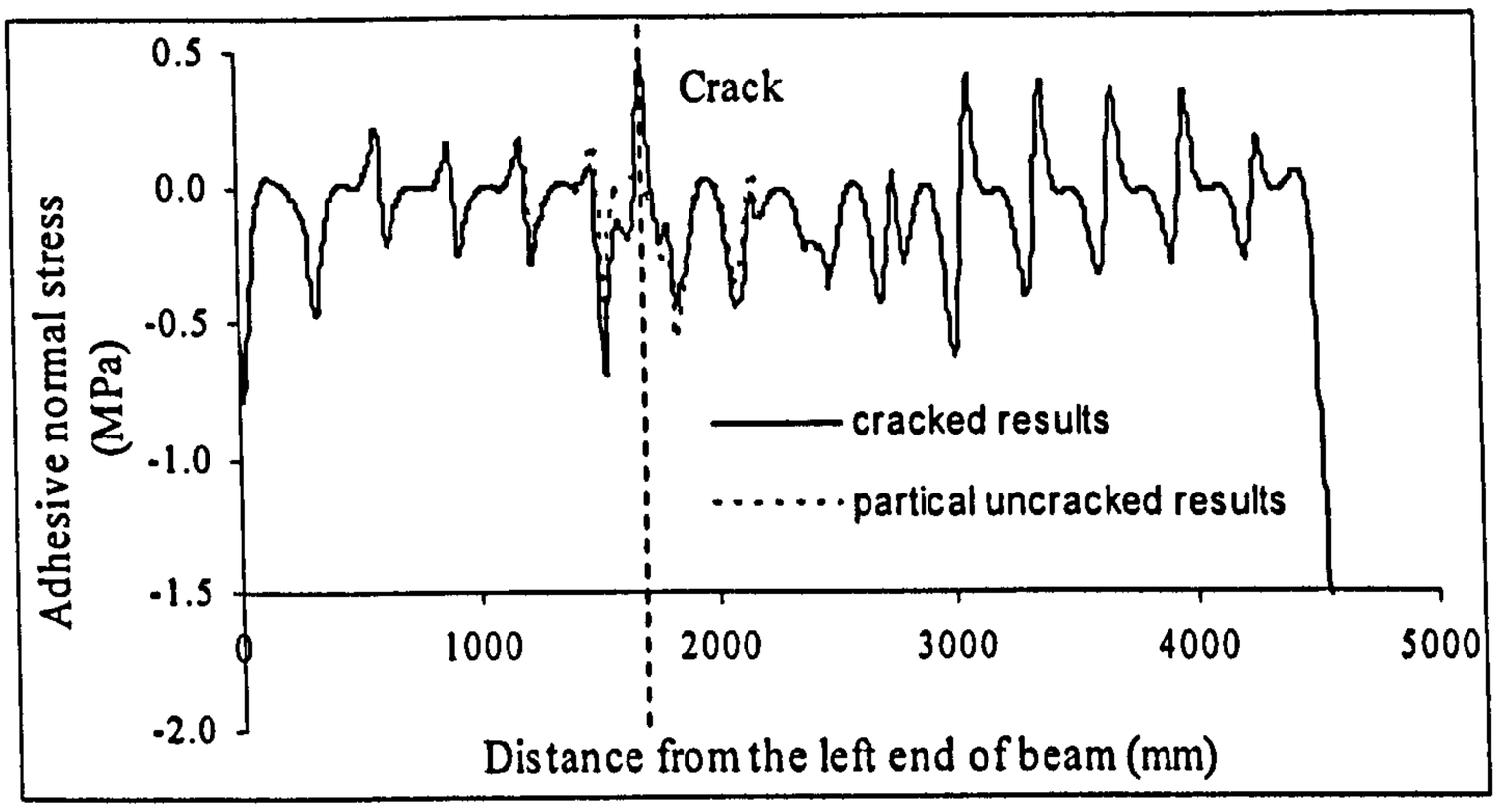

(b) Normal stress distribution

Figure 6-20 Adhesive shear and normal stress distribution

From Figure 6-21, obvious stress concentration was found near the crack area for the stress distribution of top cover concretes near adhesive layer. Figure 6-21 (a) shows that the horizontal stresses of the elements near the crack are in tension and the zero value at the crack is expected from the free crack face boundary condition.

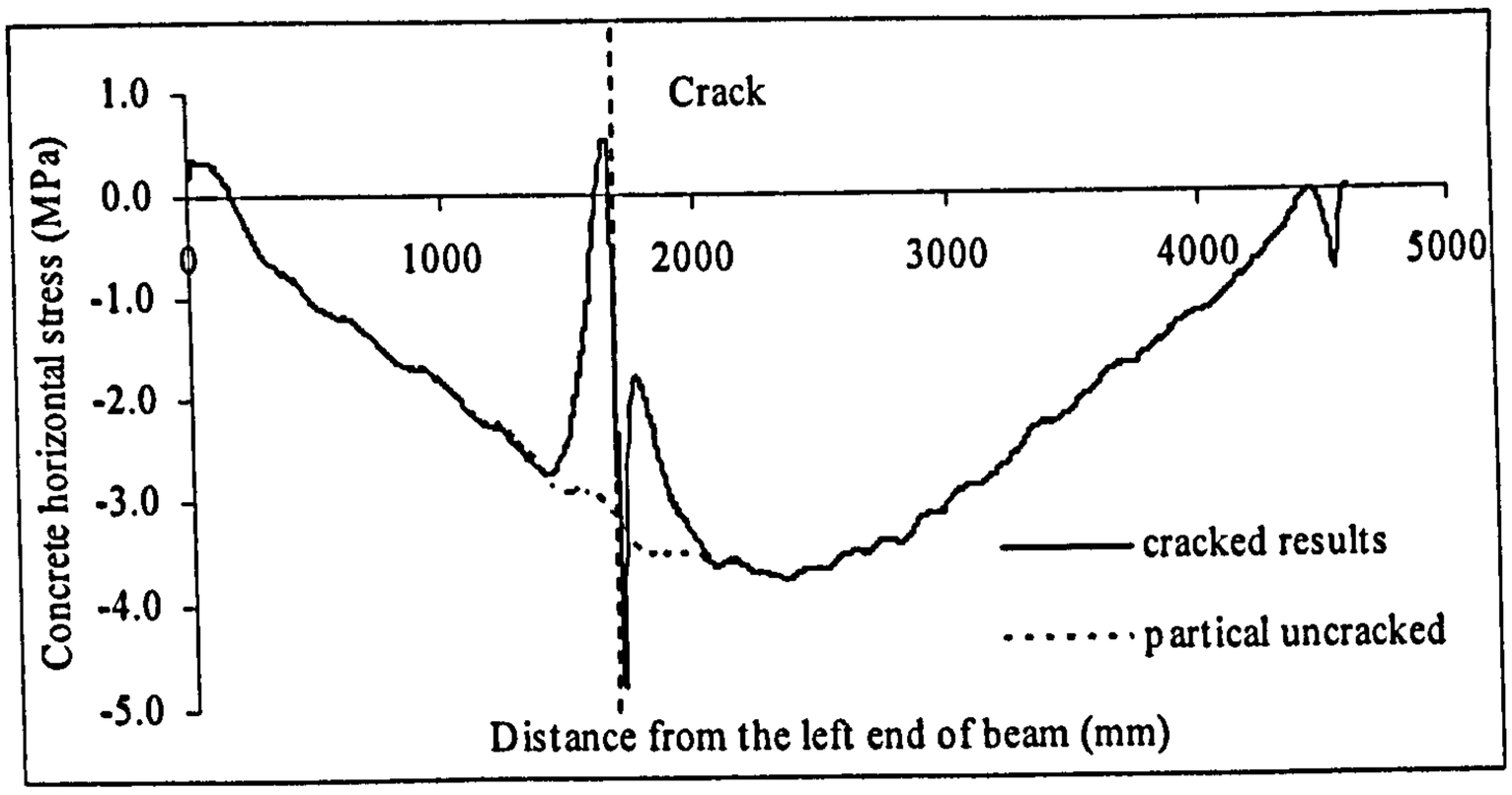

(a) Horizontal stress distribution

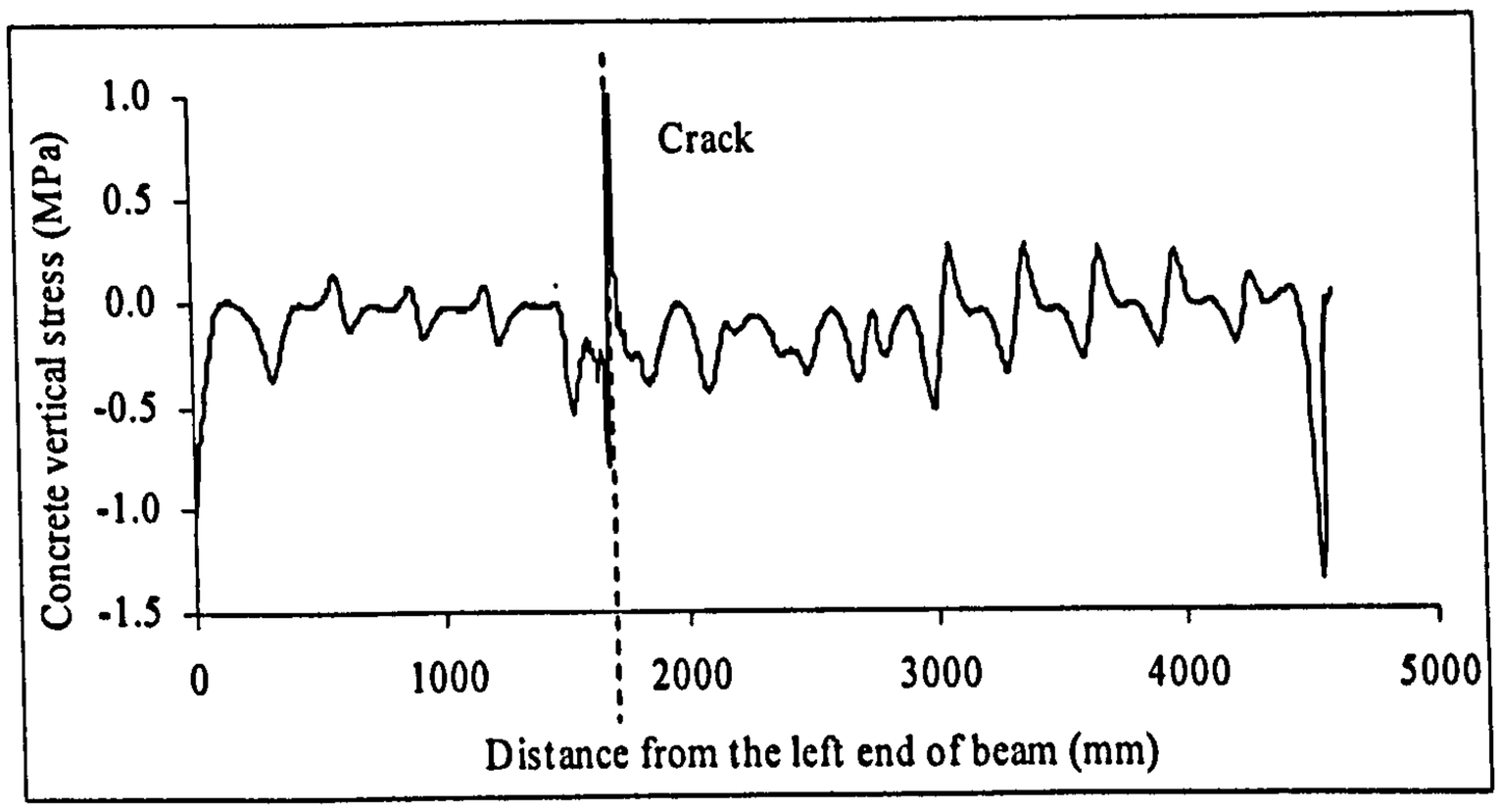

(b) Vertical stress distribution

Figure 6-21 cover concrete horizontal and vertical stress distribution

Figure 6-22 shows the axial stress distributions for both the top and bottom reinforcing steel bars. As can be seen from Figure 6-22 (a), the axial stress of the top steel near the crack area became tensile rather than compressive in order to preserve the increase of axial stress in the bar towards the crack from both sides, pushing the neutral axis up above the top reinforcing bar near the crack area. The maximum tensile stress is as high as 50 N/mm^2. For the same reason, a spike was found for the bottom steel bar near the cracked area in Figure 6-22 (b). The tensile stress in that area almost doubled the value by increasing from around 60 N/mm^2 to 120 N/mm^2. Hence

the initial crack makes a big difference on the stress distribution in the original structures.

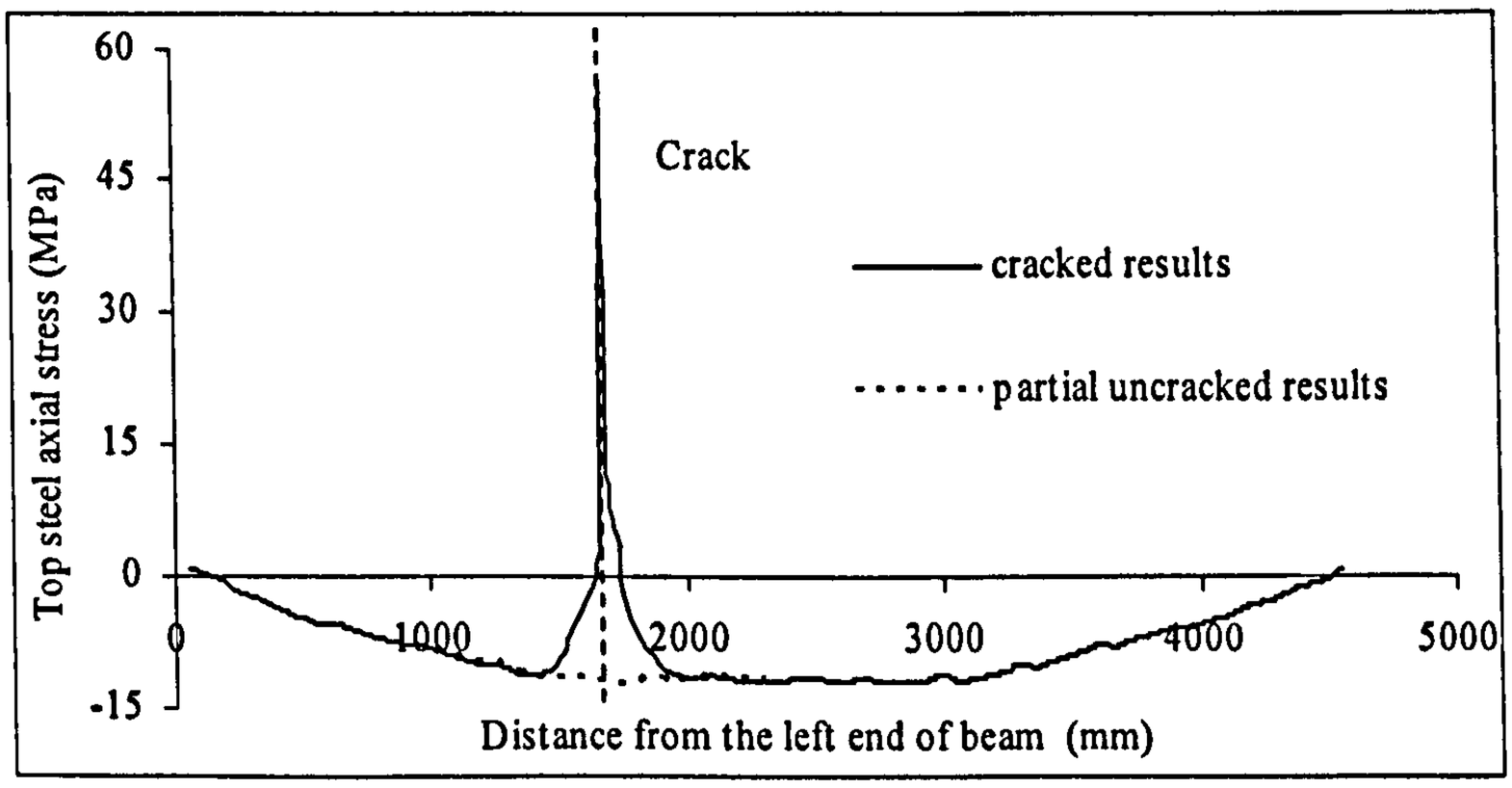

(a) Axial stress distribution for top steel reinforcing bar

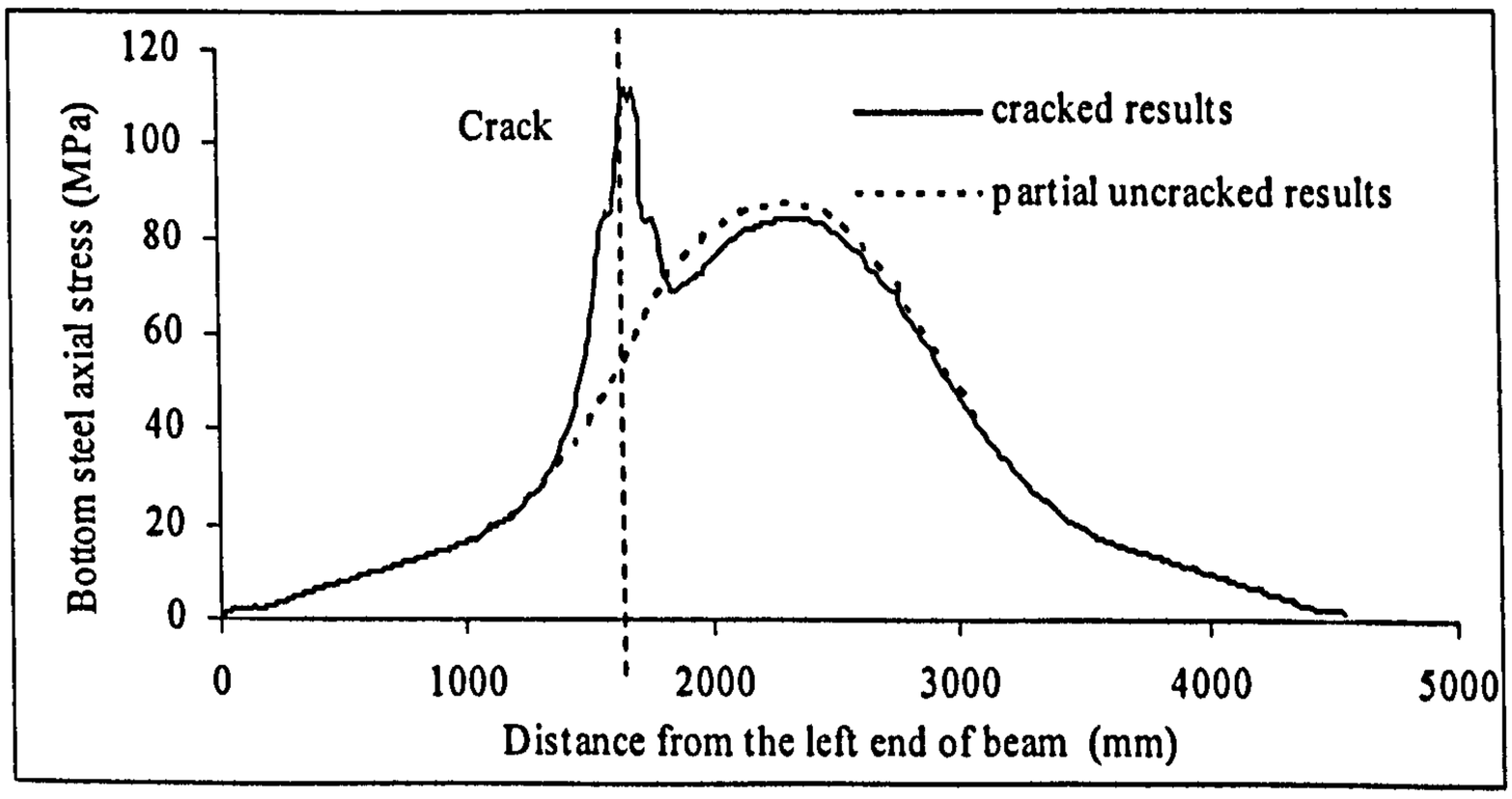

(b) Axial stress distribution for bottom steel reinforcing bar

Figure 6-22 Top and bottom steel reinforcement axial stress distribution

6.4 Double pullout test by Kankam (1997)

6.4.1 Geometry and material properties

A few 3D modelling investigations have been done in the earlier chapters, in which the specimens were modelled by using 8-noded brick elements. In certain situations, however, it maybe inappropriate to assume the rigid connection of nodes between

FRP bars and surrounding material because there is slip between them in addition to the fracture of adhesive itself. The attention is then brought forward on the simulation of this bond-slip relation between FRP and adhesive rather than assuming rigid bond.

A tentative study was then done by Kankam (1997) on a double pullout specimen (150 mm square) with a transverse anchor bar in the centre. The embedment was chosen to be 200 mm to represent a crack spacing to allow a satisfactory variation of stress in the reinforcing bar. The set up of the specimen and material properties according to the experimental data are shown in Figure 6-23.

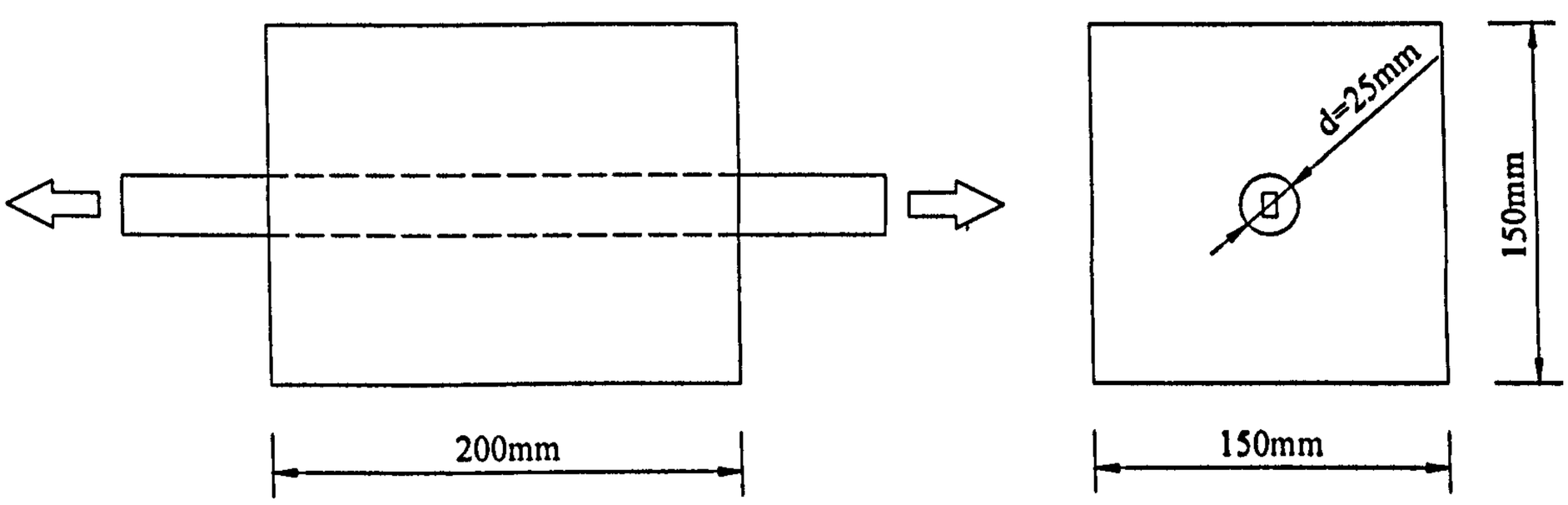

Concrete prism: $E_c = 20$ kN/mm^2, $f_{cc} = 33$ N/mm^2, $f_{tc} = 3$ N/mm^2;

Steel bars: $E_s = 200$ kN/mm^2, $f_{ys} = 500$ N/mm^2.

Figure 6-23 Set up of double pullout test

6.4.2 Measurement and calculation of experimental data

According to Kankam (1997), the strain gauges were put on the steel bar and the steel strains under different load stages are measured. Then the local bond stresses and local slips are computed based on the strain distributions along the bond length.

Considering a single circular bar of diameter D, the local bond stress τ can be expressed as follows:

$$\tau(x) = \frac{D}{4} E_s \frac{d\varepsilon}{dx} \qquad \text{(Equation 6-6)}$$

Where E_s is the modulus of bar, ε is the axial strain of the bar and x is the coordinate along the bond length, respectively.

With discrete strain readings, the above expression for the shear stress located half way between two strain gauges becomes:

$$\tau_{n+1} = \frac{D}{4} E_s \frac{\varepsilon_{n+1} - \varepsilon_n}{\Delta l} \qquad \text{(Equation 6-7)}$$

where Δl is the distance between two gauges. Using (Equation 6-7), Kankam (1997) deduced shear bond stresses based on the reinforcing steel bar strain data.

Local slip is defined as the relative displacements between the steel bar and the concrete prism. The distribution of slip along the embedded length of reinforcing bar was obtained by numerical integration of the steel strain curve, then anchored midpoint being the origin of the curve (i.e., zero slip). The contribution of concrete strain was neglected. This assumption resulted in at most 10% error in slip within the service range when an equivalent (transformed) concrete section was used to evaluate the concrete strain, varying linearly from zero at the ends to a maximum at the anchored midpoint (Kankam (1983)). The slip then can be expressed as

$$s(x) = \int_0^x \varepsilon(x) dx \qquad \text{(Equation 6-8)}$$

With discrete strain readings, the above expression becomes:

$$s_{n+1} = s_n + \frac{1}{2}(\varepsilon_n + \varepsilon_{n-1})\Delta l \qquad \text{(Equation 6-9)}$$

Then the relationship between bond stress and slip at different positions along the bar are examined. Six different positions were selected at 12.5 mm intervals along the embedded length of bar between the loaded end and the anchored midpoint. For each position the bond stress and slip values were obtained from the respective curves corresponding to several increments of tensile load. Thus the pertinent data for the relationship between bond stress and slip were obtained for each of the positions. Figure 6-24 shows the local bond-slip relationship for the specimen. It is evident that the bond stress for a given amount of slip increased in magnitude with the distance from the loaded ends of specimen. This would be expected due to the greater longitudinal steel stress at the loaded ends.

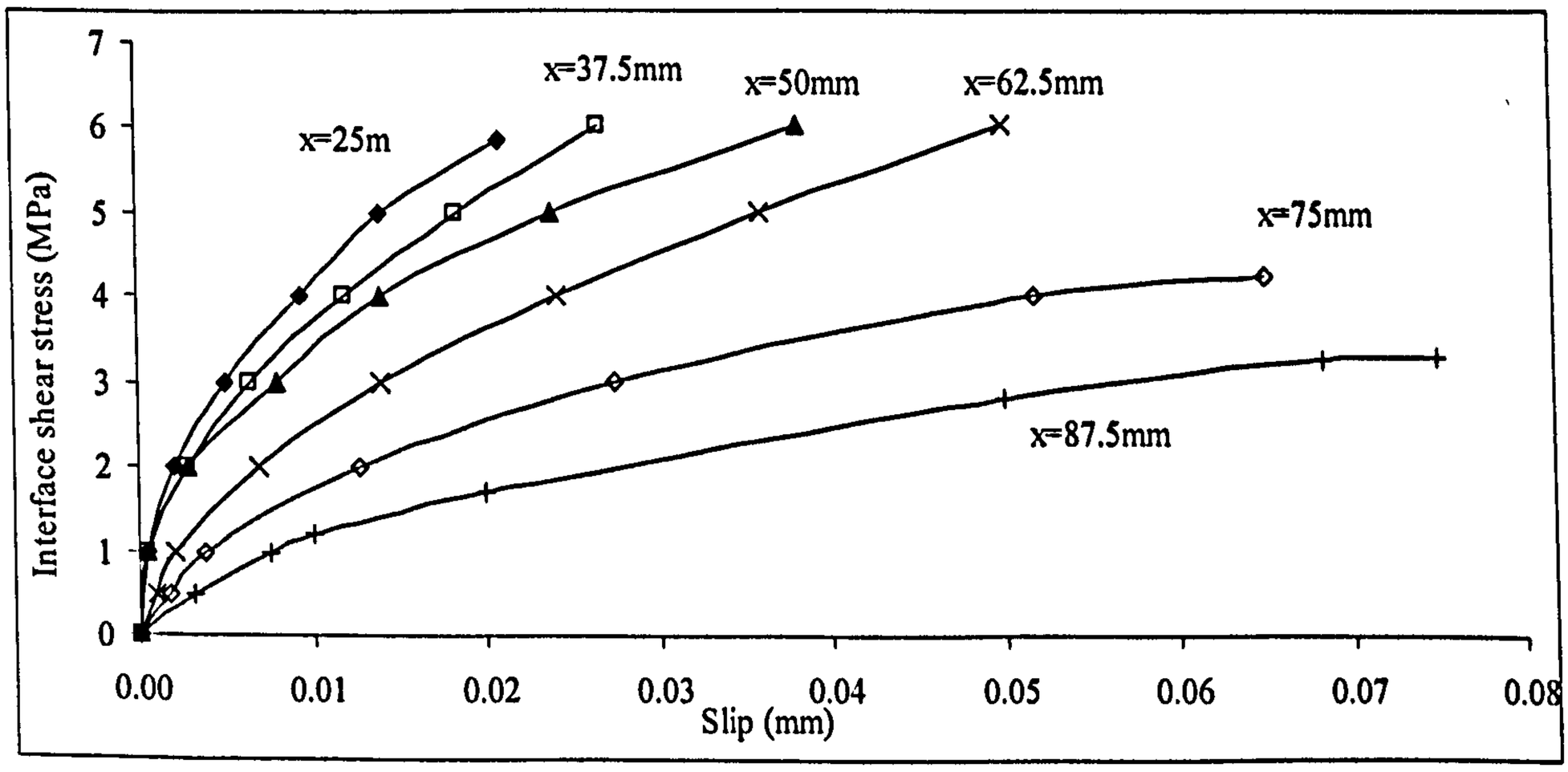

Figure 6-24 Bond-slip responses between concrete and steel bar

6.4.3 3D FE analyses of the specimen

Due to the symmetry of the structure, only one eighth of the prism was analysed with the appropriate boundary conditions and the applied load (Figure 6-25). The concrete

prism, steel bars were modelled by the 8-noded brick element HX24L. The 8-noded surface interface element Q24IF (Figure 6-26) was used to connect the concrete and steel elements so that their bond-slip behaviour can be captured. The element describes a relation between the tractions and the relative displacements across the interface. The bond-slip responses of the interface element were varied along the bond length according to experimental data, as shown in Figure 6-24.

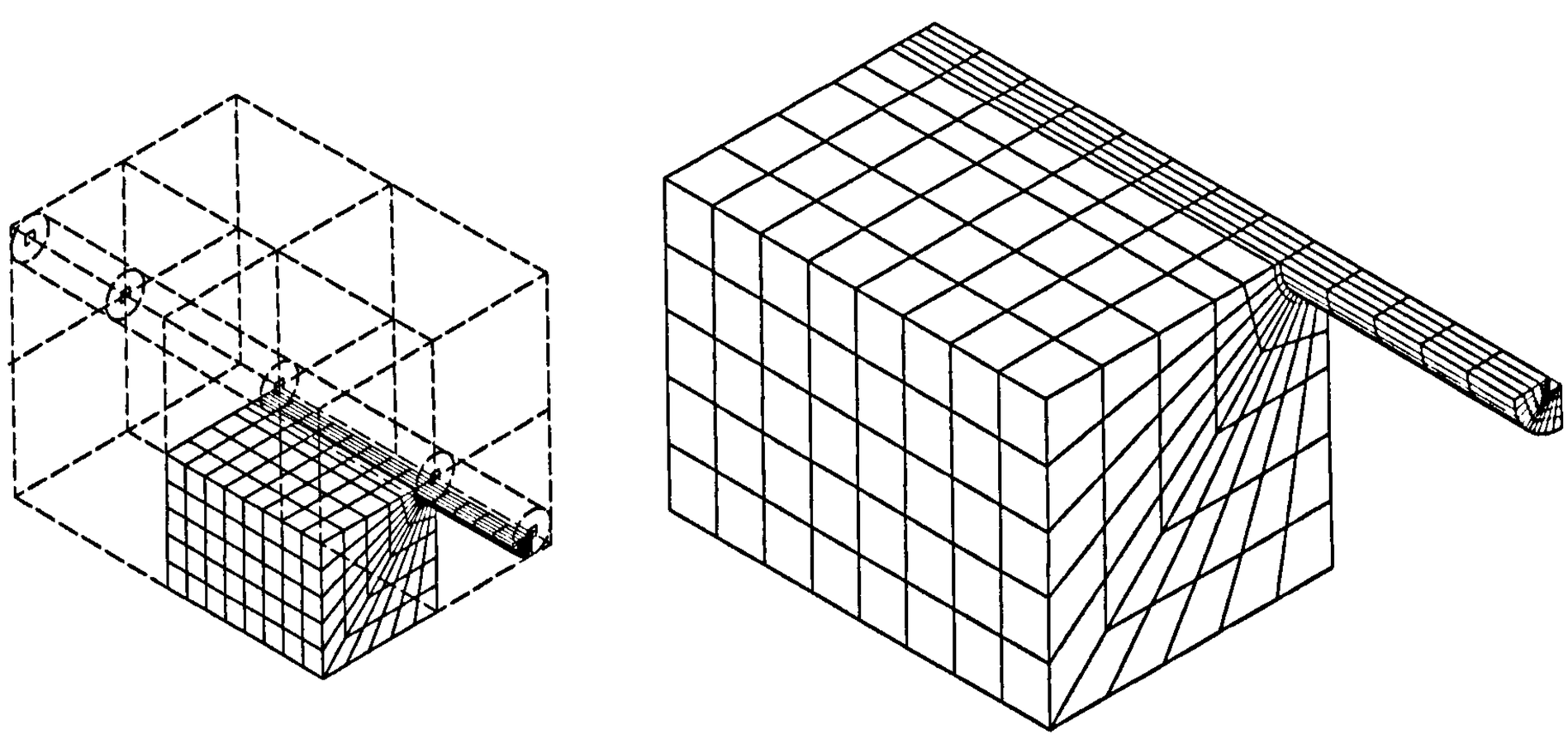

Figure 6-25 Mesh of double pull out test

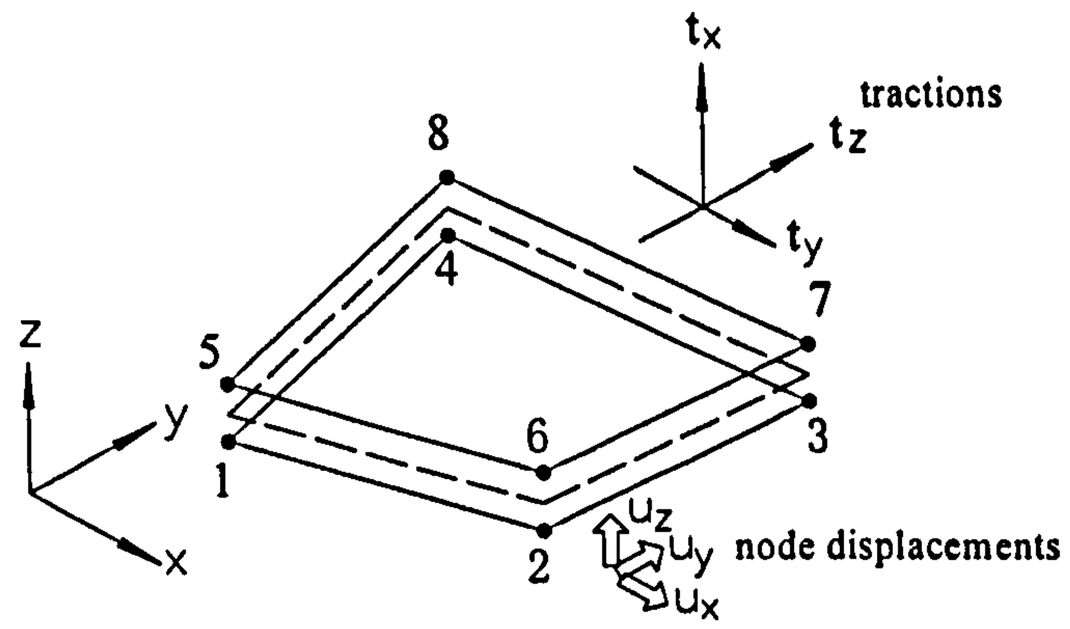

Figure 6-26 Q24IF surface interface element

Figure 6-27 shows curves of the steel strain distribution along the length of steel bar for several static tensile load stages. Although the specimens are designed to be

symmetric, the strain distributions on both sides are not exactly the same as each other. Therefore, the experimental data from both left and right sides are presented in the same quadrant and compared to the FEA results.

The typical strain distribution curve indicates a general decrease in slope towards the central anchored point. The differences of strains between the ends and the central anchored point showed a consistent increase with an increasing applied load. The FEA results agree very well with the experimental data while the gradients of experimental plots are slightly greater than those of FEA results.

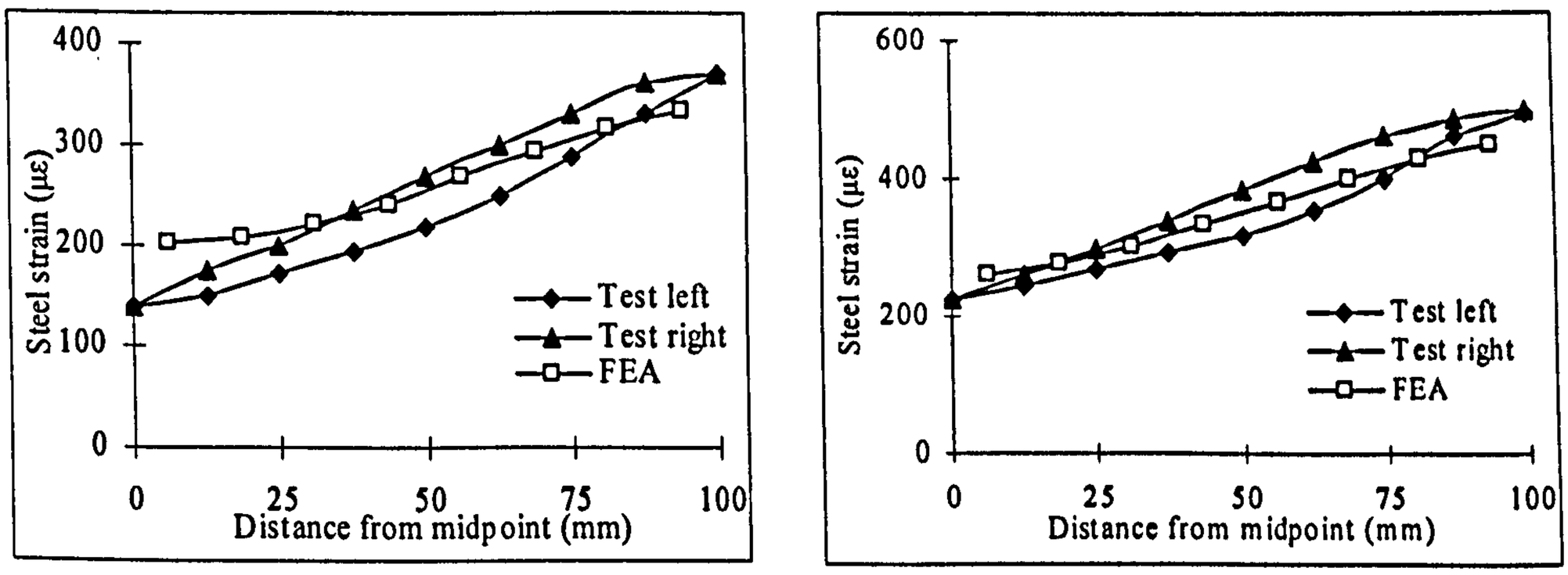

(a) P = 30 kN

(b) P = 40 kN

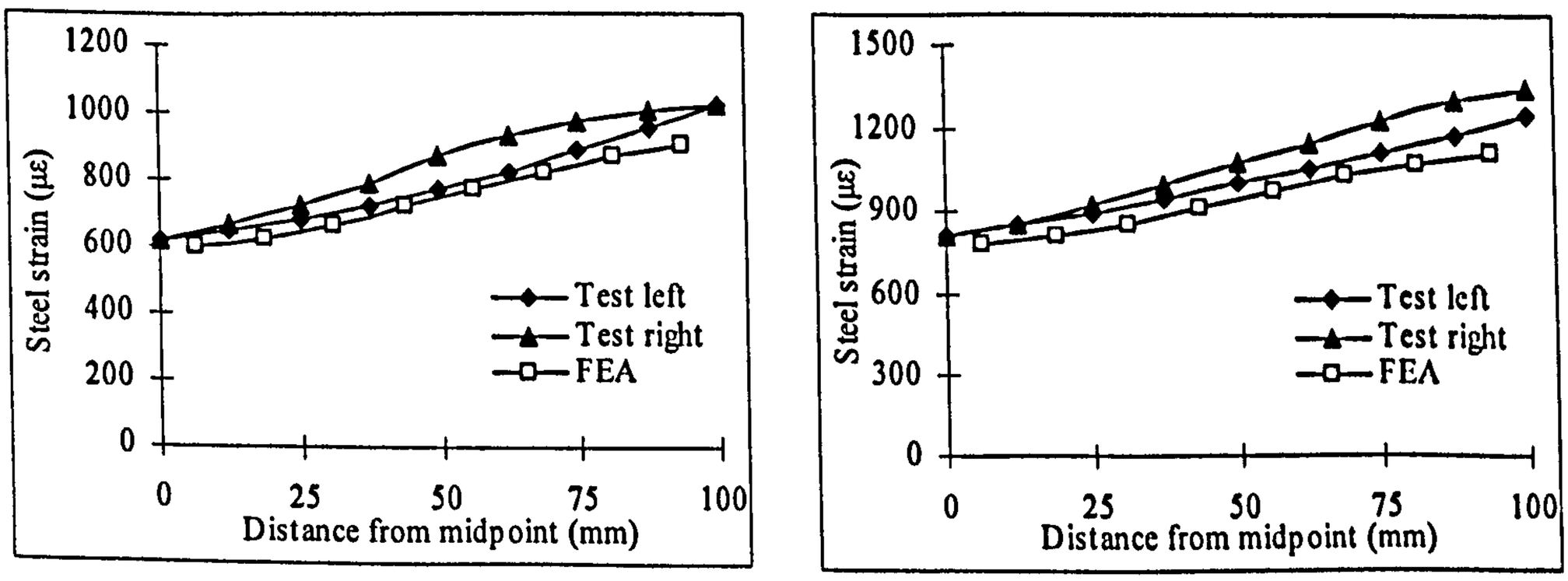

(c) P = 80 kN

(d) P = 98 kN

Figure 6-27 Steel strain distribution along the length of steel bar

Using Equation 6-4, the shear bond stresses deduced from the experimental reinforcing steel bar strain data for different applied loads are shown in Figure 6-28 (a) to (d). Also shown in Figure 6-28 are the FE predicted bond stresses. As the tensile load increased, the form of the distribution curve generally changed. Nevertheless, it was impossible to describe the curves by any simple consistent form. In general, reasonable agreements in magnitude between FEA results and experimental data are found but fluctuating shapes are different.

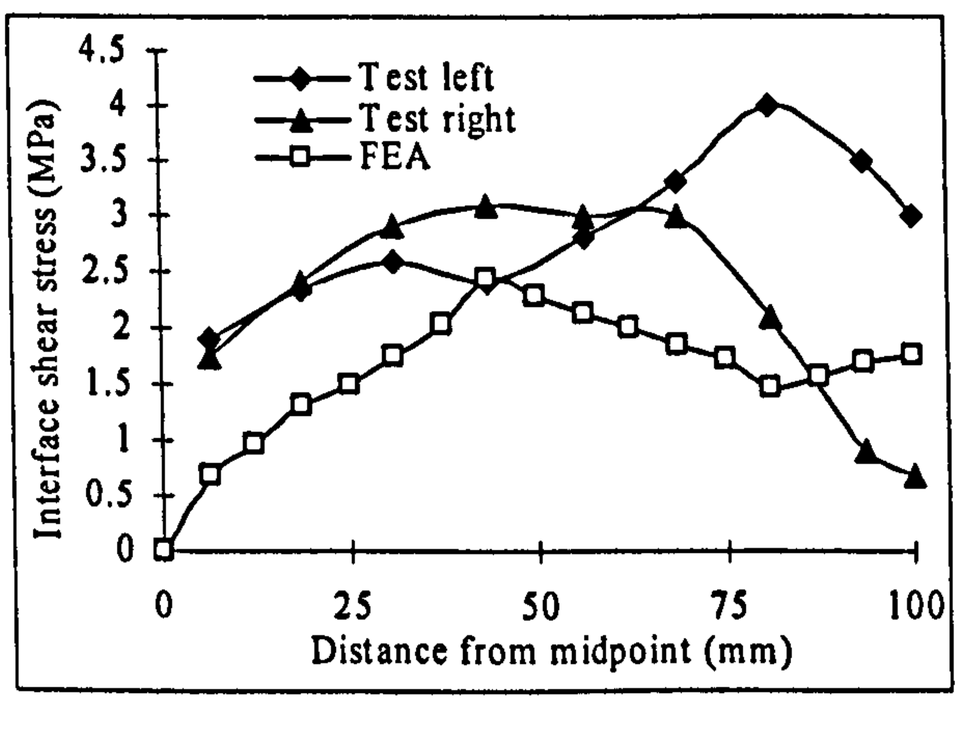

(a) P = 30 kN

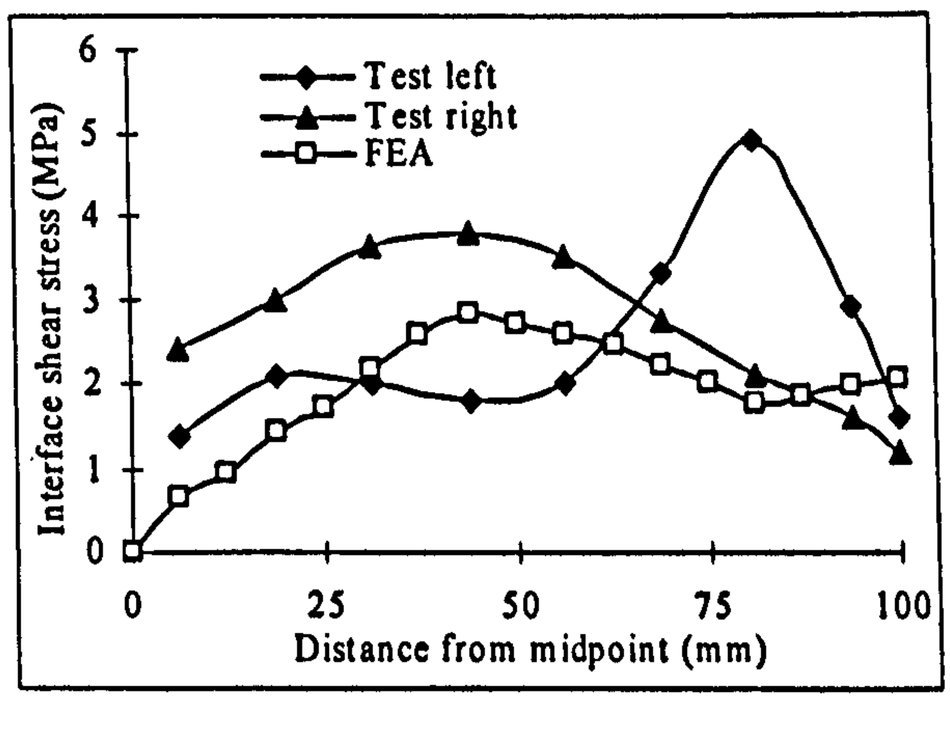

(b) P = 40 kN

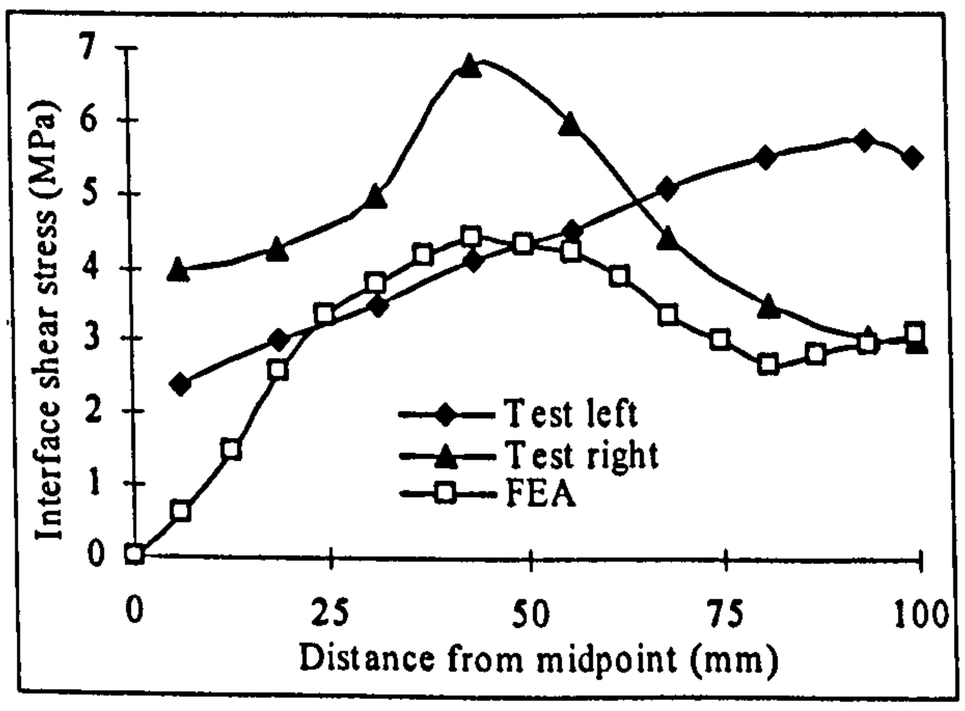

(c) P = 80 kN

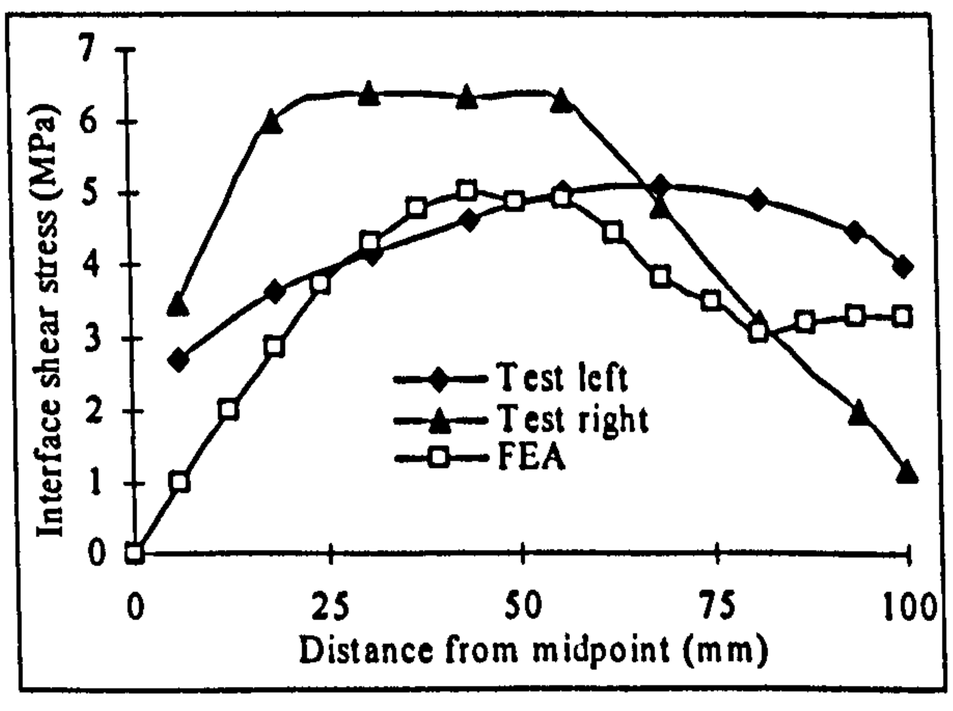

(d) P = 98 kN

Figure 6-28 Bond stress distribution along the length of steel bar

Based on Equation 6-6, the slip could be deduced from the experimental reinforcing steel bar strain data for different applied loads. Both the deduced experimental data

and FEA results of slips are shown in Figure 6-29. As can be seen, the FEA results are constantly smaller than the experimental data, which may be due to the 10% error from the neglecting of concrete strain in experimental data.

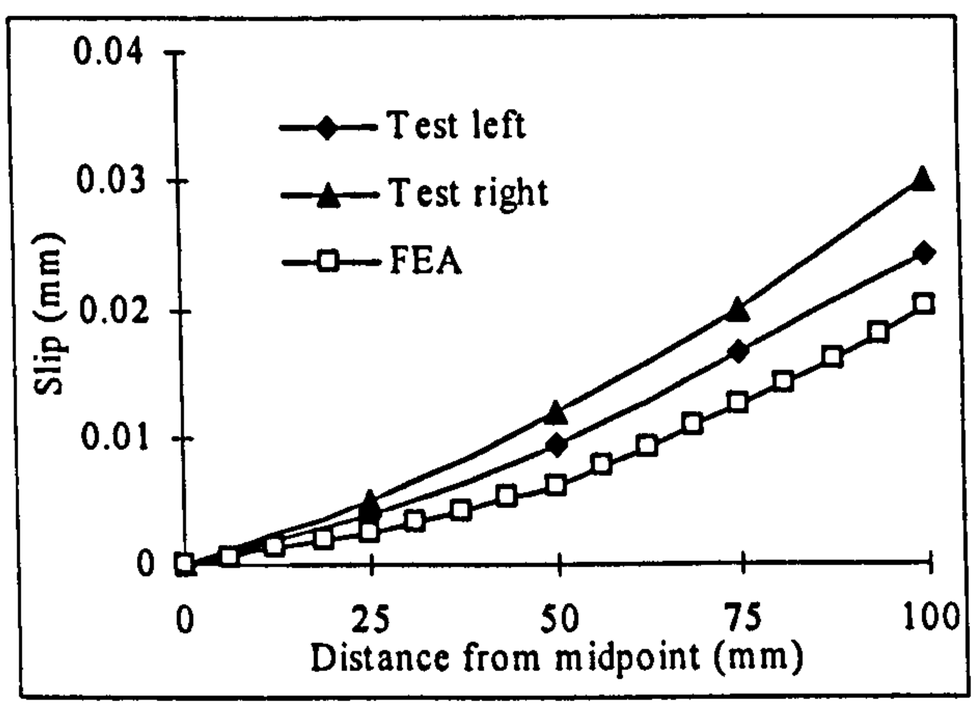

(a) P = 30 kN

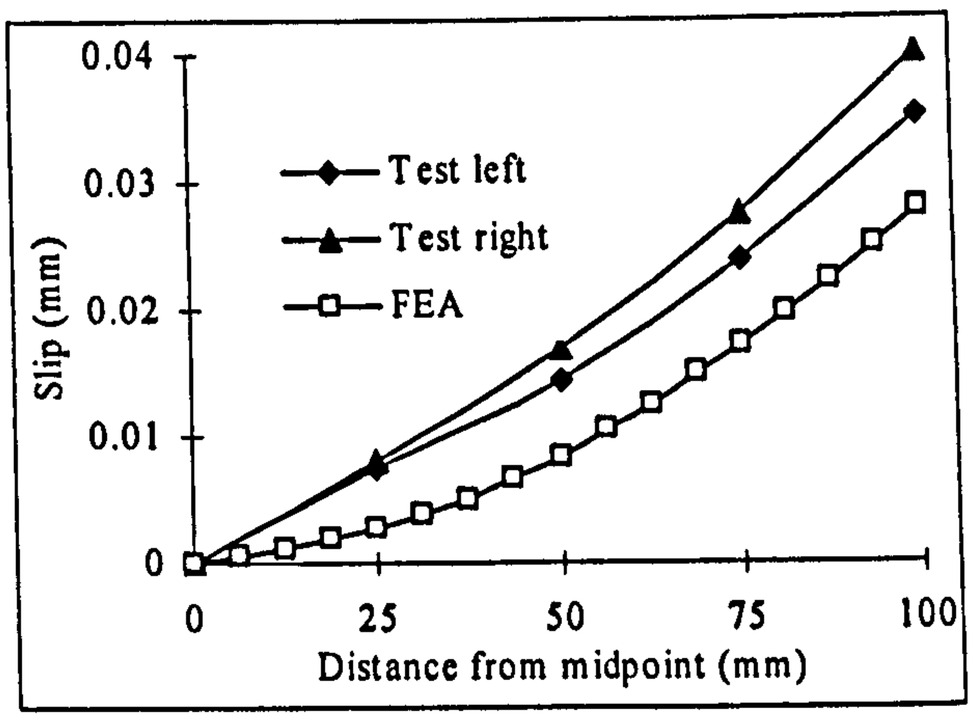

(b) P = 40 kN

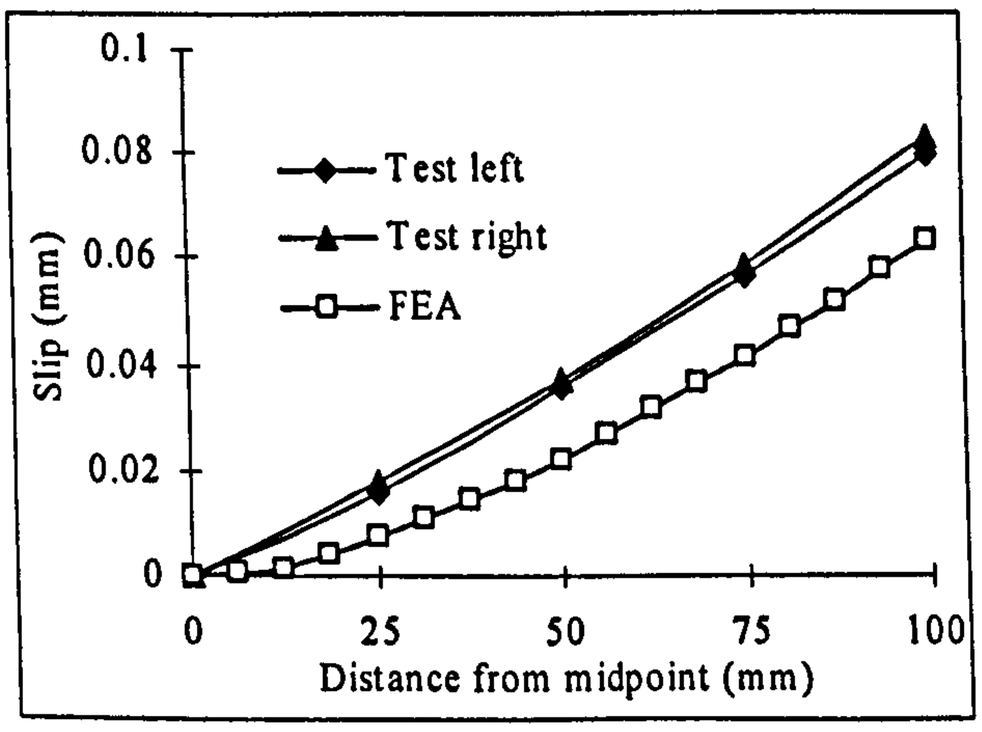

(c) P = 80 kN

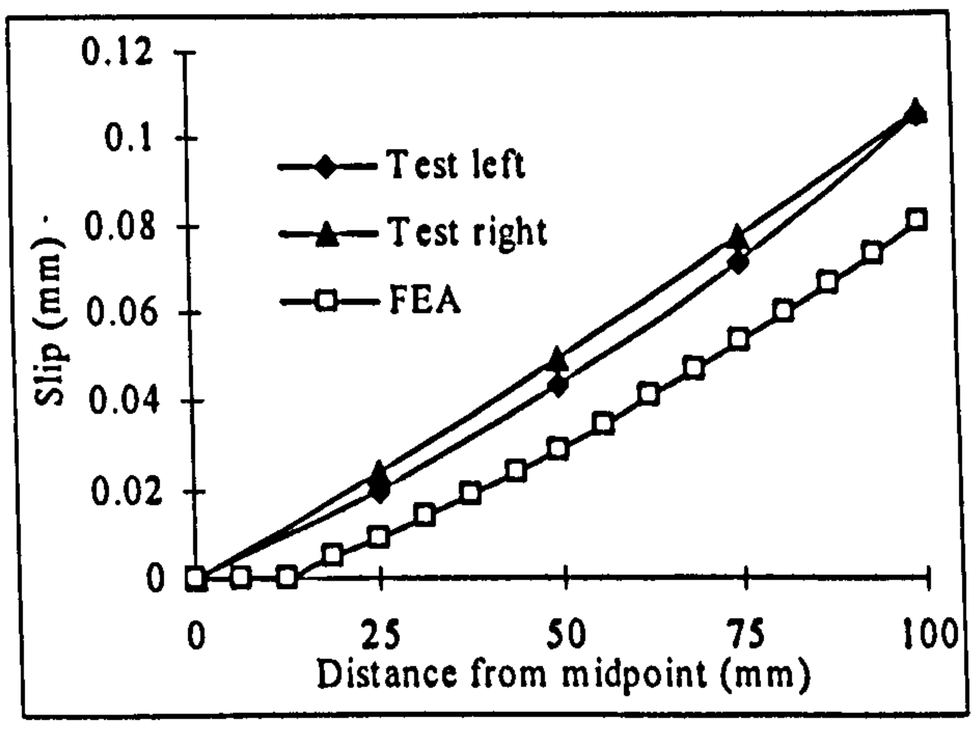

(d) P = 98 kN

Figure 6-29 Steel bar slip distribution along the length of steel bar

6.4.4 Parametric study

In the general FEA prediction studies, it could be inconvenient and inappropriate to define various bond-slip relationships for different locations of embedded strengthening bars. For simplification, one specific bond-slip response should be used to uniformly represent the behaviour of the interface elements along the bond length.

A parametric study was then performed by using alternative bond-slip responses for the interface elements. In this case, two bond-slip response plots were chosen from the experimental data and presented in Figure 6-30. As can be seen, uniform 1 has larger gradient than uniform 2 which means under the same bond stress, the slip in uniform 1 is smaller than that in uniform 2.

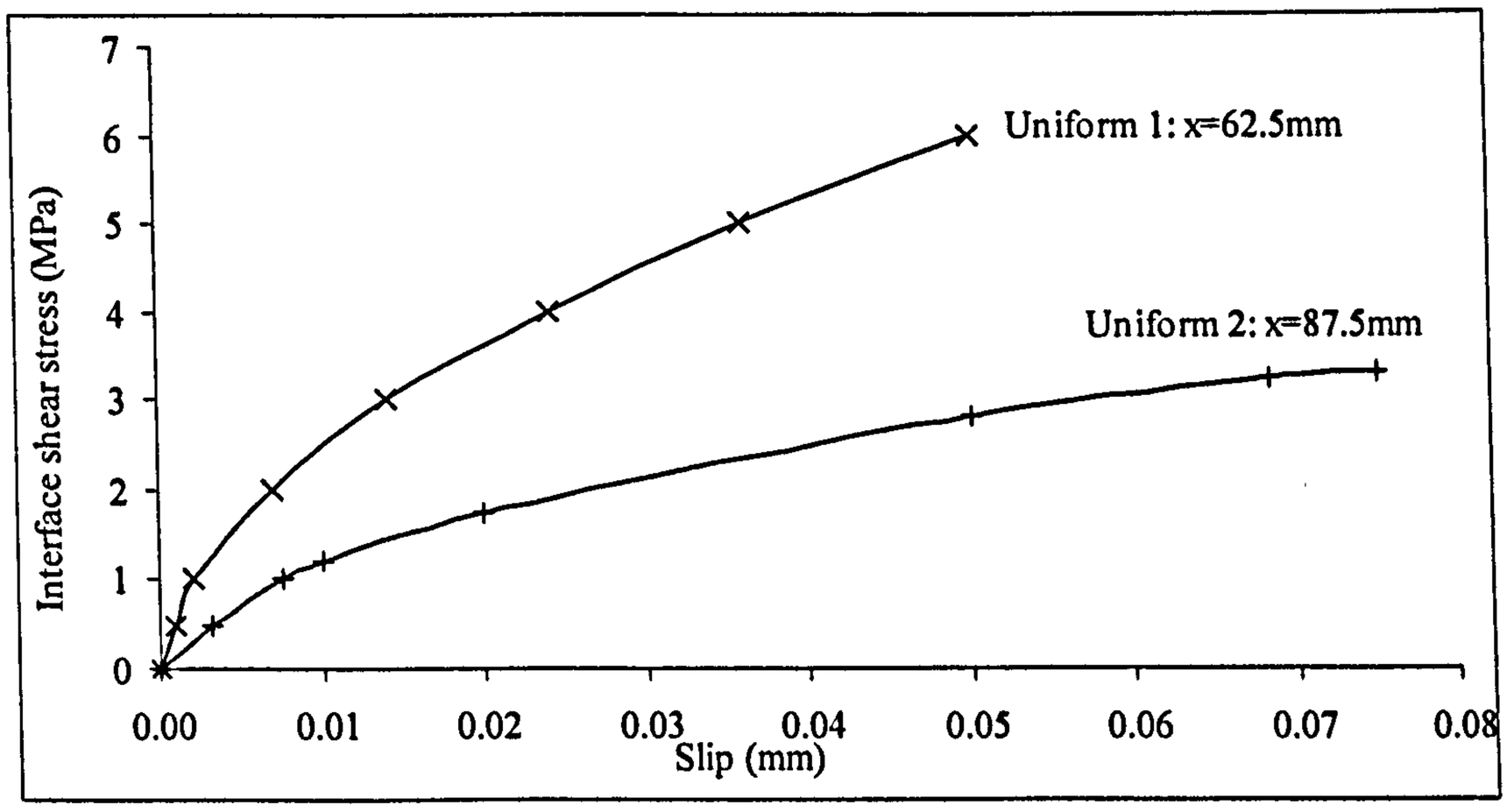

Figure 6-30 Two bond-slip responses used in parametric studies

Their computational results are presented and compared with those from FEA model with varying bond-slip responses. The comparisons are shown in Figure 6-31 to Figure 6-33.

As can be seen from Figure 6-31, the plots are relatively close to each other while the model with various bond-slip responses stay between the models with uniform bond-slip responses. Basically, the model with stiffer bond-slip relationship shows smaller steel strains.

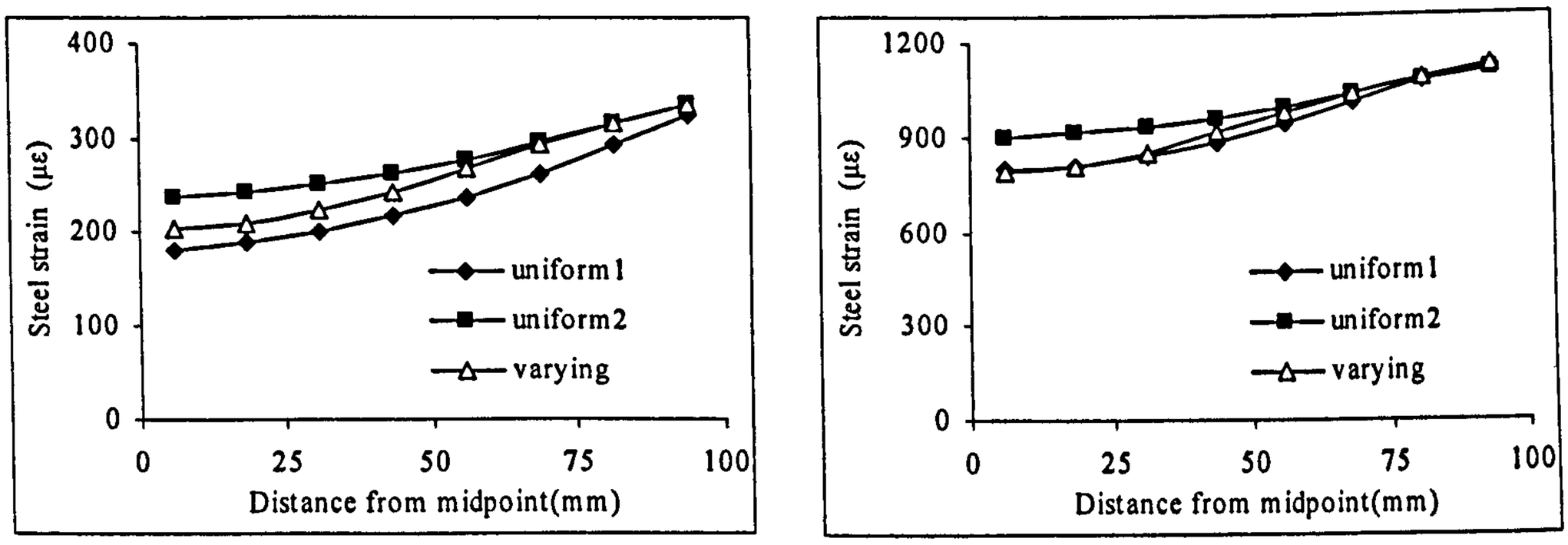

(a) P = 30 kN **(b) P = 98 kN**

Figure 6-31 Comparison of steel strain distribution along the length of steel bar

As for the bond stress distribution (see from Figure 6-32), at lower load stage, the bond stresses in two models with uniform bond-slip responses increase almost linearly with the distance from midpoint while the nonlinear behaviour was found for the model with various responses. However, the serious nonlinear plots are found for all the models at higher load stage.

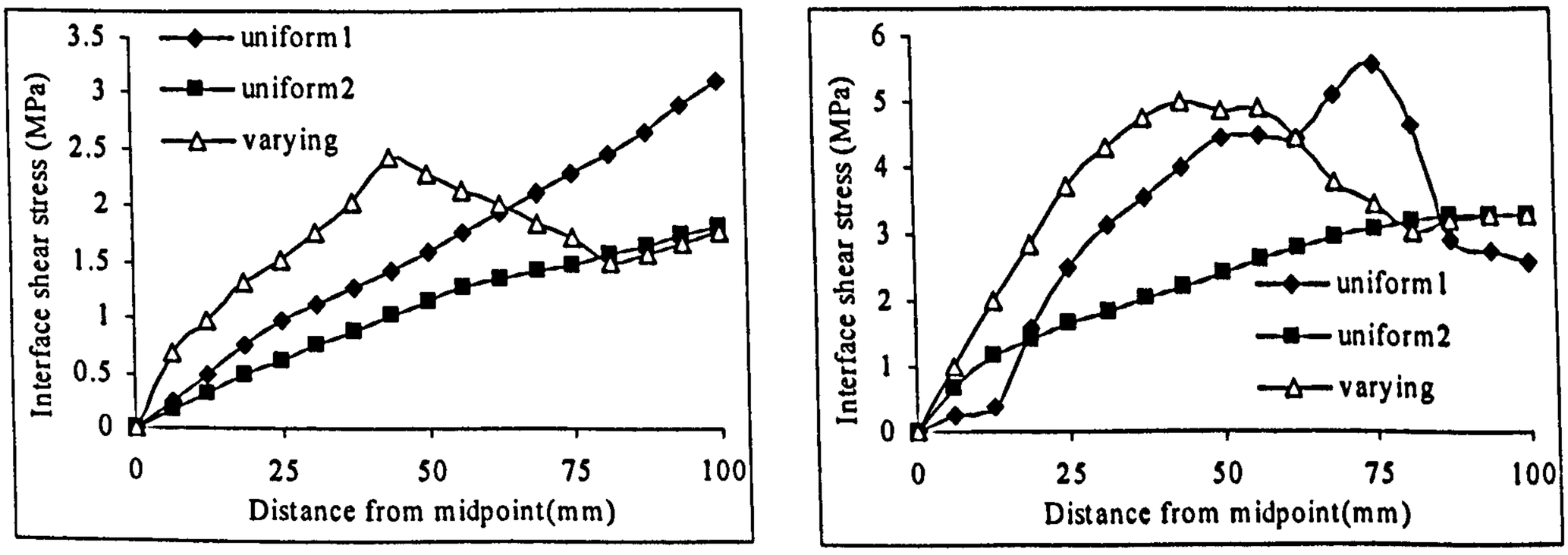

(a) P = 30 kN **(b) P = 98 kN**

Figure 6-32 Comparison of bond stress distribution along the length of steel bar

For the steel bar slip, larger slips were found for the model with smaller bond-slip gradient (Figure 6-33). Again, the model with various bond-slip responses show slips between the other two models.

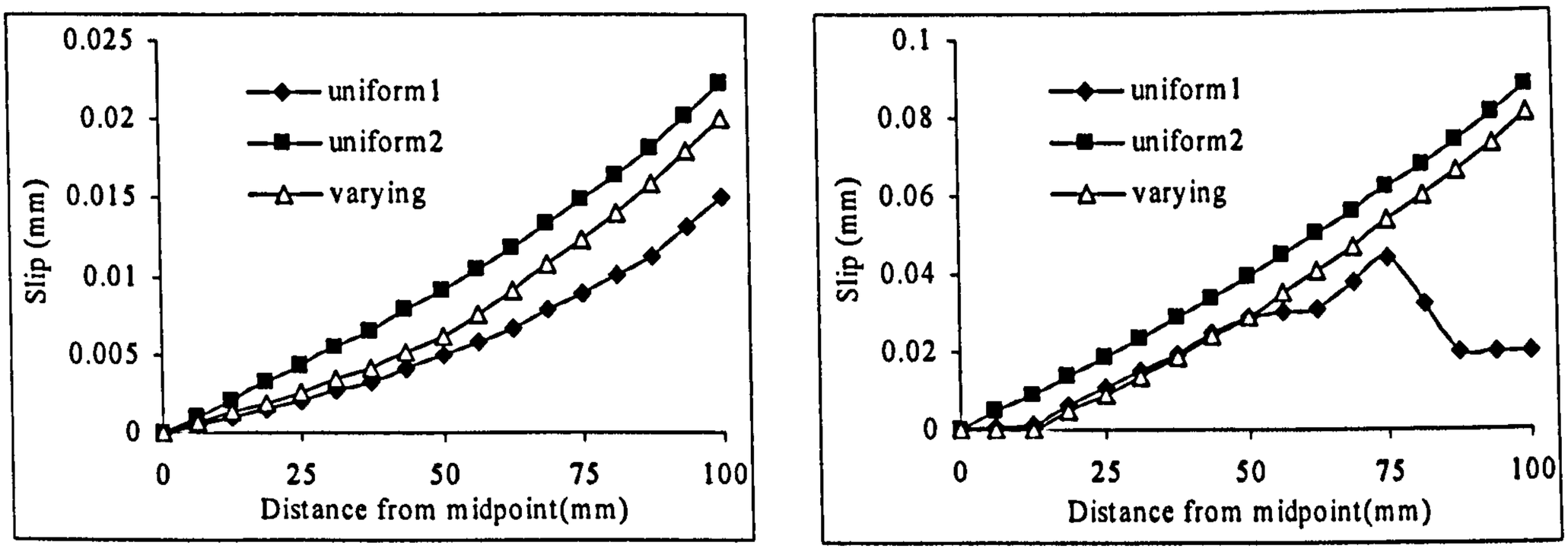

(a) P = 30 kN **(b) P = 98 kN**

Figure 6-33 Comparison of steel bar slip distribution along the length of steel bar

The application of the 3D interface element Q24IF on modelling the bond-slip relationship between steel bar and concrete was identified as a useful starting point for modelling the bond-slip relationship between FRP bar and adhesive layer in NSM FRP strengthened structure. However, according to the verification results, the input of bond-slip relationship into the FE analyses did not generate very satisfying comparisons with experimental data. Therefore, further effort should be made in this area. An extension study could be done on combining both interface element to model bond-slip action and multi-layer brick element to model through thickness stress variation across the adhesive layer.

6.5 Conclusion

In this chapter, FE analyses of three specific hybrid structural forms with internal connections and their responses to applied loads have been presented.

The first analysis is based on a RC beam discussed in the verification study of Chapter 3. The dimensions and material properties of the cracked beams are the same as the original beam, except that either vertical (flexural) cracks near the midspan or an inclined (shear) crack near the support were modelled into the concrete beam. The adhesive layer was modelled as 16 layers of plane stress elements through thickness to achieve more detailed results. The distribution of adhesive stress along the beam length either in the layer near the concrete (AC interface) or near the plate (PA interface) have been presented. In particular, the stress distributions near the cracks were emphasized and interpreted.

The second analysis focused on a composite bridge structure, being composed of a GFRP deck and concrete beam connected to each other by an adhesive layer. 2D modelling was employed and both four-noded plane stress element Q8MEM and three-noded plane stress element T6MEM were used to model the bridge deck. To investigate the effect of initial cracks on the behaviour of this composite bridge specimen, a vertical flexural crack was modelled in the concrete beam underneath the loading pad. Then, the distributions of adhesive stresses, cover concrete stresses and reinforcing steel bar axial strains along the specimen length were presented and interpreted.

The last analysis is of a 3D model of a double pullout specimen with a transverse anchor bar in the centre. The shear stress-slip relation between anchoring steel bar and surrounding concrete was modelled by using an 8-noded 3D interface element Q24IF rather than assuming rigid bond between them. Good agreement was found with test data from the literature.

From the results of the above FE analyses, the following points have emerged:

- The presence of initial cracks in the concrete beam can cause stress concentrations in the vicinal area. Up to 0.5 N/mm^2 increment of stresses is found for the cracked RC beam and up to 4 N/mm^2 is found for the composite bridge deck due to the stress concentration near cracks. It should be noted that such concentration of bond stresses at cracks is pronounced. If loads increase, especially if steel yields, then bond stresses will rise even further.
- The plane stress element Q8MEM in 2D modelling of the adhesive layer can help achieve more precise results at certain critical positions, such as the ends of the adhesive layer or near concrete beam cracks, which are the zones of connection stress concentration. For the cracked RC beam models, the cracks clearly introduce local and significant bond stress concentrations at the AC interface. These concentrations do not feed through to the PA interface.
- 3D interface element Q24IF was identified as an important element in modelling the bond-slip relationship between steel bar and concrete. Its potential could be extended to model the bond-slip relationship between FRP bar and adhesive layer in NSM FRP strengthened structure. More studies could be done on combining both interface element to model bond-slip action and multi-layer brick element to model through thickness stress variation across the adhesive layer.

Chapter 7

Conclusions

This chapter summarises the issues addressed throughout this thesis and outlines the main findings of the work. Finally, suggestions are made for extension of this work.

7.1 Summary

There is currently a significant requirement for enhancement of existing reinforced concrete (RC) structures. Due largely to the economic advantages of enhancing the existing structures rather than rebuilding them, a number of structural strengthening methods have been developed. This thesis is concerned with two of these strengthening methods, namely the near surface mounted (NSM) technique and the external bonded reinforcing (EBR) technique. In particular, this thesis focuses on both the experimental and FE analysis of stress transfer between the concrete and the strengthening materials and the corresponding brittle separation failure modes.

A survey of the literature identified that there was considerable scope for further research in relation to the following:

- Much of the work has been done for FRP plates bonded to concrete, while the stress transfer along the bonding line of concrete members with NSM FRP bars remains less investigated;
- Finding a suitable element to model the epoxy adhesive layer between concrete and FRP bars to simulate the through-thickness stress variation across the connection;
- Gaining a detailed understanding of the mechanics of brittle separation failure modes both at the mid-span and ends of the beam;
- Imperfections can arise in the adhesive connection layer and concrete members for a variety of reasons. Therefore, the effects of initial cracks on the behaviour of these structures need to be investigated carefully.

In order to investigate these issues, four CFRP NSM RC specimens were fabricated and tested to failure at the Bristol University structures laboratory. The specimens consist of one middle block and two side blocks under pure tensile load to obtain the local bond stress distribution instead of the whole length of beam. Such design enables the research to focus on the mechanical characteristics of a FRP NSM enhanced beam at the mid-span region near flexural cracks on the middle block and at the end region on the side blocks respectively. In addition, FE analyses were used to verify the experimental results and to investigate the influence of material property parameters on the mechanisms of structural behaviour. More FE analyses were done to predict the performance of other structures too.

The main conclusions drawn from these experimental and theoretical studies are presented in the next section.

7.2 Conclusions

From the results of the work presented in this thesis, the following points should be highlighted:

- Good predictions of the stress transfer behaviour between steel/FRP and concrete in the composite structures were provided by the advanced FEA package DIANA. Strains of FRP plates and steel bars, bond stress slip and slip distributions are reliably determined.
- In 2D FE modelling, it appears that the quadrilateral plane stress element shows better performance in modelling the adhesive layer rather than the line interface element. By using a few layers of plane stress elements across the thickness of the adhesive, the effects of adhesive through-thickness stress variation can be clearly demonstrated, especially at certain critical positions, such as the ends of adhesive layer or the bond near concrete beam cracks, which are the zones of connection stress concentration. The interface element is more suitable for modelling the surface between two materials rather than one certain material such as adhesive, while the surface preferably has no thickness or has much smaller thickness than the surrounding materials.
- In the 3D model, the brick elements are employed to model the adhesive layer, as well as concrete block and FRP bars. Reasonable agreements were found between FEA results and test data so that this modelling technique could be further used in other analyses.
- Although these results from FE analyses are presented for elastic response, the ideas also apply probably in magnified form after any material nonlinearity (e.g. steel yield or concrete in high compression) occurs.

- Two brittle separation modes were observed on the four RC blocks strengthened by NSM CFRP rods. The brittle separation took place either in the concrete layer horizontally due to cracks propagating along the side blocks or at the adhesive-rod interface. Consistent to the failure modes, the cracks typically occurred either through a 30mm thick concrete layer adjacent to the reinforcing steel rod or on the bond line between the adhesive and CFRP rods. Fewer cracks were observed in the specimens with shorter middle block before failure, indicating that they are more brittle than those with longer middle block so that they fail under the smaller loads without showing too much ductility.
- When the length of the middle block increased from 100mm to 300mm, the ultimate loads of the specimens with longer middle block are 24.5% to 31.7% higher than those with shorter middle block. The ultimate failure loads were not influenced by the amount of strengthening CFRP. With the same length of middle block, the ultimate load increased by a meagre 9% in spite of doubling the strengthening CFRP rod on both sides.
- Beam theory was used to investigate the mechanism of horizontal cracks on the middle block and the calculated results are consistent with experimental observation. The calculated maximum normal stress for the specimens with shorter middle block went up with the increasing of the load and reached as high as up to 10.25 N/mm^2 at the load P = 278 kN, which are higher than the tensile strength of the concrete and caused the horizontal crack at the middle block. However, throughout the loading period, the normal stress of the specimens with longer middle block stayed up to 1.12 N/mm^2, which is much lower than the tensile strength of the concrete. Therefore, no horizontal crack was observed in the test.
- 3D FE modelling was performed for the specimens from the lab test and good agreements were found between the FEA results and the average experimental data,

including the strains of the reinforcing steel bars and CFRP rods, the shear stresses of adhesive, as well as the load-displacement curve for the four specimens.

- Parametric FE analyses were done to investigate the influence of material property variations on the structural responses of the strengthened RC blocks to the load. Generally, higher stiffness and ultimate load were found in the models with higher concrete strength or higher FRP Young's modulus, especially at the post-cracking stage and before steel yielding. Inside the concrete block, both the steel and FRP strains decrease with the increment of the concrete strength because concrete with higher tensile strength can carry a larger share of the tensile load so that reinforcing bars could take smaller loads. Despite the ten-fold difference of FRP Young's modulus between the two models, the FRP strain remains similar inside the concrete block. However, the strain in the weaker model increased suddenly up to 1000 με outside of the concrete block due to the loss of concrete constraint. The influences of adhesive material properties variations on adhesive shear stress distributions increased with the load and higher shear stress values are found in the models with higher adhesive Young's modulus, tensile strength, and ratio of ultimate strain to crack strain.
- The presence of initial cracks in the concrete beam can cause stress concentrations in the vicinal area. Up to 0.5 N/mm^2 increment of stresses is found for the cracked RC beam and up to 4 N/mm^2 is found for the composite bridge deck due to the stress concentration near cracks. It should be noted that such concentration of bond stresses at cracks is pronounced. If loads increase, especially if steel yields, then bond stresses will rise even further.
- A composite bridge structure, composing a GFRP deck and concrete beam connected to each other by an adhesive layer, was analysed and good agreements were found between the FEA results and test data. Further investigation of the effect of initial

cracks on the behaviour of this composite bridge specimen found obvious stress concentration near the crack area for the stress distribution of cover concretes.

- The FEA program's capabilities are also extended to deal with the bond-slip behaviour of surface between steel reinforcement and concrete in 3D FE modelling. The steel-concrete connection is modelled by the 8-noded surface interface element with multi-linear bond slip material property input based on experimental data. The FEA results agree in certain degree with the measured or calculated experimental data but further investigation is still required.

7.3 Future work

The following ideas may form the basis of extension of this research :

- High shear bond stresses were found in the lab test, which may due to local bending of the rods caused by self-weights of middle beams. Such local bending effect could be mitigated or corrected by also attaching strain gauges to the opposite surfaces of the rod to the existing one, which could be done in the future study;
- More work has to be done on the bond-stress slip simulation to reliably predict the load carrying capacities and the corresponding deflections of FRP-reinforced RC members;
- More experimental tests should be taken to verify the influence of material properties variation on the failure behaviour of NSM strengthened concrete members as discussed by the FEA study in Chapter 5. Further, the performance of strengthened members under fatigue loading should be investigated and understood;
- FE analysis, incorporating interface elements with proper bond-slip behaviour not only between the plate and concrete, but also between the embedded steel and the concrete, should be done in the future. Use of fracture energy concepts to follow

incremental propagation of brittle separation should also be a key feature of such analysis;

- More investigation in the FE analyses, taking pre-stressing of strengthening rods and temperature effects into account, should be done. Proper elements as well as material properties should be chosen carefully.

BLANK IN ORIGINAL

References

[1] ACI 440. American Concrete Institute Technical Committee 440. Guided for the design and construction of concrete reinforced with FRP bars. 1R-03, 2003.

[2] Adams RD & Peppiatt NA. (1973). "Effect of Poisson's ratio strains in adherends on stresses of idealised lap joints", Journal of Strain Anal, 1973, v8, p135-139.

[3] Ahmed O & Van Gemert D. (1999). "Behaviour of RC beams strengthened in bending by CFRP laminates", *Proc. 8th International Conference on Structural Faults and Repair*, London, UK, 13th-15th, Jul 1999, p11.

[4] Alkhrdaji T, Nanni A, Chen G, Barker M. (1999). "Upgrading the transportation infrastructure: solid RC decks strengthened with FRP", Concrete International, *ACI*, October 1999, v21, n10, p37-41.

[5] Alampalli S, Connor JO, Yannotti, AP (2002). "Fiber reinforced polymer composites for the superstructure of a short-span rural bridge", *Compos. Struct.*, v58, n1, p21–27.

[6] Arduini M & Nanni A. (1997). "Parametric study of beams with externally bonded FRP reinforcement", *ACI Structural Journal*, v94, n5, 1997, p493-501.

[7] Asplund S. (1949). "Strengthening bridge slabs with grouted reinforcement", *Journal of American Concrete Institute*, 1949, v 20, n 6, p397-406.

[8] Bakht B, Al-Bazi G, Banthia N, Cheung M, Erki MA, Faoro M, Machida A, Mufti, AA, Neale, KW, Tadros G (2000). "Canadian bridge design code provisions for fiber-reinforced structures", *J. Compos. Constr.*, v4, n1, p3–15.

[9] Barnes RA & Mays GC. (2001). "The transfer of stress through a steel to concrete adhesive bond", *International Journal of Adhesion & Adhesives*, v21, 2001, p495-502.

[10] Barros J & Dias S. (2003). "Shear strengthening of reinforced concrete beams with laminate strips of CFRP", *Proceedings of the international conference CCC2003 composites in construction,* Cosenza, Italy, 2003, p289–294.

[11] Barros J & Fortes A.S. (2005). "Flexural strengthening of concrete beams with CFRP laminates bonded into slits", *Cement and Concrete Composites*, v27, n4, April 2005, p471-480.

[12] Bazant ZP (1983). "Crack band theory for fracture of concrete", *Materials and Structures*, RILEM, May-June, 1983, v16, n93, p155-177.

[13] Bizindavyi L & Neale KW (1999). "Transfer lengths and bond strengths for composites bonded to concrete", *Journal of Composites for Construction*, November 1999, p 153-160.

[14] Blaschko M & Zilch K (1999). "Rehabilitation of concrete structures with strips glued into slits", *Proceeding of 12th International Conference on Composite Materials*, Paris.

[15] Bonacci JF & Maalej M (2001). "Behavioral trends of RC beams strengthened with externally bonded FRP", *ASCE Journal of Composites for Construction*, v5, n2, 2001, p102-113.

[16] Brosens K & Van Gemert D (1997). "Anchoring stresses between concrete and carbon fibre reinforced laminates", *Proc. 3rd International Symposium on Non-Metallic (FRP) Reinforcement for Concrete Structures*, v1, 1997, p271-278.

[17] Brown RT & Zureick AH (2001). "Lightweight composite truss section decking", *Marine Structure*, v14, p115-132.

[18] Burgueno R, Karbhari VM, Frieder S, Kolozs RT (2001). "Experimental dynamic characterization of an FRP composite bridge superstructure assembly", *Compos. Struct.*, v54, n4, p427-444.

[19] Buyukozturk O & Hearing B (1998). "Failure behaviour of precracked concrete retrofitted with FRP", *ASCE Journal of Composites for construction*, v2, n 3, 1998, p 138-144.

[20] Buyukozturk O, Hearing B, Gunes O (1999). "FRP strengthening and repair : Where do we go from here", *Proc. 8th International Conference on Structural Faults and Repair*, London, UK, 13th-15th, Jul 1999, p12.

[21] Canning L, Hollaway LC, Thorne AM (1999). "Manufacture, testing and numerical analysis of an innovative polymer composite / concrete structure unit", *Proc. Instn Civ. Engrs Structus & Bldgs*, v134, 1999, p 231-241.

[22] Cassity P, Richards D, Gillespie J (2002). "Composite acting FRP deck and girder system", *Structural Engineering Institution*, v12, n2, p71-75.

[23] Chajes J, Finch WW, Januszka TF, Thomson TA (1996). "Bond and force transfer of composite material plates bonded to concrete", *ACI Structural Journal*, v93, n2, July 1996.

[24] Chen JF & Teng JG (2001). "Anchorage strength models for FRP and steel plates bonded to concrete", *Journal of Structural Engineering*, v 7, 2001, p 784-791.

[25] Choi MC, Gale L, Ibell TJ. (2001). "Anchorage zones for FRP-prestressed concrete structures", *Proc. 5th International Conference on Fibre-reinforced Plastics for Reinforced Concrete Structures*, Cambridge, UK, 16th-18th, Jul 2001, p 629-638.

[26] Cosenza E, Manfredi G, Realfonzo R (1997). "Behaviour and modelling of bond of FRP rebars to concrete", *ASCE Journal of Composites for Construction*, v1, n2, 1997, p40-51.

[27] Crocker H, Shehata E, Haldane-Wilsone R, Mufti A (2002). "Innovative fiber reinforced bridge deck modules", *Proceedings of 3rd International Conference on Composites in Infrastructure ICCI'02*, San Francisco, Paper 076 on CD-ROM.

[28] Crocombe AD (1995). "Modelling and predicting the effects of test speed on the strength of joints made with FM73 adhesive", *International Journal of Adhesion and Adhesives*, 1995, v 15 n 1, p 21-27.

[29] Cruz JS & Barros J (2004). "Bond between near-surface mounted carbon-fiber-reinforced polymer laminate strips and concrete", *Journal of Composites for Construction*, v 8, n 6, November/December, 2004, p 519-527.

[30] De Lorenzis L, Nanni A, La Tegola A (2000[3]). "Flexural and shear strengthening of reinforced concrete structures with near surface mounted FRP rods", *Proceedings ACMBS III*, Ottawa, Canada, 2000, p 521–8.

[31] De Lorenzis L & Nanni A (2001[1]). "Shear strengthening of RC beams with near surface mounted FRP rods", *ACI Structural* Journal, January-February 2001, v 98, n 1, p 60-68.

[32] De Lorenzis L & Nanni A (2001[2]) "Characterization of FRP rods as near-surface mounted reinforcement", *Journal of Composites for Construction*, v 5, n 2, May, 2001, p 114-121.

[33] De Lorenzis L, Rizzo A, La Tegola A (2002). "A modified pull-out test for bond of near-surface mounted FRP rods in concrete", *Composites Part B: Engineering*, v 33, n 8, December, 2002, p 589-603.

[34] De Lorenzis L & Teng JG (2007). "Near-surface mounted FRP reinforcement: An emerging technique for strengthening structures", *Composites Part B: Engineering*, v 38, n 2, March, 2007, p 119-143.

[35] Dussek IJ (1980). "Strengthening of bridge beams and similar structures by means of epoxy-resin bonded external reinforcement", *Transportation Research Record,* 1980, v 785, p 21-24.

[36] Dutta PK, Kwon SC, Lopez-Anido R (2003). "Fatigue performance evaluation of FRP composite bridge deck prototypes under high and low temperatures." *Proc., 82nd Annual Meeting, Transportation Research Board*, Washington, D.C.

[37] "Element Library", DIANA Finite Element Analysis User's Manual, Release 8.1, TNO Building and Construction Research.

[38] El-Hacha R & Rizkalla SH. (2004). "Near-surface-mounted fiber-reinforced polymer reinforcements for flexural strengthening of concrete structures", *ACI Structural Journal*, v 101, n 5, September/October, 2004, p 717-726.

[39] Fanning PJ & Kelly O (2001). "Ultimate response of RC beams strengthened with CFRP plates", *ASCE Journal of Composites for Constructions*, v 5, n 2, 2001, p 122-113.

[40] Ferreira AJ, Marques AT, De Sa, JC (2000). "Analysis of reinforced concrete with external composite strengthening", *Composites Part B: Engineering*, v31, n6-7, 2000, p 527-534.

[41] Garden HN (1997). "The strengthening of reinforced concrete members using externally bonded composite materials", PhD thesis, 1997, University of Surrey, p 556.

[42] Gentile C & Rizkalla S (1999). "Flexural strengthening of timber beams using FRP", *Technical Rep.*, ISIS Canada, University of Manitoba, Winnipeg, Manitoba, Canada.

[43] Grace NF, Soliman AK, Abdel-Sayed G, Saleh KR (1998). "Behaivour and ductility of simple and continuous FRP reinforced beams", *ASCE Journal of Composites for Construction*, v 2, n4, 1998, p 186-194.

[44] Grace NF, Sayed GA, Soliman AK, Saleh KR (1999). "Strengthening reinforced concrete beams using reinforced polymer (FRP) laminates", *ACI Structural Journal*, v 96, n5, 1999, p 865-874.

[45] Issam Harik P., Alagusundaramoorthy, Robin Siddiqui, Roberto Lopez-Anido, Steve Morton, Piyush Dutta, Bahram Shahrooz (1999). "Testing of concrete/FRP composite deck panels." *Proc., 5th Materials Engineering Congress on Materials and Construction*, L. C. Bank, ed., ASCE, Reston, Va., p351–358.

[46] Hassanen MA & Raoof M (2001). "Design against premature peeling failure of RC beams with externally bonded steel or FRP plates", *Magazine of Concrete Research*, v 53, n 4, 2001, p 251-262.

[47] Hassan T & Rizkalla S (2002). "Flexural strengthening of pre-stressed bridge slabs with FRP system", PCI Journal, v 47, p 76-93.

[48] Hassan T & Rizkalla S (2003). "Investigation of bond in concrete structures strengthened with near surface mounted carbon fiber reinforced polymer strips", *Jounral of Composites for Construction*, v 7, n 3, August 1, 2003, p 248-257.

[49] Hassan T & Rizkalla S (2004). "Bond mechanism of near-surface-mounted fiber-reinforced polymer bars for flexural strengthening of concrete structures", *ACI Structural Journal*, v 101, n 6, November/December, 2004, p 830-839.

[50] Hayes MD, Ohanehi D, Lesko JJ, Cousin TE, Witcher D (2000). "Performance of tube and plate fibreglass composite bridge deck", *Journal of Composite Construction*, v4, n2, p48-55.

[51] Hiroyuki Y & Wu Z (1997). "Analysis of debonding fracture properties of CFS strengthened member subjected to tension", *Proc. 3rd International Symposium on Non-Metallic (FRP) Reinforcement for Concrete Structures*, Japan Concrete Institute, Sapporo, v 1, 1997, p 287-294.

[52] Hogue T, Cornforth R, Nanni A (1999). "Myriad convention center floor system reinforcement", *Proceedings of the FRPRCS-4*, Dolan, Rizkalla, Nanni, Editors, ACI, Baltimore, MD, p 1145-1161.

[53] Jones R, Swamy RN, Charif A (1998). "Plate separation and anchorage of reinforced concrete beams strengthened with epoxy-bonded steel plates", *The Structural Engineering*, London, v 66, n5, p85-94.

[54] Kankam CK (1983). "Bond characteristics of reinforcing bars with reference to the deformations of concrete structures", PhD thesis, University of Leeds, England.

[55] Kankam CK (1997). "Relationship of bond stress, steel stress, and slip in reinforced concrete", *Journal of Structural Engineering*, v123, n1, January 1997, p 79-85.

[56] Keble J, Marshall G, Thoday N(2001). "Strengthening of M60 Barnes bridge, Manchester with carbon fibre composites", *Proc. 9th International conference on Structural Faults and Repair,* v 2, 4th-6th, Jul 2001, p15.

[57] Keller T (2001). "Recent all-composite and hybrid fiber-reinforced polymer bridges and buildings", Progress of Structural Engineering Material, v3, n2, p132-140.

[58] Keller T & Gurtler H (2003). "Composite action and adhesively bonded connection between FRP bridge decks and steel girders", *Journal of Composite and Construction.*

[59] Keller T, De Castro J, Schollmayer (2004). "Adhesively bonded and translucent glass fiber reinforced polymer sandwich girders", *Journal of Composite and Construction*, v8, n5, October 1, 2004, p461-470.

[60] Khalifa A, Gold WJ, Nanni A, Aziz A (1998). " Contribution of externally bonded FRP to shear capacity of RC flexural members", *ASCE Journal of Composites for Construction*, v 2, n 4, 1998, p 195-203.

[61] Khalifa A, Alkhrdaji T, Nanni A, Lansburg S (1999). "Anchorage of surface mounted FRP reinforcement", Concrete Institute: Design Construction, 1999, v 21, n 10, p 49-54.

[62] Kim D (2003). "Brittle separation failure of FRP-plated reinforced concrete beams", *PhD thesis, University of Bristol*, June 2003.

[63] Kishi N, Mikami H, Matsuoka K, Kurihashi Y (2001). "Failure behaviour of flexural strengthened RC beams with AFRP sheets", *Proc. 5th International Conference on Fibre-reinforced Plastics for Reinforced Concrete Structures*, Cambridge, UK, 16th-18th, Jul 2001, p 87-95.

[64] Kitane Y, Aref AJ, Lee GC (2004). "Static and fatigue testing of hybrid fiber-reinforced polymer-concrete bridge superstructure." *J. Compos. Constr.*, v8, n2, p182–190.

[65] Kumar P, Chandrashekhara K, Nannib A (2004). "Structural performance of a FRP bridge deck", *Construction and Building Materials*, v18, p35–47.

[66] Lees JM & Burgoyne CJ (1999). "Experimental study of the influence of bond on the flexural behaviour of concrete beams pre-tensioned with aramid fibre reinforced plastics", *ACI Structural Journal*, v96, n3, 1999, p 377-385.

[67] Li G, Lee SP, Thring RW (1999). "Nonlinear finite element analysis of stress and strain distributions across the adhesive thickness in composite single-lap joints", *Composite Structure*, v 46, 1999, p 395-403.

[68] Litton RW (1974). "A contribution to the analysis of concrte structures under cyclic loading", PhD thesis, University of California, Berkeley, 1974.

[69] Luke S, Knudsen E, Taljsten B (2002). "Advanced composite bridge decking system-project ASSET", *Structural Engineering International*, v12, n2, p76-79.

[70] Mahfuz H, Mian A, Vaidya U, Brown T, Jeelani S (1998). "Finite element study of the fibre-matrix interface behaviour of [0^o/90^o] laminated composites under tensile loading", *Journal of Materials Science*, n 33, 1998, p2965-2973.

[71] "Material Library", DIANA Finite Element Analysis User's Manual, Release 8.1, TNO Building and Construction Research.

[72] Meier U & Kaiser H (1991). "Strengthening of structures with CFRP laminates", *Proc. Specialty Conference on Advanced Composites Materials in Civil Engineering*, 31st Jan - 1st Feb 1991, p 224-232.

[73] Meier U (1992). "Carbon fibre-reinforced polymers: modern materials in bridge engineering", *Structural Engineering International*, v 1, 1992, p 7-12.

[74] Meier U, Deuring M, Meier H, Schwegler (1992). "Strengthening of structures with CFRP laminates: Research and applications in Switzerland", *Proc. 1st International Conference on Advanced Composite Materials in Bridges and Structures*, 1992, p 243-251.

[75] Meier U, Deuring M, Meier H, Schwegler (1993). "CFRP bonded sheets", *Proc. International Symposium on Fiber-Reinforced-Plastic Reinforcement for Concrete Structures*, Vancouver, ACI Special Publication n138, 28th-31st March, 1993, p 423-434.

[76] Meier U (1994). "Rehabilitation and retrofitting of existing structures through external bonding of thin carbon fibre sheets", *Bridge Assessment, Management and Design,* London, 1994, p 373-378.

[77] Meier U (2000). "Composite materials in bridge repair", *Applied Composite Materials*, 2000, p 75-93.

[78] Mindess S. & Young JF (1981). *Concrete,* Prentice-Hall, Inc., Englewood Cliffs, New Jersey, 1981.

[79] Mukhopadhyaya P, Swamy N, Lyndale C (1998). "Optimizing structural response of beam strengthened with GFRP plates", *ASCE Journal of Composites for Construction*, v 2, n 2, 1998, p 87-95.

[80] Nanni A, Alkhrdaji T, Barker M, Chen G, Mayo R, Yang X (1999). "Overview of Testing to Failure Program of a Highway Bridge Strengthened with FRP Composites", *Proceedings of the Fourth International Symposium on Non-Metallic (FRP) Reinforcement for Concrete Structures (FRPRCS-4), SP-188, C. W. Dolan, S. Rizkalla, and A. Nanni, eds., American Concrete Institute, Farmington Hills, Mich.*, p 69-75.

[81] Nanni A (2003). "North American design guidelines for concrete reinforcement and strengthening using FRP: Principles, applications and unresolved issues", *Construction and Building Materials*, v 17, n 6-7, September/October, 2003, p 439-446.

[82] Nanni A, Ludovico MD, Parretti R (2004). "Shear strengthening of a PC bridge girder with NSM CFRP rectangular bars", *Advances in Structural Engineering*, 1 August 2004, v 7, n 4, p 297-309.

[83] Neubauer U & Rostãsy FS (1997). "Design aspects of concrete structures strengthened with externally bonded CFRP-plates", *Concrete and Composites, Proc. 7th International Conference on Structural Faults and Repair*, v 2, 1997, p 109-118.

[84] Nguyen DM, Chan TK, Cheong HK (2001). "Brittle failure and bond development length of CFRP-concrete beams", *ASCE Journal of Composites for Construction*, v 5, n 1, 2001, p 12-17.

[85] Nordin H & Täljsten B (2006). "Concrete beams strengthened with prestressed Near Surface Mounted CFRP", *Journal of Composites for Construction*, ASCE, January/February 2006, p 60-68.

[86] Oehlers DJ & Moran JP (1990). "Premature failure of externally plated reinforced concrete beams", *Journal of Structural Engineering*, ASCE, v116, n4, p 978-995.

[87] Oehlers DJ (2001). "Development of design rules for retrofitting by adhesive bonding or bolting either FRP or steel plates to RC beams or slabs in bridge and buildings", *Composites Part A: Applied Science and Manufacturing*, Elsevier Science Ltd, n 32, p 1345-1355.

[88] Ozel A, Kadioglu F, Sen S, Sadeler R (2003). "Finite element analysis of adhesive joints in four-point bending load", *Journal of Adhesion*, v79, n7, 2003, p 683-697.

[89] ISSN: 0021-8464 CODEN: JADNAJ

[90] Publisher: Taylor and Francis Ltd

[91] Pandey PC, Shankaragouda H, Singh AK (1999). "Nonlinear analysis of adhesively bonded lap joints considering viscoplasticity in adhesives", *Computers and Structures*, 1999, p 387-413.

[92] Prota A, Nanni A, Manfredi G, Cosenza E. (2004). "Selective upgrade of underdesigned RC beam–column joints using CFRP", *ACI Structural Journal*, 2004, v101, n5, p 699–707.

[93] Quantrill RJ, Hollaway LC, Thorne AM (1996). "Experimental and Analytical Investigation of FRP Strengthened Beam Response: Part I", *Magazine of Concrete Research*, v48, n177, 1996, p 331-342.

[94] Quattlebaum JB, Harries KA, Petrou MF (2005). "Comparison of three flexural retrofit systems under monotonic and fatigue loads", *Journal of Bridge Engineering*, v10, n6, November/December, 2005, p 731-740.

[95] Rahimi H & Hutchinson A (2001). "Concrete beams strengthened with externally bonded FRP plates", *ASCE Journal of Composites for Construction*, v5, n1, 2001, p44-56.

[96] Roberts TM & Haji-Kazemi H (1989). "Theoretical study of the behaviour of reinforced concrete beams strengthened by externally bonded steel plates", *Proceedings of the Institution of Civil Engineers*, Thomas Telford, London, Part 2, v87, p 39-55.

[97] Ross CA, Jerome DM, Tedesco, JW, Hughes, ML (1999). "Strengthening of reinforced concrete beams with externally bonded composite laminates", *ACI Structural Journal*. v96, n2, p 212-220.

[98] Rostasy FS, Hankers C, Ranisch EH (1992). "Strengthening of RC and PC structures with bonded FRP plates", *Composite Materials in Bridges and Structures*, Sherbrooke, 1992, p253-263.

[99] Saafi M, Toutanji HA, Li Z (1999). "Behavior of concrete columns confined with fiber reinforced polymer tubes", *ACI Material Journal*, v96, v4, 1999, p 500-509.

[100] Salles NM, Melo GS, Nagato Y (2001). "T beams strengthened in shear with carbon sheet laminates (CFRP)", *Proc. 5th International Conference on Fibre-reinforced Plastics for Reinforced Concrete Structures*, Cambridge, UK, 16th-18th, Jul 2001, p239-248.

[101] Sato Y & Vecchio FJ (2003). "Tension stiffening and crack formation in Reinforced Concrete members with Fibre Reinforced Polymer sheets", *Journal of Structural Engineering ASCE*, June 2003, v129, n6, p717-724.

[102] Sebastian WM (1996). "The performance of a composite space truss bridge with glass reinforced plastic panels", PhD thesis, University of Cambridge, 1996, p258.

[103] Sebastian WM (2001). "Significance of midspan debonding failure in FRP-plated concrete beams." Journal of Structural Engineering, v7, 2001, p792-798.

[104] Sebastian WM, Geshidze, G, Zhang, C (2007). GFRP composite bridge deck experiments, University of Bristol.

[105] Shah SP, Swartz SE, Ouyang C (1995). *Fracture Mechanics of Concrete*, John Wiley & Sons, Inc., New York, New York, 1995.

[106] Sharif A, Al-Sulaimani GJ, Basunbul IA, Baluch MH, Chaleb BN (1994). "Strengthening of initially loaded reinforced concrete beams using FRP plates", *ACI Structural Journal*, v91, n2, 1994, p160-168.

[107] Shen HS, Teng JG, Yang J (2001). "Interfacial stresses in beams and slabs bonded with thin plate", *Journal of Engineering Mechanics, ASCE*, 2001, v127, p399-406.

[108] Spadea G, Bencardino F, Swamy RN (1998). "Structural behaviour of composite RC beams with externally bonded CFRP", *Jounral of Composite Construction*, August 1998, v2, n3, p132-137.

[109] Swamy RN, Jones R, Charif A (1986). "Shear adhesion properties of epoxy resin adhesives", *Proc. International Symposium Organised by RILEM Technical Committee 52*, Aix-en-Provence, 16th-19th, September 1986, p741-755.

[110] Swamy RN & Mukhopadhyaya P (1999). "Debonding of carbon-fibre-reinforced polymer plate from concrete beams", *Proc. Instn Civ. Engrs Structus & Bldgs*, v123, 1999, p301-317.

[111] Täljsten B (1994). "Plate bonding Strengthening of existing concrete structures with epoxy bonded plates of steel or fibre reinforced plastics", *PhD thesis, Luleä University of Technology*, Sweden, 1994, p189.

[112] Täljsten B (1997). "Defining anchor lengths of steel and CFRP plates bonded to concrete." *International Journal of Adhesion and Adhesives*, v17, n4, 1997, p319-327.

[113] Tann DB, Delpak R, Andereou E (2001). "Design aspects of shear strengthening of RC beams using externally bonded FRP sheets", *Proc. 9th International Conference on Structural Faults and Repair,* 4th-6th, July 2001, p13

[114] Teng JG, Zhang JW, Smith ST (2002). "Interfacial stresses in reinforced concrete beams bonded with a soffit plate: a finite element study." *Construction and Building Materials*, v16, p1-14.

[115] Teng JG, De Lorenzis L, Wang B, Li R, Wong TN, Lam L (2006). "Debonding failures of RC beams strengthened with near surface mounted CFRP strips", *Journal of Composites for Construction*, v10, n2, March/April, 2006, p92-105.

[116] The Concrete Society Technical Report No. 55 (TR55), "Design guidance for strengthening concrete structures using fibre composite materials", The Concrete Society, 2000, p71.

[117] Tommaso A, Neubauer U, Pantuso A, Rostasy S (2001). "behaviour of adhesively bonded concrete-CFRP joints at low and high temperatures", Mechanics of Composite Materials, July 2001, v37, n4, p327-338.

[118] Tumialan G, Tinazzi D, Myers J, Nanni A (1999). "Field evaluation of masonry walls strengthened with FRP composites at the Malcolm Bliss Hospital", Report CIES 99-8, University of Missouri-Rolla, Rolla, MO.

[119] Triantafillou TC (1998). "Shear strengthening of reinforced concrete beams using epoxy-bonded FRP composites", *ACI Structural Journal*, v95, n2, 1998, p107-115.

[120] Van Germert DA (1980). "Repairing of concrete structures by externally bonded steel plates", *International Journal of Adhesion*, v2, 1980, p67-72.

[121] Warren, GE (1998). "Waterfront Repair and Upgrade", *Advanced Technology Demonstration Site No. 2: Pier 12, NAVSTA San Diego, Site Specific Report SSR-2419-SHR, Naval Facilities Engineering Service Center, Port Hueneme, CA.*

[122] Warren GE (2000). "Waterfront repair and upgrade", *Advanced Technology Demonstration Site No. 3: NAVSTA Bravo 25, Pearl Harbour. Site Specific Report SSR-2567-SHR, NFESC, Port Hueneme, CA,* 2000.

[123] Yan X, Miller B, Nanni A, Bakis CE (1999). "Characterization of CFRP bars used as near-surface mounted reinforcement", *Proceedings of the Eighth International Structural Faults and Repair Conference, Edinburgh, Scotland: Engineering Technics Press*, 1999, p10.

[124] Youn SG & Chang SP (1998). "Behavior of composite bridge decks subjected to static and fatigue loading." *ACI Struct. J.*, v95, n3, p249–258.

[125] Yuan H, Wu Z, Yoshizawa H (2001). "Theoretical solutions on interfacial stress transfer of externally bonded steel/composite laminates", *Structural Engineering/Earthquake Engineering, Japan Society of Civil Engineers*, v18, n1, April, 2001, p27-39.

[126] Ziraba YN, Baluch MH, Sharif AM, Al-Sulaimani GJ, Azad AK, Basunbul IA (1995). "Modelling of damaged RC beams strengthened by fibre composite plates", *Engineering Computations (Swansea, Wales)*, v12, n7, 1995, p619-640.

Bibliography

[1] ACI 440. American Concrete Institute Technical Committee 440. Guided for the design and construction of concrete reinforced with FRP bars. 1R-03, 2003.

[2] Adhikary BB & Mutsuyoshi H. (2001). "Nonlinear fem model and design formula for externally bonded steel plates for shear enhancement of RC beams", Transactions of the Japan Concrete Institute, v23, 2001, p359-364.

[3] Bussler M & Ramesh A (1993). "Eight-node hexahedral element in FEA of part designs", Foundry Management & Technology, v 121 n 11, 1993, p 26-28.

[4] Carolin A, Nordin M, Taljsten B (2001). "Concrete beams strengthened with near surface mounted reinforcement of CFRP", Proceeding of International Conference on FRP Composites in Civil Engineering, Research Centre for Advanced Technology in Structural Engineering, Department of Civil and Structural Engineering, The Hong Kong Polytechnic University, Hong Kong, p1059-1066.

[5] Clarke J (2004). "Strengthening concrete bridges with fibre composites", Concrete (London), v 38, n 9, October, 2004, p 20-22.

[6] Darby A, Ibell T, Clarke J, Denton S, Farmer N, Luke S (2004). "Strengthening concrete structures using fibre composites", Proceedings of the Institute of Civil Engineers: Bridge Engineering, v 157, n 3, September, 2004, p 123-129.

[7] De Lorenzis L, Nanni A, La Tegola A (20001). "Bond of near surface mounted FRP rods in concrete masonry units", Proceeding of the Seventh Annual Internaltional Conference on Composites Engineering (ICCE/7), Denver, Colorado, July 2-8, 2000.

[8] De Lorenzis L, Nanni A, La Tegola, A (20002). "Strengthening of reinforced concrete structures with near surface mounted FRP rods" International Meeting on Composite Materials, PLAST 2000, Milan, Italy, May 9-11,2000.

[9] De Lorenzis L & Nanni A (2002). "Bond between near-surface mounted FRP rods and concrete in structural strengthening", ACI Structures Journal, v 99, n2, March-April 2002, p 123-133.

[10] De Lorenzis L, Galati D, La Tegola A (2004[1]). "Stiffness and ductility of fibre-reinforced polymer-strengthened reinforced concrete members", *Proceedings of the Institution of Civil Engineers: Structures and Buildings*, v 157, n 1, February, 2004, p 31-51.

[11] De Lorenzis L (2004[2]). "Anchorage length of near-surface mounted fiber-reinforced polymer rods for concrete strengthening - Analytical modelling", *ACI Structural Journal*, v 101, n 3, May/June, 2004, p 375-386.

[12] De Lorenzis L, Lundgren K, Rizzo A (2004[3]). "Anchorage Length of Near-Surface Mounted Fiber-Reinforced Polymer Bars for Concrete Strengthening - Experimental Investigation and Numerical Modeling", *ACI Structural Journal*, v 101, n 2, March/April, 2004, p 269-278.

[13] De Lorenzis L & La Tegola A (2005[1]). "Effect of the actual distribution of applied stresses on global buckling of isotropic and transversely isotropic thin-walled members: Theoretical analysis", *Composite Structures*, v 68, n 3, May, 2005, p 339-348.

[14] De Lorenzis L & La Tegola A (2005[2]). "Effect of the actual distribution of applied stresses on global buckling of isotropic and transversely isotropic thin-walled members: Numerical examples", *Composite Structures*, v 71, n 1, October, 2005, p 83-100.

[15] Emmons P, Thomas J, Sabnis GM (2001). "New strengthening technology developed—blue circle cement silo repair and upgrade", *Proceedings of the International Workshop on Structural Composites for Infrastructure Applications*, Cairo, Egypt, May 28-30, 2001, p 97-107.

[16] Foster DC, Richards D, Bogner BR (2000). "Design and installation of Fiber-Reinforced Polymer composite bridge", *ASCE Journal of Composites for Constructions*, v 4, n 1, 2000, p 33-37.

[17] Galati N, Tumialan G, Nanni A (2006). "Strengthening with FRP bars of URM walls subject to out-of-plane loads", *Construction and Building Materials*, v 20, n 1-2, February/March, 2006, 2nd International Conference, Advanced Polymers Composites for Structural Applications in Construction, p 101-110.

[127] Garden HN & Hollaway LC (1998). "An experimental study of the anchorage length of carbon fibre composite plates used to strengthen reinforce concrete beams", *Construction Building Materials*, Vol. 12, 1998, p 203-219.

[18] Garg A (1995). "2-D finite element analysis of engineering components", *Database Symposium, Computers in Engineering, ASME*, 1995, p 147-152.

[19] Gilstrap JM (1997). "Characterization of fibre reinforced polymer prestressting tendons", M.S. thesis, p 16-17.

[20] Hassan T (2002). "Flexural performance and bond characteristics of FRP strengthening techniques for concrete structures", PhD thesis, University of Manitoba, Winnipeg, Manitoba, Canada, p 304.

[21] Hordijk D (1991). "Local approach to fatigue of concrete", PhD thesis, Delft University of Technology.

[22] Ibell T (2005). "Recent research into the use of FRP to strengthen concrete structures", *Concrete (London)*, v 39, n 8, August, 2005, p 8-10.

[23] Keller T & Schollmayer M (2004). "Plate bending behavior of a pultruded GFRP bridge deck system", *Composite Structures*, v64, p 285-295.

[24] Kotsovos MD (1979). "A mathematical description of the deformation behaviour of concrete under complex loading", *Magazine of Concrete Research*, v 31, n 127, 1979, p 77-90.

[25] Li T, Galati N, Tumialan JG, Nanni A (2005). "Analysis of unreinforced masonry concrete walls strengthened with glass fiber-reinforced polymer bars", *ACI Structural Journal*, v 102, n 4, July/August, 2005, p 569-577.

[26] Liu YF & Kagawa Y (1996). "Analysis of debonding and frictional sliding in fibre-reinforced brittle matrix composites: basic problems", *Materials Science & Engineering A: Structural Materials: Properties, Microstructure and Processing*, v 212 n 1, p 75-86.

[27] Nanni A (2001). "Guides and specifications for the use of composites in concrete and masonry construction in North America", *Composites in Construction: A reality*, 2001, p 9-18.

[28] Parretti R (2004). "Strengthening of RC members using near-surface mounted FRP composites: Design overview", *Advances in Structural Engineering*, v 7, n 6, December, 2004, p 469-483.

[29] Prota A, Nanni A, Manfredi G, Cosenza E (2003). "Capacity assessment of RC subassemblages upgraded with CFRP", *Journal of Reinforced Plastics and Composites*, v 22, n 14, 2003, p 1287-1304.

[30] Raithby KD (1980). "External strengthening of concrete bridges with bonded steel plates", *Transport and Road Research Laboratory*, Supplementary Report 612, 1980.

[31] Rizkalla S & Hassan T (2001). "Various FRP strengthening techniques for retrofitting concrete structures", *CICE 2001 Conference Proceedings,* Hong Kong; December 2001.

[32] Smith ST & Teng JG (2002). "FRP-strengthened RC beams-I: Review of debonding strength models", Engineering Structures, 2002, v24, n4, p385-395.

[33] Täljsten B & Carolin A (2001). "Concrete beams strengthened with near surface mounted CFRP laminates." *Burgoyne C, editor. Proceedings of FRPRCS-5, Cambridge, UK*, 2001, p107–16.

[34] Turco V, Secondin S, Morbin A, Valluzzi MR, Modena C (2006). "Flexural and shear strengthening of un-reinforced masonry with FRP bars", *Composites Science and Technology*, v 66, n 2, February, 2006, Experimental Techniques and Design in Composite Materials, p289-296.

[35] Vaillancourt H, McCammond D, Pilliar RM (1996). "Validation of a nonlinear two-dimensional interface element for finite-element analysis." *Experimental Mechanics*, v36, n1, 1996, p19-54.

[36] Yang J, Teng JG, Chen JF (2004). " Interfacial stresses in soffit-plated reinforced concrete beams." *Proceedings of the Inst. Civil Engineers, Structures and Buildings*, v157, p77-89.